

---

# From the Sun to the Galactic Center: Dust, Stars and Black Hole(s)

Tobias Fritz

---



München 2013



---

# **From the Sun to the Galactic Center: Dust, Stars and Black Hole(s)**

**Tobias Fritz**

---

Dissertation  
an der Fakultät für Physik  
der Ludwig–Maximilians–Universität  
München

vorgelegt von  
Tobias Fritz  
aus Freiburg i. Br., Deutschland

München, den 21. May 2013

Erstgutachter: Prof. Dr. Reinhard Genzel  
Zweitgutachter: Prof. Dr. Ortwin Gerhard  
Tag der mündlichen Prüfung: 2. July 2013

# Contents

<b>Zusammenfassung</b>	<b>xv</b>
<b>Summary</b>	<b>xvii</b>
<b>1 The Galactic Center and its Galaxy</b>	<b>1</b>
1.1 Outer Components . . . . .	1
1.2 The Galactic Disk . . . . .	4
1.3 The Bulge . . . . .	6
1.4 The Central Molecular Zone . . . . .	10
1.5 The Nuclear Cluster . . . . .	15
1.6 The O-star Disks . . . . .	23
1.7 B-stars in the GC . . . . .	26
1.8 The Supermassive Black Hole Sgr A* . . . . .	29
1.9 Galaxy Overview and Transition . . . . .	33
<b>2 What is Limiting Near-infrared Astrometry in the Galactic Center?</b>	<b>37</b>
2.1 Introduction . . . . .	37
2.2 Statistical Uncertainty . . . . .	39
2.3 Astrometry in the GC . . . . .	41
2.4 Systematic Uncertainties . . . . .	43
2.4.1 Fast Atmospheric Limitations . . . . .	43
2.4.2 Slow Atmospheric Limitations . . . . .	47
2.4.3 Instrumental Limitations . . . . .	52
2.4.4 Analysis Limitations . . . . .	58
2.4.5 Astrophysical Limitations . . . . .	62
2.5 Summary & Conclusion . . . . .	65
<b>3 GC-IRS13E - A Puzzling Association of Three Early-type Stars</b>	<b>69</b>
3.1 Introduction . . . . .	69
3.2 Data Set . . . . .	71
3.2.1 NACO . . . . .	71
3.2.2 SINFONI . . . . .	72
3.3 Astrometry . . . . .	72

3.3.1	Image Processing . . . . .	72
3.3.2	Object Detection . . . . .	74
3.3.3	Proper Motions . . . . .	74
3.4	Characterization of the Objects . . . . .	76
3.4.1	Method . . . . .	77
3.4.2	Individual Objects . . . . .	77
3.5	Probability for an IMBH in IRS13E . . . . .	83
3.5.1	Stellar Surface Density in IRS13E . . . . .	85
3.5.2	The Structure of IRS13E . . . . .	85
3.5.3	The Overdensity of Young, Massive, Early-type Stars . . . . .	87
3.5.4	Cluster Mass from Velocity Dispersion . . . . .	91
3.5.5	Acceleration Limits Make an IMBH Less Likely . . . . .	92
3.5.6	Proper Motion of Sgr A* . . . . .	94
3.5.7	Total Probabilities . . . . .	95
3.6	Discussion . . . . .	96
3.6.1	Dynamics of the Young, Massive Stars . . . . .	96
3.6.2	X-ray and Radio Emission . . . . .	98
3.7	Conclusions and Summary . . . . .	100
3.8	Appendix . . . . .	101
3.8.1	Extracting the Spectral Energy Distributions . . . . .	101
3.8.2	Individual Objects in IRS13E . . . . .	102
3.8.3	Astrometric Data . . . . .	107
<b>4</b>	<b>Line Derived Infrared Extinction toward the Galactic Center</b>	<b>109</b>
4.1	Introduction . . . . .	109
4.2	Data Set . . . . .	112
4.2.1	Radio . . . . .	112
4.2.2	ISO . . . . .	114
4.2.3	SINFONI . . . . .	114
4.3	Construction of Line Maps and Flux Calibration . . . . .	117
4.3.1	Line Maps . . . . .	117
4.3.2	Flux Calibration . . . . .	117
4.4	Deriving Extinction from Hydrogen Lines . . . . .	118
4.4.1	Electron Temperature . . . . .	120
4.4.2	Extinction Calculation . . . . .	121
4.4.3	Extinction Derived . . . . .	126
4.5	Discussion . . . . .	127
4.5.1	Comparison with Literature for the GC . . . . .	127
4.5.2	A Photometric Distance to the GC . . . . .	129
4.5.3	Extinction toward Sgr A* . . . . .	130
4.5.4	Spatial Distribution of the Extinction . . . . .	131
4.5.5	The NIR Extinction . . . . .	132
4.5.6	The Optical Extinction . . . . .	134

4.5.7	The MIR Extinction . . . . .	136
4.5.8	Broadband Extinction Curve . . . . .	139
4.5.9	Dust Models . . . . .	139
4.6	Summary . . . . .	144
4.7	Appendix . . . . .	145
4.7.1	Correcting for the Flattening Bias . . . . .	145
4.7.2	Interpolating the Extinction Curve . . . . .	146
4.7.3	Effective Broadband Filter Extinctions . . . . .	147
4.7.4	Comparison with Other Methods for NIR Slope Determination . . . . .	149
<b>5</b>	<b>The Nuclear Cluster of the Milky Way I: Total Mass and Luminosity</b>	<b>155</b>
5.1	Introduction . . . . .	156
5.2	Data Set . . . . .	157
5.2.1	High Resolution Imaging . . . . .	157
5.2.2	Wield Field Imaging . . . . .	158
5.2.3	Spectroscopy . . . . .	158
5.3	Derivation of Velocities . . . . .	159
5.3.1	Proper Motions . . . . .	159
5.3.2	Radial Velocities . . . . .	161
5.3.3	Sample Cleaning . . . . .	164
5.4	Luminosity Properties of the Nuclear Cluster . . . . .	166
5.4.1	Literature about the Light Profile of the GC . . . . .	167
5.4.2	Deriving Density Profiles . . . . .	169
5.4.3	Spherical Fitting of the Stellar Density Profile . . . . .	172
5.4.4	Flattening of the Cluster . . . . .	175
5.4.5	Luminosity of the Nuclear Cluster . . . . .	177
5.5	Kinematic Analysis . . . . .	179
5.5.1	Binning . . . . .	179
5.5.2	Velocity Anisotropy . . . . .	181
5.5.3	Rotation . . . . .	181
5.5.4	Jeans Modeling . . . . .	188
5.5.5	Velocity Distribution and Fast Stars . . . . .	195
5.6	Discussion . . . . .	202
5.6.1	SMBH Mass Bias . . . . .	202
5.6.2	Comparison with the Literature . . . . .	205
5.6.3	Mass Cusp or Core? . . . . .	210
5.6.4	Cumulated Mass Profile . . . . .	211
5.6.5	Mass to Light Ratio . . . . .	213
5.6.6	The Nuclear Cluster of the Milky Way in Comparison . . . . .	216
5.7	Conclusions and Summary . . . . .	218
5.8	Appendix . . . . .	220
5.8.1	Derivation of Proper Motions . . . . .	220
5.8.2	Obtaining the Luminosity Properties . . . . .	228

5.8.3 Tabulated Values of Cumulative Mass Profiles . . . . .	234
<b>Conclusions and Outlook</b>	<b>235</b>
<b>Acknowledgements</b>	<b>267</b>

# List of Figures

1.1	The Milky Way at different wavelengths . . . . .	4
1.2	Color magnitude diagrams in the central 60'' . . . . .	7
1.3	Near-infrared spectra examples . . . . .	8
1.4	The nuclear disk in the far-infrared . . . . .	11
1.5	The nuclear disk at 4 $\mu\text{m}$ . . . . .	13
1.6	Inner six parsec in visible and near-infrared . . . . .	15
1.7	AO image of the central parsec . . . . .	18
1.8	Early- and late-type stars in the central parsec . . . . .	19
1.9	Radial distribution of different kinds of late-type stars . . . . .	22
1.10	Angular momenta of structure in the GC . . . . .	26
1.11	Components of the Galaxy . . . . .	35
2.1	Dependence of SNR on mask size and dependence of position error on SNR	40
2.2	Contributions of different noise kinds as function of magnitude . . . . .	42
2.3	Differential tilt jitter . . . . .	44
2.4	Empirical position errors as a function of stellar magnitude . . . . .	46
2.5	Astrometric shift for stars of different temperature . . . . .	49
2.6	Astrometric shift for stars suffering different strong extinction . . . . .	50
2.7	Astrometric shift for power law sources . . . . .	51
2.8	Astrometric position error as function of Strehl ratio . . . . .	53
2.9	Width of position rms of four pointings before and after correction . . . . .	54
2.10	Maps of estimated residual image distortions . . . . .	56
2.11	Position errors induced by the detector non-linearity . . . . .	57
2.12	Position errors due to halo noise . . . . .	61
2.13	Position errors due to confusion noise . . . . .	63
2.14	Summary of error sources as a function of stellar magnitude . . . . .	66
3.1	Deconvolved Ks-image of the GC . . . . .	73
3.2	Image of IRS13E . . . . .	75
3.3	Spectra of the WR-stars . . . . .	78
3.4	H+K-band spectrum of IRS13E3.0 . . . . .	80
3.5	SEDs of the example sources . . . . .	82
3.6	Surface densities of objects in IRS13E . . . . .	86

3.7	Velocities of the objects in IRS13E . . . . .	88
3.8	Probability for IRS13E as background fluctuation . . . . .	90
3.9	Expected accelerations assuming an IMBH . . . . .	93
3.10	Probabilities for different IMBH masses . . . . .	97
3.11	Pericenter distance of IRS13E . . . . .	99
3.12	Four deconvolved images from the SINFONI data . . . . .	103
3.13	SINFONI H+K-band spectrum of E6 . . . . .	107
3.14	Positions and linear motion fits for the objects in IRS13E . . . . .	108
4.1	Extinction toward Sgr A* from the literature . . . . .	111
4.2	Field of view for different measurements . . . . .	113
4.3	H II emission maps . . . . .	115
4.4	ISO-SWS spectrum of the GC . . . . .	116
4.5	Color image from J-band SINFONI data . . . . .	119
4.6	Extinction in the central $14'' \times 20''$ , binned in Brackett- $\gamma$ flux . . . . .	123
4.7	Extinction comparison with Schödel et al. (2010) . . . . .	124
4.8	Extinction toward the GC . . . . .	137
4.9	Comparison of our data with other data and dust models . . . . .	141
4.10	Measured and unextincted MIR continuum toward the GC . . . . .	147
4.11	Illustration of 'effective' wavelength choice consequences . . . . .	153
4.12	Comparison of different methods of NIR extinction slope determinations . . . . .	154
5.1	Distribution of stars with radial velocities and proper motions . . . . .	160
5.2	Mean radial velocities along the Galactic plane for our SINFONI sample . . . . .	163
5.3	Ks-surface brightness profile of the central Galaxy . . . . .	168
5.4	Extinction corrected radial distribution of stars and flux . . . . .	170
5.5	Stellar density in and orthogonal to the Galactic plane . . . . .	171
5.6	Nuker fits to the late-type stars surface density . . . . .	174
5.7	Space and projected density fits in comparison with the data . . . . .	176
5.8	Map and fit of the stellar density in the inner $r_{\text{box}} = 1000''$ . . . . .	178
5.9	Binning of the proper motion stars . . . . .	180
5.10	Binning of the inner radial velocity stars . . . . .	182
5.11	Binning of the outer radial velocity stars . . . . .	183
5.12	Average radial velocities in our bins . . . . .	184
5.13	Binned velocity dispersion used for Jeans modeling . . . . .	185
5.14	Radial and tangential dispersions as function of the radius . . . . .	186
5.15	Average radial velocities from our data and the literature . . . . .	187
5.16	Data and fits of the Jeans modeling . . . . .	193
5.17	Binwise median and maximum three-dimensional velocity . . . . .	196
5.18	Binwise maximum of the minimum binding mass . . . . .	198
5.19	Distance constraints from stars that are close to escaping . . . . .	199
5.20	Velocity histograms of our dynamics sample . . . . .	201
5.21	Fits of the dispersion in the inner $25''$ by Jeans models . . . . .	204

---

5.22	Our cumulative mass profile of the Galactic Center & literature . . . . .	207
5.23	Different cumulative mass profiles . . . . .	212
5.24	Dependence of the mass within $100''$ on the assumed IMF slope . . . . .	214
5.25	Comparison of M/L within $R < 100''$ with the literature . . . . .	215
5.26	Sizes and luminosities of nuclear clusters . . . . .	217
5.27	Residuals and dispersion in the extended field . . . . .	223
5.28	Position errors and dispersion in the large field . . . . .	225
5.29	Dependence of the dispersion on different parameters in the outer field . . . . .	228
5.30	Stellar surface density maps in the GC from VISTA data . . . . .	231
5.31	Stellar surface density maps in the GC from WFC3/IR data . . . . .	233



# List of Tables

3.1	Proper motions and acceleration limits of the objects in IRS13E . . . . .	76
3.2	Spectral properties of the objects in IRS13E . . . . .	84
4.1	Combinations of lines or continuum used for deriving extinctions . . . . .	122
4.2	Average hydrogen line extinction values toward the GC . . . . .	126
4.3	NIR infrared power law extinction fit parameters . . . . .	127
4.4	Error sources for the extinction . . . . .	129
4.5	NIR infrared extinction law from literature . . . . .	132
4.6	Relative broadband extinction values toward the GC . . . . .	140
4.7	Fit goodness of different dust models . . . . .	142
4.8	Interpolated infrared extinction curve . . . . .	148
4.9	Extinction of broadband filters for different Brackett- $\gamma$ extinctions . . . . .	150
5.1	Nuker fits of the surface density profile . . . . .	173
5.2	$\eta$ -model fits of the surface density profile . . . . .	175
5.3	Jeans model fits . . . . .	192
5.4	Fast stars . . . . .	201
5.5	Images used for the extended field . . . . .	221
5.6	Images used for the large and outer field . . . . .	221
5.7	Cumulative mass distribution . . . . .	234



# Zusammenfassung

Die Zentren von Galaxien sind die Zentren ihrer Gravitationspotentiale. Supermassereiche schwarze Löcher, Sternhaufen und Gas fallen besonders wahrscheinlich in die Zentren, da sie ihre Geschwindigkeit durch Energiegleichverteilung beziehungsweise Dissipation reduzieren können. Die in vielen Galaxienzentren beobachteten supermassereichen schwarzen Löcher und dichte zentrale Sternhaufen sind womöglich auf diese Weise dorthin gelangt. Zentrale Sternhaufen bildeten sich entweder durch Einfall von Gas oder Sternhaufen in die Zentren. Da die Milchstraße sowohl ein supermassereiches schwarzes Loch als auch einen zentralen Sternhaufen beinhaltet, können beide am besten im Zentrum der Milchstraße untersucht werden, weil dieses das nächstgelegene Galaxienzentrum ist.

In Kapitel 1 beschreibe ich die verschiedenen Komponenten der Milchstraße, insofern sie mit dem Milchstraßenzentrum in Verbindung stehen. Dann gebe ich einen Überblick der Eigenschaften des Milchstraßenzentrums, vor allem in Hinblick auf Sterneigenschaften und -verteilung. Danach berichte ich die Ergebnisse von vier verschiedenen Studien über das Milchstraßenzentrum.

In Kapitel 2 analysiere ich, wie genau Astrometrie im Milchstraßenzentrum sein kann. Dort ist es dank der hohen Sterndichte und der relativ kleinen Entfernung möglich die Bewegung von tausenden Sternen auf Bildern zu messen, die nur wenige Jahre nacheinander aufgenommen sind. Ich finde, dass es zwei hauptsächliche Einschränkungen für Astrometrie gibt: Im Falle heller Sterne limitiert die nicht perfekt korrigierbare optische Bildverzerrung die Genauigkeit. Für die Mehrheit der lichtschwachen Sterne reduzieren hingegen andere benachbarte Sterne die Genauigkeit. Die Positionsunsicherheit der lichtschwachen Sterne wird hauptsächlich durch die Seeinghalos von hellen Sternen verursacht. Ganz im Zentrum sind auch sehr lichtschwache, nicht auflösbare Sterne bedeutend für die Positionsunsicherheiten.

In Kapitel 3 beurteile ich die Belege für ein mittelschweres schwarzes Loch im kleinen potentiellen Sternhaufen IRS13E innerhalb des Milchstraßenzentrums. Mittelschwere schwarze Löcher, deren Existenz noch nicht belegt ist, liegen im Hinblick auf die Masse zwischen den zwei belegten Arten von schwarzen Löchern: den leichten stellaren und den supermassereichen in Galaxienzentren. Eine Möglichkeit für deren Entstehung sind Sternkollisionen in einem dichten jungen Sternhaufen. Solch ein Haufen könnte durch Energiegleichverteilung dann ins Milchstraßenzentrum sinken und würde dort wie IRS13E aus wenigen hellen Sternen bestehen. Erstens analysiere ich die spektrale Energieverteilung der Objekte in IRS13E. Die spektrale Energieverteilung der meisten Objekte kann durch

reine Staubemission erklärt werden. Damit sind die meisten Objekte in IRS13E reine Staubklumpen, und IRS13E besteht aus nur jungen drei Sternen. Das reduziert die Signifikanz des 'Haufens' IRS13E gegenüber dem Sternenhintergrund. Zweitens messe ich Beschleunigungslimits für diese drei Sterne. Das Fehlen von Beschleunigungen macht ein mittelschweres schwarzes Loch in IRS13E unwahrscheinlich. Da allerdings die drei Sterne eine sich gleich bewegende Sternenkonstellation bilden, die kaum durch Zufall entstehen kann, ist unklar, was IRS13E für ein Objekt ist.

In der dritten Studie (Kapitel 4) messe und analysiere ich die Extinktionskurve zum Milchstraßenzentrum. Die Extinktion ist ein Hindernis für Zentrumsbeobachtungen, da es nötig ist sie zu kennen, um die Leuchtkraft von Sternen dort zu bestimmen. Ich erhalte die Extinktionskurve, indem ich den Fluss des HII Gebiets im Zentrum in mehreren HII Linien im infraroten und im nicht extingierten Radiokontinuum messe. Ich vergleiche diese Flussverhältnisse mit den von der Rekombinationsphysik erwarteten Flussverhältnissen und erhalte die Extinktion für 22 verschiedene Linien zwischen 1 und 19  $\mu\text{m}$ . Für das K-Band leite ich  $A_{K_s} = 2.62 \pm 0.11$  her. Die Extinktionskurve folgt einem Potenzgesetz mit einem steilen Exponenten von  $-2.11 \pm 0.06$  für  $\lambda < 2.8 \mu\text{m}$ . Bei längeren Wellenlängen ist die Extinktion grauer, und es gibt Extinktionsbanden von verschiedenen Eisarten. Die Extinktionskurve bietet die Möglichkeit die Zusammensetzung des kosmischen Staubs zwischen der Sonne und dem Milchstraßenzentrum zu bestimmen. Die Extinktionskurve kann nicht durch nur zwei Staubkornarten, nämlich Kohlenstoff- und Silikatstaub, erklärt werden. Zusätzlich sind Kompositteilchen nötig, die verschiedene Eisarten enthalten.

Im letzten Teil dieser Doktorarbeit (Kapitel 5) wende ich mich den Eigenschaften der meisten Sterne im Zentrum zu. Dies sind die alten Sterne, die den zentralen Sternhaufen bilden. Ich erhalte die Massen- und Lichtverteilung dieser Sterne. Ich finde, dass die Abflachung der Sternverteilung außerhalb von  $70''$  zunimmt. Das deutet an, dass im Innern der beinahe kugelförmige Sternhaufen dominiert und weiter außen eine zentrale Scheibe das meiste Licht beiträgt. Ich zerlege das Licht in diese zwei Komponenten und erhalte für den zentralen Sternhaufen  $L_{K_s} = 2.7 \times 10^7 L_{\odot}$ . Ich ermittle Eigenbewegungen für mehr als 10000 Sterne und Radialgeschwindigkeiten für mehr als 2400 Sterne. Mit Jeansmodellierung kombiniere ich die Geschwindigkeiten und das radiale Dichteprofil und erhalte innerhalb von  $100''$  (4 pc) eine Masse von  $6.02 \times 10^6 M_{\odot}$  und eine totale Sternhaufenmasse von  $12.88 \times 10^6 M_{\odot}$ . Die Jeansmodellierung und verschiedene andere Belege deuten eher auf einen flachen Kern in der ausgedehnten Masse hin als auf eine Massenspitze dort. Das Licht der alten Sterne zeigt einen ähnlich flachen Kern. Das Masse-zu-Licht-Verhältnis der alten Sterne des zentralen Sternhaufens ist konsistent mit der üblichen Sternmassenfunktion in der Milchstraße. Das deutet darauf hin, dass sich die meisten Sterne im Zentrum in der üblichen Weise bildeten, im Unterschied zu den jungen Sternen im Milchstraßenzentrum.

# Summary

The centers of galaxies are their own ultimate gravitational sinks. Massive black holes and star clusters as well as gas are especially likely to fall into the centers of galaxies by dynamical friction or dissipation. Many galactic centers harbor supermassive black holes (SMBH) and dense nuclear (star) clusters which possibly arrived there by these processes. Nuclear clusters can be formed in situ from gas, or from smaller star clusters which fall to the center. Since the Milky Way harbors both an SMBH and a nuclear cluster, both can be studied best in the Galactic Center (GC), which is the closest galactic nucleus to us.

In Chapter 1, I introduce the different components of the Milky Way, and put these into the context of the GC. I then give an overview of relevant properties (e.g. star content and distribution) of the GC. Afterwards, I report the results of four different studies about the GC.

In Chapter 2, I analyze the limitations of astrometry, one of the most useful methods for the study of the GC. Thanks to the high density of stars and its relatively small distance from us it is possible to measure the motions of thousands of stars in the GC with images, separated by few years only. I find two main limitations to this method: (1) for bright stars the not perfectly correctable distortion of the camera limits the accuracy, and (2) for the majority of the fainter stars, the main limitation is crowding from the other stars in the GC. The position uncertainty of faint stars is mainly caused by the seeing halos of bright stars. In the very center faint unresolvable stars are also important for the position uncertainty.

In Chapter 3, I evaluate the evidence for an intermediate mass black hole in the small candidate cluster IRS13E within the GC. Intermediate mass black holes (IMBHs) have a mass between the two types of confirmed black hole: the stellar remnants and the supermassive black holes in the centers of galaxies. One possibility for their formation is the collision of stars in a dense young star cluster. Such a cluster could sink to the GC by dynamical friction. There it would consist of few bright stars like IRS13E. Firstly, I analyze the SEDs of the objects in IRS13E. The SEDs of most objects can be explained by pure dust emission. Thus, most objects in IRS13E are pure dust clumps and only three young stars. This reduces the significance of the 'cluster' IRS13E compared to the stellar background. Secondly, I obtain acceleration limits for these three stars. The non-detection of accelerations makes an IMBH an unlikely scenario in IRS13E. However, since its three stars form a comoving association, which is unlikely to form by chance, the nature of IRS13E is not yet settled.

In the third study (Chapter 4) I measure and analyze the extinction curve toward the GC. The extinction is a contaminant for GC observations and therefore it is necessary to know the extinction toward the GC to determine the luminosity properties of its stars. I obtain the extinction curve by measuring the flux of the HII region in the GC in several infrared HII lines and in the unextincted radio continuum. I compare these ratios with the ratios expected from recombination physics and obtain extinctions at 22 different lines between 1 and 19  $\mu\text{m}$ . For the K-band I derive  $A_{K_s} = 2.62 \pm 0.11$ . The extinction curve follows a power law with a steep slope of  $-2.11 \pm 0.06$  shortward of 2.8  $\mu\text{m}$ . At longer wavelengths the extinction is grayer and there are absorption features from ices. The extinction curve is a tool to constrain the properties of cosmic dust between the sun and the GC. The extinction curve cannot be explained by dust grains consisting of carbonaceous and silicate grains only. In addition composite particles, which also contain ices are necessary to fit the extinction curve.

In the final part of this thesis (Chapter 5) I look at the properties of most of the stars in the GC. These are the old stars that form the nuclear cluster of the Milky Way. I obtain the mass distribution and the light distribution of these stars. I find that the flattening of the stellar distribution increases outside 70". This indicates that inside a nearly spherical nuclear cluster dominates and that the surrounding light belongs mostly to the nuclear disk. I dissect the light in two components and obtain for the nuclear cluster  $L_{K_s} = 2.7 \times 10^7 L_{\odot}$ . I obtain proper motions for more than 10000 stars and radial velocities for more than 2400 stars. Using Jeans modeling I combine velocities and the radial profile to obtain within 100" (4 pc) a mass of  $6.02 \times 10^6 M_{\odot}$  and a total nuclear cluster mass of  $12.88 \times 10^6 M_{\odot}$ . The Jeans modeling and various other evidence weakly favor a core in the extended mass compared to a cusp. The old star light shows a similar core. The mass to light ratio of the old stars of the nuclear cluster is consistent with the usual initial mass function in the Galaxy. This suggests that most stars in GC formed in the usual way, in a mode different from the origin of the youngest stars there.

# Chapter 1

## The Galactic Center and its Galaxy

Here I introduce the components of the Galactic Center (GC) and also briefly the other components of its galaxy, the Milky Way. The size of the GC varies between different sources, see e.g. the reviews of the GC (Oort, 1977; Brown & Liszt, 1984; Genzel et al., 1994; Mezger et al., 1996; Morris & Serabyn, 1996; Genzel et al., 2010) and for example Nishiyama et al. (2006). Further, according to many theories the center and the outer parts of the Galaxy are related by physical interaction and migration. Last but not least when observing the GC, all components along the line of sight between Sun and the GC are unavoidably also observed. These components can influence observations of the GC by emission and absorption. Reviews such as Helmi (2008), Kormendy & Kennicutt (2004), Kalberla & Kerp (2009), Babusiaux (2012), Rix & Bovy (2013) and in case of the Galactic Center especially the newest, Genzel et al. (2010), are very helpful references for these different components. In my description I move from the outside to the center. I mention components with no connection to the GC only briefly. Finally, I summarize all components in one plot and introduce the themes of the four main chapters.

### 1.1 Outer Components

In this section I describe the components which are mostly at larger distance than the sun from the GC and/or are located outside the plane of the Milky Way.

From the outskirts, the first important component is probably dark matter as inferred from rotation curves in other spiral galaxies and other evidence (Babcock 1939; Kahn & Woltjer 1959; Roberts & Rots 1973; Ostriker & Peebles 1973; Einasto et al. 1974; Ostriker et al. 1974; Rubin et al. 1985; Carignan et al. 2006). These observations and many other observations can be explained with a universe dominated by a cosmological constant and cold dark matter ( $\Lambda$ CDM, see Efstathiou et al. (1990); Ostriker & Steinhardt (1995); Riess et al. (1998); Perlmutter et al. 1999). The cold dark matter is concentrated in extended halos around galaxies and galaxy clusters (White & Rees 1978; Navarro et al. 1997). From  $\Lambda$ CDM simulations (e.g. Springel et al. 2005) it follows that the dark halos are approximately spherical (with small triaxality) and that there are no sharp borders of

a galaxy. A kind of border is where the gravity of the most important neighbor is stronger than of the galaxy itself. In case of the Milky Way, the next important neighbor is Andromeda (M31). Both Galaxies are of similar mass (Reid et al. 2009), thus the border of the Milky Way is at about half the distance to M31 of 780 kpc (McConnachie et al. 2005). The existence of dark matter on the scale of galaxies is not proven, since the observations can also be explained by modifying (Milgrom 1983; Sanders & McGaugh 2002) general relativity (Einstein 1916) in a theory like TeVeS (Bekenstein 2004) and adding hot dark matter to the baryonic matter (Angus et al. 2007). The mass of the SMBHs in the center is probably not correlated with the total (dark) mass of its Galaxy, when correcting for bulge mass (Kormendy & Bender 2011).

Apart from the dark halo, there is also a spheroidal halo of stars (Eggen et al. 1962; Hesser 1992; Helmi 2008). These stars are partly field stars and partly reside in globular clusters. In the outskirts the density profile follows a power law ( $r^{-\alpha}$ ) with an index of  $n \approx 3.5$  (Harris 1976; Morrison 1993; Helmi 2008), steeper than the dark halo profile. Further inwards the radial profile of the stellar halo is less well known (Helmi 2008). Recently, Deason et al. (2011) found that the power law is broken at 27 kpc, with a flatter inner slope of  $\alpha \sim 2.3$  and a steeper outer slope of  $\alpha \sim 4.6$ . These stars are also known as population II stars, they have smaller metallicities (Baade 1944; Bond 1981; Christlieb et al. 2002; Caffau et al. 2011) than the disk stars in the Galaxy and are old. Field stars of the inner halo (close to the sun) are probably about 11 Gyrs old (Jofré & Weiss 2011; Kalirai 2012). The outer halo is possibly older but its precise age is not yet measurable for field stars.

Since the properties (e.g. ages) of globular clusters are easier to measure than the ages of halo field stars, they are often used as tracers for the halo. In the case of the Milky Way, the globular clusters are relatively old, 11 to 13 Gyrs (Rosenberg et al. 1999; Gratton et al. 2003; Pasquini et al. 2007; Dotter et al. 2011). There are, as in many galaxies, two populations of globular clusters (Zinn 1985; Minniti 1995; Brodie & Strader 2006), the inner one is more metal rich ( $[\text{Fe}/\text{H}] > -0.8$ ) and mostly younger than the outer one. The inner more metal rich globulars follow an oblate spatial distribution and belong probably not to the halo but to the bulge (Minniti 1995) or maybe instead to the thick disk (Zinn 1985). The most metal rich globular cluster is probably NGC 6528 (Harris 1996; Zoccali et al. 2004) with  $[\text{Fe}/\text{H}] = -0.1$  and  $[\alpha/\text{Fe}] \approx 0.05$ . With a distance of only 0.6 kpc to the GC it is one of the most central globular clusters of the Milky Way. But not all inner globular clusters are that metal rich, the median metallicity of the 17 globulars within  $R_0 < 1.5\text{kpc}$  is  $[\text{Fe}/\text{H}] = -0.7$  (using as in the following the database of Harris 1996). The subset of true inner bulge clusters, whose proximity to the GC is not just due to an eccentric orbit, has possibly a higher median metallicity. For example a median metallicity of  $[\text{Fe}/\text{H}] = -0.44$  is obtained from the  $R_0 < 1.5\text{ kpc}$  clusters (Harris 1996) when excluding all clusters with  $[\text{Fe}/\text{H}] < -0.8$  which are mostly associated with the halo (Zinn 1985). Probably all bulge globular clusters have slightly overabundant  $\alpha$  elements with  $[\alpha/\text{Fe}] \approx 0.2$  (Maraston et al. 2003; Zoccali et al. 2004).

There is some evidence (Burkert & Tremaine 2010; Harris & Harris 2011) that the number of globular clusters is correlated with SMBH mass for elliptical (maybe down to early-type spiral) galaxies. Taking together all globular clusters, the Milky Way has 8 times

more globular clusters than expected. This is not an observational bias, because globular clusters are not such difficult to detect around other galaxies (Harris & Harris 2011). It is disputed whether it is allowed to use only the metal rich globular clusters to say that the Milky Way has less than a factor two too many globular clusters (Burkert & Tremaine 2010; Harris & Harris 2011). In principle this  $N_{\text{globular}} - M_{\text{SMBH}}$  correlation could be a byproduct of other correlations, however the tightness of the correlation is striking according to Burkert & Tremaine (2010) and Harris & Harris (2011), but see also Rhode (2012). It seems unlikely that SMBHs and globular clusters have any direct influence on each others, more likely is an indirect connection for example if both have formed in the very early universe (Burkert & Tremaine 2010; Harris & Harris 2011). In this case many mergers could have enough time to tighten a weak correlation to a strong correlation due to the central limit theorem (Burkert & Tremaine 2010; Harris & Harris 2011). The inward migration of globular clusters due to dynamical friction is a proposed origin of nuclear clusters, see Section 1.5, Tremaine et al. (1975), Carollo (1999) and Antonini et al. (2012).

In addition to these old stars, there are also very few young stars in the halo. Many of these are B-dwarfs which move with more than the local escape velocity away from the Milky Way. These stars are called hypervelocity stars (HVS), see Brown et al. (2005). The HVSs have masses between  $2.5 M_{\odot}$  (spectral type A1) and  $9 M_{\odot}$  (spectral type B3, see Edelmann et al. 2005 and Brown et al. 2012). Due to this small mass interval and the small number of detected stars, the mass function is not constrained. The upper limit derived from the fact no F or G HVS are detected (Kollmeier et al. 2009) only excludes that the F/G to B-stars ratio of the HVS is bigger than this ratio for the whole Galaxy. The properties of the stars are best consistent with a Galactic Center origin (Brown et al. 2012). However, only for one star is the GC origin shown via the measured proper motion, the other stars lack proper motion measurements (Brown et al. 2010). Likely the HVSs are produced by binary disruption by the SMBH (alone or in a binary with an IMBH, see Yu & Tremaine 2003) in the GC (Hills 1988), see Section 1.7. The angular distribution of the HVSs is anisotropic at the  $3\text{-}\sigma$  level (Brown et al. 2009, 2012). This is difficult to explain since their traveling times from the GC differ by up to 160 Myrs. Most possible mechanism for anisotropy in the central parsec like a binary black hole in the GC (Yu & Tremaine 2003; Gualandris et al. 2005) or the clockwise disk of young stars (Lu et al. 2010) do not survive for 160 Myrs (Brown et al. 2012). It maybe that the anisotropy is a sign of a Galactic potential anisotropy in the central 10-100 pc (Brown et al. 2012).

The Fermi bubbles (Su et al. 2010), two large bubbles first detected around 5 GeV, which start close to the GC and extend about  $50^{\circ} \approx 10$  kpc below and above the Galactic plane, are probably related to the GC. Stellar activity, like Supernovae, (Su et al. 2010; Crocker et al. 2011) can probably not inject enough energy (Zubovas & Nayakshin 2012), but see Carretti et al. (2013). More likely activity of Sgr A\* 1 to 6 Myrs ago (Su et al. 2010; Guo & Mathews 2012; Zubovas & Nayakshin 2012) caused the bubbles.

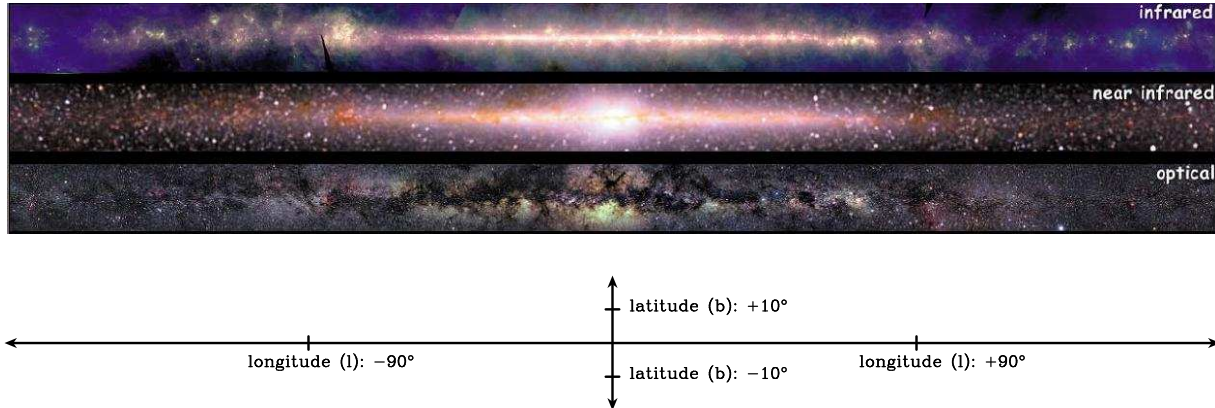


Figure 1.1 Top: The Milky way in the far-infrared (IRAS 12, 60 and 100  $\mu\text{m}$ ), near-infrared (COBE-DIRBE 1.25, 2.2 and 3.5  $\mu\text{m}$ ), and visible. Image credit <http://mwmw.gsfc.nasa.gov>; Bottom: Galactic coordinates, the center of these coordinates is, for historical reasons (Blaauw et al. 1960),  $-200''/-166''$  offset from Sgr A\*, which is very likely the center of the Galaxy.

## 1.2 The Galactic Disk

The nature of the Milky Way as a collection of very many faint stars became obvious with the first use of a telescope by Galilei (1610). Its structure as a flat disk was soon guessed. However, to uncover the position of the sun in it, three additional centuries were necessary. Herschel (1785) and others estimated that the sun is in the center in all three dimensions. Shapley (1918) measured by using standard candles in globular clusters, that the Sun is off center by about a third the radius of the Milky Way. The position of the sun close to the mid-plane of the Milky Way was confirmed later. The Sun is only 20 pc above the mid-plane, see e.g. Humphreys & Larsen (1995). Due to this structure with one preferred direction, the Galactic coordinate system is defined such that Galactic longitude (l) is measured in the Galactic plane and latitude (b) vertical to it, see Figure 1.1.

The main reason for the difficulty of determining the position of the Sun in the Milky Way is absorption of light by interstellar dust (Trumpler 1930). Since the dust is strongly concentrated in the Galactic Plane, even more so than the stars, and the Sun is close to the mid-plane, the result is a dark band in the middle of the wider stripe of stars of the Milky Way in visible light, see Figure 1.1. The dust dims the light of the stars so strongly, that Herschel (1785) could only observe stars up to a too small distance, for finding the edge of the Milky Way. In contrast, the globular clusters used by Shapley (1918) are only weakly concentrated toward the plane of Milky Way, and thus are mostly visible. However, they are slightly dimmed, resulting in an overestimated distance to the GC ( $R_0 \approx 15$  kpc) compared to today's  $R_0 \approx 8$  kpc (Reid 1993).

This dimming, the interstellar extinction, is wavelength dependent. At most wavelength the extinction decreases with increasing wavelength (Trumpler 1930; Whitford 1958; Seaton

1979; Cardelli et al. 1989; Nishiyama et al. 2008). Therefore the plane of the Milky Way is much clearer in the near-infrared, see Figure 1.1, and stars in the plane of the Milky Way, like the GC, are mostly observed in the near-infrared. However, at the distance of the Galactic Center even the near-infrared light is significantly dimmed by extinction. Thus e.g. when using standard candles in the GC for measuring its distance, it is necessary to know the absolute extinction toward the GC and its wavelength dependence. The extinction is mostly caused by small dust grains (Mathis et al. 1977; Draine 2003). The wavelength dependent extinction together with the wavelength dependent emission (the narrow emission stripe in the Galactic plane, see Figure 1.1) and the cosmic element abundances are the major constraints for the sizes and composition of cosmic dust grains (Draine 2003; Zubko et al. 2004). In Chapter 4 I measure the wavelength dependence toward the GC by means of hydrogen emission in the GC. I use this extinction curve to measure the distance of the GC using the standard candle of the red clump and to constrain the properties of the dust in the sight line toward the GC.

Apart from the dust, there is a much larger amount of gas (measured by mass), atomic and molecular (mostly traced by CO) hydrogen in the Galactic Disk. Since this gas rotates nearly circularly around the GC it is possible to derive kinematic distances (see e.g. Clemens 1985 and Kolpak et al. 2003) of most gas of the Milky Way from the velocities and positions on the sky of this gas. For this it is necessary to know the distance to the Galactic Center ( $R_0$ ) and the rotation velocity at the position of the sun ( $\Theta_0$ ). Both parameters are also essential for determining the mass of the Galaxy, see e.g. Reid et al. (2009). They can be derived for example from parallaxes and proper motions of sources in the GC (Reid & Brunthaler 2004; Reid et al. 2009), see also Section 1.8 and 1.9. Most of the atomic and molecular gas is in two to four spiral arms (Oort et al. 1958; Dame et al. 2001; Russeil 2003). Maser measurements over most of the Galaxy are soon expected to clarify the number of arms (Brunthaler et al. 2011). A big part of the molecular gas is at around 4 kpc distance from the GC, maybe in a molecular ring (Stecker et al. 1975; Cohen & Thaddeus 1977) but see also Dobbs & Burkert (2012). In these molecular clouds star formation occurs also today with a total star formation rate of about  $1 M_\odot/\text{yr}$  (Robitaille & Whitney 2010), derived using young stellar objects (YSO). Due to the ongoing star formation there are many young stars in the Galactic Disk (Rocha-Pinto et al. 2000).

The older stars in the Galactic Disk (the thick disk) have bigger random motion out of the Galactic plane than the younger stars (the thin disk). However, it is uncertain if the separability in thick and thin disks carries information about bimodal formation (Gilmore & Reid 1983) or is only a sign of radial mixing with time (Schönrich & Binney 2009). Recently, Bovy et al. (2012) claimed that the thick disk is not a distinct entity. Within the plane of the disk, the Milky Way star density follows the typical galactic disk profile, an exponential profile. Such a profile is also used as a defining property of disks and pseudobulges, see Section 1.3. The scale length is uncertain and depends partly on the data used: a scale length of about 3.5 kpc is derived from stars in the optical (Gilmore 1984; López-Corredoira et al. 2002; Larsen & Humphreys 2003), most infrared studies obtain values around 2.3 kpc (Porcel et al. 1998; Drimmel & Spergel 2001), while from HI gas one finds a scale length around 3.15 kpc (Kalberla & Kerp 2009). The stellar density of

the thin disk probably declines faster than the exponential profile outside of  $R \approx 14$  kpc (Robin et al. 1992; Sale et al. 2010; Minniti et al. 2011). As in many galaxies, the atomic hydrogen is more extended than the stars, see e.g. Kalberla & Kerp (2009).

In observations of the GC, foreground Galactic Disk stars make up only a small fraction of the total number of stars due to the very high stellar density in the GC. Outside of the central parsec, they can however contribute a significant part of the hot stars (stars which have Br  $\gamma$  lines) observed there, see Figure 1.2. This effect is caused by a higher fraction of hot young stars in the disk compared to the GC. Further, intrinsically fainter stars are can be detected in the closer and less extinguished Galactic Disk intrinsic fainter stars, but not in the GC. At intrinsic fainter magnitudes also stars of spectral type A and F can contribute to the hot stars, while in the GC only OB-stars are detectable. Since A/F-stars live much longer than OB-stars, they increase the number of detectable hot stars in the Galactic Disk compared to the GC. Because these Galactic Disk stars are less extinguished than GC stars, they can be separated from them by their color, see Figure 1.3.

### 1.3 The Bulge

The bulge is the central component of the Milky Way. It is thicker and brighter than the disk and it is visible at optical wavelengths as the brightest areas outside of the dust lanes, see Figure 1.1. It was probably suggested and discovered by Baade (1944, 1946) and first studied in windows with low extinction (Arp 1965; Oort 1977; Whitford 1978; Frogel 1988). However, the structure of the bulge is difficult to determine in the optical due to extinction in the Galactic Disk. The bulge of the Milky Way is primarily a bar. This was discovered by Blitz & Spergel (1991) and Dwek et al. (1995) by using full sky near-infrared images, and from Stanek et al. (1994) by using red clump distances. The bar is seen close to edge-on from the sun ( $\approx 20^\circ$  deviation, see Binney et al. (1991); Dwek et al. (1995); Binney et al. (1997); Launhardt et al. (2002)). The observed change of this angle close to  $l = |4|^\circ$  (Gonzalez et al. 2011) is probably an usual effect for a boxy bulge (Gerhard & Martinez-Valpuesta 2012). The axis ratios are about 1:0.33:0.23 (Dwek et al. 1995; Launhardt et al. 2002). The exact form and size of the bar is difficult to determine (Dwek et al. 1995), a pure exponential profile with a largest scale length of about 1 kpc fits the data (Dwek et al. 1995; Launhardt et al. 2002). New work indicates possibly a bigger bar, see the review of Babusiaux (2012).

There are two kinds of bulges, classical bulges and pseudobulges (the second are also called a boxy/peanut bulges), see Kormendy & Kennicutt (2004), which is also the primary reference for the following. Classical bulges form through violent mergers mostly in the first half of time since the big bang, while pseudobulges form more recently from disks through slow secular processes. It is not settled as to which kind the bulge of the Milky Way belongs. It depends mostly on which tracer is more reliable for dissecting the types, see Kormendy & Kennicutt (2004). The boxy structure of the bulge (Blitz & Spergel 1991; Dwek et al. 1995; Wyse et al. 1997) is a strong indication for secular evolution and thus for a more recent bulge formation. However, Kuijken & Rich (2002), Clarkson et al. (2008),

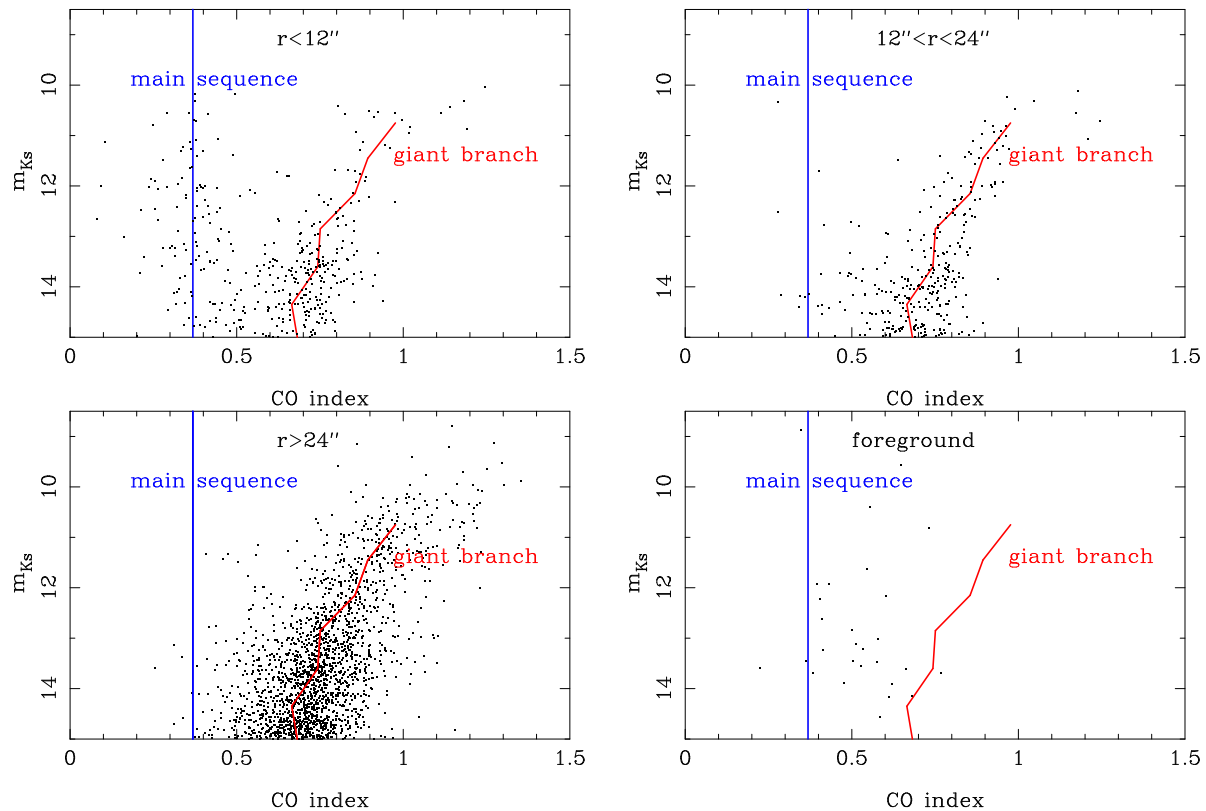


Figure 1.2 Color magnitude diagrams (CMDs) of stars toward the Galactic Center. I use as temperature proxy my photometrically (VLT program 087.B-0182) measured strength of the CO band-heads (the CO index), the strongest signature of late-type stars in the K-band, see Figure 1.3. Stars with lower temperature have a larger CO index. The fraction of stars on the main-sequence decrease in the GC from the inside out. In the foreground are again more stars on the main sequence and the intrinsic fainter giants are hotter than the intrinsic brighter GC giants at the same observed magnitudes.

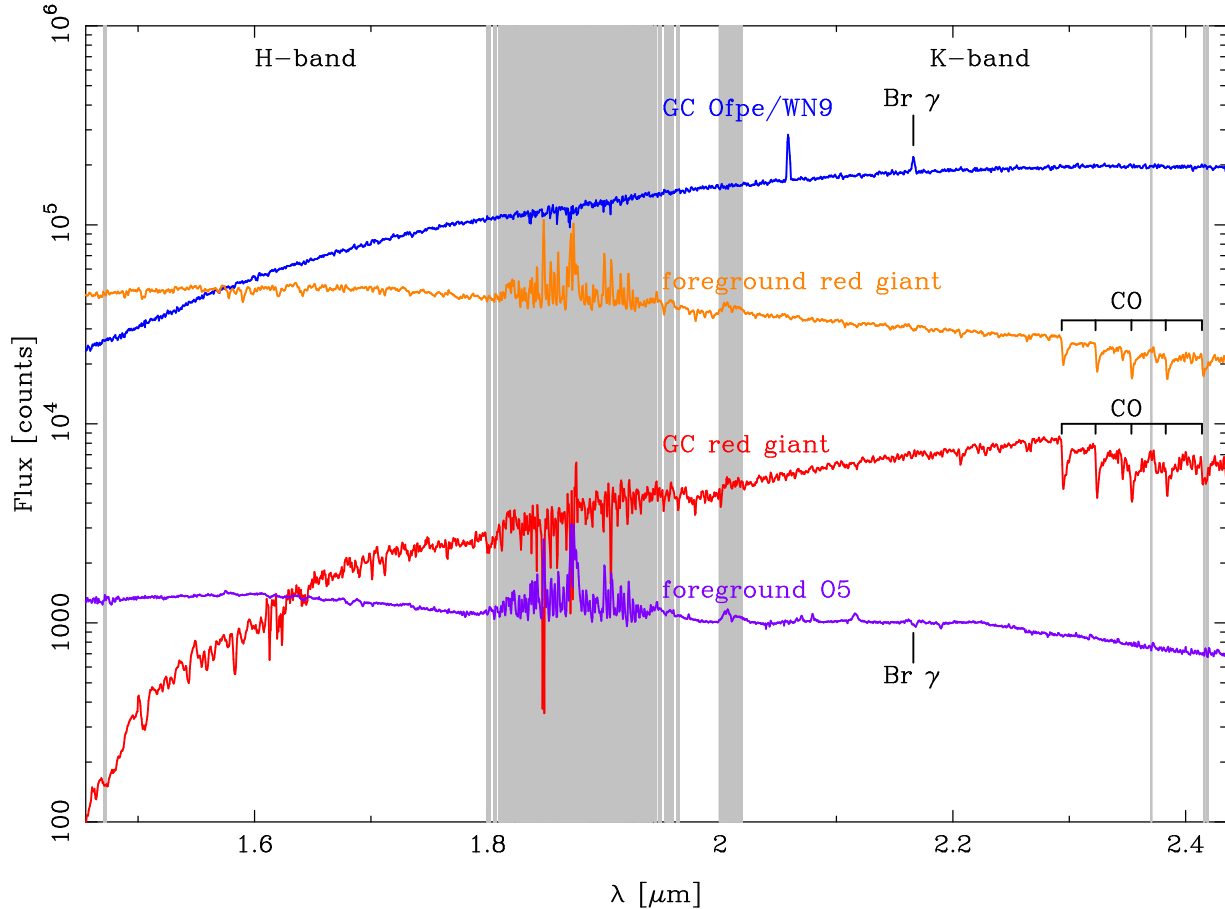


Figure 1.3 Near-infrared spectra: example spectra of old red giants and young O-stars in the Galactic Center and the foreground Galactic Disk in the near-infrared H-/K-bands. The gray bands mark wavelengths where the atmosphere is not transparent enough for high quality observations. Due to the high extinction the K-band is the best band for spectroscopy of GC sources. The overall slope of the spectra shows the importance of extinction toward the GC. The strong extinction has a much stronger influence than the star temperature on the H-K color. Extinction is also the reason that the foreground O5 is slightly redder than the foreground red giant. This O5 star ( $d \approx 4$  kpc) still has significant extinction, while the foreground late-type giant has only little extinction. The most prominent feature of the red (in the vast majority old) stars are the CO band-heads around  $2.3 \mu\text{m}$ . Intrinsically brighter red giants are mostly colder and have stronger CO band heads than fainter red giants. This is visible in the comparison of the intrinsically bright GC red giant and the fainter foreground red giant and in CMDs, see Figure 1.2. Hot stars have different lines, the most common lines are the hydrogen lines, of which Brackett  $\gamma$  is the line with the highest SNR for GC stars. Depending on the stellar type, these lines can appear in emission or in absorption.

and Zoccali et al. (2003) used photometric CMDs of bulge stars and obtain an age of 10 to 13 Gyrs for the majority of these stars. van Loon et al. (2003) and Bensby et al. (2011) find with mid-IR photometry and high-resolution spectroscopy respectively, that parts of the bulge are younger. Possibly the truth lies in between (Nataf & Gould 2012). In case of the lensed stars of Bensby et al. (2011) it is also possibly that these are not located in the bulge, but in the far side of the disk (Ness et al. 2013). All studies agree that the bulge is older than the thin disk. It is established that the  $\alpha$  to iron ratio of the metal poor bulge stars is super solar (Babusiaux 2012). Lecureur et al. (2007) find that the  $\alpha$  to iron ratio is slightly higher than in the thick disk, but most newer works point toward values as they are found for the thick disk, see Alves-Brito et al. (2010) and Bensby et al. (2011). It is disputed whether also the more metal rich stars are  $\alpha$  enhanced: Rich & Origlia (2005), Zoccali et al. (2006), Minniti & Zoccali (2008), and Rich et al. (2012) find an  $\alpha$  enhancement, in contrast to Hill et al. (2011). The majority of authors have measured a supersolar  $\alpha$  to iron ratio, indicative of rapid formation a long time. The mean metallicity increases toward the Galactic plane from  $-12^\circ$  to  $-4^\circ$  (Zoccali et al. 2008) but is constant further inwards (Rich et al. 2012). The iron abundance distribution at each position is broad with a long tail to low metallicities (Zoccali et al. 2008). That distribution is probably caused by a bimodal or multimodal intrinsic distribution and measurement errors (Babusiaux et al. 2010; Ness et al. 2013). This could be an indication for a classical bulge inside the bar (Babusiaux et al. 2010); however this classical bulge contains according to Ness et al. (2013), less than 1/3 of its stars. Radial velocities follow nearly pure cylindrical rotation and thus support the idea that the 'bulge' is mostly a bar (Howard et al. 2009; Ness et al. 2013). (A small classical bulge is difficult to exclude dynamically, see Saha et al. 2012.) The picture is further complicated by the discovery of two red clumps in most bulge lines-of-sight, which is likely caused by an X-shaped bulge (Nataf et al. 2010; Saito et al. 2011), which may be simply a general feature of bar (boxy/peanut) bulges (Fux 1999; Ness et al. 2013). Possibly the tension in age between the boxy bulge of the Milky Way and of most pseudobulges is only a reflection of a difference in the stellar ages in the inner disks of these galaxies. In this, case the Milky Way would have a pseudobulge which, because the inner disk of the Milky Way is older than in most galaxies, contains older stars than most pseudobulges. Then the bulge of the Milky Way formed rather recently out of old stars. A variant of this theory could be that the pseudobulge of the Milky Way formed earlier secularly. A possibility for secular formation is clump migration to the center, around a redshift of 2, as indicated by observations at this redshift (Genzel et al. 2008). Overall the bulge is complex and no consensus is reached about its origin, see e.g. Minniti & Zoccali (2008), Rich et al. (2012), Zoccali (2012), and Ness et al. (2013).

The dispersion in bulges and elliptical galaxies is related to their SMBH mass by the  $M$ - $\sigma$  relation (Ferrarese & Merritt 2000; Gebhardt et al. 2000). One current formulation of this relation is:

$$\log(M_{\text{BH}}/M_{\odot}) = (8.24 \pm 0.08) + (4.24 \pm 0.41) \times \log(\sigma/200\text{km/s})$$

(Gültekin et al. 2009). Since this correlation is probably the strongest correlation of SMBH mass with any galaxy parameter, it is probably the primary correlation, which needs phys-

ical explanation, and the other correlations could be byproducts of the  $M$ - $\sigma$  relation and other relations (Ferrarese & Merritt 2000; Gebhardt et al. 2000; Kormendy et al. 2011; Kormendy & Bender 2011). The origin of this relation is uncertain, the preferred option is quenching of bulge growth by output of the SMBH (Silk & Rees 1998). The discovery that quasars at high redshift are more massive than expected (Peng et al. 2006) could be evidence for the opposite scenario: SMBHs are starved earlier than bulges, see Peng et al. (2006), but see also Alexander et al. (2008) for the opposite observations in case of sub-mm galaxies. Further the central limit theorem, acting in many mergers, can produce tight correlations even when no relation was present at the beginning (Peng 2007; Jahnke & Macciò 2011). The dispersion of the bulge of the Milky Way is  $105 \pm 20$  km/s. It is more difficult to determine  $\sigma$  of the Milky Way than for other Galaxies because of the extinction toward it and its large solid angle on the sky (Ferrarese & Merritt 2000; Gebhardt et al. 2000; Tremaine et al. 2002; Freeman 2008; Gültekin et al. 2009; Howard et al. 2009). With the dispersion above the SMBH of the Milky Way is about a factor two too light compared to the  $M$ - $\sigma$  relation. However, the general scatter in the sample of Gültekin et al. (2009) is a factor three. Compared to the relation for ellipticals, in which no pollution by pseudobulges (Kormendy et al. 2011) occurs, Sgr A\* is a factor three too small. But also this deviation is not significant because the error caused by the bulge dispersion uncertainty is a factor two. Thus, although there seems to be no  $M$ - $\sigma$  relation in pseudobulges (Kormendy et al. 2011) the Milky Way alone is not a clear example for the breakdown of the relation in case of pseudobulges.

The bulge is essentially free of dust and gas, which is obvious above the Galactic plane see Figure 1.1. A negligible gas content can also be derived for the plane of the Milky Way between 1.5 and 3.5 kpc from gas observations, see e.g. Cox & Mezger (1989) and Mezger et al. (1996). This dust free zone in the plane is caused by the bar potential which makes corotating circular orbits unstable at these radii (Binney et al. 1991).

## 1.4 The Central Molecular Zone

Around the Galactic center the Galactic disk appears to be brighter and hotter in the far-infrared, see Figure 1.4. This dust is not only visible in emission, it also causes the extinction toward the GC to be higher than toward most other areas of the Galactic Disk, see Marshall et al. (2006). This high extinction makes the K-band the most efficient band for spectroscopy in the central molecular zone and further inward, see Figure 1.3. The additional extinction has the advantage that foreground bulge stars can mostly be disentangled from the nuclear disk by their smaller extinction.

This additional dust is close to the Galactic Center. Since it was first detected in emission with tracer molecules (mainly CO, e.g. Dame et al. 1987) it is called the central molecular zone (CMZ, Serabyn & Morris 1996). The same region also hosts a flattened concentration of stars (see Becklin & Neugebauer (1978), Catchpole et al. (1990), Mezger et al. (1996), Launhardt et al. (2002) and Figure 1.5). This has been interpreted as an extension of the nuclear cluster, see Serabyn & Morris (1996). Other authors like



Figure 1.4 The inner Galaxy (box of  $12.5^\circ^2$ ) in the (far-) infrared (25, 60, 100  $\mu\text{m}$ ). The image is in equatorial coordinates, thus the Galactic plane is diagonal on the image. The bright warm (yellow) nuclear disk (FIR size  $\approx 2^\circ$ ) is visible in the center of the (red) Galactic Disk. Image credit: IRAS at <http://irsa.ipac.caltech.edu/data/ISSA>

Lis & Carlstrom (1994) and Launhardt et al. (2002) call it the nuclear (stellar) disk, as also observed in the centers of other galaxies (Carollo et al. 1997; Kormendy & Kennicutt 2004). I use here the name nuclear disk if I mean its stars. However, it is easier seen in emission of dust, gas or molecules since the bulge is devoid of this emission. The CMZ has a diameter of about  $6^\circ$ , which corresponds to 420 pc (Mezger et al. 1996; Launhardt et al. 2002). Its size is somewhat wavelength dependent: it is smaller in the mid-infrared and at 3 cm, and bigger in the sub-mm, longer radio wavelengths and in CO (Launhardt et al. 2002). This implies that cold gas and dust is distributed over a larger area but is heated and ionized mainly in the center. Especially the cold gas is asymmetrically distributed. There is more gas, and it extends further, at positive Galactic longitudes than at negative Galactic longitudes, see e.g. Mezger et al. (1996). In total the CMZ contains about 5-10 % of the molecular gas mass of the Galaxy in a much smaller volume, implying higher densities (Morris & Serabyn 1996). This gas follows a peculiar velocity pattern rather than a pure circular rotation (Bania 1977; Bally et al. 1988). This pattern is probably explained by the potential of the bar (Binney et al. 1991): orbits are only stable in the orbit families  $x_1$  and  $x_2$  (Contopoulos & Mertzaniides 1977; Contopoulos & Papayannopoulos 1980). Apart from a circular component close to the center, the gas is mainly at the intersection of the two orbit families and on the  $x_2$  orbits further inside (Blitz & Spergel 1991; Mezger et al. 1996).

The majority of the mass is in stars, but it is more difficult to measure due to the extinction. In some parts the extinction is so high that, even in the Ks-band, it blocks practically all emission from behind (Becklin & Neugebauer 1978; Vollmer et al. 2003). This extinction is caused by giant molecular clouds (GMC) in the CMZ. These clouds are also visible in dust and molecule emission (Lis & Carlstrom 1994). Since only in parts of the nuclear disk are big GMCs visible (Lis & Carlstrom 1994), the Ks-band can still be used to derive the global properties of the nuclear disk. The observed size of about 200 pc radius (Launhardt et al. 2002), slightly smaller than the cold gas extension, is considered reliable. The nuclear disk is flattened, but the precise parameters are uncertain mainly due to resolution limitations in Launhardt et al. (2002). In Chapter 5 we obtain higher resolution data of the inner nuclear disk. It is unclear whether the nuclear disk is asymmetric (Alard 2001). Since the nuclear disk covers only a small angular size a symmetric bar cannot explain this asymmetry, since this would require an unrealistically long bar seen nearly directly edge-on. Thus either there is an asymmetric bar or the asymmetry is an artifact caused by the difficulty of extinction correction and bulge subtraction. The spatial scale of this asymmetry is slightly larger than required to explain the observed HVS anisotropy (Brown et al. 2012).

The fraction of red young stars (red supergiants and TP-AGB stars) increases toward Sgr A\* on a scale of  $2^\circ$  (Catchpole et al. 1990; Lindqvist et al. 1992; Narayanan et al. 1996; Ramírez et al. 2008; Schultheis et al. 2009). Thus there are more stars with ages between 20 and 200 Myrs in the nuclear disk than in the bulge. The detailed star formation history is not known due to the lack of CMDs. Figer et al. (2004) claim that their extinction corrected K-band luminosity function (KLF) supports continuous star formation. However, Antonini et al. (2012) can fit the same data with rather different star formation histories.

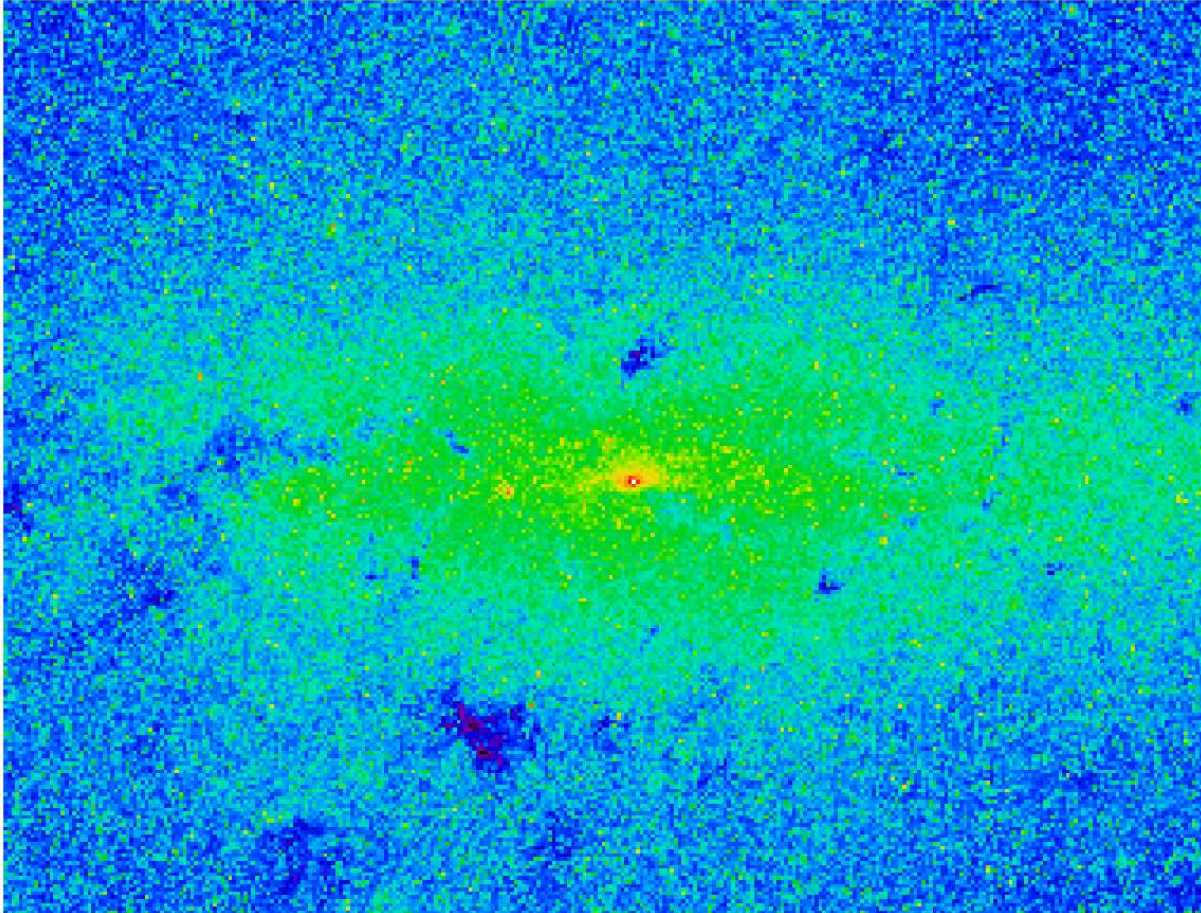


Figure 1.5 The central molecular zone (nuclear disk) at  $4.5 \mu\text{m}$  (The two central GLIMPSE mosaics from SPITZER/IRAC2; image source: <http://irsa.ipac.caltech.edu/data/SPITZER/GLIMPSE>). The native resolution is reduced to improve the visibility of surface brightness trends by smearing most stars out. The image covers a scale of  $2.1/1.6^\circ$  in l/b. The Galactic plane runs horizontally through the image. The nuclear cluster is the biggest light concentration close to the center. In the plane to its left is the Quintuplet cluster, visible as another light concentration. The emission is mostly dominated by cool stars; at some places, especially in the center and in the Quintuplet cluster, warm dust is more important. The dark patches in the image are caused by extinction. Since the extinction decreases with distance from the plane, the disk is thinner after extinction correction.

At the short age end of red stars, periods of Cepheids (Matsunaga et al. 2011) indicate more star formation in the inner nuclear disk  $25 \pm 8$  Myrs ago compared to  $50 \pm 20$  Myrs ago.

There are two young massive clusters within the nuclear disk, Arches (Cotera et al. 1996; Figer et al. 2002) and Quintuplet (Glass et al. 1990; Okuda et al. 1990; Figer et al. 1995). The Arches cluster has an age of about 2.5 Myrs (Martins et al. 2008). From proper motions of massive stars one can determine its mass of about  $1.5 \times 10^4 M_{\odot}$  (Clarkson et al. 2012). An important parameter to characterize star formation is the initial mass function (IMF). In this work we use the following definition of the IMF as a power law:  $N(m)dm \propto m^{\alpha}$ . The IMF of the Arches cluster is consistent with the -2.35 Salpeter (1955) slope for the detectable stars ( $M > 1.3 M_{\odot}$ , see Kim et al. 2006 and Espinoza et al. 2009). However, the mass measured by Clarkson et al. (2012) implies fewer low mass stars than the standard IMF of Kroupa (2001) and Chabrier (2003). This small mass could also be a sign of mass segregation of the more massive stars to the center (talk by C. Olczak at<sup>1</sup>). The Quintuplet cluster is about 4 Myrs old (Figer et al. 1999) and contains a photometric mass of  $6 \times 10^3 M_{\odot}$  within  $r < 0.5$  pc (Hußmann et al. 2012). Its IMF is with  $\alpha = -1.68$  (Hußmann et al. 2012) flatter than the Salpeter (1955) IMF. This flattening may also be caused by mass segregation (private communication A. Stolte). There are two metallicity measurements in the nuclear disk: both the metallicity of the very young red supergiant VR 5-7 in the Quintuplet cluster (Cunha et al. 2007) and of some bright hot stars in the Arches cluster (Martins et al. 2008) point to a slightly supersolar iron abundance and a more significant supersolar  $\alpha$  to Fe ratio.

Young blue stars outside these two clusters and the central cluster have recently been detected within the nuclear disk (Muno et al. 2006; Mauerhan et al. 2010; Wang et al. 2010). Due to the selection via X-ray emission or Paschen  $\alpha$  excess all of these stars are massive post main-sequence stars. About 50% of the young stars found in these surveys (covering the central  $0.1^{\circ 2}$ ) are located outside the three known cluster and form no new cluster (Dong et al. 2012). They conclude from the Paschen  $\alpha$  equivalent width and the magnitudes of these stars that they consist of two age groups. One is similar in age to the Quintuplet cluster and the other one is probably older than the O-stars in the central parsec. Detailed age and star formation history modeling from spectra is still missing for these fields stars.

Due to the high density in many GMCs, Serabyn & Morris (1996) and Mezger et al. (1996) predicted ongoing star formation in the nuclear disk. This is now confirmed by the detection of young stellar objects (YSO). The first photometrically selected YSOs (Felli et al. 2002; Schuller et al. 2006; Yusef-Zadeh et al. 2009) are now partly spectroscopically confirmed, implying a star formation rate of  $\approx 0.07 M_{\odot}/\text{yr}$  (An et al. 2009, 2011; Immer et al. 2012). Most of the YSOs are found at positive longitudes close to the Sgr B molecular complex. The rate is 5-10% of the Milky Way integrated star formation rate, as expected from the fraction of the molecular gas in the nuclear disk compared to the whole Galaxy. However, the conclusion that star formation is proportional to the molecular gas

<sup>1</sup>[http://www.astro.uni-bonn.de/~sambaran/program\\_nb2012.html](http://www.astro.uni-bonn.de/~sambaran/program_nb2012.html)

mass is not supported by observations outside the nuclear disk. For example Kennicutt (1998) and Gao & Solomon (2004) show that the star formation efficiency increases in high density molecular gas. Thus, the current star formation rate in the nuclear disk is surprisingly low compared to the high density of the molecular gas there (Longmore et al. 2013; Kruijssen et al. 2013).

The current epoch of star formation, probably also the epoch of TP-AGB stars ( $t \leq 200$  Myrs), in the nuclear disk is likely due to the inflow to the center caused by the bar (Binney et al. 1991; Serabyn & Morris 1996). For stars older than about 200 Myrs there is not enough spectroscopy available for determining the star formation history even qualitatively. These stars would offer the possibility to constrain the history of the bar: around epochs with a (strong) bar there should be more star formation in the nuclear disk than in epochs without a bar or only a weak bar.

## 1.5 The Nuclear Cluster



Figure 1.6 Inner 5.7 parsec ( $144''^2$  box) in the visible and near-infrared: left visible (irg-band RGB) image constructed from raw VST Galactic Center images (Image credit: program ESO177.D-3023), right: near-infrared (2.25, 2.09 and  $1.71 \mu\text{m}$ ; RGB image credit <http://www.eso.org/public/images/potw1047a/>) image of the Galactic Center. No truly GC source is detectable in the visible image, which shows only sources in front of the GC. Some of the red sources in the visible image are significantly extinguished. For example, the red star close to the lower edge at 5 o'clock (arrow) is the O5 star from Figure 1.3. The images are orientated equatorially, thus the nuclear/Galactic disk runs from 5 to 11 o'clock. However, it is nearly invisible in the central few parsecs.

As is the case for the nuclear disk, the nuclear cluster is absolutely invisible in the optical because of extinction, see Figure 1.6. In contrast, it is bright in the near-infrared, it has a magnitude of  $m_{K_s} \approx 3.6$  integrated over the central arcminute. With a resolution of only  $5''$  already Becklin & Neugebauer (1968) discovered this high surface brightness in the center of the Milky Way, which is clearly higher than what one would expect from extrapolating the bulge. (High spatial resolution) spectroscopy was necessary to uncover the nature of this central light excess (see e.g. Rieke et al. (1989); Sellgren et al. (1990); Krabbe et al. (1991); Genzel et al. (1997); Eisenhauer et al. (2005); Pfuhl et al. 2011). High resolution observations of the centers of other galaxies (Lauer et al. 1993; Phillips et al. 1996; Kormendy et al. 1996; Carollo et al. 1997; Bender et al. 2005; Côté et al. 2006) are helpful for comparing the GC with other galaxies.

The central light excess has probably three major components, the nuclear disk (Section 1.4), the nuclear cluster and disks of young stars (Section 1.6 and Figure 1.7). The nuclear cluster is relatively old, the majority of its stars are more than 5 Gyrs old (Blum et al. 2003; Pfuhl et al. 2011). The star formation history has a minimum between 200 Myrs and 5 Gyrs ago. Again there are more stars younger than 200 Myrs. The age of the oldest stars is difficult to determine, because the main sequence turn off cannot be observed at this age in the GC. The IMF of the nuclear cluster cannot be determined directly from its KLF, since one can only observe giants, which cover only a very small mass range. However, a top-heavy IMF, which is more than about 0.7 flatter than Salpeter (1955) for  $M_\odot > 1$ , can be excluded, because it would require more mass in remnants, more processed gas and less diffuse light than is observed (Pfuhl et al. 2011). Thus, the standard IMF (Kroupa 2001; Chabrier 2003) could fit the stars of the nuclear cluster. Dynamically the central nuclear cluster is probably isotropic (Trippe et al. 2008; Schödel et al. 2009). Its mass is not well determined in the inner parsec. Different methods yield different result with a range from 0.5 to  $1.5 \times 10^6 M_\odot$  (Trippe et al. 2008; Schödel et al. 2009). The synthesis of Genzel et al. (2010) prefers a mass of  $10^6 M_\odot$  in the central pc, with a factor two uncertainty on its mass. In Chapter 5 we obtain a better mass estimate for the nuclear cluster which is also useful to constrain its IMF further. Rotation of the nuclear cluster is visible in radial velocities (McGinn et al. 1989; Genzel et al. 1996; Trippe et al. 2008) and proper motions (Trippe et al. 2008). In the inner parsec the rotation is clearly smaller than the dispersion (Trippe et al. 2008; Schödel et al. 2009). The importance of rotation increases with increasing distance to Sgr A\*. It is, however, disputed how fast the rotation increases (McGinn et al. 1989; Trippe et al. 2008; Schödel et al. 2009). We determine the rotation curve in Chapter 5. The rotation does not lead to an obvious flattening of the nuclear cluster in the central  $\sim 30''$ , see Schödel et al. (2007). The nuclear disk (at 30 to 200 pc) shows a clear sign of flattening (Launhardt et al. 2002). In between Vollmer et al. (2003) state an axis ratio of 1.4 for the light there. However, inside of 30 pc an analysis of how the flattening evolves with radius is missing, which I provide in Chapter 5.

The old nuclear cluster and the O-star disks (Section 1.6) are distinct not only by their age: firstly, the (inner) nuclear cluster is nearly isotropic with only weak rotation in the Galactic plane (McGinn et al. 1989; Genzel et al. 1996; Trippe et al. 2008). In contrast, 3/4 of the young massive stars are in two disks of different orientations. However, since

vector resonant relaxation (Alexander & Hopman 2009) erases disks fast (few tens of Myrs), and the nuclear stars are much older than few tens of Myrs, even a strong rotation at the formation of the nuclear cluster would be invisible today. (The fact that rotation is visible in the nuclear cluster possibly implies that this rotation is enforced by forces from further out.) Secondly, the disk structure is much stronger concentrated on Sgr A\* than the old stars, see Figure 1.8 and e.g. Sellgren et al. (1990); Genzel et al. (1996); Paumard et al. (2006); Bartko et al. (2010). This difference in radial distribution is not only seen in comparison to really old stars, but also in comparison with most supergiants and TP-AGB stars (Sellgren et al. 1987; Genzel et al. 1996). This result is confirmed by the analysis of Blum et al. (2003) and Pfuhl et al. (2011) who use current stellar evolution models and temperatures for separating bright old giants from intermediate-age late-type stars, see Figure 1.9. Blum et al. (2003) worked with bright late-type stars, which have  $-7 < M_{\text{Bol}} < -3$ . Pfuhl et al. (2011) also included fainter intermediate age late-type stars, down to  $M_{\text{Bol}} \approx 3$ . Since the radial distribution of stars depends on energy, it can only be changed by non-resonant relaxation on a scale of few Gyrs, see Alexander (2007). Thus the intermediate age stars are, at around 100 Myrs, too young for their radial distribution to have changed by relaxation. Thirdly, the IMFs of the two are different. The power law slope  $\alpha$  of the OB-stars is about 1.9 more top-heavy (Bartko et al. 2010) than the standard IMF slope, while the nuclear cluster is at most 0.7 more top-heavy (Pfuhl et al. 2011) than the standard IMF. There is also an indication that the main disk is even more extreme, this disk could contain nearly no stars below  $14 M_{\odot}$  (see Section 1.6). No stars that massive can be detected in the nuclear cluster, since after their short lifetime only very faint remnants are left behind. An IMF difference of this order cannot be caused by evolutionary effects, like mass segregation because mass segregation is not strong enough to cause such a big change in the distribution of the less massive component (Alexander & Hopman 2009).

At large radii, the case for separating the nuclear disk from the nuclear cluster is probably less convincing. This distinction is also not used by all, see e.g. Serabyn & Morris (1996). Launhardt et al. (2002) obtained in their dissection of nuclear cluster and nuclear disk, a nuclear cluster of a half light radius of 8 pc, larger than most nuclear clusters (Böker et al. 2004). The data used by Launhardt et al. (2002) are not homogeneous and are partly of limited resolution. Especially around the transition from the nuclear cluster to the nuclear disk their resolution is too small to dissect them reliably. In Chapter 5 I use data with higher spatial resolution to obtain a new estimate for the size of the nuclear cluster.

In other galaxies nuclear clusters and disks are also observed, sometimes both together (Kormendy & Kennicutt 2004; Seth et al. 2006), and sometimes alone (Böker et al. 2004; Kormendy & Kennicutt 2004; Seth et al. 2006). However, not all of these structures are of the small scale of the GC, and partly the naming conventions used may be confusing. The dissection into nuclear disk and nuclear cluster is not discussed as a problem in other galaxies. However some galaxies in Carollo et al. (2002) have large nuclear clusters of about 20 pc half light radii which could be an indication that the Milky Way is not unique in this respect.

Concerning the gas, the biggest gas structure on scale of the nuclear cluster is the

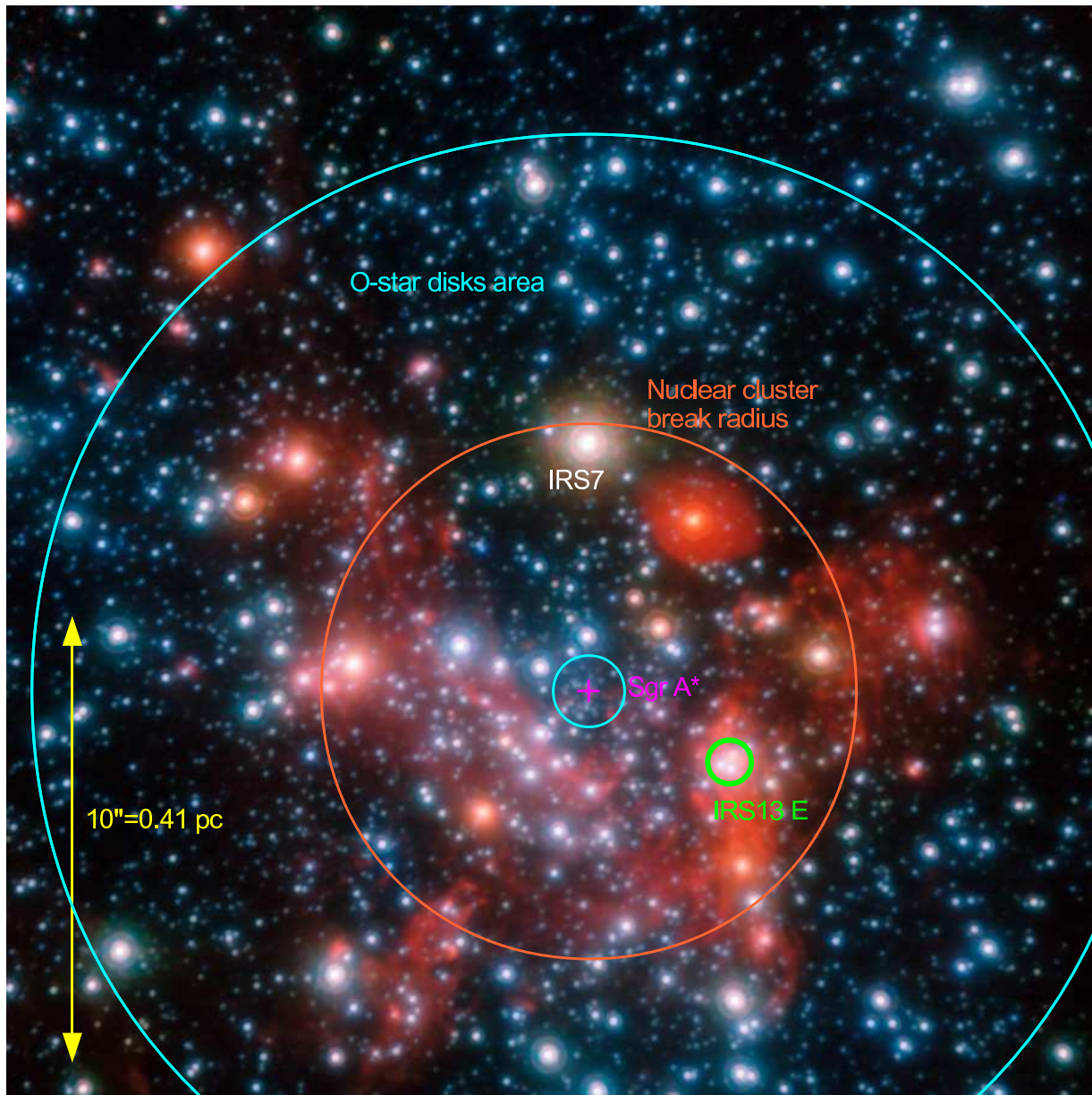


Figure 1.7 Adaptive optics image of the central parsec: On this VLT/NACO image (LKsH RGB-image, image credit: <http://www.eso.org/public/images/eso0846a/>) the positions of the important objects are marked. These are: the potential star cluster IRS13E, the SMBH Sgr A\*, the region of the O-star disks between inner and outer break radii at  $0.8''$  and  $12.5''$  (Buchholz et al. 2009; Bartko et al. 2010), and the break radius of the nuclear cluster, at  $\approx 6''$  (Buchholz et al. 2009). The red supergiant IRS7, which is used as the AO guide star, belongs also to the O-star population. B-stars extend in a scale free power law over the full image, they are dominating in the central  $0.8''$ .

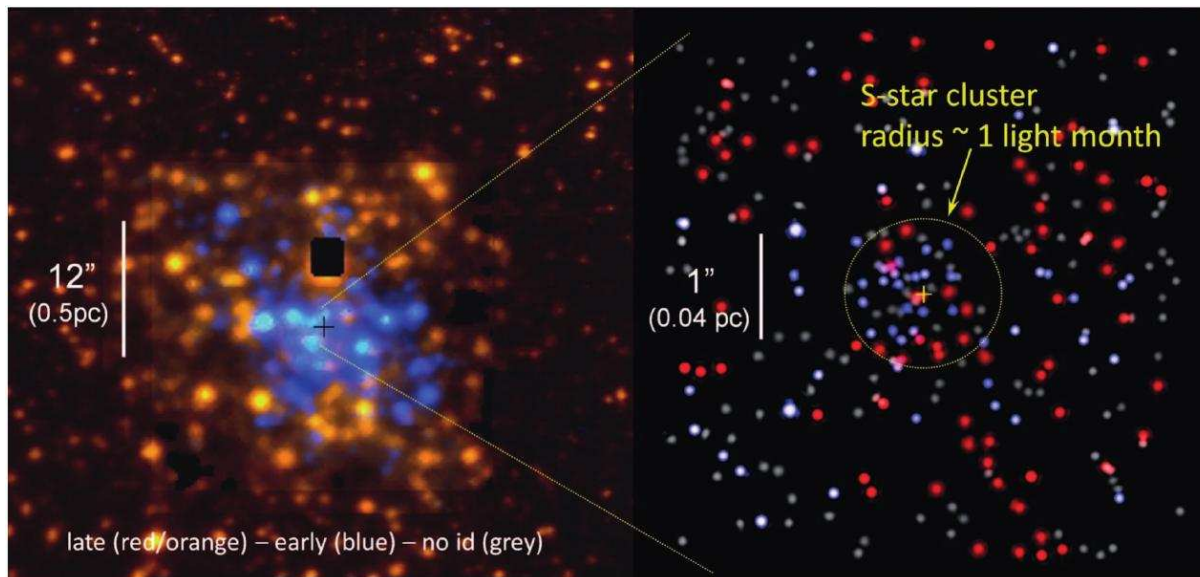


Figure 1.8 Early- and late-type stars in the central parsec: left, CO band-heads maps from seeing limited spectroscopy. The hole in the map covers the bright red (but young) supergiant IRS7. right: coloring of sources on a deconvolved NACO image according to their spectral types. Image credit: Genzel et al. (2010)

circumnuclear disk (CND) (Becklin et al. 1982) at about 1.5 to 5 pc distance with a mass of about a few  $10^4 M_{\odot}$  (Genzel et al. 1985; Mezger et al. 1989; Requena-Torres et al. 2012), only about a 1/100 of the nuclear cluster mass of  $8 \times 10^6 M_{\odot}$  (Genzel et al. 2010) within 5 pc. In the central 1.5 pc the gas fraction is smaller than further out, see Guesten et al. (1987) and Launhardt et al. (2002). This is a consequence of the central cavity (Guesten et al. 1987) which is likely created by the short lived O-stars in the center. Therefore it is not clear whether the gas fraction of the nuclear cluster is smaller than the gas fraction of the nuclear disk. Only in the outer CMZ is the gas fraction clearly bigger, see Launhardt et al. (2002).

The star formation histories of the nuclear cluster and nuclear disk can currently barely be used to distinguish them, since the star formation history of the nuclear disk is not well known. Launhardt et al. (2002) derive a factor four higher mass-to-light ratio of  $M/L=2$  for the nuclear disk compared to the nuclear cluster. However, the flux data source used by them changes at the border of the two components, such that the different  $M/L$  could be an artifact. Overall, there is not much convincing physical evidence for distinguishing the nuclear disk from the nuclear cluster. Thus, the simple assumption of one component maybe be better from a theoretical perspective. However, from an observer perspective it is still useful to distinguish the nuclear disk from the nuclear cluster because they are radially separated and are usually not observed together.

The chemical abundances of the stars in the Nuclear cluster  $[Fe/H] \approx 0.1 \pm 0.07$ ,

slightly supersolar with remarkably small scatter (Genzel et al. 2010; Ramírez et al. 2000; Cunha et al. 2007). Especially the narrow metallicity distribution is inconsistent with the bulge properties (Cunha et al. 2007). The alpha elements are probably enriched with  $[\alpha/\text{Fe}] \approx 0.35 \pm 0.2$  (Genzel et al. 2010; Ramírez et al. 2000; Cunha et al. 2007); however Davies et al. (2009) derived solar metallicities for IRS7 after correction for evolutionary effects. Most stars analyzed are less than 200 Myrs old. For four stars of the sample in Cunha et al. (2007) the age is disputed: according to Blum et al. (2003) they are old ( $> 5$  Gyrs) giants but according to Cunha et al. (2007) they are younger than 1 Gyr. It therefore remains uncertain whether the metallicity in the GC is slightly supersolar with small scatter for all formation periods. Thus further metallicity measurements for bona fide old stars are necessary for establishing the high metallicity at all ages and for starting to measure the width of the metallicity distribution also for the old stars. The stated mean metallicities, which are similar to the bulge, and the IMF constraints, can qualitatively be explained on the one hand by recent gas inflow from the inner disk. Thereby it is necessary that this gas is enriched in  $\alpha$  by recent star formation. This could possible happen in the nuclear disk via core collapse supernova or AGB winds (Morris & Serabyn 1996; Genzel et al. 2010). On the other hand, the mean metallicities are similar to the bulge, and can be explained in case of old stars in the same way as for true bulges by a short burst of star formation a long time ago. Confirmation of the small Fe spread for the old stars would invalidate the second scenario and make the formation in bar induced gas inflows a little more than 5 Gyrs ago more likely.

The radial distribution of the old stars outside the central parsec follows a power law slope of about -0.8 (Becklin & Neugebauer 1968; Haller et al. 1996; Philipp et al. 1999) out to about  $600''$ . A flattening is visible in the center when counting bright late-type stars (Genzel et al. 1996) or the diffuse light of the unresolved background of relative faint stars on seeing limited images (Philipp et al. 1999). The lack of CO in speckle spectra indicated already in Genzel et al. (1997) that the fainter late-type stars are similarly distributed. Thanks to AO based observations this flattening is now confirmed for red clump giants (Eisenhauer et al. 2005; Bartko et al. 2010; Buchholz et al. 2009; Do et al. 2009). Also fainter giants seem to be similarly distributed (Gillessen et al. 2009; Pfuhl et al. 2011). Within the errors the profile is flat in the central  $\approx 8''$  (Buchholz et al. 2009; Bartko et al. 2010). Although it is difficult to derive the unprojected density profile from the projected one, it needs to be flatter (Do et al. 2009) than the expected Bahcall & Wolf (1976) cusp slope of  $-7/4$ . The reason for this apparent core is unclear, since mass segregation probably does not work strongly enough for these solar mass stars, see Alexander & Hopman (2009). The two main possibilities are: the nuclear cluster had not enough time for relaxation after an (black hole) merger event (Merritt 2010) or collisions destroy giants in the GC (Lacy et al. 1982; Genzel et al. 1996; Davies et al. 2011). Preferable the explanation should not only explain the core in the  $> 5$  Gyrs old stars but also in the 100 Myrs old stars, see Figure 1.9. It is unlikely that a big enough merger event occurred in the last 100 Myrs. A physical destruction seems to be a natural way of destroying big stars, however, it is unlikely that the destruction of late-type stars creates cores of the same size for stars of different luminosity (Dale et al. 2009). Maybe a very top heavy IMF over long times

with many black hole remnants can create cores of the right size, see Davies et al. (2011). However, the IMF of the nuclear cluster cannot be sufficiently top-heavy for making enough black holes (Pfuhl et al. 2011). Also, it is not clear whether black holes are the main remnants of the top-heavy IMF, see Section 1.6. Physical destruction scenarios which destroy giants but not main sequence stars can be tested by observations of their precursor main sequence stars. However, only for some of the brightest and youngest red giants, are the precursors currently detectable. In this case the comparison with fainter B-stars, although complicated by star formation history effects, may soon offer some constraints. For most giants only the diffuse light can be used for comparison. However, that is of course difficult to measure, and probably cannot be trusted as much as one can trust measurements based on resolved stars. The diffuse light seems to be more concentrated to the center than the old stars, see Yusef-Zadeh et al. (2012). Possibly this is one of the few cases in which JWST with its relatively small and stable PSF will be able to improve near-infrared GC science. Indirectly, the quiescent X-ray radiation around Sgr A\* could be useful for constraining the dwarf density close to it. Sazonov et al. (2012) proposed that the quiescent X-ray radiation around Sgr A\* is caused by dwarfs in the central arcsecond. If on the other hand, CHANDRA grating spectroscopy (Nowak et al. 2012) can show that the extended X-ray emission is caused by the accretion flow, then the idea of Sazonov et al. (2012) can be used the other way round to set an upper limit on the dwarf density in the central arcsecond. Also a precise determination of the mass in stars in the central 1 pc can answer the question of whether the missing Bahcall & Wolf (1976) cusp is also missing in the mass profile. I make a step to a precise mass profile in Chapter 5.

Since the similarity of the distribution of very old and moderately old stars of the nuclear cluster is surprising, especially in case of merger explanations, more precise age and density measurements can be useful constraints on the scenarios. Also, it might turn out that a different explanation than the ones mentioned before is necessary for explaining the radial profile of the nuclear cluster.

Nuclear clusters preferentially exist in small and medium sized galaxies which contain often no measurable SMBH (Ferrarese et al. 2006). However, there are also galaxies which contain both, a nuclear cluster and SMBH, see Graham & Spitler (2009). Thus, the idea of Ferrarese et al. (2006) that the nucleus (either the SMBH or a nuclear cluster) weighs a constant mass fraction (about 0.2%) of its galaxy cannot be true in the strict version, which allows only for one of them in a galaxy. Kormendy et al. (2009) collect data showing a similar mass fraction relation between the central massive objects and their galaxies. However, they assume that this relation is an accident. They suspect that nuclear clusters and SMBHs are only indirectly connected by the fact that both are partly feed by gas from the disk.

For the origin of nuclear clusters there are mainly two theories (Kormendy & Kennicutt 2004; Böker 2010): firstly, formation via migration of (globular) clusters to the center (Tremaine et al. 1975; Andersen et al. 2008; Capuzzo-Dolcetta & Miocchi 2008), and secondly star formation in situ directly after gas inflow (Emsellem & van de Ven 2008; Milosavljević 2004). The recent epoch (from 20 to 200 Myrs ago) of star formation occurred likely in situ out of the gas in the nuclear disk, see also Section 1.4. Given its

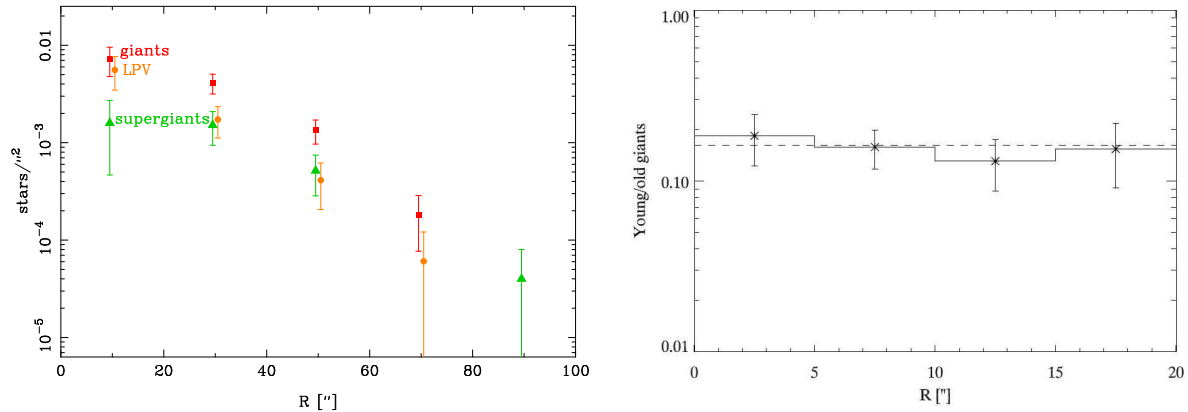


Figure 1.9 Radial distribution of different kinds of late-type stars; left: star densities of different kind of late-type stars constructed using stars listed in Blum et al. (2003). I exclude the youngest red supergiant (IRS7) from the calculation because it is with an age of about 7 Myrs (Carr et al. 2000) much younger than the other red supergiants (few tens of Mys, see Blum et al. 2003). IRS7 belongs probably to the O-star disks (Pfuhl et al. 2011). The sample is not complete but unbiased in spectral type. right: relative abundance of young (around 100 Myrs) to old giants for stars with magnitudes between  $0 < M_{\text{bol}} < -4$  from Pfuhl et al. (2011). The radial distributions of these different old stars (from about 20 to 6 Gyr) are identical.

different IMF and spatial distribution this epoch of star formation was likely different from the current one in the very center, which resulted in the stellar disks (Section 1.6). Possibly, in case of the stellar disks, the gas clouds approached the SMBH closer than in the other cases. Recent infall of clusters is unlikely since there are not enough young clusters close to the Galactic Center. Nuclear clusters are not more common in barred galaxies than in other galaxies (Carollo et al. 2002; Böker et al. 2004; Kormendy & Kennicutt 2004). Bright nuclear clusters with  $L_V > 5.3 \times 10^6 L_\odot$ , like the Milky Way’s nuclear cluster are usually associated with nuclear disks (Carollo 1999).

In the Galaxy the recent star formation epoch ( $t \leq 200$  Myrs) contributed less than 10% of the mass of the nuclear cluster (Pfuhl et al. 2011). Therefore the major part of the mass could originate from a different process. Antonini et al. (2012) claim that a globular cluster infall for most stars is consistent with the observed morphology and star formation history. However, the measured metallicity of the nuclear cluster is higher than the metallicity of all globular clusters and its scatter is also smaller. Still, it is possible that none of these metallicity measurements belongs to the old population of stars. Further, since there is no clear distinction between the nuclear cluster and the nuclear disk, a formation theory should probably explain also the properties of this disk. (However, that there is no clear distinction between them is due to the fact that there is less information about the properties of the nuclear disk available.) Since the globular cluster population is less flattened than the nuclear disk it is difficult to create the nuclear disk from globular clusters. It follows from this that most of the nuclear cluster formed in situ following

gas inflowing, possibly in contrast to most other galaxies (Kormendy & Kennicutt 2004). However, this conclusion is assumption dependent, the most important one is that the stellar properties in nuclear cluster and nuclear disk are similar.

Since the nuclear disk and nuclear cluster seem to be identical in most of their measured properties, the star formation history in the nuclear cluster may be identical to the star formation history of the nuclear disk. Thus the star formation history of the nuclear cluster may serve as an indicator for the presence of a bar, see Section 1.4. The low star formation rate between 200 Myrs and 5 Gyrs could be an indication that the (strong) bar is a rather young structure. This means that the bar did not reform often in the second half of the Galaxy's life or that the bar was at least on average smaller and weaker than today. Since this seems to be in contradiction to the secular evolution explanation of the bar (Kormendy & Kennicutt 2004) further studies are necessary to shed light on this.

## 1.6 The O-star Disks

Apart from the relatively old ( $15 > \text{Myrs}$ ) stars, there are also young stars in the Galactic Center. The apparently brightest star IRS7, at a projected distance of  $6''$  to Sgr A\*, was recognized as a young red supergiant (Neugebauer et al. 1976; Treffers et al. 1976; Lebofsky et al. 1982). It is the only red supergiant with an age of less than 10 Myrs in the GC (Blum et al. 2003; Pfuhl et al. 2011).

In addition to this red young star, there are many more blue young stars. The first, a Wolf-Rayet star was discovered by Forrest et al. (1987) and Allen et al. (1990). Later, more stars like WR-stars, OB-(super)giants (Allen et al. 1990; Krabbe et al. 1991; Genzel et al. 1996, 2000) and O-dwarfs (Paumard et al. 2006; Bartko et al. 2009) were discovered. Probably all of these stars have an age of about 6 Myrs (Paumard et al. 2006; Martins et al. 2007). These stars are concentrated much more toward Sgr A\* than the nuclear cluster (Krabbe et al. 1991; Genzel et al. 1996; Bartko et al. 2010; Buchholz et al. 2009; Do et al. 2013), the half number radius is about  $7''$ , and only very few are outside of  $r > 15''$ . (to calculate the half number radius I use the O-star density within  $r < 25''$  in Bartko et al. 2010), The density evolution outside of  $20''$  and thus the transition to the nuclear disk (Section 1.4) is still very uncertain because only spectra of very bright stars have been taken there (Blum et al. 2003; Geballe et al. 2006). No O-star is found with  $r < 0.8''$  from Sgr A\*, although some would be expected (Bartko et al. 2010), extrapolating the density profile from the outside, see Figure 1.11. The angular momenta of these stars are not randomly oriented: slightly more than half of them orbit Sgr A\* in one clockwise disk (Genzel et al. 2003; Paumard et al. 2006; Lu et al. 2009) which is warped (Löckmann & Baumgardt 2009; Bartko et al. 2009), see also Figure 1.10. There is evidence that 20 % of the O/WR-stars rotate in a second disk, the counterclockwise disk, (Genzel et al. 2003; Paumard et al. 2006; Bartko et al. 2009, 2010). The remaining 25% seem to have randomly oriented angular momenta (Bartko et al. 2009). Since this second disk contains fewer stars, its existence is disputed, see Lu et al. (2009).

The IMF of the young stars between  $0.8''$  and  $12''$  is top-heavy with a power law of

$\alpha = -0.45 \pm 0.3$  (Paumard et al. 2006; Bartko et al. 2010). Do et al. (2013) and Lu et al. (2013) find  $\alpha = -1.7 \pm 0.2$ , excluding both a Salpeter IMF and  $\alpha = -0.45$  with  $3.8\sigma$ . However, the cleaning of the sample of late-type stars in Do et al. (2013) and Lu et al. (2013) is likely imperfect, since their young stars luminosity function shows a bump at the magnitude of the red clump. The red clump consists of old giants. Since there are nearly no fainter B-stars ( $M_{\odot} \lesssim 14$ ) on disk orbits, see Section 1.7, the IMF of stars truly belonging to the disk, is likely even more extreme. Probably it is not possible to extend this extreme IMF slope to larger masses, pointing toward an IMF with varying slope like in Kroupa (2001). According to Chabrier (2003) the IMF below  $1 M_{\odot}$  can be parametrized in as lognormal:

$$N(m)dm \propto \exp\left(-\frac{((\log(m) - \log(m_c))^2)}{2\sigma^2}\right)$$

In case of the standard IMF the characteristic mass ( $m_c$ ) is  $0.08M_{\odot}$  (Chabrier 2003). From the log-normal formulation follows a local power law  $-0.3$  at the characteristic mass (Chabrier 2003; Bastian et al. 2010). This power law slope is consistent with the IMF of the disk structure. Thus, if the GC IMF follows a lognormal function, the characteristic mass is in the mass range around 20 to 40  $M_{\odot}$  at least a factor 250 bigger than in the Galactic Disk. Due to this extreme IMF it is uncertain whether the mass of about  $1.5 \times 10^4 M_{\odot}$  obtained from the KLF (Bartko et al. 2010) is the mass of the disks. Possibly, very massive stars, which are now less massive remnants, increase the mass of disks, especially in the first 3 Myrs after formation. The mass of the disks depends on the uncertain maximum stellar mass (Figer 2005; Crowther et al. 2010; Banerjee et al. 2012). Maybe the modeling of disk evolution (Löckmann et al. 2009), which is sensitive to the life time integrated mass of the disks can reach enough accuracy to exclude disks with too many extremely massive stars. This could be also interesting in the context of very massive stars in general. Since the disk structure contains probably no long living stars it is not surprising that the older stars (Section 1.5) do not show disk-like characteristics. It follows that these older stars cannot be used for constraining earlier epochs of disk formation, and it is uncertain how often it occurred in the past. The stellar remnants set a limit on the occurrence rate in a way similar to the IMF constraints in Pfuhl et al. (2011). However, when most remnants are neutrons stars (NS), as recent models and observations suggest for metal rich very massive ( $M \gtrsim 40 M_{\odot}$ ) stars (Heger et al. 2003; Ritchie et al. 2010), this limit is less strong, possibly nearly a factor  $M_{\text{NS}}/M_{\text{stellar BH}} \approx 1/5$  lower. Maybe the gas processed by these stars delivers better constrains via metallicity (which is probably slightly supersolar for the current disk stars, see Martins et al. (2007)) if the outflow effects are not too strong. Since it is difficult to imagine that no gas falls into the SMBH when these stars have formed locally (Levin & Beloborodov 2003; Genzel et al. 2003; Nayakshin & Cuadra 2005) the SMBH mass delivers a weak limit on the mass processed in disk formation during the history of the Galaxy.

The O-stars in the central parsec cannot be formed in situ in normal giant molecular clouds (GMC), since the tidal force exerted by the SMBH destroys normal GMCs (Morris 1993). Further, they cannot be transported to the center as single stars, because they are much too young for relaxation (Alexander 2007). Transportation by the Hills-

mechanism (Hills (1988), see Section 1.7) is excluded by the too low eccentricities of the disk stars (Paumard et al. 2006; Lu et al. 2009; Bartko et al. 2009; Gillessen et al. 2009). There are two main theories for the origin of the O-stars. In the first, one or two GMC fall toward Sgr A\*, get compressed by (self-)collisions and self-gravity, and form disk(s) around Sgr A\* (Levin & Beloborodov 2003; Genzel et al. 2003; Nayakshin & Cuadra 2005; Hobbs & Nayakshin 2009; Bonnell & Rice 2008). In the second theory, a massive cluster migrates due to dynamic friction to the center (Gerhard 2001). To not disrupt the cluster too early in this process it is necessary that the cluster contains an intermediate mass black hole (IMBH), see Portegies Zwart & McMillan (2002) and Hansen & Milosavljević (2003). The observed warp of the brighter disk can be explained qualitatively by any of the different non-spherical structures (other O-star disk, CND) in the GC (Nayakshin & Cuadra 2005; Šubr et al. 2009; Löffmann & Baumgardt 2009). In case of a cluster infall the warp is difficult to explain, since then there has not been sufficient time for warping (Bartko et al. 2010). The observation of two disks of the same age is very surprising for the case of an infall, since two independent clusters of the same age would have to infall. The formation of two disks occurs in some simulations during in situ formation, see Hobbs & Nayakshin (2009), Alig et al. (2013) and Lucas et al. (2013). In the in situ simulations of Hobbs & Nayakshin (2009) and Bonnell & Rice (2008) the resulting IMF is top-heavy as observed. However, the IMF slopes obtained by Hobbs & Nayakshin (2009) are radius dependent in contrast to the observations. For the infall scenario, a top-heavy IMF can be caused by mass segregation in the cluster and losing the less massive stars further out in the GC. In some simulations this results in an IMF slope of -1.1 in the center (Gürkan & Rasio 2005). The infall scenario predicts that there are many low mass stars further out in the GC. The detailed spatial distribution of these lower mass stars depends on the infall cluster parameters, like its density. However, the prediction of a usual Salpeter IMF, when integrating over all young stars in the GC within about 4 pc, is robust. But observations measure few low mass stars inside 1 pc, and in addition they are not on disk like orbits (Bartko et al. 2010). Also the strong concentration of the O-stars toward Sgr A\* is broadly consistent with local formation (Hobbs & Nayakshin 2009; Bonnell & Rice 2008), and not with cluster inspiral without mass segregation (Hansen & Milosavljević 2003). Even with mass segregation it is difficult to hide the B-stars far enough outside to explain the non-detection in the available observations (Bartko et al. 2010). It would be necessary to further extend the search area for B-stars to exclude the most extreme infall scenarios (Fujii et al. 2009).

In the context of the necessity of an IMBH for the infall scenario it is interesting that there are two concentrations of young massive stars within  $r < 5''$  to Sgr A\*, the rather loose IRS16SW concentration (Lu et al. 2005) and the IRS13E cluster (Maillard et al. 2004). Both are proposed to be remnants of infalling clusters and could contain an IMBH (Lu et al. 2005). In case of the IRS16SW association the surface density is not enhanced (Paumard et al. 2006), it is probably only a part of the clockwise disk with a coincidentally reduced dispersion. In case of IRS13E the case is less clear, it is a strong concentration of stars on the sky (Paumard et al. 2006). I analyze in Chapter 3 the case for an IMBH in IRS13E. In general nearly no IMBH is unambiguously confirmed, see e.g. the review of

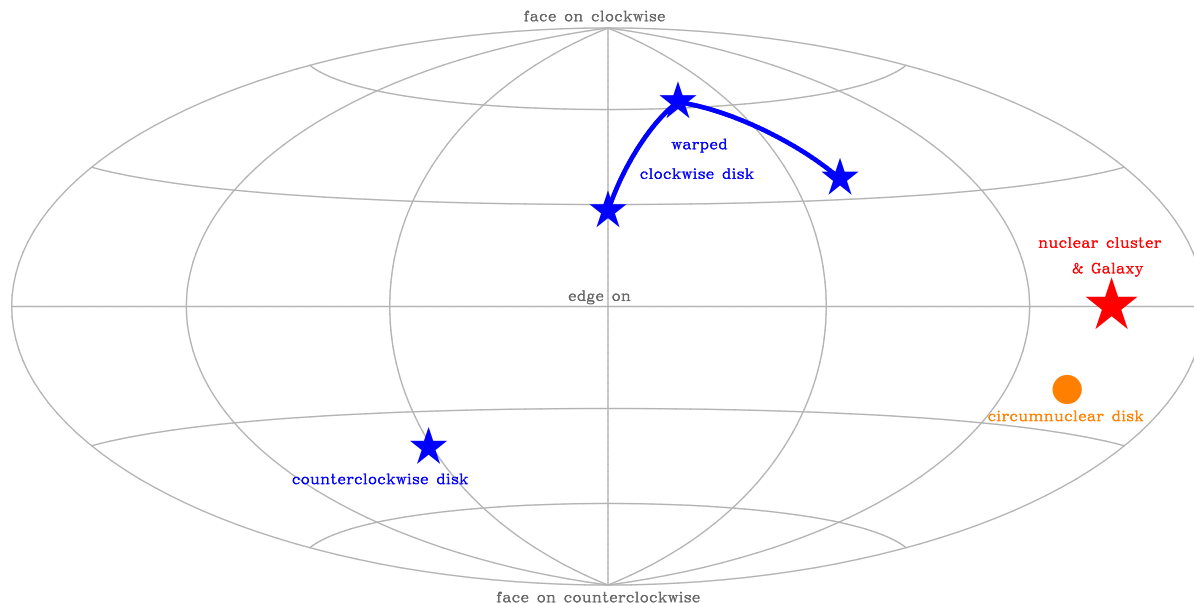


Figure 1.10 Angular momenta orientation of massive components of the GC: the nuclear cluster (consisting of stars  $> 20$  Myrs) rotates only weakly, in same direction as the Galaxy (Trippe et al. 2008; Bartko et al. 2009). In contrast, the young O-stars and the bright B-stars ( $14 < m_K < 15$ ) live in the bigger, warped clockwise disk (Bartko et al. 2009) and the smaller counterclockwise disk (Bartko et al. 2010). The gaseous circumnuclear disk is somewhat misaligned to the Galactic Disk (Jackson et al. 1993).

IMBHs by van der Marel (2004) and the review of ultra luminous X-ray sources (ULX) by Feng & Soria (2011). There is also discussion about globular clusters harboring IMBHs, see e.g. the disputed case of  $\omega$  Cen in Noyola et al. (2008), van der Marel & Anderson (2010), and Strader et al. (2012).

## 1.7 B-stars in the GC

A priori, there is no reason why B-stars ( $m \leq 20M_{\odot}$ ) should not have the same distribution in phase space as the slightly more massive O-stars. However, since observations show that they are distributed differently, I discuss the B-stars here separately. The first B-stars ( $m_K \geq 14$ ) discovered were some of the so called S-stars in the central arcsecond (Eckart & Genzel 1996, 1997). The first clue about the nature of these S-stars came from the non-detection of CO band-heads in speckle spectra (Genzel et al. 1997). Later most brighter S-stars were confirmed as B-stars by the detection of Brackett- $\gamma$  absorption lines (Ghez et al. 2003; Eisenhauer et al. 2005; Gillessen et al. 2009). In contrast to  $r > 0.8''$ , there are only B-stars and no O-stars in the region of the S-stars ( $r < 0.8''$ ).

Later, these B-stars were also discovered outside the central arcsecond, primarily by

Paumard et al. (2006), Bartko et al. (2010), and Do et al. (2013). Compared to the O-stars there are relatively few B-stars out to  $12''$ . Outside of this radius the number of detections is small, but there seem to be more B-stars than O-stars. The IMF outside of  $12''$  and inside of  $0.8''$  is consistent with a young single generation Salpeter IMF. (In this case a young single generation means that the star formation occurred recently enough that also the most massive B-stars have not yet died.) Between  $0.8''$  and  $12''$  the IMF is with very top-heavy  $\alpha = -0.45 \pm 0.3$  (Bartko et al. 2010). The O-stars follow approximately an exponential profile with a central hole, the bright B-stars follow a very steep power law profile with  $\alpha = -1.5 \pm 0.2$  (Figure 1.11). From the semi-major axis distribution of the early-type S-stars follows  $\alpha = -1.1 \pm 0.3$  (Gillessen et al. 2009), consistent with the outer B-star slope. This means the B-stars are concentrated on Sgr A\*: using the B-stars with  $r < 25''$  and  $14.5 < m_{K_s} < 15.5$  from Bartko et al. (2010). I obtain a half number radius of about  $13''$ .

The orbital properties of the B-stars are well studied in the central arcsecond, because their individual orbits can be measured (Eisenhauer et al. 2005; Ghez et al. 2005; Gillessen et al. 2009). The orbits are randomly oriented and the eccentricities are  $1.8 \sigma$  hotter than for an isotropic, thermal velocity distribution. Further out, half of the B-stars with  $14 < m_{K_s} < 15$  are consistent with being in the clockwise disk (Bartko et al. 2010). In contrast, only one of the 14 fainter stars in Bartko et al. (2010) and Pfuhl et al. (2011) is consistent with the clockwise disk. The Poisson probability for observing only one in 14 consistent with the main disk is only 0.05% when assuming that the B-stars disk membership has the same probability value of 50% as the brighter stars. Thus the observation of only 1 in 14 is already significant, and the disk structure contains nearly no faint B-stars, see Section 1.6 for discussing this in the context of the disk IMF. The eccentricities of the B-stars outside the central arcsecond cannot yet be measured from orbits. It is possible to measure eccentricities as for the O-star disks (Bartko et al. 2009) with statistical methods, see Madigan et al. (2013). Their results indicate that brighter B-stars ( $14 < m_{K_s} < 15$ ) have eccentricities colder than thermal while the fainter ones have hotter than thermal eccentricities. Measuring whether the (outer) B-stars rotate weakly in the same direction as the nuclear cluster and the nuclear disk could in the future constrain their relationship.

The B-stars in the central arcsecond form a 'paradox of youth' (Ghez et al. 2003) since they are so close to Sgr A\* that they cannot have formed in situ due to the tidal force of the SMBH. Further, they are so young that classical transportation mechanisms are too slow. The possibility that they only seem to be young, but are giants stripped of their envelopes (Genzel et al. 2003), is excluded by high quality spectra (Eisenhauer et al. 2005; Martins et al. 2008). Thus only fast transportation mechanisms remain as an explanation. There are two main contenders for this transportation mechanism. The first possibility is a two step process. In this process, they firstly come to the central parsec in a similar way as the O-stars. Either they are born locally in a disk, either the current one (Löckmann et al. 2008) or an older one (Madigan et al. 2011), or they were brought to the center by the inspiral of a star cluster with an IMBH (Merritt et al. 2009; Gualandris & Merritt 2009; Fujii et al. 2010). Afterwards a second process is necessary for bringing them closer to the center than the O-stars. Because the mass difference between B- and O-stars is rather

small, it is difficult to bring so many more B-stars than O-stars to the center, when starting from the current disks, see L $\ddot{o}$ ckmann et al. (2009). The difficulties in explaining the B/O-ratio can be reduced by making the B-stars older than the current disk. Then there is more time to change their orbits (Madigan et al. 2011). In the second theory the B-stars originate further out in the region of the GMCs in the CMZ, see Section 1.4. Binaries that are born there are scattered by massive perturbers, i.e. GMCs to the center (Perets et al. 2007). In the center, the tidal force of the SMBH disrupts the binary (Gould & Quillen 2003), scattering one partner on a very eccentric short orbit around the SMBH and the other as an HVS to the halo (Hills 1988), see Section 1.1. As a last step, resonant relaxation (Perets & Gualandris 2010) reduces the eccentricity to the only slightly superthermal observed value.

The theory should not only explain the B-stars in the central arcsecond, but also further out, since the processes discussed work also outside the central arcsecond, see Perets & Gualandris (2010). I now discuss the observed properties and the two scenarios: the binary disruption scenario predicts the observed high eccentricities in the central arcsecond and further out (Hills 1988; Perets & Gualandris 2010). The radial density profile is less constraining since the radial profile predicted by the Hills scenario depends on the binary separation distribution, which is not well known. This can be seen in the different B-stars profiles in Perets et al. (2007) and Perets & Gualandris (2010) caused by different binary properties. The randomly distributed angular momenta of the B-stars further out (Bartko et al. 2010) also fits better to the Hills scenario. The single generation Salpeter IMF for the S-stars is a major problem for an origin in the current disk (L $\ddot{o}$ ckmann et al. 2009). The S-star mass function can maybe be explained by quasicontinuous star formation in many disks with top-heavy IMFs, but only if they contain any faint B-stars, in contrast to current indications. In case of the Hills scenario, the predictions are not so certain. The IMF depends on the unknown star formation history outside the central few parsecs, the mass dependence of the binary fraction and the mass dependence of the semi major axis distribution (Perets & Gualandris 2010). In case of continuous star formation and no mass dependence of the close binary fraction, the mass function should be steeper than that measured. The binary disruption itself causes probably no relevant mass bias: the analysis of Kobayashi et al. (2012) finds that in most cases there is no relevant preference for ejection. In case of a bound binary which is disrupted relatively far out, the primary could be significantly more likely to be caught as an S-star (Antonini et al. 2011; Kobayashi et al. 2012). In all other cases when the binary is close to a parabolic orbit, the primary to secondary mass ratio does not change the ejection (capture) probability. This reason is that the relatively small velocity of the primary causes capture/ejection if it orbits the binary mass center against/with the orbit around the SMBH (Kobayashi et al. 2012).

Overall, the Hills-scenario is the best fitting one. However, this is partly due the fact that it has more free parameters than the local scenarios. Especially nearly everything outside of the central arcsecond remain uncertain. Perets (2009) made the first steps in using the HVS and S-star properties together for constraining their origin. However, since nearly all S-stars are younger and more massive than nearly all HVSs, he could not compare

the exact same population. This mass effect is apparent in the study of Zhang et al. (2012): they find that there are more S-stars compared to HV-stars than expected. They correct this for their preferred model, which is formation from the clockwise disk (Lu et al. 2010), by an IMF slope of -1.6. In case of formation from binaries via the Hills mechanism a top heavy IMF with a slope flatter than -1.6, is necessary to match observation and Hills mechanism modeling in Zhang et al. (2012). Possibly they define the mass interval of S-stars to be too narrow ( $7 - 15 M_{\odot}$ ). This narrow mass range increases the number of HV-stars with respect to S-stars. The need for a top-heavy IMF is qualitatively consistent with the single generation Salpeter IMF of the S-stars. Apart from a top heavy IMF, also the overabundance of close binaries for massive stars (compare Duquennoy & Mayor (1991) and Sana et al. 2012) can cause a more top-heavy S-star mass function than usual. Further, non-continuous star formation with a recent burst can increase the fraction of S-stars compared to the simple model of Zhang et al. (2012).

Now I look on the question whether the Hills scenario can explain all B-stars in the GC (Perets & Gualandris 2010). The co-rotation of the brighter B-stars with the disk (Bartko et al. 2010) makes it likely that not all B-stars have the same origin as the S-stars. Probably most bright B-stars ( $14 < m_{K_s} < 15$ ) outside the central arcsecond formed together with the O-stars in the disk, while the fainter stars in the same radial range have the same random angular momenta as the S-stars (Bartko et al. 2010). Thus, the origin of the B-stars is probably complex and cannot be explained by single mechanism for all stars. For more detailed dissections of the B-star origin by mass and maybe also radius, more B-star detections are necessary.

## 1.8 The Supermassive Black Hole Sgr A\*

Already in the very first radio data the coordinates of the brightest position, which were obtained by extrapolation, were consistent with the center of the Milky Way (Jansky 1932, 1933). This was confirmed later by Reber (1944). With higher resolution this emission was resolved into different sources. Sgr A is the name of the brightest radio source in Sagittarius (Piddington & Minnett 1951), which then was suggested as the nucleus of the Milky Way by McGee & Bolton (1954), see Goss & McGee (1996) for the history. With further increased resolution Sgr A was separated in Sgr A West and Sgr A East by Downes & Martin (1971). Finally, Balick & Brown (1974) separated Sgr A\*, which at this time and for many years to follow, was an unresolved point source, from the surrounding HII region Sgr A West.

This search was motivated by Lynden-Bell & Rees (1971) who proposed that also the Milky Way contains a supermassive black hole (SMBH), a dormant quasar (Lynden-Bell 1969; Schmidt 1963). Soltan (1982) quantified this dead quasar argument by integration the quasar luminosity function to redshift 0 to derive a black hole mass of about  $10^5 M_{\odot}$  per cubic Megaparsec nowadays. Now this argument is known as the Soltan argument. In addition to discussing SED arguments for an SMBH in the Milky Way, Lynden-Bell & Rees (1971) suggested to weigh it by measuring gas velocities close to it. Wollman et al. (1977),

Lacy et al. (1979), Serabyn & Lacy (1985), Schwarz et al. (1989), and Roberts et al. (1996) measured velocities of different gas components down to  $3''$  distance to Sgr A\*. The derived mass of  $3 \times 10^6 M_{\odot}$  within  $r < 0.13$  pc by Roberts et al. (1996) was already six times more than the expected stellar mass within this radius. However, more exotic stellar populations with many dark remnants could also be an explanation for the high mass close to the center. Since gas can be influenced not only by gravity, and because most luminosity of the GC is not associated with Sgr A\*, some (e.g. Allen & Sanders (1986); Ozernoy (1989); Rieke et al. (1989); Kormendy & Richstone 1995) concluded that Sgr A\* was not a convincing case for an SMBH.

Thus stellar velocities were needed. The earlier stellar velocity measurements for constraining the mass used velocities derived from the strong CO band-heads of late-type stars, either from single star velocities (Sellgren et al. 1987; Rieke & Rieke 1988) or beam integrated dispersion and velocities (McGinn et al. 1989; Sellgren et al. 1990). The results varied: from no evidence for a black hole (Rieke & Rieke 1988) to an SMBH with a mass of  $(5.5 \pm 1.5) \times 10^6 M_{\odot}$  (Sellgren et al. 1990). The mean of the derived SMBH masses using old stars (Genzel et al. 1996; Haller et al. 1996) is around  $2.5 \times 10^6 M_{\odot}$ . Possibly, the reason for the difficulty of deriving the right black hole mass from the late-type stars is the small number of later stars truly close to the SMBH, due to their shallow radial distribution, see Section 1.5.

The detection of the O-stars (see Section 1.6) was first used as an argument against an SMBH, since its tidal force makes star formation close to it more difficult (Sanders 1992). However, since they are more concentrated on Sgr A\* than the late-type stars, they were used to probe the gravitational potential closer to Sgr A\*. Krabbe et al. (1995), Haller et al. (1996), and Genzel et al. (1996) found a nearly constant mass between about 0.1 and 1 pc, of about  $3 \times 10^6 M_{\odot}$ , resulting in a density of  $10^9 M_{\odot}/\text{pc}^3$  and  $M/L_K > 100$  in the center. The modeling of Genzel et al. (1996) excluded most non-BH explanations for the central mass. Only a single compact object (likely an SMBH) or a cluster of stellar mass black holes (Morris 1993) were still considered possible. With the discovery of the spatial orientation of the O-stars in mainly one disk, it was possible to determine more accurate SMBH masses from them. Beloborodov et al. (2006) used an orbital roulette technique for the clockwise disk to derive a mass of  $(4.3 \pm 0.5) \times 10^6 M_{\odot}$ , assuming  $R_0 = 8$  kpc. With the same distance Schödel et al. (2009) used the Leonard & Merritt (1989) mass estimator for deriving a mass of  $4.5 \times 10^6 M_{\odot}$  from the proper motions of most early-type stars. (Since some stars out to  $25''$  are used for this estimate, this mass includes also a part of the nuclear cluster.)

Diffraction limited images in the near-infrared (Hofmann et al. 1992) allowed resolving of individual stars (the S-stars, see Section 1.7) closer than  $1''$  to Sgr A\*. Measuring their proper motions (Eckart & Genzel 1996; Genzel et al. 1997) was then the next step to conclude that Sgr A\* is indeed a single compact object. Genzel et al. (1997) showed that the  $2.6 \times 10^6 M_{\odot}$  within the innermost stars is concentrated to  $2.2 \times 10^{12} M_{\odot}/\text{pc}^3$ . Since no such dense stellar remnant cluster is stable against collapse for more than  $10^7$  yrs (Maoz 1995; Genzel et al. 1997), the concentration must be a SMBH or something more exotic, like e.g. a boson star (Torres et al. 2000) or a fermion ball (Viollier et al.

1993; Munyaneza & Viollier 2002). Later, measurements of accelerations (Ghez et al. 2000; Eckart et al. 2002) and finally orbits (Schödel et al. 2002; Ghez et al. 2003) of these stars made it obvious that the mass depends not on the details of the fitted models but can be also obtained with simple Keplerian physics. In Schödel et al. (2002) the central mass concentration in the extended mass Plummer model of more than  $10^{17} M_{\odot}/\text{pc}^3$  excludes also most fermion balls. This progress convinced also skeptics from the early nineties and the Milky Way's SMBH is now the best case for an SMBH (Kormendy & Richstone 1995; Kormendy 2004).

The current mass determinations (Gillessen et al. 2009; Ghez et al. 2008) from orbit fitting yield consistently a mass of about  $(4.0 \pm 0.05) \times 10^6 M_{\odot}$  for a fixed distance of  $R_0 = 8$  kpc. The orbit fitting of Gillessen et al. (2009) shows that Sgr A\* is within 2 mas of the position of the central mass. Because there is a big mass close to Sgr A\* and because the proper motion of Sgr A\* is within 1 km/s of zero (Backer 1996; Reid & Brunthaler 2004), it is possible to conclude from equipartition (excluding very unlikely geometries) that Sgr A\* has  $M > 4 \times 10^5 M_{\odot}$  (Genzel et al. 1997; Reid & Brunthaler 2004; Genzel et al. 2010). From the small size of Sgr A\* obtained with mm-VLBI observations (Rogers et al. 1994; Doeleman et al. 2008) of about 3.7 times the event horizon of a  $4.4 \times 10^6 M_{\odot}$  SMBH at 1.3 mm (Doeleman et al. 2008) it can be deduced that Sgr A\* has a density of at least 0.5 % of the density of an SMBH of  $(4.4 \pm 0.4) \times 10^6 M_{\odot}$  (Genzel et al. 1997; Reid & Brunthaler 2004; Genzel et al. 2010). In the future the imaging of the black hole's shadow with (sub-) mm-VLBI (Weintroub 2008) or the astrometry of an orbit of a hotspot with a 20 min period with GRAVITY (Eisenhauer et al. 2008) may probe even deeper into the potential and further confirm or falsify the concepts general relativity and black holes (Einstein 1916; Schwarzschild 1916; Kerr 1963).

Sgr A\* is now firmly detected in the radio down to  $350 \mu\text{m}$  (Serabyn et al. 1997; Shcherbakov et al. 2012), in the infrared between  $4.7 \mu\text{m}$  and  $1.45 \mu\text{m}$  (Genzel et al. 2003; Hornstein et al. 2007; Yusef-Zadeh et al. 2009) and in the X-rays between about 2 and 10 keV (Baganoff et al. 2001; Porquet et al. 2003). Most energy is emitted around  $800 \mu\text{m}$ . The total luminosity of Sgr A\* is  $260 L_{\odot}$ , which is only about  $2 \times 10^{-9} L_{\text{Edd}}$  (Genzel et al. 2010). This low energy output was used in the past as an argument against the black hole nature of Sgr A\* (Allen & Sanders 1986; Kormendy & Richstone 1995) and is still not easy to understand. The gas inflow rate to the Galactic Center decreases with radius (Genzel et al. 2010), but also at the innermost measurement at about  $50 R_S$  it is with about a few  $10^{-8} M_{\odot}/\text{yr}$  much too large (a factor 1000 assuming perfect mass to energy conversion) for explaining the low luminosity with standard accretion (Genzel et al. 2010). Thus, the accretion must occur in a radiatively inefficient accretion flow (RIAF). Compatible with the observed radio spectrum are an advection-dominated accretion flow (Yuan et al. 2003) or a short jet (Falcke et al. 2000). Both models are probably simplifications of the reality which likely contains both a jet and an accretion flow. To get a more realistic picture, general relativistic magneto-hydro-dynamic simulations are necessary (Mościbrodzka et al. 2009; Dexter et al. 2010). From these simulations, an accretion disk, which is tilted compared to the spin of the SMBH (Dexter & Fragile 2012), currently fits the observations best.

Apart from this steady emission there is also variable emission (Baganoff et al. 2001; Genzel et al. 2003), for which the variability increases with frequency (Genzel et al. 2010). The X-ray variability seems to occur mostly in distinct events (flares) of up to 200 times the quiescent brightness (Porquet et al. 2003). Probably, the variation of the radiation originating from close to the SMBH is even bigger, since the quiescent emission originates likely from the more extended Bondi accretion region (Shcherbakov & Baganoff 2010). The X-ray flux distribution is not yet quantitatively analyzed, in contrast to the near-infrared (Dodds-Eden et al. 2011), because the faintness in the faintest X-ray state makes such an analysis difficult. The X-ray flares are associated with simultaneous near-infrared flares (Eckart et al. 2004; Marrone et al. 2008; Dodds-Eden et al. 2009), but the flux ratio between the two bands is not constant, see Trap et al. (2011). In the NIR it is unclear if bright flares (Genzel et al. 2003; Dodds-Eden et al. 2011) are different from low level variations. Either they constitute distinct flares on top of quasi steady state emission (Genzel et al. 2003, 2010; Dodds-Eden et al. 2011), or they are only the brightest excursions from a single state, which consists of all brightness levels of Sgr A\* (Dodds-Eden et al. in prep. and Witzel et al. 2012). In some of these bright flares, periodic fluctuations with a period of about 20 minutes are detectable (Genzel et al. 2003), which are for some flares rather significant (Meyer et al. 2006). However, when large data sets are analyzed together, this period is not significant compared to a red noise model which has a break in the slope around 100 minutes (Do et al. 2009; Meyer et al. 2009; Witzel et al. 2012). The 20 min period could be a sign of an orbiting hot spot close to the last stable orbit (Genzel et al. 2003). In the future, GRAVITY (Eisenhauer et al. 2008) will likely be able to test this model by measuring the position of Sgr A\* accurately enough to detect the motion of a hot spot on the last stable orbit.

The emission mechanism of the NIR infrared emission is probably synchrotron emission (Yuan et al. 2003). This is supported by the linear polarization of the NIR event (Genzel et al. 2003; Eckart et al. 2006). The x-ray emission during flares is either inverse Compton or also synchrotron emission (Yuan et al. 2003, 2004). At least for one bright NIR/X-ray flare the synchrotron mechanism is preferred (Dodds-Eden et al. 2009).

There is also some radio and sub-mm variability seen, see e.g. Herrnstein et al. (2004), Mauerhan et al. (2005), Yusef-Zadeh et al. (2006) and Shcherbakov et al. (2012). In this wavelength range the variability is at most a factor 3 from peak to valley (Zhao et al. 2003). The typical variability is smaller, about 20 %, at 850  $\mu\text{m}$ , see e.g. Haubois et al. (2012). Marrone et al. (2008) and Eckart et al. (2008) propose that this variability is partially caused by flares which are delayed with respect to shorter wavelengths. These delayed radio flares could be caused by adiabatic expansion of a blob which becomes transparent later at longer wavelengths (Marrone et al. 2008; Eckart et al. 2008). However, it is unclear whether the brightening at different wavelengths is not only coincidentally close in time (Dexter & Fragile 2012). In the model of Dodds-Eden et al. (2010) the submillimeter variability are dips following flares at shorter wavelength. The dip is caused by the energy loss in the accretion flow. The fact that the delay is similar for most reported cases (Morris et al. 2012) makes the case stronger for a true relation. To solve this issue, a combined analysis of a lot of sub-mm and near-infrared simultaneous data without preselection

of flares is probably necessary.

Apart from this current variability, which leads at most to a doubling of the bolometric luminosity, there is also evidence that Sgr A\* was much brighter about 100 years ago (Sunyaev et al. 1993; Koyama et al. 1996; Ponti et al. 2010; Capelli et al. 2012). Its presence is deduced from scattered X-ray (primarily Fe-K $\alpha$  line) emission at GMCs in the CMZ. However, also the brightest X-ray flux (Inui et al. 2009; Terrier et al. 2010) of about  $3 \times 10^{39}$  ergs/s (nearly  $10^7$  times more than today's quiescent radiation in the X-rays) is still much less than the Eddington (1926) limit.

Currently a gas cloud, possibly originating from winds of massive stars (Cuadra et al. 2005), is falling toward the SMBH (Gillessen et al. 2012). Some of its gas will probably be accreted to the SMBH (Schartmann et al. 2012). With a mass of about  $3 M_{\oplus}$  (Gillessen et al. 2012; Burkert et al. 2012) the gas cloud could sustain Eddington accretion (assuming 10% efficiency in the conversion of mass to energy) for only 3000 seconds. In one model of Burkert et al. (2012), the shell model, in which the cloud is part of a larger shell-like structure, the mass is 60 times larger, but still not enough to turn Sgr A\* into a quasar. Assuming that Sgr A\* in its brightest phase (Inui et al. 2009) radiated 10 % of its energy in the X-rays, a  $3 M_{\oplus}$  gas cloud can power this luminosity for only 1.9 yrs, less than the duration of the outburst responsible for the X-ray reflections (Capelli et al. 2012). On the one hand, the mass in the shell model (Burkert et al. 2012; Schartmann et al. 2012) or a slightly larger cloud would be sufficient to power this outburst. On the other hand, it is possible that the energy fraction in the X-rays in this outburst was smaller than 10%, then the energy released from this outburst would be larger. In this case small gas clouds, caused by stellar winds (Cuadra et al. 2005), cannot anymore explain the past X-ray activity. Further, it is not obvious that an infalling gas cloud, can cause a light curve consistent with the observed complex X-ray light curve (Capelli et al. 2012).

## 1.9 Galaxy Overview and Transition

We have seen that the Galaxy and its center harbor different components. In Figure 1.11 these components are visible. Different components dominate at different distances. Star counts offer first clues about these components. However, in order to really understand the nature of the components (e.g. finding disks) and measure masses which can lead to the discovery or exclusion of dark components like black holes, it is necessary to measure motions. In the GC both radial velocities and proper motions can be obtained.

This thesis compiles the work from the last four years, presenting four papers. In the first, I analyze the method to get proper motions, astrometry, see Chapter 2. This is done on near-infrared adaptive optic images, which are the currently best suited instrument/telescope combination for resolving stars in the GC. Then I apply this tool astrometry (together with other techniques) on the stellar group IRS13E, which could contain an intermediate mass black hole, see Chapter 3. In Chapter 4, I derive the extinction curve toward the GC and apply it to the distance measurement toward the GC using the red clump, and for determining the properties of the dust in Galactic and nuclear disk. The

mass of the SMBH in the GC is well determined. However, the mass, luminosity, shape and size of the nuclear cluster around it, is much less well determined. Therefore, in Chapter 5 I measure the motions of thousands of stars in three dimensions to derive the mass of the nuclear cluster. Further, I derive a map density map of the cluster to determine its size and ellipticity. I use the results obtained to put the nuclear cluster in the context of the Galaxy and other nuclear clusters.

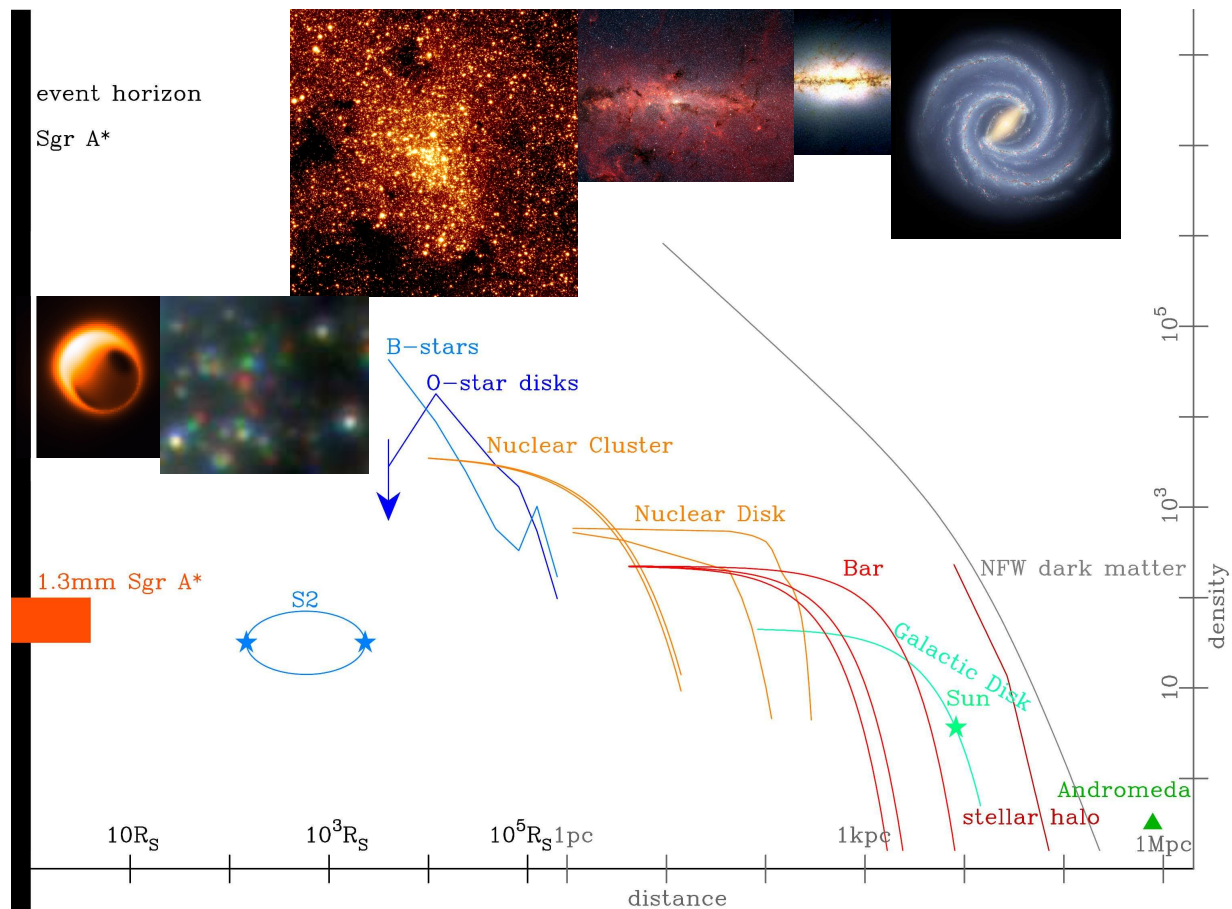


Figure 1.11 Components of the Galaxy: the top insets show the main components. Projected density is used for the nuclear cluster and further in, and space density further out. The different densities are offset to each other. Their ordering shows approximately which component dominates the light in each radial range. The halo components are shifted upwards for visibility. The colors of the lines indicate the age of the components: blue is younger than red. The sources are: event horizon,  $M_{\text{SMBH}}$  from Gillessen et al. (2009) assuming a Schwarzschild (1916) metric, mm size of Sgr A\*: Doeleman et al. (2008), early-type stars: Bartko et al. (2010), nuclear cluster: my own light decomposition in Chapter 5, nuclear disk: Launhardt et al. (2002), bar: Dwek et al. (1995); Launhardt et al. (2002), Galactic Disk with a scale length of 3.2 kpc, stellar halo: Deason et al. (2011), dark halo: Navarro et al. (1997). All assume  $R_0 = 8.2$  kpc (Genzel et al. 2010). The images in the top show the black hole shadow (image credit: [www.eventhorizontelescope.org](http://www.eventhorizontelescope.org)), the moving S-stars (my creation from NACO Ks-images, RGB from 2002/07/13), the central  $86''^2$  of the nuclear cluster (my creation from an NACO Ks-image), the central molecular zone in the mid-infrared (image credit: <http://www.spitzer.caltech.edu/images>), the bulge in the near-infrared ([www.atlasoftheuniverse.com/2mgalaxy.jpg](http://www.atlasoftheuniverse.com/2mgalaxy.jpg)) and a Milky Way model (image credit: [www.nasa.gov/missionpages/spitzer/multimedia/20080603a.html](http://www.nasa.gov/missionpages/spitzer/multimedia/20080603a.html)).



# Chapter 2

## What is Limiting Near-infrared Astrometry in the Galactic Center?

**Original publication:** T. Fritz, S. Gillessen, S. Trippe, T. Ott, H. Bartko, O. Pfuhl, K. Dodds-Eden, R. Davies, F. Eisenhauer & R. Genzel, 2010, *What is limiting near-infrared astrometry in the Galactic Centre?* MNRAS, 401, 1177

**Abstract:** We systematically investigate the error sources for high-precision astrometry from adaptive optics based near-infrared imaging data. We focus on the application in the crowded stellar field in the Galactic Center. We show that at the level of  $\lesssim 100 \mu\text{as}$  a number of effects are limiting the accuracy. Most important are the imperfectly subtracted seeing halos of neighboring stars, residual image distortions and unrecognized confusion of the target source with fainter sources in the background. Further contributors to the error budget are the uncertainty in estimating the point spread function, the signal-to-noise ratio induced statistical uncertainty, coordinate transformation errors, the chromaticity of refraction in Earth's atmosphere, the post adaptive optics differential tilt jitter and anisoplanatism. For stars as bright as  $m_K = 14$ , residual image distortions limit the astrometry, for fainter stars the limitation is set by the seeing halos of the surrounding stars. In order to improve the astrometry substantially at the current generation of telescopes, an adaptive optics system with high performance and weak seeing halos over a relatively small field ( $r \lesssim 3''$ ) is suited best. Furthermore, techniques to estimate or reconstruct the seeing halo could be promising.

### 2.1 Introduction

The Galactic Center (GC) is a unique celestial laboratory. It hosts a super massive black hole (SMBH) the existence of which is now widely accepted in astronomy (Wollman et al. 1977; Genzel et al. 1996; Ghez et al. 1998; Schödel et al. 2002). The tightest constraints on the mass have been put by observing the motions of individual stars as they orbit the SMBH (Ghez et al. 2008; Gillessen et al. 2009). The statistical error of the mass is as low

as  $\approx 1.5\%$ , the systematic error is considerably higher with  $\approx 10\%$  owed to the uncertainty in  $R_0$  of  $\approx 5\%$ , the distance to the GC.

These astonishing measurements rely on high-angular resolution, adaptive optics (AO) assisted, near-infrared observations, obtained at large telescopes; namely the Keck and VLT facilities. From imaging data astrometric positions are derived, reaching an accuracy of  $\approx 300 \mu\text{as}$ . This is a factor of 200 smaller than the maximum possible image resolution of  $\approx 60 \text{ mas}$  in K-band, while the apparent orbit of the most important star of these so-called S-stars, S2, measures  $\approx 190 \text{ mas}$ .

With the black hole paradigm now being well established, the efforts turn toward detecting post-Newtonian effects. From General Relativity, one expects a prograde periastron shift of  $0.2^\circ$  per revolution of 15.8 years for S2 (Rubilar & Eckart 2001). This corresponds to an apparent position shift of  $\approx 800 \mu\text{as}$ , which however is not as easily detected as it seems, since it needs to be measured from the same data from which also the orbital elements have to be determined. Secondly, a population of dark stellar remnants such as stellar mass black holes and neutron stars might be present around the SMBH (Morris 1993). Such an extended mass component will lead to a retrograde periastron shift. If for example  $\approx 0.1\%$  of the mass inside the S2 orbit were extended, the resulting retrograde shift would cancel the relativistic prograde precession (Rubilar & Eckart 2001). Detecting either of these shifts would be astrophysically extremely interesting.

Future ground-based telescopes will further increase the spatial resolution accessible, thus potentially increasing the astrometric accuracy further. Trippe et al. (2010) investigate in general the astrometric performance of an extremely large telescope. Weinberg et al. (2005) simulated the expected advance in monitoring stellar orbits in the GC when using an extremely large telescope, concluding that the upcoming facilities indeed will be capable of measuring the post-Newtonian effects and that mass of and distance to Sgr A\* can be determined with unprecedented precision.

High-precision astrometry is important for other scientific cases, too. Intermediate mass black holes might be found by detecting accelerations of stars in the vicinity of the black hole. Potential sites are for example  $\omega \text{ Cen}$  (Noyola et al. 2008; Anderson & van der Marel 2010) or the compact stellar group GC IRS13E (Maillard et al. 2004; Schödel et al. 2005; Fritz et al. 2010). Another area where AO-assisted high-resolution imaging profits from excellent astrometric capabilities is the domain of binaries and substellar companions (Chauvin et al. 2004; Neuhäuser et al. 2007, 2008; Köhler et al. 2008; Lagrange et al. 2009; Kervella et al. 2013).

This paper aims at investigating the limits of astrometry, in particular in the GC. This is of great value both for current and future studies of stellar orbits. Our approach is to estimate the various error sources mostly empirically, i.e. from existing VLT data. The main parameters characterizing the reachable accuracy for any given star are its magnitude and distance from Sgr A\*, and for any given image the Strehl ratio. The empirical numbers used were determined for the VLT NIR-AO imager NACO, operated in Ks-band with a pixel scale of  $13 \text{ mas/pix}$ . The field of view being of interest here is  $\Theta_{\text{FoI}} = \pm 2''$ , given by the apparent size of the GC stellar system. We concentrate on the data set from 13 March 2008, which was of good quality (Strehl ratio larger than 30%) and therefore is well-suited

to study systematic effects<sup>1</sup>. In that sense, this paper is a case study, but the dependencies on the Strehl ratio which we exploit make the results applicable for a wider range of data.

## 2.2 Statistical Uncertainty

The fundamental limit to astrometry for diffraction limited data is given by the number of photons recorded and the image resolution, with higher SNR and smaller point spread function (PSF, FWHM  $\Theta$ ) increasing the positional accuracy. For a circular aperture of size  $D$  and an observation wavelength  $\lambda$  one has

$$\Theta_{\text{FWHM}} = 1.028 \frac{\lambda}{D} . \quad (2.1)$$

Lindgren (1978) gives the following equation for the position error:

$$\sigma_x = \frac{1}{\pi} \frac{\lambda}{D} \frac{1}{\text{SNR}} . \quad (2.2)$$

We have verified this equation explicitly by simulating different SNR for a simple Gaussian PSF. The sampling was chosen to be similar to VLT data from imaging GC observations with  $\Theta_{\text{FWHM}} \approx 6$  pix which occurs for a Strehl ratio of 18%<sup>2</sup>. We generated a set of noise images, in each of which the PSF was added. First, we searched the optimum radius for the source region for the given sampling. We determined the SNR as ratio of flux inside a certain radius and the standard deviation of the flux inside the same area in the noise image. The optimum was 4 pixels (Figure 2.1, left), independent from the peak intensity. Next, we varied the SNR by adding the PSF several times to each noise map with the peak intensity ranging from  $0.3 \times$  to  $200 \times$  the noise level. We determined the position of the PSF by a Gaussian fit to each image. The standard deviation over the set of noise images per intensity then measures the positional uncertainty for that intensity level. The corresponding SNR was calculated with the optimum radius. We plot the positional error as a function of SNR in Figure 2.1, right, which shows that our explicit simulation matches equation (2.2). While the  $1/\text{SNR}$  behavior is obvious, this checks mainly that the numerical factor in equation (2.2) correctly describes the accuracy for the optimum signal extraction.

Empirically, we find for the VLT data that a source in K-band creates a total current (photo electrons per second) on the detector (in its high dynamic mode with the readout scheme double read-reset-read) of

$$\Sigma_{\text{pix}} \dot{n}_{\text{e, obj}} [\text{el}/\text{sec}] = 10^{0.4(25.4 - m_K)} \quad (2.3)$$

If source photon noise were the only error source, for a  $m_K = 14$  source (i.e. S2), within one second the position uncertainty would drop to  $50 \mu\text{as}$ . However, also the noise of

<sup>1</sup>We are using data from ESO program 179.B-0261.

<sup>2</sup>This is taken from the actual data, spanning the years 2002-2009. Since 2007 we are getting consistently smaller FWHM values and higher Strehl ratios.

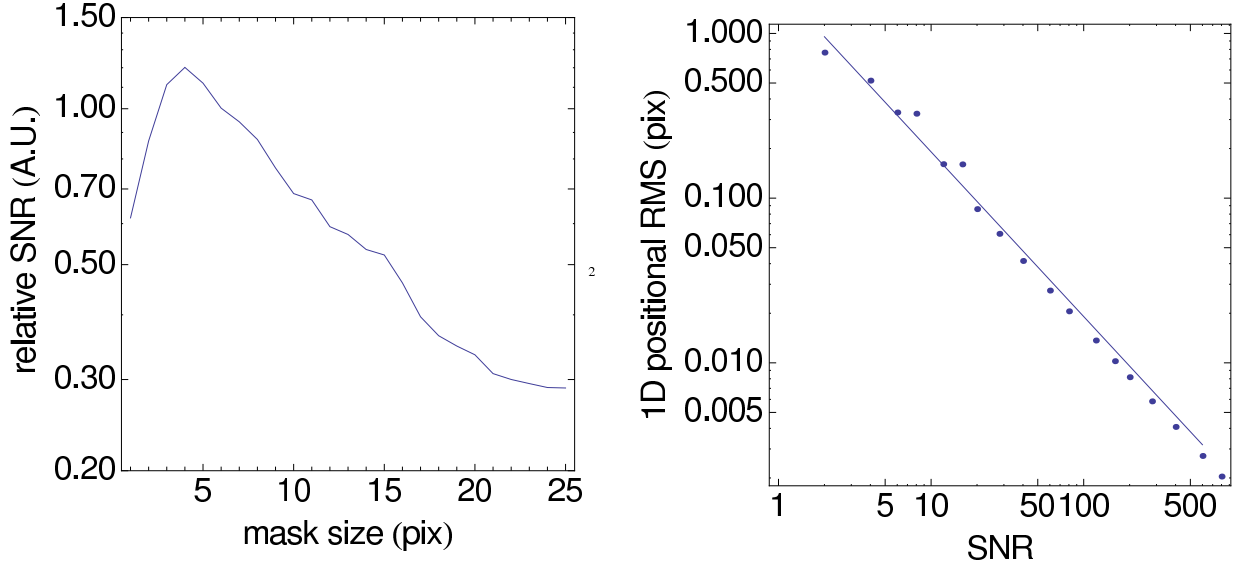


Figure 2.1 Left: SNR for a source with  $\text{FWHM} = 6$  pix and Gaussian shape in a noise image as a function of the integrating radius used, showing that a source area with  $r = 4$  pix is optimal. Right: The data points show the positional uncertainty in simulated images as function of the SNR. The solid line is the prediction from equation (2.2).

the sky background and the read noise of the detector have to be taken into account in equation (2.2).

In a single pixel in a single-pointing, combined frame the noise after the usual data reduction steps of sky subtraction and flat fielding should be (assuming that the flat field on average equals 1 and that  $N_{\text{sky}}$  frames with the same exposure time as the  $N_{\text{obj}}$  object frames were averaged for the sky)

$$\sigma_e^2 = \sigma_f^2 s^2 + \frac{n_{e,\text{obj}}}{N_{\text{obj}}} + \left( \frac{1}{N_{\text{obj}}} + \frac{1}{N_{\text{sky}}} \right) \times (\sigma_{\text{RON}}^2 + n_{e,\text{sky}}), \quad (2.4)$$

where  $\sigma_f = 0.15\%$  is the empirically determined relative noise of the flat field,  $s = (n_{e,\text{obj}} - n_{e,\text{sky}})/f$  the reduced signal per pixel and  $\sigma_{\text{RON}} = 46.2$  the read noise of the detector in electrons. Typically, the sky brightness per pixel for the given setup is

$$\dot{n}_{e,\text{sky}}[\text{el}/\text{sec}] = 21.5. \quad (2.5)$$

The solid lines in Figure 2.2 illustrate the noise behavior for a single pixel as given by equation (2.4). With the noise (equation 2.4) and the signal (equation 2.3), it is straight forward to evaluate equation (2.2) if one assumes a certain PSF shape. As a simple example, we show the resulting positional uncertainty for a case in which the position is estimated from a Gaussian shaped PSF-core with a FWHM of 6 pixels that contains 30% of the stellar light. As above, the light from inside a 4-pixel radius was used. The error so obtained represents the statistical limit to the positional accuracy for a single, reduced

frame. Usually, astrometry is done on combined objects frames with varying pointing positions ('mosaics'). This improves the statistical precision limit by a factor  $\sqrt{N_{\text{pointing}}}$  compared to equation (2.4).

## 2.3 Astrometry in the GC

We briefly describe the method by which we obtain astrometric positions. The lack of any extragalactic background source in the NIR is one of the main obstacles for astrometry in the GC. Therefore all position measurements are relative to other sources in any given image. The link to the international celestial reference frame ICRF is only possible due to a set of SiO maser stars, which are both NIR and radio sources. The position vectors relative to Sgr A\* of the latter can be measured with high accuracy (Reid et al. 2003, 2007). The position and motion of Sgr A\* in the ICRF in turn is well known (Reid et al. 1999; Reid & Brunthaler 2004).

An additional complication is that with the current  $1k \times 1k$  NACO detector, a suitable sampling ( $\approx 4 \text{ pix}/\text{FWHM} = 13 \text{ mas}/\text{pix}$ , Trippe et al. 2010) is only reached for the central few arcseconds (depending on the dithering scheme), while the SiO maser stars are found out to  $20''$ . Therefore it is more practical to measure the SiO maser positions with a larger pixel scale ( $27 \text{ mas}/\text{pix}$  for NACO) and relate the finer scale to the coarser sampling by a set of reference stars that can be reliably detected in both scales. That also helps to overcome the large dynamic range needed, given that the brightest SiO maser star used for astrometry has a magnitude of  $m_K \approx 8.5$  (Blum et al. 2003; Reid et al. 2007) and that one is interested in the positions of stars as faint as  $m_K \approx 19$ .

In practical terms, the procedure is as follows: From a set of images, obtained between 2002 and 2009 in the  $27 \text{ mas}/\text{pix}$  scale, we derive astrometric positions and proper motions for a set of  $\approx 100$  reference stars. This relies on the work of Reid et al. (2007), which allows us to calculate the astrometric positions of the SiO maser stars for the given NIR epochs. We use mosaics corrected for their geometric distortion (Trippe et al. 2008) and a full, 6-parameter linear transformation to relate pixel and astrometric positions of eight SiO masers. For any given image in the  $13 \text{ mas}/\text{pix}$  scale we determine the PSF from the image and deconvolve it using the Lucy-Richardson algorithm (Lucy 1974). After beam restoration with a Gaussian beam we determine the stellar pixel positions by Gaussian fits to the positions, both to the reference stars and the sources targeted. The transformation used to link the astrometric reference star positions to their pixel positions is a 20-parameter, third order polynomial transformation, which should also implicitly correct for any large scale ( $5''$ ) image distortion. This is useful since for the smaller pixel scale we were not able to construct a reliable distortion model, indicative that the effect is fairly small (Trippe et al. 2008). For a more complete description of the procedure see Gillessen et al. (2009).

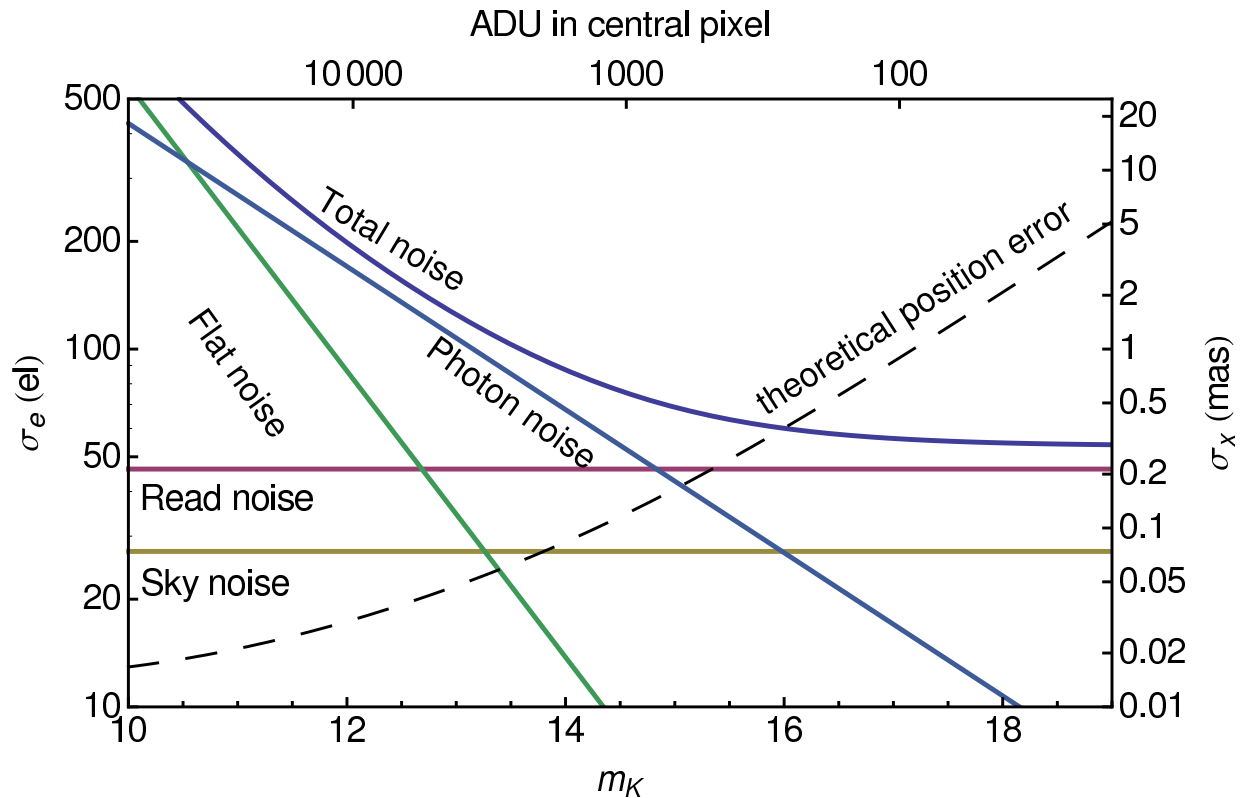


Figure 2.2 The solid lines (referring to the left ordinate) show the noise contributions per pixel as function of illumination according to equation (2.4) for a single image, which actually is the combination of two object and two sky frames of 17.2 sec each. (Our data is mostly obtained in a mode with 2 detector reads of 17.2 sec per data file, a setting that is chosen to avoid saturation effects for most of the stars and minimizes overheads.) The total noise at faint magnitudes is dominated by the read noise. For realistic data sets, we use more than two sky frames, such that the read noise contribution from the sky is reduced compared to this illustration. For brighter objects, the photon noise is the dominant contribution. The regime in which the noise of the flat becomes important already is in the highly non-linear regime of the detector which normally is not used. For the conversion to magnitudes, a sampling of 6 pix per FWHM and a Gaussian PSF that contains 30% of the light were assumed. The dashed line (referring to the right ordinate) gives the resulting positional error according to equation (2.2) for the total noise.

## 2.4 Systematic Uncertainties

A multitude of systematic uncertainties are present in the astrometric data, the most important ones being atmospheric turbulence, image distortions, unrecognized source confusion and uncertain PSF halos. The time scales involved are very different; atmospheric effects are present even in a single frame, while confusion of sources happens on time scales of years. The section discusses the error sources (roughly) by increasing time scale involved.

### 2.4.1 Fast Atmospheric Limitations

#### Anisoplanatism

Time variable refraction in Earth's atmosphere, induced by turbulence cells, blurs ground-based astronomical images, an effect which is called 'seeing'. For the observations discussed here, the seeing is partly corrected by the adaptive optics (AO) system. The resulting PSF is a superposition of a close to diffraction-limited core with a seeing-limited halo. Useful parameters to describe the performance of the AO are the Strehl ratio (SR; the ratio of measured central flux compared to the diffraction-limited central flux) and the FWHM of the PSF. The AO correction in our data is achieved with a single guide star (single-conjugate AO).

The tip-tilt component of the wavefront errors between any two objects in the field of view gets less and less correlated with increasing distance between the two objects, an effect which is called anisoplanatism. Complete decorrelation is reached for the so-called isoplanatic angle, which has a typical value of  $10'' - 20''$ . As a result of anisoplanatism, one observes random variations in the relative positions of any two objects. Anisoplanatism is seen as PSF elongation during individual exposures, and as residual, differential tilt jitter between successive frames.

#### Differential Tilt Jitter

The differential tilt jitter between any two stars in good approximation linearly increases with distance between the two stars. The effect averages out with exposure time. For a Komolgorov turbulence spectrum the dominant term of the differential tilt jitter scales with telescope diameter  $D$  and integration time  $t$  like (Cameron et al. 2009)

$$\begin{pmatrix} \sigma_{\parallel, \text{TJ}}^2 \\ \sigma_{\perp, \text{TJ}}^2 \end{pmatrix} = \alpha \begin{pmatrix} 3 \\ 1 \end{pmatrix} \theta^2 D^{-7/3} \frac{\tau}{t}. \quad (2.6)$$

The effect is  $\sqrt{3}$  times bigger in the direction connecting the two stars than perpendicular to it. The time constant  $\tau$  characterizes the time it takes a turbulence cell to move over the telescope aperture. The constant  $\alpha$  is related to the second moment of the atmospheric turbulence profile. A typical value, following from the numbers in Cameron et al. (2009), is  $\alpha \approx 3$  when  $\sigma$  is measured in mas,  $D$  in meters and  $\theta$  in arcseconds.

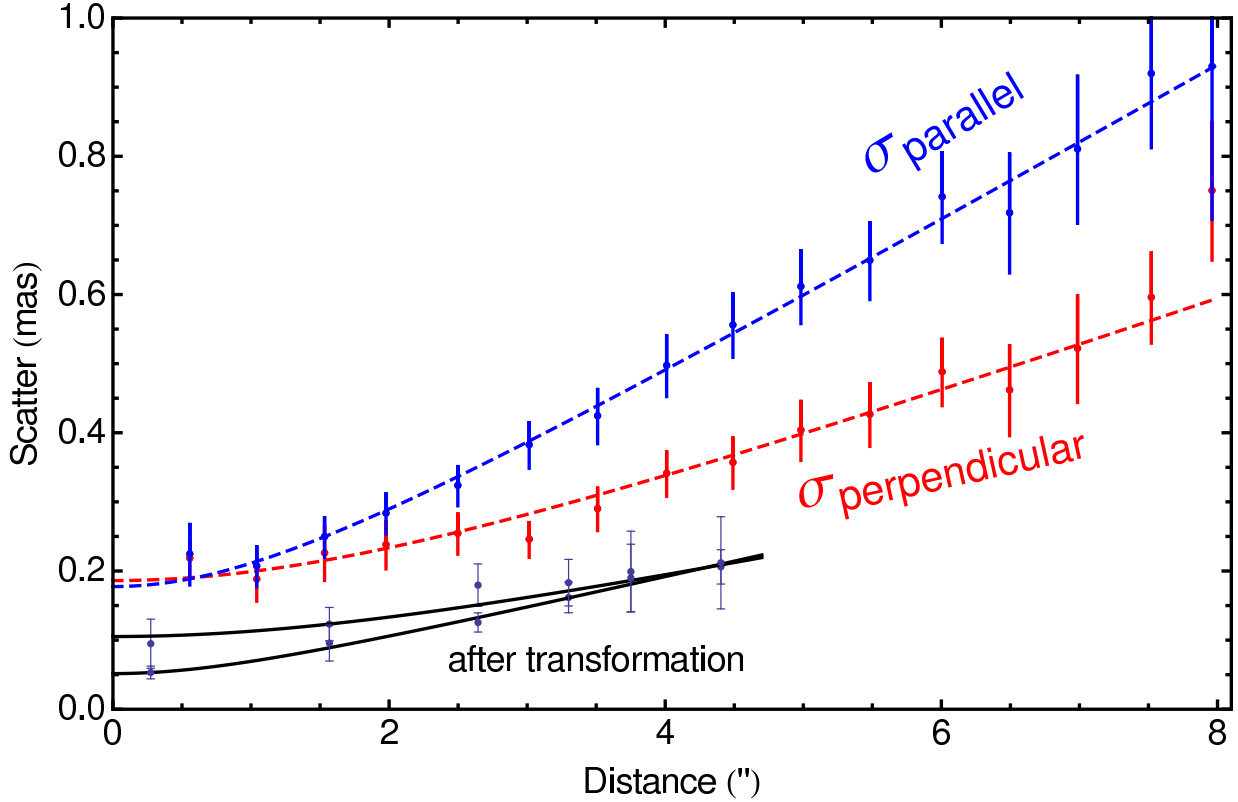


Figure 2.3 Differential tilt jitter in the data from 13 March 2008. The dashed lines show linear fits to the positional scatter between pairs of stars in the direction parallel or perpendicular to difference vector between the two stars. The empirical model used was  $\sigma^2 = \sigma_0^2 + \beta^2\theta^2$ . The fitted slopes  $\beta$  for large distances are  $0.114 \pm 0.002$  mas/'' (blue) and  $0.071 \pm 0.003$  mas/'' (red). The solid, black line and corresponding data show the remaining astrometric effect in R.A. and Dec. after a full linear transformation (the range is smaller since positions are counted from the center of the field then).

We looked for the effect in the data set from 13 March 2008 by calculating the variance of stellar distances in a sequence of subsequent exposures that were obtained at exactly the same pointing position. We decomposed the difference vectors into the directions parallel and perpendicular to the vector connecting the two respective stars. Figure 2.3 (dashed lines) shows the resulting scatter as a function of distance between the two stars. Clearly the differential tilt jitter is visible and the measured ratio  $\sigma_{\parallel}/\sigma_{\perp} = 1.62 \pm 0.05$  is consistent with the expected value of  $\sqrt{3}$ . Since we do not have the data to evaluate the turbulence profile for our observation, we can check for plausibility only. From the slope of the relation  $d\sigma_{\text{TJ}}/d\theta = 0.071 \pm 0.03$  and given the exposure time of 34.4 s we estimate the wind crossing time over the telescope aperture of 8 m to be 0.4 s, corresponding to a wind speed of  $v \approx 20$  m/s, which seems reasonable.

Since the field of interest  $\Theta_{\text{FOI}} = \pm 2''$  is practically always smaller than the isoplanatic

angle, the tilt jitter will act in a correlated way on all of the stars. Hence, the effect will to a large extent cancel out for astrometric positions defined as relative positions to a set of reference stars (Cameron et al. 2009). The effect of the corresponding full linear transformation (i.e. including shear terms) is shown for the test data in Figure 2.3 (solid lines). The remaining astrometric error for a single frame is  $< 0.2 \text{ mas}$  and in the center even  $< 0.1 \text{ mas}$ . Due to the mosaicking, that number will decrease further by  $\sqrt{N_{\text{frames}}}$  and for a typical data set of  $\gtrsim 70$  images differential tilt jitter should contribute less than  $20 \mu\text{as}$ . Hence, using a simple linear transformation is sufficient to effectively eliminate this error source. The more elaborate approach by Cameron et al. (2009) is not necessary for our current GC data sets.

### PSF Elongation

The AO corrects the tip-tilt jitter optimally for the the guide star. Since the exposure times are much longer than the time constant for the AO, the image retrieved can be thought as a superposition of many short images, each of which is centered on the guide star. As a result, the random errors from equation (2.6) vanish at the guide star and the image is sharpest there. Further away, the integrated jitter increases the PSF width with distance to the guide star, and the particular form of equation (2.6) leads to an elongation of the PSF in direction toward the guide star. Since the analysis uses a constant PSF (either for deconvolution or PSF fitting) when estimating stellar positions, the effect will lead to increased position errors.

We assessed the error by comparing the differences of extracted position from various PSF estimates, obtained from stellar images with similar brightnesses at different positions in the field of view. We used the high-quality data set from 13 March 2008. Using two different PSF estimates from the same region leads to a typical position difference of  $50 \mu\text{as}$ . When the two PSF estimates are extracted from two samples  $3.5''$  apart, we only find a small increase of the typical position difference to  $70 \mu\text{as}$ . At  $6''$  distance, the effect starts to hurt more severely since it reaches  $\approx 180 \mu\text{as}$ . At  $7''$  distance, it even reaches  $400 \mu\text{as}$ . These values illustrate the effect of the isoplanatic angle. It is worth noting that anisoplanatism can be significantly more severe for worse atmospheric conditions.

For the analysis, the effect will contribute only at a very low level, if the set of stars from which the PSF is constructed is chosen carefully; i.e. within  $\Theta_{\text{FoI}} \approx \pm 2''$  of the target region. In GC data sets, this can easily be achieved and therefore we expect anisoplanatism to be only a very small error contribution. If the size of the target region exceeds  $4''$ , as for example in the work of Trippe et al. (2008) or Schödel et al. (2009), the anisoplanatic effects should be taken into account for astrometric measurements by varying the PSF over the field.

### Comparison with Data

Figure 2.4 compares the expected position errors with the actual scatter in the data, using again the data set from 13 March 2008. We obtained the expected errors by simulating

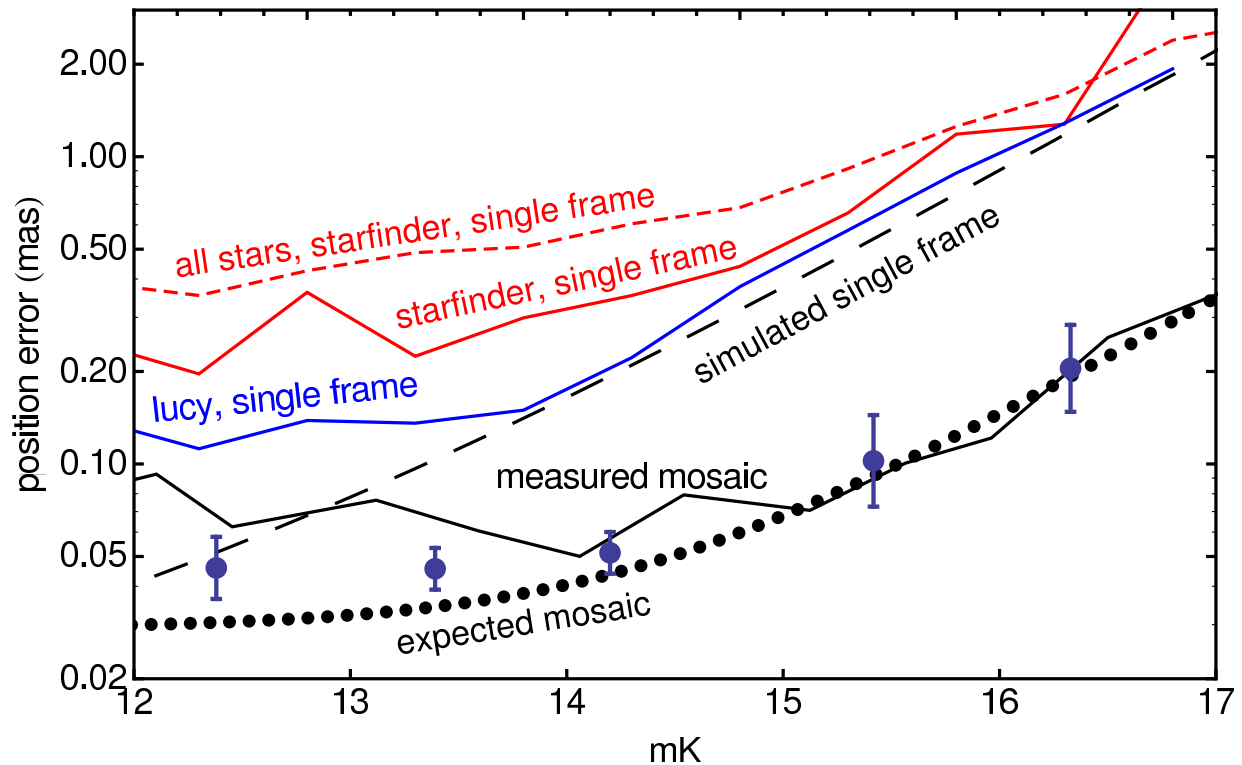


Figure 2.4 Empirical position errors as a function of stellar magnitude, estimated using a PSF extracted from the respective data. The red, dashed line indicates the errors for all stars found by STARFINDER in a single frame and is dominated by anisoplanatism at brighter magnitudes. The red, solid line shows the errors for isolated stars obtained from STARFINDER on the same single image in a restricted area (the central  $2''$ ,  $\Theta_{\text{FOI}}$ ). The blue line indicates for the same stars the errors obtained by applying a Lucy-Richardson deconvolution to the single frame, and fitting the sources with Gaussian functions. The black, dashed line shows the errors obtained by simulating isolated stars and finding them back. The black dotted line is showing the expectation for a mosaic, obtained by describing the blue line with an empirical function and square root scaling with the number of frames used in the mosaic. The black, solid line shows the measured errors on the mosaic which flatten at a level of  $\approx 70 \mu\text{as}$ . The data points show the measured, statistical errors for the mosaic from 13 March 2008.

isolated stars and remeasuring their positions, using a noise floor as measured in single frames and using the respective PSF also obtained from the data. The position scatter between subsequent single frames is a useful estimator for the position error due to the statistical limit and atmospheric turbulence, since the frames were taken with exactly the same pointing position. This means neither image distortions nor confusion events bias the scatter.

We find that compared to the simulations, star positions found by STARFINDER (Diolaiti et al. 2000) scatter as expected from anisoplanatism. The scatter gets reduced, if one restricts the analysis to stars that are sufficiently isolated in a small area ( $\Theta_{\text{FoI}} = \pm 2''$ ). For  $m_K > 15$ , the scatter is only moderately higher than in the simulation. In comparison, our technique of Lucy-deconvolving the image performs a bit better than STARFINDER and is for  $m_K > 14$  essentially as good as predicted by the simulation. The reason why STARFINDER is performing a bit worse might be that it was allowed to calculate a (spatially varying) background map for each single image, which however is not needed for the data. The additional degree of freedom then introduces extra noise, from which the deconvolution technique does not suffer. Both for STARFINDER and deconvolution, the brighter stars have a higher scatter than what one would expect from the simulations and the values reach a floor. Its level of  $\approx 125 \mu\text{as}$  is consistent with being the combination of PSF uncertainty (Section 2.4.4) and differential tilt jitter as present in Figure 2.3 (data after transformation).

The empirical curve for the deconvolution of a single frame was then parametrized by a simple model of type  $\sigma_x^2 = \alpha \sigma^2(m_K) + \sigma_0^2$ . For the given data,  $\alpha = 1.1$  and  $\sigma_0 = 100 \mu\text{as}$  are an excellent description of the measured errors. We scaled this relation by  $\sqrt{N_{\text{frames}}} = \sqrt{24}$  in order to estimate the expected positional uncertainty for a single-pointing mosaic (Figure 2.4). For  $m_K > 15$  the actual data (obtained again with deconvolution) follows the expected relation and flattens for sources with  $m_K \lesssim 14$  at about  $70 \mu\text{as}$ . This is the value as expected from the PSF uncertainty (Section 2.4.4) and the anisoplanatism over the field. Hence, we conclude that no additional terms come in by combining multiple frames to a single-pointing mosaic.

For comparison, we also show in Figure 2.4 (data points) the positional errors as obtained by comparing two mosaics created from subsamples using the data from 13 March 2008. The match with the simulated is actually a combination of the fact that  $1.5\times$  more single frames were used here for each submosaic, and that the error is composed of the fitting error plus the positional difference between the two submosaics.

## 2.4.2 Slow Atmospheric Limitations

### Differential Refraction

Refraction in Earth's atmosphere displaces stellar images toward the zenith by

$$R \approx \frac{n_0^2 - 1}{2n_0^2} \frac{p T_0}{p_0 T} \tan z \approx 44'' \tan z , \quad (2.7)$$

where  $z$  is the zenith angle of the observation and the constant of  $44''$  is the refraction constant for typical conditions at Paranal as evaluated from the refractive index  $n_0$  at standard conditions of  $p_0 = 1013.25$  mbar and  $T_0 = 273.15$  K, scaled by the current pressure and temperature. Since we are using relative astrometry, only the differential effect is relevant. It amounts to

$$\delta R \approx \Theta_{\text{FoI}}[\text{rad}] \times 44'' / \cos^2 z . \quad (2.8)$$

Numerically, this evaluates to values around  $3.5$  mas for  $z = 60^\circ$  and  $\Theta_{\text{FoI}} = \pm 2''$ . It would thus be a large error source. However, the effect is absorbed into the shear terms of the transformation; a full linear transformation leaves a remaining second order effect that is less than  $3 \mu\text{as}$ .

### Chromatic Effects

The dependence of the refractive index  $n$  on the observation wavelength (e.g. as given by Edlen 1953) for the H- and K-band and typical Paranal conditions is approximated by

$$n_1 \cdot 10^7 = 2029.94 - 2.87\lambda_2 + 2.16\lambda_2^2 - 1.44\lambda_2^3 + 0.92\lambda_2^4 \quad (2.9)$$

where  $n_1 = n - 1$  and  $\lambda_2 = \lambda[\mu\text{m}] - 2$ . Thus the atmosphere acts as weak spectrometer, as a result of which the effective position for a source is the weighted average of the wavelength dependent positions over the band (Helminiak 2009). The weighting factor is the number of photons per wavelength which in turn is the convolution of the input spectrum with the interstellar extinction and the atmospheric and instrumental transmission numbers. The size of the net effect grows quadratically with the bandpass used and hence narrow band filters help to suppress the atmospheric chromatic effects on the astrometry.

Figure 2.5 shows the resulting effect for black body type emission compared to a fictitious object with  $10^5$  K. For young, hot stars (most of the S-stars have  $T \approx 25000$  K, see Ghez et al. (2003) and Martins et al. 2008) the K-band measured positions for typical zenith angles are altered by  $\approx 20 \mu\text{as}$ . For stars with a temperature of  $6000$  K the K-band shift would be  $\approx 70 \mu\text{as}$ . Below  $5000$  K, the approximation as black body breaks down due to the presence of the broad CO absorption features around  $2.3 \mu\text{m}$ , and the shift does not get larger anymore but rather is close to 0 with a typical spread of  $< \pm 20 \mu\text{as}$  compared to the fictitious emitter.

Since our position measurements are relative to other sources in the field, the differential effect between reference stars and target sources is an error source for the positions obtained. The reference frame is constructed from early- and late-type stars in roughly equal numbers, such that in K-band it refers to coordinates shifted by  $\approx 10 \mu\text{as}$  compared to the fictitious object. Individual stars are then shifted again depending on their stellar type by  $\approx 10 \mu\text{as}$  compared to the coordinate system. Only G-type stars would experience a shift of  $\approx 50 \mu\text{as}$ ; but main sequence stars of that type are by far too faint to be detected in the GC field. The net effect for K-band based astrometry is thus very small.

For H-band data the effect is larger in the first place (Figure 2.5) and secondly late-type stars actually can be approximated by black bodies in H-band. For  $z = 40^\circ$  and a late-type

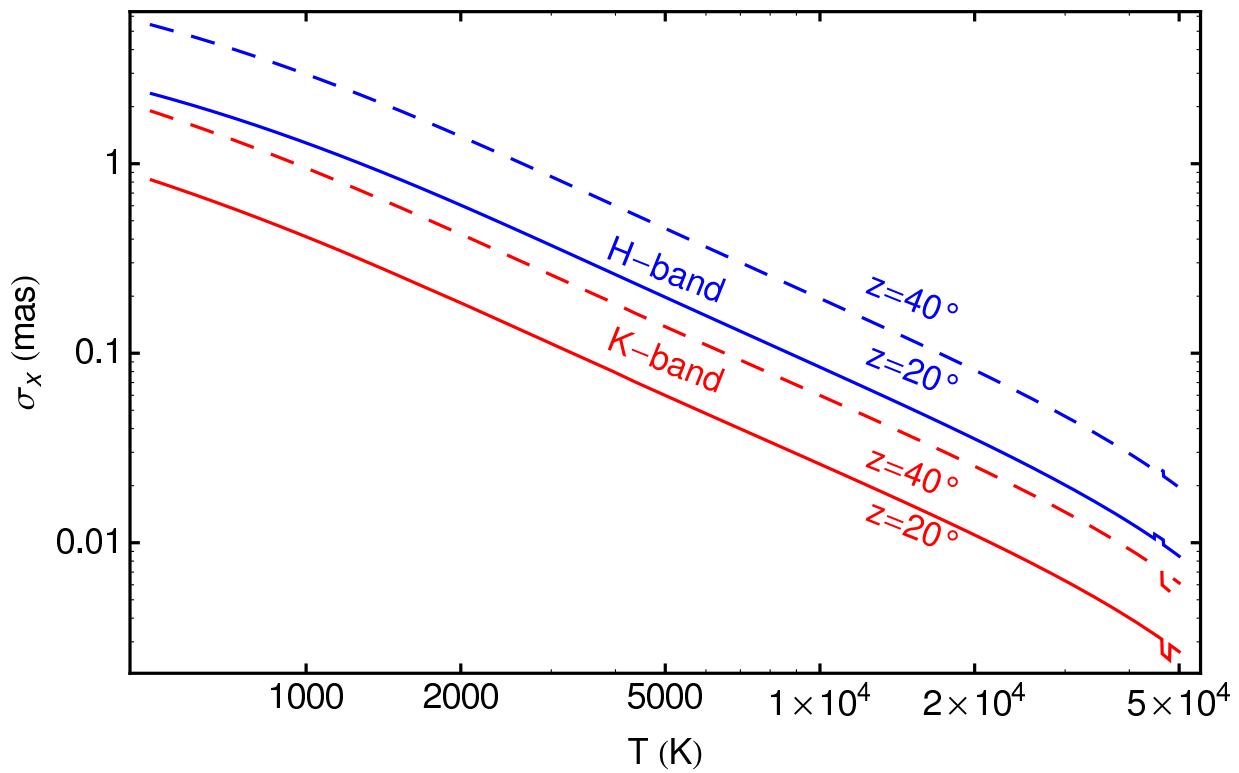


Figure 2.5 Assuming black body emission, the astrometric shift of a source due to the chromatic effects of Earth's atmosphere compared to a fictitious emitter of  $T = 10^5$  K is shown as a function of temperature. The red lines assume a K-band measurement, the blue lines H-band. The solid lines are for a zenith angle of  $20^\circ$ , the dashed lines for  $z = 40^\circ$ .

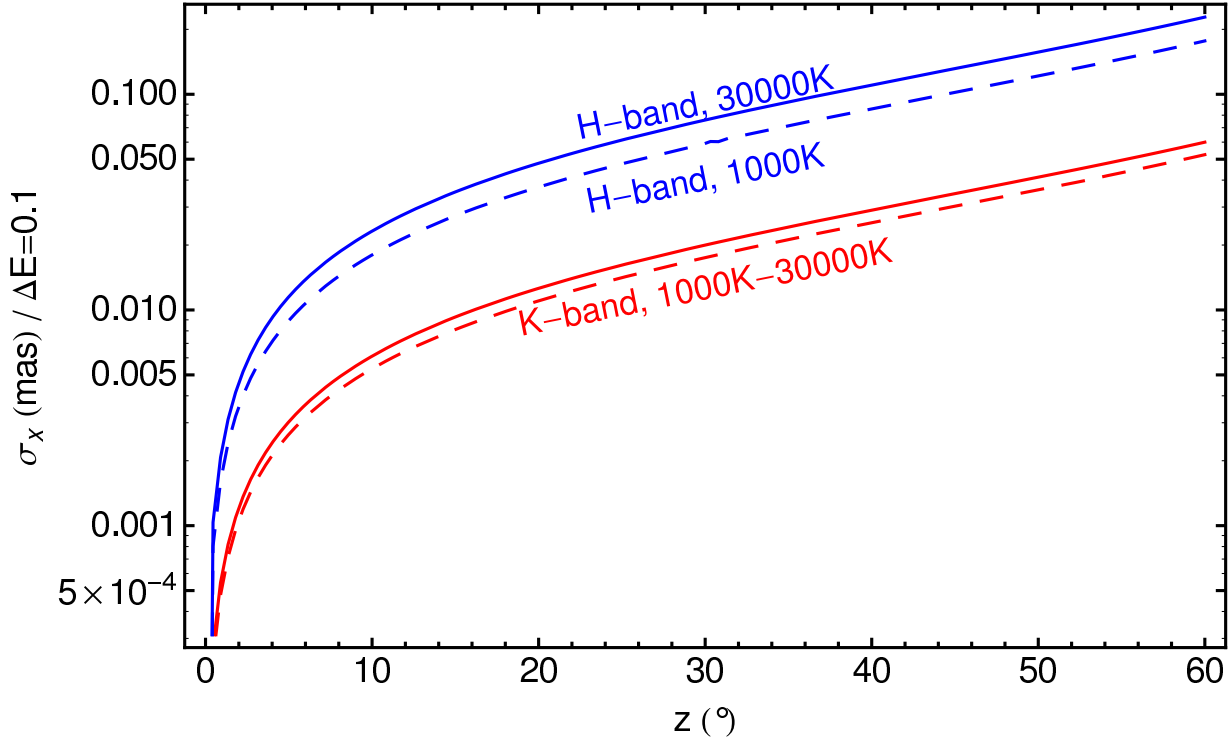


Figure 2.6 Positional shift of a black body source per 0.1 mag change in extinction as a function of zenith angle as it results from the chromaticity of Earth’s atmosphere. The red lines show that the effect for K-band data is nearly independent from the source temperature. For H-band data (blue lines), the effect slightly increases with temperature.

star the chromatic shift can reach  $400 \mu\text{as}$  compared to the  $10^5 \text{ K}$  emitter. For hot, young stars a more typical value is  $50 \mu\text{as}$ . The astrometric net effect will thus be  $\approx 175 \mu\text{as}$ .

Of course, these values strongly depend on the actual zenith angle and the exact input spectrum. Also, this error source is correctable, given that the zenith angle is known and if the input spectrum is at least approximately known.

More subtle is the combined effect of the patchy nature of the extinction screen toward the GC and the chromaticity of the atmosphere. Extinction variations lead to a change in observed color for each object as it moves behind the screen, the change in color in turn leads to a positional offset. By looking at the scatter of the observed K-band magnitudes of some isolated, bright stars (e.g. S8, S10, S30, S65, S87 in the nomenclature of Gillessen et al. 2009) we conclude that the extinction variation  $\Delta A_K \lesssim 0.1$  for the central field of interest  $\Theta_{\text{FoI}}$ . Figure 2.6 plots the positional shift per 0.1 mag extinction variation as a function of zenith angle. For K-band data, the effect is  $\sigma_x \lesssim 20 \mu\text{as}$ , for H-band data  $\sigma_x \lesssim 100 \mu\text{as}$ . Also note that for larger regions in the GC of a few arcsecond, values of  $\Delta E \approx 0.5$  are reported (Buchholz et al. 2009), which yields a correspondingly larger chromatic effect.

Finally, it is worth investigating the chromatic effects for Sgr A\*, the SMBH itself, which

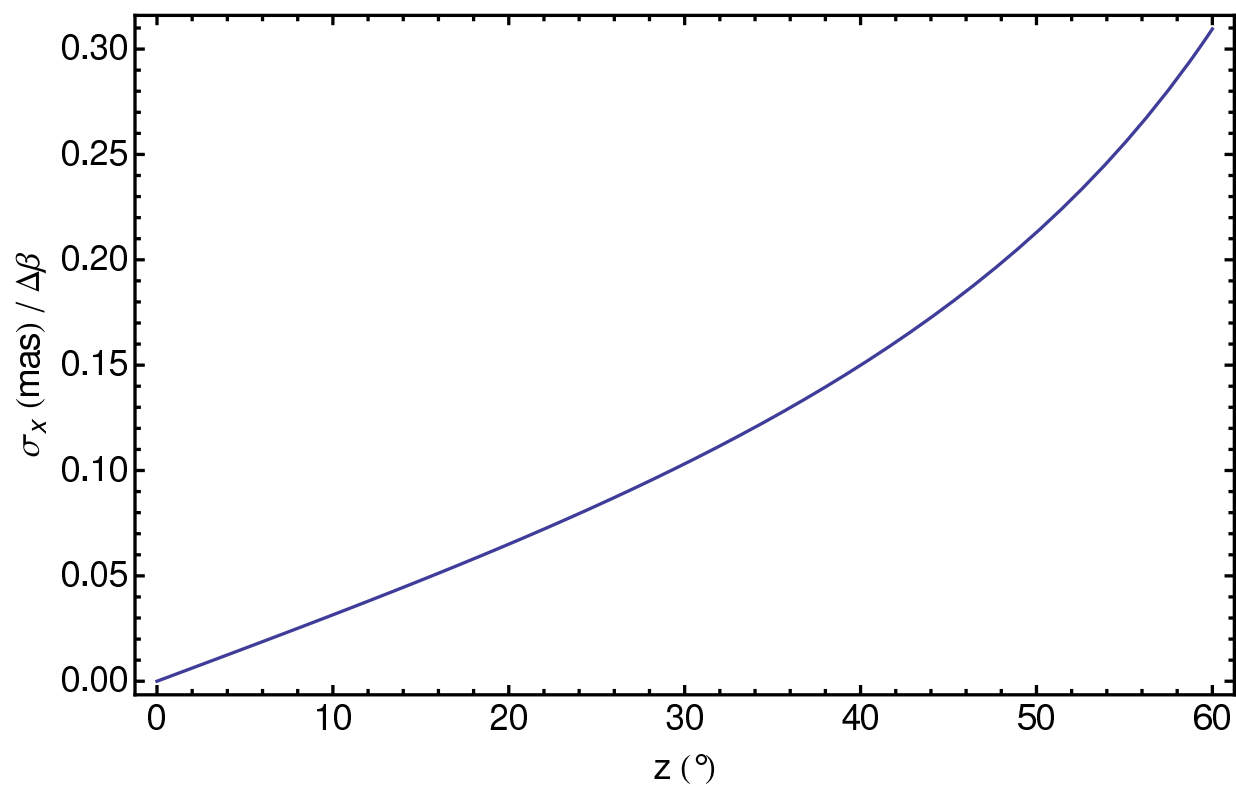


Figure 2.7 Positional shift in Ks-band of a power law type spectral energy distribution source (like Sgr A\*) per change in power law slope  $\Delta\beta$ ,  $\nu S_\nu \sim \nu^\beta$ , as a function of zenith angle as induced by the chromatic nature of refraction in Earth's atmosphere.

in the NIR is a variable source powered by the synchrotron emission of relativistic electrons and possibly changes its power law index  $\beta$  ( $\nu S_\nu \sim \nu^\beta$ ) with flux (Eisenhauer et al. 2005; Gillessen et al. 2006; Krabbe et al. 2006), but see also Hornstein et al. (2007). The astrometric effect  $\sigma_x$  per unit change of  $\beta$  is shown in Figure 2.7 as a function of zenith angle. The effect reaches  $\approx 200 \mu\text{as}$  for a zenith angle of  $\gtrsim 30^\circ$  and a change of  $\Delta\beta = 2$ . This is still a bit smaller than the currently achieved astrometric accuracy, but it can be a big systematic effect for future studies using extremely large telescopes. The easiest way to overcome the problem probably is the use of a narrow band filter, but also atmospheric dispersion compensators are feasible. Interferometric studies of Sgr A\* (Eisenhauer et al. 2008) will use several spectral channels over the K-band. In each channel, the effective wavelength will be altered by a change in color of Sgr A\*. Using five spectral pixels of  $\Delta\lambda = 0.1 \mu\text{m}$  will already lower the astrometric effect to  $< 10 \mu\text{as}$ , and in addition a first order correction will be possible because the color of the source can be measured simultaneously.

### Influence of Strehl Ratio

For any given AO image, it is common practice to characterize its quality by the SR. It is strongly correlated with the FWHM of the PSF, and hence from equation (2.2) follows that the SR limits the reachable accuracy. We simulated the influence of the SR by placing measured PSFs into noisy background maps and finding these isolated stars back using STARFINDER. The resulting errors as a function of SR followed very well power laws with power law indices between  $-0.7$  and  $-1.3$  for stars between  $m_K = 11$  and  $m_K = 18$  (Figure 2.8). The power laws get steeper with increasing magnitude since the readout noise is more important for faint sources. As a consequence, the SNR induced position error for fainter stars is more sensitive to the observing conditions than for brighter stars. As suggested by Figure 2.8 and in practice, the SR induced position errors are smaller than other error terms, most notably the halo noise (Section 2.4.4). Hence, our current data sets are not SNR limited.

## 2.4.3 Instrumental Limitations

### Distortion

Each imaging system suffers to some degree from optical distortions. These can either be a global effect for the image (such as classical optical aberrations) or small scale imperfections. The global terms should mainly be absorbed by the third order transformation between pixel positions and astrometric positions, but a floor of residuals is unavoidable. If we would use only one pointing position, these residuals would not influence the precision of the data, but would of course affect the accuracy. However, we use various pointing settings from run to run and even during one run (to increase area coverage). The residual image distortions effectively act like a random error.

Our  $13 \text{ mas/pix}$  observations are typically dithered in a scheme that four positions,

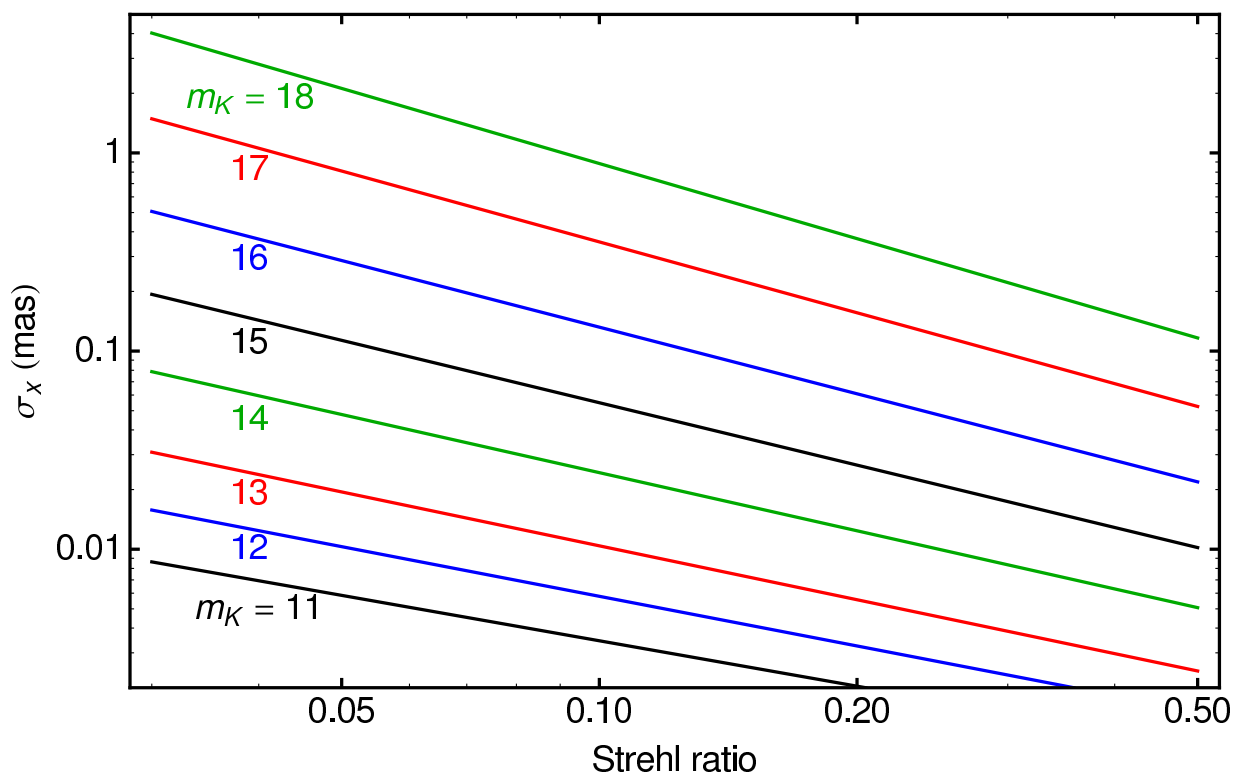


Figure 2.8 SNR induced position error in a Ks-band mosaic of 96 single frames as a function of Strehl ratio for stars of magnitudes between 11 and 18. The darker a star is, the more its SNR induced position error is sensitive to the atmospheric conditions.

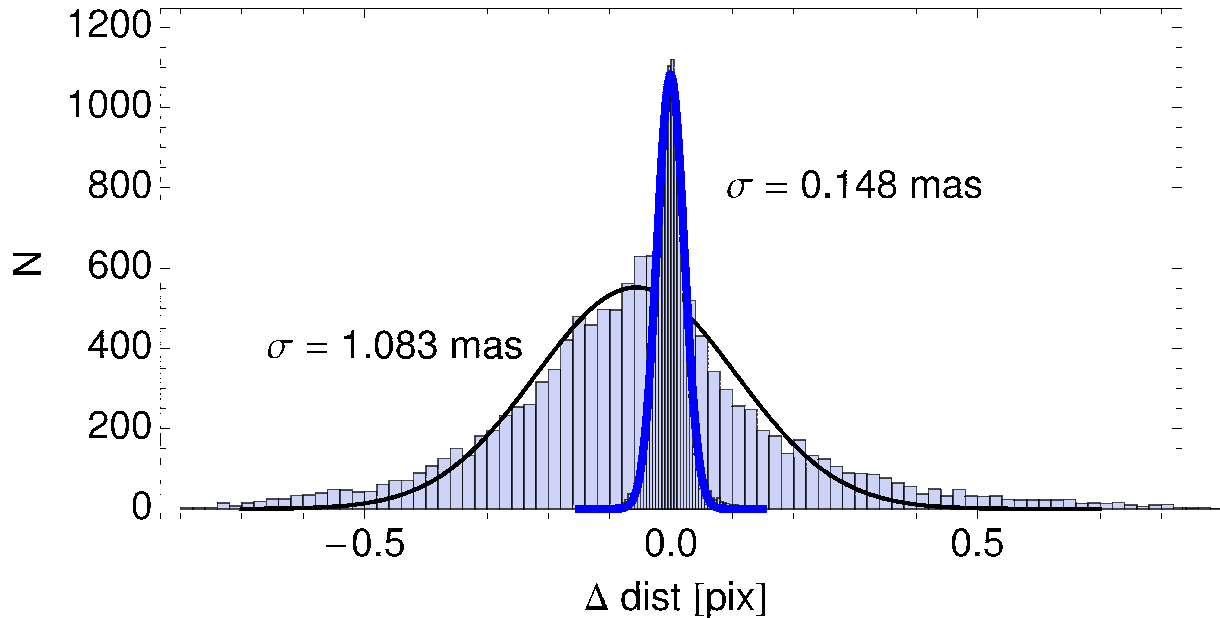


Figure 2.9 Compensation of image distortions by means of a cubic transformation for the data from 13 March 2008. The broad histogram is the distribution of differences of bona fide stellar positions from four pointing positions with a dither offset of  $7''$  after having mapped the positions onto each other with a full linear transformation. If the stars are mapped onto each other by a cubic transformation the same differences yield a much narrower distribution since image distortions are removed. The corresponding one-dimensional position errors  $\sigma_x$  are given, too.

offset by  $3.5''$  from Sgr A\* in both axes, are obtained. Since the field of view is  $\approx 13.5''$ , the central  $\approx 7''$  are covered by each frame. From these data, we usually construct multi-pointing mosaics. The effect of the image distortions here is a) that each source gets broadened slightly and b) that a superposition of the global distortions is present in the area which is covered by several pointings. Both the area of interest and the reference stars are taken from the central  $7''$  which are covered by all pointings, and hence the resulting distortion pattern might be a complicated function, which we represent by a cubic transformation with 20 parameters.

Following the approach in Gillessen et al. (2009) we estimate the size of the effect for the data from 13 March 2008 by creating four single-pointing mosaics and comparing the distances of stars common in all pointings after having transformed them with a cubic transformation onto each other (Figure 2.9). The width of distribution of position differences then measures the residual image distortions, but includes also the effects of PSF uncertainty and differential tilt jitter. We obtained a value of  $\sigma_x = 148 \mu\text{as}$ , of which  $\approx 50 \mu\text{as}$  are due to the uncertainty in the PSF,  $\approx 40 \mu\text{as}$  due to anisoplanatism, and  $\approx 125/\sqrt{24} \mu\text{as} \approx 25 \mu\text{as}$  due to differential tilt jitter. The SNR induced position error is

$< 5 \mu\text{as}$  here, since the mean magnitude for the set of stars used was  $m_K = 13.1$ . Hence, we conclude that the residual image distortions affect the astrometry at a level of  $\approx 130 \mu\text{as}$ . This value is smaller than the corresponding number in Gillessen et al. (2009) who had not taken into account the other effects subtracted here and who were looking at a different data set from a time before the instrument got realigned.

A different route to estimate the residual image distortions is to compare the high order terms of the transformations between several epochs. For this purpose we calculated the inverse of the third order transformations for each of the 73 NACO epochs with 13 mas/pix data to convert a regular grid on sky back to the respective pixel positions in each frame. Then we mapped these pixel positions to a common epoch with a full linear transformation which was determined from the reference stars for the given epoch. Like this we take into account image shifts, rotations, scale changes and shear terms and therefore the resulting jitter of the grid points measures the variations of the higher order distortions. Since the set of reference stars on average still might be moving in a linear fashion we actually determined the jitter as the residuals to a temporal linear fit for each grid point. We broke up the entire data set into three periods, corresponding to three hardware configurations: From 2002 to June 2004 a different detector was used than in the following years, and NACO underwent a major realignment late 2007. From the residuals we constructed maps of the residual distortions (Figure 2.10). For the first two periods, a typical value for the central arcsecond is  $\sigma_x \approx 300 \pm 50 \mu\text{as}$ , while for the last period a significant improvement to  $\sigma_x \approx 120 \pm 30 \mu\text{as}$  is observed. This estimate agrees with the number quoted in the previous paragraph for the data set from 13 March 2008.

For the 27 mas/pix camera of NACO, the residual distortions in absolute terms are higher. The procedure of Trippe et al. (2008) leads to residuals of order 1.2 mas, (see their Figure 2, bottom; or Figure 6 in Gillessen et al. 2009). Over time, the distortion appears stable, given that the distortion parameters of Trippe et al. (2008) are consistent with each other for all data analyzed since 2002. For a distance of  $10''$  from the optical axis (which differs from the center of the detector), the uncertainty of the geometric model is 0.4 mas and hence is smaller than the residuals. We have not analyzed further, what limits the positional accuracy for the 27 mas/pix data. For our data sets, the residuals of this plate scale matter when the positions need to be related to an absolute coordinate system, for example for answering the question where radio-Sgr A\* is located on the frames. For many questions, however, this does not matter, e.g. when one is trying to detect accelerations. For a more detailed discussion see Gillessen et al. (2009).

### Detector Non-linearity

Nominally, the current NACO detector is regarded as a linear device up to 2/3 of its capacity, corresponding to 14000 ADU for the readout mode of our data sets. Using a set of flat exposures with varying exposure times, we checked the linearity behavior of the detector and found that at 10000 ADU the non-linearity is 7%, at 7000 ADU 4% and at 5000 ADU still 2%. This would in turn mean that a PSF estimate is worse for brighter stars, possibly leading to positional biases. Hence, we calculated a pixel-wise map of polynomial

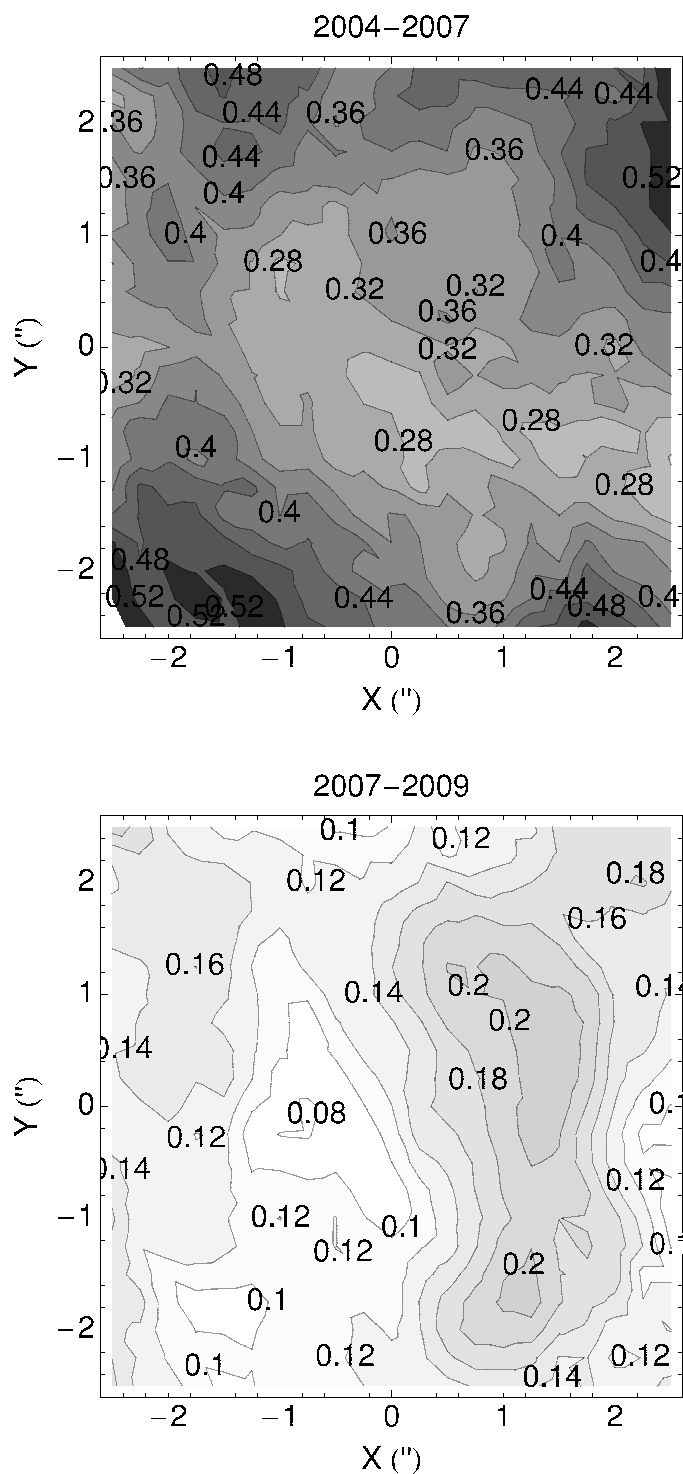


Figure 2.10 Maps of estimated residual image distortions. Contour labels are in mas. Top: For the period between June 2004 and fall 2007. Bottom: For the period after the realignment in 2007 until 2009. Note that identical color maps have been used, pronouncing the fact that the residual distortions are much less severe after the realignment.

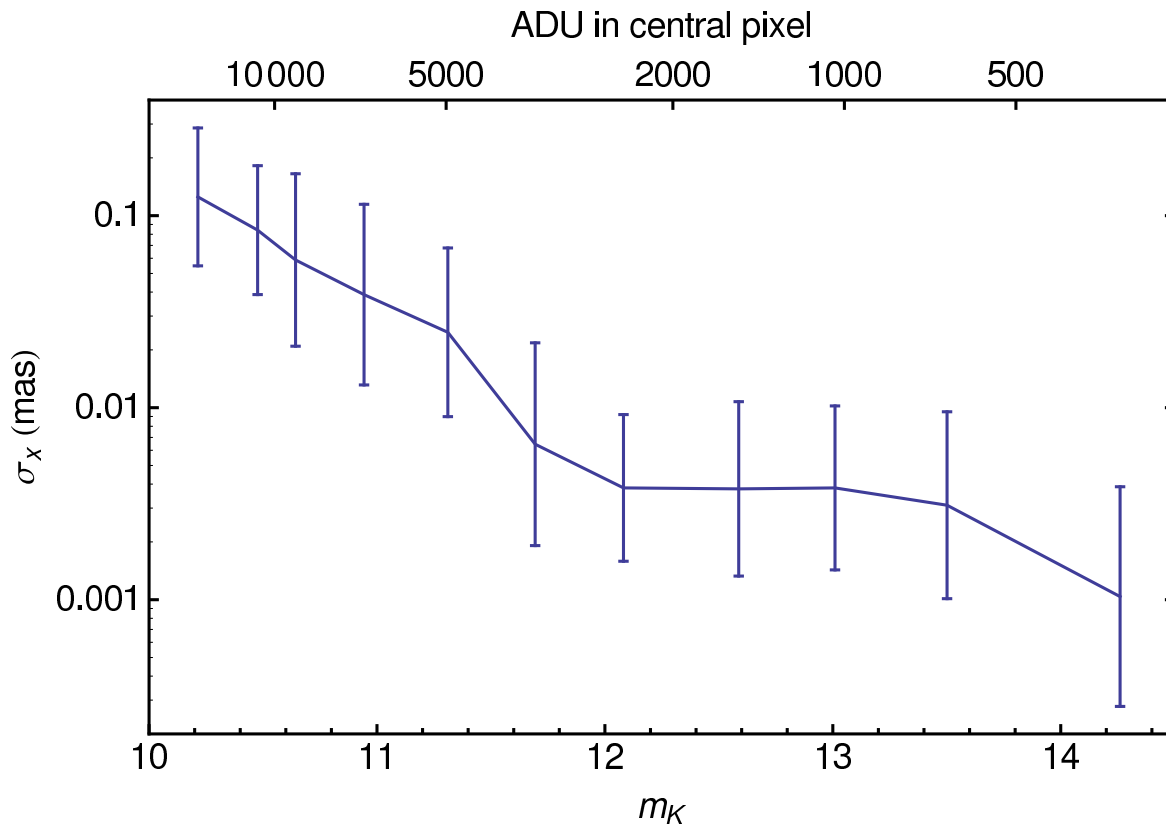


Figure 2.11 Position errors induced by the detector non-linearity under good observing conditions as a function of flux in ADU (top axis) and stellar magnitude (bottom axis) assuming an image with DIT= 17.2s. The error bars show the standard deviation of the position errors and hence measure the scatter per bin.

coefficients to correct the effect, which is now applied to all data. That correction doubles the usable dynamic range of the detector and thus allows the use of brighter stars. It is now linear to 2% up to 12 000 ADU, which for the data from 13 March 2008 corresponds to  $m_K = 10.7$ .

We also tested for the potential astrometric bias by comparing the positions from a linearity-corrected and an uncorrected frame. Figure 2.11 shows that the effect in a mosaic for the brightest S-stars with  $m_K \approx 14$  is  $\lesssim 50 \mu\text{as}$  and decreases for fainter stars.

Stars that are affected by saturation are offset sporadically up to  $100\times$  the usual positional error, i.e. in the multi-mas range. Such a big effect is easily detected in the data and hence such cases can be flagged as outliers. We thus don't assign a formal error here but rather expect that for some data sets, for bright stars saturation effects make the positions unusable. Furthermore, heavily saturated stars (showing for example a flux plateau at the highest flux value) are not described at all by the PSF estimate; such stars are even recognized earlier, since the deconvolution does not yield a point-like structure in these cases.

### 2.4.4 Analysis Limitations

#### Knowledge of the PSF

Astrometry in a crowded stellar field necessarily needs as input an estimate for the PSF. Just using local maxima in the image as position estimates is not sufficient, since essentially all stars are located on the seeing halo of neighboring sources. This yields a background flux with a gradient and thus biases the positions of local maxima. Even worse, the background will vary with the AO correction from image to image and lead to a position jitter. Moreover, very faint stars in a seeing halo of a bright star do not produce a local maximum (but only change the shape of the seeing halo) and would be missed by an algorithm looking for local maxima.

These problems are overcome by using the knowledge of the PSF, which can be obtained from the image itself with an iterative procedure, e.g. using STARFINDER (Diolaiti et al. 2000). Given a certain PSF estimate, there are two basic options to obtain position estimates.

- **PSF fitting.** A program like STARFINDER (Diolaiti et al. 2000) iteratively fits local maxima to the image until the image is sufficiently well represented by the set of sources found, each of which is characterized by a position and flux.
- **Deconvolution.** The image on the detector is the convolution of the PSF with the original object distribution. Since a convolution in image space corresponds to a multiplication in Fourier space, the inverse operation deconvolution in the Fourier domain is a division. The presence of noise and the limited range of spatial frequencies complicate the actual algorithm. Various methods are available and have been compared (Ott et al. 1999). We mostly use the Lucy-Richardson algorithm (Lucy 1974) for astrometry.

Since both methods use the same input, one does not expect a major difference in astrometric performance. The fact that in Figure 2.4 the STARFINDER errors are larger than the corresponding deconvolution errors might reflect a non-optimum user choice for the parameters of the STARFINDER algorithm and/or it might be due to the differences how the non-stellar background is dealt with.

The fact that the input PSF is not perfectly known but has to be estimated needs to be accounted for in the error budget. In order to quantify the error, we used various sets of PSF stars and compared the resulting positions. Also, we compared the positions depending on the number of iterations used for the extraction of the PSF. From the scatter of the positions (after having transformed them linearly onto each other) we conclude that the uncertainty of the PSF knowledge yields a positional error of  $50 \mu\text{as}$ .

#### Transformations

The fact that we need to transform the measured pixel positions with a set of reference stars is an error source because the transformation parameters also have errors. Fortunately,

the corresponding statistical error can be lowered to a very low level. If  $N$  stars are used as reference stars, each with a typical position error of  $\sigma_x$ , the additional error for the target sources due to the transformation is of order  $\sigma_x/\sqrt{N}$ . By choosing a large enough sample of reference stars, this statistical error can thus be lowered to any desired value as long as a sufficient number of reference stars is available. Of course, this holds only if the reference stars can all be chosen from within the field in which the PSF can be treated as constant. Recently Gillessen et al. (2009) used  $N \approx 100$  reference stars in the GC field, which suppresses effectively the transformation error to below  $50 \mu\text{as}$ . Former studies (Schödel et al. 2002) had used  $N \approx 10$  reference stars, which hence at the time was contributing at the few 10% level to the errors.

### Deconvolution

We also investigated systematically the number of iterations to be used with our implementation of the Lucy-Richardson algorithm. Using a set of 66 well isolated stars in the data set from 20 July 2007 we obtained pixel positions for different deconvolution depths.

For less than 500 iteration steps, the resulting positions are biased up to  $0.5 \text{ mas}$  for bright stars compared to the positions in the undeconvolved image and compared to more deeply deconvolved images. For different stars the bias acts in different directions, and hence globally it appears to be a scatter of up to  $0.5 \text{ mas}$ . For 2000 steps, both bias and scatter for bright stars drop below  $120 \mu\text{as}$ . The optimum is reached for  $\approx 10000$  iterations; also fainter sources are unbiased with that number of iterations. Much larger values (like 50000 steps) tend to put the flux of any star into a single pixel, which of course corresponds to larger positional errors again. The optimum depth in practice is between 5000 and 15000 steps, with better data needing less deep deconvolution.

### Halo Noise

Visual inspection of the deconvolved frames shows that the background in the images is not flat but rather has a noise-like structure, see for example Figure 1 in Gillessen et al. (2009). The deconvolution algorithm does not discriminate between sources and background and therefore any extended light present gets concentrated into this floor of faint local maxima. That light is due to the imperfections in the knowledge of the PSF wings (the dominant source) and real, physical extended background light as expected from interstellar gas. Astrometrically, the spurious deconvolution peaks act as a noise source. It turns out that this halo noise is the main limitation for fainter sources. Experimentally indistinguishable from this is the confusion noise due to unresolved background sources, see in Section 2.4.5.

While the term halo noise describes the influence of the imperfectly known PSF halo of surrounding stars, the PSF uncertainty refers to the effects of the imperfectly known PSF on the source itself. The PSF uncertainty would be present also for sufficiently isolated sources, the importance of the halo noise is a consequence of the stellar crowding. It is also worth noting that the halo noise is not specific to the deconvolution technique. Also a STARFINDER-like algorithm is not free from that noise source. It generally arises from

the fact that the seeing halo of neighboring, brighter stars cannot be subtracted perfectly, which owes to the large dynamic range in the images and the high surface density of stars.

As a first test to estimate the effect of halo noise, we added Gaussian peaks with the same width as the typical width for real stars into the deconvolved frame from 13 March 2008 at random positions, avoiding positions at which the added source would overlap with an already existing and detected star. We then re-identified the random sources and determined their positional uncertainty by calculating the median deviation of the distribution of differences between the respective initial and re-identified positions. This tests by how much simulated stellar sources are shifted due to the combined deconvolution and confusion noise. The resulting positional error can be described very well by a relation of type

$$\sigma_x = \Sigma_x(r) \times 10^{0.4(m_K - 14)}, \quad (2.10)$$

where  $\Sigma_x(r)$  is a characteristic error for a source with  $m_K = 14$  at a given radial distance  $r$  from Sgr A\*. In the chosen data set  $\Sigma_x$  has the following radial dependence:

$r''$	0.22	0.47	0.77	1.07	1.36	2.07	3.18	$M$
$\Sigma_x[\mu\text{as}]$	273	176	122	133	110	105	82	63

The last bin, labeled  $M$ , corresponds to manually selected, well-behaved background regions in the deconvolved image. There are two reasons why the deconvolution and confusion noise decreases with radius: a) The unrecognized, faint stellar population falls off with radius. b) The stray light, leading to a variable background on top of the PSF, follows the general trend that the light is roughly concentrated toward Sgr A\*.

In a second test we added the full PSF into the undeconvolved frame, neglecting the effects of anisoplanatism. The modified frame was then deconvolved as before and stars were identified, yielding again an estimate for the error introduced by the deconvolution with imperfectly known background and PSF halo. This procedure yielded the errors as a function of magnitude and radius from Sgr A\* as shown in Figure 2.12. The numbers obtained are broadly consistent with the results from the first test where Gaussian peaks were added to the deconvolved frames.

Hence, the combination of halo and confusion noise is a severe limitation. Only for the brightest S-stars ( $m_K \approx 14$ ) it gets as small as the errors due to residual image distortions. In the next section, we show that the confusion noise actually contributes much less than the halo noise and we have to conclude that halo noise is limiting the astrometric accuracy for stars fainter than  $m_K \approx 15$ .

Due to the importance of the halo noise, we have repeated the last test (putting full PSFs into an existing image and finding the stars back) using PSF fitting (STARFINDER) instead of Lucy-deconvolution. We used 100 artificial stars per magnitude bin on the image from 13 March 2008, the positional error again is the width of the distribution of the differences between detected and simulated position. The results are very similar to what we found with deconvolution. The positional uncertainty using STARFINDER is slightly larger than for the deconvolution, similar to the findings in Figure 2.4. The photometric correctness on the other hand is slightly better for the PSF fitting method.

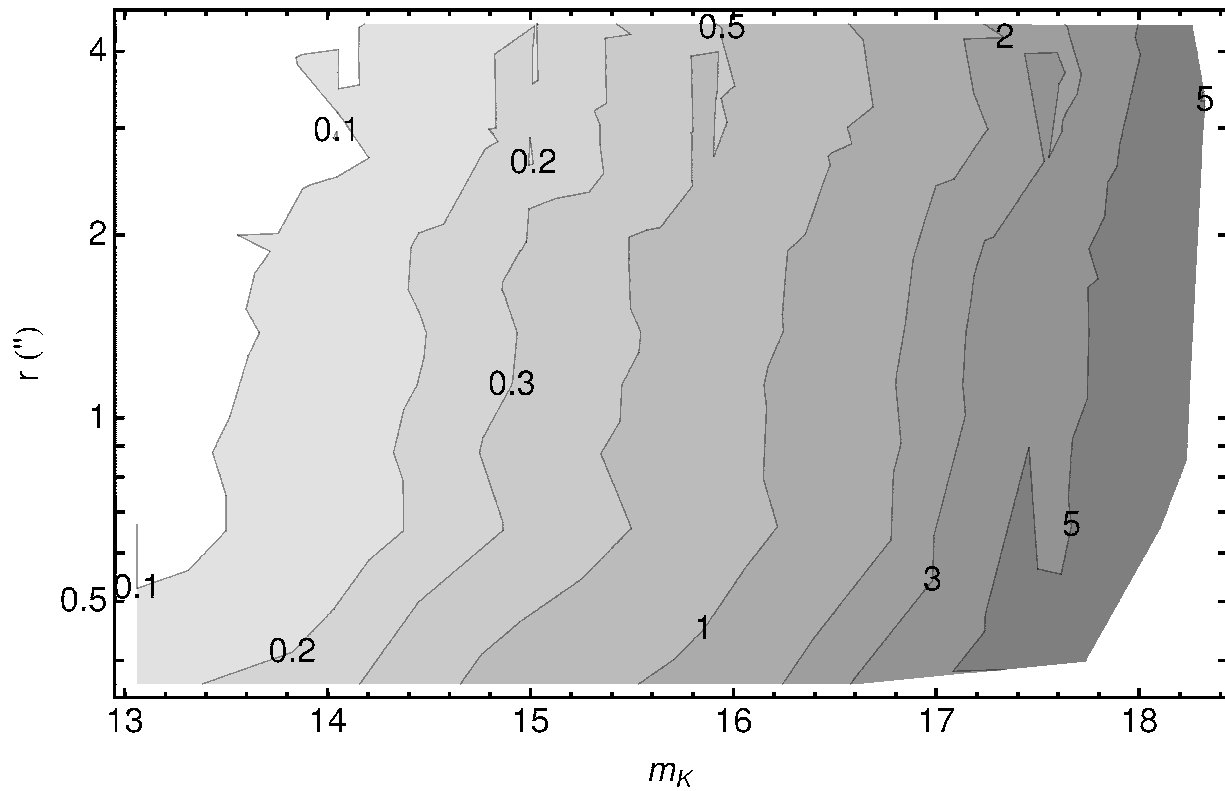


Figure 2.12 Position errors due to halo (and confusion) noise as a function of stellar magnitude and distance from Sgr A\*. The errors are obtained by adding simulated stars to an undeconvolved frame and finding the sources back after deconvolution. The contour label units are mas.

This can be understood, since the Lucy algorithm tends to pull flux from the surroundings into local maxima during the iterative procedure. For a low SNR source this can bias the flux estimate. Overall, we conclude that halo noise is an important noise source, and it is not specific to the method used to extract positions.

### 2.4.5 Astrophysical Limitations

#### Confusion

Astrometry in the GC is affected by the stellar crowding close to the SMBH. The S-stars reside in a cusp with a steep density profile. As a consequence, the closer a star is to the SMBH, the more frequently it is confused with some other source. Not all confusion events are recognized, and therefore unrecognized confusion events will contribute to the positional error budget. This error is already included in the Halo noise (Section 2.4.4). It is nevertheless instructive to single out the effect of the stars, since that limit would remain even if the instrumental halo noise could be removed.

As an extreme example for a possible confusion error, it is worth mentioning that the orbit of the star S2 possibly was affected in 2002, during its pericenter passage, by such an event. Both recent analyses (Ghez et al. 2008; Gillessen et al. 2009) therefore treat the respective 2002 data separately; either by ignoring it or by assigning large errors to it.

In order to assess the magnitude of the confusion noise, we simulated stellar background populations in a Monte-Carlo fashion. That needed two basic input distributions: a K-band luminosity function and the radial surface density profile. We based these on the findings of Genzel et al. (2003). We used three radial bins for our simulations:  $0'' < r_1 < 0.2''$ ,  $0.2'' < r_2 < 0.8''$  and  $r_3 = 3.5''$ . Since we had to assume the density also for stars much fainter than what can be measured, some assumptions had to be used. For  $r_3$  we extrapolated the cluster KLF of Genzel et al. (2003) down to  $m_K = 24$ . For  $r_{1,2}$  and  $m_K \leq 18$  we used the KLF as estimated from the S-stars cusp, scaled to the respective expected surface density from the radial profile. At fainter magnitudes we extrapolated with a KLF from the same radial region that only counts stars which are not identified as late-type stars. This essentially assumes that for  $m_K > 18$  only main sequence stars are present. Figure 2.13 shows the densities used.

Using the assumed densities per magnitude we simulated stellar fields, using Gaussian profiles with a FWHM of 30 mas – 42 mas (magnitude dependent, to mimic the FWHM of real sources in the deconvolved frames) and a binning of 13 mas/pix. For each image, the target star was placed in the center of a box of 12 pixels width and background stars fainter than the target star were added. The positional error of the target star is given by the difference between input position and the position at which it is found back by fitting the star with a Gaussian profile plus a floor. We used up to  $10^5$  simulated images per magnitude bin. The distribution of positional differences per magnitude bin was then fit with a Gaussian, the width of which estimates the position error. The resulting errors as a function of magnitude are shown in Figure 2.13.

For the S-stars cluster ( $r \lesssim 0.8''$ ) the error due to unrecognized confusion is of similar

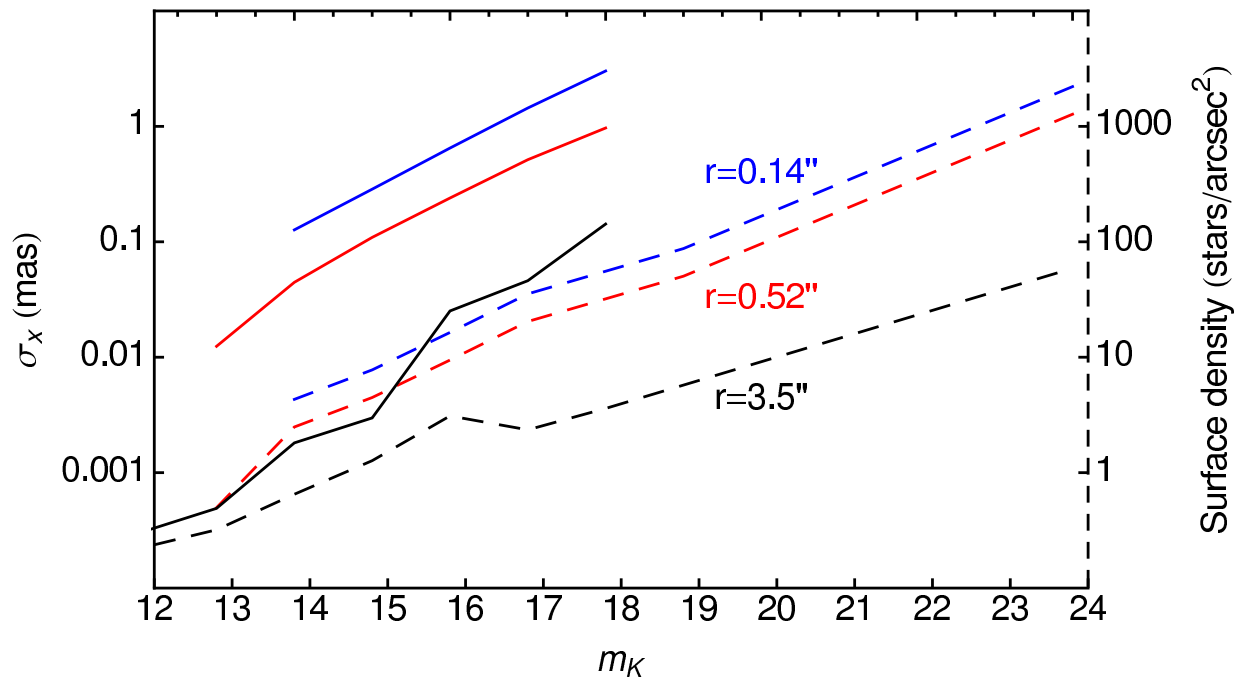


Figure 2.13 Assumed stellar densities and resulting position errors due to confusion noise: Dashed lines and right axis: assumed stellar surface density as a function of magnitude. Solid lines and left axis: resulting positional errors due to unrecognized confusion events with fainter stars. The blue lines are for  $0'' < r < 0.2''$ , the red for  $0.2'' < r < 0.8''$  and the black for  $r = 3.5''$ .

magnitude as the error due to halo noise. For larger radii, the confusion induced error is smaller than the halo noise as the stellar densities drop rapidly with radius. The increase of confusion error with stellar magnitude is well described by a power law of type  $C \times 10^{0.4m_K}$  (as the halo noise).

### Relativistic Effects

Currently, relativistic effects have not yet been detected in the data of any star orbiting the GC SMBH. Actually, detecting  $\beta^2$  effects will be possible probably first in radial velocity measurements (Zucker et al. 2006). Astrometrically detectable deviations from Newton's law have not yet been seen in the GC. Vice versa, the effects can currently be neglected in the analysis. Still, a few effects are worth discussing here.

- **Gravitational light deflection by the SMBH.** The deflection angle for a star sufficiently far behind the SMBH (at distance  $z$ ) can be approximated by

$$\theta \approx 20 \mu\text{as} \frac{z}{b} \quad (2.11)$$

where  $b$  is the impact parameter (Nusser & Broadhurst 2004). For smaller values of  $z$ ,  $\theta$  decreases compared to equation (2.11), and for  $z = 0$  it is half of it. Generally the effect leads to very faint secondary images ( $m_K \approx 22$  at best), and lensing only can become important when a star crosses the line of sight to Sgr A\* behind Sgr A\*. Currently none of the stars tracked is in that regime and we neglect the effect. On the other hand, detecting the effects of secondary images would be extremely interesting. Bozza & Mancini (2005, 2009) calculate the appearance of the secondary images for the known orbits. It will be extremely difficult to detect these faint sources in the crowded field around Sgr A\* ever. Another application would be the idea of Alexander (2001) who suggested to use the secondary images of background stars to pinpoint the position of the SMBH.

- **Gravitational light deflection by the Sun.** Light deflection by the gravitational field of the sun can be approximated by Lindegren & Bastian (2006)

$$\theta \approx 4 \text{ mas} \times \cot \Psi / 2, \quad (2.12)$$

where  $\Psi$  is the angle between Sun and the observed object. While the absolute magnitude of the effect is as large as 22 mas for  $\Psi = 20^\circ$  (the minimum useful distance), the differential effect (relevant for relative astrometry as in our case) over a field of view of  $20''$  is always well below  $10 \mu\text{as}$  and would even mainly be absorbed in the linear terms of the transformations.

- **Differential aberration.** The classical light aberration yields for a small field of view effectively a change in plate scale in one direction (Lindegren & Bastian 2006). The effect will be absorbed into the parameters of the transformation when converting

pixel positions to astrometric positions via reference stars if and only if one allows also for the linear shear terms in the transformation. Otherwise, a positional error of

$$\theta \approx \Theta_{\text{FoI}} \frac{v}{c} \cos \Psi , \quad (2.13)$$

can occur, where  $v \approx 30 \text{ km/s}$  is the speed of Earth and  $\Psi$  the angle between the apex point and the target. Numerically, this evaluates to  $1 \text{ mas} \times \cos \Psi$  for a field of interest of  $\pm 2''$  and hence would be a huge effect. It is, however, absorbed into the shear terms of the transformation.

## 2.5 Summary & Conclusion

We have analyzed a multitude of error sources that potentially influence and bias stellar positions as obtained from adaptive optics assisted imaging data in crowded stellar fields. The domain of application in this work is the stellar cusp in the Galactic Center. Figure 2.14 summarizes the various error sources for a mosaic of 48 frames with  $\text{DIT} = 17.2 \text{ s}$  and  $\text{NDIT} = 2$  using NACO in K-band and the  $13 \text{ mas/pix}$  image scale, assuming the current instrumental setup and good observing conditions.

We find that for stars fainter than  $m_K \approx 15$  the main error source for position measurements is halo noise, resulting from the imperfectly subtracted PSF seeing halos of surrounding, brighter stars. For stars of  $m_K \approx 14$  and brighter, the main limitation is residual image distortions and the uncertainty in the PSF. In order of importance for a star with  $m_K = 15$  in the central arcsecond, we estimate the following error contributions:

- Halo noise:  $300 \mu\text{as}$
- Residual image distortions:  $130 \mu\text{as}$
- Confusion noise:  $100 \mu\text{as}$
- PSF uncertainty:  $50 \mu\text{as}$
- SNR induced position uncertainty:  $45 \mu\text{as}$
- Coordinate transformations:  $30 \mu\text{as}$
- Differential tilt jitter:  $15 \mu\text{as}$
- Extinction uncertainty:  $10 \mu\text{as}$
- Differential chromatic aberration:  $10 \mu\text{as}$
- Detector non-linearity:  $< 5 \mu\text{as}$

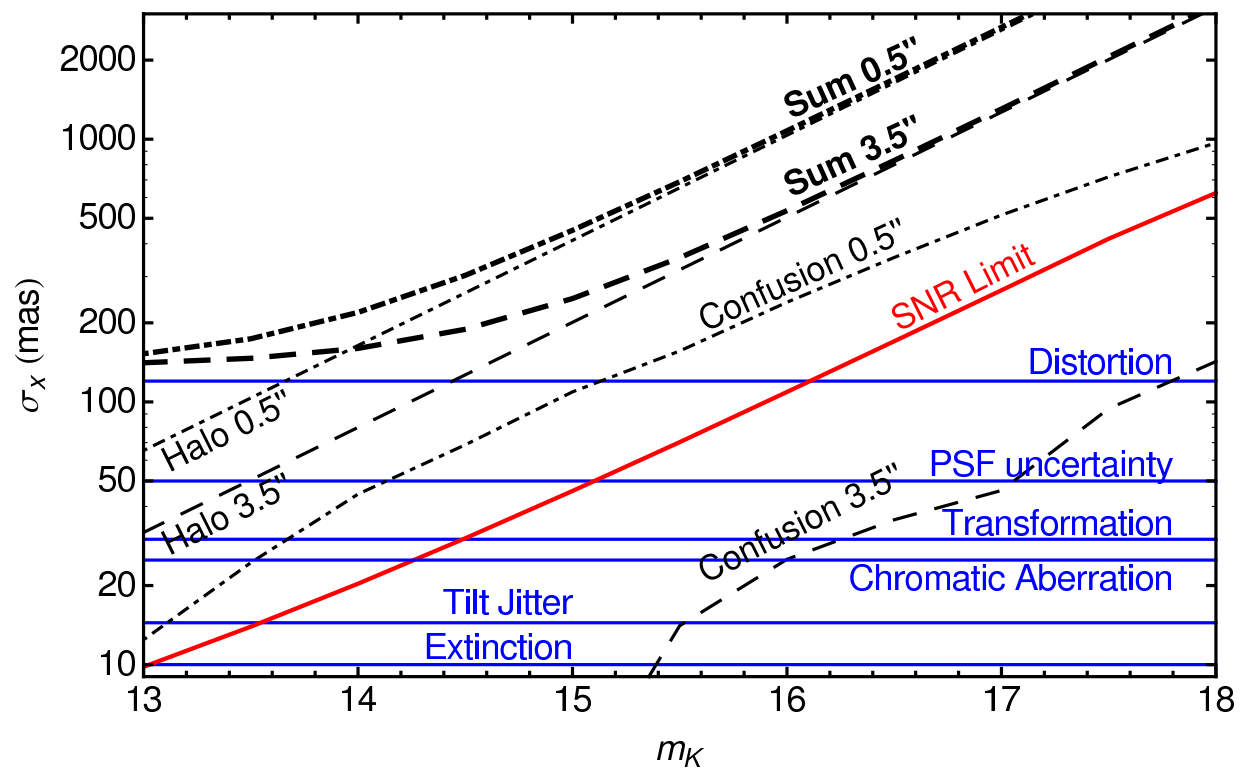


Figure 2.14 Summary of error sources as a function of stellar magnitude. The blue, horizontal lines are constant contributions. From top to bottom these are: residual image distortions, PSF uncertainty, coordinate transformations, differential chromatic aberration, differential tilt jitter and extinction uncertainty. The red, diagonal, solid line is the SNR limit. The dot-dashed curves are for the central cusp ( $r = 0.5''$ ) and show from bottom to top the confusion error, the halo error and in thick the sum of the errors for that radius. The dashed curved are the same for  $r = 3.5''$ .

It is worth noting that our Figure 2.14 cannot be compared to Figure 3 of Ghez et al. (2008), who only show the centroiding uncertainties and not the astrometric accuracy. The proper comparison is with our figure 2.4.

Given the dominance of the halo noise in the error budget, the most promising route to improve the astrometry on existing data is to get better PSF estimates, in particular for the large seeing halo. This task is complicated due to the stellar crowding which is so dense that essentially no star has an unperturbed halo. It may also be worthwhile to think about blind deconvolution, which extracts the PSF while finding stars in an iterative way and in principle could use as much information as possible from any image. The advantage would be that basically all stars are used to estimate the PSF halo, and not just the ones which a user has selected a priori. Another way to improve the PSF estimates might be the techniques of PSF reconstruction from the wavefront sensor data (Gendron et al. 2006).

For the brightest stars ( $m_K \approx 14$ ), the next step of improvement would come from a better handling of residual image distortions. One possible route could be to actually map the distortions and then apply a correction to the pixel positions obtained from the data. For that, it is also important to have a well designed, well aligned and stable optical system.

Other, desirable improvements which could be implemented in the analysis using current data are: a) take into account anisoplanatism during the deconvolution process (moderately important), b) correct for the atmospheric chromatic bias due to the different stellar types (important in H-band only) and c) extend the linearity correction to earlier data obtained with another detector (barely important).

It should also be noted that most of the errors effectively act as random errors, if many epochs are considered. Hence, we expect that observing at many epochs will average out many errors discussed. Nevertheless some care needs to be taken that this actually happens. The halo noise might get correlated between epochs if consistently the same PSF stars and same PSF size get used. Using different bands, experiencing variable atmospheric conditions, the motion of stars and varying the way to estimate the PSF during the analysis help to avoid that the error turns into a bias. For the analysis, this means that from a given data set frames should be added up until the faintest stars of interest are well detected, but not beyond that. If more frames are available, it is better to create a second mosaic, thus lowering the halo noise induced error. The only source of error which unavoidably leads to correlated position errors is unrecognized confusion events, since for typical proper motions, stars are confused for a few years.

Our results also indicate that further instrumental improvements mainly would come from better angular resolution and higher Strehl ratios. It is somewhat trivially clear that this would yield better astrometry. The value of our analysis is mainly to show that this indeed is limiting the astrometry in the Galactic Center. Current observations are not SNR limited, for example. Also, we cannot exclude that at the level of  $\approx 200 \mu\text{as}$  the astrometry has reached a limit, given current telescopes and adaptive optics systems.

Since the resolution is essentially set by the apertures of the telescopes, only extremely large telescopes (with 30 m to 40 m aperture) or interferometric means in the future will further improve the angular resolution.

The Strehl ratio deserves a bit more discussion. Clearly, the astrometry in the Galactic Center would benefit from an adaptive optics system that yields the highest Strehl ratio possible over a relatively small field. This means that adaptive optics systems that yield a more moderate correction over wider fields are not well-suited for studying stellar dynamics close to the massive black hole in our Milky Way. Interesting for the GC seem the concepts for extreme adaptive optics systems that should deliver Strehl ratios up to 90% over a limited region (Macintosh et al. 2003; Conan et al. 2004) Finally, good astrometry will continue to depend on suitable atmospheric conditions.

In a nutshell: Further improving the astonishing measurements of stellar orbits in the GC requires larger telescopes, higher Strehl ratios, better knowledge or reconstruction of the seeing halo of the PSF, correction of residual image distortions - and ideally even a combination of these.

# Chapter 3

## GC-IRS13E - A Puzzling Association of Three Early-type Stars

**Original publication:** T.K. Fritz, S. Gillessen, K. Dodds-Eden, F. Martins, H. Bartko, R. Genzel, T. Paumard, T. Ott, O. Pfuhl, S. Trippe, F. Eisenhauer & D. Gratadour, 2010, *GC-IRS13E - A Puzzling Association of Three Early-type Stars* ApJ, 395, 441

**Abstract:** We present a detailed analysis of high resolution near-infrared imaging and spectroscopy of the potential star cluster IRS13E very close to the massive black hole in the Galactic Center. We detect 19 objects in IRS13E from Ks-band images, 15 of which are also detected reliably in H-band. We derive consistent proper motions for these objects from the two bands. Most objects share a similar westward proper motion. We characterize the objects using spectroscopy (1.45 to 2.45  $\mu\text{m}$ ) and (narrow-band) imaging from H- (1.66  $\mu\text{m}$ ) to L'-band (3.80  $\mu\text{m}$ ). Nine of the objects detected in both Ks- and H-band are very red, and we find that they are all consistent with being warm dust clumps. The dust emission may be caused by the colliding winds of the two Wolf-Rayet stars in the cluster. Three of the six detected stars do not share the motion or spectral properties of the three bright stars. This leaves only the three bright, early-type stars as potential cluster members. It is unlikely that these stars are a chance configuration. Assuming the presence of an IMBH, a mass of about  $14000 M_{\odot}$  follows from the velocities and positions of these three stars. However, our acceleration limits make such an IMBH nearly as unlikely as a chance occurrence of such a star association. Furthermore, there is no variable X-ray source in IRS13E despite the high density of dust and gas. Therefore, we conclude that is unlikely that IRS13E hosts a black hole massive enough to bind the three stars.

### 3.1 Introduction

The innermost parsec of the Galaxy hosts the supermassive black hole (SMBH) Sgr A\* (Schödel et al. 2002; Ghez et al. 2003), accompanied by a population of young WR/O-stars (Forrest et al. 1987; Allen et al. 1990; Krabbe et al. 1991; Genzel et al. 1996). Most

of these stars reside in one or two disk-like structures (Genzel et al. 2003; Paumard et al. 2006; Lu et al. 2009; Bartko et al. 2009). A group of at least three such bright stars called IRS13E at a distance of  $3.5'' = 0.13$  pc from Sgr A\* is of special interest. This group has a diameter of about  $0.5''$ . Maillard et al. (2004) identified two of the stars, E2 and E4, from their emission lines as early-type stars. In addition they identified four other early-type stars in IRS13E from broad-band SED fitting. The four brightest stars share a common proper motion (Ott 2002). Maillard et al. (2004) concluded without using a statistical test that such an association of young stars cannot be a coincidence. From the radial velocities of two of the stars they estimated a cluster mass of at least  $750 M_{\odot}$  if the two stars are bound. This mass is higher than the stellar mass seen in IRS13E. They explained the additional mass by the presence of an intermediate mass black hole (IMBH).

In the simulations of stellar clusters of Portegies Zwart & McMillan (2002) the core of a dense cluster collapses and forms an IMBH. Such an IMBH would be necessary, if IRS13E were an inspiraling cluster that survives the infall into the Galactic Center (GC) and reaches the central parsec before disintegrating (Hansen & Milosavljević 2003). A cluster without central mass would be disrupted (Gerhard 2001) by the tidal forces of the SMBH.

Schödel et al. (2005) measured the proper motions of the four brightest sources more accurately and estimated that the cluster has a mass of about 10000 to 50000  $M_{\odot}$  if it is gravitationally bound. According to these authors, an IMBH of this mass is unlikely, mainly because of the lack of radio and X-ray emission in IRS13E, despite the presence of a lot of dust. They suggested that IRS13E could also be a cluster in the process of dissolution or a chance association.

Paumard et al. (2006) identified the spectral types of the three brightest early-type stars. In addition, they measured the stellar surface density around IRS13E on a deconvolved H-band image. Inside a radius of  $0.30''$ , the core of IRS13E, they found at least twelve stars. Furthermore, they found an over-density out to  $0.68''$  which has a total significance of  $4.5\sigma$ . They concluded that IRS13E is a cluster. Given that velocities had been measured for only four of the stars, Paumard et al. (2006) argued that the total velocity dispersion could be small. Then no dark mass is needed to explain IRS13E. Trippe et al. (2008) measured the velocities of the stars between  $0.30''$  and  $0.68''$ . The velocities of most of these stars are different from the stars in the center. Therefore most of them are not cluster members and thus the overdensity is less significant compared to Paumard et al. (2006).

IRS13E2 and IRS13E4 are candidate members of the face-on counterclockwise disk (Paumard et al. 2006; Bartko et al. 2009). In this case the physical distance of these stars to Sgr A\* is identical with the projected one. According to Paumard et al. (2004, 2006) IRS13E is embedded in the bar of the minispiral at a distance of  $z = 7 - 20''$  of Sgr A\* (Liszt 2003). In this case IRS13E is rather far away from Sgr A\* and IRS13E2 and IRS13E4 would not be candidates members of the counterclockwise disc (Bartko et al. 2009).

Accordingly, the nature of IRS13E is still a matter of debate. This is largely because the proper motions and the nature of the member objects are known only for very few sources in the core with a radius of about  $0.3''$ . In particular, it is not clear whether all

objects identified by previous works actually are stars. In this paper we analyze seven years of imaging data (presented in Section 3.2). We identify 19 objects in the core of IRS13E, for all of which we can measure proper motions (Section 3.3). For the brightest sources E1 and E2, we obtain acceleration limits which start to constrain the nature of IRS13E (Section 3.3). From H- to L'-band photometry and H+K-band spectra we constrain the nature of the objects (Section 3.4). In Section 3.5 we calculate the probability that our acceleration limits occur for the two cases that a) IRS13E is bound by an IMBH and b) that it is a chance association. Section 3.6 considers other data in a more qualitative fashion and theoretical models. Finally we summarize and conclude in Section 3.7. We assume a distance to the GC of  $R_0 = 8$  kpc (Reid 1993) and a mass of the SMBH of  $M = 4 \times 10^6 M_\odot$  (Ghez et al. 2008; Gillessen et al. 2009).

## 3.2 Data Set

This study uses seven years of adaptive optics based imaging data and spectroscopic data obtained with an integral field spectrograph in 2004 and 2009. This section briefly describes our data set.

### 3.2.1 NACO

We obtained images with NAOS/CONICA (NACO) mounted on UT4 (Yepun) at the VLT (Lenzen et al. 2003; Rousset et al. 2003)<sup>1</sup>. The camera CONICA, together with the adaptive optics (AO) system NAOS, achieves diffraction limited images in the near-infrared. For this study, we use mainly the 13 mas/pixel image scale. On this scale, the point spread function (PSF) is oversampled. This is suited better for highly crowded fields than a strict Nyquist sampling (Trippe et al. 2010).

For source detection and astrometry, we use data from nearly every observing run from April 2002 to May 2009, excluding only the worst 10% of the observing runs by eye. In total, our sample consists of 37 H-, 74 Ks- and 5 L'-band images.

We base the broad-band photometry on four H-, four Ks- and three L'-band images that were of particularly good quality. Furthermore, we use four narrow-band images for photometry, which we obtained at  $2.06 \mu\text{m}$ ,  $2.24 \mu\text{m}$  (12-06-2004),  $2.17 \mu\text{m}$  and  $2.33 \mu\text{m}$  (13-06-2004).

All images are flat-fielded, bad pixel corrected and sky subtracted. In addition, we correct images in which saturation is important for the nonlinearity of the detector (Fritz et al. 2010).

We combine single images of typically 30 seconds exposure into stacked images. Because the faint additional sources in IRS13E lie in the PSF halos of the bright stars, the prime goal of the data reduction is to obtain the highest Strehl ratio possible for each data set,

<sup>1</sup>We use NACO data from ESO programs 70.B-0649, 71.B-0077, 71.B-0078, 71.B-0365, 072.B-0285, 073.B-0084, 073.B-0085, 073.B-0665, 073.B-0775, 075.B-0093, 077.B-0014, 078.B-0136, 179.B-0261, 179.B-0932, 183.B-0100.

even at the cost of smaller total exposure (Fritz et al. 2010). For this reason, we select frames of good quality (small FWHM) for a combined image of an observing run only.

### 3.2.2 SINFONI

Spectroscopy allows one to obtain a secure identification of spectral types and to measure radial velocities. We use spectra obtained with the integral field spectrometer SINFONI (Eisenhauer et al. 2003; Bonnet et al. 2003) at UT4 of the VLT<sup>2</sup>. We analyze high-quality H+K-band laser and natural guide star data from May 21 and 23, 2009. The data from the latter date have a Strehl ratio of 28% at  $2.11\ \mu\text{m}$  and a total of 2400 s exposure. The spatial sampling is  $12.5\ \text{mas} \times 25\ \text{mas}\ \text{pixel}^{-1}$ , the spectral resolution is 1500. We apply the standard data reduction for SINFONI data, including detector calibrations (such as bad pixel correction, flat-fielding and distortion correction) and cube reconstruction. The wavelength scale is calibrated by means of emission line lamps and finetuned with atmospheric OH lines. The remaining uncertainty corresponds to typically (less than) 10 km/s.

## 3.3 Astrometry

### 3.3.1 Image Processing

One of the main aims of this study is to characterize the faint objects in the core of IRS13E, the velocities of which are unknown. We base our analysis on deconvolution of the images, which requires the determination of the PSF for each image.

For creating a PSF we use STARFINDER version 1.2 (Diolaiti et al. 2000). We extract the PSF from ten to 15 stars brighter than  $m_{\text{Ks}} = 13.5$  and symmetrically distributed around IRS13E up to a distance of  $4''$ . We then use the Lucy-Richardson algorithm (Lucy 1974). Depending on the image quality, we choose between 6000 and 20000 iterations. We are confident that the LR algorithm applied in this way also mostly correctly handles extended sources. For example, the extended object IRS2L (Blum et al. 1996) contains only one maximum after deconvolution, and a large fraction of the flux remains detached from the central maximum. Relatively faint sources which are in the same distance from a bright star as the radius of the PSF are sometimes influenced by deconvolution rings. Most (and all important) sources are either clearly outside or clearly inside of these rings. We do not smooth the result of the deconvolution at all and find stellar positions by centroids around local maxima.

We deconvolve all H- and Ks-band images. We then select by visual inspection the images for the subsequent analysis, on which at least some of the fainter objects are visible. These are 61 Ks-band images and 18 H-band images. This subjective quality selection is nearly identical to a Strehl ratio cut of 9% in both bands.

---

<sup>2</sup>We use SINFONI data from ESO program 183.B-100.

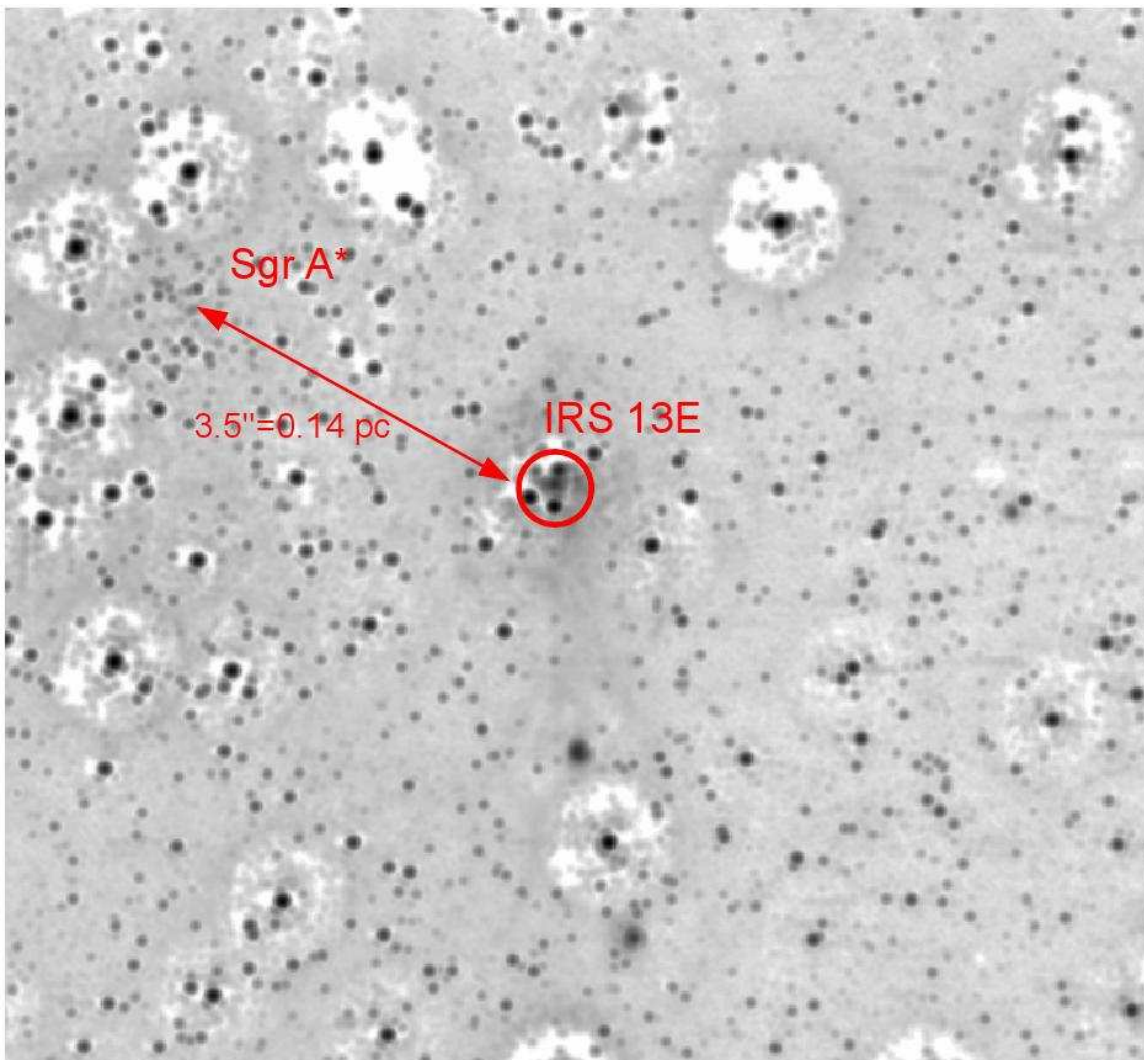


Figure 3.1 Lucy-deconvolved Ks-image of the GC from 13-03-2008, smoothed with a Gaussian with a FWHM of 4 pixels. The intensity scale is logarithmic. Sgr A\* and IRS13E are marked.

### 3.3.2 Object Detection

Some care is needed to distinguish between real and spurious sources since we are dealing with a crowded field imaged at the diffraction limit. Our procedure is as follows. We start by measuring the positions of the local maxima on the quality-selected, deconvolved images. We treat each frame individually, such that we can neglect maxima that are unlikely to correspond to a real source. These are for example maxima only marginally brighter than the noise floor or the background from the minispiral, or maxima that apparently are affected by deconvolution artifacts.

We consider an object to be well-detected if it is found in either at least three images in both H- and Ks-band, or in at least ten Ks-band images. This is a robust criterion, since the objects are present in images that sample a wide range of PSF shapes. According to these criteria, we detect 19 sources in the core ( $r \lesssim 0.3''$ ) of IRS13E (Figure 3.2). The rms position deviation of these sources to a linear fit after transformation into the astrometric reference frame to the Ks-band data is 7 mas in median. Thus all measured positions of the 19 sources lie within an area of 4000 mas<sup>2</sup>, only 1/50 of the area of the cluster core. Therefore the sources are not random fluctuations.

We test by means of simulated images that indeed our detection procedure is robust. Using a variety of PSFs we find that it is only possible to continue to obtain the same sources after deconvolution if indeed these sources had been put into the simulation.

### 3.3.3 Proper Motions

Given the pixel positions, we go to an astrometric coordinate system by constructing a full linear transformation using ten bright, isolated stars from the astrometric list of Trippe et al. (2008) close to IRS13E. Proper motions are in turn obtained by fitting the positions as a function of time by linear functions. Since we are using many position measurements for the fitting, we simply use an unweighted fit. The errors for any given object are set to the scatter of the data around the linear motion model. For the fit,  $5\sigma$  outliers are rejected. There are only two such cases in H and Ks for all the objects. The absolute position toward Sgr A\* has an additional uncertainty of about 2 mas (Reid et al. 2007; Trippe et al. 2008; Gillessen et al. 2009) corresponding to a relative error of  $\approx 0.05\%$  which safely can be neglected in our analysis.

In the L'-band the exclusion of  $5\sigma$  outliers becomes important, and the errors are mostly larger. The L'-band velocities differ significantly from the velocities obtained from the other bands for the three brightest stars. The differences can be as large as  $16\sigma$  and 2.5 mas/yr. The differences are probably caused by L'-band dust emission that is important around IRS13E. The L'-band velocities are less useful and we neglect them in our analysis.

The proper motion fits are presented in Table 3.1 and Figure 3.14. For the bright stars E1, E2 and E4.0 we also fit second order polynomials to the stellar positions as a function of time to test for accelerations. The accuracy reached for the three brightest stars starts to constrain the mass of a putative IMBH.

For most objects the velocities derived from H- and Ks-band data are consistent. The

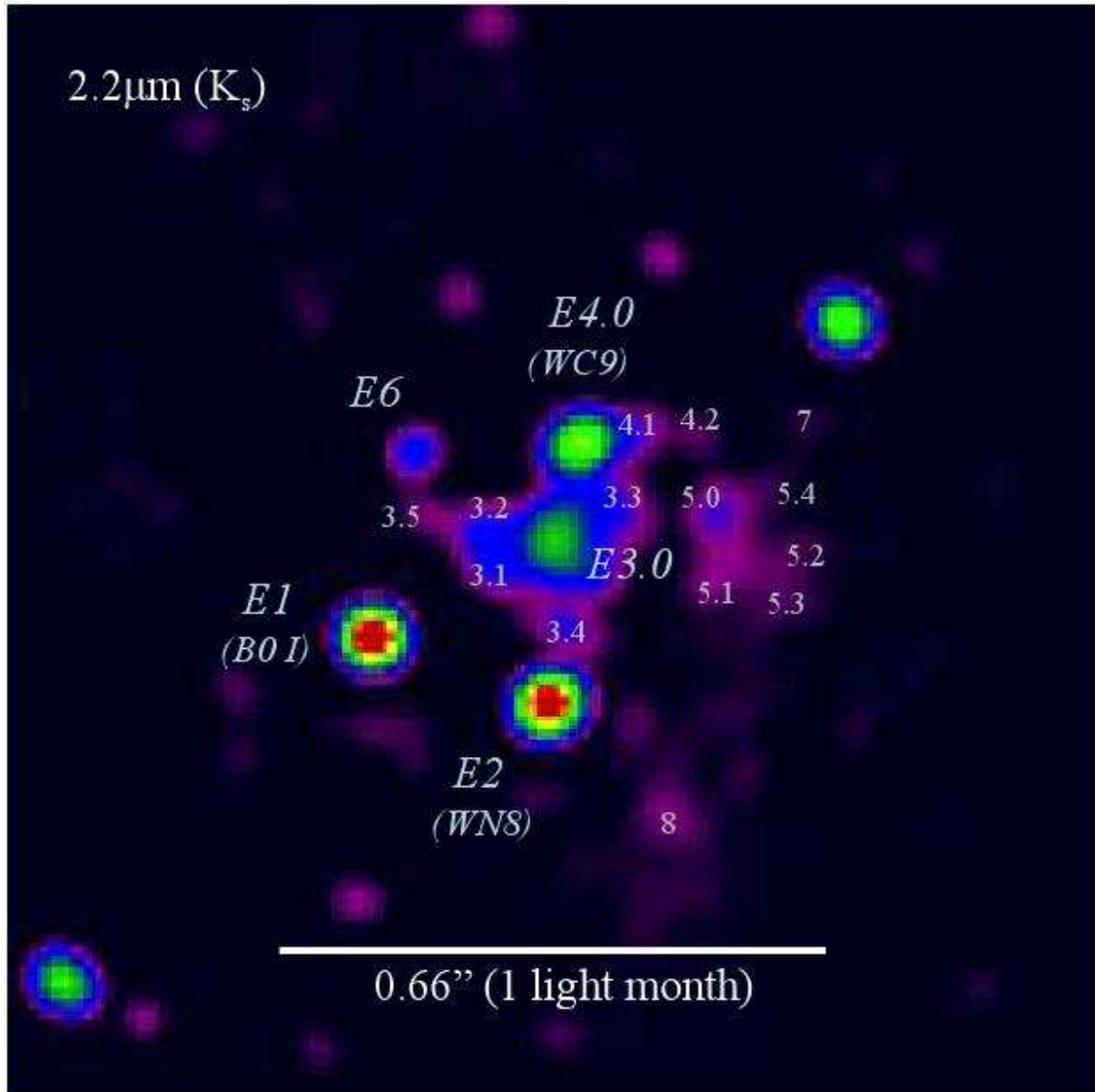


Figure 3.2 Coadd of four Lucy-deconvolved  $K_s$ -images of IRS13E between 2002 and 2007, smoothed with a Gaussian with a FWHM of 2 pixels. The intensity scale is logarithmic. The sources which we consider real are marked with numbers. Nearly all of these objects are also found in H-band images.

Table 3.1. Proper motions and acceleration limits of the objects in IRS13E

Object	band	R.A. [as]	v <sub>R.A.</sub> [km/s]	Dec. [as]	v <sub>Dec.</sub> [km/s]	a <sub>R.A.</sub> [ $\mu$ as/yr <sup>2</sup> ]	a <sub>Dec.</sub> [ $\mu$ as/yr <sup>2</sup> ]
E1	H and Ks	-2.958	-142.5 $\pm$ 1.3	-1.645	-105.5 $\pm$ 0.7	22 $\pm$ 20	11 $\pm$ 14
E2	H and Ks	-3.171	-249.2 $\pm$ 1.1	-1.732	23 $\pm$ 0.7	20 $\pm$ 19	-14 $\pm$ 16
E3.0	Ks	-3.184	-82 $\pm$ 9	-1.528	8 $\pm$ 9		
E3.1	Ks	-3.126	19 $\pm$ 39	-1.562	19 $\pm$ 43		
E3.2	Ks	-3.093	-74 $\pm$ 38	-1.525	84 $\pm$ 24		
E3.3	Ks	-3.252	-262 $\pm$ 17	-1.491	2 $\pm$ 15		
E3.4	Ks	-3.203	-97 $\pm$ 20	-1.632	-23 $\pm$ 27		
E3.5	H	-3.026	-12 $\pm$ 51	-1.501	-126 $\pm$ 48		
E4.0	H	-3.210	-227 $\pm$ 4	-1.409	26 $\pm$ 4	80 $\pm$ 70	-30 $\pm$ 80
E4.1	Ks	-3.281	-211 $\pm$ 21	-1.410	206 $\pm$ 18		
E4.2	H	-3.364	-25 $\pm$ 43	-1.402	-80 $\pm$ 27		
E5.0	Ks	-3.382	-136 $\pm$ 12	-1.502	175 $\pm$ 14		
E5.1	Ks	-3.391	-87 $\pm$ 38	-1.569	42 $\pm$ 34		
E5.2	Ks	-3.474	-340 $\pm$ 38	-1.541	3 $\pm$ 28		
E5.3	Ks	-3.458	-139 $\pm$ 39	-1.607	163 $\pm$ 30		
E5.4	Ks	-3.446	-68 $\pm$ 38	-1.469	30 $\pm$ 34		
E6	H and Ks	-3.010	-133 $\pm$ 7	-1.423	23 $\pm$ 7		
E7	Ks	-3.495	-227 $\pm$ 29	-1.391	167 $\pm$ 28		
E8	Ks	-3.320	-118 $\pm$ 18	-1.866	95 $\pm$ 20		

Note. — The positions refer to reference epoch 12-05-2005 and are measured relative to Sgr A\*. The dominating uncertainty of the position is caused by the coordinate uncertainty of about 2 mas (Reid et al. 2007; Trippe et al. 2008; Gillessen et al. 2009).

biggest discrepancy happens for E4.0 that shows a velocity difference of 16 km/s or  $3.7\sigma$  in R.A. The value for the R.A.-velocity in Ks lies between the velocities obtained from H- and L'-band data. Therefore, we assume that dust perturbs the position of this star also in Ks-band, not only in L'-band. Consequently we only use the astrometry from H-band data for this star, and we also don't trust the marginally significant acceleration in Dec. direction.

Similarly, for the faint or confused objects (E3, E4.1, E4.2, E5, E7, E8) we adopt the measurements derived from the band where the source is more prominent compared to the local background level. For the relatively blue objects E3.5, E4.0 and E4.2 this is the H-band, for the other ones Ks-band. For the unconfused objects E1, E2 and E6 we use the weighted average of the two bands.

### 3.4 Characterization of the Objects

In order to address the question of whether IRS13E hosts an IMBH, it is important to know the nature of its constituent objects. Only stars can be used as fiducial tracers for a gravitational potential, and an overdensity of objects compared to the stellar background is only meaningful if these are actually stars. In this section we first describe the combined photometric and spectroscopic method to construct a SED. Then we use it to constrain

the nature of the individual objects. We present the results for the most important objects here and leave for the appendices a description of the details of the method and the results for the remaining objects.

### 3.4.1 Method

For each object we construct a spectral energy distribution (SED), ideally ranging from H- to L'-band. For this we use broad- and narrow-band images plus the two spectro-imaging data cubes in the combined H+K-band.

Where possible, we identify the objects in the SINFONI data by their spectral features as late- or early-type stars. In this way we show that E1, E2, E4.0 and E6.0 are stars. For the other objects we construct SEDs from a deconvolved SINFONI cube and the narrow-band imaging data (Appendix 3.8.1). We then estimate whether a stellar component is required to explain the SED.

Following the approach of Maillard et al. (2004), we consider models composed of an extinction parameter and either one or two temperatures corresponding to a star and dust. We derive the temperature of the stellar component from the lines in the spectrum when possible. Otherwise we assume a temperature of 9480 K (corresponding to the spectral type A0V) for the star. This is sufficient, since the shape of the SEDs in our wavelength range depends only weakly on the assumed temperature for the stellar component of the SED model.

We use the extinction law of Draine (1989) shortward of Brackett- $\beta$  and  $A_{K_s}/A_{L'} = 1.75$  (Lutz et al. 1996). When fitting models to the less well measured SEDs, we only use extinction values that differ less than  $\Delta A_{K_s} = 0.3$  from the value for E1. This range seems adequate given the extinction map of Schödel et al. (2010) and our result does not depend strongly on this assumption. We neglect the nebular lines originating from the interstellar gas. At our precision their contributions to the flux are negligible.

For the bright early-type stars we have well-measured spectra such that an explicit comparison with atmosphere models becomes viable. We use the radiative transfer code CMFGEN (Hillier & Miller 1998) to derive the main parameters of the stellar atmospheres of E1, E2 and E4.0. The code computes non-LTE atmosphere models including wind and line-blanketing. We proceed as in Martins et al. (2007). A slight improvement in the method is the use of iterations on the hydrodynamic structure to ensure a better consistency between the atmosphere model per se and the density/velocity structure (Martins et al. 2009). The derived stellar parameters rely on line ratios and photometry. In addition, we derive the extinction by fitting the shape of the infrared SEDs. Hence, for each star, we have computed several models with different luminosities and looked for the best combination of luminosity, extinction and dust emission.

### 3.4.2 Individual Objects

This section describes the nature of the most important objects in IRS13E. For a description of the other objects, see Appendix 3.8.2. Table 3.2 presents the values of the model

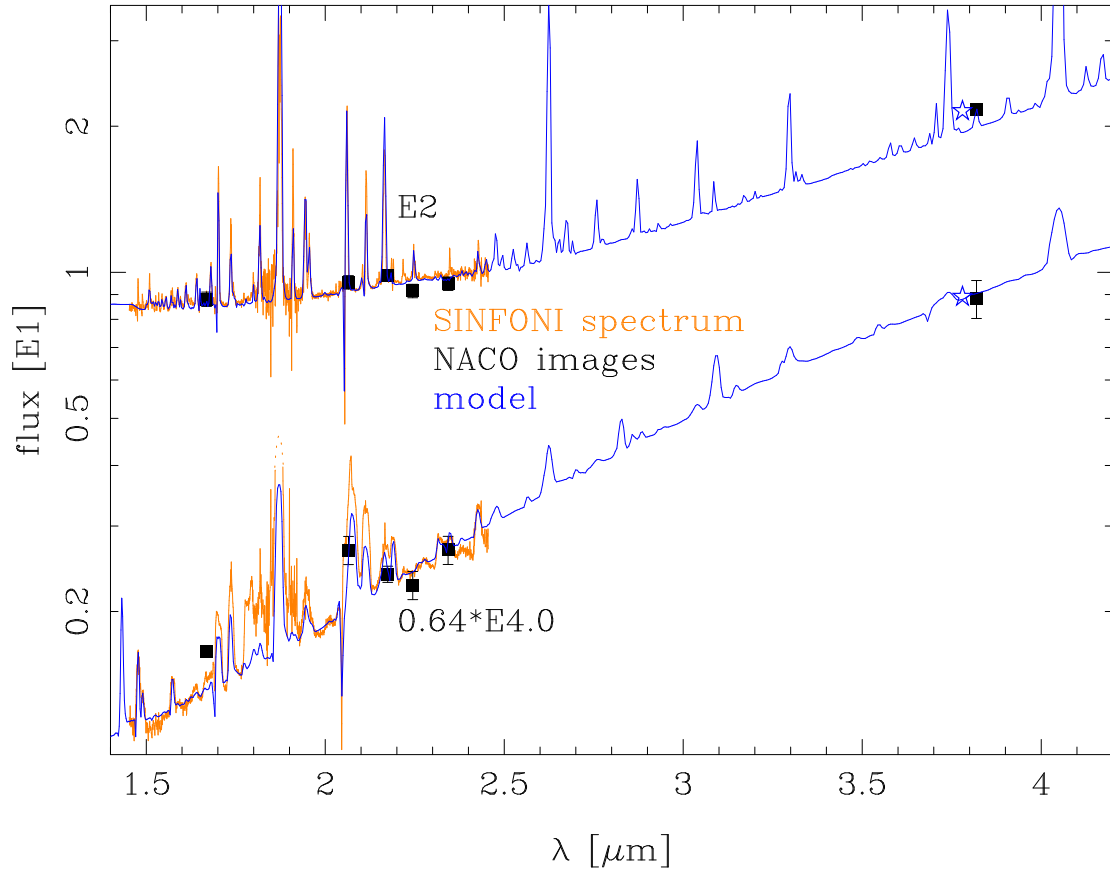


Figure 3.3 H+K-band spectra and photometry of the two WR-stars in IRS13E: E2 (WN8) and E4.0 (WC9). We fit full atmosphere models plus blackbodies with dust-like temperatures to the observed spectra and L'-band flux points. The asterisks denote the average flux of the models in L'-band, to which the measured flux needs to be compared.

parameters for all objects, for which our data allow an identification.

### IRS13E3.0

We resolve E3 on the deconvolved images into six stable sources and name them E3.0, E3.1, E3.2, E3.3, E3.4 and E3.5. This section describes the brightest component E3.0, which likely is extended or multiple at our resolution. Its flux increases significantly by 0.25 mag between 2002 and 2008 in H- and Ks-bands, the main increase happens between 2004 and 2006. This is not caused by confusion.

We extract a spectrum from the SINFONI data at the position of E3.0 (Figure 3.4). This spectrum also contains flux from the other five E3 sources and the extended background, but E3.0 completely dominates due to its brightness.

No stellar line (absorption line, or broader emission line) is visible in E3.0, but many narrow emission lines from H, Fe and He are present. Nearly all these lines are very similar

to the surrounding nebular background. A few lines like  $\text{H}_2$  at  $2.122 \mu\text{m}$  and  $2.223 \mu\text{m}$  are only present in the background. Most identifiable lines ( $\text{HI}$ ,  $\text{HeI}$ ,  $\text{FeII}$ ,  $\text{FeIII}$ ) are known from the minispiral (Lutz et al. 1993) or are other hydrogen lines.

Stellar absorption lines of fainter stars are likely too weak for being detectable against the strong narrow emission lines of the surrounding gas. However, that there are any WR-stars in E3.0 seems unlikely, since the strong, broad emission lines of such stars would be visible. For example, E4.0 (a WC9 star) scaled down to  $m_{\text{Ks}} = 15$  would be detectable against the narrow emission lines. Given that a WR-star cannot be fainter than  $m_{\text{Ks}} = 16.5$  (Crowther 2007), only a few types of WR-stars could be hidden in E3.0. Also, E3.0 does not resemble a dusty WR-star (of which E4.0 is one), in which case the lines would be diluted but still visible.

It is worth noting that also the background emission is well determined from our data. The seeing halo of E3.0 is of no concern since the lines in the background are stronger in relative terms. The extinction appears to be similar in the whole region, since we do not measure any change in the relative line strengths for lines from one ionization state of an element over the spectral cube. In contrast, the line strength ratios of different elements differ between the background and E3.0 (see for example the  $\text{HI}$ ,  $\text{FeII}$  pseudo doublet at  $1.64 \mu\text{m}$  in Figure 3.4). These spatial changes in the spectral properties appear to be gradual, consistent with a gaseous nature of E3.0. They are strongest at the position of E3.0, but they do not correlate in general with the positions of the red sources in IRS13E.

The radial velocity of E3.0 determined from the Brackett- $\gamma$  line is  $v_{\text{LSR}} \approx -25 \text{ km/s}$ , measured at the position of the continuum peak of E3.0. Paumard et al. (2006) measured a velocity of  $v_{\text{LSR}} = 87 \pm 20 \text{ km/s}$  for E3 but did not identify the type of star. Probably Paumard et al. (2006) measured an average of E2 and E4.0 instead of the E3 velocity.

Given the photometric variability of E3.0, we fit the SED based on the narrow-band data set from 2004 and the one based on the SINFONI spectroscopy from 2009 separately. Using the latter we obtain  $A_{\text{Ks}} = 3.89 \pm 0.16$  and a warm dust component of  $T = 970 \pm 17 \text{ K}$ , see Table 3.2 and Figure 3.5. The  $1\sigma$  flux limit on the stellar component is  $m_{\text{Ks}} = 16$ . Using the earlier imaging data yields consistent results. Also in this case, no stellar component is needed, however the limit is less constraining due to the smaller wavelength coverage. The extinction value  $A_{\text{Ks}} = 3.5 \pm 0.7$  is consistent with the former one. We also obtain an independent extinction estimate of  $A_{\text{Ks}} = 3.44 \pm 0.15$  from the Brackett series of E3.0 by using the relative line strengths of Hummer & Storey (1987) and the electron densities and temperatures from Lutz et al. (1993). Our different extinction estimates appear to be sufficiently consistent with each other. Using a value around  $A_{\text{Ks}} = 3.4$  in conjunction with the 2009 data yields that the magnitude of a possible stellar component is less than  $m_{\text{Ks}} = 18$ .

We also compare the spectrum of E3.0 with those of young stellar objects (YSO). Such objects are not expected to reside in the central parsec, because the gas density there is much too low for star formation (Christopher et al. 2005; Bonnell & Rice 2008). Eckart et al. (2004) and Mužić et al. (2008) speculate that some of the objects of IRS13N nevertheless could be YSO, arguing that shocks could allow star formation to take place. The combination of color and luminosity for E3.0 argues against a typical Herbig-Be-star.

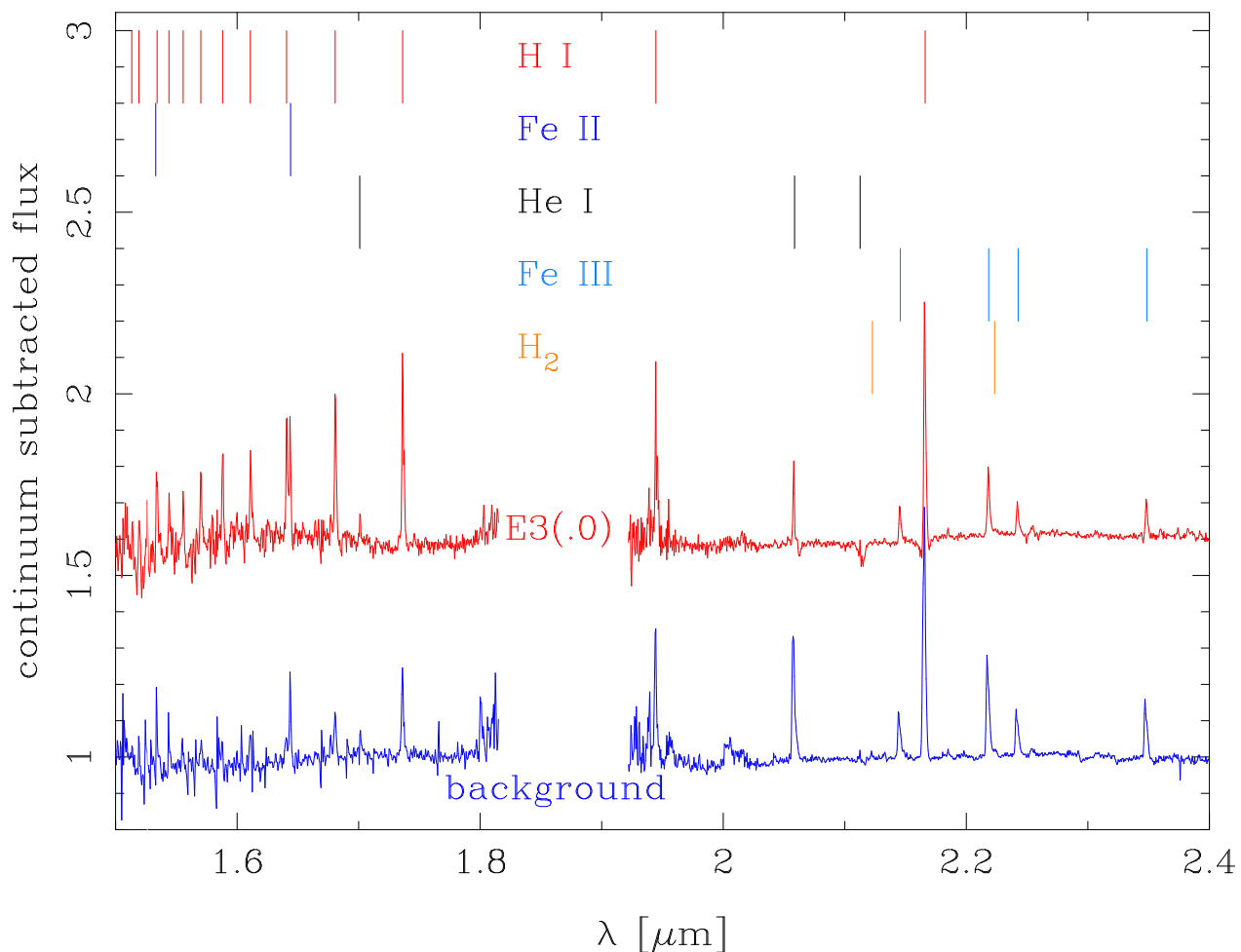


Figure 3.4 H+K-band spectrum (red) of the brightest component of IRS13E3: E3.0. For comparison the spectrum of the nebular background is shown, too (blue, shifted). In the upper part, the line positions for various transitions are marked. The weak CO band heads in the background spectrum are caused by stray light of late-type stars. The weak absorption feature of E3.0 around Brackett- $\gamma$  and Helium are likely caused by the slightly imperfect subtraction of the stellar emission lines.

Also, no distinctive feature of a massive YSO is visible in E3.0. Except for the Brackett lines, the lines observed in E3.0 are unknown (e.g. FeIII) or weak (e.g. He) in massive YSO. A massive YSO does not necessarily show other lines apart from Brackett- $\gamma$  in the K-band, but often CO-band heads, H<sub>2</sub>, or the Pfund series in emission can be visible (Bik et al. 2006; Martín-Hernández et al. 2008). Such a clear indication for a YSO is not observed in E3.0, nor in other parts of IRS13E. Furthermore, there is no additional local extinction toward E3.0 while YSOs show locally enhanced extinction. We conclude that it is unlikely that E3.0 is a YSO.

The source E3.0 in the H-band has a velocity similar to the the radio source in IRS13E (Zhao et al. 2009). Therefore the H-band emission is likely due to dust associated with the gas, which causes the radio continuum emission. Hence, also qualitatively a higher extinction value (like for example expected in YSO) seems not to be needed.

Maillard et al. (2004) found two similarly bright components E3A and E3B, which is different from our result at higher resolution. Their additional stellar components do not fit our SED for E3.0. Our flux at 1.48  $\mu\text{m}$  is a factor  $\approx 1.8$  lower than the sum of the flux models for E3A and E3B, but at 2.18  $\mu\text{m}$  our flux is only a factor  $\approx 1.15$  lower. The hint for the stellar component in Maillard et al. (2004) is only based on the 1.6  $\mu\text{m}$ -flux measured in the filter F160W from NICMOS. Since this is a very broad filter, and E3.0 is a very red source, the central wavelength of the filter is considerably bluer than the effective wavelength. Hence, using the central wavelength will overestimate the flux. We speculate that this effect made the stellar component necessary. Also, the amount of stellar flux contributing at that wavelength to the total flux is small, and hence a small measurement error might change the conclusion from Maillard et al. (2004).

To summarize; the potential stellar component in E3.0 is fainter than most known WR-stars. A main sequence star in E3.0 would need to be fainter than B1.5V. This seems unlikely, however, since these stars do not produce dust. With three different methods we obtained consistent extinction values, similar to the extinction toward E1 and E2. We conclude that E3.0 is neither a star nor a YSO, but rather a concentration of warm dust and gas.

The source E3.0 is not the only dust source of its brightness in the GC. For example, the source IRS2L resembles E3.0 in many respects and also shows extended H-band emission.

### E7, E8 and the Surrounding Gas

The background around IRS13E is not only visible in gaseous emission lines (Figure 3.4) but also in the continuum. The deconvolution artifacts hamper any photometric measurement of this continuum. Instead, we use the objects E7 and E8 (Figure 3.2) that are less affected. These objects are farther away from the center of IRS13E than the other sources and likely do not belong to IRS13E but to the background. Spectroscopically, E8 appears to be indeed a local overdensity in the gas.

E7 and E8 are not detected in the H-band. We fit a blackbody model to each of the two objects, fixing the extinction to its upper bound at  $A_{K_s} = 3.9$ . We find that no star is needed to explain the SED of these two objects. We obtain a temperature of  $T = 692 \pm 55$  K

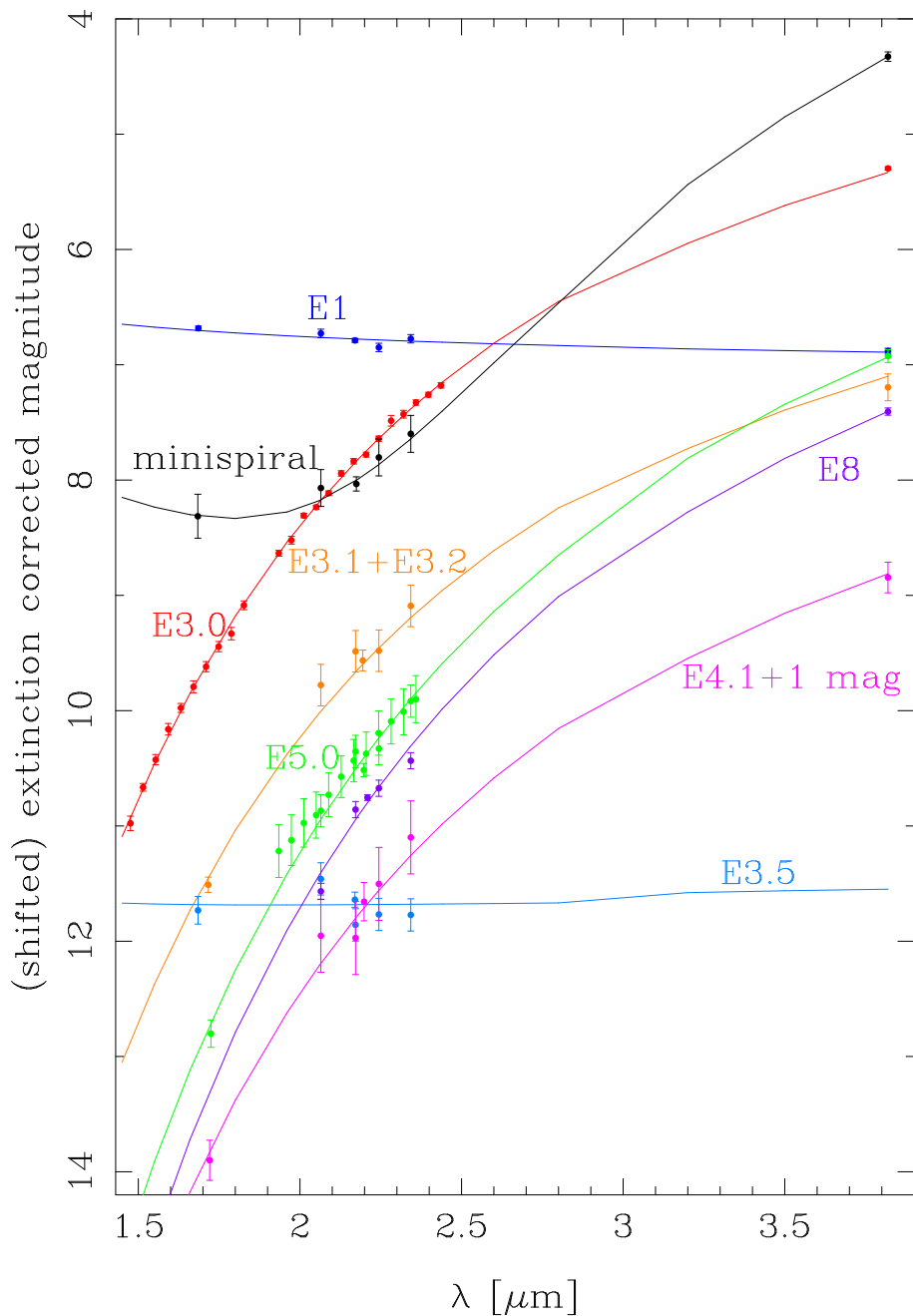


Figure 3.5 SED data and model fits for E1, E3.0, E3.5, E4.1, E5.0, E8, the minispiral and the sum of E3.1 and E3.2. All data and fits are offset from each other for clarity. For all sources the extinction correction of E1 is applied. E1 and E3.5 are fit well by single blackbodies of stellar temperature. The objects E3.0, E3.2+E3.3, E4.1, E5.0 and E8 can be fit as single blackbodies with a dust-like temperature. Stellar components do not improve these fits. The SED of the minispiral shows two blackbodies: A warm dust component and stellar stray light.

for E7 and of  $T = 732 \pm 10$  K for E8. Thus, E7 and E8 are colder than most objects in IRS13E.

We also detect three faint stars ( $m_{\text{Ks}} \approx 15$ ) in the SINFONI data at the approximately same distance ( $\approx 450$  mas) to E3.0. All these stars show CO band heads. Buchholz et al. (2009) correctly identify the star with the strongest CO-band heads as late-type, the others are misidentified as early-type stars. The radial velocities of these stars are different from the radial velocity of IRS13E. Thus, the stars differ from IRS13E not only in proper motion (Trippe et al. 2008) but also in stellar type and radial velocity. We conclude that they are fore- or background objects.

The background around IRS13E is part of the minispiral (Lo et al. 1983; Paumard et al. 2004; Zhao et al. 2009). The minispiral is visible in our L'- and Ks-band data. In order to measure its SED, we select seven boxes of  $\approx 0.2''$  diameter far away from bright stars at a distance of around  $1.5''$  to IRS13E. We exclude the narrow-band data around Brackett- $\gamma$  because of the strong emission line there. We calibrate the flux from the narrow-band filters by fitting these flux values as a linear function of wavelength and setting equal the flux at  $2.18 \mu\text{m}$  to the measured Ks-band flux. We fit two blackbodies to the SED data (Figure 3.5). One accounts for the stellar stray light, the other represents the dust. The fits for all fields are similar. The average extinction is  $A_{\text{Ks}} = 3.64 \pm 0.55 \pm 0.56$ , consistent with the extinction value derived for E1. The average dust temperature is  $T = 585 \pm 22 \pm 33$  K. Thus, the minispiral is colder than the dust in IRS13E.

One of the seven fields contains the central sources of IRS13N (Eckart et al. 2004; Moutaka et al. 2005; Mužić et al. 2008). In this case the fit yields  $A_{\text{Ks}} = 3.7 \pm 1.6$  and  $T = 664 \pm 174$  K. This argues against a highly extinguished object (like a YSO) as these authors had proposed. The object IRS13N $\beta$  is within the field of view of our SINFONI data. We do not find any significant differences between its spectrum and the spectrum of the gas around IRS13E. Also, the velocity of IRS13N in L'-band (Mužić et al. 2008) and at radio wavelengths (Zhao et al. 2009) make it more likely that IRS13N actually consists of dust blobs. They appear denser than in other regions in the GC, but still they are much less prominent than E3.0. The common proper motion of these sources (Mužić et al. 2008) could also be explained by a recent formation of the dust clouds.

## 3.5 Probability for an IMBH in IRS13E

We now discuss the nature of IRS13E considering our NIR observations. There are four main explanations:

- IRS13E is a cluster in the process of dissolution, one of various possibilities suggested by Schödel et al. (2005). This is very unlikely, because it would get diluted extremely quickly. In the case of IRS13N with a similar dispersion as IRS13E Mužić et al. (2008) show in their Figure 2 that such an association is diluted quickly in the GC. We estimate that after just 200 years one would not recognize anymore the overdensity of three young, massive stars of IRS13E as such. We exclude this option.

Table 3.2. Spectral properties of the objects in IRS13E

Name	data	spectrum	$A_{K_s}$	$T_1$ [K]	$T_2$ [K]	star $m_{1, K_s}$	dust $m_{2, K_s}$
E1	NB, H, K, L	OB I	$3.64 \pm 0.07$	26000		$10.38 \pm 0.06$	
E2	SINF, NB, H, K, L	WN 8	3.51	30000	712	10.43	14.74
E3.0	SINF, NB, H, K, L	gas	$3.89 \pm 0.16$	9480	$970 \pm 17$	> 16	$11.42 \pm 0.05$
E3.(1+2)	NB, H, K, L	gas	3.9	9480	$955 \pm 24$	> 18.03	$13.24 \pm 0.18$
E3.3	NB, H, K, L	gas	3.9	9480	$987 \pm 54$	> 15.16	$13.65 \pm 0.35$
E3.4	NB, H, K, L	gas	3.9	9480	$954 \pm 49$	> 16.53	$14.15 \pm 0.36$
E3.5	NB, H, K		$3.49 \pm 0.36$	4000-19000		$15.30 \pm 0.26$	
E4.0	SINF, NB, H, K, L	WC 9	3.64	41000	1400	11.95	12.51
E4.1	NB, H, K, L	gas	3.9	9480	$844 \pm 24$	> 18.36	$14.38 \pm 0.21$
E4.2	NB, K, H		3.9	4000-19000	$517 \pm 252$	$15.77 \pm 0.11$	$16.64 \pm 2.5$
E4.3	K						$15.48 \pm 0.10$
E5.0	SINF, NB, H, K, L	gas	3.4	9480	$700 \pm 8$	> 18.46	$14.08 \pm 0.10$
E5.1	NB, H, K, L	gas	3.9	9480	$947 \pm 25$	> 17.75	$14.25 \pm 0.14$
E5.2	NB, K, L	gas	3.9	9480	$642 \pm 70$	> 15.6	$15.49 \pm 0.10$
E5.3	NB, H, K	gas	3.9	9480	$978 \pm 524$	> 16.04	$15.1 \pm 1.6$
E5.4	NB, K	gas	3.4		$817 \pm 474$		$15.54 \pm 2$
E6	NB, H	K3III	$3.68 \pm 0.09$	4300		$13.82 \pm 0.10$	
E7	NB, K, L		3.9	9480	$692 \pm 55$	> 16.71	$16.02 \pm 0.40$
E8	NB, K, L	gas	3.9	9480	$732 \pm 10$	> 17.14	$14.51 \pm 0.11$

Note. — We fit one or two blackbodies with temperatures  $T_1$  and  $T_2$  and one extinction parameter to our SED data. We allow extinction values between  $A_{K_s} = 3.4$  and  $A_{K_s} = 3.9$  and clip it if needed at the respective edge of the interval. We derive the temperature of the stellar component from an atmosphere model or from the observed lines when possible. Otherwise the temperature is set to  $T = 9480$  K. All limits are  $1\sigma$  limits. In column two, SINF means the SED fitting results are based on SINFONI data, NB that the narrow band images are used. The fourth row fits E3.1 and E3.2 together.

- IRS13E is a cluster bound by stellar mass. From our detection limits, we estimate that the total stellar mass of the cluster could at most be  $2000 M_{\odot}$ .
- IRS13E is a cluster bound by additional mass, e.g. an IMBH.
- IRS13E is a chance association.

### 3.5.1 Stellar Surface Density in IRS13E

A physical cluster leads to an overdensity in projection compared to the local background density. Detecting a local, significant overdensity in the stellar surface density would hence be a strong indication that IRS13E is a cluster. From our data we measure the projected space densities of stars in IRS13E. Paumard et al. (2006) found 13 objects with  $m_H < 19.4$  inside a radius of  $0.3''$  in IRS13E. Similarly, we find 15 objects in H- and Ks-band with  $m_H < 18.5$  inside a radius of  $0.27''$ .

We determine the density of background stars in a non-confused region with a size of  $5.15 \text{ sqas}$  north of IRS13E for stars fainter than  $m_H = 14$ . Because there the extinction is higher than toward IRS13E according to the extinction map of Schödel et al. (2010), we shift the magnitudes of all the stars in this field by 0.4 magnitudes to brighter magnitudes. For stars brighter than  $m_H = 14$  we use the results from Genzel et al. (2003) to estimate the background density. We find that the density of objects in IRS13E is higher than in the surrounding field at nearly all magnitudes (Figure 3.6), if all objects are considered. However, only for six of these objects a star is required to explain the observed SED. For the other objects, a possible stellar component needs to be fainter than about  $m_{Ks} \approx 15.5$ . This corresponds to a stellar surface density of  $26 \text{ as}^{-2}$ , which is five times higher than the background. However, E6 (Figure 3.7) is not a member of the cluster, given its age well above 6 Myr. Furthermore, the two faint stars E3.5 and E4.2 have magnitudes consistent with the red clump and hence are likely also older than the bright stars. In the magnitude bin of E3.5 and E4.2, the background population accounts already for one of the two stars. Thus, the overdensity in this bin is insignificant, too.

We conclude that the magnitude integrated overdensity of objects in IRS13E (with a chance probability of  $2 \times 10^{-5}$ , Paumard et al. 2006) is caused by dust clumps and not by stars. This overdensity cannot be used as evidence for a cluster. Nevertheless, the concentration of the three bright early-type stars in IRS13E remains puzzling, an argument which we analyze quantitatively in Section 3.5.3.

### 3.5.2 The Structure of IRS13E

A significant number of dust clumps in the GC are found far away from stars (Mužić et al. 2007). But most of these dust clump are invisible in Ks-band and none of them is visible in H-band. In the H-band the dust blobs in IRS13E are among the brightest non-stellar structures in the central parsec. The dust clumps close to E3.0 are nearly twice as hot as the minispiral and also denser ( $\approx 4\times$  for E3.0, estimated from surface brightness and

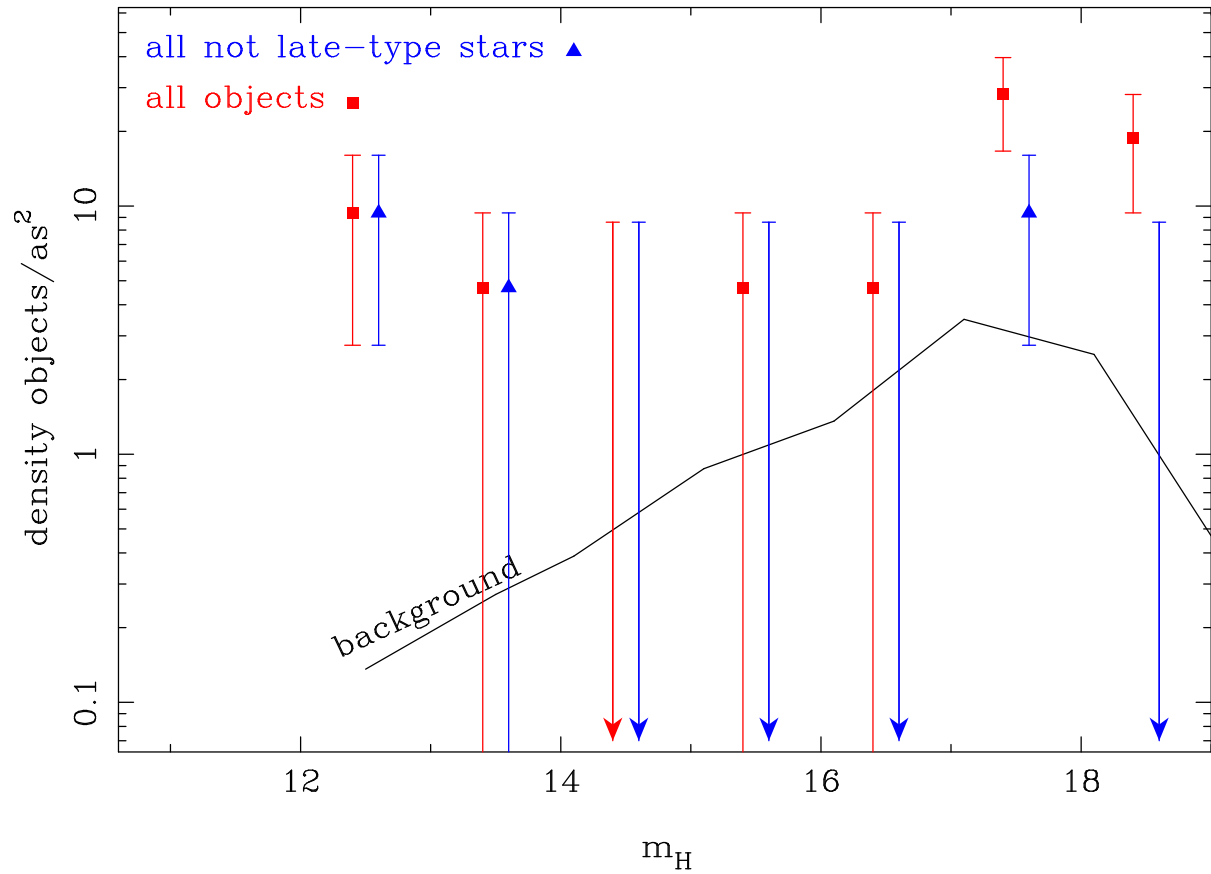


Figure 3.6 Surface densities of objects in the core ( $r = 0.27''$ ) of IRS13E. The errors are Poisson errors. The upper limits are  $1\sigma$  limits. Red: All objects. Blue: Cluster member candidates only. The red and blue data are offset slightly in the horizontal direction for clarity. The solid line shows the estimated background density for our data.

temperature) than the minispiral. The brightest and hottest dust blobs (around E3.0) are located between the two bright WR-stars E2 and E4.0. The star E2 is the brightest of all WR stars in the GC and E4.0 is a dusty WR with the hottest dust in IRS13E.

Therefore E4.0 might be the most important dust source in IRS13E. But it seems unlikely that E4.0 is responsible alone for the bright dust blob E3.0, given that it does not move away from E4.0, while the motions of the blobs E4.1 and E4.3 are consistent with being outflows from E4.0. Instead, we assume that the winds of E2 and E4.0 collide in the E3 region and cause the bright dust blobs in this way. For this model it is not necessary that the dust originates from the stars but only that it is heated by the two stars. The fact that the velocities of these blobs are not pointing toward either of the two WR stars supports this picture. Also, the eastward component of the R.A. motion of the blobs increases from west to east as expected in this model. Accordingly, E2 and E4.0 would not only be close in projection, but would indeed have a small 3D distance.

A potential weakness of that model is that the motions of the blobs E3.3 and E4.1 do not seem to fit. But this is only a worry if no other forces than repulsion from the stars act on the winds. For example, the presence of the gas from the minispiral might decelerate the winds. A second problem might be that it is not clear whether the conditions for dust formation are satisfied, given that our system is very different from WR140 (Monnier et al. 2002).

Most likely E1 does not contribute to the dust production. It is further away and supergiants have weaker winds than WR-stars. Furthermore, the velocities of some dust clumps are pointing toward E1. Therefore E1 can, but needs not to be close in real space to the WR-stars.

The dust clumps in E5, E7 and E8 fit less well into our simple model of two WR stars because of their velocities. They are also mostly colder than the dust clumps in E3 and E4, but still warmer than the minispiral. In addition, they are farther away from E2 and E4.0. Likely the minispiral is more important for their formation.

### 3.5.3 The Overdensity of Young, Massive, Early-type Stars

Because most of the fainter objects in IRS13E are dust clumps, the most prominent feature of the potential cluster IRS13E is the concentration of the three bright early-type stars. Therefore we quantitatively evaluate the argument of Maillard et al. (2004), that this association cannot be a chance occurrence. On the one side, the number of stars is very small, and one could argue that IRS13E cannot be a significant overdensity. On the other hand, five or even six phase space coordinates of these stars are similar.

We calculate the probability that a star association like IRS13E occurs randomly, i.e. a pseudocluster, by means of Monte Carlo simulations. IRS13E cannot be part of the clockwise disk of young stars (Paumard et al. 2006). Consequently, the size of the sample of stars considered is chosen to equal the observed population of those O- and WR-stars that are not part of the clockwise disk, which yields 96 stars with  $r < 10''$ . We assume that as many of the counterclockwise moving stars are in a disk-like configuration as suggested by Bartko et al. (2009); the rest is on randomly oriented orbits. The disk thickness and

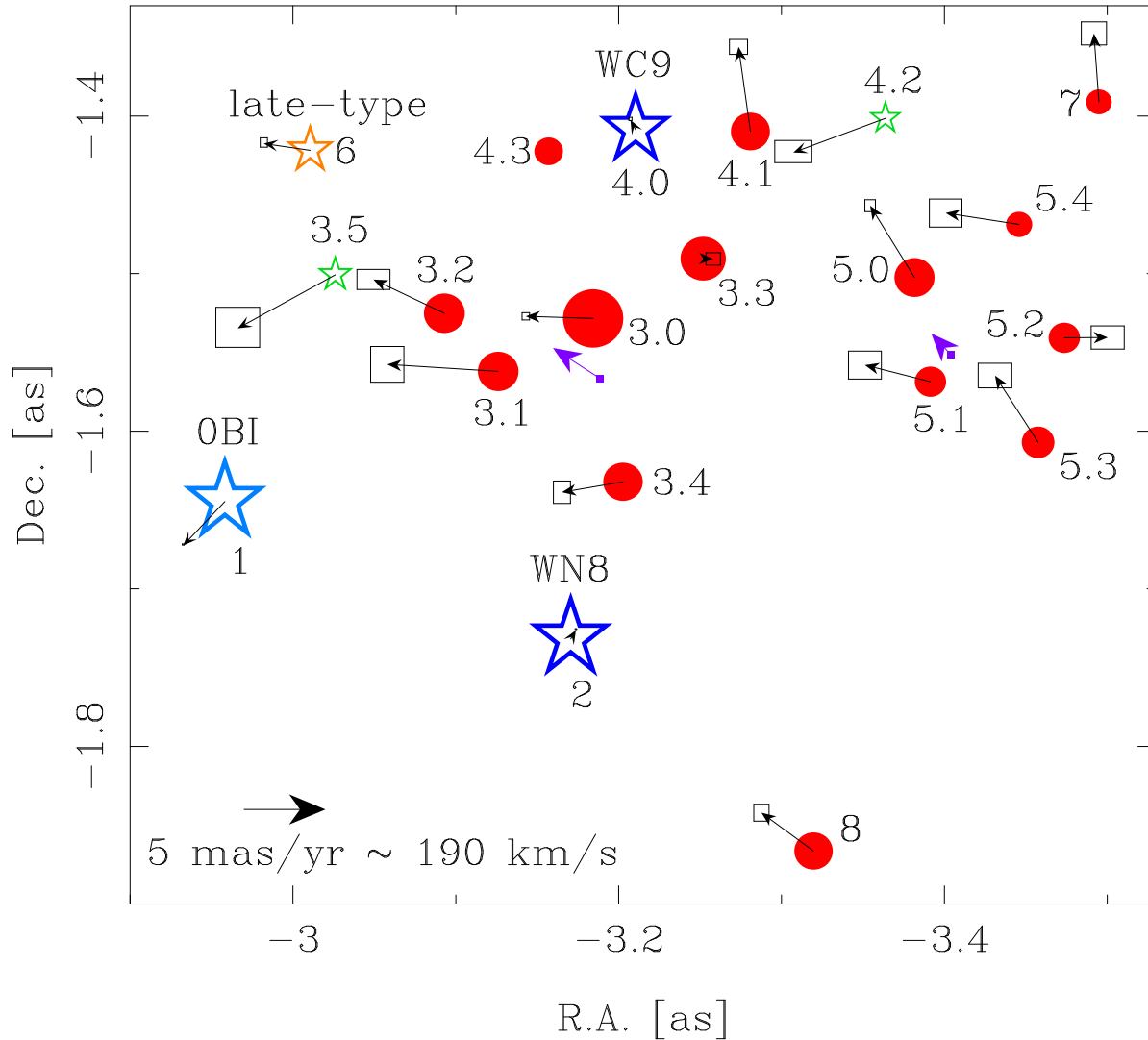


Figure 3.7 Velocities of the objects in IRS13E relative to the mean motion of the two WR-stars E2 and E4.0. The near-infrared motions are marked with black arrows, the boxes denote the 1- $\sigma$  errors. Stars are marked with asterisks (blue: young stars; green: stars without spectral identification). Dust clumps are marked by red disks. The sizes of symbols indicate the Ks-band flux. The 13 mm radio motions (violet) of Zhao et al. (2009) are shown, too.

eccentricity distribution of the counterclockwise disk are not well known. The thickness is likely larger than  $10^\circ$  (the value for the clockwise disk) and smaller than  $25^\circ$ , because a thicker disk would be invisible (Bartko et al. 2009). The eccentricity distribution is more uncertain. For each realization we have a set of eccentricities with an rms width of 0.22 (Bartko et al. 2009) and a median eccentricity which is varied for each realization. The median values are chosen such that they are distributed symmetrically around the mean eccentricity of the clockwise disk, in the range from 0.17 to 0.60 (Paumard et al. 2006; Bartko et al. 2009). We use these eccentricity distributions for the counterclockwise disk and for the random stars. The impact of the width of the eccentricity distribution on the derived probabilities is small compared to influence of the median eccentricity. The distribution of semi-major axes is chosen such that the final surface density profile resembles the one observed for the stars that are not part of the clockwise disk. A change of the semi-major axis distribution compatible with the errors of the observations has nearly no influence on the derived probabilities. The actual number of stars is varied, too. On purpose, we don't restrict the sample to the stars at least as bright as the IRS13E members. Fainter O-stars are barely less massive, and dynamically they would not behave any differently (Portegies Zwart et al. 2007).

The criteria for finding a cluster from the simulated stars are motivated by the observed properties of IRS13E. If anywhere in the simulated set three stars are found for which the following four conditions are met, the set is marked as containing a pseudo-cluster of three stars. The following cut values are the measured values plus the  $1\sigma$  errors: We require that  $r_{\text{cluster}, 2\text{D}} \leq 0.19''$  and that the proper motion dispersion  $\sigma_{v, 2\text{D}} \leq 94$  km/s. Furthermore, we demand that for any two stars of the three  $r_{3\text{D}} \leq 0.46''$  and for any (other) two stars of them  $\Delta v_z \leq 76$  km/s. A pseudo-cluster of two stars is defined by the criteria  $d_{2\text{D}} \leq 0.33''$ ,  $\sigma_{v, 2\text{D}} \leq 23$  km/s, and  $d_{3\text{D}} \leq 0.46''$ . In the following we give the probabilities to find such configurations, and in brackets we give the values if the requirement that two stars need to be close in the  $z$ -coordinate is omitted.

By randomly drawing a stellar distribution many times and varying the assumptions on the dynamical properties of the O/WR stars population, we find that a triple of stars matching the criteria for a pseudo-cluster of three stars out of 96 has a chance probability of 0.2 % to 2% (0.6% to 4%) with the most likely probability being 0.8%. Finding a pair of stars out of 96 that matches the criteria for a pseudo-cluster has a chance probability of 0.4% to 5% (4% to 14%, Figure 3.8). Demanding in addition that E2 and E4.0 have similar masses lowers the chance probability for such a pair to 0.1%, since only 28 of the 96 stars from which we draw the pseudo-clusters have masses comparable to that of E2 and E4.0.

The dominant error source here are the assumptions on the dynamical properties of the O/WR stars population, as indicated by the ranges of values in the previous paragraph. The uncertainties of the probabilities induced by the measurement errors of the proper motions are very small. They lead to relative errors of the probabilities well below 10%. Also the influence of  $\delta v_z$  on the probability is small with 13% (relative error). We conclude that the occurrence of a pseudo-cluster similar to IRS13E is not expected, but still not

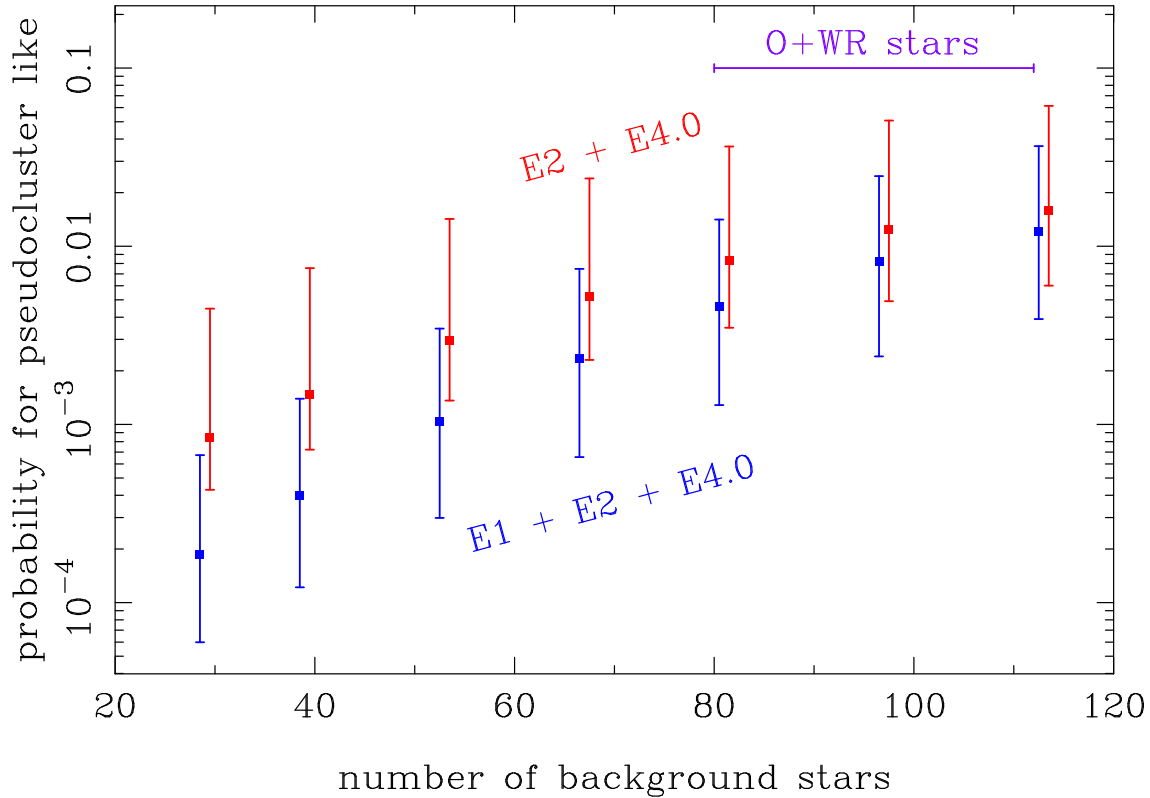


Figure 3.8 Probability for observing a cluster of two (red) or three (blue) early-type stars that resemble IRS13E in a background population of given sample size. The errors are derived from assuming different distributions of orbital elements for the simulated stars. The red and blue data are shifted for clarity horizontally. The background population consists of the O/WR early-type stars outside of the clockwise disk. The violet bar marks the range applicable for the GC.

impossible<sup>3</sup>.

We also note that E2 and E4.0 could be a binary in an orbit with a pericenter distance of more than 1.3 pc (see Section 3.5.4). Heavy binaries indeed often consist of two similarly massive stars (Kobulnicky & Fryer 2007). On the other hand, the hypothesis that all three stars are physically connected and reside outside the central parsec seems improbable since such young, massive stars actually are very rare in the Galaxy. And regardless of the location of IRS13E along the line-of-sight, the high velocity dispersion would require additional, unseen mass to bind the cluster.

<sup>3</sup>In the clockwise disk one also finds a comoving group of stars: The IRS16-SW group (Lu et al. 2005). This group is less concentrated than IRS13E.

### 3.5.4 Cluster Mass from Velocity Dispersion

Because the probability for IRS13E being a chance association is relatively small, it is reasonable to exploit the idea that IRS13E indeed is a cluster. Therefore we estimate the mass needed to bind the cluster by analyzing the velocity dispersion.

#### Assuming E1, E2 & E4.0 are Cluster Members

Classical mass estimators are very uncertain when applied to a sample of three stars only. Hence, we simulate clusters of three stars around a central mass in a Monte Carlo fashion for deriving the probability distribution for the value of the mass. For this one needs to marginalize over many parameters, mainly the 18 orbital elements of the three stars. Since we assume here that IRS13E is a cluster, we normalize the probability such that the total probability of clusters accepted over the full mass range is 1.

We assume that all angles and phases are randomly distributed and that the eccentricities follow a thermal distribution  $n(e) \propto e$ . The semi-major axes  $a$  are drawn from  $a = 0.4'' \times p^{0.9}$ , where  $p$  is a random number in  $[0,1]$ . This makes the distribution of projected distances similar to the observed one. In this way we simulate  $5 \times 10^8$  clusters around different IMBHs with masses between  $300 M_{\odot}$  and  $3 \times 10^5 M_{\odot}$  in steps of  $\Delta M/M = 0.15$ .

The peculiar property of IRS13E is that one star has a significantly different velocity compared to the other two. Thus, we choose from the simulated clusters the ones, which have nearly the same velocity differences as the observed cluster: Between any two stars this is  $|V_{2D, \text{sim}} - V_{2D, \text{obs}}| < 10 \text{ km/s}$  and between two of them additionally  $|V_{z, \text{sim}} - V_{z, \text{obs}}| < 39 \text{ km/s}$ . We neglect the exact spatial distribution of the stars in IRS13E. But on average the simulated stars from the chosen clusters are at similar positions as the observed stars.

The uncertainties of the derived probability density due to the measurement errors and due to the assumptions on the semi-major axis distribution are small. Even though the exact shape of the distribution changes slightly, it will continue to be a concave function normalized to 1, with a broad maximum around  $2 \times 10^4 M_{\odot}$ .

We derive that the most likely mass is  $M_{\text{IMBH}} = 16900 M_{\odot}$  with a 68.3 % confidence region from 4000 to 59400  $M_{\odot}$ . The probability distribution for  $M_{\text{IMBH}}$  is highly non-Gaussian, see black curve in Figure 3.10. The large uncertainty on the mass is due to the low number of stars. Nevertheless, the mass needed to bind IRS13E exceeds the mass of the three stars. Hence, if IRS13E is a cluster of three stars, it needs to be bound by additional mass that is not detected by our observations. This mass could be present in the form of an IMBH.

#### Assuming Only E2 & E4.0 are Cluster Members

If one assumes that E2 and E4.0 form an equal-mass binary, the measured velocity difference yields a mass for each star of  $180 M_{\odot}$ . The two stars have almost certainly a much lower mass, but the argument illustrates that an IMBH with a mass similar to the equal-mass binary is sufficient to bind the two stars, too. Since this mass is less than the limit on the stellar mass in IRS13E ( $2000 M_{\odot}$ ), one would not need an IMBH to explain IRS13E.

The simple binary hypothesis is problematic for other reasons. The tidal forces of the SMBH disrupt a binary with a separation larger than the Hill-radius (Binney & Tremaine 2008) during pericenter passage. For a bound, equal mass binary there exists no value of the unknown line-of-sight distance  $|z|$  that would make the binary survive a pericenter passage (Figure 3.11). Also, the destruction timescale for such a soft binary in a distance of  $3.5''$  to the SMBH is only 19000 years (calculated for the observed projected separation of E2 and E4.0, Binney & Tremaine 2008). Furthermore, a mass of  $180 M_{\odot}$  per star seems unrealistic, but this mass estimate could be too high due to the measurement errors. A mass per star of  $85 M_{\odot}$  is excluded only at the  $2\sigma$  level. Taken together, these arguments make the binary hypothesis unlikely, and it seems more natural to assume that additional mass is needed for binding E2 and E4.0.

### 3.5.5 Acceleration Limits Make an IMBH Less Likely

A binding IMBH can manifest itself in the accelerations it imposes on surrounding stars. Vice versa, the absence of accelerations makes it more likely that IRS13E is a chance occurrence. Thus, we calculate now the probability for observing the observed (insignificant) accelerations, firstly for the case that a binding IMBH is present and secondly for the case that no additional mass is present in IRS13E.

#### Binding IMBH Present

From our data we can only test for accelerations in the proper motions:

$$a_{2D} = \frac{r_{2D}}{R_{3D}} \cdot \frac{G M_{\text{IMBH}}}{R_{3D}^2} = G M_{\text{IMBH}} \frac{r_{2D}}{(r_{2D}^2 + z^2)^{3/2}} \quad (3.1)$$

We do not measure any significant accelerations (Table 3.1). Firstly, this sets only limits on the location of the stars relative to the IMBH along the line of sight ( $z$ ). But secondly, it is unlikely that a cluster extends much more in the  $z$ -dimension than in the plane of sky, and this actually constrains the mass  $M_{\text{IMBH}}$  of the IMBH.

We use again as in Section 3.5.4 the Monte Carlo simulated cluster, which are similar to IRS13E. For all this clusters, we calculate the expected values of  $a_{2D}$ .

Figure 3.9 shows that E2 is nearly not constraining, since for nearly all simulated clusters the expected value of  $a_{2D}$  is smaller than the  $1\sigma$  acceleration limit. In case of E4.0 the expected accelerations are similar to E2. Since the measurement errors of E4.0 are four times larger than for E1 and E2, this star is of least importance. As consequence, only the acceleration limit of E1 is important. This is due to the fact that its velocity differs from the one of E2 and E4.0. As pointed out by Schödel et al. (2005) in their Figure 2, the IMBH is likely closest to E1. Therefore its motion is most sensitive to the mass of the IMBH.

It is apparent in Figure 3.9 that E1 excludes an IMBH of lower mass more efficiently than an IMBH of higher mass. This seems paradoxical, but results from the fact that the lower the mass is, the more likely it is that the IMBH resides close to E1. If the IMBH is

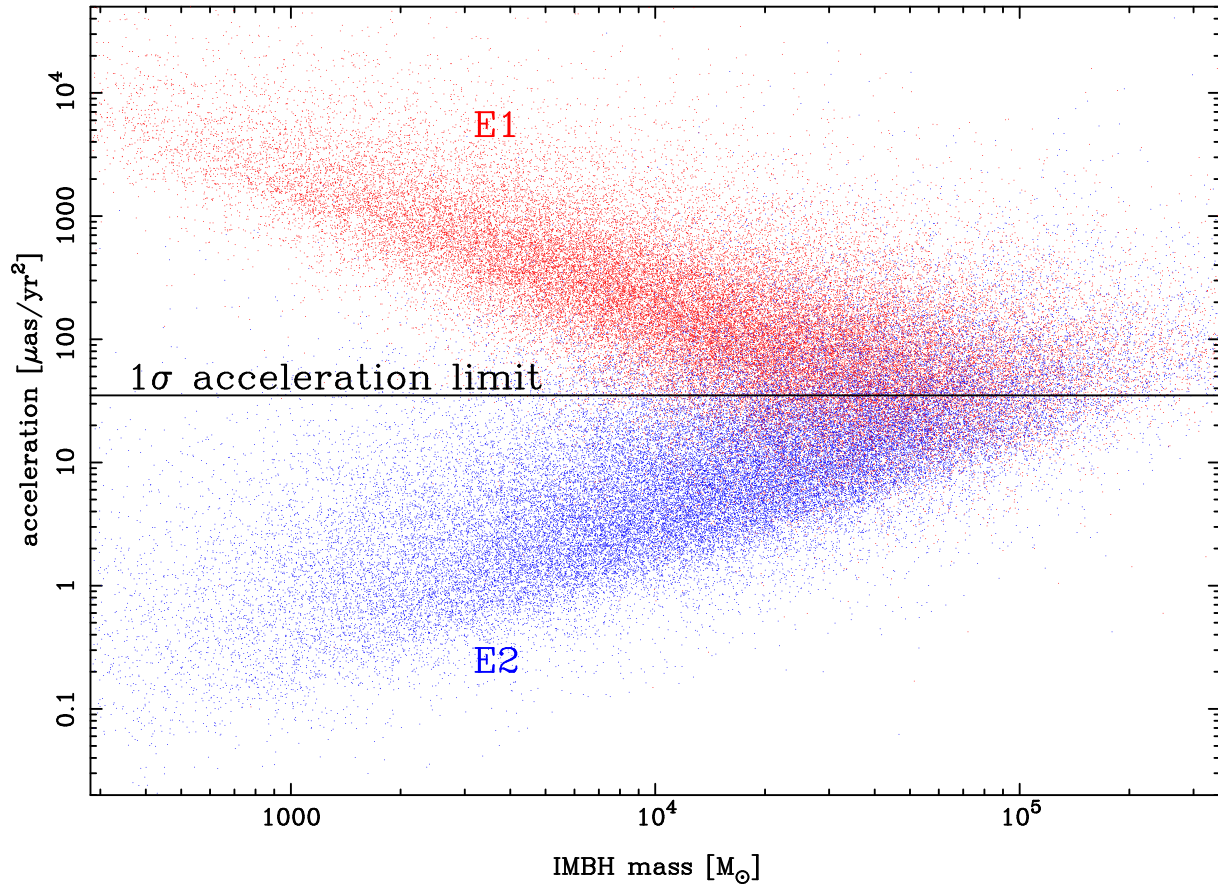


Figure 3.9 Plane of sky accelerations of the simulated stars in our Monte Carlo clusters. Every red dot marks an acceleration of E1 in one of the 50000 simulated clusters. The blue dots stands for E2 in the same simulations. The horizontal line represents our acceleration limit. The region above the line is excluded at the 1 $\sigma$  level.

close to E1, the full velocity difference between E1 and the other stars is due to E1 and one can write.

$$\frac{m_{\text{E1}}(\delta v)^2}{r_{\text{E1}}} = \frac{G M_{\text{IMBH}} m_{\text{E1}}}{r_{\text{E1}}^2} \rightarrow r_{\text{E1}} = \frac{M_{\text{IMBH}}}{(\delta v)^2} \quad (3.2)$$

Reducing  $M_{\text{IMBH}}$  thus lowers  $r_{\text{E1}}$  if the velocity difference has to stay at the measured value. For the acceleration  $a_{\text{E1}}$  follows

$$a_{\text{E1}} \propto \frac{M_{\text{IMBH}}}{r_{\text{E1}}^2} \propto \frac{(\delta v)^4}{M_{\text{IMBH}}} \quad (3.3)$$

This anti-proportionality of acceleration to  $M_{\text{IMBH}}$  is apparent in the simulations (red points in Figure 3.9).

We now calculate how probable the observed accelerations are, if one assumes a certain  $M_{\text{IMBH}}$ . Hence, we use those simulated clusters from Section 3.5.4 that fall into the corresponding mass bin and calculate for each case the  $\chi^2$  for the observed accelerations given their errors and the simulated acceleration values. This in turn is then converted to a probability. Because all simulated clusters are equally likely, we use the average over this mass bin as probability for obtaining the measured accelerations (Figure 3.10).

All IMBHs with  $M_{\text{IMBH}} < 10000 M_{\odot}$  have a probability of less than 0.9% to be consistent with our acceleration limits. At the most probable mass of  $14000 M_{\odot}$  the probability of not detecting an acceleration is 2.5%. For all mass bins the probability of  $M_{\text{IMBH}} > 0$  is less than 3%. The mass that yields acceleration values that are least unlikely is about  $60000 M_{\odot}$ .

The main uncertainty for the derived probabilities is due to the assumption on the semi-major axis distribution  $a = 0.4'' \times p^{0.9}$ . Using  $0.28''$  or  $0.52''$  instead of  $0.4''$  (which makes the simulated clusters still look reasonably similar to IRS13E) changes the resulting probabilities by up to a factor of  $\approx 2$ .

### No Additional Mass

If there is no IMBH in IR13E we expect zero acceleration. We calculate the  $\chi^2$  to the accelerations for this case, too, and obtain a probability of 39 % for observing the measured acceleration values under the assumption that no additional mass is present in IRS13E.

The mass estimate of  $\approx 1000 M_{\odot}$  from the assumption that only E2 and E4 are bound would yield an acceleration of  $\approx 3 \mu\text{as}/\text{yr}^2$ . This is much smaller than our measurement accuracy and we cannot test this hypothesis.

## 3.5.6 Proper Motion of Sgr A\*

### Binding IMBH Present

Gualandris & Merritt (2009) show that the proper motion of Sgr A\* perpendicular to the plane of the Galaxy (Reid & Brunthaler 2004) is the most promising method for excluding an IMBH at distances similar to that of IRS13E. For IRS13E itself, we can take advantage of

the fact that we know the velocity of the potential cluster and hence of the proposed IMBH. Thus we can predict the expected reflex motion of Sgr A\* via momentum conservation. We do not need to assume circular motion in the plane of sky, as Gualandris & Merritt (2009) had to.

We use the value from Reid & Brunthaler (2004) who find that the motion perpendicular to the Galactic plane is  $-0.4 \pm 0.9$  km/s. We estimate the uncertainty of the motion of the IMBH simply by the velocity dispersion of the potential cluster IRS13E.

We proceed as in Section 3.5.5. For a given mass bin, we calculate the expected reflex motion of Sgr A\* due to the IMBH the motion of which is varied by the estimated uncertainty. We compare the such calculated reflex motion with the measured value. The corresponding probabilities we again obtain from the  $\chi^2$  values. Finally we use the average per mass bin to estimate the probability of the radio data of Sgr A\* under the assumption that an IMBH of that mass is present (Figure 3.10). The small insignificant proper motion of Sgr A\* is quite probable for small ( $< 20000M_\odot$ ) IMBH masses. But for  $M_{\text{IMBH}} > 46000M_\odot$  the data are inconsistent with the model at the 90% level.

### No Additional Mass

We also calculate probability for that the measured motion occurs when no additional mass is present. We obtain a probability of 65.7%.

## 3.5.7 Total Probabilities

### Binding IMBH Present

In Section 3.5.4 we have shown that if an IMBH massive enough to bind IRS13E is present, its most likely mass is (given the velocity differences between E1, E2 and E4)

$$M_{\text{IMBH}}^{\text{pos, vel}} = 17000_{-13000}^{+43000} M_\odot. \quad (3.4)$$

The corresponding distribution of probabilities  $p_{\text{pos, vel}}(m)$  is the solid, black curve in Figure 3.10, which is normalized to 1, since it assumes the presence of an IMBH.

Next, we calculate combined probabilities. For each mass bin  $m$ , the probability that the measured acceleration limits and the radio data are compatible with an IMBH of mass  $m$  is

$$p_{\text{acc, radio}}(m) = p_{\text{acc}}(m) \times p_{\text{radio}}(m) \quad (3.5)$$

(Figure 3.10; red, dashed curve). Hence, at any given mass the probability for the data under the assumption that an IMBH is present is smaller than 0.8%.

Further, we can calculate the most likely probability value, by evaluating a weighted average of  $p_{\text{acc, radio}}(m)$  over all mass bins, using as weights  $p_{\text{pos, vel}}(m)$ , i.e.

$$\bar{p}_{\text{comb}} = \frac{\int p_{\text{acc, radio}}(m) \times p_{\text{pos, vel}}(m) dm}{\int p_{\text{pos, vel}}(m) dm}, \quad (3.6)$$

where the denominator equals 1 due to our normalization. The result is

$$\bar{p}_{\text{comb}} = 0.4\%. \quad (3.7)$$

This value is uncertain by a factor of  $\approx 2$ .

Normalizing the nominator from equation (3.6) to 1, i.e.

$$p_{\text{comb}}(m) = \frac{p_{\text{acc, radio}}(m) \times p_{\text{pos, vel}}(m)}{\int p_{\text{acc, radio}}(m) \times p_{\text{pos, vel}}(m) dm}, \quad (3.8)$$

is equivalent to a Bayesian approach, for obtaining a combined probability distribution of the mass. This results in the green, solid curve in Figure 3.10. It is normalized to 1 by construction which reflects the fact that the presence of an IMBH is assumed. The most likely mass of an IMBH is thus

$$M_{\text{IMBH}}^{\text{comb}} = 20000_{-8000}^{+12000} M_{\odot}.$$

### No Additional Mass

For the case that no additional mass is present, we obtain  $p_{\text{acc, radio}}(m = 0) = 26\%$ . In Section 3.5.3 we showed that  $p_{\text{pos, vel}}(m = 0)$  is 0.8%, which yields  $p_{\text{comb}}(m = 0) \approx 0.2\%$ . The error on this value is a factor of  $\approx 3$ .

## 3.6 Discussion

We are left with a puzzle. The probability to obtain the observed data (positions, velocities, accelerations, radio reflex motion of Sgr A\*) when no IMBH is present is 0.2%. Similarly unlikely is the probability of getting the same data if one assumes the presence of an IMBH. For any mass assumed, the probability is smaller than 0.8%. Hence, both scenarios are similarly unlikely given their errors of about a factor 2.5. We therefore consider additional arguments.

### 3.6.1 Dynamics of the Young, Massive Stars

The clockwise disk of early-type stars in the GC is significantly warped (Bartko et al. 2009). Such a warp can be the consequence of another non-spherical mass (Nayakshin & Cuadra 2005; Löckmann & Baumgardt 2009), and thus an IMBH might manifest itself via the warp. However, there are many other possibilities to explain the warp: The counterclockwise disk might suffice, or the warp can also happen in the gaseous phase during the disk formation (Hobbs & Nayakshin 2009). Dynamical friction will make an IMBH spiral down to the SMBH (Fujii et al. 2009), such that it would stay only for a very short time in the radial region of the disks. Hence, an IMBH is a less efficient warper per mass than a disk.

One possible origin of a potential IMBH is the core collapse of a young, massive star cluster (Portegies Zwart & McMillan 2002). IRS13E could be the remainder of such an

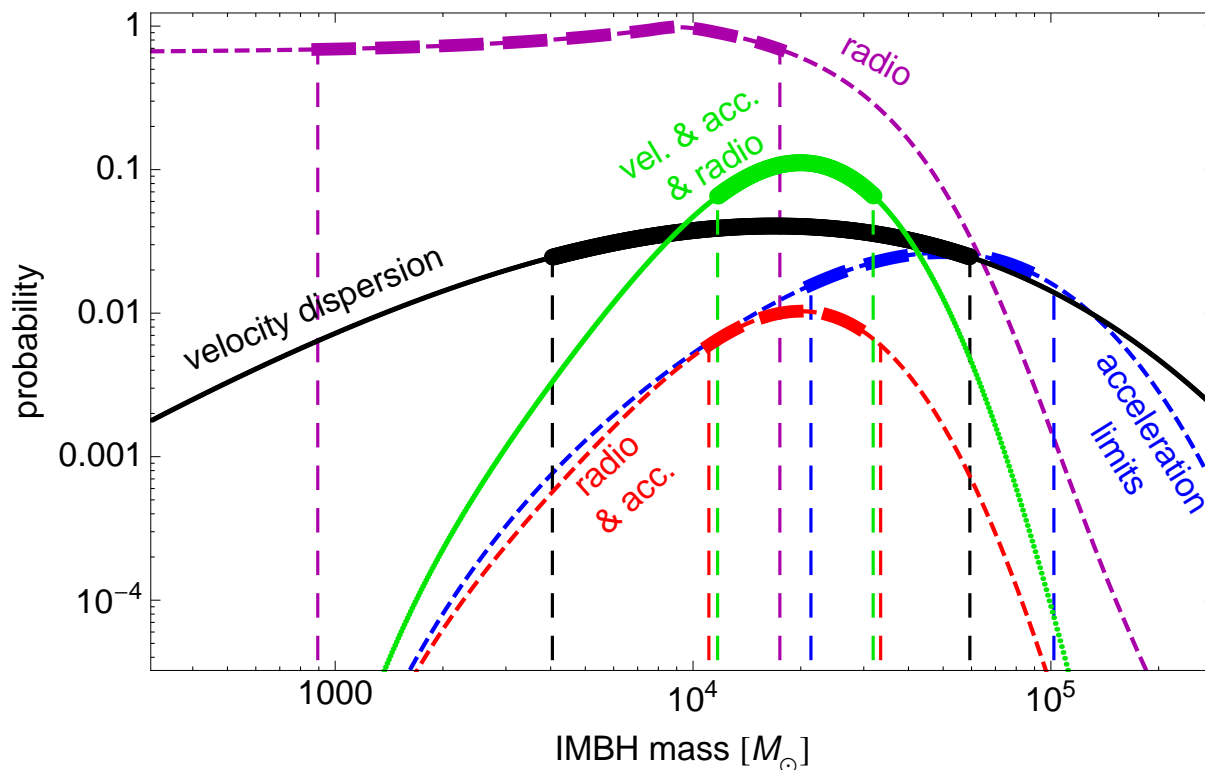


Figure 3.10 Probabilities for different IMBH masses, if IRS13E is a gravitationally bound star cluster of 3 stars (E1,E2, E4.0). Solid lines are probability densities per logarithmic mass bin of size  $\Delta M/M = 0.15$  and are normalized to 1. Dashed curves are probabilities calculated binwise. The thick regions mark the respective 68.3 % confidence regions of the most likely masses. Black, solid: probability distribution of the mass of the IMBH from the measured velocity differences. Blue, dashed: probability to observe the measured acceleration limits for an assumed mass of the IMBH. Magenta, dashed: probability to observe measured radio motion of Sgr A\* for an assumed mass of the IMBH. Red, dashed: combining acceleration and radio information yields for every mass bin the probability that the observed values for the accelerations and radio motions occur. Green, solid: Probability distribution of the mass of the IMBH, combining velocity, acceleration and radio-based information,

object that currently is spiraling in. Schödel et al. (2005) firstly indicated that using the simulations of Portegies Zwart & McMillan (2002) a cluster of an unrealistic high mass is necessary for a such massive IMBH as in IRS13E. In addition, we compare the number of young, massive stars in the GC with the expectation for the most likely mass of an IMBH of  $20000 M_{\odot}$ .

In the simulations of Portegies Zwart & McMillan (2002), Portegies Zwart et al. (2004), and Fujii et al. (2009) the IMBH obtains a mass of 0.1% to 9% of the total initial mass of the cluster, depending on the assumptions on the IMF, the radii and winds of very massive stars, the density of the cluster and whether a single supernova stops the formation of the IMBH. Thus, for the most likely IMBH mass one needs an initial cluster mass of at least  $2 \times 10^5 M_{\odot}$  (Fujii et al. 2009). Assuming a Salpeter IMF between 1 and  $140 M_{\odot}$  (Fujii et al. 2009), stars more massive than  $40 M_{\odot}$  would merge into the IMBH. The lighter stars should still be observable today, and one would expect to find 790 O-stars ( $20 - 40 M_{\odot}$ ) and 1950 early B-stars ( $10 - 20 M_{\odot}$ ).

In the GC there are in total only  $\approx 290$  O/WR-stars, correcting the currently detected number of such stars upward by a factor of 2.4, as estimated from incomplete areal coverage and detection incompleteness (Figure 2 in Bartko et al. 2010). However, not all of them are compatible with the idea that they originate from IRS13E.

Figure 3.11 shows that it is not possible that an IMBH binds IRS13E, and that at the same time IRS13E is located in the counterclockwise disk. Hence, the inspiraling cluster scenario requires that the orbits of the stars stripped off the cluster are found in edge-on orbits in a common orbital plane. We estimate that at most 50 O/WR-stars could have such orbits. We observe, however, a factor 15 fewer O-stars than expected for an IMBH of  $20000 M_{\odot}$ . For the bright B-stars, the discrepancy is even larger. We conclude that the formation of an IMBH of  $20000 M_{\odot}$  in IRS13E is inconsistent with the observed number of young stars.

### 3.6.2 X-ray and Radio Emission

Apart from Sgr A\*, IRS13E is the only source with significant emission detectable in the NIR, radio, and X-ray regime (Zhao & Goss 1998; Wang et al. 2006). At 13 mm, the morphology of the minispiral is similar to the one in L'-band. This emission traces hot gas, probably associated with the dust visible in the NIR.

The X-ray spectrum of IRS13E (Wang et al. 2006) is similar to the diffuse X-ray emission from the local background and from the region around Sgr A\*. Coker et al. (2002) argue, that IRS13E is a wind nebula excited by a star, which left the Luminous Blue Variable (LBV) phase a short time ago. Maybe this scenario also works for the two WR-stars the winds of which probably collide in E3. The accuracy of the position of the X-ray source is not sufficient to decide whether the X-ray source can be identified with any of the bright NIR sources in IRS13E.

The observed flux in IRS13E is  $L_X(2 - 10 \text{ keV}) = 2 \times 10^{33} \text{ erg/s}$  (Wang et al. 2006), corresponding to  $\approx 10^{-9}$  Eddington luminosities ( $L_{\text{Edd}}$ ) for an IMBH of  $20000 M_{\odot}$ . This number is much smaller than for the X-ray binaries detected in the GC (Muno et al. 2005).

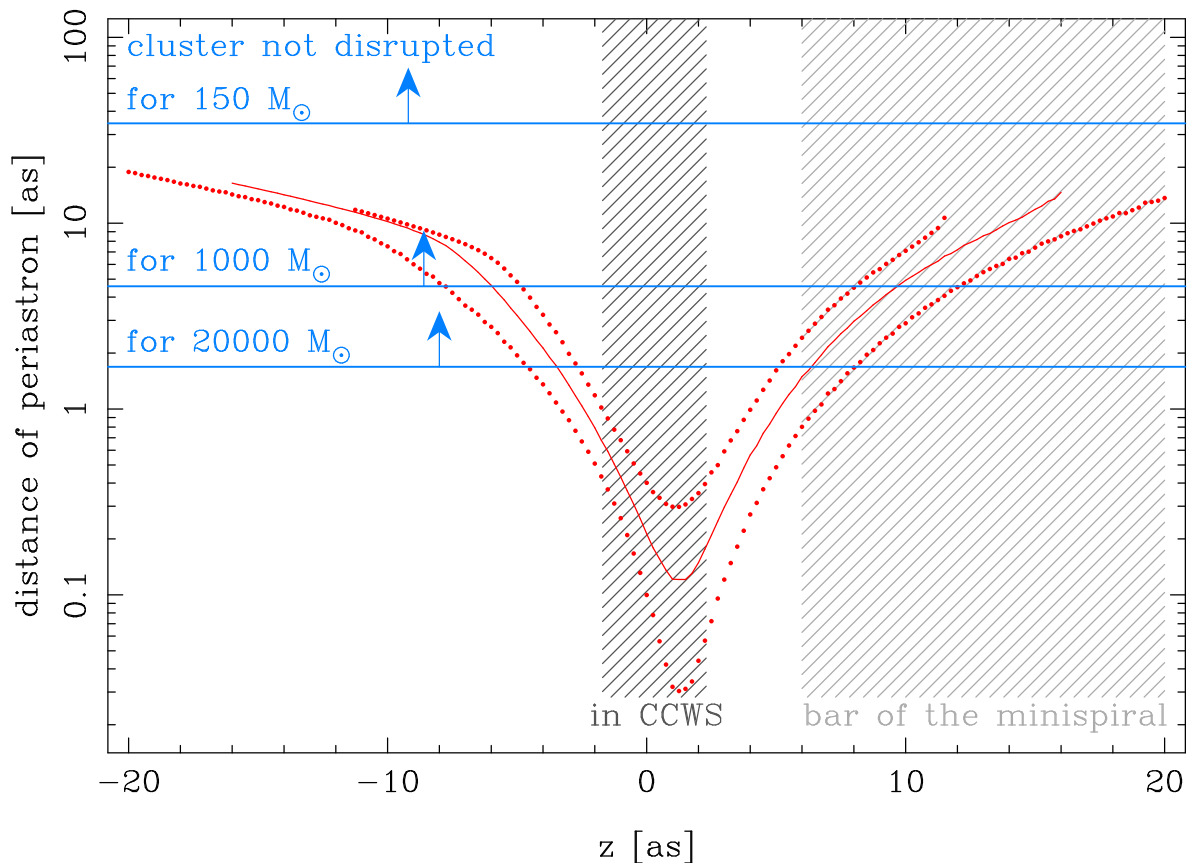


Figure 3.11 Periastron distance of IRS13E for possible locations along the line of sight ( $z$ ) in the point mass potential of the SMBH. The dotted lines mark the  $1\sigma$  error band. Considering tidal disruption, only the  $z$  positions corresponding to periastron distances above the blue lines are possible for the respective masses. The two lower lines for 1000 and 20000  $M_{\odot}$  assume a cluster with an IMBH, the upper line is for the case that E2 and E4.0 form a binary with 150  $M_{\odot}$  per star. The shaded region close to  $z = 0''$  corresponds to the cases in which IRS13E is in the counterclockwise disk (CCWS, Bartko et al. 2009). The shaded region to the right corresponds to a location of IRS13E in the minispiral (Paumard et al. 2004), which is possible for all configurations. It is not possible, that an IMBH binds IRS13E, and that at the same time IRS13E is located in counterclockwise disk.

The faintness of the X-ray source in IRS13E was the main argument of Schödel et al. (2005) against an IMBH in IRS13E. However, Sgr A\* itself is radiating in quiescence with only  $L_X(2 - 10 \text{ keV}) = 4 \times 10^{-12} L_{\text{Edd}}$  (Baganoff et al. 2001) such that a low radiative efficiency does not exclude the presence of an IMBH right away. A comparison on basis of the X-ray flux only is difficult, since the environment and accretion state might differ significantly between Sgr A\* and an IMBH in IRS13E.

There is no variability reported for IRS13E in the X-rays (Muno et al. 2005), despite the fact that during roughly half of the observations of Sgr A\* IRS13E was observed, too. Many black holes are variable in the X-ray domain (examples are X-ray binaries, see Muno et al. (2005), and Sgr A\*, see Baganoff et al. (2001) and Porquet et al. 2003). In Section 3.5.2 we argue that the dust seen in IRS13E is physically connected with the group of stars. Comparing the Br- $\gamma$  emission in IRS13E and close to Sgr A\* shows that the gas reservoir in the IRS13E is much richer than close to the SMBH. Taken together, this makes it unlikely that the reported, steady source is due to an IMBH.

### 3.7 Conclusions and Summary

We present a detailed analysis of the potential cluster IRS13E in the GC. We use AO-based images in H- and Ks-band from 2002 to 2009 for identifying objects in IRS13E and for performing astrometry. We detect 19 objects on most high Strehl ratio images in Ks-band and 15 of them also in H-band. The proper motions of the objects are well determined.

In addition, we characterize the SED of the objects in IRS13E using AO-based integral field spectroscopy (1.45 to 2.45  $\mu\text{m}$ ) for the brighter objects and (narrow-band) imaging from H- (1.66  $\mu\text{m}$ ) to L'-band (3.80  $\mu\text{m}$ ) for the fainter objects. We fit the SED of the objects by a model consisting of two blackbodies and an extinction parameter. From this we conclude that 13 objects are dust clumps without embedded stars and that the extinction appears to be constant in the IRS13E region. Three objects are fainter stars: One is a spectroscopically identified late-type star. The two fainter stars of the magnitude of the red clump are consistent with the expected number of stars per area at this magnitude bin. Thus, these three stars are likely background stars. Therefore, IRS13E is only a concentration of the remaining three early-type stars E1, E2 and E4.0.

They have the following properties:

- E2 and E4.0 are probable located close in 3D, because of the bright hot dust clumps between them.
- A chance association of three early-type stars has a probability of around 0.2%. Depending on the assumptions on dynamical properties of the stellar population this value varies between 0.06% and 0.6%.
- In the case of a binding mass, we use Monte Carlo Simulations of a cluster of three stars around all reasonable masses of IMBHs (300 to  $3 \times 10^5 M_\odot$ ). From those simulations we select the ones that agree with the constraints from the observed positions

and velocities of the stars. The most likely mass is about  $20000 M_{\odot}$ . This mass exceeds the stellar mass (inclusive faint, invisible stars) in IRS13E.

- We find that at any given mass less than 0.8% of the previously selected simulations agree with the observed acceleration limits of the three stars and the fact that Sgr A\* appears to be at rest. This value is uncertain by a factor of  $\approx 2$ .
- There are roughly 15 times too few young stars in the GC for the formation of an IMBH as massive as  $20000 M_{\odot}$ .
- The weak and non-variable X-ray source in IRS13E makes the presence of an IMBH unlikely.

Overall, we conclude that it is more likely that IRS13E does not host an IMBH.

## 3.8 Appendix

### 3.8.1 Extracting the Spectral Energy Distributions

#### Deconvolution of SINFONI Data

In order to distinguish between objects in the SINFONI data, we deconvolve the cube in small bandpasses, taking into account the variation of the PSF with wavelength. We extract line maps at three wavelengths at which single stars prominently dominate the respective images: at  $1.49 \mu\text{m}$  the dominant star is E4, at  $1.70 \mu\text{m}$  and  $2.11 \mu\text{m}$  it is E2. We manually remove apparent artifacts and smooth the PSF wings azimuthally. We then spectrally inter- and extrapolate these single-wavelength PSFs over the whole wavelength range, either resampled to 24 spectral channels or at the original spectral sampling. We then used two sets of PSFs to perform deconvolution of the cube at the different samplings. We use the deconvolution at the original sampling for extracting the spectra of the WR stars E2 and E4.0. The resampled deconvolution is used for E3.0 and 5.0.

We also use the PSFs interpolated at the original sampling for creating a subtracted cube in which the four brightest stars (E1, E2, E4.0 and the bright late-type star north-west of IRS13E) are subtracted. For this purpose we fit in each spectral plane the stars with Gaussians to determine their flux as a function of wavelength. Then we subtract the correspondingly scaled, interpolated PSFs from the original data cube. We use the resulting cube for analyzing the spectral features of the gas and the fainter stars.

We flux-calibrate the SINFONI data by using the early-type star E1, in the spectrum of which we manually replace the (few) spectral lines by continuum. The photometric errors from the SINFONI data are estimated by varying the selection of source pixels. During the fit of the such obtained data with an SED model, we rescale them such that the reduced  $\chi^2 = 1$ .

### Photometry from NACO Images

In order to measure the SED of the objects fainter or more confused than E5.0, we determine fluxes from the deconvolved broad-band and narrow-band images. We measure the flux of each object at each available wavelength by manually selecting the respective object pixels in the frames. For the broad-band images we estimate the flux errors from the standard deviation of the measured fluxes at the different epochs. For the narrow-band images we simply adopt the same flux errors as obtained from the broad-band images.

For the images in H- and Ks-bands, we calibrate the magnitudes following Maness et al. (2007)<sup>4</sup>. We derive the narrow-band calibration from the broad-band calibration by using the empirical extinction law

$$A_\lambda = A_{Ks} * \lambda / \lambda_{Ks}^\alpha = A_{Ks} * \lambda / \lambda_{Ks}^{-1.75} \quad (3.9)$$

from Draine (1989). As calibrators we use eight isolated, bright early-types stars with known temperatures within a distance of less than 2.5'' to IRS13E. Since there is no suitable L'-band calibrator close to IRS13E, we use an indirect method by extrapolating the dereddened SED of the calibrators to L'-band and applying the extinction law from Lutz et al. (1996) longward of Brackett- $\beta$  and short-ward the power law of Draine (1989). This results in  $A_{Ks}/A_{L'} = 1.75$ . The slope of the power law in equation (3.9) is uncertain:  $\alpha = -1.6$  (Rieke & Lebofsky 1985; Rieke 1999),  $\alpha = -2$  (Nishiyama et al. 2009) and  $\alpha = -2.21$  (Schödel et al. 2010). Recent works may indicate that the extinction law used here is outdated (Stead & Hoare 2009; Gosling et al. 2009). But at our precision the value of  $\alpha$  does not affect the SED fitting because the shape of the derived SED is relatively insensitive to the value of  $\alpha$  adopted. Nevertheless it introduces an uncertainty to the extinction values. Thus, it is important for the absolute luminosities of the early-type stars. To estimate these uncertainties, we use both the originally adopted extinction and the law from Schödel et al. (2010) plus the magnitudes of the calibration stars in H, Ks and L' published by Schödel et al. (2010).

For the SED fits, we calculate the effective wavelength of the bands for each object. First, we apply an extinction value of  $A_{Ks} = 2.8$  together with the atmospheric and the filter transmission to the source spectrum (either a blackbody or the output from the atmosphere modeling). For the broad-band data it is necessary to perform a second iteration using the resulting SED in order to improve the effective wavelength.

## 3.8.2 Individual Objects in IRS13E

### IRS13E1

E1 is a hot OB supergiant (Paumard et al. 2006). Its flux is constant in our data, and the spectrum does not reveal any signs of binarity. We use the H-band lines from the Brackett-series to determine the radial velocity (in K-band, the emission lines from nebular

<sup>4</sup>The calibration of Schödel et al. (2010) is about 0.3 mag fainter in both bands.

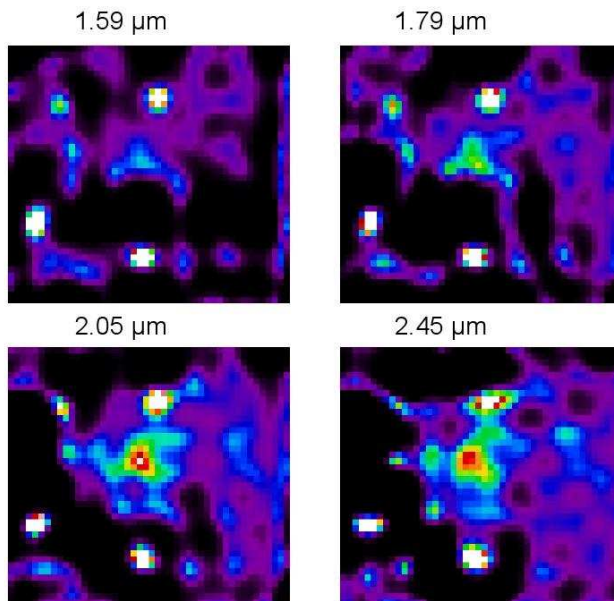


Figure 3.12 Four of the 24 deconvolved narrowband images created from the high-quality H+K-band SINFONI cube of IRS13E.

background are more dominant). We obtain  $v_{\text{LSR}} = 134 \pm 10$  km/s. This is  $3\sigma$  different to  $v_{\text{LSR}} = 71 \pm 20$  km/s, the Brackett- $\gamma$  based value reported in Paumard et al. (2006).

We compare our atmosphere model of E1 to a simple blackbody model of  $T = 26000 \pm 1000$  K and do not see differences between the two models which would matter for the broad-band photometry. Therefore, we fit the extinction using the photometric data and a blackbody model. We obtain  $A_{\text{Ks}} = 3.64 \pm 0.07$  (Figure 3.5). Contrary to Maillard et al. (2004), we do not find a weak dust component. This is likely because of the higher resolution of our data, since the SINFONI data show that the star is surrounded by gas probably also associated with dust. Fitting a supergiant model to the observed SED we obtain  $\log L/L_{\odot} = 6.23 \pm 0.07$ . Thus E1 would be more luminous than all known supergiants of this spectral class. When using the calibration and extinction law of Schödel et al. (2010) we obtain  $\log L/L_{\odot} = 5.90 \pm 0.07$ , consistent with the brightest known OB supergiants.

### IRS13E2

E2 is a Wolf-Rayet star of type WN8 (Paumard et al. 2006; Martins et al. 2007). There is no sign of binarity in its light curve or in its spectrum. The latter shows strong, broad emission lines. In addition, WR-stars have strong winds causing a near-infrared excess. Therefore it is necessary to use a full atmosphere model for the SED fit of E2. We manually adjust the temperature of a possible dust component and the extinction parameter to make the atmosphere model match the observed spectrum.

The SED fit yields a second blackbody component of around  $T = 712$  K and  $A_{\text{Ks}} = 3.51$ .

This result is qualitatively consistent with the findings of Maillard et al. (2004). The smaller dust temperature they find is likely caused by their assumption that E2 can be modeled with a blackbody. We find that the dust component is significant in L'-band, but in Ks-band the stellar component dominates (see Figure 3.3), contrary to the proposal by Martins et al. (2007).

We obtain for E2  $\log L/L_{\odot} = 6.14 \pm 0.1$  when using the standard calibration and extinction law of this paper and  $\log L/L_{\odot} = 5.81 \pm 0.1$  when using calibration and extinction law of Schödel et al. (2010). Thus, E2 is relatively luminous for its classification as WN8 star. E2 could be more massive and even younger ( $\approx 3$  Myr) than most of the young, massive stars in the central parsec. However, due to the particular shape of the evolutionary tracks, E2 could equally well have the same age as the other stars of similar type. In their Figure 23 Martins et al. (2007) gave for E2 only an upper limit in luminosity because of the unknown dust contribution at the time. From our SED fit we were able to show that the Ks-luminosity is to about 96% of stellar origin. Therefore the luminosity of E2 in Martins et al. (2007) is nearly identical with the value derived here. In any case, E2 is brighter than the other WN8 stars in the GC. This fact is unaffected by calibration uncertainties. Also, binarity would not be able to fully explain the luminosity of E2.

We use the  $2.24 \mu\text{m}$  NIII line from the full atmosphere model for deriving the radial velocity of E2, which is more accurate compared to previous works. We obtain  $v_{\text{LSR}} = 65 \pm 30$  km/s while Paumard et al. (2006) reported  $v_{\text{LSR}} = 40 \pm 40$  km/s and Maillard et al. (2004) gave  $v_{\text{LSR}} = 30$  km/s. All these values are consistent with each other.

### IRS13E3.1 to IRS13E3.4

The extracted PSFs of the SINFONI data are not good enough to measure the H-band part of the SEDs of the fainter objects around E3.0. Qualitatively, the spectra of E3.1 to E3.4 do not show any new spectral features compared to E3.0. There is only a gradual change in the spectral properties, such as the line velocities. Hence, these sources also likely consist mostly of gas and dust. This is confirmed by the SED fits, which are based on the narrow-band images. Because of the faintness of the sources we cannot reliably fit the extinction, which we restrict for pure dust sources to  $A_{\text{Ks}} = 3.4 - 3.9$ .

On most images in K-band (including the narrow-band images before 2005) and all L'-band data, the sources E3.1 and E3.2 are strongly overlapping. Therefore we fit a combined SED for the two (Figure 3.5). The properties of the fitted blackbody are similar to E3.0 apart from its brightness. A stellar component is not necessary, the  $1 \sigma$  limit is  $m_{\text{Ks}} = 18.0$ , and thus again we can exclude that a WR star of the most common types is hidden in E3.1 and E3.2. We suspect that Maillard et al. (2004) found a stellar component in the eastern part of their source E3 due to the same bias as for E3.0 (Section 3.4.2). Also for the less well constrained objects E3.3 and E3.4 (Table 3.2) no stellar components are required. This conclusion does not depend on the assumption for the extinction.

### IRS13E3.5

The SED of E3.5, derived photometrically, differs from the other sources in E3 (Figure 3.5). Its color is consistent with that of a star, and no dust is necessary to explain the SED of this object. Unfortunately, it is too confused and too faint for deriving its spectral type. Any temperature between 4000 K and 19000 K is possible, which also implies an uncertainty of  $\Delta A_{Ks} = 0.4$ . The absolute magnitude of E3.5 corresponds to the red clump, which makes it likely that E3.5 is an old, late-type star. In addition, this star does not share the proper motion of the three brightest stars in IRS13E. We conclude that E3.5 most likely does not belong to IRS13E.

### IRS13E4.0

E4.0 is a Wolf-Rayet (WC9) star (Paumard et al. 2006; Martins et al. 2007). Its radial velocity is very uncertain. Paumard et al. (2006) report  $v_{LSR} = 56 \pm 70$  km/s, Maillard et al. (2004) claim  $v_{LSR} = -30$  km/s. From our atmosphere model (Figure 3.3) including wind induced line broadening we obtain  $v_{LSR} = 200 \pm 200$  km/s.

As for E2 we manually adjust the atmosphere model with an additional dust component to match the measured spectrum (Figure 3.3). Clearly two components are needed to describe the SED, but the derived values are very uncertain. The dust component with  $T = 1400$  K is significant. It contributes 38% of the flux in the Ks-band, as indicated by Martins et al. (2007). Our measurement is more precise than the one from Maillard et al. (2004), because we use a full atmosphere model and extend the wavelength coverage to L'-band. We obtain the same extinction as for E1. The luminosity of E4.0 is  $\log L/L_{\odot} = 5.23$ . Because of the difficult modeling of this star and WC9 stars in general it is not possible to conclude whether E4.0 has an age similar to the other WC9 in the GC.

### IRS13E4.1 to IRS13E4.3

Besides H- and Ks-band, E4.1 is detected also in L'-band and has overall a red SED. It is too close to E4.0 to allow the broadband SED to be extracted from the SINFONI data. The spectrum shows only gas lines and no stellar features. For fitting the SED it was necessary to fix the extinction at the upper end of the possible range to  $A_{Ks} = 3.9$ . With this the data are fit well by a single blackbody of  $T = 844 \pm 24$  K. Any stellar component has to be fainter than  $m_{Ks} = 18.4$ .

E4.2 does not show any spectral features and is not detected in L'-band. Therefore, there is less data than for the previous sources. We fix  $A_{Ks} = 3.9$ . From a single blackbody fit we get a temperature of less than 2800 K, which is too cold for a star of  $m_{Ks} = 15.4$ . Thus, we need to add a second blackbody to the fit, which means we classify E4.2 as a star. As in the case for E3.5, this faint star matches the typical luminosity of red clump stars. Hence, it is most likely an old late-type star. Its motion, being slower westward than for the three bright stars in IRS13E, argues against E4.2 being a physical member of IRS13E.

For E4.3 we are only able to photometry in Ks-band, yielding  $m_{Ks} = 15.5 \pm 0.1$ .

### IRS13E5.0

The source E5.0 is isolated enough to extract its broadband SED in the Ks-band from the SINFONI data (Figure 3.5), but because of its location close to the edge of the data cube, the SINFONI H-band measurements are not reliable. Hence, we combine the NACO-based fluxes with the SINFONI data. We allow for a global scaling factor to match the two data sets, which yields an offset of 0.24 mag. In any case, the fit does not change significantly by either including or excluding the SINFONI data. The preferred fit yields  $A_{Ks} = 3.22$  and a dusty blackbody. Thus, we fix the extinction value to the lowest value from the range assumed here to  $A_{Ks} = 3.4$ . Again, no stellar component is needed, and any star inside is fainter than  $m_{Ks} = 18.5$ . The dust of E5.0 is with  $T = 700 \pm 8$  K colder than for most other objects in E3 and E4. Maillard et al. (2004) were only able to identify one source in E5. The scatter in their data points is so high that it is not clear how significant the stellar component is in their fits.

### IRS13E5.1 to IRS13E5.4

The other sources of E5 are also red but fainter than E5.0. They appear embedded in the brightest part of the minispiral. It is not possible to measure their SEDs separated from the minispiral at our resolution, because the background is inhomogeneous and therefore the background subtraction too uncertain. This holds both for the NACO photometry and for the SINFONI data. In addition, the sources E5.2 and E5.3 are located on the deconvolution ring of the bright source E1. Thus, the fluxes of these two sources are biased to high values, especially in H-band. Finally many of the objects are not detected in all our NACO bands. Consequently, the characterization of these source is considerably more uncertain than for the other sources. The spectra of these sources show only gaseous emission lines. We again assume that the continuum emission is mainly caused by dust, and thus we restrict  $A_{Ks}$  to the range 3.4 – 3.9.

The source E5.1 is a double source on the higher quality Ks-band images obtained since 2008, but we are not yet able to disentangle them. This source is also detected in the L'-band. With our assumption for the extinction, the best fit is a blackbody with  $T = 947 \pm 25$  K; any stellar component needs to be fainter than  $m_{Ks} = 17.8$ .

The source E5.2 is not detected in H-band but in L'-band, where it is nearly overlapping with E5.3. We nevertheless simply assume that all of the L'-flux is caused by E5.2. With this we obtain a temperature of  $T = 642 \pm 70$  K from the SED fit, which is consistent with the non-detection in the H-band. Any star hidden in E5.2 must be fainter than  $m_{Ks} = 15.6$ . Given the lower temperature, E5.2 is likely a part of the minispiral.

Contrary to E5.2, the object E5.3 is not detected in L'-band but in H-band. Our fit does not require a stellar component. The  $1\sigma$  limit is  $m_{Ks} = 16.0$  and we obtain a temperature of  $T = 978 \pm 524$  K. The large error is caused by the smaller wavelength range on which the SED fit is based.

The source E5.4 is located close to E5.0. It is detected only in Ks- and the narrow bands. Hence we fit only a single blackbody with the restricted extinction interval. We

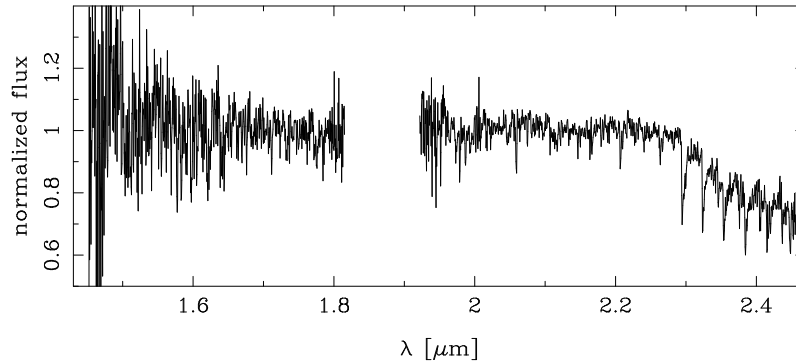


Figure 3.13 SINFONI H+K-band spectrum of E6.

obtain a temperature of  $T = 817 \pm 474$  K.

### IRS13E6

The spectrum (Figure 3.13) of E6 ( $m_{Ks} = 13.82 \pm 0.10$ ) shows CO-band heads in H- and Ks-band and lines of NaI and CaI. Thus, E6 is a late-type star with a spectral class around K3III. Maillard et al. (2004) identified E6 as an O-star, but they used data from three relatively broad bands for their photometric identification. Buchholz et al. (2009) used narrow bands around the CO-band heads and determined correctly that E6 is a late-type star. We derive a radial velocity of  $v_{LSR} = 106 \pm 10$  km/s from the CO-band heads in Ks-band.

In order to avoid biases, we exclude from the SED fit the bands which contain flux of the CO band heads. The fitted extinction value of  $A_{Ks} = 3.68 \pm 0.09$  is consistent with the extinction of E1. Due to its faintness E6 cannot be a red supergiant and it is thus older than the three bright early-type stars.

### 3.8.3 Astrometric Data

We present the positions and fits of most objects in Figure 3.14.

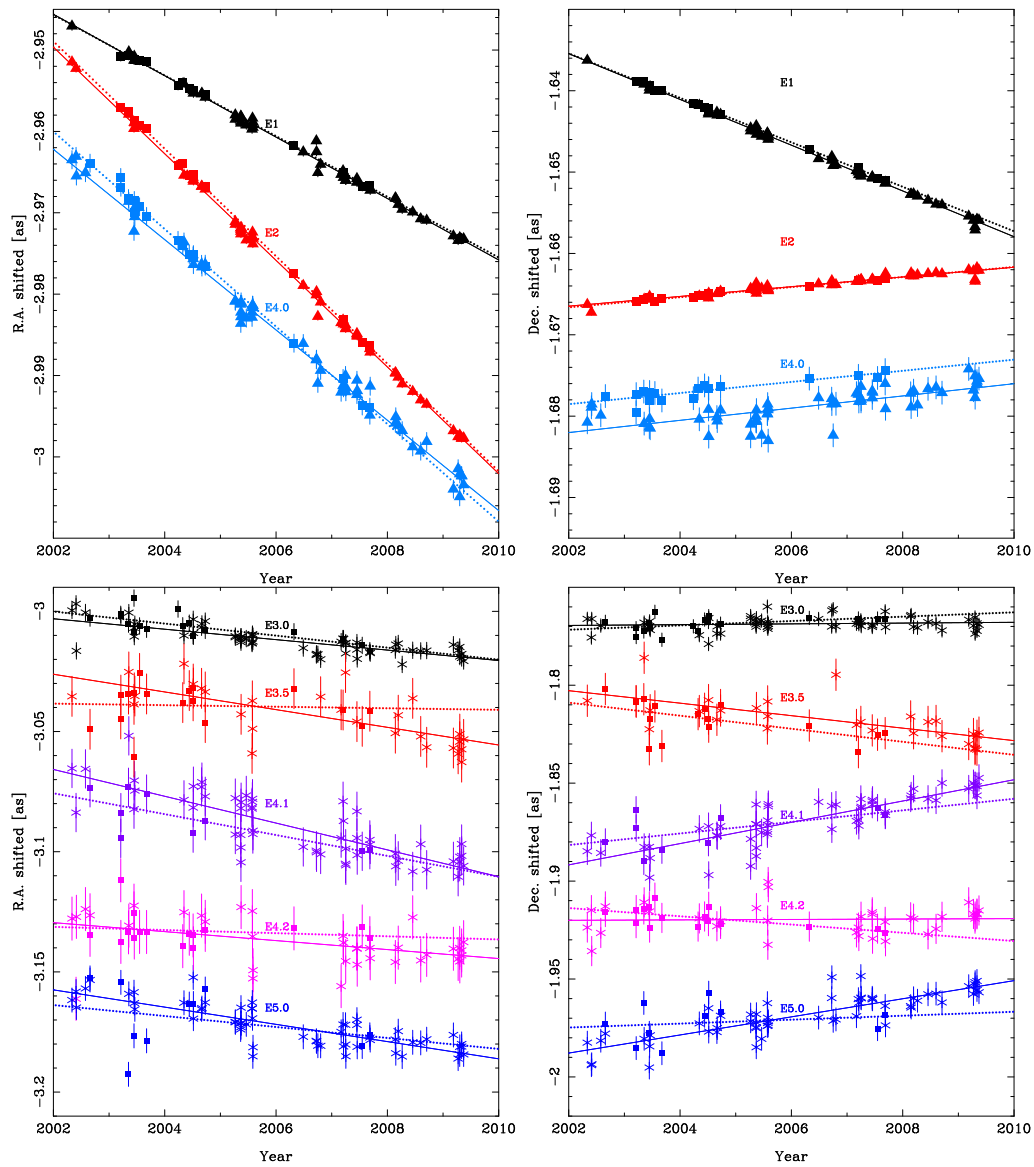


Figure 3.14 Positions and linear motion fits for the objects in IRS13E. Top: The three bright stars in Ks-band (asterisks and solid lines) and H-band (boxes and dotted lines). Bottom: Some of the fainter objects. All data and fits are offset from each other for clarity.

# Chapter 4

## Line Derived Infrared Extinction toward the Galactic Center

**Original publication:** T.K. Fritz, S. Gillessen, K. Dodds-Eden, D. Lutz, R. Genzel, W. Raab, T. Ott, O. Pfuhl, F. Eisenhauer, & F. Yusef-Zadeh, 2011, *Line Derived Infrared Extinction toward the Galactic Center* ApJ, 737, 73

**Abstract:** We derive the extinction curve toward the Galactic Center from 1 to 19  $\mu\text{m}$ . We use hydrogen emission lines of the minispiral observed by ISO-SWS and SINFONI. The extinction free flux reference is the 2 cm continuum emission observed by the VLA. Toward the inner  $14'' \times 20''$  we find an extinction of  $A_{2.166\mu\text{m}} = 2.62 \pm 0.11$ , with a power law slope of  $\alpha = -2.11 \pm 0.06$  shortward of 2.8  $\mu\text{m}$ , consistent with the average near-infrared slope from the recent literature. At longer wavelengths, however, we find that the extinction is *grayer* than shortward of 2.8  $\mu\text{m}$ . We find it is not possible to fit the observed extinction curve with a dust model consisting of pure carbonaceous and silicate grains only, and the addition of composite particles, including ices, is needed to explain the observations. Combining a distance dependent extinction with our distance independent extinction we derive the distance to the GC to be  $R_0 = 7.94 \pm 0.65$  kpc. Toward Sgr A\* ( $r < 0.5''$ ) we obtain  $A_{\text{H}} = 4.21 \pm 0.10$ ,  $A_{\text{Ks}} = 2.42 \pm 0.10$  and  $A_{\text{L}} = 1.09 \pm 0.13$ .

### 4.1 Introduction

Knowledge of the extinction in the infrared (Schultz & Wiemer 1975; Cardelli et al. 1989; Mathis 1990) is important for obtaining the intrinsic luminosities of highly extinguished objects. In addition, the extinction curve provides important constraints on the properties of interstellar dust (see e.g., Compiègne et al. 2011). Using the extinction curve together with the dust emission it is possible to derive the composition and sizes of interstellar dust grains. In this way it has been found that interstellar dust is mainly composed of silicate and carbonaceous dust grains (Draine 2003). However, it is still uncertain if composite par-

ticles are also required (Mathis 1996; Li & Greenberg 1997; Weingartner & Draine 2001; Zubko et al. 2004), including, for example ices and voids in addition to the basic dust grains.

The Galactic Center (GC), invisible in the optical, is one well-known example of a highly extinguished region (Becklin & Neugebauer 1968). Because of this, it should be relatively easy to measure the infrared extinction, without the large relative errors implicated in using regions of small absolute extinction. Rieke & Lebofsky (1985), for example, used infrared photometry of a few red supergiants present in the GC together with a visible to near-infrared extinction law obtained outside of the Galactic Center, in order to derive a universal infrared extinction law (Figure 4.1). This measurement was later slightly improved by adding NICMOS near-infrared measurements by Rieke (1999).

Another method of measuring the IR extinction is to use a stellar population of known infrared luminosity (Nishiyama et al. 2006), such as the red clump for which the absolute luminosity is measured locally (Groenewegen 2008). For this method, however, it is also necessary to know a precise distance to the object, which makes the method difficult for most objects. In the case of the GC the distance is however well known (Reid 1993; Genzel et al. 2010). Using this method Schödel et al. (2010) obtained  $A_H = 4.35 \pm 0.18$ ,  $A_{K_s} = 2.46 \pm 0.12$  and  $A_{L'} = 1.23 \pm 0.20$  toward Sgr A\*.

As an alternative to methods involving stars, one can also use nebular hydrogen lines to measure extinction. As a case in point, Lutz et al. (1996) and Lutz (1999) used ISO-SWS spectra of the minispiral (a bright HII region in the GC; Lo et al. 1983) to derive extinction from 2.6 to 19  $\mu\text{m}$ . Typically this method is more precise, since the intrinsic uncertainty of the relative line strengths in this case (Hummer & Storey 1987) is smaller than the spectral uncertainty of stellar emission. An additional advantage is that the lines are much narrower than the bandpasses of the broadband filters, so that the effective wavelength is known a priori, while for broadband filters it is extinction dependent. Furthermore, there are many more lines in the IR than the number of broadband filters in frequent use, such that it is easier to obtain a well-sampled extinction curve, that includes also extinction features.

Although it is only possible, using infrared lines alone, to obtain *relative* extinction measurements within the infrared, stellar methods often have the same problem. Absolute extinction calibration is made possible by comparing with longer wavelengths where the extinction is negligible. The absolute extinction toward the GC for the Paschen- $\alpha$  line at 1.87  $\mu\text{m}$  was obtained in this way in Scoville et al. (2003) using 6 cm continuum data.

The extinction toward Sgr A\* from the various measurements mentioned above is shown in Figure 4.1. However, there is apparently some discrepancy between the different studies. The uncertainty in extinction creates, in turn, uncertainty in determining the intrinsic luminosities of young massive stars in the GC (Martins et al. 2007; Fritz et al. 2010), as well as the intrinsic luminosity of Sgr A\* (Genzel et al. 2003). In addition, there is no study that covers the full wavelength range, and only a few studies of this kind are available outside of the Galactic Center.

In this paper we use the emission of the minispiral from 1.28 to 19  $\mu\text{m}$  to derive relative extinction values from line emission, which are compared to 2 cm radio continuum data

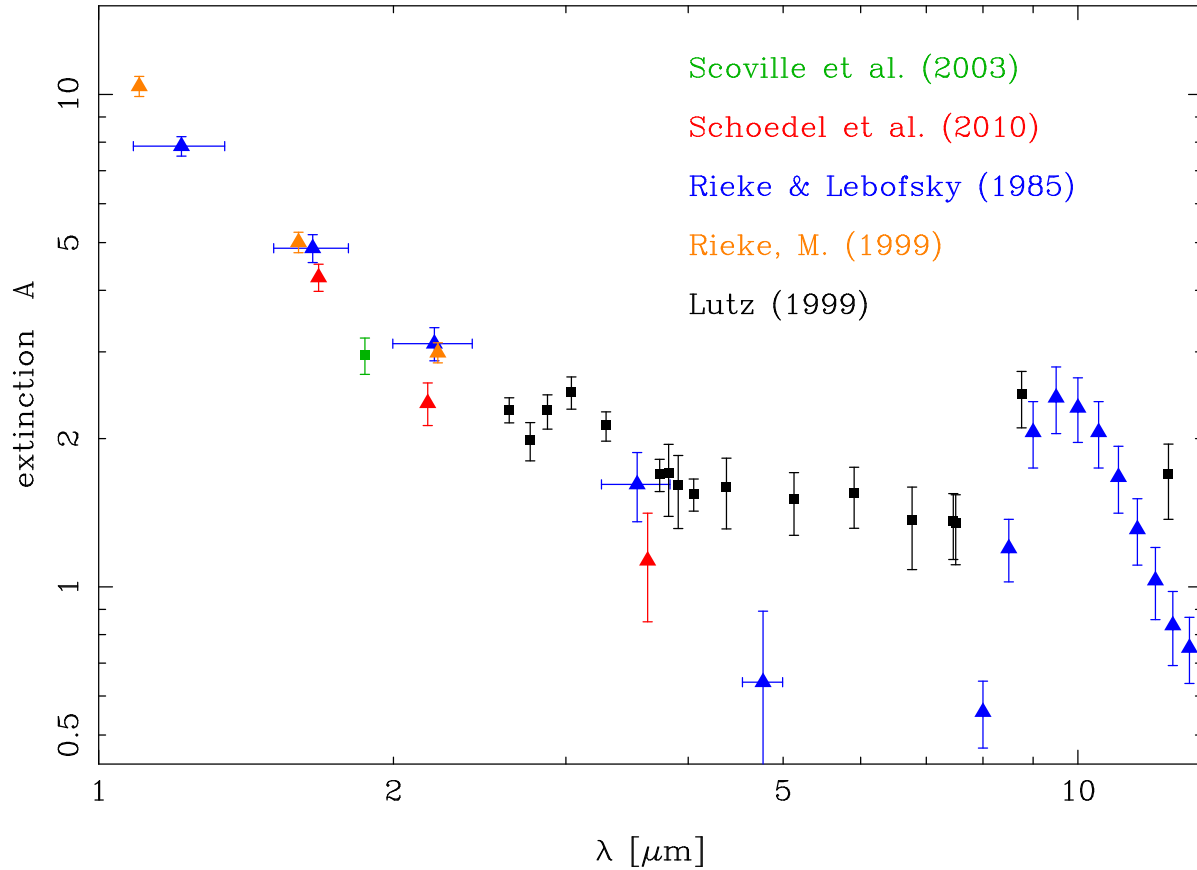


Figure 4.1 Extinction toward Sgr A\* from the literature: triangles represent values derived from stars, boxes values derived from gas lines. Most values were obtained using slightly different regions around Sgr A\*. For the comparison, we convert the values to the direct sight line toward Sgr A\* (i.e. the central  $0.5''$ , see Section 4.5.3) using the extinction map of Schödel et al. (2010). In the case of Rieke & Lebofsky (1985) we use the extinction law of Rieke & Lebofsky (1985) and the absolute extinction of Rieke et al. (1989).

to compute the absolute extinction. In Section 4.2 we present our data, and discuss the extraction of line maps and flux calibration in Section 4.3. In Section 4.4 we derive the extinction. We discuss the results in Section 4.5. We compare the results with other works for the GC and for other parts of the Galaxy and with theoretical dust models. We also use the data for estimating the distance to the Galactic Center,  $R_0$ . We summarize in Section 4.6.

## 4.2 Data Set

In this section we describe the observations used to derive the extinction curve toward the Galactic Center. We used a VLA radio (2 cm continuum) map, ISO-SWS spectra (2.4 to 45  $\mu\text{m}$ ) and SINFONI imaging spectroscopy (1.2 to 2.4  $\mu\text{m}$ ), of which the latter is used to construct line maps at Brackett- $\gamma$  (2.166  $\mu\text{m}$ ), Brackett- $\zeta$  (1.736  $\mu\text{m}$ ), and Paschen- $\beta$  (1.283  $\mu\text{m}$ ). The fields of view for the different datasets are compared in Figure 4.2.

### 4.2.1 Radio

Figure 4.2 presents the radio and near-infrared data used combined with the field of views of all measurements. The radio data consists of combined 2 cm continuum observations in the A, B, C and D configurations of the VLA. The phase center of the multi-configuration data set at 2 cm is on Sgr A\*. Standard calibration was done on each data set before each data set was combined in the  $uv$  plane. Details of phase and amplitude calibration of each data set taken in different configurations of the VLA can be found in Yusef-Zadeh & Wardle (1993) and Yusef-Zadeh et al. (1998). The combination of these configurations makes high resolution possible, while at the same time ensuring good coverage of extended structure. Due to the use of the smallest, D, configuration, we are able to detect structures of up to 50'' in size. The resolution of the final image is  $0.42'' \times 0.3''$  with the longer axis of the Gaussian oriented approximately north (P.A.  $\approx 4^\circ$ ). The image extends at least 48'' from Sgr A\* in all directions. We use a radio continuum map because, for the data available to us, the SNR and the resolution are better than for line maps.

We chose to use a map at 2 cm because non-thermal emission, redder than the thermal emission of the minispiral, is less dominant at shorter wavelengths (Scoville et al. (2003), on the other hand, used a 6 cm map). Naturally, some non-thermal contamination is expected at 2 cm as well. We control for this by testing whether there is a correlation between minispiral emission and extinction strength (see Section 4.4.2). Sgr A\* is a clearly visible non-thermal source in the radio map, see Figure 4.2. However, due to our high resolution it is well isolated from the minispiral. We are thus able to fit the source by a Gaussian and subtract it, smoothing the area around it. As a result, Sgr A\* is not visible in our final radio map (Figure 4.3).

Two particularly problematic regions are IRS2 and IRS13, for which Roberts et al. (1996) and Shukla et al. (2004) derived significantly higher than average electron temperatures. In our analysis we simply ignore these regions, masking out IRS13 and IRS2.

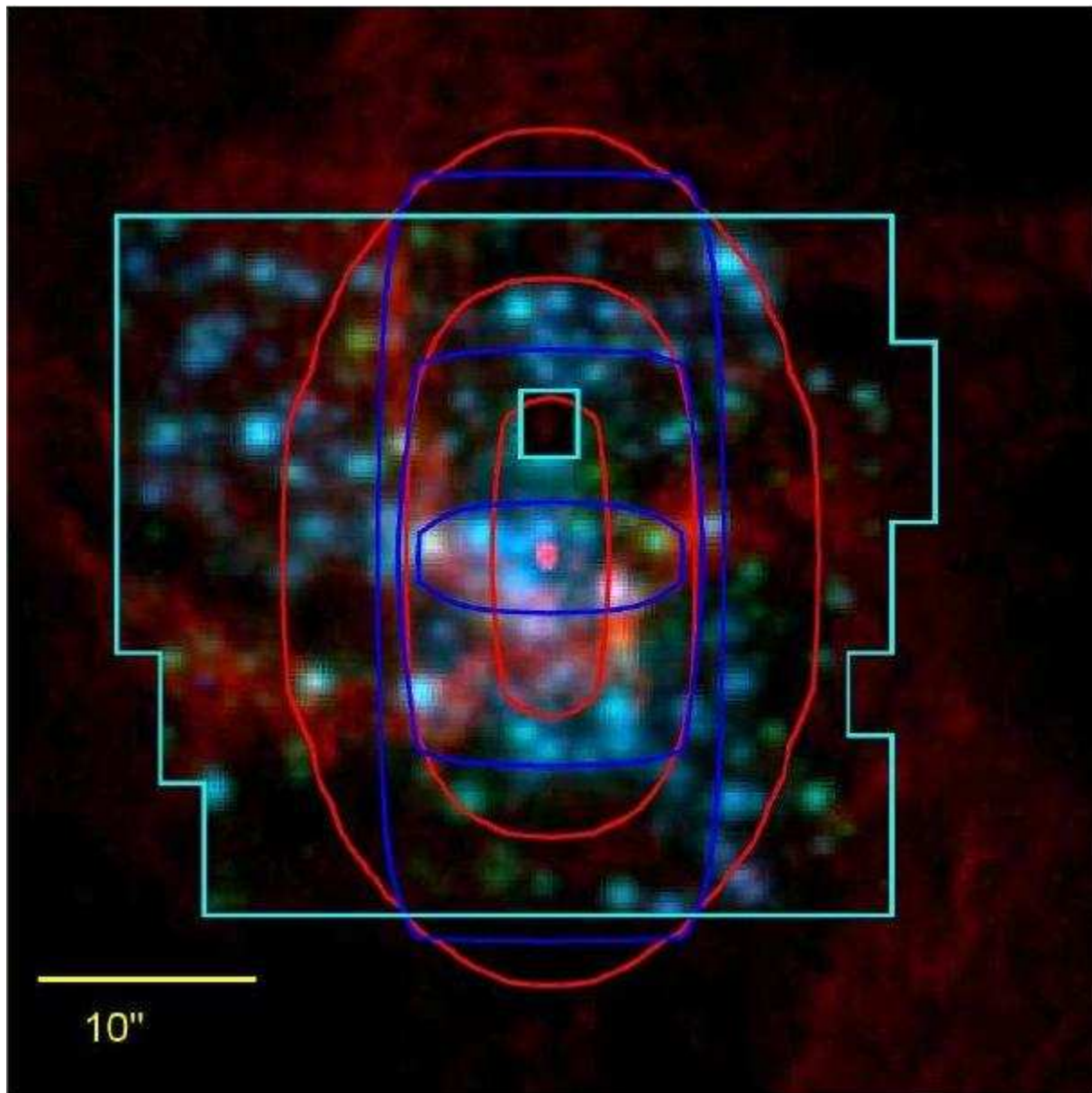


Figure 4.2 Field of view for different measurements. In red, the radio 2 cm continuum image; in blue and green, respectively, are the H and Ks broadband images constructed from SINFONI HK data. The radio image is larger than displayed here, but the outer areas are not used in this publication. Light green lines mark the borders of the SINFONI field which has a hole around IRS7. Blue lines indicate the contours of the ISO PSF around  $2.6 \mu\text{m}$ , representing 90% , 50% and 10% of the central intensity. The red lines indicate the same for the ISO PSF around  $19 \mu\text{m}$ .

Difficulties can also arise, for interferometric observations, from the fact that only a finite range of spatial frequencies can be sampled. This has the consequence that structure larger than the fringe spacing of the shortest baseline is not measured, which can result in an underestimate of the flux, if the observed object is much larger than the largest angular scale sampled. For us, however, this is not a problem, since our map, due to the use of D configuration as mentioned above, we are able to detect structures of sizes up to  $50''$ , while nearly all of the flux of the minispiral is concentrated within  $50''$  diameter (Figure 1 of Scoville et al. 2003).

### 4.2.2 ISO

We use the ISO-SWS data of Lutz (1999). These data are reduced with the SWS interactive analysis system (Wieprecht et al. 1998). The data consist of a single aperture spectrum extending from 2.4 to  $45 \mu\text{m}$ , shown in Figure 4.4.

The field of view of SWS (de Graauw et al. 1996) is approximately rectangular; it can be seen in Figure 4.2. We consider the deviations from rectangularity (Beintema et al. 2003) in Section 4.3.2. In our observations the longer axis of the field of view is oriented north-south (P.A.  $\approx 0^\circ$ ). The field of view is approximately  $14'' \times 20''$ , shortward of  $12 \mu\text{m}$ , and  $14'' \times 27''$  between 12 and  $28 \mu\text{m}$ . The observations are centered on Sgr A\*.

### 4.2.3 SINFONI

For shorter wavelengths (1.2 to  $2.4 \mu\text{m}$ ) we use spectra obtained with the integral field spectrometer SINFONI (Eisenhauer et al. 2003; Bonnet et al. 2003) at UT4 of the VLT<sup>1</sup>. We use the following data: H+K-band (spectral resolution 1500), seeing limited cubes (FWHM= $0.85''$ ) covering an area of about  $37'' \times 30''$  around Sgr A\* from 2003 April 9 with a spatial sampling of  $250 \text{ mas pixel}^{-1} \times 250 \text{ mas pixel}^{-1}$ . J-band (spectral resolution 2000), seeing limited cubes (FWHM= $0.6''$ - $1''$ ) of most areas of the minispiral obtained 2010 May 21 and July 6, with a spatial sampling of  $125 \text{ mas pixel}^{-1} \times 250 \text{ mas pixel}^{-1}$ . We apply the standard data reduction SPRED (Abuter et al. 2006; Schreiber et al. 2004) for SINFONI data, including detector calibrations (such as bad pixel correction, flat-fielding, and distortion correction) and cube reconstruction. The wavelength scale is calibrated with emission line lamps and finetuned with atmospheric OH lines. The HK data is atmosphere corrected and kept in ADU count units. No conversion in energy is applied. We flux calibrate the J-band data with standards which were observed directly after the science observations, as is described in more detail in the next section. The Brackett- $\gamma$  map, one of three line maps derived from the SINFONI observations (described in the next section), can be seen in Figure 4.3.

<sup>1</sup>We use SINFONI data from ESO programs 70.A-0029(A), 183.B-100(P) and 183.B-100(R).

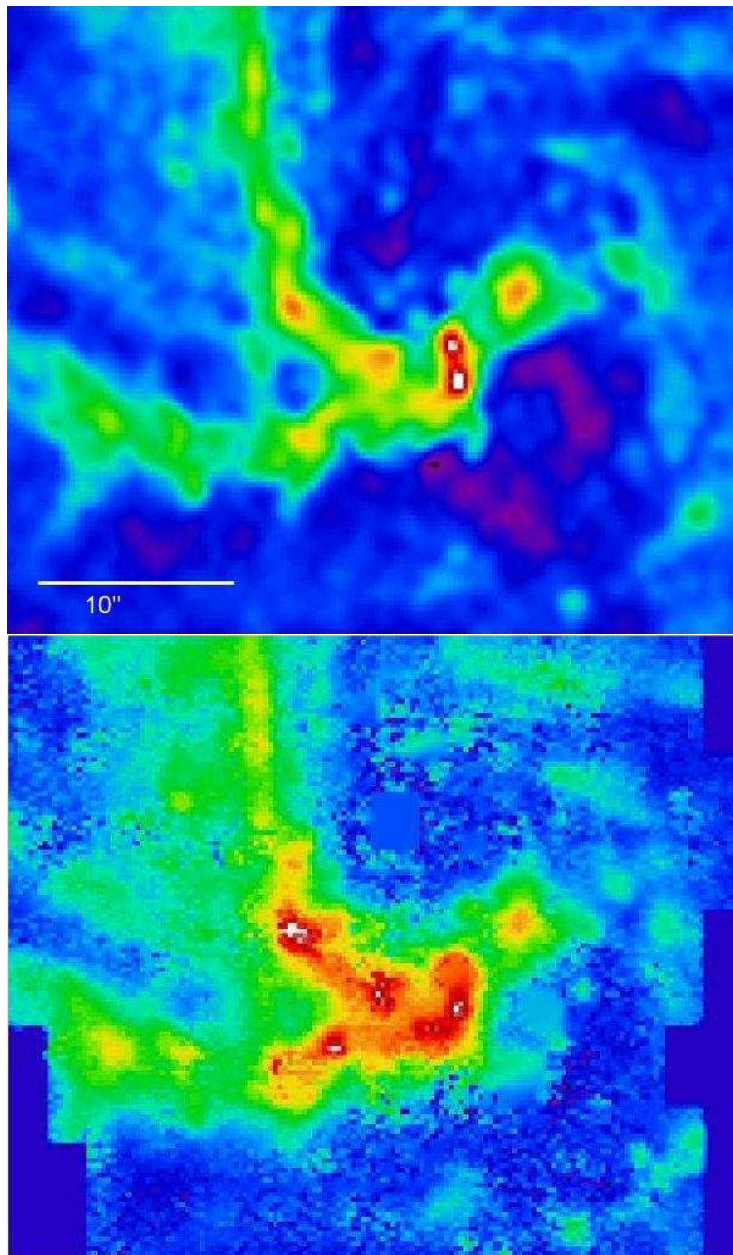


Figure 4.3 Top: 2 cm continuum radio image from VLA. We subtracted Sgr A\* by fitting a Gaussian to it. The resolution is smoothed to  $0.85''$ . Bottom: Brackett- $\gamma$  map derived from SINFONI. Areas with stellar lines are replaced by the neighboring gas emission. Some areas at the border were not mapped and are given zero flux. We fill the area around IRS7 that was not covered by the observations with the median flux of the surrounding. Both maps show the same area, with  $250 \text{ mas pixel}^{-1}$ , the same resolution, and the same color scaling.

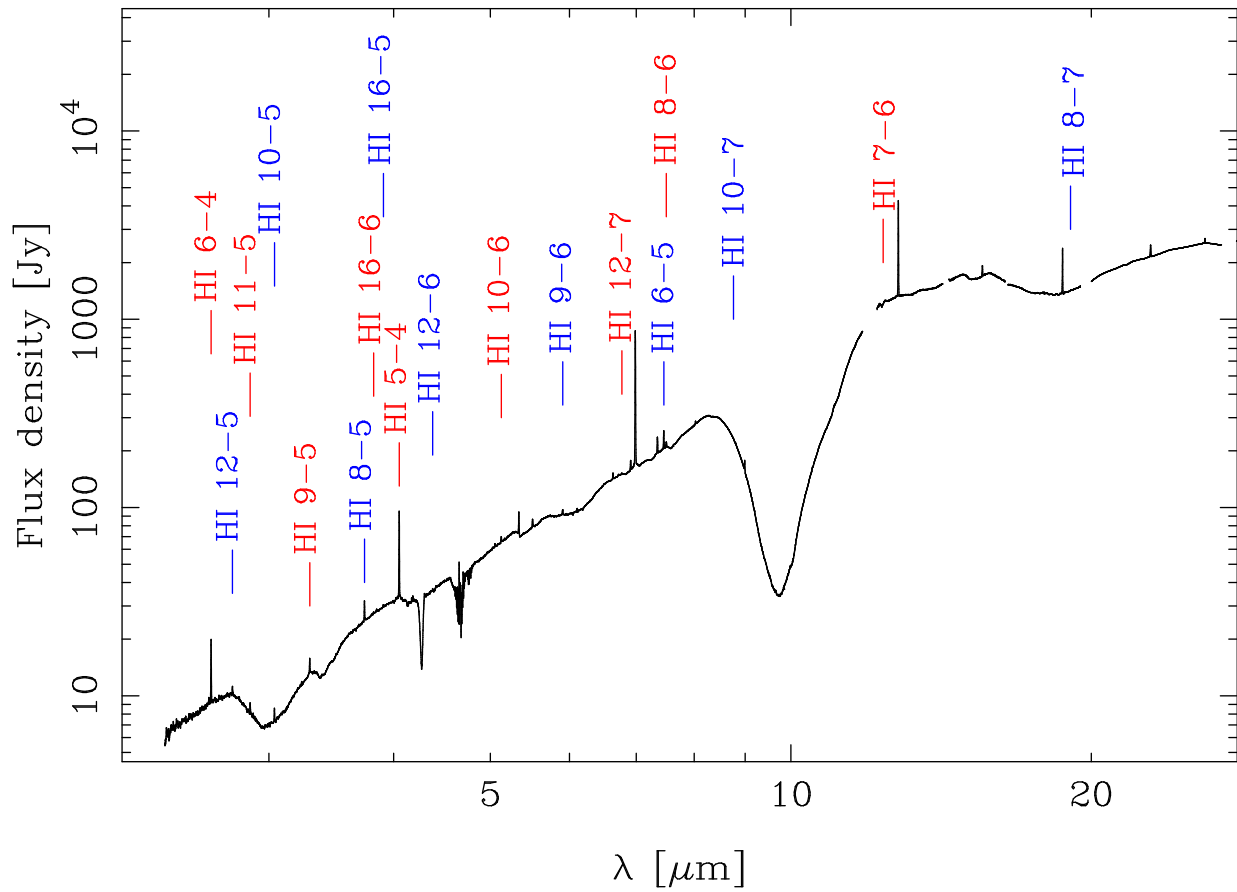


Figure 4.4 ISO-SWS spectrum of the GC. The hydrogen lines used for the extinction measurements are marked by colored vertical lines.

## 4.3 Construction of Line Maps and Flux Calibration

### 4.3.1 Line Maps

In this section we describe the construction of Brackett- $\gamma$ , Brackett- $\zeta$ , and Paschen- $\beta$  line maps from the SINFONI data, see Table 4.1. In order to do this, we integrate over the channels which contain the nebular emission and subtract the average of the adjacent spectral channels on both sides as background. The line maps contain the following types of artifacts, unrelated to the minispiral emission:

- Bad pixels, in the sense of a large deviation of a few pixels from their neighbors. We identify them mostly manually.
- Gaps between cubes, when not well aligned
- Emission and absorption line stars

We interpolate these artifacts, treating them like bad pixels in the data reduction. We also replace the hole around IRS7 in our map with the median flux of the surrounding for obtaining line maps, see the Brackett- $\gamma$  map in Figure 4.3.

### 4.3.2 Flux Calibration

We flux calibrate the Brackett- $\gamma$  map with a NACO Ks-image of the GC from April 29, 2006. On this day, a standard star was observed with a zero-point uncertainty of 0.06 mag. In order to translate this calibration to the SINFONI data, we extract a mock Ks-image ( $F_{\text{SINFONI Ks}}$ ) from the SINFONI cube. This is done by multiplying the atmosphere corrected SINFONI data slice by slice with factors which represent the product of atmospheric and NACO Ks-filter transmission<sup>2</sup> for every slice. The factors are scaled such that their integral is one. In this way we calibrate a single SINFONI slice at the isophotal wavelength of the Ks-band.

We measure the full flux in the NACO image and in  $F_{\text{SINFONI Ks}}$  over the area covered by the SINFONI data. We estimate the uncertainty of the cross-calibration by dividing the two images in nine parts and measuring in each part the count ratio. We obtain an uncertainty of 0.03 mag from the standard deviation of the nine count ratios.

In total we use the following factor for calibration of the Brackett- $\gamma$  line map:

$$f = \frac{F_{\lambda_{\text{Ks}}} \lambda_{\text{iso Ks}}}{R \lambda_{\text{Br}\gamma}} 10^{-0.4 \text{ZP}} \quad (4.1)$$

$$= \frac{F_{\lambda_{\text{Ks}}} \lambda_{\text{iso Ks}}}{R \lambda_{\text{Br}\gamma}} 10^{-0.4 \left( \text{ZP}_{\text{NACO}} + 2.5 \log \frac{F_{\text{SINFONI Ks}}}{F_{\text{NACO Ks}}} \right)} \quad (4.2)$$

<sup>2</sup>We use the NACO Ks-filter transmission from the NACO web site: <http://www.eso.org/sci/facilities/paranal/instruments/naco /inst/filters.html>

Here,  $F_{\lambda_{\text{Ks}}}$  is the Ks calibration of Vega (Tokunaga & Vacca 2005),  $R$  the number of slices per  $\mu\text{m}$  and  $ZP$  the zero point in magnitudes of the SINFONI data. We assume an error of 0.03 mag for  $F_{\lambda_{\text{Ks}}}$ . Because we use ADU spectral data, the amount of energy per ADU depends on wavelength. Since the calibration is at the isophotal wavelength (Tokunaga & Vacca 2005), we multiply  $F_{\lambda_{\text{Ks}}}$  by  $\lambda_{\text{iso Ks}}/\lambda_{\text{Br}\gamma}$ . Compared to using a standard star, our calibration has the advantage that we use the same NACO data as Schödel et al. (2010) for calibration. In this way we reduce the uncertainty when comparing our results with theirs, see Section 4.5.2.

We calibrate Brackett- $\zeta$  in a similar way to Brackett- $\gamma$ , using the integrated flux of an H-band NACO image from April 29, 2006, which is compared to a H-band image constructed from the SINFONI cube. The errors of the calibration are 0.05 mag (NACO zero point), 0.04 mag (cross-calibration) and 0.03 mag uncertainty from the conversion to energy ( $F_{\lambda_H}$ ).

We use data cubes flux calibrated with standard stars for Paschen- $\beta$  (see Figure 4.5), because a flux calibrated GC image in the J-band was not readily available. By comparing the fluxes of different standard stars from the two nights in April and July 2010 in which the data was obtained, we validate that the calibration is stable, with only 0.034 mag rms scatter and 0.005 mag bias over the J-band spectrum. We test the calibration accuracy further by comparing adjacent areas in the data from April and July. In doing so, we do not find signs of significant discontinuities in the Brackett- $\gamma$  to Paschen- $\beta$  ratio at the border between the two areas. We estimate the systematic calibration error to be the same as for Brackett- $\gamma$ : 0.075 mag.

For the ISO data we use the absolute calibration of Lutz et al. (1996). The calibration error dominates the total error for bright lines. It is 10% below 4.06  $\mu\text{m}$  and 20% above.

Since the emission of the minispiral is not homogeneous, it is necessary to compute the NIR and radio comparison fluxes from the same area as the ISO-SWS beam profile. Because of this we multiply the ISO-SWS beam profile (Beintema et al. 2003) in every ISO band with the Brackett- $\gamma$  line map and obtain the Brackett- $\gamma$  flux within the ISO-SWS beam profile. Since the Brackett- $\gamma$  map does not cover the full ISO beam, we also calculate the radio flux contained in the ISO-SWS beam profile in the same way. Over the Brackett- $\gamma$  field the difference in the beam correction is 3 % between using radio and using Brackett- $\gamma$ . This difference could be caused by non-thermal emission. Therefore, we use the radio data only for calculating how much flux is missed due to the smaller field of the Brackett- $\gamma$  data. In total, we find that the flux is about 7% smaller below 12  $\mu\text{m}$  and about 6% higher above 12  $\mu\text{m}$  compared to a sharp  $14'' \times 20''$  field. The sudden change at 12  $\mu\text{m}$  is an artifact caused by the field size increase to  $14'' \times 27''$  at this wavelength.

## 4.4 Deriving Extinction from Hydrogen Lines

The ratios between different hydrogen recombination lines in HII regions depend only weakly on the local physics (Hummer & Storey 1987). Hence, it is possible to derive the relative extinction ( $A$ ) between two lines  $a$  and  $b$  by comparing the observed flux ratio

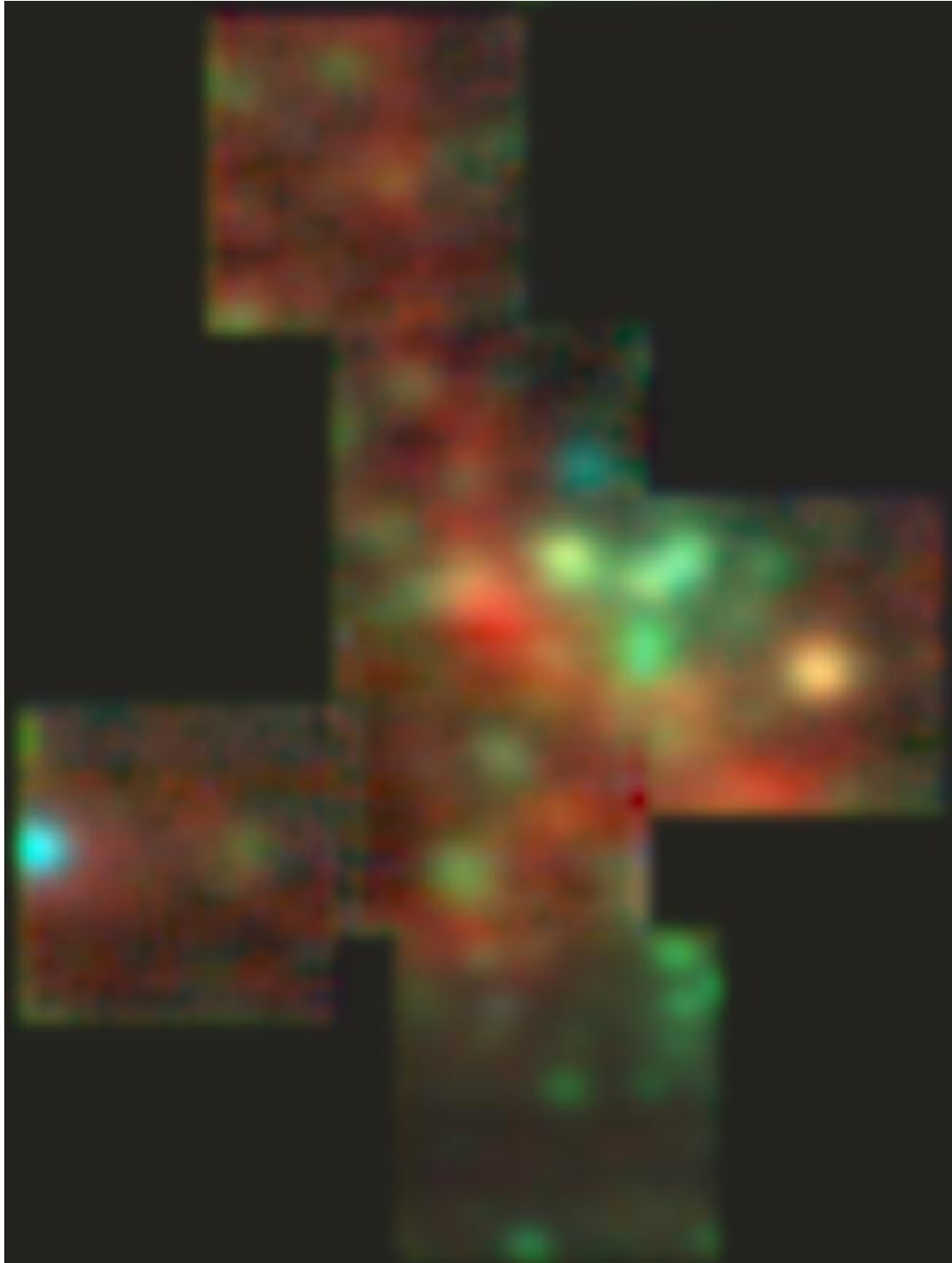


Figure 4.5 Color image from J-band SINFONI data: blue  $1.18 \mu\text{m}$  image, green  $1.3 \mu\text{m}$  image, red Paschen- $\beta$  line map.

$(F(a)_{\text{obs}}/F(b)_{\text{obs}})$  with the expected (extinction-free) flux ratio  $(F(a)_{\text{exp}}/F(b)_{\text{exp}})$ :

$$A_{a-b} = -2.5 \times \log \left( \frac{F(a)_{\text{obs}}/F(b)_{\text{obs}}}{F(a)_{\text{exp}}/F(b)_{\text{exp}}} \right) \quad (4.3)$$

Using infrared data only, and without making further assumptions about the shape of the extinction curve, it is only possible to obtain the relative extinction. In order to obtain absolute extinction values it is necessary to use a wavelength for  $b$  at which the extinction is known independently, or negligible. Then it is possible to calculate the expected flux at  $a$  from the observed flux at  $b$  using the known flux ratios for emission from a gaseous nebula (Baker & Menzel 1938). We use their Case B, for which the nebula is opaque to Lyman radiation but transparent to all other radiation (in Case A the nebula is also transparent to Lyman radiation.):

$$F(a)_{\text{exp}} = c \times F(b)_{\text{obs}} \quad (4.4)$$

$c$  follows from the Case B calculation and depends on the radio frequency and infrared line used, as well as on the electron temperature, see also Section 4.4.1.

In our analysis, we use radio data for  $b$  and infrared lines in place of  $a$ . The equation for absolute extinction is thus:

$$A_{\text{IR}} = -2.5 \times \log \left( \frac{F(\text{IR})_{\text{obs}}}{c \times F(\text{radio})_{\text{obs}}} \right) \quad (4.5)$$

We use the Case B line ratios in Hummer & Storey (1987) for the  $F_{\text{obs}}$  ratios in equation (4.3). The unextincted ratios of hydrogen emission originating from different atomic levels depend on the radiation state (like Case B; Lutz 1999). As a first test of the validity of Case B we use the hydrogen line in the ISO-SWS spectrum at  $7.50 \mu\text{m}$ , which is a blend of the lines 6-8 and 8-11. After accounting for the blending the  $7.50 \mu\text{m}$  extinction differs only by 0.05 mag from the extinction for the 6-5 line at  $7.46 \mu\text{m}$ , assuming Case B. This implies that Case B is indeed valid for the Galactic Center (Lutz 1999).

#### 4.4.1 Electron Temperature

The physical conditions of the plasma, in particular the electron temperature ( $T_e$ ), have an important influence on the extinction free flux ratios of the IR line fluxes to the radio flux. For example the dependence of Paschen- $\alpha$  to radio continuum (free-free) emission ( $S_{\text{ff}}$ ) is  $F_{\text{Pa}\alpha}/S_{\text{ff}} \propto T_e^{-0.52}$  (Scoville et al. 2003). Accordingly, it is necessary to know  $T_e$  for deriving the absolute extinction.

The electron temperature has been derived at H92 $\alpha$  (8.3 GHz) by Roberts & Goss (1993) and at H41 $\alpha$  (92 GHz) by Shukla et al. (2004). Both obtain  $T_e \approx 7000$  K in most parts of the minispiral. The consistency of both measurements shows that all conditions, thus also Case B, (Roberts et al. 1991) for deriving  $T_e$  are fulfilled, even at the smaller and more problematic frequency of 8.3 GHz. In this work, we take the measurement by Roberts & Goss (1993) of  $T_e = 7000 \pm 500$  K, since it has the highest SNR, however we correct it to account for the He<sup>+</sup> fraction (see below).

According to Roberts & Goss (1993), there is no significant spatial variation in the electron temperature. Thus, we think it is justified to simply assume a constant electron temperature. Even if the electron temperature varies, the variation does not matter as long as the value used is equal to the flux weighted average of  $T_e$  of the area over which we integrate.

The absolute value of  $T_e$  also depends on the Helium<sup>+</sup> ( $\text{He}^+$ ) fraction:  $Y^+ = \text{He}^+/\text{H}^+$ . Roberts & Goss (1993) derived a  $2\sigma$  limit for  $Y^+$  of 3%, and measured  $Y^+ = 5\% \pm 2\%$  in another area. Krabbe et al. (1991) derived  $Y^+ \approx 4\%$  from the He I line at  $2.06 \mu\text{m}$ . We obtain  $Y^+ = 2\% \pm 0.7\%$  using the same line. Considering all information, we assume  $Y^+ = 3\% \pm 1\%$  for the calculation of  $T_e$ .

The electron temperature depends in the following way on  $Y^+$  (Roelfsema et al. 1992; Roberts et al. 1996):

$$T_e = \left( T_{e\text{raw}} \frac{1}{1 + Y^+} \right)^{0.87} \quad (4.6)$$

$T_{e\text{raw}}$  is the  $T_e$  obtained assuming  $Y^+ = 0$ . Since Roberts & Goss (1993) used  $Y^+ = 0$ , they calculated  $T_{e\text{raw}}$ . We therefore calculate the real  $T_e$  from the  $T_{e\text{raw}}$  of Roberts & Goss (1993) using our value of  $Y^+ = 3\%$ . We obtain  $T_e = 6800 \pm 500 \text{ K}$ , and use this value hereafter. The error in the electron temperature results in an absolute extinction error of 0.043 mag. In principle, it is also necessary to know the electron density of the emitting plasma to calculate the absolute extinction from infrared lines and radio emission (Hummer & Storey 1987). We use an electron density of  $10^4 \text{ cm}^{-3}$  (Shukla et al. 2004), but the results are not very sensitive to the actual value used (Hummer & Storey 1987).

#### 4.4.2 Extinction Calculation

We first compute the Brackett- $\gamma$  extinction from direct comparison of the Brackett- $\gamma$  map with the radio data (Figure 4.3), following equation (4.5). We then calculate all other extinction values with respect to the Brackett- $\gamma$  data. This method has the advantage that we can select the fiducial area by comparing with the high SNR Brackett- $\gamma$  data (Table 4.1). This is done by calculating the extinction relative to Brackett- $\gamma$  extinction following equation (4.3). The Brackett- $\gamma$  extinction is then added to this value to obtain the absolute extinction.

To calculate the expected flux ratio we convert equation 3 of Scoville et al. (2003) to Brackett- $\gamma$ , our continuum frequency of 15 GHz, and mJy, using the relative line strength in Hummer & Storey (1987):

$$\left( \frac{F_{\text{Br}\gamma}}{S_{\text{ff}}} \right)_{\text{exp}} = (1.327 \pm 0.052) 10^{-11} \text{ erg s}^{-1} \text{ cm}^{-2} \text{ mJy}^{-1} \quad (4.7)$$

Inserting this expected ratio and the measured Brackett- $\gamma$  to radio ratio in equation (4.5) we obtain a Brackett- $\gamma$  extinction map.

In order to estimate the impact of non-thermal emission, we measure the resulting extinction in Brackett- $\gamma$  flux bins, see Figure 4.6. For most line fluxes, the extinction is

Table 4.1. Combinations of lines or continuum used for deriving extinctions

Line A	Line B	area used ('good' area)
2 cm continuum	Brackett- $\gamma$	'ISO beam', excluding: low Br- $\gamma$ flux, IRS(16C+16NE+13+2)
Brackett- $\gamma$	Brackett- $\zeta$	'ISO beam', excluding: low Br- $\gamma$ flux, Br- $\gamma$ / Br- $\zeta$ outliers, IRS(16C+16NE+13+2)
Brackett- $\gamma$	Paschen- $\beta$	'ISO beam' inside the J-band data, excluding: low Br- $\gamma$ flux, IRS(16C+16NE+13+2)
Brackett- $\gamma$	ISO lines	in each case the adequate ISO beam

approximately constant. However for line fluxes smaller than  $3.7 \cdot 10^{-16} \text{ ergs s}^{-1} \text{ cm}^{-2} \text{ pixel}^{-1}$  the extinction is anticorrelated with the Brackett- $\gamma$  flux. Most likely the anticorrelation is caused by non-thermal emission of Sgr A East which becomes more important in fainter regions of the minispiral. Because of this, we mask out areas with fluxes smaller than  $3.7 \cdot 10^{-16} \text{ ergs s}^{-1} \text{ cm}^{-2} \text{ pixel}^{-1}$ . The choice of this flux cut is somewhat arbitrary. However, since we only use the integrated flux of the whole ISO beam, which is dominated by the brighter fluxes, the uncertainty of the flux cut only introduces an extinction error of 0.03 mag. In addition, we mask out IRS2 and IRS13 (see Section 4.2.1), as well as IRS16NE and IRS16C because of remaining stellar emission line flux there.

The extinction in the areas defined by the above constraints is similar to the extinction map of Schödel et al. (2010). However, there is a scatter of about 0.4 mag in our map, when comparing pixel by pixel, due to the low SNR per pixel in Brackett- $\gamma$  and radio data. Because of this, our extinction map is not of direct use. Nevertheless, the small SNR per pixel does not affect our absolute measurement, because we use the flux from a total of 2854 pixels for deriving the Brackett- $\gamma$  extinction.

For a comparison with Schödel et al. (2010) we add up the Brackett- $\gamma$  and radio fluxes within 0.1 mag bins. We use the extinction map of Schödel et al. (2010) to bin according to extinction. We then calculate the extinction in every bin from the total fluxes therein by means of equation (4.7), see Figure 4.7. The differences between the extinction values from Schödel et al. (2010) and this work have an rms scatter of 0.10 mag. This scatter is bigger than would be expected from the SNR of both maps, but systematic problems, such as residual anisoplanatism in Schödel et al. (2010), or  $T_e$  variations for our map, could cause increased scatter. We assume that half of the scatter is caused by our data and add therefore 0.07 mag as additional extinction error. This estimate is conservative, because many problems should average out over the full area.

Our aim is to measure the wavelength dependent extinction curve in one line of sight. Spatially variable extinction can however cause deviation of the line of sight extinction curve, if different measurement areas are used at different wavelengths. In addition, for comparison with Schödel et al. (2010), it is also necessary to correct for the difference between the average extinction of this map and the Brackett- $\gamma$  flux weighted extinction in the same area. In order to take both effects into account, we calculate the average extinction of the extinction map of Schödel et al. (2010) within the region of the ISO beam, and the flux weighted extinction within the ISO beam for the different line maps.

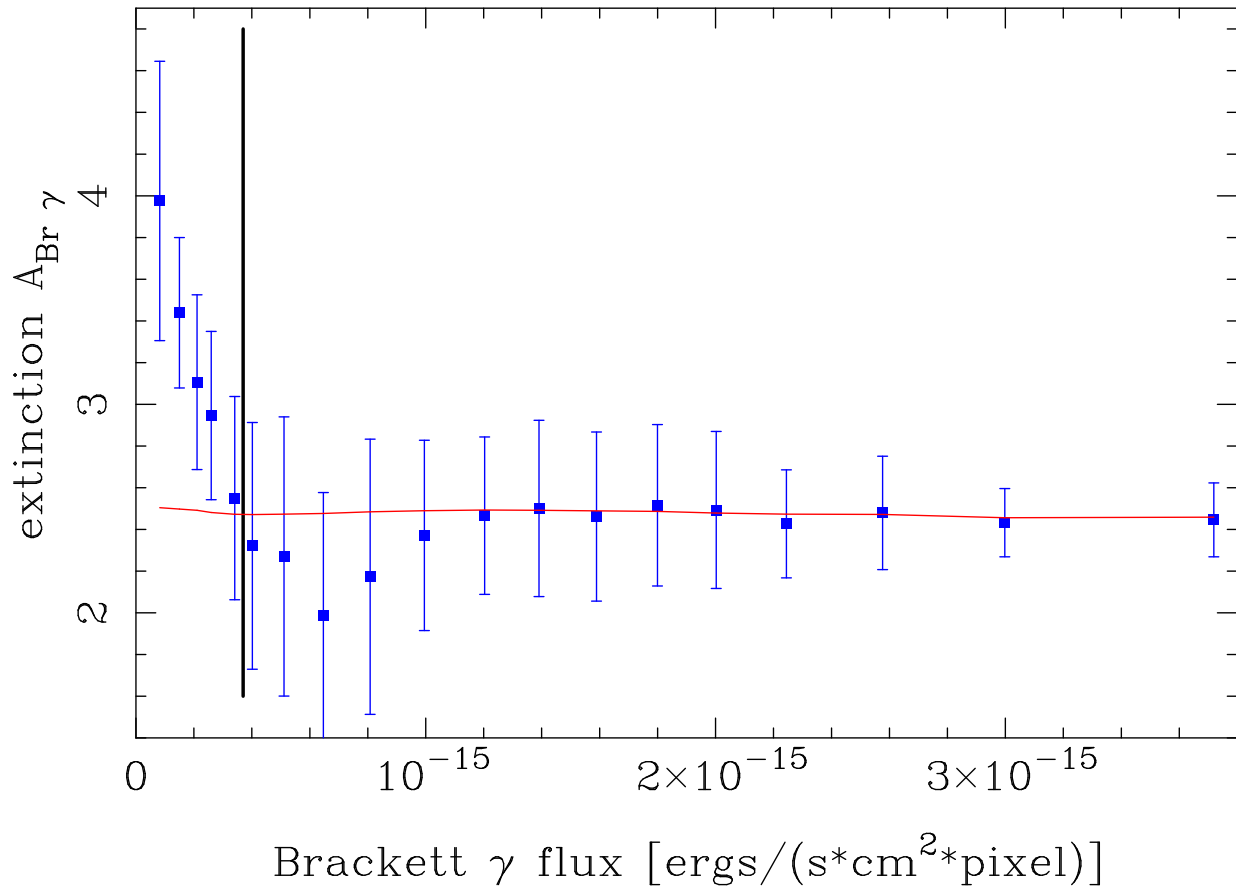


Figure 4.6 Extinction in the central  $14'' \times 20''$ , binned in Brackett- $\gamma$  flux. The squares and error bars mark the median extinction per flux bin. (The error is based on the median deviation, scaled to a Gaussian  $1\sigma$  error by multiplying it with 1.483.) While for small fluxes the extinction is anticorrelated with the flux, there is no such correlation at fluxes larger than the vertical line at  $3.7 \times 10^{-16} \text{ ergs s}^{-1} \text{ cm}^{-2} \text{ pixel}^{-1}$ . The red line is the integrated extinction using all pixels with a flux larger than or equal than the flux in the given bin. There is nearly no variation.

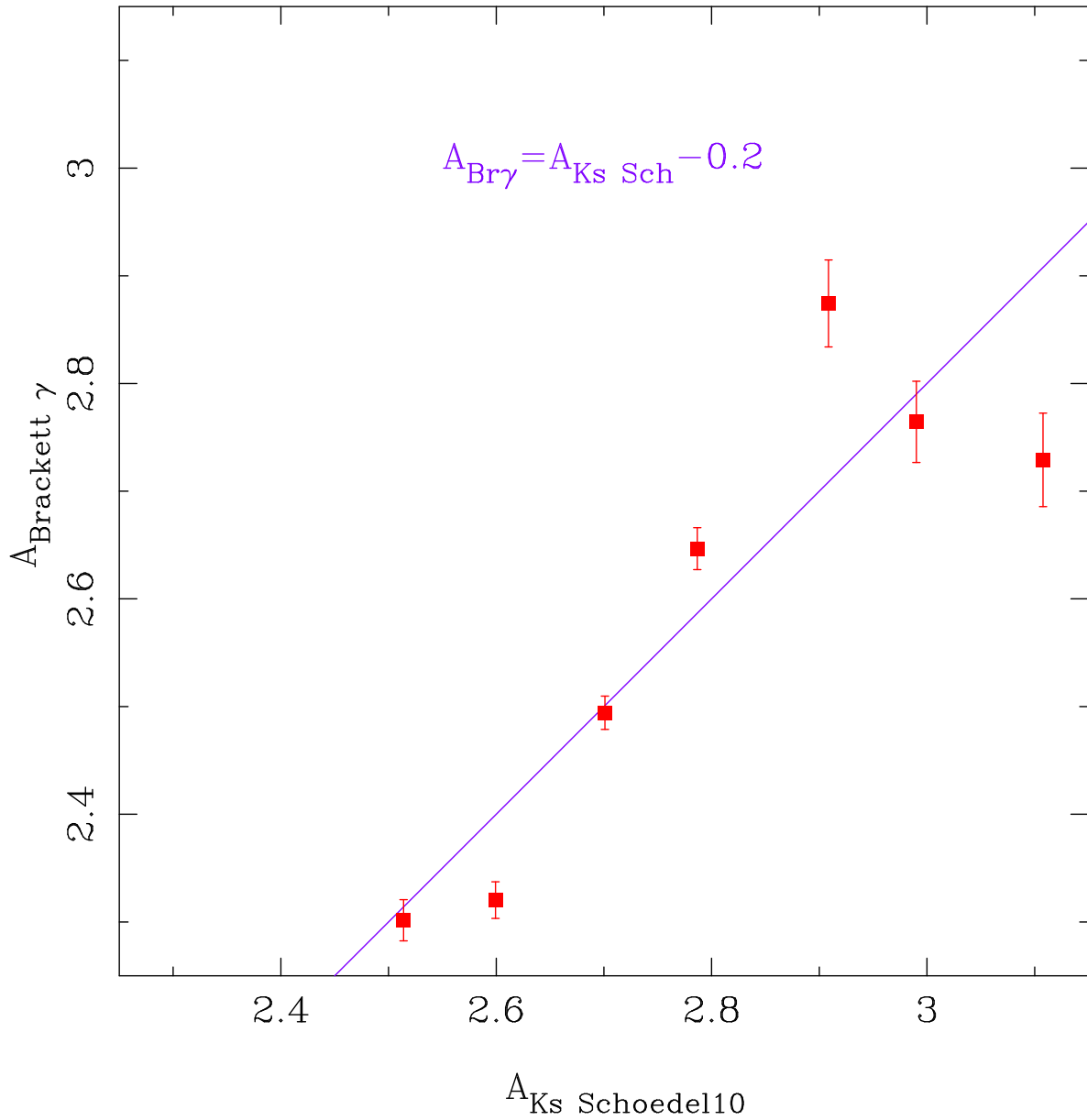


Figure 4.7 Comparison of the extinction derived from our data and that of the Ks extinction map of Schödel et al. (2010). We bin our data according to the map of Schödel et al. (2010) and measure the extinction in every bin. The error bars show the expected error due to the single pixel SNR. The rms scatter in the plot is 0.1 mag, exceeding the expectation.

The difference in extinction is small for all lines. We find the biggest deviation is -0.03 mag for Paschen- $\beta$ , for which line the smallest area was covered, see Figure 4.5. We apply these corrections to our raw extinction values.

There is an additional bias in integrated extinction measurements that can cause apparent flattening of the extinction law, and is especially important for integrated galaxy SEDs (Calzetti et al. 2000). This bias arises because the measurement of the extinction is flux-weighted: this flux being the observed (extincted) flux. This creates a problem, because if the extinction is spatially variable, the extincted flux will be brighter in low-extinction subregions of the image. Thus more weight will be given to these bright, low-extinction sub-regions of the image. A similar effect of very inhomogeneously distributed extinction in the case of galaxy integrated measurements (mixed case) is visible in the top left panel of Figure 2 in Calzetti (2001). The effect of this bias is negligible for negligible extinction (i.e. at long wavelengths), but increases toward shorter wavelength together with the extinction, producing an apparent flattening of the measured extinction law. We test and correct for this bias in our measurements, which is however small (up to 0.08 mag, see Appendix 4.7.1).

In the H-band, the hydrogen lines are weaker, both intrinsically as well as being subject to higher extinction. The atmospheric OH-lines are also stronger in H-band. Because of this, only Brackett- $\zeta$  at  $1.736 \mu\text{m}$  is easily detectable, although even this line is polluted by an atmospheric OH-line, despite sky subtraction. The structure of this remaining OH-line emission/absorption follows the cubes which are combined to the mosaic and is caused by the time variability of the sky. The sky has to be observed offset from the GC in space and thus also in time due to the brightness of the GC. To correct the sky remnants, we derive OH-line strength maps from the next two strongest OH-lines at longer wavelengths, and subtract the average of the two maps from the raw Brackett- $\zeta$  map. We scale the subtraction such that any observable structure due to individual cubes in the combined cube vanishes. We use the uncertainty of the scaling factor and the difference between the two OH-line maps to estimate the error. In order to further exclude unphysical outliers we do not use pixels which deviate by more than  $2.5 \sigma$  from the median Brackett- $\gamma$ / Brackett- $\zeta$  flux ratio. Integrating over the useful area of both lines we obtain  $F_{\text{Br}\gamma}/F_{\text{Br}\zeta} = 16.1 \pm 1.3$ . The error due to the OH line subtraction and the pixel selection uncertainty adds an error of 0.081 mag to the extinction for Brackett- $\zeta$ .

For Paschen- $\beta$  we used the smaller area (Figure 4.5) within its overlap with the central  $14'' \times 20''$ . We use the hydrogen lines detected in the ISO-SWS spectrum (Figure 4.4) to derive extinction values at the corresponding wavelengths. For the ISO data, which is not spatially resolved, stellar emission could be a problem. We test this by comparing the total Brackett- $\gamma$  from our map with that computed upon declaring stars visible in the line map to be 'bad pixels'. The flux difference between the two cases is only 0.04 mag. This contribution, compared to the extinction error of the ISO data of at least 0.14 mag, is therefore not relevant. Since the intrinsic (non extincted) line ratios follow Case B (Section 4.4.2), the intrinsic ratios are well known and do not cause an additional error apart of the  $T_e$  uncertainty.

Table 4.2. Average hydrogen line extinction values toward the GC

$\lambda$ [ $\mu\text{m}$ ]	extinction
1.282	$7.91 \pm 0.11$
1.736	$4.30 \pm 0.13$
2.166	$2.49 \pm 0.11$
2.625	$1.83 \pm 0.13$
2.758	$1.51 \pm 0.19$
2.873	$1.84 \pm 0.19$
3.039	$2.07 \pm 0.19$
3.297	$1.66 \pm 0.15$
3.74	$1.19 \pm 0.14$
3.819	$1.19 \pm 0.31$
3.907	$1.09 \pm 0.3$
4.052	$1.01 \pm 0.13$
4.376	$1.09 \pm 0.29$
5.128	$0.99 \pm 0.24$
5.908	$1.04 \pm 0.24$
6.772	$0.84 \pm 0.29$
7.459	$0.81 \pm 0.23$
7.502	$0.79 \pm 0.24$
8.76	$2.04 \pm 0.34$
12.371	$1.34 \pm 0.32$
19.062	$1.34 \pm 0.5$

Note. — All values scaled to the central  $14'' \times 20''$  of the GC.

### 4.4.3 Extinction Derived

The extinction derived in this analysis is presented in Table 4.2 and Figure 4.8. It decreases with wavelength, following a linear relation in this log-log plot between 1.2 and 2.8  $\mu\text{m}$ . At longer wavelengths, the extinction curve changes shape: it contains more bumpy features, and is higher than expected from linear extrapolation. For the purpose of investigating the extinction, it is useful to separate the two regimes. Therefore, we define the near-infrared (NIR) as the wavelength regime from 1.2 to 2.8  $\mu\text{m}$  and the mid-infrared (MIR) as the wavelength regime from 2.8 to 26  $\mu\text{m}$ . The linear relation within the NIR in the log-log plot implies a power law:

$$A_b = A_a \times (\lambda_a/\lambda_b)^\alpha \quad (4.8)$$

For the five NIR lines we obtain  $\alpha = -2.11 \pm 0.06$  and  $A_{\text{Br}\gamma} = 2.62 \pm 0.11$ , see Table 4.3. The  $\chi^2$  of the fit is 2.70 given 3 degrees of freedom. Hence, a power law is a good description of the NIR extinction. Since the extinction is obviously grayer beyond 3.7  $\mu\text{m}$ , we test if there is any indication for flattening within the NIR by fitting the red and blue part of the 5 NIR lines separately, see Table 4.3. The slope of the red part, with  $\alpha = -1.76 \pm 0.39$ , is only 0.9  $\sigma$  flatter than the blue part. Because this change in slope is not significant, we use the power law obtained from all 5 NIR lines for deriving the broadband extinction values (Appendix 4.7.3). The extinction between 3.7 and 8  $\mu\text{m}$  is fitted by the following power

Table 4.3. NIR infrared power law extinction fit parameters

Used range [ $\mu\text{m}$ ]	$A_{B-r\gamma}$	slope $\alpha$	$\chi^2/\text{d.o.f}$
1.282 to 2.166	$2.60 \pm 0.11$	$-2.13 \pm 0.08$	2.05/1
2.166 to 2.758	$2.50 \pm 0.11$	$-1.76 \pm 0.39$	0.54/1
1.282 to 2.758	$2.62 \pm 0.11$	$-2.11 \pm 0.06$	2.70/3

law:

$$A(\lambda) = (1.01 \pm 0.08) \times (\lambda/4.9\mu\text{m})^{-0.47 \pm 0.29}$$

Thus, the MIR extinction is grayer than the NIR extinction.

## 4.5 Discussion

### 4.5.1 Comparison with Literature for the GC

We now compare and discuss the extinction curve obtained in this work with the literature.

First of all, we compare with Rieke & Lebofsky (1985), who used mainly data from GC stars to derive the infrared extinction law up to 13  $\mu\text{m}$ . Their finding, however, a single power law of slope  $\approx -1.54$  from J- to M-band, is in contrast with our results. The differences probably lie (i) in their assumption of an universal IR extinction law, whereby  $R_V$  is determined only indirectly, and (ii) variability of the stars used. Firstly, for absolute calibration of the extinction law they used *o* Sco, which is also detectable in the optical, together with the relation  $E_{V-K}/E_{B-V} = 2.744$  from Schultz & Wiemer (1975) and Sneden et al. (1978). However, this relation was obtained outside of the GC, making their extinction law vulnerable to line of sight variations, see Section 4.5.5. Secondly, they employ the  $E_{V-M}/E_{B-V}$  of the GC and the bolometric luminosity of IRS7 to estimate  $R_V = A_V/E_{B-V} = 3.09$ . In the process they use measurements of three stars in the M-band, which is dominated by atmospheric emission, to estimate their lower limit on  $R_V$ . Not only are all of the GC stars used by Rieke & Lebofsky (1985) supergiants, which are in general variable, but variability has, in particular, been reported for IRS7 (Blum et al. 1996). Their indirectly determined  $R_V$  could introduce a systematic error in their extinction measurement. For example, if we reduce  $R_V$  to 2.98 in their calculation, we obtain from their data  $\alpha = -2.04$  between J and K. This is compatible with our  $\alpha$ .

In a later work, Rieke (1999) updated Rieke & Lebofsky (1985) using NICMOS data (F110M, F145M, F160W, F222M), again of stars in the GC region. They used spectra of the IRS16 stars (Tamblyn et al. 1996) for deriving absolute extinctions. The extinction curve they found is flatter in 'HK' ( $\alpha = -1.58$ ) than in 'JH' ( $\alpha = -1.95$ ), in contrast to our extinction law (Section 4.4.3) and to most other publications which derive a constant slope in the NIR (e.g, Draine 1989). In order to test whether the NICMOS data generally contradict our NIR extinction law (Section 4.4.3) we use stars which have NICMOS magnitudes

published in Maillard et al. (2004). We use only stars which have been spectroscopically identified as early-type (Paumard et al. 2006; Bartko et al. 2009). Early-type stars have colors  $\approx 0$  in the NIR. We exclude IRS13E2 and IRS13E4.0 from the analysis because they are dusty (Fritz et al. 2010). Using the rescaled versions of the extinction map and the Ks-band magnitudes of Schödel et al. (2010), the NICMOS data are consistent with a single power law with a slope of  $\alpha = -2.16 \pm 0.08$ . Thus, the NICMOS data do not contradict our result of  $\alpha = -2.11 \pm 0.06$  (Section 4.4.3).

In another study, Viehmann et al. (2005) performed seeing-limited ISAAC L- and M-band photometry. Assuming stellar colors they derived a flat extinction slope from L to M:  $A_M/A_L = 0.966 \pm 0.05$ . From our NACO broadband extinction values (Appendix 4.7.3) we obtain a consistent value:  $A_M/A_L = 0.88 \pm 0.23$ . However, these results are not directly comparable, because Viehmann et al. (2005) used a narrow M-band with a FWHM =  $0.10 \mu\text{m}$  at  $4.66 \mu\text{m}$ . At this wavelength, a CO absorption feature is visible in the ISO spectra (Lutz et al. 1996; Moneti et al. 2001), see Figure 4.8.

Scoville et al. (2003) obtained an absolute extinction map of the GC for Paschen- $\alpha$ . To do this, they used NICMOS narrowband imaging at Paschen- $\alpha$  ( $1.87 \mu\text{m}$ ) and at  $1.90 \mu\text{m}$  to construct the line map. They took a VLA continuum map at 6 cm to use as extinction-free data. Using their extinction map, we compute an average extinction of  $A_{\text{Pa}\alpha} = 3.54$  integrated over the ISO beam. This value is consistent with our value of  $A_{\text{Pa}\alpha} = 3.56 \pm 0.11$ , obtained from the best-fit power law.

Schödel et al. (2010) measured the extinction toward the GC using NACO data in H-, Ks- and L'-band. By comparing the magnitude of the peak of the luminosity function (the red clump) with its expected magnitude, they obtained the total light modulus of the GC. They then used a distance to the GC of  $8.03 \pm 0.15$  kpc, derived from different works, to obtain the extinction:  $A_H = 4.48 \pm 0.13$ ,  $A_{\text{Ks}} = 2.54 \pm 0.12$  and  $A_{L'} = 1.27 \pm 0.18$ .

Schödel et al. (2010) also derived the selective extinction  $E_{\text{H-Ks}} = (A_H - A_{\text{Ks}})/A_{\text{Ks}}$  from the red clump extinction values. They then used  $E_{\text{H-Ks}}$  for obtaining a Ks-band extinction map from the observed stellar colors. Surprisingly, the average of the map is, with  $A_{\text{Ks}} = 2.70$ , larger than the extinction obtained from the red clump. It can be seen from Table A.2 in Schödel et al. (2010) that most individual stars have larger values of H-Ks than the stellar population of the red clump in the luminosity function, the reason for which is not clear.

We do not know which of the two Schödel et al. (2010) extinction values should be preferred. Because of this, we use the average and enlarge the error by adding  $\sqrt{1/2} \times (A_{\text{Ks}1} - A_{\text{Ks}2}) = 0.11$  mag. We obtain  $A_{\text{Ks}} = 2.62 \pm 0.16$  for the full field of Schödel et al. (2010). Their extinction map has an average of  $A_{\text{Ks}} = 2.70$  over the full map. However, the average is  $A_{\text{Ks}} = 2.68$  over the ISO field of view. Therefore, we correct the average by multiplying with  $2.68/2.70$  and obtain  $A_{\text{Ks}} = 2.60 \pm 0.16$  as a final value for comparison with our extinction.

The issue of two possible extinction values in the Ks-band also extends to the other bands. We assume a linear scaling of the extinction values based on stellar colors with the extinction values derived from the red clump in each band. We again use the average of red clump extinction and the selective extinction. We obtain  $A_H = 4.58 \pm 0.24$  and

Table 4.4. Error sources for the extinction

Error source	$\Delta\text{mag}$ for Brackett- $\gamma$	$\Delta\text{mag}$ for other lines
• IR calibration error and line SNR	0.073	0.073 to 0.50
• electron Temperature	0.043	0.043
• selection of good pixels in Brackett- $\gamma$	0.03	0.03
• scatter comparing with Schödel et al. (2010)	0.07	0.07
• selection of good pixels in other lines	0	0 to 0.088
total	0.114	0.114 to 0.507

$A_{L'} = 1.30 \pm 0.19$  as final values for comparison with our extinction values.

If we now compare with our broadband extinction values (see Appendix 4.7.3), we obtain the following differences between our results and Schödel et al. (2010):  $A_{H\text{ lines}} - A_{H\text{ Sch}} = 0.07 \pm 0.25$ ,  $A_{Ks\text{ lines}} - A_{Ks\text{ Sch}} = 0.07 \pm 0.17$  and  $A_{L'\text{ lines}} - A_{L'\text{ Sch}} = -0.10 \pm 0.23$ . For the calculation of the errors here, we exclude the zero-point errors in the H and Ks-band because both results use the same calibration data, and we also exclude the error due to  $R_0$  because we use the differences to measure  $R_0$ , see Section 4.5.2. To summarize, our values are all consistent with the values of Schödel et al. (2010).

In Table 4.4 we present the various sources of error for our extinction values. Our data are well fitted with a power law in the NIR ( $\chi^2/d.o.f = 0.71$ ), see Section 4.4.3 as expected from the established literature (Cardelli et al. 1989). An error in the radio data (such as an error on  $T_e$ ) affects all values in the same way, such that its influence on the  $\chi^2$  of the power law fit is much smaller than the influence of independent errors in the NIR data. Because the power law does not continue to the MIR till to negligible extinction in our data, it is not possible to obtain the absolute extinction independent of the radio data, as was done in Landini et al. (1984). However, the value for  $T_e$  which we use is consistent with both Roberts & Goss (1993) and Shukla et al. (2004). Therefore, it is unlikely that there is a relevant systematic error in the extinction due to the radio data.

## 4.5.2 A Photometric Distance to the GC

The distance to the Galactic Center  $R_0$  is used to derive distances to all but the closest regions of the Galaxy and is one of the fundamental parameters for building Milky Way models. Knowing  $R_0$  is hence of general relevance. Prior to this publication there was no reliable measurement for the GC extinction that was independent of  $R_0$ . Works that did derive  $R_0$  photometrically (Nishiyama et al. 2006; Groenewegen et al. 2008; Dambis 2009; Matsunaga et al. 2009) used stars in the bulge, not directly in the GC. On the other hand, stars directly in the GC have been used to derive  $R_0$  from the dynamics of their stellar orbits around the SMBH (Eisenhauer et al. 2003; Ghez et al. 2008; Gillessen et al.

2009), and by using the statistical parallax of the population of late-type stars in the GC (Genzel et al. 2000; Trippe et al. 2008).

With our extinction measurement we can obtain a photometric  $R_0$  from stars in the GC. We combine our extinction measurement with the extinction measurement of Schödel et al. (2010). These authors obtained the total luminosity modulus of the red clump stars in the GC. Because the luminosity modulus involves both the extinction and the distance modulus it was necessary for Schödel et al. (2010) to assume a distance for calculating extinction values, for which they used  $R_0 = 8.03 \pm 0.15$  kpc. Here, we can use the extinction differences between the two works, see Section 4.5.1 in order to estimate  $R_0$ . For the Ks-band, we obtain  $R_0 = 7.78 \pm 0.63$  kpc. From the H-band we obtain  $R_0 = 7.78 \pm 0.95$  kpc, and from the L'-band we obtain  $R_0 = 8.41 \pm 0.94$  kpc. The errors follow from the errors of the extinction differences between our extinction values and those of Schödel et al. (2010), see Section 4.5.1. We use the weighted average of all values as our final value:  $R_0 = 7.94 \pm 0.65$  kpc. For the error we use the smallest single error, the relative error of Ks-band, because the errors are correlated between the filters.

Nishiyama et al. (2006) used red clump stars in the inner bulge to derive a photometric distance and obtained  $R_0 = 7.52 \pm 0.36$  kpc. Our value is about  $0.6 \sigma$  larger. Since in both works the same absolute red clump magnitude is used, the consistency indicates only that other uncertainties (like the extinction) are not larger than assumed. However, it is still possible that the absolute magnitude has a bigger error than assumed. Our result is also consistent with the review of Reid (1993), who determined  $R_0 = 8.0 \pm 0.5$  kpc, and the recent review of Genzel et al. (2010), who determined  $R_0 = 8.15 \pm 0.14 \pm 0.35$  kpc from direct and indirect measurements, and  $R_0 = 8.23 \pm 0.2 \pm 0.19$  kpc from only direct measurements.

Conversely, assuming that the direct estimate of  $R_0$  by Genzel et al. (2010) is correct we can test the red clump magnitude: The red clump in the GC has then a magnitude of  $M_{Ks} = -1.59 \pm 0.13$ . The value used by us and Schödel et al. (2010) is  $M_{Ks} = -1.47$ , and the two values are consistent, although the GC star formation history (Blum et al. 2003; Pfuhl et al. 2011) and metallicity (Cunha et al. 2007) was not modeled to obtain  $M_{Ks}$ . Therefore, as expected according to Salaris & Girardi (2002),  $M_{Ks}$  of the red clump is therefore relatively independent of the star formation history and metallicity and thus is a reliable distance indicator.

### 4.5.3 Extinction toward Sgr A\*

Our data do not have enough SNR to obtain a good extinction map. However, because our absolute values for the extinction are more accurate than the extinction of Schödel et al. (2010), combining our absolute value and the extinction map of Schödel et al. (2010) is useful. For this, we adjust the extinction map of Schödel et al. (2010) such that in it the extinction is the same as our interpolated  $A_{Br\gamma}$  of the same area. This means that we multiply the map of Schödel et al. (2010) by 0.976.

From the adjusted map we use  $A_{Br\gamma}$  toward Sgr A\* to derive broadband extinctions (Appendix 4.7.3) of:  $A_H = 4.21 \pm 0.10$ ,  $A_{Ks} = 2.42 \pm 0.10$  and  $A_{L'} = 1.09 \pm 0.13$ . Effectively,

this is the extinction to the stars with  $r \leq 0.5''$  around Sgr A\* due to the procedure used by Schödel et al. (2010). However, it is adjusted for the SED difference between stars and Sgr A\* (Appendix 4.7.3).

#### 4.5.4 Spatial Distribution of the Extinction

The light that reaches Earth from the GC crosses many regions of the Galaxy. It is possible that dust associated with the minispiral extinguishes the light in the GC itself. However, because the extinction derived from the minispiral is consistent with the extinction derived from stars of Schödel et al. (2010), the extinction must occur mainly in front of the GC. For testing this further, we smooth the Brackett- $\gamma$  flux to the resolution of the extinction map of Schödel et al. (2010). This we compare with the extinction map of Schödel et al. (2010) in bins defined by the smoothed minispiral flux. We do not find a correlation between the minispiral flux and the extinction derived from stars. Furthermore, the scatter of the median extinction is only 0.04 mag over the different flux means. In addition, the small far-infrared flux (Becklin et al. 1982; Guesten et al. 1987) of the central few parsecs shows that hardly any UV radiation is absorbed there (Brown & Liszt 1984). All in all, the NIR extinction must be very small (at least  $A_{K_s} < 0.1$ ) inside the central parsec.

In order to further constrain the location of the extinction in the line of sight, we use the  $H - K_s$  values of the stars in Table A.2 of Schödel et al. (2010). Since the intrinsic color  $|H - K_s| < 0.2$  for nearly all stars, the  $H - K_s$  of each star depends nearly only on the extinction. We then measure how many stars in the table have a  $H - K_s$  compatible with zero extinction. Thereby, we exclude stars which are so blue and faint in  $K_s$  that they would be too faint for detection if they would have the extinction of the GC. We exclude them in order to avoid a bias toward foreground stars. After this, we obtain that only five of 6324 stars have a  $H - K_s$  color compatible with zero extinction. According to Philipp et al. (1999), the Galactic Disk and bulge (outside of 300 pc) have 2.3 % of the flux of the GC at  $r = 10''^3$ . Because the ratio of extinction free stars to all stars of 0.1% is much smaller than the flux contribution of Galactic bulge and Disk to the flux in the center of 2.3 %, there must be extinction within the Galactic Disk. We then measure up to which extinction it is necessary to include stars in order to account for the 2.3 % star contribution of Galactic Disk and bulge. We find that it is necessary to include stars with extinction up  $A_{K_s} = 2.0$ . This is about 3/4 of the total extinction toward the GC.

Therefore, the measured extinction is mainly not associated with the Giant Molecular Clouds in the nuclear bulge (Mezger et al. 1996) and as such is not related to special processes in the central 50 pc. Because most bulges do not contain a lot of dust, it is likely that most of the extinction is caused by dust in the Galactic Disk. As a result, the measured extinction curve is likely a typical extinction curve of dust in the Galactic Disk.

The extinction toward the GC is higher than the average extinction of the bulge behind the Galactic plane (Marshall et al. 2006). However there are also regions with much higher

---

<sup>3</sup>We exclude the central  $10''$  because there the total flux is dominated by young stars. Since there are only a few young stars due to the top heavy IMF (Bartko et al. 2010) they are irrelevant for the star number ratio.

Table 4.5. NIR infrared extinction law from literature

Publication	$E_{J-H}/E_{H-K}$	slope $\alpha$
Indebetouw et al. (2005)		$-1.65 \pm 0.12$
Messineo et al. (2005)		$-1.9 \pm 0.1$
Nishiyama et al. (2006)		$-1.99 \pm 0.08$
Straizys & Laugalys (2008)	$2 \pm 0.13$	$-2.07 \pm 0.23$
Gosling et al. (2009)		$-2.64 \pm 0.52$
Nishiyama et al. (2009)	$2.09 \pm 0.13$	$-2.23 \pm 0.23$
Stead & Hoare (2009)		$-2.14 \pm 0.045$
Zasowski et al. (2009)	$2.11 \pm 0.1$	$-2.26 \pm 0.17$
Schödel et al. (2010)		$-2.21 \pm 0.24$
Our work		$-2.11 \pm 0.06$
weighted average		$-2.07 \pm 0.16$

Note. — NIR extinction slope measurements of diffuse ISM extinction since 2005. When  $\alpha$  is not given in the publication, or the effective wavelength are unusual we calculate  $\alpha$  from  $E_{J-H}/E_{H-K}$ . Thereby we use for  $\lambda'_{\text{eff}}$  the wavelength 1.24, 1.664 and 2.164  $\mu\text{m}$  (Nishiyama et al. 2009). The error is either the measurement error in the publication or the scatter of different sight lines. From Nishiyama et al. (2009) we only use the 2MASS data, since the SIR-IUS data are identical to Nishiyama et al. (2006). We use all values for the calculation of the weighted average.

extinction close to the GC (Ramírez et al. 2008). Therefore, the extinction of the Galactic Center is not exceptional for an 8 kpc view through the Galactic Disk.

#### 4.5.5 The NIR Extinction

Our NIR data can be well fitted with a power law of  $\alpha = -2.11 \pm 0.06$  ( $\chi^2/d.o.f. = 2.70/3$ ). This strengthens the case for the use of a power law as model for the extinction in the NIR (e.g., Cardelli et al. 1989). Our slope is steeper than the slope of  $\alpha \approx -1.75$  of most reviews, see e.g. Savage & Mathis (1979); Mathis (1990) and Draine (2003). However, most of the measurements (e.g., Schultz & Wiemer 1975; Landini et al. 1984; Whittet 1988; He et al. 1995) combined in these reviews used relatively few stars; these stars are detectable in the optical and partly also in the UV, have  $A_V \leq 5$  and are mostly closer than 3 kpc, see e.g. He et al. (1995). The extinction measurement of Rieke & Lebofsky (1985) toward the GC was also tied partly to measurements of stars which are visible also in the optical.

Since about 2005, large infrared surveys have become available and are now used by most publications about extinction. Since now no detection in the optical is necessary, and because it is easier to characterize high extinction, many publications (see Table 4.5) measured the extinction toward the highly extinguished inner Galactic Disk and bulge, at about 8 kpc distance. Most of these publications measure  $\alpha \approx -2.1$ .

It is possible that the change in the measured  $\alpha$  around 2005 is due to systematic errors. Stead & Hoare (2009), for example, suggested that the use of the isophotal wavelength instead of the effective wavelength caused the flatter slope in the measurement prior to

2005. We think, however, that it is unlikely that errors in the effective wavelengths are the reason for the discrepancy: while it is correct that using the isophotal filter wavelengths can lead to errors in  $\alpha$ , using the effective wavelength as presented in Stead & Hoare (2009) overestimates  $\alpha$  slightly, see Appendix 4.7.4. Furthermore, even if the isophotal wavelength is used, the systematic error on  $\alpha$  is at maximum 0.07 for the hot stars (see Appendix 4.7.4 for a 9480 K star) used in most works before 2005. Additionally, Fitzpatrick (2004) used 2MASS data of solar neighborhood stars and, using the effective wavelength, obtained  $\alpha \approx -1.84$ .

Since the dust probed by studies which obtain  $\alpha \approx -1.75$  and  $\alpha \approx -2.1$ , respectively, is not identical it seems likely that the extinction law varies between these regions. A strong piece of evidence for truly variable extinction is the correlation of  $R_V$  with  $\alpha$  in Fitzpatrick & Massa (2009), whereas for the standard  $R_V = 3.1$   $\alpha = -1.77 \pm 0.05$ . This work used 14 stars with observations from 120 nm to Ks-band. All in all, we think it is likely that there is a transition of a mostly flatter NIR extinction in the solar neighborhood to a steeper one in most parts of the Galactic Disk. Naturally, further tests of the NIR extinction slope variation via measurement of the NIR extinction slope in the local low extinction sight lines, and in the Galactic Disk, using the best methods available today would be very valuable.

For most molecular clouds, the extinction is, with  $\alpha \approx -1.8$  (Román-Zúñiga et al. 2007; Naoi et al. 2006; Kenyon et al. 1998; Flaherty et al. 2007; Lombardi et al. 2006), flatter than for the Galactic Disk sight lines. However, there are also clouds with deviating  $\alpha$ , with an  $\alpha$  range from -1 to -2.4 (Froebrich & del Burgo 2006; Whittet 1988; Racca et al. 2002; Naoi et al. 2007).

There are some features typical of molecular clouds that are visible in the ISO-SWS spectrum. Whittet et al. (1997) determined that about a third of the extinction toward the GC is caused by molecular clouds with substructure and the rest by diffuse extinction. A relatively small contribution of the extinction by molecular clouds is also supported by the fact, that the extinction variation toward the central parsec is less than one third of the maximum extinction, as can be seen in the extinction map of Schödel et al. (2010). This means also that the molecular cloud contribution is not visible in terms of star counts as it is in the case of e.g. the coalsack. Accordingly, the line of sight toward the GC is not dominated by molecular cloud extinction. Thus, we exclude molecular cloud extinction in our quantitative comparison with the GC.

For comparison we use publications about the extinction toward the Galactic Disk and bulge. In practice this means only publications since 2005, see Table 4.5. We use these data for calculating the weighted average:  $\alpha = -2.07 \pm 0.16$ . Of these 9 publications used, only Indebetouw et al. (2005) is inconsistent with the others. Hence, the extinction law is likely constant toward the inner Galactic Disk and bulge and can probably be used also for other fields in that region.

Due to the high absolute extinction in the inner Galactic Disk, this region contributes more to the global extinction of the Galaxy than the solar neighborhood, or the halo of the Galaxy (Schlafly et al. 2010). Therefore, the steeper extinction law in the NIR of the inner Galactic Disk is probably more important when integrated over the volume of the Milky

Way. Similarly, for other galaxies for which our Galaxy is typical, a steeper extinction law could also be more important.

### 4.5.6 The Optical Extinction

Rieke et al. (1989) estimated an optical extinction of  $A_V = 31$  toward the GC using the extinction law of Rieke & Lebofsky (1985). The GC is, due to this high extinction, undetectable in the optical. As a result, any estimate of  $A_V$  for the GC is indirect. Since both this paper and Schödel et al. (2010) obtain a different infrared extinction law to Rieke & Lebofsky (1985), it seems possible that the optical extinction toward the GC is also different from the one assumed in Rieke & Lebofsky (1985).

In order to test this, we use data which has a more direct connection to the GC than *o* Sco which was used by Rieke & Lebofsky (1985). The shortest wavelength at which the GC has been observed is the z-band (Henry et al. 1984; Rosa et al. 1992; Liu et al. 1993). In order to estimate the z-band extinction, we use the magnitudes of the IRS16 stars from these works, because these stars and their intrinsic colors are well known. We neglect the data for IRS16C in Liu et al. (1993) because the star is brighter in this work compared to all other works. We use the extinction map and the IRS16 magnitudes of Schödel et al. (2010) in order to calculate the dereddened Ks-band magnitudes of the IRS16 stars. We then subtract the dereddened Ks-band magnitudes and an intrinsic color of  $z - Ks = -0.25$  from the measured z-band magnitudes of IRS16 to obtain z-band extinctions.

We convert the z-band extinctions into an extinction power law between Paschen- $\beta$  and the true effective wavelength for extinction measurements ( $\lambda_{\text{true}}$ ) of the GC (see Appendix 4.7.4). In the case of Henry et al. (1984) and Liu et al. (1993) the wavelengths given in the publications are probably  $\lambda_{\text{true}}$ . We assign to them an error of  $0.01 \mu\text{m}$ . Rosa et al. (1992) give the central wavelength for stars extinguished by GC extinction and unextinguished stars. Since both are incorrect, see Appendix 4.7.4, we calculate from the given central wavelength and FWHM of the optical system  $\lambda_{\text{true}} = 0.97 \mu\text{m}$ . Due to the additional uncertainties in calculating the effective wavelength we assume an error of  $0.015 \mu\text{m}$ . The effective wavelength uncertainty and the scatter of the IRS16 stars are used for the calculation of the errors.

In this way we obtain  $\alpha = 1.99 \pm 0.09$ ,  $\alpha = 1.91 \pm 0.14$  and  $\alpha = 2.165 \pm 0.13$  from Henry et al. (1984), Rosa et al. (1992), and Liu et al. (1993). The average slope is, with  $\alpha = -2.02 \pm 0.07$ , consistent with our determined NIR-slope of  $\alpha = 2.11 \pm 0.06$  (Section 4.4.3). Using the average of the three Paschen- $\beta$  z slopes we obtain  $A_{1\mu\text{m}} = 13.11 \pm 0.30$ . This extinction is slightly higher than interpolating Rieke et al. (1989) although our K-band extinction is smaller, see Figure 4.8.

We now consider how the z-band extinction should be extrapolated into the optical. Molecular cloud features are probably responsible for a third of the extinction toward the GC, see Section 4.5.4. An above average contribution of molecular cloud extinction to the GC is also supported by the fact, that the extinction toward the GC is higher than the average bulge extinction (Section 4.5.4). If we assume a high  $R_V = 5.5$  for the molecular cloud extinction and 3.1 for the other two thirds, the average  $R_V \approx 3.9$  for the GC.

Use a Cardelli et al. (1989) curve with this  $R_V$  (but with  $\alpha = -1.85$  between  $0.91 \mu\text{m}$  and  $1 \mu\text{m}$  for reducing the jumps in the slope) to extrapolate to the optical, we obtain  $A_{\lambda=0.55\mu\text{m}} = 30.3$ .

However, most molecular clouds do not have an  $R_V$  of 5.5. Thus, even assuming that one third is caused by molecular cloud extinction and two thirds by normal extinction, the real  $R_V$  is probably closer to 3.1. In addition, the high strength of aliphate ( $3.4 \mu\text{m}$ ) and silicate ( $9.7 \mu\text{m}$ ) features are different from the extinction in molecular clouds (Section 4.5.7). These features are even stronger than in most diffuse extinction sight lines. Furthermore the steep NIR extinction slope of  $\alpha = -2.11$  is not typical of molecular cloud extinction (Section 4.5.5). Therefore, we obtain another estimate, extrapolating to the visible also with the normal  $R_V = 3.1$  (using  $\alpha = -1.95$  between  $0.91 \mu\text{m}$  and  $1 \mu\text{m}$ ). In this case we obtain  $A_{\lambda=0.55\mu\text{m}} = 33$ .

A much steeper extinction law than the standard  $R_V = 3.1$  from B-band to J-band is measured (Udalski 2003; Sumi 2004; Revnivtsev et al. 2010; Nishiyama et al. 2008) toward parts of the bulge which have a much smaller extinction than the GC ( $A_V < 7$  in case of Nishiyama et al. (2008)). In particular, Nishiyama et al. (2008) measured  $A_V/A_J = 5.32 \pm 0.14$ , while according to Rieke & Lebofsky (1985)  $A_V/A_J = 3.55 \pm 0.16$  for the standard  $R_V = 3.1$ . We fit these bulge data points with a Cardelli et al. (1989) curve with  $R_V = 2.0$  (using  $\alpha = -2.02$  between  $0.91 \mu\text{m}$  and  $1 \mu\text{m}$ ). Extrapolating the z-band extinction of the GC with this curve we obtain  $A_{\lambda=0.55\mu\text{m}} = 44$ . The aliphate and silicate features toward the GC are stronger than in diffuse extinction, while they are even weaker in molecular cloud extinction, see Section 4.5.7. This means, that the strength of these features is anticorrelated with  $R_V$  for  $3.1 \leq R_V \leq 5.5$ . Extrapolating this anticorrelation to the stronger feature toward the GC implies, that  $R_V < 3.1$  toward the GC, which in turn implies an  $A_V > 33$ .

Figure 4 in Fitzpatrick & Massa (2009) shows a correlation between the infrared power law slope  $\alpha$  and  $R_V$ . The correlation implies that the slope in the infrared approximately continues into the red. Using a second order polynomial to fit their 13 measurements (neglecting one outlier) we obtain  $R_V = 2.48 \pm 0.06$  for the GC, using our measurement of  $\alpha = -2.11 \pm 0.06$  in the GC. Thus, because a small  $R_V$  implies a high  $A_V$ , this again implies the optical extinction toward the GC is probably large.

X-rays can shed another light on  $A_V$ . X-ray photons, for example, are attenuated by scattering and absorption which are related to the extinction (Morrison & McCammon 1983; Predehl & Schmitt 1995). At the energy at which the GC is observed ( $\approx 3$  to  $8$  keV), absorption by astronomical metals is much stronger than scattering by dust grains (Predehl & Schmitt 1995; Porquet et al. 2008). For the absorption the chemical state of the absorbing material is irrelevant and depends only on the integrated column density of astronomical metals. Thus the X-ray absorption can be used to constrain dust models and the extinction.

Here we investigate the implications only for the extinction. Observationally, the X-ray absorption is well correlated with  $A_V$  (Predehl & Schmitt 1995) in most Galactic sight lines. However, there are AGNs with different X-ray absorption to  $A_V$  ratios (Maiolino et al. 2001; Li 2007). Toward Sgr A\* we obtain a column density of  $N_H = 10.5 \pm 1.4 10^{22} \text{cm}^{-2}$ ,

averaging over the different states (Porquet et al. 2008). Thereby we assume an intrinsic X-ray power law for the flares of Sgr A\* (Dodds-Eden et al. 2009). We thus obtain an X-ray derived  $A_V = 56.7 \pm 7.4$  for the GC (Figure 4.8) using the  $N_H/A_V$  relation of Predehl & Schmitt (1995). Using UV derived  $N_H/A_V$  relations (Bohlin et al. 1978; Draine 1989; Zubko et al. 2004) we obtain  $A_V$  from 53 to 59. Our best fitting dust model (Section 4.5.9) gives  $A_V \approx 48$  for the measured  $N_H$ .

There is the possibility, that part of the column density toward Sgr A\* arises in ionized gas in the halo of the SNR Sgr A East (Maeda et al. 2002; Porquet et al. 2008), in which case not all of the  $N_H$  (measured by X-rays) toward Sgr A\* is caused by dust. For example, Sakano et al. (2004) measured an  $N_H = 15 \cdot 10^{22} \text{cm}^{-2}$  for hot plasma, and  $N_H = 7 \cdot 10^{22} \text{cm}^{-2}$  for somewhat colder plasma of Sgr A East. The second value is perhaps typical of plasma lying in the line of sight to Sgr A\*. Accordingly, it is possible that the column toward the colder plasma corresponds to the column to Sgr A\*. If this is the case we obtain a lower  $A_V = 37.8$ , using the relation of Predehl & Schmitt (1995). However, probably the foreground extinction toward Sgr A East and Sgr A\* is not fully homogeneous. In principle it is possible to obtain a better  $N_H$  toward the Sgr A region by measuring  $N_H$  toward point sources outside of Sgr A East. By comparing such a map with an IR excess map, it should be possible to obtain a better estimate for  $N_H$  for the GC.

Overall, the evidence for an  $R_V < 3.1$  is slightly larger than for  $R_V > 3.1$ , which means that,  $A_{\lambda=0.55\mu\text{m}} > 33$ . However, it is clear that only a direct measurement in the visible can clarify the value of  $R_V$ . The GC extinction attenuates 16NW, the brightest blue star in the GC with unextincted  $m_V \approx 5.5$ , to a magnitude of  $m_V = 34$  to 43 depending on  $R_V$  (since this simulated measurement integrates over the V-band the extinctions are smaller than the corresponding  $0.55 \mu\text{m}$  extinctions).

### 4.5.7 The MIR Extinction

At wavelengths  $> 2.8 \mu\text{m}$  extinction features are visible in the ISO-SWS spectrum, even shortward of the deep silicate feature at  $9.7 \mu\text{m}$  (Figure 4.4). These features are known from Butchart et al. (1986), Willner et al. (1979), Lutz et al. (1996), and Chiar et al. (2000).

Most of these features are caused by ices like the  $\text{H}_2\text{O}$  feature at  $3.1 \mu\text{m}$  (Butchart et al. 1986; Lutz et al. 1996; Chiar et al. 2000) and the  $\text{CO}_2$  feature at  $4.3 \mu\text{m}$  (Lutz et al. 1996; de Graauw et al. 1996). Among others, Whittet et al. (1988), Rosenthal et al. (2000), and Knez et al. (2005) detected these features in many other sight lines with different strengths, both compared to one other as well as to the continuum extinction. Rawlings et al. (2003) and Whittet et al. (1997) did not detect  $\text{H}_2\text{O}$  ice in sight lines consisting of diffuse interstellar material with  $A_V \approx 10$ . Thus, these features are likely only visible in sight lines through molecular clouds and not in purely diffuse extinction regions (Whittet et al. 1997; Chiar et al. 2000). This view is supported by the CO clouds in the Galactic arms in front of the GC (Sutton et al. 1990). This CO is also visible in the ISO-SWS spectrum (Lutz et al. 1996; Moneti et al. 2001). The detection of molecular cloud features toward the GC is not unique, ice features are also detected toward the Quintuplet cluster at a distance of about  $12'$  to the GC, where they are slightly weaker compared to the continuum extinction

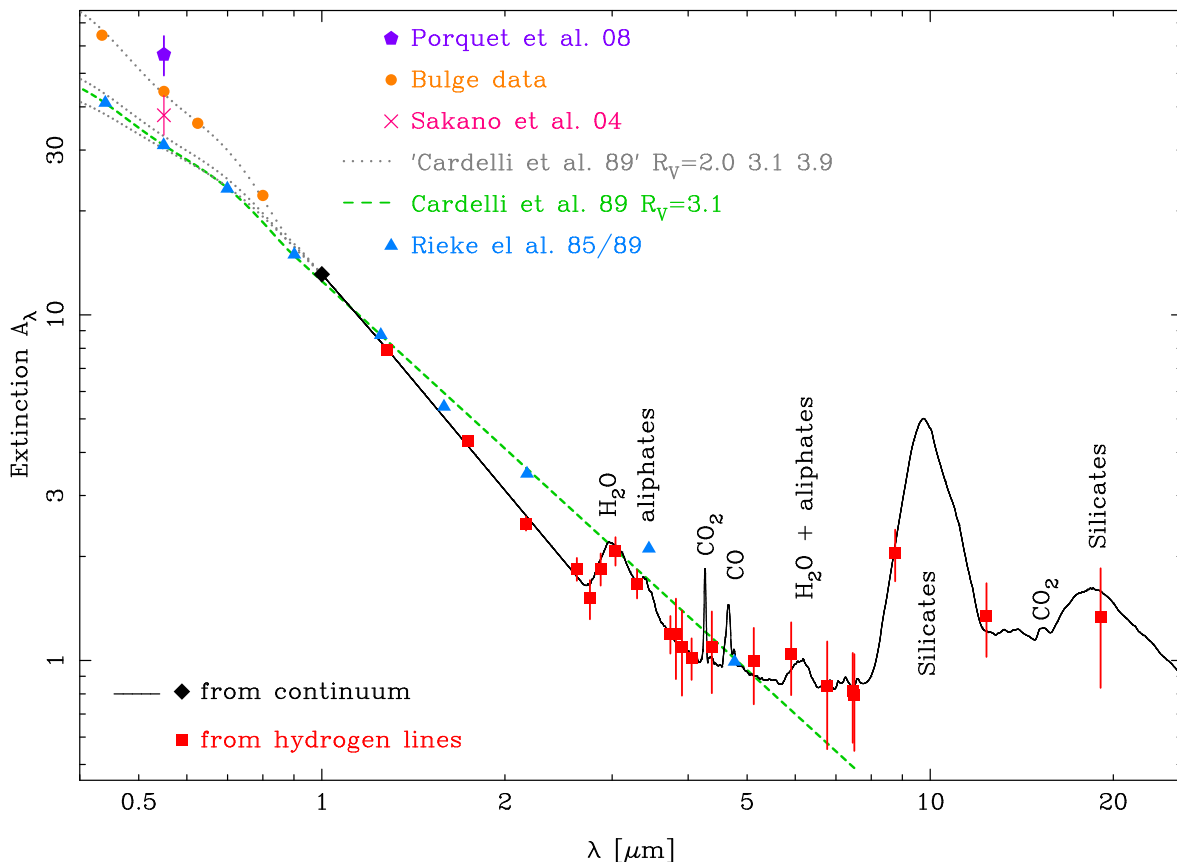


Figure 4.8 Extinction toward the central  $14'' \times 20''$  of the GC. We use hydrogen lines for obtaining the extinction between  $1.28$  and  $18 \mu\text{m}$  (red boxes) and stellar colors for  $1 \mu\text{m}$  (black diamond). We interpolate the data by use of the continuum emission (black line). The spectral resolution of the interpolation is not high enough to resolve all features like the CO feature at  $4.7 \mu\text{m}$  fully. We mark the larger extinction features (Lutz et al. 1996; Chiar et al. 2000). We use the central bulge data of Sumi (2004), Nishiyama et al. (2008), and Revnivtsev et al. (2010) for extending the extinction curve to the visible (orange dots). For comparison we add a value for  $A_V$  derived from the X-ray spectrum of Sgr A\* (Porquet et al. 2008) (violet pentagon). In the same way we use the gas in front of Sgr A East (Sakano et al. 2004) (pink cross). The extinction curve differs from Rieke & Lebofsky (1985), Rieke et al. (1989) (blue triangles), the results of which are only partly based on GC data. The GC data differs also from the Cardelli et al. (1989) curve (fitted to  $R_V = 3.1$  observations; green dashed line). The optical extinction toward the GC is uncertain. We use three curves of the type used by Cardelli et al. (1989) with  $R_V = 2.3, 3.1, 3.9$  (dotted grey lines from top down) for showing the possible range.

(Chiar et al. 2000).

Other extinction features, like the strong aliphatic hydrocarbon feature at  $3.4 \mu\text{m}$  (Willner et al. 1979), are caused by diffuse dust and are thus a general visible feature of extinction (Chiar et al. 2000; Rawlings et al. 2003). The feature at  $3.4 \mu\text{m}$  is about a factor of two stronger toward the GC than in the local diffuse extinction (Rawlings et al. 2003; Gao et al. 2010). The  $3.4 \mu\text{m}$  feature is typical for diffuse dust. In molecular clouds it is not detected (Pendleton & Allamandola 2002).

In order to better constrain the shape of the extinction curve, we use the continuum of the ISO-SWS spectrum, see Appendix 4.7.2 and Figure 4.8.

For the silicate feature at  $9.7 \mu\text{m}$  we obtain an optical depth of  $\Delta\tau_{\text{Si}9.7} = 3.84 \pm 0.52$  relative to the continuum at  $7 \mu\text{m}$  from our interpolated extinction curve. The depth is similar to that obtained by Chiar et al. (2000) of  $\Delta\tau_{\text{Si}9.7} = 3.46$  and by Roche & Aitken (1985) of  $\tau_{\text{Si}9.7} = 3.6$ . According to van Breemen et al. (2011) the shape of  $9.7 \mu\text{m}$  silicate feature of the GC is identical to sight lines with diffuse extinction and slightly different to sight lines with molecular clouds. Using our broadband extinction values (Appendix 4.7.3) we obtain  $\Delta\tau_{\text{Si}9.7}/E(J-K) = 0.70 \pm 0.10$ , consistent with (Roche & Aitken 1985). This is more than the value of  $\Delta\tau_{\text{Si}9.7}/E(J-K) = 0.34$  in nearly all other diffuse sight lines (Roche & Aitken 1984; van Breemen et al. 2011). Sight lines with molecular clouds also have  $\tau_{\text{Si}9.7}/E(J-K) = 0.34$  or even smaller values (van Breemen et al. 2011). The large  $\Delta\tau_{\text{Si}9.7}/E(J-K)$  toward the GC is probably caused by an abnormally high  $\Delta\tau_{\text{Si}9.7}$ . A larger silicate dust to carbon dust ratio in the inner Galaxy compared to the local diffuse medium (Roche & Aitken 1985; van Breemen et al. 2011) could explain the high  $\Delta\tau_{\text{Si}9.7}/E(J-K)$  toward the GC. With a higher silicate abundance  $\Delta\tau_{3.4\mu\text{m}}/E(J-K)$  toward the GC should be identical to the local value. However, it is twice the local value. Porous dust grains cause both a strong  $3.4 \mu\text{m}$  and a strong  $9.7 \mu\text{m}$  feature (Gao et al. 2010). Porosity is also one element of the dust model of Zubko et al. (2004), which best fits our continuum extinction data, see Section 4.5.9.

In the continuum,  $\text{CO}_2$  is visible at  $15 \mu\text{m}$  (Gerakines et al. 1999). It is, however, much weaker than in the observations of extinction in molecular clouds observed by Knez et al. (2005). In contrast, the silicate feature at  $18 \mu\text{m}$  toward the GC is much stronger than the  $\text{CO}_2$  feature, see Figure 4.8.

Rieke & Lebofsky (1985) and Rosenthal et al. (2000) can fit all their extinction values up to  $7.5 \mu\text{m}$  with a single power law. This single power law extinction is inconsistent with the flattening of the extinction curve in our data at around  $4 \mu\text{m}$ , see Section 4.4.3. In the continuum, there are no strong extinction features apparent between  $3.7$  and  $8 \mu\text{m}$ , see Figure 4.8. Some weak features due to  $\text{H}_2\text{O}$ ,  $\text{NH}_3$ ,  $\text{CO}_2$ ,  $\text{HCOOH}$  and aliphatic hydrocarbon are tentatively identified by Lutz et al. (1996) and Chiar et al. (2000). All the features are weaker than  $\tau = 0.15$ . Thus, these features are too weak to explain a significant part of the extinction difference between the measured extinction and a single power law. There is some indication for a steeper slope around  $3.9 \mu\text{m}$  and a flatter one at longer wavelengths. Also, the data of Nishiyama et al. (2009) and most theoretical models (Section 4.5.9) exhibit a smooth flattening in the transition region.

Zasowski et al. (2009), Jiang et al. (2003, 2006), Gao et al. (2009), Román-Zúñiga et al.

(2007), Flaherty et al. (2007), Nishiyama et al. (2009), and Indebetouw et al. (2005) also detected a flattening of the extinction at MIR wavelengths toward different regions of the Galaxy. Some of these observations, such as, Nishiyama et al. (2009) and Zasowski et al. (2009), targeted diffuse extinction in the bulge and the Galactic Disk. Therefore, the flattening of the curve in the MIR is not caused by the molecular cloud in front of the GC.

The extinction curves of other galaxies in the MIR are more difficult to interpret, because the extinction in other galaxies is not likely to be caused by an uniform foreground screen. However, since a mixed model (Förster Schreiber et al. 2001) produces a flattening of the extinction curve at higher extinction, while in the GC a flattening at smaller extinction is observed, it is still possible to find qualitative signs for the GC extinction curve in the spectra of other galaxies. The fact that a single power law extinction is slightly preferred when fitting the continuum in some ULIRGS (Tran et al. 2001) could also partially be caused by a GC-like extinction and the mixed model. On the other hand, Thuan et al. (1999) found an extinction curve similar to our results for the extremely metal poor galaxy SBS 0335-052, also using continuum emission. In the case of the central region of M82, Förster Schreiber et al. (2001) found, using hydrogen lines, that an extinction curve similar to the one in the GC provides a better fit to the data than a single power law. All in all, it is likely that the GC extinction (Lutz et al. 1996), considered to be unusual at the time of discovery, is in general the more widely spread type of extinction.

### 4.5.8 Broadband Extinction Curve

Since the GC extinction is consistent with many extinction measurements outside of the GC (Section 4.5.5 and 4.5.7), the extinction curve toward the GC (Appendix 4.7.2) is also useful for other sight lines. We derive from this extinction curve broadband extinction values (Appendix 4.7.3). In principle it is necessary to know the extinction amplitude and the intrinsic object spectrum for deriving precise broadband extinctions. The error caused by neglecting these aspects is below 2 %. On the other hand, the error due to transmission differences between slightly different, but equally named broadband filters can be up to 2.5 % (Appendix 4.7.3). We give in Table 4.6 broadband extinctions ratios relative to the NACO Ks-band. For extinction values of many additional filters and for different source spectra, see Appendix 4.7.3.

### 4.5.9 Dust Models

Extinction curves, together with the emission spectrum of dust, as well as the elemental abundances and depletions, constrain the properties of interstellar dust. Ideally, the dust model should also be plausible with regards to the formation and destruction of the dust (Compiègne et al. 2011). We use published extinction models which fulfilled most constraints at the time of their publication and compare them with the extinction curve toward the GC.

The classical grain model (Mathis et al. 1977) is composed of silicate and graphite grains, where both follow a power law size distribution with a lower and an upper cutoff

Table 4.6. Relative broadband extinction values toward the GC

Broadband	$A_{\text{band}}/A_{\text{Ks}}$
VIRCAM Y	$4.634 \pm 0.103$
NACO J	$3.051 \pm 0.069$
NACO H	$1.737 \pm 0.027$
NACO Ks	$1.000 \pm 0.000$
NACO L'	$0.450 \pm 0.053$
NACO M'	$0.391 \pm 0.094$
IRAC 1	$0.547 \pm 0.052$
IRAC 2	$0.396 \pm 0.082$
IRAC 3	$0.340 \pm 0.094$
IRAC 4	$0.383 \pm 0.116$

Note. — The extinction ratios are obtained from the average of two calculations for the effective filter extinction as described in Appendix 4.7.3 using Vega-like stars with  $A_{Br\gamma} = 1$  and  $A_{Br\gamma} = 5$ . The errors are made up of half of the extinction ratio difference between the two different Brackett- $\gamma$  extinction and the extinction curve errors. We assume that the NIR extinction follows a power law of  $\alpha = -2.11 \pm 0.06$ . Broadband filters of other instruments can have another transmission curve. This can result in an additional error of up 3.5%. For further filters, see Appendix 4.7.3.

for the exclusion of very large and very small grains. Li & Draine (2001) improved this simple model to size distributions which include even smaller grains in order to account for the PAH emissions by interstellar clouds. We use a slight variant of this dust model considered by Weingartner & Draine (2001) (Wg-model), who also consider different  $R_V$ . This model consists of a trimodal carbonaceous grain size distribution and a simple silicate grain size distribution. With increasing  $R_V$ , the number of small grains decreases while the maximum grain size increases.

Similarly to most later models the Wg-models do not have the  $\text{H}_2\text{O}$  features at  $3 \mu\text{m}$  and  $6 \mu\text{m}$ . For constraining the dust properties, independent of the features, we exclude the four lines concerned in our quantitative comparisons. We also exclude the lines beyond  $8 \mu\text{m}$  because the silicate feature is not modeled in all works and in no case matches our silicate extinction toward the GC. In addition, excluding these features we are also more likely to match other extinction measurements in the infrared, such as, for example Indebetouw et al. (2005) and Nishiyama et al. (2009), where the features could not be measured due to too low spectral resolution. We fit all models to the data by adjusting the extinction curve with a global scaling factor.

All Wg-models have a relatively flat NIR slope  $\alpha \geq -1.7$  and hence fit the data badly in the NIR ( $\lambda < 2.8 \mu\text{m}$ ), see Table 4.7. They differ in the MIR from each other. There the models with higher  $R_V$  are flatter. On the one hand, when fitting all lines the models with  $R_V \geq 4.0$  have a worse  $\chi^2$  than the  $R_V = 3.1$  model because of the flatter slope of the  $R_V \geq 4.0$  models in the K-band, which is due to the smaller extinction errors there

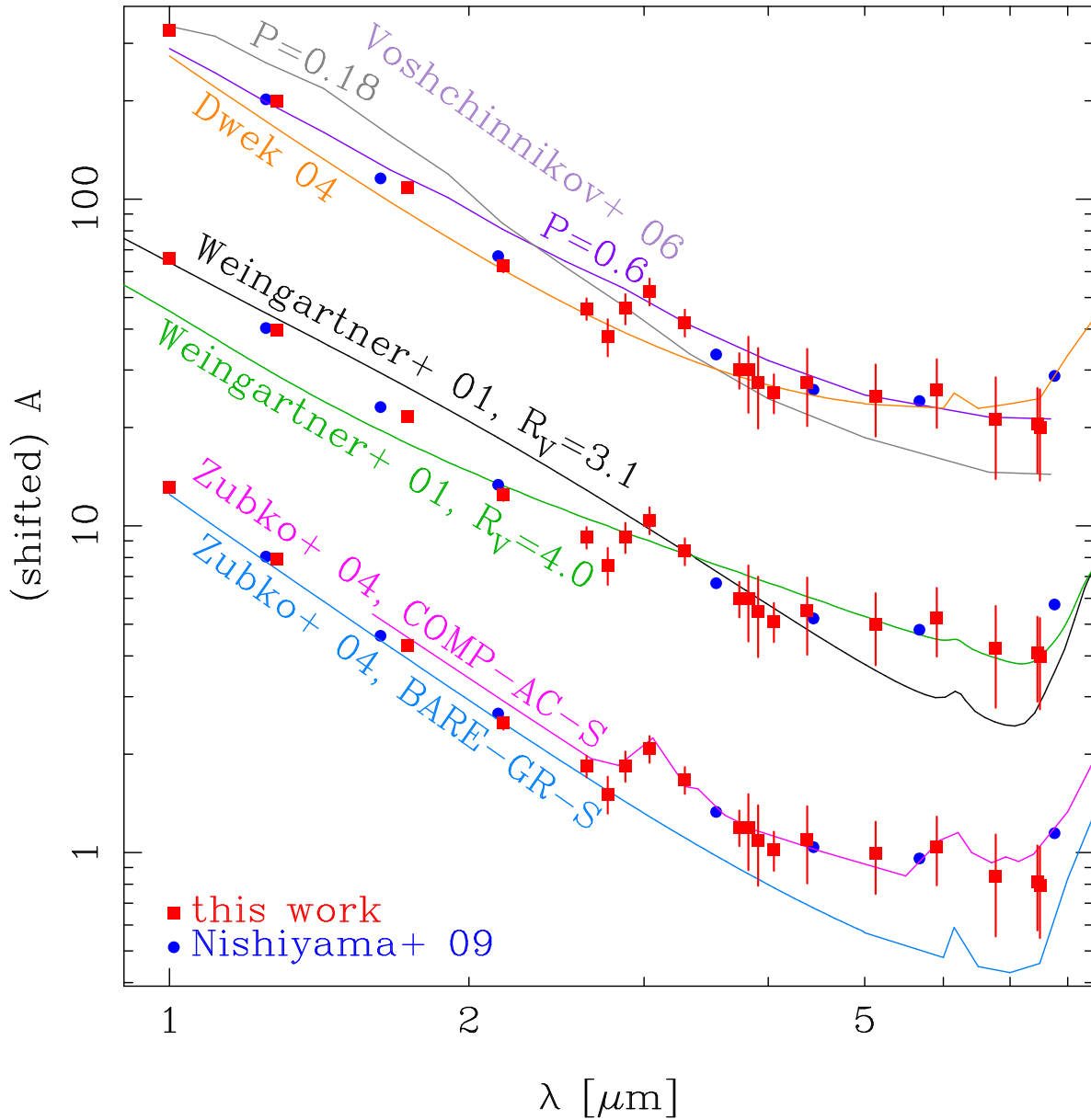


Figure 4.9 Comparison of our data with other data and dust models. To our extinction measurements derived from hydrogen lines (red boxes) we add the inner bulge observations of Nishiyama et al. (2009) (blue circles) scaled to our  $A_{\text{Br}\gamma}$ . The models (lines) are from Weingartner & Draine (2001), Zubko et al. (2004), Dwek (2004), and Voshchinnikov et al. (2006). Everything apart from the lowest data is shifted for better visualization.

Table 4.7. Fit goodness of different dust models

Author	model	total $\chi^2$ /d.o.f.	best fit $\chi^2$ /points of NIR	best fit $\chi^2$ /points of MIR
Wg01	$R_V = 3.1$	114.3/14	106.6.3/6	7.7/9
Wg01	case B $R_V = 4.0$	228/14	178/6	51/9
Zu04	BARE-GR-S	18.9/14	4.4/6	14.5/9
Zu04	COMP-AC-S	6.4/12	4.7/4	1.7/9
Dw04		30.9/14	21.7/6	9.2/9
Vo06	$p = 0.18$	111/14	66/6	45/9
Vo06	$p = 0.6$	117/14	111/6	5.2/9

Note. — We fit the different dust models to our data by scaling the full extinction curve. The NIR data are between 1 and  $2.8 \mu\text{m}$ , the MIR lines are between  $3.7$  and  $7.5 \mu\text{m}$ . In  $\chi^2$ /points we give the number of data points used for the fitting which are within the NIR and MIR. The models are from Weingartner & Draine (2001), Dwek (2004), Zubko et al. (2004), and Voshchinnikov et al. (2006).

more important than the MIR. On the other hand, the  $R_V = 3.1$  model is incompatible with the data of Nishiyama et al. (2009) in the MIR, see Figure 4.9. Compared with the Nishiyama et al. (2009) data, the models with  $R_V \geq 4.0$  are a better fit, although none of the Wg-models show such a strong and sharp flattening from NIR to MIR as observed.

One possibility for more complex dust models is the inclusion of voids in the dust grains (Voshchinnikov et al. 2006). In this model, mainly two size distributions of porous silicate grains and one of small graphite grains contribute to the extinction. Still, the extinction features shortward of  $7 \mu\text{m}$  are unexplained. This model has the advantage that the NIR slope between J and K depends on the porosity. None of their three models with different porosity and also no linear combination of these models can fit our data, see Figure 4.9 and Table 4.7.

Zubko et al. (2004) obtained dust models by fitting grain size distribution to an  $R_V = 3.1$  extinction curve, dust emission and elemental abundances. They use the extinction dispersion between different sight lines as their error estimate. Thus, the extinction has a relatively small weight which could be part of the reason that various dust models can fit their data. Zubko et al. (2004) used different element abundances which have some impact on the result in the case of carbon abundances. We only use their solar abundances. More likely, the real solar abundances (Asplund et al. 2009) are smaller than those used by Zubko et al. (2004). However the abundances in HII regions are higher than the solar abundances (Asplund et al. 2009) and at least the B-star carbon abundance is too small for causing the observed magnitude of extinction (Li 2005).

The simplest model of Zubko et al. (2004), BARE-GR, consists of only graphite, PAHs and silicates grains and as such is similar to the Wg-models. BARE-GR only uses graphite grains smaller than  $300 \text{ nm}$  while the Wg-models use grains up to  $0.8 \mu\text{m}$  and  $5 \mu\text{m}$  respectively. Since grain sizes around  $300 \text{ nm}$  cause the steepest infrared slopes in contrast to grains of other sizes (Moore et al. 2005; Gao et al. 2009), the NIR extinction slope of the BARE-GR model is steeper than that of Wg-models. Overall, the BARE-GR model

can fit the data with  $\chi^2/d.o.f. = 18.9/14$  relatively well. But this model does not have the H<sub>2</sub>O features in contrast to the ISO-SWS spectrum. Because this model nearly does not flatten at all in the MIR, it cannot fit the inner bulge data of Nishiyama et al. (2009), see Figure 4.9.

The COMP models of Zubko et al. (2004) use, in addition to silicate and carbonaceous grains, composite grains consisting of silicates, organic refractory material, water ice and voids. These models seem to be more promising for the GC, because they contain water ice which is visible in extinction features toward the GC. The best fitting subtype is AC in which the carbon is mainly amorphous. The composite particles are, with sizes up to 0.8  $\mu\text{m}$ , bigger than the other particles. The other subtypes of composite models have a steeper slope, at least in the MIR, and hence make a worse fit to the data. The COMP-AC-S model has a  $\chi^2/d.o.f. = 6.4/12$ , slightly better than the BARE-GR-S model. In contrast to the other models, it also matches the Nishiyama et al. (2009) data, see Figure 4.9.

Dwek (2004) added metallic needles to the BARE-GR model of Zubko et al. (2004). The extinction caused by the needles rises with wavelength up to 8  $\mu\text{m}$ , thus flattening the Wg-model between 3 and 8  $\mu\text{m}$ , see Figure 4.9. The extinction due to needles drops fast longward of 8  $\mu\text{m}$  for avoiding a weakening of the silicate feature. This model does not fit the data with  $\chi^2/d.o.f. = 30.9/14$ . The inconsistency is caused by an overly gradual transition to a flatter slope around 3  $\mu\text{m}$ , while the observed slopes changes faster, see Figure 4.9. While it might be possible to fit our data better with some dust model variant which consists of metallic needles as well as simple carbonaceous and silicate grains, finding a fit to the data will not be easy, since the extinction due to both components varies so slowly with wavelength that it is difficult to obtain the observed sharp flattening around 3  $\mu\text{m}$ .

All together, the COMP-AC-S model of Zubko et al. (2004) seems to be the best model for extinction toward the GC because of its best  $\chi^2/d.o.f.$  and the presence of the H<sub>2</sub>O features. However, the lack of H<sub>2</sub>O ice features in most sight lines (Rawlings et al. 2003; Whittet et al. 1997), while MIR-flattening is observed in many regions (Zasowski et al. 2009; Jiang et al. 2003, 2006; Gao et al. 2009; Flaherty et al. 2007; Román-Zúñiga et al. 2007; Nishiyama et al. 2009; Indebetouw et al. 2005) renders the idea that composite particles glued by ices are responsible the flat MIR extinction questionable, also for the GC. This is because if composite particles can exist only together with ices, the other regions should show a steeper MIR extinction than the GC. However, because the sight lines with extinction probed in the MIR do not overlap with the sight lines which are tested for H<sub>2</sub>O ice, it is still possible that the ice feature could exist in most sight lines with flatter MIR extinction.

An alternative model could be that something else aside from ices produces the flat extinction in the MIR toward the GC and elsewhere, and toward the GC additional pure ice grains produce the extinction features. However, all other models tested here have the problem that they do not have at once a steep NIR extinction and a flat MIR extinction. It is perhaps possible to change the shape of the extinction curves within the models, without changing the type of particles in the model. However, this seems difficult for the pure carbonaceous and silicate grain model, because a smooth particle size distribution

of carbonaceous and silicate grains should also produce a smooth extinction curve. It might be possible, on the other hand, to change the extinction shape only around  $3 \mu\text{m}$  by omitting only  $\text{H}_2\text{O}$  ice from the composite particles in the COMP-AC-S model. If this does not change the other extinction properties of the dust such model could fit the extinction also in other sight lines.

For solving the issue, further modeling seems to be necessary, maybe concentrating first on the detailed extinction curve toward the Galactic Center. In the future, similarly detailed extinction curves in other sight lines would also be very useful. Especially promising could be searching for the  $\text{H}_2\text{O}$  ice feature in sight lines which are already probed by broadband measurements. Also, adding more extinction measurements in between for testing the commonness of the sharp transition to a flatter extinction in the MIR might be very interesting for further study.

## 4.6 Summary

The simplest way to derive an extinction curve is to observe a well understood object at different wavelengths, including at least one extinction-free wavelength. The minispiral in the GC fulfills these conditions. It is a HII region and Case B is valid. As extinction-free emission we use the 2 cm radio continuum observed with the VLA. In the infrared, we obtain line fluxes between  $1.28 \mu\text{m}$  and  $2.17 \mu\text{m}$  from SINFONI. For lines at longer wavelengths of up to  $19 \mu\text{m}$  we use ISO-SWS observations. We obtain the following results:

- By interpolation we obtain  $A_{2.166 \mu\text{m}} = 2.62 \pm 0.11$  as the average  $2.166 \mu\text{m}$  extinction of the ISO field of  $14'' \times 20''$  about Sgr A\*.
- Using the extinction map of Schödel et al. (2010) for the relative spatial extinction we obtain, for the direction toward Sgr A\*:  $A_{\text{H}} = 4.21 \pm 0.10$ ,  $A_{\text{Ks}} = 2.42 \pm 0.10$  and  $A_{\text{L'}} = 1.09 \pm 0.13$ .
- Schödel et al. (2010) measured the total luminosity modulus of the red clump consisting of the extinction and distance modulus toward the Galactic Center. Since we measure the extinction independent of the distance, the combination of Schödel et al. (2010) with our extinction yields the distance  $R_0$ , the distance to the Galactic Center: we obtain  $R_0 = 7.94 \pm 0.65$  kpc in agreement with current measurements.
- The extinction in the NIR ( $1.2$  to  $2.8 \mu\text{m}$ ) is well fitted by a power law of slope  $\alpha = -2.11 \pm 0.06$ . This law is steeper than the value of about  $\alpha \approx -1.75$ , which was mostly reported in the literature before 2004, see for example (Draine 1989). However, since 2005 most publications about diffuse extinction toward the bulge and Galactic Disk (for example Stead & Hoare 2009) yield a steeper law. We obtain  $\alpha = -2.07 \pm 0.16$  as weighted average of all publications about diffuse extinction since 2005.

- At longer wavelengths, several extinction features are visible, such as H<sub>2</sub>O at 3.1  $\mu\text{m}$  and silicates at 9.7  $\mu\text{m}$ . Even aside from such features, the extinction is higher than expected from extrapolating the NIR power law. Our data agree well with several IRAC publications for the inner bulge, such as Nishiyama et al. (2009) for example. Because we are able to use many lines, it is apparent that the change in slope is sharper and stronger than in any of the extinction curves produced by pure carbonaceous and silicate grains (Weingartner & Draine 2001). The best fitting model adds composite particles which contain also H<sub>2</sub>O ice (Zubko et al. 2004).

## 4.7 Appendix

### 4.7.1 Correcting for the Extinction Law Flattening Bias due to Inhomogeneous Extinction

Here, we estimate the extinction law flattening bias due to inhomogeneous extinction.

We make the assumption that the true extinction map  $A_i(\lambda)$ , for resolution element  $i$  and wavelength  $\lambda$ , has the same relative spatial distribution of extinction as the map of Schödel et al. (2010), such that we can obtain the extinction map at a given wavelength  $\lambda$  via a simple scaling of an (as yet unknown) factor  $x(\lambda)$ :

$$A_i(\lambda) = x(\lambda) \times A_{i\text{Sch}} \quad (4.9)$$

We then derive an unextincted Brackett- $\gamma$  flux map from our observed Brackett- $\gamma$  flux map, using the extinction map of Schödel et al. (2010) (scaled to our measured Brackett- $\gamma$  extinction) as model for the spatial inhomogeneity in the extinction at this wavelength. For resolution element  $i$ , the unextincted flux map can be written as:

$$F_i(\lambda = \text{Br } \gamma)_{\text{unext}} = F_i(\lambda = \text{Br } \gamma)_{\text{obs}} * 10^{0.4x_0 A(\text{map})_{\text{Sch}}}. \quad (4.10)$$

Here we use as scaling factor,  $x_0$ , our integrated measurement of the Brackett- $\gamma$  extinction (Section 4.4.2), divided by the (observed) flux-weighted extinction of the map of Schödel et al. (2010):

$$x_0 = A(\lambda = \text{Br } \gamma)_{\text{integrated,measured}} \left( \frac{\sum_{i \in \text{ISO}} F_i(\lambda = \text{Br } \gamma)_{\text{ext}} A_{i\text{Sch}}}{\sum_{i \in \text{ISO}} F_i(\lambda = \text{Br } \gamma)_{\text{ext}}} \right)^{-1}. \quad (4.11)$$

We use the unextincted Brackett- $\gamma$  flux map as a model for the spatial distribution of the intrinsic (unextincted) flux at all wavelengths (i.e. the correct distribution of relative flux weights).

The true (extinction-law-conserving) integrated extinction should be flux-weighted by the unextincted flux, not the observed flux:

$$A(\lambda)_{\text{integrated,true}} = x(\lambda) \times \frac{\sum_{i \in \text{ISO}} F_i(\lambda = \text{Br } \gamma)_{\text{unext}} A_{i\text{Sch}}}{\sum_{i \in \text{ISO}} F_i(\lambda = \text{Br } \gamma)_{\text{unext}}} \quad (4.12)$$

Our extinction measurement, on the other hand, measures rather the ratio of integrated fluxes:

$$A(\lambda)_{\text{integrated,measured}} = -2.5 \times \log \left( \frac{\sum_{i \in \text{ISO}} F_i(\lambda = \text{Br } \gamma)_{\text{ext}}}{\sum_{i \in \text{ISO}} F_i(\lambda = \text{Br } \gamma)_{\text{unext}}} \right) \quad (4.13)$$

In this equation, areas with smaller extinction have higher observed fluxes relative to the unextincted flux and thus are given a higher weight. Upon integration this then leads to a smaller measured extinction than the true integrated extinction of equation (4.12).

To estimate this bias, we simulate our extinction measurements, weighting the intrinsic extinction,  $x(\lambda)A_{i\text{Sch}}$ , by the unextincted flux weights derived from the Brackett- $\gamma$  map:

$$A(\lambda)_{\text{integrated,simulated}} = -2.5 \times \log \left( \frac{\sum_{i \in \text{ISO}} 10^{-0.4 x(\lambda) A_{i\text{Sch}}} F_i(\lambda = \text{Br } \gamma)_{\text{unext}}}{\sum_{i \in \text{ISO}} F_i(\lambda = \text{Br } \gamma)_{\text{unext}}} \right) \quad (4.14)$$

For every SINFONI line at wavelength  $\lambda$  we find an  $x(\lambda)$  which, when substituted in equation (4.14), results in our measured extinction  $A(\lambda)_{\text{integrated,measured}}$ . The calculation is carried out over the same area (ISO) used in the extinction measurement for each line. The bias at a given wavelength  $\lambda$  is then:

$$\Delta A(\lambda) = A(\lambda)_{\text{integrated,true}} - A(\lambda)_{\text{integrated,simulated}} \quad (4.15)$$

This correction must be applied to  $A(\lambda)_{\text{integrated,measured}}$  in order to obtain the correct (extinction-law-conserving) extinction. The biggest correction occurs for the highest extinction (Paschen- $\beta$ ). Even for this line the correction is only 0.08 mag, smaller than the extinction error of 0.11 mag.

## 4.7.2 Interpolating the Extinction Curve

We use the continuum of the ISO-SWS spectrum in order to constrain the shape of the extinction curve in the MIR. The unextincted continuum cannot be modeled with a single simple model such as a single black- or gray body. Instead, we correct the measured continuum close to the hydrogen lines by using the extinction of the lines. We then interpolate the resulting points using simple models for sections of the spectrum, described in the paragraph below. After this, we obtain the extinction curve by dividing the interpolated extinction-corrected continuum by the observed continuum. By applying this method, we use the extinction of the hydrogen lines to obtain extinction values in regions where no hydrogen lines are available.

Between 2.62 and 7.6  $\mu\text{m}$  we fit the extinction corrected continuum points with a second order polynomial in log-log space. At longer wavelengths however the interpolation is less certain, due to the fact that there are fewer lines, larger extinction errors and silicate emission in the GC region (Kemper et al. 2004). For the continuum up to 12  $\mu\text{m}$  we use the GC continuum of Kemper et al. (2004), which contains silicate emission, scaled such that it fits our two data points in this wavelength range. A 240 K blackbody is a good approximation to the extincted continuum between 12 and 15  $\mu\text{m}$ . In this range there are

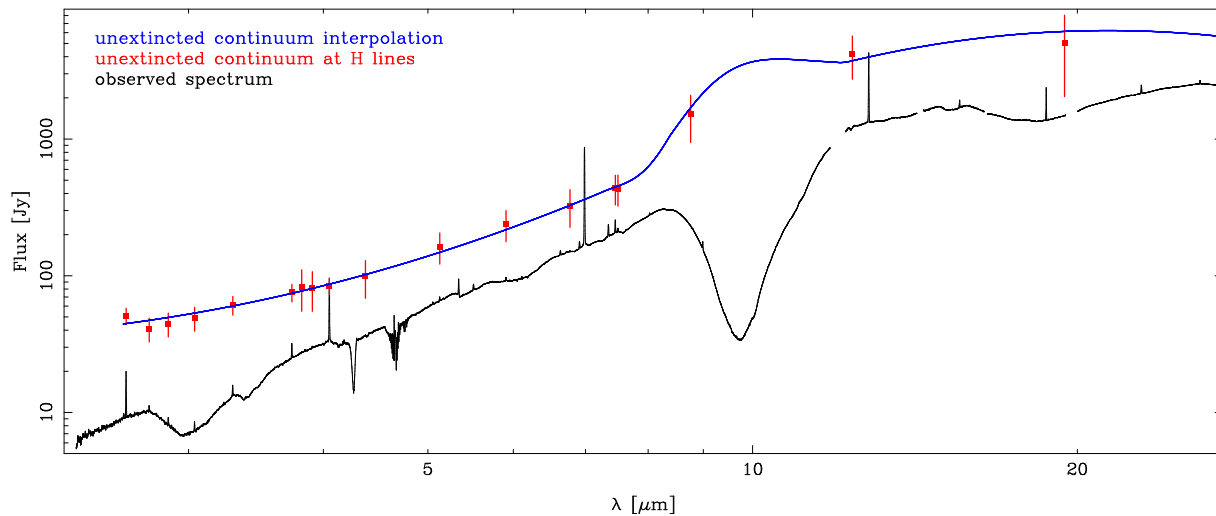


Figure 4.10 Measured and unextincted MIR continuum toward the GC. The black line is the observed ISO-SWS spectrum. We unextinct the continuum around the hydrogen lines by the hydrogen line extinctions there (red boxes). We interpolate these points to obtain the unextincted continuum (blue line).

no significant extinction features. We extrapolate this blackbody up to  $26 \mu\text{m}$ , scaling it such that the unextincted continuum close to both lines in this range is fit by the blackbody, and use it as a model for the continuum between  $12$  and  $26 \mu\text{m}$ . We combine the three different continua with smooth transitions around  $7 \mu\text{m}$  and  $12 \mu\text{m}$ , see Figure 4.10.

In a similar way, we make a smooth transition to the  $\alpha = -2.11$  power law shortward of  $2.75 \mu\text{m}$ . We continue the interpolation by a  $\alpha = -2.02$  power law shortward of  $1.28 \mu\text{m}$ . We also correct unphysical jumps in the extinction curve, such as the one at  $4.07 \mu\text{m}$ , due to calibration errors of the ISO-SWS data. For this we adjust the extinction curve locally with linear interpolation. We interpolate the extinction curve we obtain, excluding spectral lines, with splines (Table 4.8). The spectral resolution of this interpolation is not high enough to fully resolve all features, such as, e.g., the CO feature at  $4.7 \mu\text{m}$ .

### 4.7.3 Effective Broadband Filter Extinctions

A complication in correcting for extinction in broadband flux measurements is that the extinction that should be associated with a given filter varies with both the intrinsic spectrum of the source and the strength of the extinction.

Since we use spectral lines in this paper to constrain the extinction law, the wavelengths to associate with the extinction measurements are well-defined. Also the interpolated extinction (Appendix 4.7.2) has well defined wavelengths. Thus, we can explicitly calculate the extinction values for a given broadband filter, like Espinoza et al. (2009), using the

Table 4.8. Interpolated infrared extinction curve

$\lambda[\mu\text{m}]$	A(GC)	$\delta A$ (GC)
1.00009	13.1075	0.3
1.00984	12.8529	0.2925
1.0197	12.6033	0.285
1.02964	12.3586	0.2776
1.03969	12.1186	0.2701
1.04983	11.8832	0.2626
1.06007	11.6525	0.2551
1.07041	11.4262	0.2477
1.08086	11.2043	0.2402
1.0914	10.9867	0.2327

Note. — Our extinction curve. The second column is the average extinction toward the central  $14'' \times 20''$  of the GC. The errors includes all effects. Some effects matter only for comparison over big wavelength ranges. Locally the error is smaller for most of ISO-SWS range (2.6 to 27  $\mu\text{m}$ ). This curve can be used for  $A(\lambda)$  in equation (4.16) for obtaining the extinction for other objects and filters. Scaled to other absolute extinctions it can be also useful outside the Galactic Center. The full table is available in the electronic edition.

equation:

$$A_{\text{filter}} = -2.5 \times \log \left( \frac{\int \lambda F_{\lambda}(\lambda) S(\lambda) R(\lambda) d\lambda}{\int \lambda F_{\lambda}(\lambda) S(\lambda) d\lambda} \right). \quad (4.16)$$

Here  $F_{\lambda}(\lambda)$  is the intrinsic flux density of the source, which when multiplied with the wavelength,  $\lambda$ , is proportional to the number distribution of photons with wavelength.  $S(\lambda)$  is the wavelength dependent throughput of telescope, instrument and atmosphere. We also define here  $R(\lambda) = 10^{(-0.4A(\lambda))}$  as a 'reddening factor' to separate the extinction from the intrinsic flux.

We use our interpolated extinction curve for  $A(\lambda)$  (see Section 4.7.2 and Table 4.8) in equation (4.16) to calculate the effective broadband filter extinction values for a range of commonly used infrared filters. The results are presented in Table 4.9. As source spectrum we use primarily a blackbody of 9480 K. For stars of this temperature, there is no major difference between the real spectrum and the correct blackbody in the infrared. The use of such a star also has the advantage that a similar star is used for the definition of the Vega magnitude system. In addition, we also compute the effective filter extinctions for a bright Sgr A\* like spectrum (Eisenhauer et al. 2005; Gillessen et al. 2006) which follows a power law with a slope  $\beta = 0.5$  in  $\nu L_{\nu}$  (Hornstein et al. 2007; Dodds-Eden et al. 2009) as example of a very red source. For  $S(\lambda)$  we use the atmospheric transmission multiplied with the instrument transmission. For all Paranal filters we use the atran transmission models (Lord 1992) from Cerro Panchon for the atmosphere, with airmass 1 and 2.3 mm

water vapor column from the Gemini web site<sup>4</sup>. For the VISIR filters we use the filter transmissions from the instrument web site<sup>5</sup>. We obtain the VIRCAM filters from the instrument web site<sup>6</sup>. For the NIRC2 filters, which we obtain from the instrument web site<sup>7</sup>, we use a Mauna Kea atmosphere of airmass 1.5 and 1.6 mm water vapor column from the Gemini web site (see footnote 4). For these instruments only in case of VIRCAM the wavelength dependent quantum efficiency and mirror reflectivity are available. We use them for our calculation. However, including QE and mirror reflectivity change the extinction only by less than 0.07% relatively. For the other instruments we assume that the throughput of the instrument is apart of the filter not wavelength dependent within a filter. For 2MASS we use the full transmissions including the atmosphere from the project web site<sup>8</sup>. We obtain the NICMOS transmissions from the instrument web site<sup>9</sup> as in case of the IRAC transmissions<sup>10</sup>.

Although, strictly speaking, it is necessary to calculate the effective broadband extinction on a per spectrum basis, the differences in the effective extinction for different source SEDs are mostly relatively small, even for the high extinction of the GC. For example, the difference in effective extinction between a blue spectrum (Vega) and a red spectrum (Sgr A) is only 0.056 mag in the H-band and 0.026 mag in the Ks-band.

We test the influence of difference magnitudes of extinctions on broad band extinctions. The H-band extinction derived from  $A_{Br\gamma} = 2.62$  is 4.65 mag, while the H-band extinction derived from  $A_{Br\gamma} = 0.5$  is 0.91 mag. Assuming linear scaling of the H-band extinction with the Brackett- $\gamma$  extinction the expected H-band extinction (scaled up from  $A_{Br\gamma} = 0.5$ ) is  $0.91\text{mag} \times 2.62/0.5 = 4.77$  mag. Thus, the deviation from linearity (the non-linearity) is 0.12 mag in this case. In the Ks-band the non-linearity is, with 0.029 mag, much smaller for the same value of  $A_{Br\gamma}$ . We find that the non-linearity is of the order of the measurement error for  $A_{\text{band}} \leq 4$ .

For most objects, for which the extinction is not significantly higher than in the GC, it is sufficient to use the extinction closest to the measured extinction in Table 4.9 renormalized to the correct absolute extinction. For very high extinctions or different filters it is necessary to calculate the filter extinctions from equation (4.16) using the interpolated extinction curve given in Table 4.8.

#### 4.7.4 Comparison with Other Methods for the Determination of the NIR Extinction Slope

We derive the NIR extinction slope  $\alpha$  from absolute extinction values at known wavelength. Another way commonly used to compute the near-infrared extinction slope  $\alpha$  is to use

<sup>4</sup><http://www.gemini.edu/?q=node/10789>

<sup>5</sup><http://www.eso.org/sci/facilities/paranal/instruments/visir/inst/index.html>

<sup>6</sup><http://www.eso.org/sci/facilities/paranal/instruments/vircam/inst/>

<sup>7</sup><http://www2.keck.hawaii.edu/inst/nirc2/filters.html>

<sup>8</sup>[http://www.ipac.caltech.edu/2mass/releases/second/doc/sec3\\_1b1.html#s16](http://www.ipac.caltech.edu/2mass/releases/second/doc/sec3_1b1.html#s16)

<sup>9</sup><http://www.stsci.edu/hst/nicmos/design/filters>

<sup>10</sup><http://ssc.spitzer.caltech.edu/irac/calibrationfiles/spectralresponse>

Table 4.9. Extinction of broadband filters for different Brackett- $\gamma$  extinctions

Instrument	Filter	A ( $A_{Br\gamma} = 2.62$ ) 9480 K	A ( $A_{Br\gamma} = 0.5$ ) 9480 K	A ( $A_{Br\gamma} = 6$ ) 9480 K	A ( $A_{Br\gamma} = 2.40$ ) $\beta = 0.5$
NACO	J	$8.16 \pm 0.12$	$1.62 \pm 0.03$	$17.90 \pm 0.26$	$7.42 \pm 0.11$
NACO	H	$4.65 \pm 0.11$	$0.91 \pm 0.02$	$10.29 \pm 0.25$	$4.21 \pm 0.10$
NACO	Ks	$2.67 \pm 0.11$	$0.52 \pm 0.02$	$6.02 \pm 0.26$	$2.42 \pm 0.10$
NACO	L'	$1.20 \pm 0.14$	$0.23 \pm 0.03$	$2.73 \pm 0.32$	$1.09 \pm 0.13$
NACO	M'	$1.05 \pm 0.25$	$0.20 \pm 0.05$	$2.37 \pm 0.57$	$0.95 \pm 0.23$
VISIR	PAH1 (8.6 $\mu\text{m}$ )	$1.73 \pm 0.54$	$0.34 \pm 0.10$	$3.83 \pm 1.23$	$1.60 \pm 0.50$
VISIR	PAH2.2 (11.9 $\mu\text{m}$ )	$1.61 \pm 0.36$	$0.31 \pm 0.07$	$3.66 \pm 0.83$	$1.47 \pm 0.33$
NICMOS	110M	$10.42 \pm 0.19$	$2.07 \pm 0.04$	$22.86 \pm 0.40$	$9.49 \pm 0.18$
NICMOS	145M	$6.00 \pm 0.11$	$1.16 \pm 0.02$	$13.44 \pm 0.25$	$5.47 \pm 0.10$
NICMOS	160W	$4.89 \pm 0.11$	$0.97 \pm 0.02$	$10.61 \pm 0.25$	$4.40 \pm 0.10$
NICMOS	170M	$4.33 \pm 0.11$	$0.83 \pm 0.02$	$9.80 \pm 0.25$	$3.95 \pm 0.10$
NICMOS	222M	$2.50 \pm 0.11$	$0.48 \pm 0.02$	$5.70 \pm 0.26$	$2.28 \pm 0.10$
IRAC	Band 1	$1.47 \pm 0.14$	$0.28 \pm 0.03$	$3.27 \pm 0.32$	$1.31 \pm 0.13$
IRAC	Band 2	$1.06 \pm 0.22$	$0.20 \pm 0.04$	$2.40 \pm 0.50$	$0.97 \pm 0.20$
IRAC	Band 3	$0.91 \pm 0.25$	$0.17 \pm 0.05$	$2.08 \pm 0.57$	$0.83 \pm 0.23$
IRAC	Band 4	$1.02 \pm 0.31$	$0.21 \pm 0.06$	$2.19 \pm 0.67$	$1.01 \pm 0.30$
NIRC2	H	$4.75 \pm 0.11$	$0.93 \pm 0.02$	$10.56 \pm 0.25$	$4.31 \pm 0.10$
NIRC2	K'	$2.73 \pm 0.11$	$0.53 \pm 0.02$	$6.15 \pm 0.26$	$2.48 \pm 0.10$
NIRC2	L'	$1.24 \pm 0.14$	$0.24 \pm 0.03$	$2.80 \pm 0.32$	$1.12 \pm 0.13$
NIRC2	Ms	$1.17 \pm 0.25$	$0.23 \pm 0.05$	$2.66 \pm 0.57$	$1.07 \pm 0.23$
VIRCAM	Y	$12.40 \pm 0.27$	$2.40 \pm 0.05$	$27.77 \pm 0.58$	$11.33 \pm 0.25$
VIRCAM	J	$8.21 \pm 0.12$	$1.60 \pm 0.03$	$18.30 \pm 0.26$	$7.48 \pm 0.11$
VIRCAM	H	$4.68 \pm 0.11$	$0.91 \pm 0.02$	$10.41 \pm 0.25$	$4.24 \pm 0.10$
VIRCAM	Ks	$2.67 \pm 0.11$	$0.51 \pm 0.02$	$6.04 \pm 0.26$	$2.42 \pm 0.10$
2MASS	J	$8.26 \pm 0.12$	$1.64 \pm 0.03$	$18.14 \pm 0.26$	$7.51 \pm 0.11$
2MASS	H	$4.65 \pm 0.11$	$0.90 \pm 0.02$	$10.37 \pm 0.25$	$4.22 \pm 0.10$
2MASS	Ks	$2.58 \pm 0.11$	$0.50 \pm 0.02$	$5.84 \pm 0.26$	$2.34 \pm 0.10$

Note. — We calculate filter extinctions for different Brackett- $\gamma$  (2.166  $\mu\text{m}$ ) extinctions. We use blackbodies and power law source spectra. The error is the uncertainty due to the extinction error. The first column is the average extinction of stars in the central  $14'' \times 20''$  of the GC. The last column is the extinction toward the power law source Sgr A\* (i.e. using stars in the central  $r \leq 0.5''$  of the GC for scaling of  $A_{Br\gamma}$ ).

stellar colors, using an assumed wavelength to associate with the broadband filters (we hereafter call this the effective wavelength method). For example, the following equation is commonly used to compute the extinction slope  $\alpha$  from JHK(s) colors (Stead & Hoare 2009):

$$\frac{E_{J-H}}{E_{H-Ks}} = \frac{\left(\frac{\lambda_J}{\lambda_H}\right)^\alpha - 1}{1 - \left(\frac{\lambda_{Ks}}{\lambda_H}\right)^\alpha} \quad (4.17)$$

where  $\lambda_J$  is some assumed wavelength of the  $J$  filter, and so on for the other filters. Obviously, it is necessary to know the wavelength that can correctly be associated with the filters for the given source and extinction in order to derive  $\alpha$ . One possibility would be to use the isophotal wavelength ( $\lambda_{\text{iso}}$ , see Tokunaga & Vacca 2005):

$$F_\lambda(\lambda_{\text{iso}}) = \frac{\int F_\lambda(\lambda) S(\lambda) d\lambda}{\int S(\lambda) d\lambda} \quad (4.18)$$

This means that  $\lambda_{\text{iso}}$  is the wavelength at which the monochromatic flux  $F_\lambda(\lambda_{\text{iso}})$  equals the mean flux in the passband.

The effective wavelength (Tokunaga & Vacca 2005) is more commonly used for extinction purposes:

$$\lambda'_{\text{eff unext}} = \frac{\int \lambda^2 F_\lambda(\lambda) S(\lambda) d\lambda}{\int \lambda F_\lambda(\lambda) S(\lambda) d\lambda} \quad (4.19)$$

The effective wavelength defined this way is the average wavelength of received photons, weighted by the number distribution of received photons at the detector, appropriate for photon counting detectors. This equation is used in two variants: for the calculation of  $\lambda'_{\text{eff unext}}$  the source spectra are not extinguished.

For the calculation of the other variant ( $\lambda'_{\text{eff ext}}$ ) the source spectra are extinguished, see Stead & Hoare (2009) and Schödel et al. (2010):

$$\lambda'_{\text{eff ext}} = \frac{\int \lambda^2 F_\lambda(\lambda) S(\lambda) R(\lambda) d\lambda}{\int \lambda F_\lambda(\lambda) S(\lambda) R(\lambda) d\lambda} \quad (4.20)$$

We test the accuracy of the methods concentrating on the two definitions of the effective wavelength. To do this we compare the explicitly calculated filter extinctions to those obtained with the effective wavelength method for an extinguished, 9480K Vega-like blackbody. As test filters we use the NACO JHKs filters plus atmosphere and our  $\alpha = -2.11$  extinction law. Using equation (4.16) we obtain slightly higher extinctions for the explicit calculation than obtained by applying the extinguished effective wavelength method (equation 4.17), with differences of  $A_{Ks \text{ true}} - A_{Ks \lambda' \text{ eff ext}} = 0.05$  for  $A_{Br \gamma} = 2.5$  (for lower extinction the difference is much less  $A_{Ks \text{ true}} - A_{Ks \lambda' \text{ eff ext}} = 0.013$  for  $A_{Br \gamma} = 1$ ). Similarly we obtain  $A_{Ks \text{ true}} - A_{Ks \lambda' \text{ eff unext}} = -0.012$  for  $A_{Br \gamma} = 2.5$  when we use the unextinguished effective wavelengths.

The reason for these discrepancies is illustrated via an exaggerated example in Figure 4.11. To obtain the correct value of the true extinction it is necessary to consider the

photon distribution, integrated over the filter, of both the unextincted and of the extincted source. Yet the two effective wavelength methods each consider only one of the above photon distributions. In the case of the unextincted source: because a larger proportion of the photons is transmitted through the extinction at longer wavelength than at  $\lambda'_{\text{eff unext}}$ , the true filter extinction is smaller than at  $\lambda'_{\text{eff unext}}$ . The opposite is true at  $\lambda'_{\text{eff ext}}$ .

In summary both 'effective' wavelengths deviate from the true extinction, because these effective wavelengths are not the effective extinction wavelengths. As a result it is not correct to use these 'effective' wavelengths to calculate the extinction appropriate for broadband filters from our extinction curve. The true wavelength for extinction measurements  $\lambda_{\text{true}}$  is the wavelength at which the extincted object is extincted by the same amount of extinction as in the explicit calculation of equation (4.16).  $\lambda_{\text{true}}$  depends on the optical system, object SED, strength of extinction and the shape of the extinction law. However, since e.g. Stead & Hoare (2009) and Schödel et al. (2010) measured the broadband extinctions directly their extinctions are correct at least for the specific source, filter and extinction strength combinations used in the determination.

More important is the issue of effective wavelengths for the determination of  $\alpha$  from measured broadband extinctions. To test this we calculate alpha, using either  $\lambda_{\text{iso}}$ ,  $\lambda'_{\text{eff unext}}$  or  $\lambda'_{\text{eff ext}}$  in equation (4.17) (method of relative extinction). We also calculate  $\alpha$  from the absolute  $A_{\text{H}}$  and  $A_{\text{Ks}}$  using  $\lambda'_{\text{eff ext}}$ , as is done in Schödel et al. (2010). We then compare the obtained values of  $\alpha$  with the input  $\alpha = -2.11$ , see Figure 4.12.

Since none of the methods obtains the true extinction values, it is not surprising that none of the methods obtains the true extinction slope  $\alpha$ . The best method for obtaining  $\alpha$  is using  $\lambda'_{\text{eff ext}}$  and equation (4.17): for extinctions  $A_{\text{Br } \gamma} \leq 4$  there is less than 0.046 deviation of  $\alpha$  from the input  $\alpha = -2.11$ . The other methods can result in larger deviations of up to 0.11 for the same range of extinction.

The difference between the  $\alpha$  obtained using  $\lambda'_{\text{iso}}$  and  $\lambda'_{\text{eff unext}}$  is only  $\Delta\alpha \approx 0.01$ . In contrast Stead & Hoare (2009) obtain a difference of around  $\Delta\alpha = 0.2$ . The reason for this could be the slightly different photometric system, but perhaps more likely, the difference between a 9480 K blackbody and a K2III spectrum. Given this big difference in  $\Delta\alpha$ , it is unclear if using  $\lambda'_{\text{eff unext}}$  is also the best approximation to the true  $\alpha$  for instruments and source spectra other than tested here.

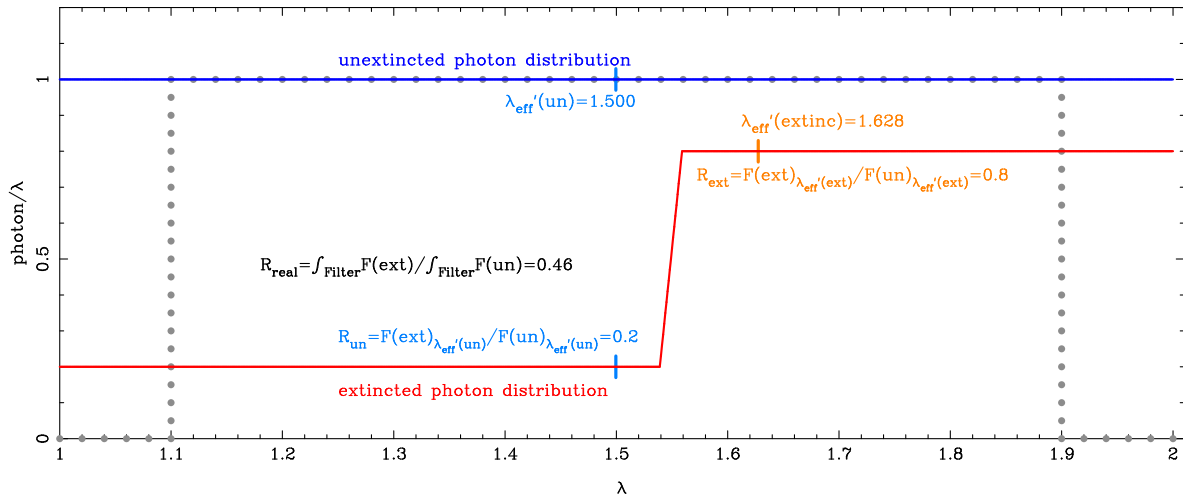


Figure 4.11 Difference between the extinction at (extincted and unextincted) effective wavelengths, and the filter-integrated extinction. A source (blue line, showing unextincted flux) is observed with a broad filter (gray dots). Via an (unrealistic) extinction, the source is extincted to the orange line. In this example the effective wavelength of the unextincted flux is in the part with high extinction, and the effective wavelength of the extincted flux is in the part with small extinction. The true reddening factor, however, is determined by the integrals over the filter range and has a value between the reddening factors at the two effective wavelengths. For more realistic extinction curves this effect is much smaller, but not always negligible.

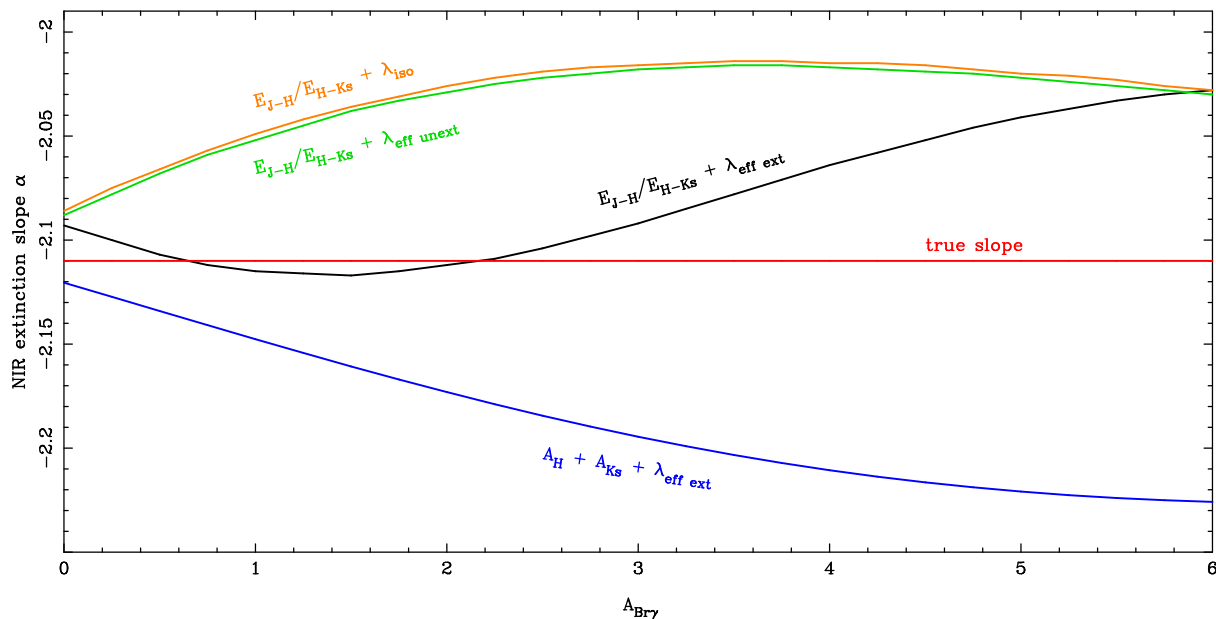


Figure 4.12 Comparison of the true near-infrared extinction slope  $\alpha$  with the  $\alpha$  obtained using common methods. We use the NACO JHKs filters with atmosphere and a 9480 K blackbody, simulating common measurements. For obtaining  $\alpha$  from  $E_{J-H}/E_{H-Ks}$  we use equation (4.17). The results are displayed as follows: (orange) the use of the isophotal wavelength in equation (4.17); (green) the use of the effective wavelength of the unextincted flux in equation (4.17); (black) the use of the effective wavelength of the extincted flux in equation (4.17); and (blue) the computation of  $\alpha$  from absolute  $A_H$  and  $A_{Ks}$ , using the extincted effective wavelengths. The true slope is shown as the red line.

# Chapter 5

## The Nuclear Cluster of the Milky Way I: Total Mass and Luminosity

**Original publication:** T.K. Fritz, S. Chatzopoulos, O. Gerhard, S. Gillessen, K. Dodds-Eden, R. Genzel, T. Ott, O. Pfuhl, F. Eisenhauer *The Nuclear Cluster of the Milky Way I: Total Mass and Luminosity*<sup>1</sup>, ApJ, in prep.

### Abstract:

Like many other late-type galaxies, also the Milky Way contains a nuclear star cluster. In this work we obtain the basic properties of its dominant old stellar population. Firstly, we derive its structural properties by constructing a stellar density map of the central  $1000''$  using extinction corrected star counts from VISTA, WFC3/IR and NACO data. We can describe the profile with a two-component model built from Sersic profiles. The inner, almost spherical component is the nuclear cluster. Its half-light radius is  $110'' \approx 4.4\text{pc}$ , and with  $M_{\text{Ks}} = -15.30 \pm 0.26$  it is a bright specimen. The outer component can be identified with the stellar component of the circumnuclear zone, and it has a flattening ratio of 3.85. Secondly, we enlarge the field of view over which detailed dynamics are available from 1 pc to 4 pc. We obtain more than 10000 individual proper motions from NACO data, and more than 2400 radial velocities from SINFONI data. By means of isotropic Jeans modeling and assuming spherical symmetry, we obtain a power law slope of the mass profile of  $\delta = 1.19 \pm 0.07$ . We get a nuclear cluster mass within  $100''$  of  $M_{100''} = (6.02 \pm 0.51|_{\text{fix}R_0} \pm 0.96|_{R_0}) \times 10^6 M_{\odot}$ , which corresponds to a total cluster mass of  $M_{\text{NC}} = (12.88 \pm 2.69|_{\text{fixed}R_0} \pm 2.05|_{R_0}) \times 10^6 M_{\odot}$ . Our results slightly favor a core over a cusp in the mass profile. By minimizing the number of unbound stars in our sample we obtain a distance estimate of  $R_0 = 8.51^{+0.18}_{-0.14}$  kpc, where an a priori relation between  $R_0$  and SMBH mass from stellar orbits is used. Combining our mass estimate and the light profile we calculate  $M/\text{Ks} = 0.50 \pm 0.12 M_{\odot}/L_{\odot, \text{Ks}}$  for the central  $100''$ . This is consistent with a Chabrier IMF.

---

<sup>1</sup>Based on observations collected at the ESO Paranal Observatory (programs 060.A-9026, 70.A-0029, 071.B-0077, 073.B-0084, 073.B-0085, 073.B-0775, 077.B-0014, 078.B-0136, 179.B-0261, 179.B-2002, 183.B-0100, 087.B-0182)

## 5.1 Introduction

In the center of many late-type galaxies one finds massive stellar clusters, the nuclear star clusters (Phillips et al. 1996; Matthews & Gallagher 1997; Carollo et al. 1998; Böker et al. 2002). The nuclear clusters are central light overdensities on a scale of about 5 pc (Böker et al. 2002) compared to the light profile in the galaxies further out. Also the central light concentration of the Milky Way (Becklin & Neugebauer 1968), is probably a nuclear star cluster (Philipp et al. 1999; Launhardt et al. 2002). Nuclear clusters are comparably dense as globular clusters, but are typically more massive (Walcher et al. 2005). In some galaxies the clusters coexist with a supermassive black hole (SMBH), see e.g. Graham & Spitler (2009). The formation mechanism of nuclear stars cluster is debated (Böker 2010). There are two main scenarios: on the one hand formation of stars in dense star cluster, which are possibly globular clusters, followed by cluster infall (Andersen et al. 2008; Capuzzo-Dolcetta & Miocchi 2008). On the other hand in situ star formation from the cosmological gas inflow (Milosavljević 2004; Emsellem & van de Ven 2008).

Due to the proximity of the center of the Milky Way with a distance of  $R_0 \approx 8$  kpc (Reid 1993; Genzel et al. 2010), the nuclear cluster of the Milky Way can be observed in much higher detail than any other nuclear cluster. It is particularly useful to shed light on the properties and the origin of nuclear clusters in general. The access is hampered by the high foreground extinction of  $A_{K_s} = 2.42$  (Fritz et al. 2011). The vicinity makes high-resolution observations possible, which for practical reasons however cannot cover the full apparent angular size of  $r \approx 300''$  (Launhardt et al. 2002), and thus multiple data sets at different image scales need to be combined. Progress on the full extent of the nuclear cluster was also slowed down by the fact that in the last years most observations concentrated on the central parsec (Genzel et al. 2010).

The light in the very center ( $r \approx 0.4$  pc) is dominated by 6 Myrs old stars (Forrest et al. 1987; Krabbe et al. 1991; Paumard et al. 2006; Bartko et al. 2009) with a top-heavy IMF (Bartko et al. 2010; Lu et al. 2013). However, these stars do not dominate in number or mass. Most stars in the central  $r \approx 2.5$  pc formed more than 5 Gyrs ago (Blum et al. 2003; Pfuhl et al. 2011). The determination of the light profile is hampered by the severe extinction. Most profiles (Becklin & Neugebauer 1968; Haller et al. 1996; Philipp et al. 1999) show a central light excess of at least  $400''$  on top of the bulge. More recent works (Graham & Spitler 2009; Schödel 2011) claim that the nuclear cluster transits at  $150''$  to the bulge. Launhardt et al. (2002) state that there is another stellar component between nuclear cluster and bulge, a strongly flattened edge-on disk of  $3^\circ$  length, the nuclear disk.

The mass of the SMBH is well-determined to  $4.3 \times 10^6 M_\odot$  with an error of less than 10% (Gillessen et al. 2009; Ghez et al. 2008). In difference the mass of the nuclear cluster is less well constrained. The mass within  $r \leq 1$  pc is  $10^6 M_\odot$  with about 50 % systematic uncertainty (Genzel et al. 2010). In the central parsec the potential is dominated by the SMBH. Further the core in the profile of the stellar distribution (Buchholz et al. 2009; Do et al. 2009; Bartko et al. 2010) yields a small number of stars in the center and the deprojection is not well constrained. As a result also the newer works of Trippe et al. (2008) and Schödel et al. (2009) have still about 50 % mass uncertainty in the central parsec,

similar to Haller et al. (1996) and Genzel et al. (1996) who used fewer radial velocities. The mass determination outside the central parsec is based on radial velocities of late-type stars, either maser stars (Lindqvist et al. 1992; Deguchi et al. 2004), or stars with CO band-heads (Rieke & Rieke 1988; McGinn et al. 1989). The absence of proper motion information makes the derived masses outside the central parsec more sensitive to anisotropy than in the center. Further radial velocities of gas in the circumnuclear disk (CND) are useful for mass determination outside the central parsec (Genzel et al. 1985; Serabyn & Lacy 1985; Serabyn et al. 1986).

In conclusion, although the nuclear cluster of Milky Way is the closest such cluster, its mass and luminosity profiles are surprisingly bad constrained. In this paper we improve the constraints on these parameters.

- We extend the area in which all three velocity dimensions of stars are measured to  $r \approx 4$  pc.
- We construct a stellar number count based density map of the GC out to  $r_{\text{box}} = 1000''$ .

We use these data for employing Jeans modeling of the cluster, assuming isotropy and spherical asymmetry. These assumptions will be relaxed in the work of Chatzopoulos et al in prep.

In Section 5.2 we present our data, and describe the extraction of velocities in Section 5.3. In Section 5.4 we derive the surface density properties of the nuclear cluster and fit it with an empirical model. In Section 5.5 we describe the kinematic properties mostly qualitatively and derive the mass of the nuclear cluster in Jeans modeling. We discuss in Section 5.6 our results and conclude in Section 5.7. Where a distance to the GC needs to be assumed, we adopt  $R_0 = 8.2$  kpc (Genzel et al. 2010; Gillessen et al. 2013).

## 5.2 Data Set

In this section we describe the observations used for deriving proper motions, radial velocities, and the luminosity properties of the nuclear cluster. In this study we use the kinematics of the main, old stellar population of the GC. We explain in Section 5.3.3 how we avoid pollution by younger stars.

### 5.2.1 High Resolution Imaging

For deriving proper motions and for determining the stellar density profile in the center we use adaptive optics images with a resolution of  $\approx 0.080''$ . In the central parsec we use the same NACO/VLT images (Lenzen et al. 2003; Rousset et al. 2003) as described in Trippe et al. (2008) and Gillessen et al. (2009). We add to them images obtained in further epochs since then, in the 13 mas/pixel scale matching to the Gillessen et al. (2009) data set and in the 27 mas/pixel scale extending the Trippe et al. (2008) data set. The images are listed in Appendix 5.8.1.

For obtaining proper motions outside the central parsec we use adaptive optics images covering a larger field of view. These are four epochs of NACO/VLT images, one epoch of MAD/CAMCAO at the VLT (Marchetti et al. 2004; Amorim et al. 2006) and one epoch of Hokupa'a+Quirc (Graves et al. 1998; Hodapp et al. 1996) Gemini North images, see Appendix 5.8.1. Most images cover the Ks-band, some are obtained with H-band or narrower filters within the K-band. The VLT images are flat-fielded, bad pixel corrected and sky subtracted. In case of the Gemini data we use the publicly available images. These images are combinations of reduced images with nearly the same pointings.

### 5.2.2 Wide Field Imaging

To obtain the structural properties of the nuclear cluster outside of the central  $r_{\text{box}} = 20''$  we use two different additional data sets. Here, high resolution is less important than for the proper motion determination, but area coverage and extinction correction are the keys.

1. Closer to the center we use HST data<sup>2</sup>. The central  $r_{\text{box}} \approx 65''$  around Sgr A\* are covered in the filters M127, M139 and M153. Primarily, we use the images in M127 and M153 in our analysis. We optimize the data reduction compared to the pipeline in order to achieve Nyquist-sampled final pixels and to avoid having pixels without flux. We use MultiDrizzle to combine the different images in the same filter, with a drop size parameter of 0.6 with boxes and a final pixel size of 60 mas. We do not subtract the sky background from the images, since it is difficult to find a source free region from where one could estimate it. Since we use only point source fluxes this does not affect our analysis. We change the cosmic removal parameters to 7.5, 7, 2.3 and 1.9 to avoid removal of actual sources. Due to the brightness of the GC sources cosmics are only of minor importance. The final images have an effective resolution of  $0.15''$ .
2. On a larger scale we use the public VISTA Variables in the Via Lactea Survey (VVV) data. We use from data release 1 the central tile 333. The data contain flux calibrated, but not background subtracted images in J, H and Ks-band. The resolution is about  $1''$ . These images cover more than one square degree around the GC. We only use a  $r_{\text{box}} \approx 1000''$ . In the center the crowding is severe and nearly all sources are saturated in the Ks-band. This is not a limitation, since there we use the higher resolution images from NACO.

### 5.2.3 Spectroscopy

For obtaining spectra of the stars we use data cubes obtained with the integral field spectrometer SINFONI (Eisenhauer et al. 2003; Bonnet et al. 2003). We use data with the

---

<sup>2</sup> Based on observations made with the NASA/ESA Hubble Space Telescope, obtained from the Data Archive at the Space Telescope Science Institute, which is operated by the Association of Universities for Research in Astronomy, Inc., under NASA contract NAS 5-26555. These observations are associated with program 11671 (P.I. A. Ghez).

combined H+K-band (spectral resolution 1500) and K-band (spectral resolution 4000) grating. The spatial scale of the data vary between the smallest pixel scale ( $12.5 \text{ mas pixel}^{-1} \times 25 \text{ mas pixel}^{-1}$ ) and the largest scale  $125 \text{ mas pixel}^{-1} \times 250 \text{ mas pixel}^{-1}$ . The spatial resolution of the data correspondingly varies between 70 mas and  $2''$ . It has been matched at the time of the observations to the stellar density that increases steeply toward Sgr A\*. Thus, we can detect many sources in the center, and can sample also large areas at larger radii. Also, the actual resolution achieved depends on the availability of adaptive optics and the atmospheric conditions during the observations. We apply the standard data reduction SPRED (Abuter et al. 2006; Schreiber et al. 2004) for SINFONI data, including detector calibrations (such as bad pixel correction, flat-fielding, and distortion correction) and cube reconstruction. The wavelength scale is calibrated with emission line lamps and finetuned with atmospheric OH lines. Finally, we correct the data for the atmosphere by dividing with a late B-star spectrum and multiplying with a blackbody of the same temperature.

## 5.3 Derivation of Velocities

The primary constraint for estimating the mass of the nuclear cluster is velocity data. Due to the small distance of the nuclear cluster it is possible to measure individual proper motions and radial velocities. That is more suitable for calculating velocity dispersions than integrated dispersions, see Section 5.3.2. Thus, all our velocity dispersions are derived from individual velocities. As a result, too conservatively estimated errors for the velocities, cause a bias in the calculated dispersions, which is different from directly measured dispersions. Therefore, realistic error estimates are essential in our analysis. Further, it is necessary to estimate the uncertainty of the errors for deciding whether data are reliable, and for estimating the final uncertainties.

### 5.3.1 Proper Motions

We combine in this work proper motions obtained from four different data sets: central field, extended field, large field and outer field, see Figure 5.1. Trippe et al. (2008) used the extended field. In the central field the stellar crowding is high and a different analysis is needed than further out. Also, the number of epochs and their similarity decrease from inside out which requires a more careful and separated error analysis. We give here a short overview of the data and methods used. The details are explained in Appendix 5.8.1.

- In the central ( $r \leq 2''$ ) we use the same method for astrometry as in Gillessen et al. (2009). We now track stars out to  $r_{\text{box}} \approx 2''$ . With this increased field of view, we more than double the number of stars compared to Gillessen et al. (2009). Also some of the old, late-type stars have significant accelerations (Gillessen et al. 2009), but the curvature of their orbits is not important compared to their linear motion, and thus the linear motion approximation is sufficient. This sample consists of 80 stars.

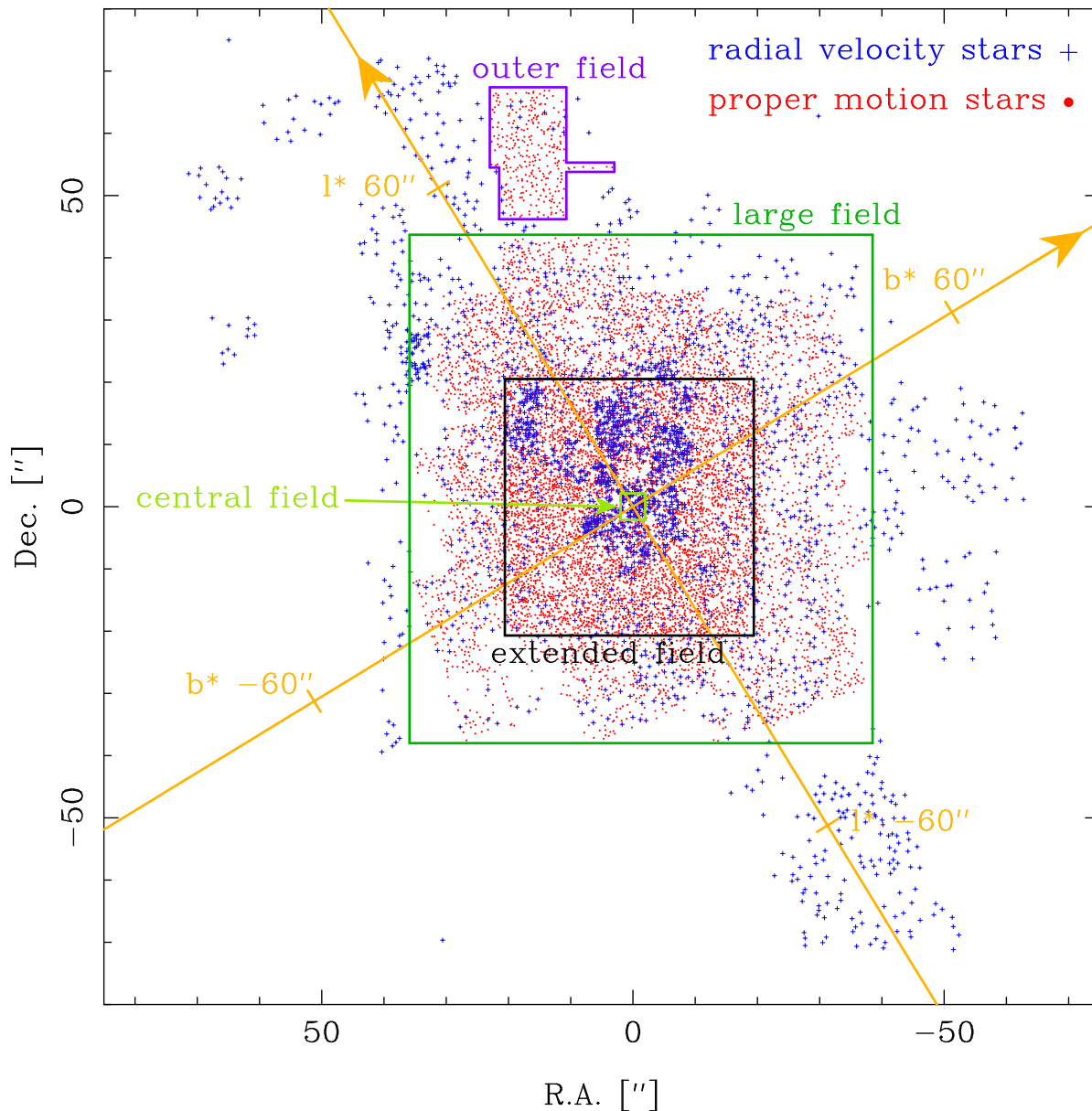


Figure 5.1 Distribution of stars with radial velocities and proper motions. For the proper motions we combine four different data sets: the central field in the central  $2''$ . The extended field from  $2''$  outwards to  $\approx 20''$ , the large field from there outwards to  $\approx 40''$  and a separate, outer field in the north. The yellow lines define our coordinate system, shifted Galactic coordinates  $l^*/b^*$  (Deguchi et al. 2004; Reid & Brunthaler 2004) where the center is shifted to Sgr A\*.

Thus, here the Poisson error of the dispersion derived is much larger than all other errors, such as the one originating in the uncertainties of the velocity errors.

- In the radial range between a box radius of  $2''$  and  $20''$  (extended field) we expand slightly on the data and method used by Trippe et al. (2008). We do not change the field of view and the selection of well isolated stars compared to Trippe et al. (2008). The number of stars with velocities has increased a bit due to the addition of new images. In total we have dynamics for 5835 stars in this field. We obtain a proper motion dispersion of  $\sigma_{1D} = 2.671 \pm 0.018$  mas/yr using all stars and averaging the two dimensions. The error includes only Poisson noise, which is likely the dominating error, because the dispersion value and error are the same when splitting the sample up into a fainter and a brighter half.
- Outside a box radius of  $20''$  (large field) nearly no proper motions were available, with the exception of a small area in Schödel et al. (2009), which however the authors did not use for their analysis. From the images we collected with sufficiently good AO correction we obtain velocities for 3831 stars. For the proper motion dispersion we obtain  $\sigma_{1D} = 2.333 \pm 0.019$  mas/yr. The comparison of the dispersion for fainter and brighter stars shows that the error on the dispersion (after subtracting the velocity errors in quadrature) of the fainter stars is  $2\sigma$  larger than for the brighter stars. Since this is barely significant we assign Poisson errors to the dispersions for the large field, too.
- For expanding our coverage of proper motions to  $70''$  we use the outer field. These data do not cover the full circle around Sgr A\*, but only a small field. We have two epochs for this field: Gemini data from 2000 and NACO data from the 29<sup>th</sup> May 2011. In this field we have velocities for 379 stars. We exclude in this field the faintest third of all stars, because we obtained a higher velocity dispersion for them than for the brighter two thirds. We also exclude stars which might be affected by an insufficient distortion correction. From the 297 stars with good velocities we obtain  $\sigma_{1D} = 1.792 \pm 0.073$  mas/yr using both dimensions together. We assume again that the Poisson error dominates over other error sources for the stars selected.

In the literature there are only few proper motion measurements outside the central 2 pc. Clarkson et al. (2012) measured the velocity dispersion of the field around the Arches cluster located at  $l^* = 635''$  and  $b^* = 227''$ . They measured  $\sigma_l = 2.72 \pm 0.12$  mas/yr and  $\sigma_b = 1.69 \pm 0.1$  mas/yr.

### 5.3.2 Radial Velocities

Since we can resolve the stellar population in the GC, the line of sight velocity dispersion can be obtained in two ways, either as direct dispersion measurement of the integrated light for a certain area or by measuring many radial velocities and calculating the dispersion from them. McGinn et al. (1989) used the first method. They measured the velocity dispersion

in overlapping apertures of  $20''$ . The pointing-to-pointing variations are larger than what one would expect from the measurement errors (see their Figure 4). This is probably due to individual bright stars that can dominate the measurement. The second method, using only resolved stellar spectra circumvents that problem. An additional advantage is that a lower spectral resolution suffices then. Due to the advent of integral field spectroscopy obtaining sufficient area coverage is less of a problem as it used to be.

For measuring the radial velocities we use the strong and sharp CO band head features between 2.29 and 2.37  $\mu\text{m}$ . We cross-correlate the spectra with a template and correct the radial velocities to the LSR. The statistical error on the radial velocity is obtained by the uncertainty of the best crossmatch in the correlation. This error is typically larger than 4 km/s. The median velocity error obtained in this way is 7 km/s. For a subset of more than 300 stars we have velocities available extracted from two or more entirely independent different data sets, which allows us to check the velocity error. The median velocity difference is 8.4 km/s, consistent with our error estimate. In total we have CO radial velocities for 2425 stars. The line-of-sight velocity dispersion of these stars is  $\sigma_z = 102.51 \pm 1.48$  km/s after the minor correction for the velocity error of 8 km/s.

Hence, the statistical uncertainty of the velocities is small and negligible. However, this check does include systematic problems due to calibration errors or template mismatch. A possibility to check our velocity accuracy is the comparison with the LSR. No relative motion is expected between the average motion of the solar neighborhood and the nuclear cluster in radial direction. The determination of the LSR is difficult in the direction of Galactic rotation (Dehnen & Binney 1998; Schönrich et al. 2010; Bovy et al. 2012), but here only the radial component  $U$  matters. We use the LSR calculation of the ATCA array<sup>3</sup>, which uses  $U=10.25$  km/s, consistent with the recent values of 10.5 km/s (Bovy et al. 2012) and  $11.1 \pm 1.2$  km/s (Schönrich et al. 2010). The nuclear cluster is rotating in the Galactic plane (McGinn et al. 1989; Lindqvist et al. 1992; Genzel et al. 1996; Trippe et al. 2008). Since our coverage is not homogeneous we cancel the rotation by using stellar number counts weighted bins in  $|l^*|$ , see Figure 5.2. The mean radial velocity over all bins is  $5.7 \pm 3.9$  km/s, consistent with 0. Reverting the argument, assuming that the calibration is correct, we can conclude that the nuclear cluster is radially moving less than 15 km/s relative to the LSR. In conclusion it seems likely that Poisson errors are dominating the dispersion uncertainty for our radial velocity sample, and we only include those in the final analysis.

In order to expand our radial velocity dataset to larger radii we use the radial velocities from the literature (Lindqvist et al. 1992; Deguchi et al. 2004). Lindqvist et al. (1992) used the VLA for detecting OH masers in a blind Galactic Center survey. This survey covered the GC out to  $\approx 3000''$  from Sgr A\*. Stars with an absolute velocity greater than 217 km/s were not detectable due to the limited spectral range. Since only very few stars have a velocity close to this value probably only very few stars were missed. Lindqvist et al.

<sup>3</sup><http://www.narrabri.atnf.csiro.au/cgi-bin/obstools/velo.cgi?radec=17%3A45%3A40+-29%3A00%3A28&velo=0&frame=bary&type=radio &date= 03%2F07%2F11&freq1=0&freq2=100&telescope=atca>

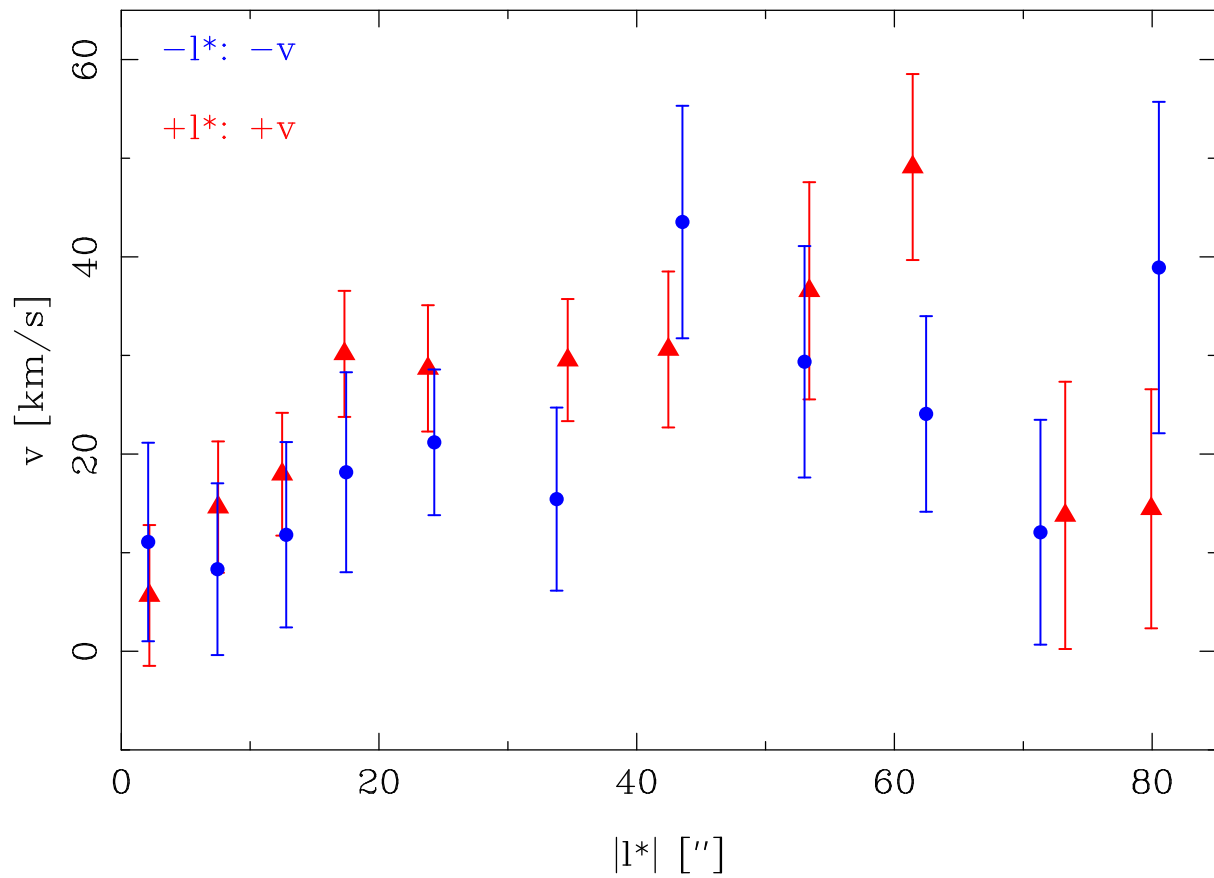


Figure 5.2 Mean radial velocities along the Galactic plane for our SINFONI sample. The signs of the velocities at negative  $l^*$ -values are reversed for better comparison.

(1992) subdivided the masers into two classes according to their age (as estimated from the the expansion velocity  $v_{\text{exp}}$  of the masers), but found that both follow the same projected rotation curve, with the same sign and orientation as the Galactic rotation. The rotation does not follow solid body rotation, it decreases with increasing distance from Sgr A\*. Deguchi et al. (2004) targeted large amplitude variables within  $950''$  from Sgr A\* as SiO Masers with the 45 m Nobeyama radio telescope. The beam of the observations was  $40''$ . Their sample probably contains multiple-identifications, as there are suspiciously many close neighbors ( $r < 40''$ ) that have velocity differences of less than 5 km/s. We clean the sample and remove also stars already present in the Lindqvist et al. (1992) sample. As a side product of this matching, we confirm that the typical velocity uncertainty is less than 3 km/s as stated in Lindqvist et al. (1992) and Deguchi et al. (2004). Due to the big position errors for the masers it is difficult to find the corresponding IR stars. We therefore exclude from the combined list the eleven stars that overlap spatially with the areas in which we obtained spectra, with the aim of avoiding using stars twice. Overall we use 274 radial velocities outside the central field. After exclusion of outliers, see Section 5.3.3, 261 stars remain in our final maser sample.

### 5.3.3 Sample Cleaning

In order to probe the gravitational potential we need to use a relaxed population. The main population in the GC is indeed older than the relaxation time (Alexander 2005; Genzel et al. 2010), or at least close to relaxed (Merritt 2010). The more massive stars have already evolved into giants, while the less massive stars on the main sequence remain unobservable due to the high stellar crowding. The giants share the dynamic and distribution properties of the main stellar population in the GC, if they are not subject to violent destruction (Dale et al. 2009). Spectroscopically the old stars are easily identified as late-type stars.

The young stars are dynamically not relaxed, and follow different radial profiles. We thus exclude the young stars from our sample. These are the early-type stars, the WR-, O- and B-stars (Paumard et al. 2006; Bartko et al. 2009, 2010) and the red supergiant IRS7, that has the same age as the WR/O-stars of around 6 Myrs (Blum et al. 2003; Pfuhl et al. 2011). We do not exclude the intermediate-age stars with ages of about 20 to 200 Myrs that constitute about 10% of all old stars (Pfuhl et al. 2011). Although, a priori relaxation is not guaranteed for that age, observationally no difference is detected in dynamics or radial distribution (Blum et al. 2003; Pfuhl et al. 2011) between them and the majority of the stars, which are more than 5 Gyrs old (Pfuhl et al. 2011). Apart from the age selection we also exclude foreground sources and stars which due to their high measured velocity most likely are outliers.

Since the ratio of young to old stars is a strong function of radius (Krabbe et al. 1991; Buchholz et al. 2009; Bartko et al. 2010; Do et al. 2013), the selection criterion for old stars is radius dependent. In the central arcsecond spectroscopically one has identified more early-type stars than late-type stars, see Figure 1 of Gillessen et al. (2009). Since the KLF slope of the young stars in the central arcsecond (Bartko et al. 2010) is identical to

the one of the late-type stars (Buchholz et al. 2009; Pfuhl et al. 2011), the majority of the stars without spectral identification is probably young here. Outside the central arcsecond the fraction of young stars decreases, but remains high for  $r \leq 2''$  (Buchholz et al. 2009; Do et al. 2009; Bartko et al. 2010). We therefore include for  $r \leq 2''$  only stars in our sample that are spectroscopically<sup>4</sup> identified as late-type stars.

Outside of  $r \geq 2''$  there are clearly less early-type than late-type stars (Bartko et al. 2010; Do et al. 2009; Buchholz et al. 2009; Pfuhl et al. 2011). In this radial range we include all stars, for which we did not record an early-type spectrum. This selection is not radius independent, because we have a better spectral coverage close the center (Bartko et al. 2010): at  $2''$  we have spectral identifications for about 50% of the stars, for which we have dynamics. This fraction decreases to 13 % at  $20''$ . Further, our spectroscopic completeness decreases toward fainter stars. In conjunction with the top-heavy IMF for young stars in this radial range (Bartko et al. 2010; Lu et al. 2013) this means that the pollution of our sample with young stars is reduced compared to what would follow from the overall fractions. For example, we see that stars without spectra cluster around  $m_K = 15.5$  - a signature of the red clump. Quantitatively, we calculate the number young stars that we still expect in our sample by a simple completeness correction, multiplying in each radius and magnitude bin the number of unidentified stars with the measured early-type fraction. We obtain that we include about 140 early-type stars in the extended sample of 5864 stars. The pollution fraction of 2.4% increases only to 3.7% in the inner radial half. For  $r > 20''$  we even find only 6 early-type stars, less than 1% of all stars with spectra. Thus, we are confident that our dispersions (or higher moments) are not biased in a significant way.

From the radial trend further in it is expected that there are very few early-type stars outside of  $20''$ . Surprisingly, Nishiyama & Schödel (2013) found from narrowband imaging a rather high early-type candidate fraction of  $\approx 7$  % for bright ( $m_K < 12.25$ ) stars. At  $r > 0.5$  pc they found 35 stars. We have spectra for 24 of them, and see clear late-type signatures in 22 of them. Only 2 of our spectra show early-type signatures. Thus, the contamination fraction is around 90 %, and not 20 % as claimed by Nishiyama & Schödel (2013). The problem in their analysis is probably that they misidentify stars from the population of warm giants (Pfuhl et al. 2011).

We also exclude stars, which due to their low extinction belong to the Galactic disk or bulge, similar to what is done in Buchholz et al. (2009). The selection criterion for foreground stars is  $H - K_s < 1.3$ , except in regions with unusual extinction where we use a local value. In total we exclude 97 stars as foreground stars. For many stars no H-band magnitude is available. These stars are included in our sample, since it is obvious from the more than 7000 stars with H-band information that only few stars belong to the foreground. We do not make any attempt to correct for stars in the background, since that will even be less of a problem than the foreground.

Outside of  $20''$  we have at most four epochs for proper motions and the velocities might be affected by outliers. The velocity histogram for stars at  $r > 20''$  shows an excess of stars at velocities above  $|9|$  mas/yr compared to the Gaussian distribution obtained from stars

<sup>4</sup>Here and everywhere we use our SINFONI spectra for spectral classifications.

between  $7''$  and  $20''$ . In order to avoid such a bias to high velocities we exclude proper motions which are faster than  $1.7\times$  the escape velocity, which we calculate using the mass profile in Genzel et al. (2010). This criterion excludes 22 stars. Afterwards the velocity histogram for the outer stars looks more similar to the one for the radial range from  $7''$  to  $20''$  (Section 5.5.5). In principle, it is also possible that the high velocities are not flukes. They could be high velocity stars, similar to the hypervelocity stars (Brown et al. 2005); Since we are only interested in the relaxed stars, it is correct to exclude them in any case.

For the radial velocities most of the problems discussed for the proper motions do not exist: a star is per definition old when it has CO band heads. Also it is very unlikely to measure a too high fluke velocity. In the maser sample there are some surprisingly fast stars, see Lindqvist et al. (1992), Deguchi et al. (2004) and Section 5.5.5. After spatial binning of these stars (Section 5.5.1) we inspect the binwise velocity histograms and exclude stars that are apparent outliers. We exclude this way 13 of the 274 stars. The scatter in mean velocity and dispersion of the bins is notably reduced by this procedure.

## 5.4 Luminosity Properties of the Nuclear Cluster

In order to be able to derive a mass profile from the velocities it is necessary to know the spatial distribution of the velocity tracers (Binney & Tremaine 2008; Genzel et al. 1996; Schödel et al. 2009; Das et al. 2011). Given the inhomogeneous and spatially incomplete nature of our dynamics sample, it would be very cumbersome (if not impossible) to derive the spatial distribution from that data set. There are two ways how this can be overcome.

- One can use the luminosity profile of the cluster. The usual assumption of a constant mass to light ratio will fail, however, because of the young stars in the center that dominate the luminosity. Hence, spectral information is needed in addition.
- A better way for the GC cluster is to extract the surface (star) density profile, not requiring that the dynamics are known for these stars. Still, one then needs to correct for the early-type stars that contribute an important fraction of all stars in the center.

After an overview on the literature of the large scale properties of the nuclear cluster in Section 5.4.1, we obtain in Section 5.4.2 density maps, the radial profile of the nuclear cluster and also the profile in direction of and perpendicular to the Galactic plane. Assuming spherical symmetry we then empirically fit the radial profile in Section 5.4.3 to obtain the deprojected properties for the Jeans modeling (Section 5.5.4). In the Jeans modeling we will actually fit our surface density and dynamics data at once, since also the dynamics yields a weak constraint on the tracer profile. However, in order to be able to check whether the obtained solutions are realistic we fit the density profile beforehand. In Section 5.4.4 we use the density maps to separate nuclear cluster and nuclear disk. Finally, we obtain in Section 5.4.5 the total luminosity of the nuclear cluster.

### 5.4.1 Literature about the Light Profile of the GC

The first measurement of the K-band luminosity profile in the center of the Milky Way was performed by Becklin & Neugebauer (1968). This work and Haller et al. (1996) obtained a surface brightness profile of  $\Sigma \propto r^{-0.8 \pm 0.1}$  between  $6''$  and  $300''$ . Philipp et al. (1999) decomposed the GC emission in bright stars ( $m_K \lesssim 14$ ) and diffuse background ( $m_K \gtrsim 14$ ). Their measurement indicated that the increase in flux in the central  $20''$  is caused by few bright stars. This has been confirmed explicitly by the discovery of the early-type stars and their steep density profile (Bartko et al. 2010). The data from also Philipp et al. (1999) show that the diffuse flux decreases by more than a factor five from the central core following a power law slope of  $-0.6$ . In all these measurements the central light excess on top of the bulge is relatively extended, i.e. larger than  $250'' \approx 10$  pc, see Figure 5.3.

In contrast to the aforementioned measurements, the profiles from Graham & Spitler (2009) and Schödel (2011) flatten at about  $80''$  (Figure 5.3) indicating that the bulge dominates already there. A possible reason for the discrepancy might be the omission of sky background subtraction in these data sets. Graham & Spitler (2009) used the light profile from Schödel et al. (2008) constructed from public 2MASS images, while Schödel (2011) used SIRIUS images of the GC. Both data sets are not optimized for diffuse flux detection in the GC. 2MASS as an all sky survey is not optimized for the high background in the GC. The sky background in Ks is around  $13 \text{ mag}/''^2 = 4.2 \text{ mJy}/''^2$  in Paranal. This is also approximately the bulge surface brightness in the data of Graham & Spitler (2009). This interpretation is strengthened by the fact that Vollmer et al. (2003) using 2MASS and subtracting a sky background obtained a smaller Ks-flux of about  $1 \text{ mJy}/''^2$  at distance of  $200''$  to Sgr A\*. The same problem might affect the SIRIUS GC data, a project that was designed to characterize the properties of point sources in the GC. For the space-based COBE/DIRBE data used by Launhardt et al. (2002), the background is much lower in the NIR than for ground-based data sets. Their data show that the Galactic bulge is not as bright as obtained by Graham & Spitler (2009) and Schödel (2011). Also our VISTA data support the results of Becklin & Neugebauer (1968), Haller et al. (1996), and Philipp et al. (1999): the nuclear light excess is important out to  $300''$  (Figure 5.3). Hence, Graham & Spitler (2009) and, Schödel (2011) might have mistaken the sky background emission as a detection of the bulge.

Launhardt et al. (2002) corrected the COBE/DIRBE data for extinction and combined it with the radial profile of Philipp et al. (1999) to show that there is another component in size between the nuclear cluster and the Galactic bulge, which they called the nuclear disk. It is strongly flattened with an axis ratio of approximately 5:1 and has a major axis FWHM of about 300 pc. The authors derived a size of the nuclear cluster of  $\approx 10 - 20$  pc and a steepening of the radial slope toward its outskirts. However, since they missed higher resolution data at the outer edge of the nuclear cluster, they could not determine the shape of the nuclear cluster very well. Catchpole et al. (1990) and Alard (2001) also see the flattening inside the main bulge on a scale of about  $1^\circ$  using number counts of bright stars.

The rotation of the nuclear cluster with the Galaxy probably causes a flattening aligned

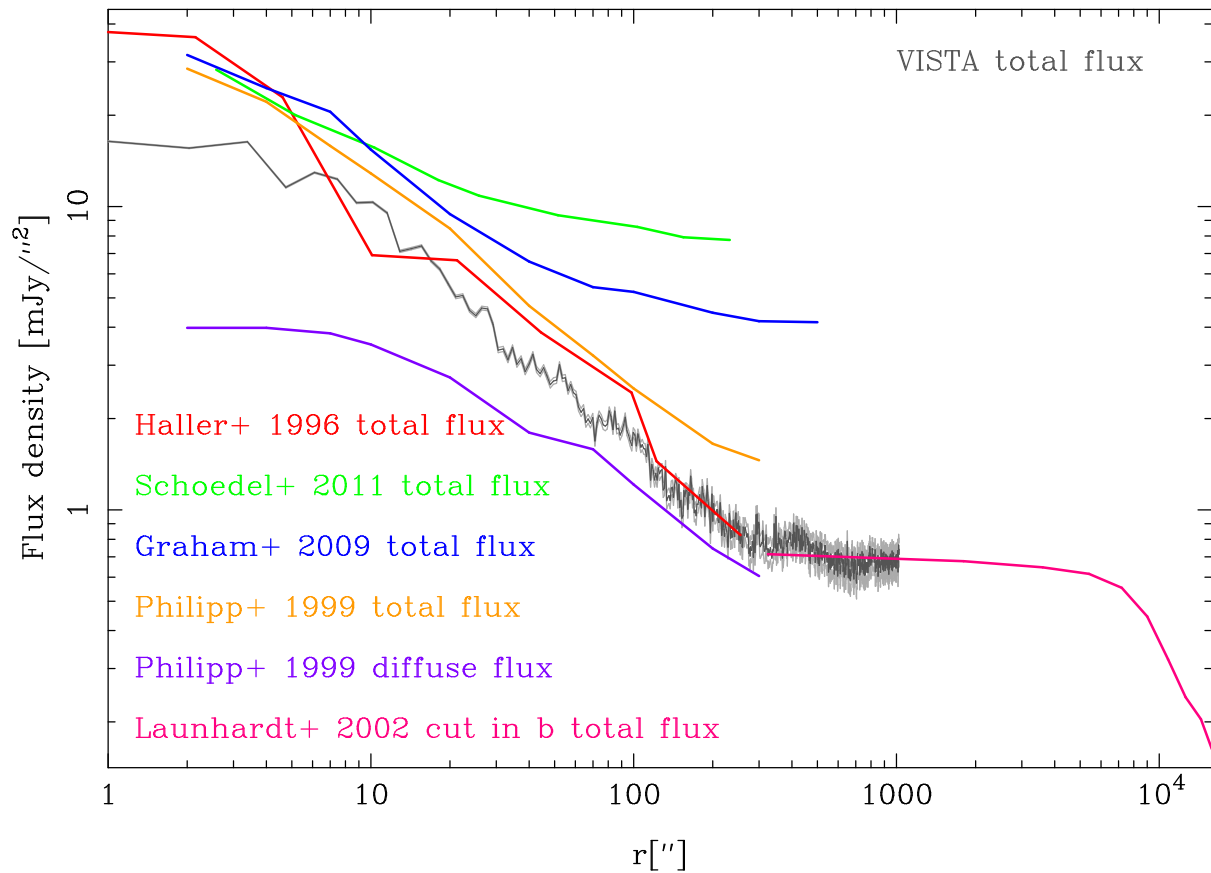


Figure 5.3 Ks-surface brightness profile data of the central Galaxy from Haller et al. (1996), Philipp et al. (1999), Launhardt et al. (2002), Graham & Spitler (2009), Schödel (2011) and VISTA; the nuclear cluster profiles from Haller et al. (1996), Philipp et al. (1999), Graham & Spitler (2009), and Schödel (2011) are obtained from ground based K(s)-band data. From Launhardt et al. (2002) we show the cut through the Galactic Center at  $l=0$  using the  $2.2 \mu\text{m}$  obtained with COBE/DIRBE (their Figure 2a). All data are not corrected for extinction. The central core in the VISTA data is caused by saturation.

to the Galactic plane. Vollmer et al. (2003) mention that the Ks-isocontours follow an ellipsoid of 1.4:1 in the range of about  $200''$ . However, the radial profile of the flattening is not well known for the nuclear cluster. We use in Section 5.4.2 different data sets to measure the radial profile and its flattening.

### 5.4.2 Deriving Density Profiles

For deriving the light properties of the nuclear cluster we use three different data sources, because the images either do not cover the full area of interest or are highly incompletely in the center. For the largest scales ( $r_{\text{box}} = 1000''$ ) we use VISTA images with  $1''$  resolution. Within  $r_{\text{box}} = 66''$  we use WFC3/IR images with a resolution of  $0.15''$ . In the central  $r = 20''$  we use diffraction limited NACO images with  $0.08''$  resolution. In the overlap regions we use the data with the higher resolution. We use both methods to construct the density profile, stars counts and the surface brightness, allowing us to obtain a robust error estimate, except for the WFC3/IR data which are obtained in a different band such the resulting surface brightness profile would not be comparable.

We use the following steps to derive the stellar distribution:

- We exclude stars younger than 10 Myrs from our sample.
- We correct the star counts for completeness.
- We correct for extinction using two NIR filters. The resulting map is still patchy in some areas because of the optical depth being too high for correction.
- We create masks to exclude the emission from these areas, comparing the four quadrants of the maps assuming such symmetry in  $|l^*|$  and  $|b^*|$ .
- We also exclude very bright foreground stars and GC clusters like the Arches.
- The excluded areas are then replaced with the average of the other areas at the same  $|l^*|$  and  $|b^*|$  to conserve symmetry.

Not all steps are necessary for all data subsets, and the procedures are described in detail in Appendix 5.8.2.

In Figure 5.4 we present the profiles obtained. The profiles obtained from the integrated flux and from stellar number counts are similar but not identical within the errors. The differences are probably caused by imperfection in the extinction treatment. Splitting the number counts based profile into a  $|l^*|$  and  $|b^*|$  component (Figure 5.5) yields profiles similar to the model of Launhardt et al. (2002). For the NACO and WFC3 data the number counts in  $|l^*|$  and  $|b^*|$  are measured using the half of the circular aperture which is closer to  $|l^*|$  respectively to  $|b^*|$ . With this method we use all available information and are such able to measure the small flattening at  $r < 66''$ . Further out the flattening is so large that this method would reduce the signal. There we use for the density along major and minor axis only the data which is closer than  $39''$  to the axes.

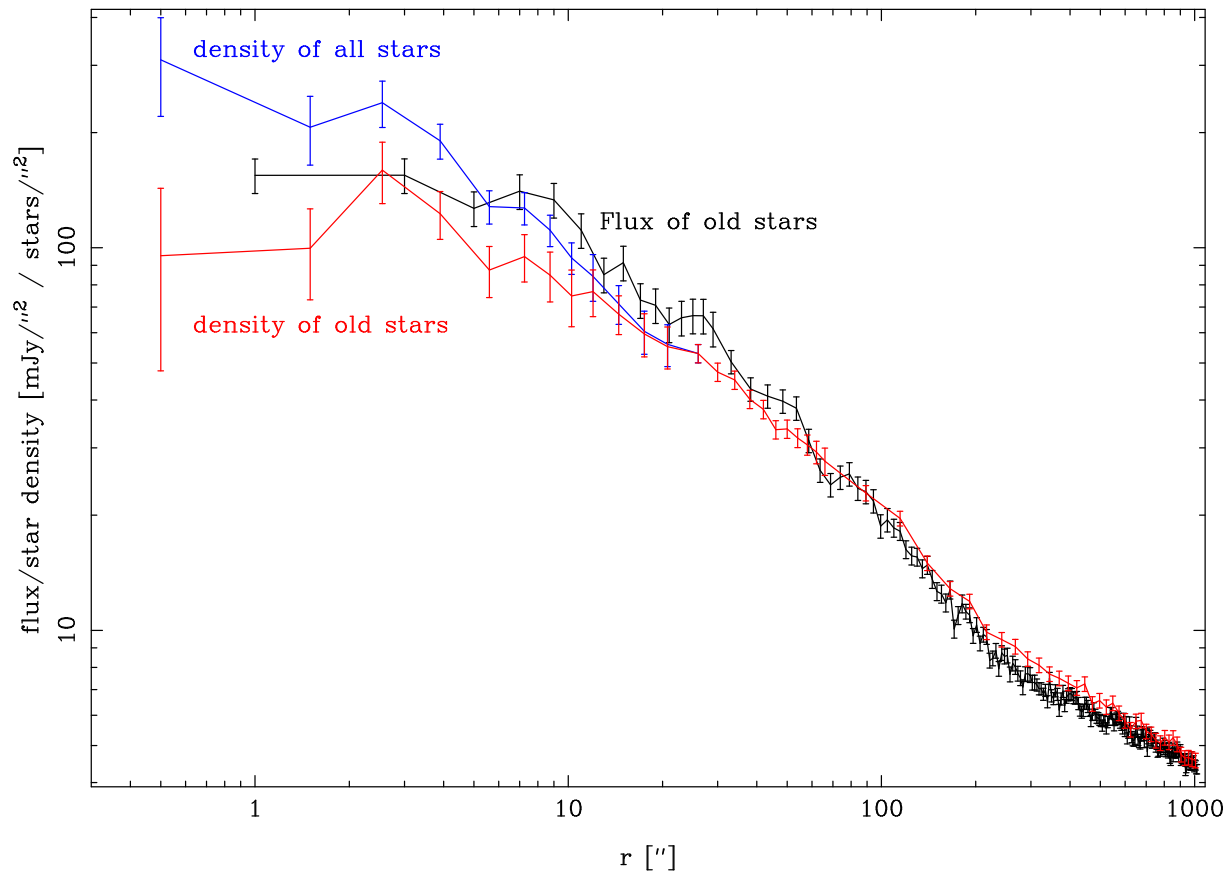


Figure 5.4 Radial distribution of stars. We construct the radial stellar/flux density profile from NACO, WFC3/IR and VISTA images (in order of increasing field of view).

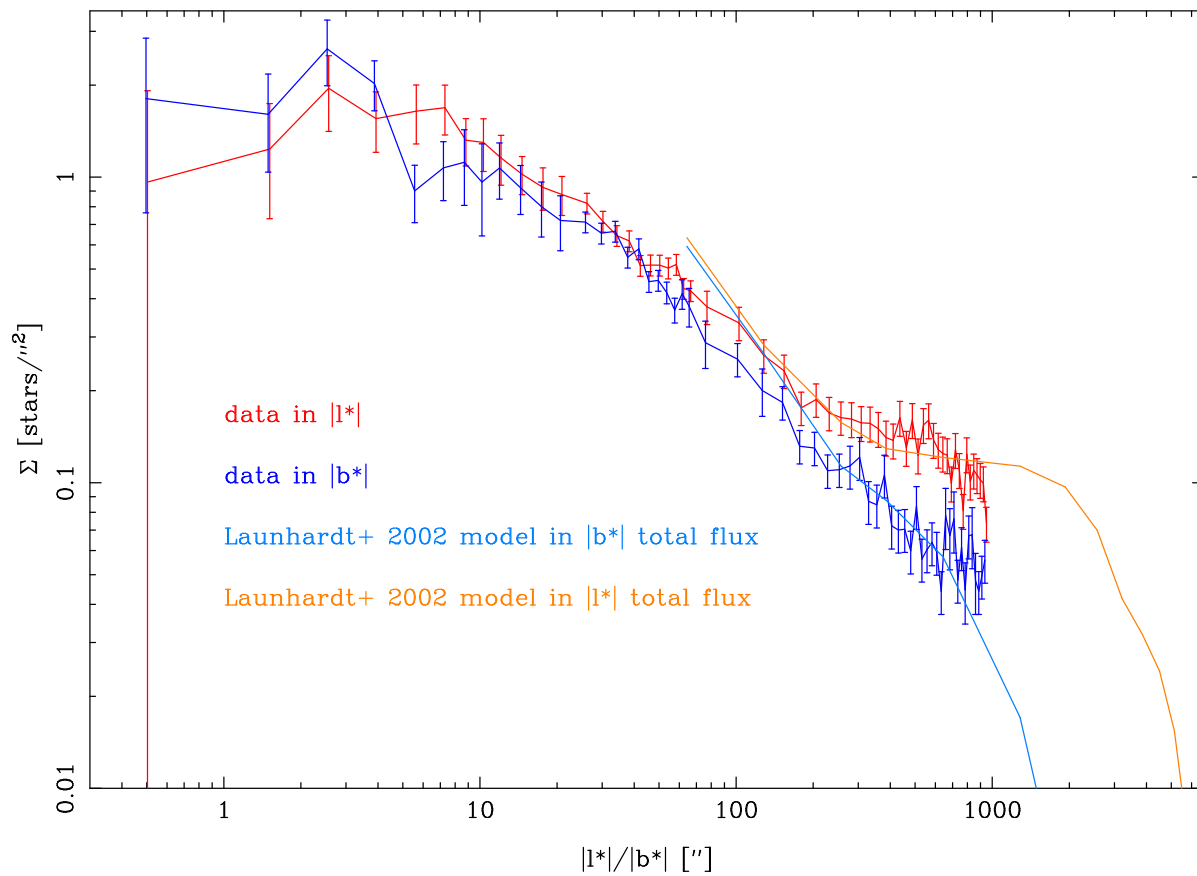


Figure 5.5 Stellar density in and orthogonal to the Galactic plane. From Launhardt et al. (2002) we show the model presented in their Figure 12, scaled to our data. Their model does not include Galactic Disk and bulge, which are included in our data.

### 5.4.3 Spherical Fitting of the Stellar Density Profile

We now fit the density profile assuming spherical symmetry. This assumption apparently is not correct. However, the cluster is close to spherical in the center such that this assumption does not lead to large errors there, and also the mass profile obtained from Jeans modeling (Section 5.5.4) is not very sensitive to this assumption. For the Jeans modeling we need a space density profile. Nevertheless, here we parametrize the projected density in order to compare our data set with the literature. Usually projected surface densities in the GC were fitted with (broken) power laws (Genzel et al. 2003). A generalization of that model is the Nuker profile (Lauer et al. 1995):

$$\rho(r) = \rho(r_b) 2^{(\beta-\gamma)/\alpha} \left(\frac{r}{r_b}\right)^{-\gamma} \left[1 + \left(\frac{r}{r_b}\right)^\alpha\right]^{(\gamma-\beta)/\alpha} \quad (5.1)$$

Therein,  $r_b$  and  $\rho_b$  are the break radius and the density at the break radius. The exponent  $-\gamma$  is the inner (usually flatter) power law slope, and  $-\beta$  is the outer (usually steeper) power law slope. The parameter  $\alpha$  is the sharpness of the transition; a large value of  $\alpha$  yields a very sharp transition, essentially a broken power law. Using  $\alpha = 100$  (fixed) our fits can be compared with the literature.

Firstly, we try to fit the full data range of the stellar and flux density profiles. In both cases the reduced  $\chi^2$  of these fits is much larger than 1, see Rows 1 and 2 of Table 5.1. In case of the flux density the fit even transits from a steeper profile in the center to a flatter further out. The reason for this behavior is the break feature around  $220''$ . This feature is mainly caused by the flattening of the nuclear cluster/disk in the Galactic plane (Figure 5.5). Due to this flattening our assumption of spherical symmetry is not fulfilled outside of this break. Hence, we constrain the following fits to  $r < 220''$  (Table 5.1).

Rows 3 and 4 in Table 5.1 give our fits for stellar number counts and the flux profile, respectively. Row 3 can be directly compared to the literature. Buchholz et al. (2009) conducted the largest area study so far. They obtained  $\beta = -0.17 \pm 0.09$  and  $\gamma = 0.70 \pm 0.09$  for  $R_b = 6.0''$ . This fit is broadly consistent with our data, although we obtain for this radial range no clear sign for a power law break. The break radius of Buchholz et al. (2009) is smaller than ours, although its error is not given. The binned data of Buchholz et al. (2009) look similar to our data. The same is true for the data in Bartko et al. (2010) who do not attempt to fit the profile. These works find a very weak increase of the density with radius inside of  $\approx 5''$  and then a somewhat stronger decrease of the density with radius further out. This is also the case in Do et al. (2009, 2013). Do et al. (2013) used data out to  $14''$  and find  $\beta = 0.16 \pm 0.07$ .

Overall, most data seem to be consistent with a break radius for the late-type stars around  $20''$ . When counting stars regardless of their age, a smaller break radius of about  $8''$  is found (Genzel et al. 2003; Schödel et al. 2007). Do et al. (2013) were able to fit their density with a single power law, but Buchholz et al. (2009) going to larger radii and using photometric classifications of stars needed a broken power law. Also for our much larger radial coverage, a single power law fails to fit our data, even when we restrict our data

Table 5.1. Nuker fits of the surface density profile

No.	data source	radial range	$\alpha$	$\chi^2/\text{d.o.f}$	$R_b$ ["]	$\Sigma(R_b)$	$\beta$	$\gamma$
1	star density	all r	100	143.2/55	$11 \pm 21$	$1.21 \pm 0.45$	$0.669 \pm 0.007$	$0.171 \pm 0.089$
2	flux density	all r	100	747.95/205	$350 \pm 14$	$6.94 \pm 0.15$	$0.420 \pm 0.010$	$0.677 \pm 0.006$
3	star density	$r < 220''$	100	26.66/25	$23 \pm 3$	$0.86 \pm 0.09$	$0.771 \pm 0.018$	$0.277 \pm 0.054$
4	flux density	$r < 220''$	100	74.11/50	$24 \pm 2$	$71.2 \pm 4.6$	$0.934 \pm 0.016$	$0.304 \pm 0.030$
5	star density	$r < 90''$	100	11.43/20	$13 \pm 3$	$1.11 \pm 0.15$	$0.645 \pm 0.040$	$0.186 \pm 0.084$
6	star density	$r < 220''$	1	15.28/25	$21 \pm 14$	$0.84 \pm 0.28$	$0.972 \pm 0.089$	$0.059 \pm 0.146$
7	flux density	$r < 220''$	1	50.71/50	$10 \pm 3$	$110 \pm 20$	$1.048 \pm 0.040$	$-0.163 \pm 0.148$

to the range for which we have spectral classifications ( $r < 90''$ ). The best fit broken power law has  $\chi^2/\text{d.o.f} = 11.43/20$  (Row 5 in Table 5.1), while a single power law yields  $\chi^2/\text{d.o.f} = 53.12/23$ .

When we set  $\alpha = 1$ , the  $\chi^2$  of both fits gets considerably better (Rows 6 and 7 in Table 5.1). This indicates that the transition between the two slopes is softer than for a broken power law. Figure 5.6 shows our data together with these fits.

The older literature used single power law profiles to describe the density profile. Between  $20''$  and  $220''$  our data can be fit relatively well by a single power law of  $0.765 \pm 0.018$  (stellar density) and of  $0.915 \pm 0.015$  (flux density). These slopes show again that the two data sets are not consistent. Becklin & Neugebauer (1968), Allen et al. (1983), Haller et al. (1996) obtain a slope of 0.8, while Philipp et al. (1999) obtain a flatter slope of 0.6. None of these works uses two color information to correct for extinction. The single power law fit of Catchpole et al. (1990) with a slope of 1.1 in the radial range from  $140''$  to  $5700''$  is not well comparable to our data set.

For our Jeans-modeling (Section 5.5.4) we need a parametrization of the space density profile  $n(R)$ , which is connected to the observable surface density profile  $\Sigma(r)$  by the following Abel integral:

$$\Sigma(r) = 2 \int_R^\infty n(R) R dR / \sqrt{R^2 - r^2} \quad (5.2)$$

We use the spherical  $\eta$ -model (Tremaine et al. 1994):

$$n(R) = \frac{\eta}{4\pi} \frac{K}{R^{3-\eta}} \frac{a}{(R+a)^{1+\eta}} \quad (5.3)$$

Therein  $K$  is the total mass of the model as used in Tremaine et al. (1994). In our case, it is the total flux, respectively the star counts.  $a$  is scale of the core of the model. The density slope is  $\eta - 3$  within the core and  $-4$  at  $\infty$ . The  $\eta$ -model has the advantage that its solutions are usually positive distribution functions which we will employ in Chatzopoulos et al. in prep. More complex profiles, like for example a Nuker model, contain many poorly constrained parameters for our data set. In the Jeans modeling (Section 5.5.4)

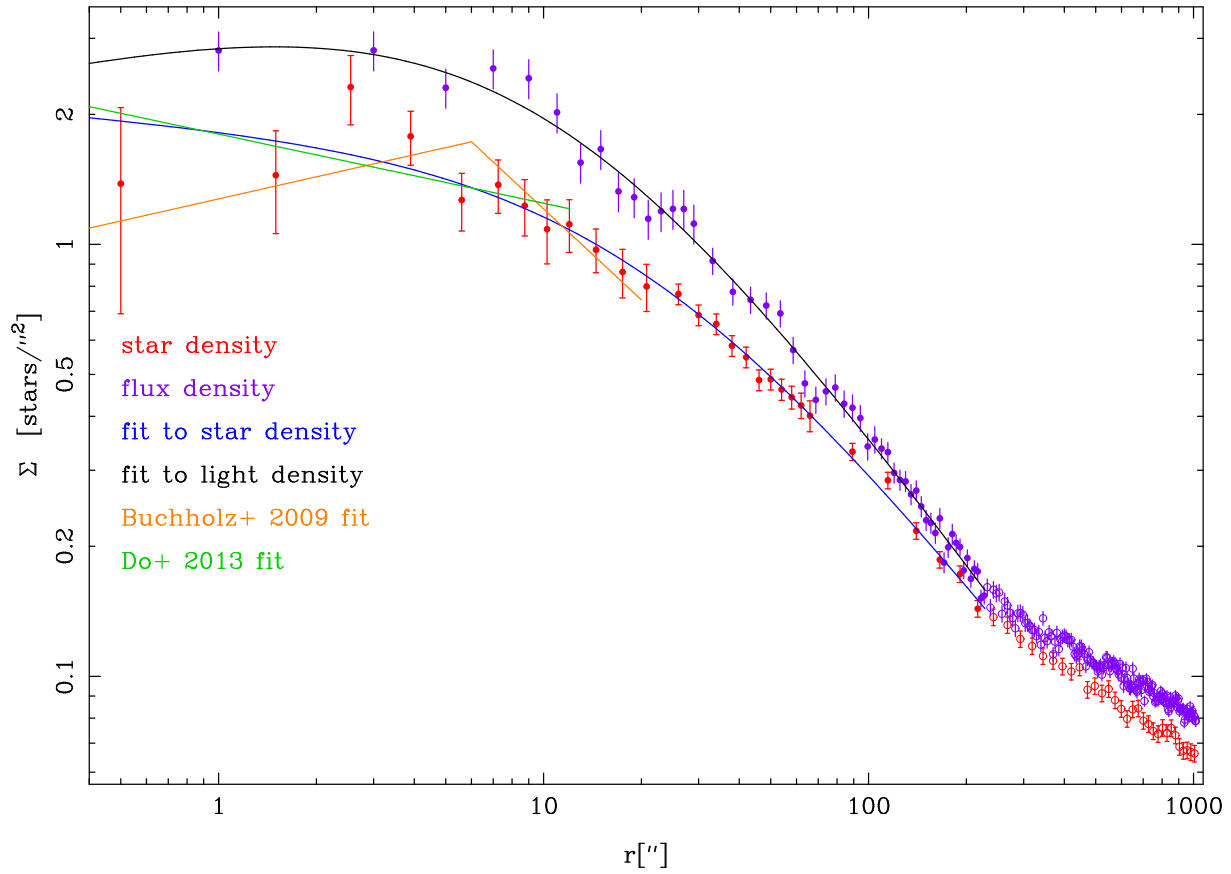


Figure 5.6 Nuker fits (with  $\alpha = 1$ ) to the late-type stars surface density, either their star density or their flux density. We present here fits to the inner data ( $r < 220''$ , filled dots). The outer data outside the break is presented by open dots. We also plot the fits of Buchholz et al. (2009) and Do et al. (2013).

Table 5.2.  $\eta$ -model fits of the surface density profile

No.	data source	r range	$\chi^2/d.o.f.$	$K_{\text{inner}}$	$a_{\text{inner}}['']$	$\eta_{\text{inner}}$	$K_{\text{outer}}$	$a_{\text{outer}}['']$
1	star density	all r	29.11/50	$67 \pm 8$ ks	$194 \pm 33$	$2.10 \pm 0.11$	$7.1 \pm 1.5$ Ms	$3396 \pm 458$
2	flux density	all r	220.287/204	$3.4 \pm 0.1$ kJy	$117 \pm 10$	$2.24 \pm 0.08$	$548 \pm 38$ kJy	$3711 \pm 158$
3	star density	$r < 220''$	18.84/24	$288 \pm 34$ ks	$626 \pm 93$	$1.86 \pm 0.06$	-	-

Note. — The units for  $K$  are star (s) or Jansky(Jy), given in kilo (k) or Mega (M) units.

we will fit the surface density and dynamics data at once, since also the dynamics yields a (weak) constraint on the tracer profile. However, for being able to check whether the obtained solutions are realistic, we also fit the density alone. Since the GC light profile has two breaks (Figure 5.6), we cannot fit the full data range with one  $\eta$ -model. We use instead two independent  $\eta$ -models. The central slope of the outer component is difficult to determine from the data and we fix it to be flat by setting  $\eta_{\text{outer}} = 3$ . A larger value would correspond to a central depression, and values  $< 2$  can create profiles in which the outer component dominates again at very small distances. We obtain the fits presented in Rows 1 and 2 in Table 5.2.

The two best fitting profiles are similar (Figure 5.7) to each other, but again not consistent within their errors as already noticed during the Nuker profile fits. The mean central of slope of the cluster is consistently  $\eta_{\text{inner}} - 3 = -0.83 \pm 0.12$ . However, the small error is a consequence of the functional form which we use, other function yield a range of inner slopes that appears to be consistent with the uncertainty reported by Do et al. (2009). The outer  $\eta$ -model is needed even inside of  $220''$ . Row 3 in Table 5.2 shows a fit with a single component. The resulting  $\eta_{\text{inner}} - 3$  is unrealistically small ( $< -1$ ) when comparing with Do et al. (2009).

The space density models in the literature do not describe our data well, even when restricted to the inner  $220''$ , see Figure 5.7. The density model of Schödel et al. (2009) combines a large break radius with a relatively small outer slope and thus overestimates the density further out and underestimates it in the center. The models of Genzel et al. (1996) and Trippe et al. (2008) fit our data somewhat better, however their core radii appear to be too small.

#### 5.4.4 Flattening of the Cluster

Our profiles show that the flattening (defined as the axes' ratio) of the nuclear cluster increases with radius, see Figure 5.5. Inside of  $66''$  the flattening is small, with an average of about 1.20. The error on this number is around 10% as estimated from the bin-to-bin variations and the different data sets. Outside of  $66''$ , where the data are based on VISTA star counts the flattening increases. At  $l^* = 100''$  it is around 1.3 and increases to 1.5 at

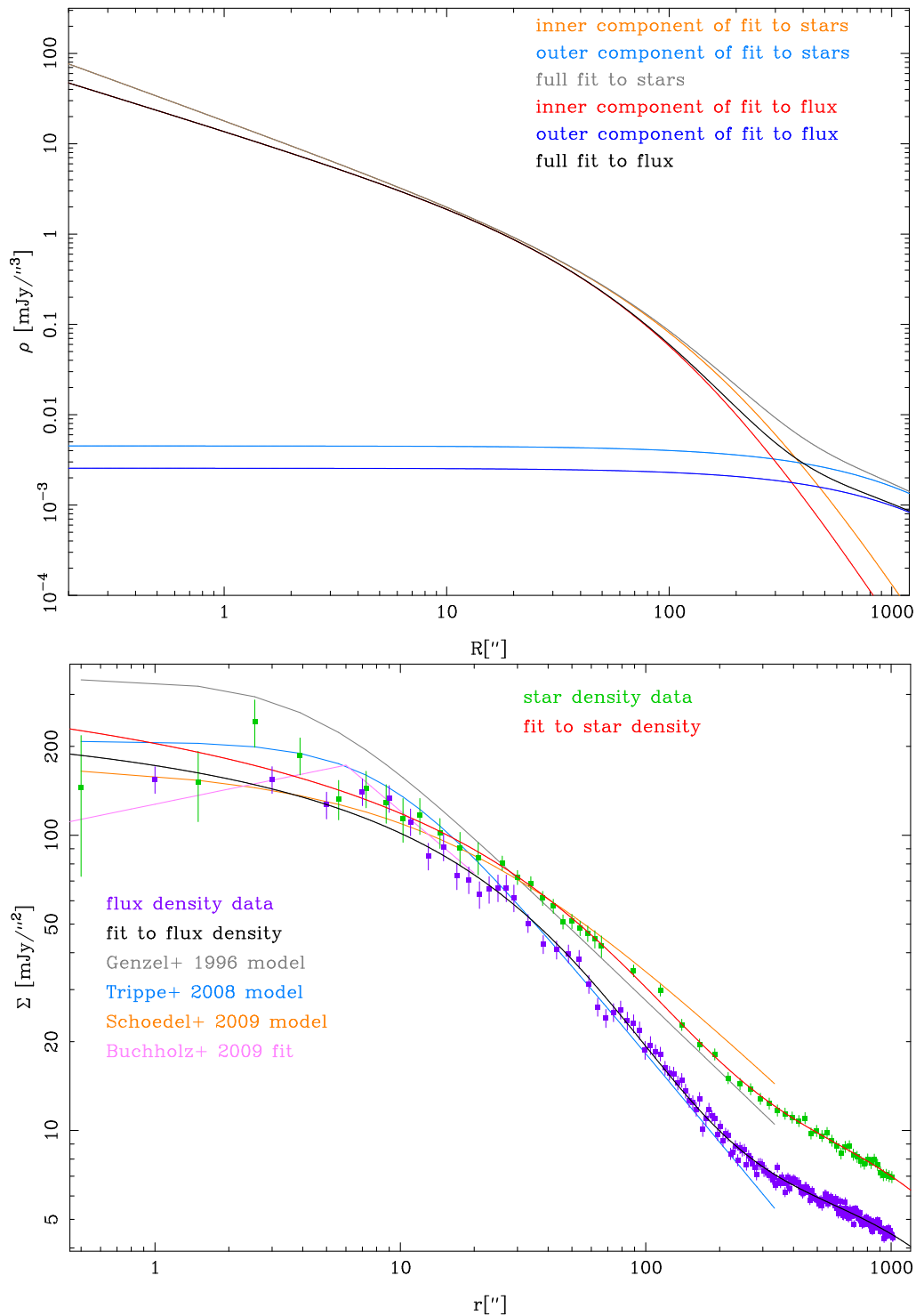


Figure 5.7 Space and projected density fits in comparison with the star and flux density data. For illustration purposes the stellar density is shifted. We fit two  $\eta$ -models. We also show the models of Genzel et al. (1996), Trippe et al. (2008), and Schödel et al. (2009). The Schödel et al. (2009) model fits neither our data sets nor the fit of Buchholz et al. (2009).

$l^* = 200''$ , to 2.1 at  $l^* = 500''$ , and reaches at the edge of the field of view ( $l^* = 1000''$ ) a value of 3.2. The flattening increases further outside of our field of view, as it is visible in large scale IRAC data and in Launhardt et al. (2002). They model the inner  $r_{\text{box}} = 2^\circ$  of the GC and obtain a maximum flattening of 5 at around  $l^* = 3100''$ . The quick change of the flattening ratio around  $100''$  could be sign of a two component nature of the light distribution, as suggested by Launhardt et al. (2002). They call the inner component the nuclear (stellar) cluster and the outer one the nuclear (stellar) disk, in analogy to other galaxies. In contrast, Serabyn & Morris (1996) assumed that the central active star forming zone inside the inactive bulge of the Milky Way consists of a single component, a central stellar cluster of  $r = 100$  pc.

We can use our two dimensional data to distinguish between nuclear cluster and nuclear disk, where the outer, disk component is used to estimate the background for the cluster in the following. In the central  $66''$  we use the density profiles shown in Figure 5.5 in the corresponding quadrants. Further out, we use the VISTA data. Figure 5.8 shows the resulting map. For finding an empirical description we use GALFIT (Peng et al. 2002). We fix the center to its known location and enforce an alignment of the flattening with the Galactic plane. We find that a combination of two Sersic profiles (Sersic 1968) describes our data well. The properties of the inner component are well constrained, and they depend only weakly on the outer component. For the outer component we fix  $n_{\text{outer}} = 3$ . We obtain for the inner component  $n_{\text{inner}} = 1.42 \pm 0.03$ ,  $r_e = 110 \pm 10''$ , a flattening of  $1.1 \pm 0.07$  and an integrated counts uncertainty of 13%. The outer component has a flattening of  $3.85 \pm 0.30$ . In the very center the outer component contributes 22% of the star counts of the inner component, the outer component dominates outside about  $90''$ . While the formal fit uncertainties are quite small, we estimate the errors instead by fits with  $n_{\text{outer}} = 3.87$  and  $n_{\text{outer}} = 2.4$ , the range of  $n_{\text{outer}}$  which seems acceptable given our data.

### 5.4.5 Luminosity of the Nuclear Cluster

To obtain the Ks-luminosity of the central GC we integrate the flux of the old stars (Figure 5.4). The total extinction-corrected flux within projected  $100''$  is  $1044 \pm 200$  Jy. The absolute error of 20% contains the uncertainty of the extinction law toward the GC (Fritz et al. 2011: 11%), the calibration uncertainty (7%), and 14% account for the differences between the stellar density and flux density profiles. The last error term is probably caused by assuming screen extinction for the flux density. To estimate the luminosity of the nuclear cluster, we use the two-dimensional decomposition of the star counts in nuclear cluster and nuclear disk (Section 5.4.4). We use only the inner  $200''$  within which 79% of the nuclear cluster is included, since integrating into a larger region where the cluster is negligible increases the uncertainties. Combined with a nuclear cluster fraction of 43% within this radius, this leads to a total luminosity of  $1248 \pm 288$  Jy for the nuclear cluster. The error includes now in addition 13% for the uncertainty in the decomposition. This corresponds to a luminosity of  $M_{\text{Ks}} = -15.3 \pm 0.26$  or  $2.7 \pm 0.62 \times 10^7 L_\odot$  for the nuclear cluster, consistent but on the low side of the estimate of  $6 \pm 3 \times 10^7 L_\odot$  from Launhardt et al. (2002). The difference might be due to our smaller cluster size, which is caused by the use

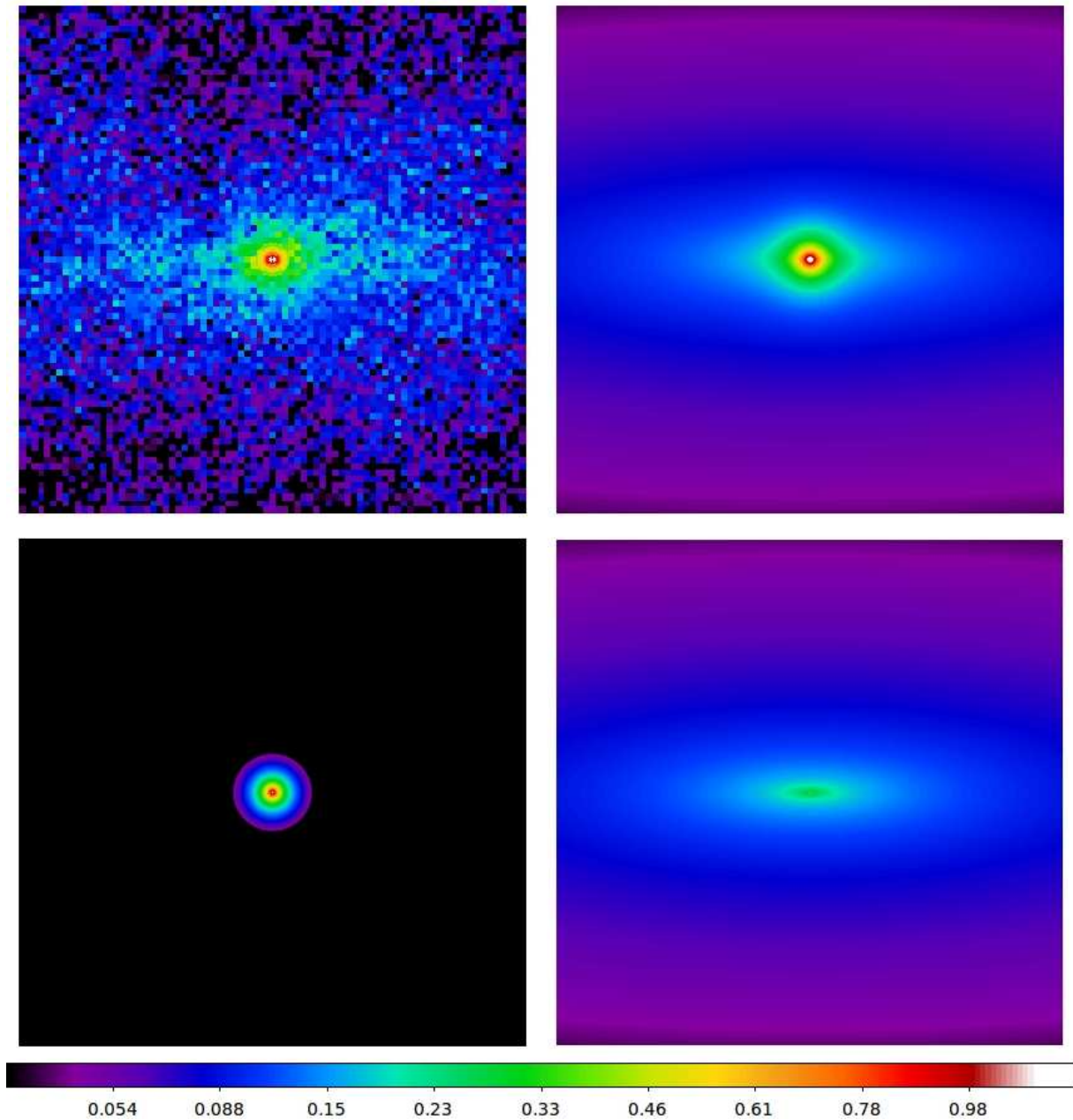


Figure 5.8 Map of the stellar density in the inner  $r_{\text{box}} = 1000''$ . All panels use the same color scale. Upper left: stellar density from VISTA/WFC3/NACO star counts, corrected for completeness and extinction. Upper right: GALFIT fit to the data. The fit consists of two Sersic components, which are shown in the lower two panels. Lower left: central component, a nearly circular, close to exponential Sersic profile ( $n = 1.41$ ), lower right: a Sersic profile with  $n = 3$  and a flattening ratio of 3.7. The properties of the outer component are (apart from the flattening) not well characterized since it extends well outside of our field of view.

of two-dimensional information for the separation of nuclear cluster and disk.

The young O(B)-stars in the center, which are not included in our sample, add 25 Jy in the Ks-band. Although they are such irrelevant for the light in the Ks-band, this is different in other bands: for calculating the V-band magnitude we assume aligned to Pfuhl et al. (2011) that the old star Ks-flux is caused to 80% by giants (assuming K5III with  $V - K = 3.6$ , Cox (2000), Masana et al. 2006) and to 20% of turnoff main sequence stars (assuming G2V with  $V - K = 1.5$ ). For the O(B)-stars we assume  $V - K = -0.8$ . This results for the young stars in  $M_V = -11.8$  and a similar flux of  $M_V = -12.5$  for the old stars. The bolometric luminosity of the young stars is about  $L_{UV} \approx 10^{7.5} L_\odot$  and  $M_{\text{bol}} = -14.1$  (Genzel et al. 2010; Mezger et al. 1996) and thus much larger than what we obtain for the old stars,  $M_{\text{bol}} = -12.8$ . Also, the young stars are concentrated on an about 100 times smaller area than the old stars.

## 5.5 Kinematic Analysis

We now use our kinematic data to measure the mass of the nuclear cluster. In Section 5.5.1 we explain the binning used. Section 5.5.2, 5.5.5 and 5.5.3 discuss anisotropy, fast stars and rotation, respectively. In this work we use isotropic spherical symmetric Jeans modeling (Binney & Tremaine 2008) for obtaining a mass estimate (Section 5.5.4). In a subsequent work (Chatzopoulos et al. in prep.) we will use two-integral modeling with self-consistent rotation (Hunter & Qian 1993), which allows one to include intrinsic flattening and rotation in a self-consistent way.

### 5.5.1 Binning

For simplicity, we choose to bin our data. The loss of information (Merritt & Tremblay 1994; Feigelson & Jogesh Babu 2012; Scott 1992) is small, since we use a large amount of data. We choose different binnings for the radial velocities and for the proper motions, since the stars used respectively are distributed differently in these dimensions (Figure 5.1). Further, the velocity pattern aligned with the Galactic plane (McGinn et al. 1989; Lindqvist et al. 1992; Genzel et al. 2000; Trippe et al. 2008) has different symmetries in proper motion and in radial velocity.

#### Proper Motion bins

Rotation and flattening of the GC cluster are expected to occur in direction along the Galactic plane, and hence we choose proper motion bins reflecting that. We use two-dimensional circular coordinates  $(r, \phi)$ , where  $r$  is the distance from the center and  $\phi$  is the absolute value of the smallest angle between the Galactic plane and the respective star, thus  $0^\circ \leq \phi \leq 90^\circ$ . This definition of  $\phi$  uses the symmetry of the edge-on system, in which the dispersion can only vary by  $r$  and  $\phi$ . Our bins contain a relative similar number of stars (Figure 5.9), between 120 and 295 with an average of 168 stars outside

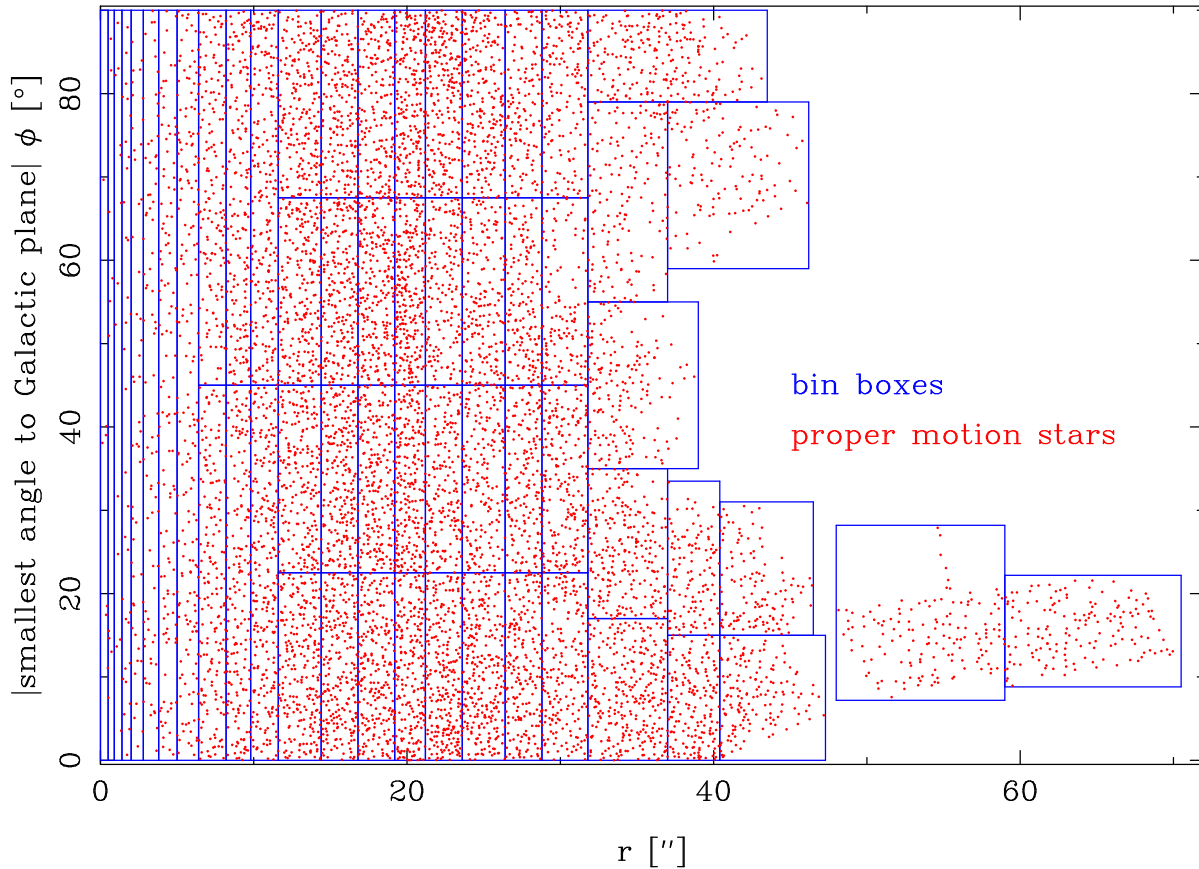


Figure 5.9 Binning of the proper motion stars. The figure shows the parameter space which we use for binning, radial distance from Sgr A\* and the smallest absolute value of angular distance from the Galactic plane.

of  $12''$ . Inside of that we have less stars, but we need a higher resolution there in order to resolve the increased velocity dispersion caused by the SMBH. The innermost bin with  $r < 0.5''$  contains 7 stars. Between  $5''$  and  $32''$  we choose four azimuthal bins for being able to measure robustly azimuthal variations, for  $r < 5''$  we do not bin the stars azimuthally.

### Radial Velocity Bins

The rotation of the cluster causes a change of the mean radial velocity with  $l^*$  (McGinn et al. 1989; Lindqvist et al. 1992; Genzel et al. 2000) from negative velocities at negative  $l^*$  to positive values for positive  $l^*$ . Rotation does not depend on the sign of  $b^*$  due to the symmetry. Hence, a natural choice for the binning coordinates is  $(l^*, |b^*|)$ . We again choose our bins such that the bins are relatively even populated with stars, but the overall number of stars is smaller than for the proper motions. Outside the central  $4''$  there are on average 50 stars per bin. In the central  $4''$  we disregard the sign of  $l^*$  since the rotation is much smaller there compared to the velocity dispersion peaking there due to the presence of the

SMBH. We choose there quadrangular rings as bins to transit smoothly to the rectangular bins further out. The inner most bin includes all stars with  $|l^*| < 0.5''$  and  $|b^*| < 0.5''$ , see Figure 5.10. Further out, in the regime of the maser stars we adopted from the literature, we use more complex bins to achieve comparable star numbers per bins (Figure 5.11).

### Binned Velocity Data

Figure 5.13 shows the binned dispersion data in all three dimensions ( $l^*$ ,  $b^*$ ,  $z$ ). The mean radial velocities are shown in Figure 5.12. Note that by construction, the mean velocities in  $l^*$  and  $b^*$  are 0.

### 5.5.2 Velocity Anisotropy

An unrelaxed cluster can be anisotropic, which would manifest itself by a difference in the dispersions in tangential and radial direction (Leonard & Merritt 1989; Schödel et al. 2009). The uneven angular distribution of stars together with the dispersion difference between  $l^*$  and  $b^*$  can mimic anisotropy. To counter this effect we firstly restrict the analysis here to  $r < 40''$  for having approximately full angular coverage. Secondly, we obtain the dispersions by taking the average of the dispersions within  $\phi < 45^\circ$  and  $\phi > 45^\circ$ . We obtain  $\beta_{pm} = \sigma_r/\sigma_t = 1.018 \pm 0.011$  (Figure 5.14). The scatter of the data points is consistent with the error. Similar to the what was found by Schödel et al. (2009) we see that  $\beta_{pm}$  is somewhat larger in the center, but the data are completely consistent with a flat slope ( $\chi^2/d.o.f. = 32.25/39$ ). The increase in the center could be entirely due to pollution with early-type stars, which are on average have more tangential orbits (Genzel et al. 2000; Bartko et al. 2009, 2010).

The deprojected anisotropy parameter  $\beta$  is more different from 1 than  $\beta_{pm}$ :  $\beta = \beta_{pm}(1 - 1/\xi)$ , see van der Marel & Anderson (2010). For cluster without true cores, the dilution factor  $1 - 1/\xi$  is between 0.5 and 0.83, and we obtain a  $3\sigma$  limit of 1.1 on  $\beta$ . Thus, it is justified to ignore anisotropy in the following.

### 5.5.3 Rotation

The cluster shows a gradient in the mean radial velocity as a function of  $|l^*|$  (Figure 5.12). This is an unambiguous sign of rotation. Trippe et al. (2008) interpreted also the difference in dispersion between  $l$  and  $b$  (Figure 5.13) as a sign of rotation. However, this difference is primarily a sign of flattening (Chatzopoulos et al. in preparation). The rotation velocity does not depend on  $|b^*|$ . Combining the data from Figure 5.2 and the maser data (Section 5.3.2) we obtain Figure 5.15.

Inside of  $25''$  our velocities are consistent with the velocities of Trippe et al. (2008), since the data set is largely identical. Outside of  $25''$  our new SINFONI radial velocities are on average smaller than the velocities of Trippe et al. (2008), who used only a subset of the velocities in McGinn et al. (1989), a problem already pointed out by Schödel et al. (2009). Surprisingly, our new high resolution data do not yield roughly the average of

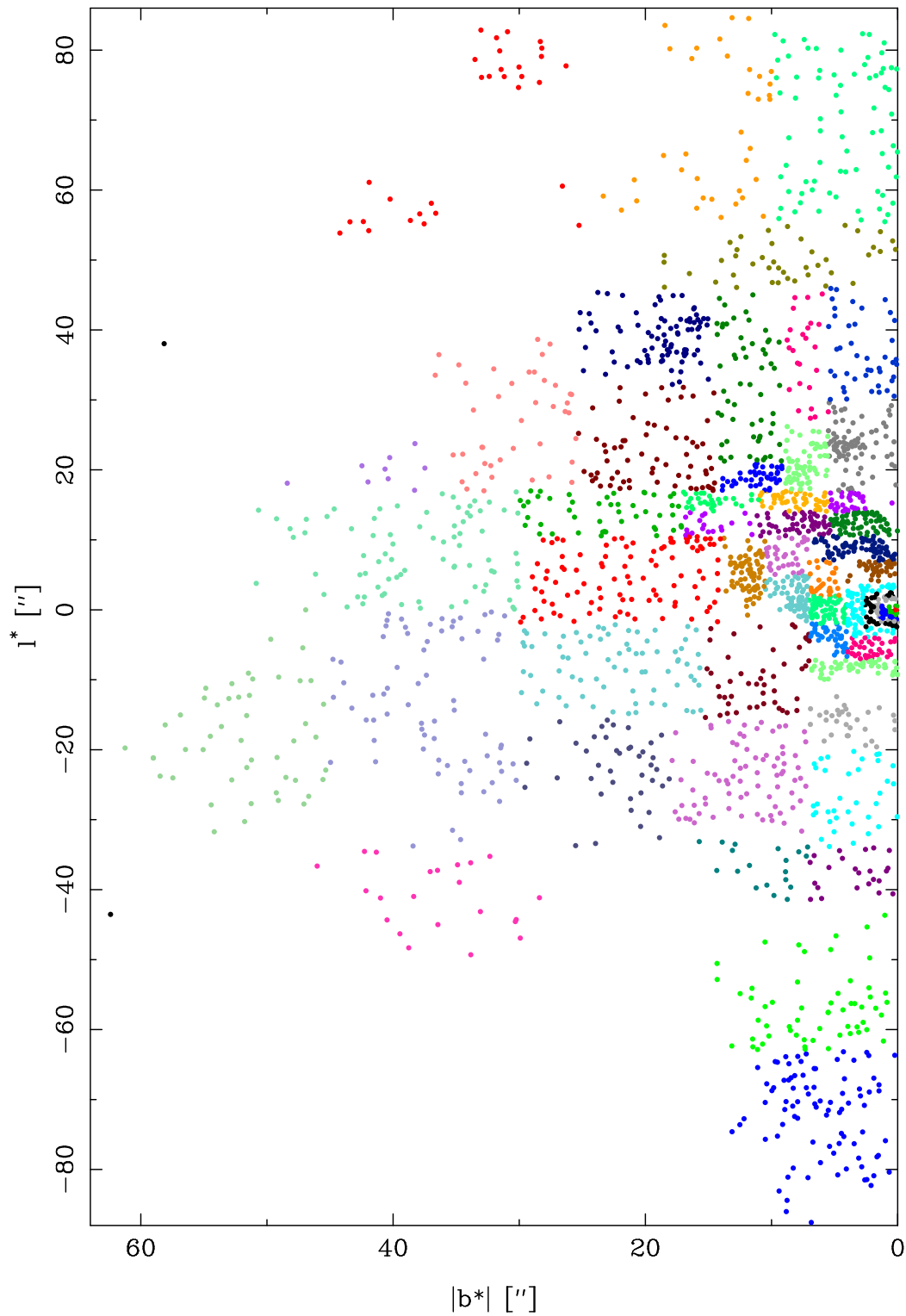


Figure 5.10 Binning of the inner radial velocity stars. These stars are binned in  $l^*$  and  $|b^*|$ . Different colors mark different bins

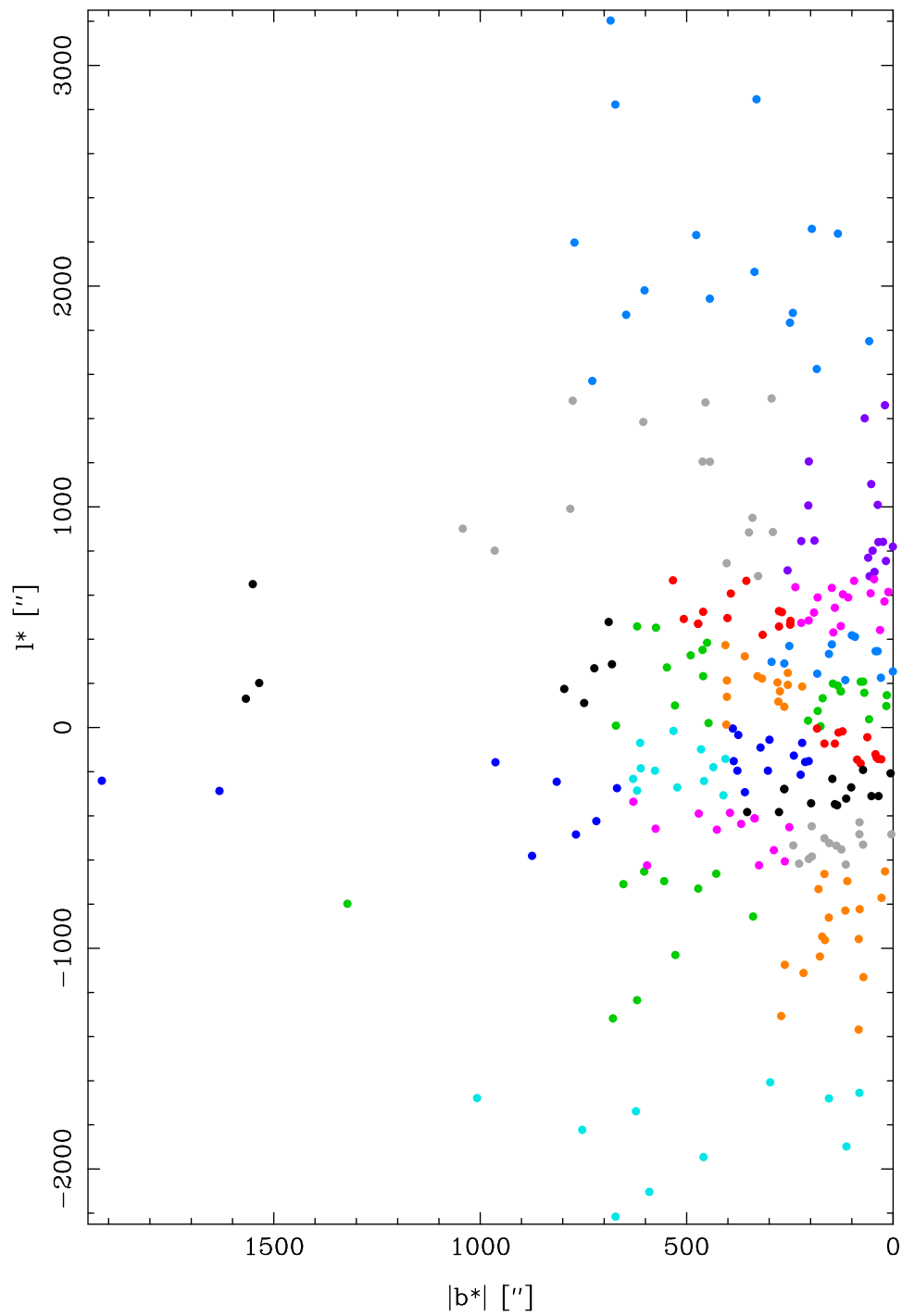


Figure 5.11 Binning of the outer radial velocity stars, the maser sample from the literature (Lindqvist et al. 1992; Deguchi et al. 2004). These stars are binned in  $l^*$  and  $|b^*|$ . Different colors mark different bins.

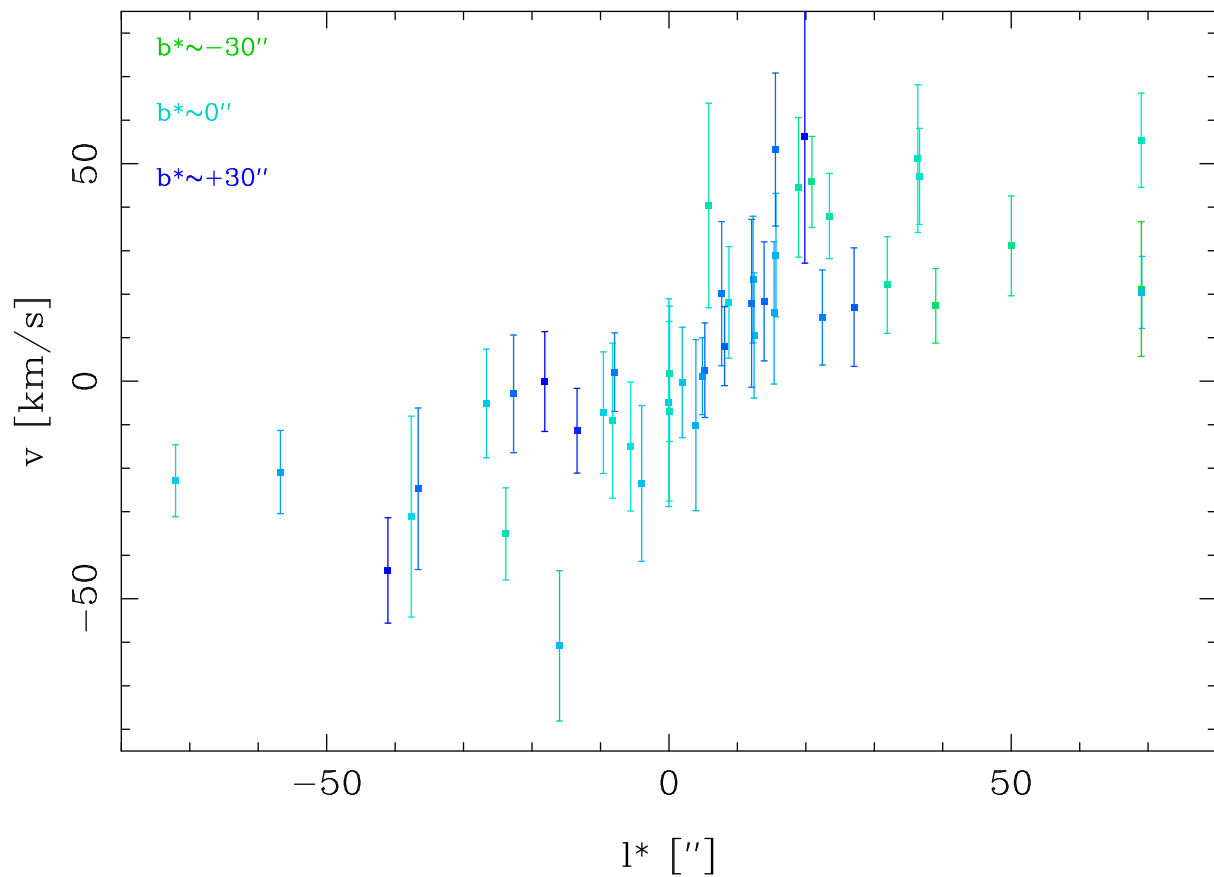


Figure 5.12 Average radial velocities in our bins. Data points with an error larger than 30 km/s, which occur all in the center, are excluded for better visibility.

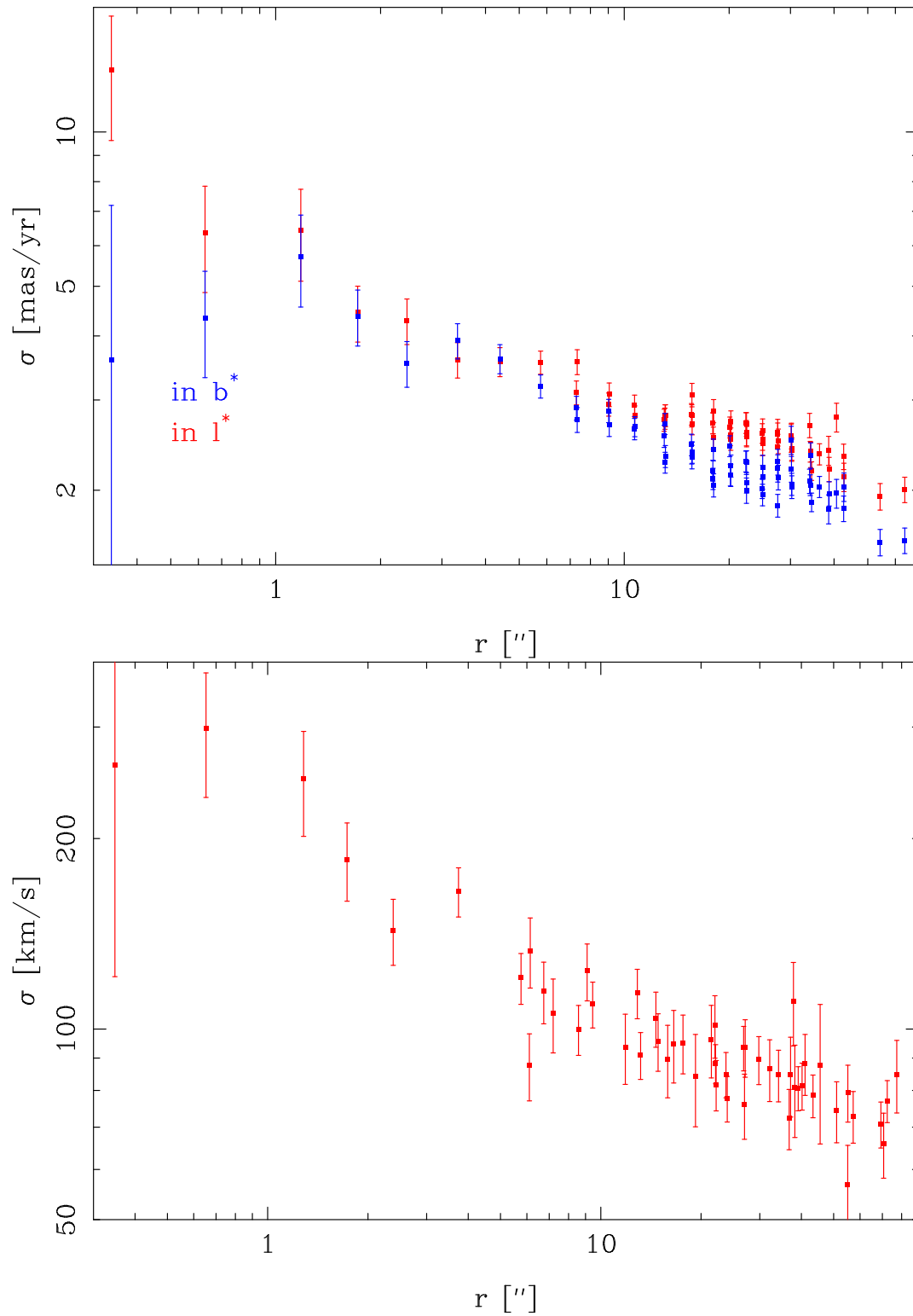


Figure 5.13 Binned velocity dispersion used for Jeans modeling. The upper panel presents the proper motion data, the lower one the radial velocity data.

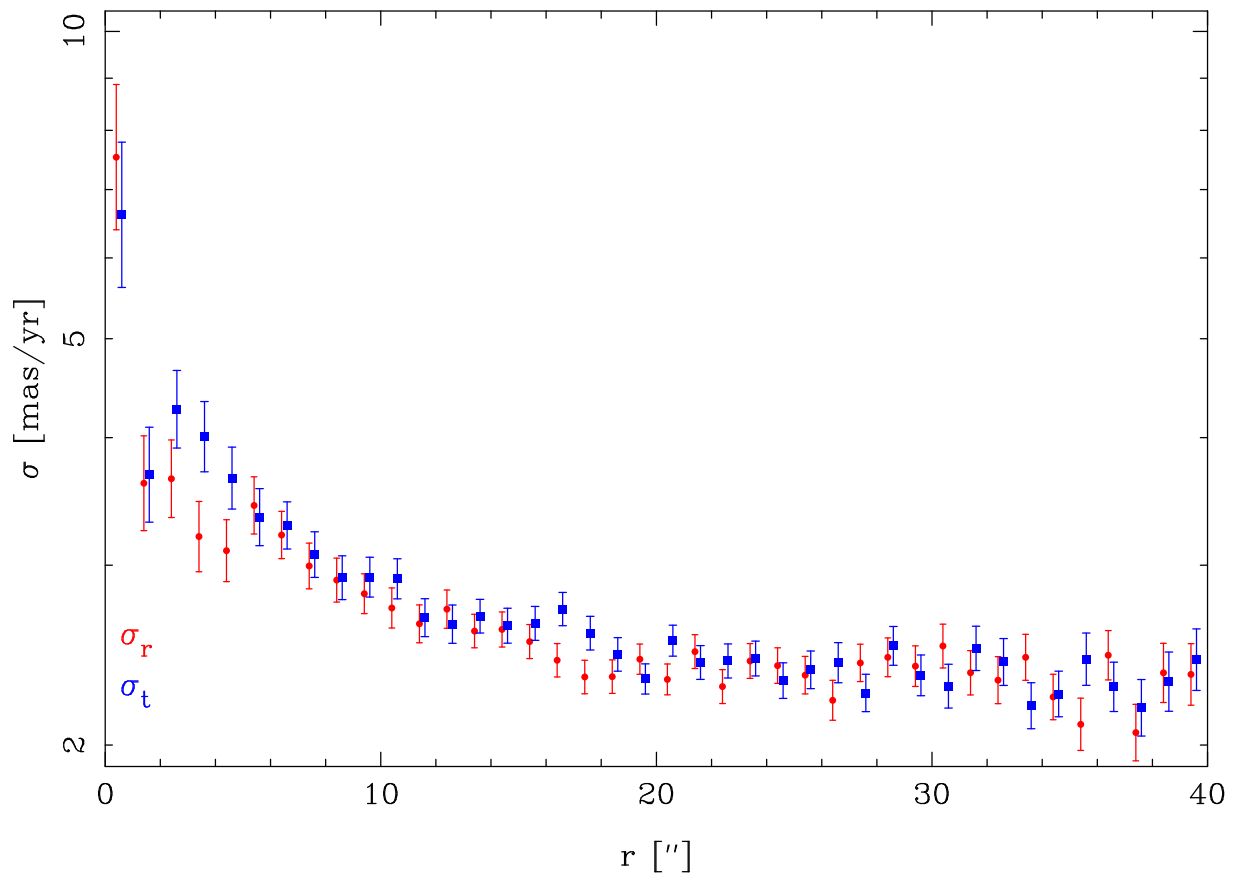


Figure 5.14 Radial and tangential dispersions as function of the radius. The points are offset from each other for better visibility.

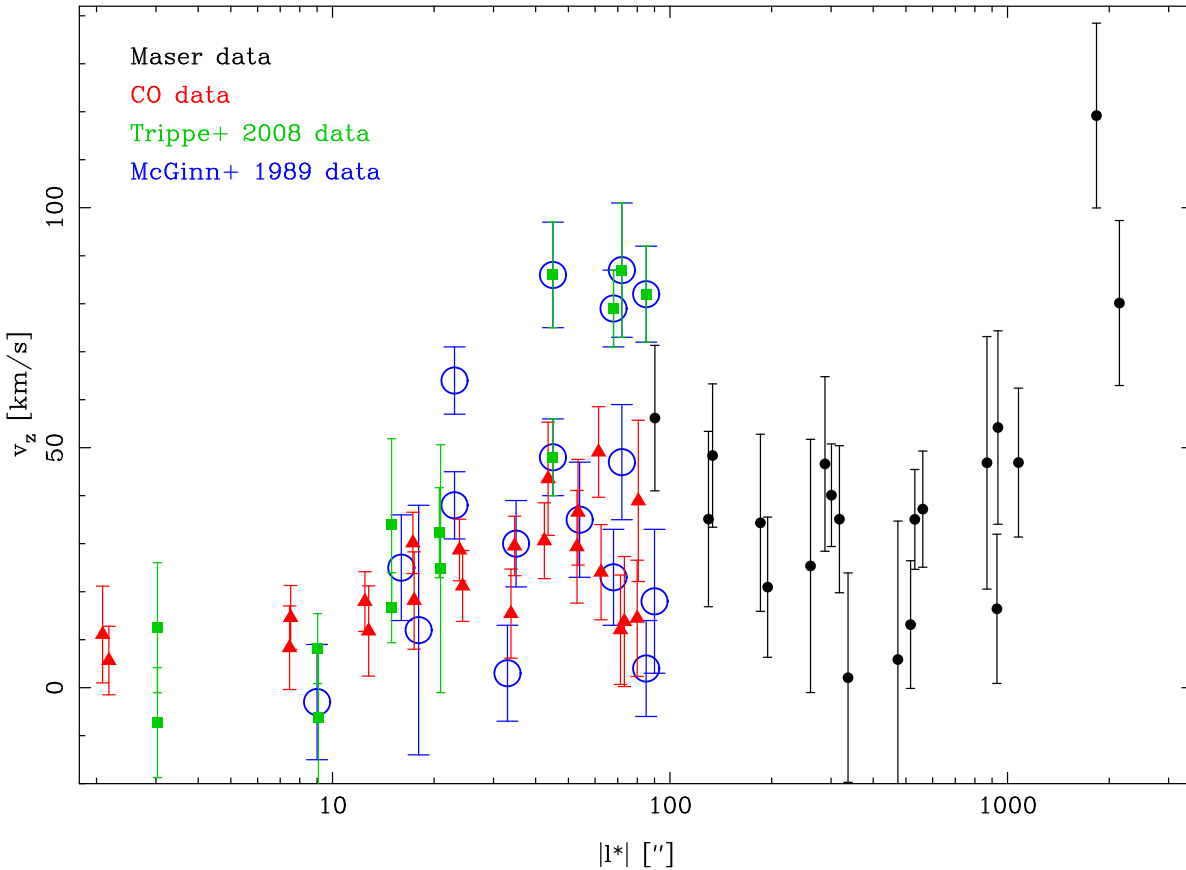


Figure 5.15 Average radial velocities from our data and the literature. We assume symmetry of the rotation pattern and reverse for data points with  $l^* < 0$  the sign of the radial velocities. For the maser data we use the velocities from Lindqvist et al. (1992) and Deguchi et al. (2004). The data from Trippe et al. (2008) overlaps within  $|l^*| < 25''$  largely with our data. Further out Trippe et al. (2008) utilized a subsets of the dataset of McGinn et al. (1989).

the velocities reported by McGinn et al. (1989), but agree roughly with the lower end of values found. The maser data of Lindqvist et al. (1992) and Deguchi et al. (2004) agree with the lower velocity data of McGinn et al. (1989) and our CO velocities. Overall we are confident that our smaller rotation of the cluster compared to Trippe et al. (2008) is correct.

### 5.5.4 Jeans Modeling

We use only the most simple kind of Jeans-modeling (Binney & Tremaine 2008) assuming isotropy and spherical symmetry for mass and light. More complicated variants that include flattening may lead to solutions that are impossible to achieve in phase space, and two-integral modeling (Chatzopoulos et al. in prep.) is better suited. Two variants of isotropic Jeans modeling were used in the past for the GC:

- Genzel et al. (1996) and Trippe et al. (2008) parametrized the deprojected dispersion.
- Schödel et al. (2009) used a direct mass parametrization.

### Dispersion-parametrized Method

This method was useful in the past to decide on the presence of a SMBH in the GC. The Jeans equation is

$$GM(R)/R = \sigma(R)^2 \times c_{\text{geo}} , \quad (5.4)$$

with

$$c_{\text{geo}} = -d \ln[n(R)]/d \ln R - d \ln[\sigma(R)^2]/d \ln R . \quad (5.5)$$

Genzel et al. (1996) and Trippe et al. (2008) used the following parametrization of the dispersion:

$$\sigma(R)^2 = \sigma(\infty)^2 + \sigma(10'')^2 (R/10'')^{-2\beta} \quad (5.6)$$

The a priori incorporation of the mass of the central SMBH is only approximately possible by demanding that in the center the dispersion shall follow Keplerian power law slope of -0.5. The approximation is that this implies  $c_{\text{geo}}=1$ , which is only approximately true for our data set.

### Mass-parametrized Method

In case of the mass-parametrized method the Jeans equation is (Schödel et al. 2009):

$$\sigma^2(r)/G = \frac{\int_r^\infty dr R^{-2}(R^2 - r^2)^{1/2}n(R)M(R)}{\int_r^\infty dr R(R^2 - r^2)^{-1/2}n(R)}, \quad (5.7)$$

and one needs to choose a mass parametrization for  $M(R)$ . The assumption which has the fewest degrees of freedom is a constant mass to light ratio (D’Souza & Rix 2013), or a theoretically predicted profile of that ratio (Lützendorf et al. 2012). The GC data sets have been rich enough to leave the shape of the extended mass distribution as a free parameter (Schödel et al. 2009). Given that the presence of the central SMBH is well established in the GC, one can add it ( $M_\bullet$ ) to  $M(R)$ , as done in Schödel et al. (2009). The straight-forward inclusion of such physical arguments is the main advantage of the mass-parametrized method compared to the dispersion-parametrized one.

### Deprojection

In both cases one needs to deproject the observed radii  $r$  into true 3D radii  $R$ , for which one needs to know the space tracer density distribution  $n(R)$ , see Section 5.4.3. This is done by two Abel integrals, namely equation (5.2) and the following integral:

$$\Sigma(r)\sigma_r(r)^2 = 2 \int_R^\infty n(R)\sigma_r(R)^2 R dR / \sqrt{R^2 - r^2} \quad (5.8)$$

### Averaging the 3D-dispersions

In the Jeans equation a one-dimensional dispersion  $\sigma$  is used. We have data in all three dimension and thus need to average them. We use proper motions and radial velocities separately since they cover different areas and have different errors.

- For the proper motion we combine both dimension in each bin to  $\sigma_p^2(r) = 1/2 \times (\sigma_l^2(r) + \sigma_b^2(r))$  to reduce the impact of the flattening. By definition of our coordinates, there is no rotation term in the proper motions.
- For the radial velocities, there is significant rotation (Figures 5.12 and 5.15). For including there the energy in rotation we do not use  $\sigma_z$ , but  $\langle v_z^2 \rangle^{1/2}$  (Tremaine et al. 2002) instead; i.e. we use the dispersions relative to  $v_{\text{LSR}} = 0$  instead of the local mean.

### Errors of the Dispersions

Calculation the error of the dispersion from  $\delta_\sigma = \sigma \times 1/\sqrt{2N}$  is problematic when there are only few stars in a bin (as in our radial velocity data), since the weight of the individual

bins will scale inversely with the dispersion value, and the weight is thus affected by the Poisson statistics. Instead, we determine the errors with an iterative procedure: We fit the binned profile  $\sigma(r)$  with an empirical function (a fourth order log-polynomial) using our errors. Then we use the values of the fit in the bins to estimate the errors. With these errors we repeat the fit and get refined error estimates. After four iterations the procedure converges.

For the proper motions we have a sufficient number of stars per bin such that the effect is not relevant. In the innermost bin the non Gaussian velocity distribution increases the error. We estimate there an error of 140 km/s in each dimension from the comparison of three dimensions.

### Tracer Distribution Profiles

We fit our data using three different types of profiles for the three-dimensional tracer distribution:

- For most fits we assume a double  $\eta$ -profile (Section 5.4.3).
- For checking the robustness of these, we also use a single Nuker profile which we fit only to our inner density data.
- For comparison with the literature, we also use the single component tracer models of Genzel et al. (1996), Trippe et al. (2008) and Schödel et al. (2009).

### Mass Parametrization

Our mass model contains the SMBH at the center and an extended component made of stars. It is justified to ignore gas clouds, since even the most massive structure, the circumnuclear disk, has a mass of only a few times  $10^4 M_\odot$  (Mezger et al. 1996; Launhardt et al. 2002; Requena-Torres et al. 2012). We use two different ways of parameterizing the extended mass:

- We use a power law, similar to Schödel et al. (2009):

$$M(R) = M_{100''} \times (R/100'')^\delta \quad (5.9)$$

The fact that the total mass is not finite is not a problem, since our tracer profile  $n(R)$  falls more rapidly than  $M(R)$ .

- We use a constant mass to light ratio for the extended mass, similar to D'Souza & Rix (2013). The most important features of these profiles are the steep decrease around  $200''$ , flanked by flatter profiles further in and further out.

To both we add the SMBH. For the normalization we choose  $100''$  in both cases, since that mass is well determined from our data.

## Fitting

We present the fits corresponding to the various choices of how to set up the Jeans model of the nuclear cluster in Table 5.3. The robustness of the results can be assessed by comparing the different fits. We use the fitting routine `mpfit` (Markwardt 2009).

In few of our fits the central slope of the inner component is larger than -0.5. Such a flat slope is problematic, because a slope larger than -0.5 causes anisotropy when a central point mass is dominating (Schödel et al. 2009). Thus, this solution is not self-consistent with our assumption of isotropy. We thus fix the inner slope to -0.5 if necessary. Also, the inner slope of the outer component is not well constrained and we fix it usually to 0. Both restrictions have no relevant influence on the mass obtained.

Initially, we fit with a free SMBH mass (Rows 1 and 2 in Table 5.3). However, for the power law mass model with more freedom for the cluster shape, the resulting mass of the SMBH is smaller than the direct mass measurements by means of stellar orbits (Ghez et al. 2008; Gillessen et al. 2009). Hence, in the following we fix the central mass to  $M_{\bullet} = 4.17 \times 10^6 M_{\odot}$ , corresponding to our fixed distance of  $R_0 = 8.2$  kpc, and we neglect the small uncertainty of 1.5% (Gillessen et al. 2009). We discuss the small SMBH mass further in Section 5.6.1. The reason for the too small SMBH mass probably is a too low dispersion value in the center, and hence fixing the SMBH mass to the supposedly correct value can also lead to a mass bias for the cluster mass, i.e. a too low cluster mass.

## Results

Table 5.3 presents our fits. Our most trustworthy fits are in rows 3, 4, 5 and 6. They use a range of  $10'' < r < 100''$  for the dynamics data. The SMBH mass bias in the cluster mass is visible for the fits in row 7 and 8, using  $r < 100''$  for the dynamics data (i.e. including the central region) and allowing the cluster shape to vary (in the power law mass model). All other fits are less biased and yield a mass range between  $5.4$  and  $6.8 \times 10^6 M_{\odot}$ . The model-to-model variance is higher than the formal fit errors.

Figure 5.16 illustrates the fits of rows 1, 3, and 5. Our models are not very good fits for  $r < 10''$ , where the influence of the SMBH bias is highest, and outside of  $100''$ . The reason for the latter is

- We don't have density data outside of  $1000''$ , and hence the outer slope of the tracer profile is not well-constrained over the full range over which we have dynamic information.
- The assumption of spherical symmetry gets a poor approximation outside of  $\approx 300''$ .

Hence, we can determine best the mass in the central  $100''$ , and ignore the discrepancy. Restricting the range even to  $10'' < r < 100''$  removes in addition the mass bias, and thus this is our most trustworthy range for the dynamics data.

Beyond the mass bias, the selection of the range for the dynamics data is less important than the choice of the tracer source. The latter is particularly true when choosing a constant mass-to-light ratio as the mass model. Choosing the stellar number counts or the flux as

Table 5.3. Jeans model fits

No.	mass model	tracer model	tracer source	tracer range	dynamics range	$M_{\bullet}$ [ $10^6 M_{\odot}$ ]	$M_{100''}$ [ $10^6 M_{\odot}$ ]	$\delta$	$\chi^2/\text{d.o.f}$
1	power law	double $\eta$	stars	all	all r	$2.28 \pm 0.27$	$9.17 \pm 0.47$	$0.92 \pm 0.04$	184.94/182
2	M/L=const	double $\eta$	stars	all	all r	$4.36 \pm 0.13$	$5.16 \pm 0.24$		269.68/183
<b>3</b>	<b>power law</b>	<b>double <math>\eta</math></b>	<b>stars</b>	<b>all</b>	<b><math>10'' &lt; r &lt; 100''</math></b>	<b>4.17</b>	<b><math>5.71 \pm 0.28</math></b>	<b><math>1.22 \pm 0.06</math></b>	<b>144.61/137</b>
<b>4</b>	<b>power law</b>	<b>double <math>\eta</math></b>	<b>flux</b>	<b>all</b>	<b><math>10'' &lt; r &lt; 100''</math></b>	<b>4.17</b>	<b><math>6.03 \pm 0.25</math></b>	<b><math>1.26 \pm 0.05</math></b>	<b>347.88/286</b>
<b>5</b>	<b>M/L=const</b>	<b>double <math>\eta</math></b>	<b>stars</b>	<b>all</b>	<b><math>10'' &lt; r &lt; 100''</math></b>	<b>4.17</b>	<b><math>5.63 \pm 0.17</math></b>		<b>152.71/138</b>
<b>6</b>	<b>M/L=const</b>	<b>double <math>\eta</math></b>	<b>flux</b>	<b>all</b>	<b><math>10'' &lt; r &lt; 100''</math></b>	<b>4.17</b>	<b><math>6.76 \pm 0.28</math></b>		<b>340.39/287</b>
7	power law	double $\eta$	stars	all	$r < 100''$	4.17	$4.83 \pm 0.32$	$1.36 \pm 0.06$	197.35/163
8	power law	double $\eta$	flux	all	$r < 100''$	4.17	$5.15 \pm 0.31$	$1.40 \pm 0.05$	431.26/312
9	M/L=const	double $\eta$	stars	all	$r < 100''$	4.17	$5.53 \pm 0.16$		192.24/164
10	M/L=const	double $\eta$	flux	all	$r < 100''$	4.17	$6.64 \pm 0.16$		411.71/313
11	power law	double $\eta$	stars	all	$10'' < r$	4.17	$6.03 \pm 0.18$	$1.13 \pm 0.03$	180.20/157
12	power law	double $\eta$	flux	all	$10'' < r$	4.17	$6.44 \pm 0.16$	$1.12 \pm 0.03$	395.04/306
13	M/L=const	double $\eta$	stars	all	$10'' < r$	4.17	$5.57 \pm 0.16$		234.82/158
14	M/L=const	double $\eta$	flux	all	$10'' < r$	4.17	$6.58 \pm 0.16$		427.85/307
15	power law	double $\eta$	stars	all	all r	4.17	$5.48 \pm 0.17$	$1.20 \pm 0.03$	243.96/183
16	power law	double $\eta$	flux	all	all r	4.17	$5.93 \pm 0.16$	$1.19 \pm 0.03$	502.24/332
17	M/L=const	double $\eta$	stars	all	all r	4.17	$5.44 \pm 0.15$		271.98/184
18	M/L=const	double $\eta$	flux	all	all r	4.17	$6.47 \pm 0.16$		495.45/333
19	power law	single Nuker	stars	$r < 220''$	$10'' < r < 100''$	4.17	$5.86 \pm 0.23$	$1.27 \pm 0.07$	126.34/107
20	power law	single Nuker	flux	$r < 220''$	$10'' < r < 100''$	4.17	$6.34 \pm 0.21$	$1.29 \pm 0.06$	174.85/132
21	M/L=const	single Nuker	stars	$r < 220''$	$10'' < r < 100''$	4.17	$6.27 \pm 0.21$		127.38/108
22	M/L=const	single Nuker	flux	$r < 220''$	$10'' < r < 100''$	4.17	$7.29 \pm 0.17$		167.40/133
23	power law	Schödel+ 2009	stars	$r < 220''$	$10'' < r < 100''$	4.17	$5.70 \pm 0.26$	$1.17 \pm 0.06$	194.84/110
24	power law	Trippe+ 2008	stars	$r < 220''$	$10'' < r < 100''$	4.17	$7.11 \pm 0.17$	$1.21 \pm 0.05$	451.99/110
25	power law	Genzel+ 1996	stars	$r < 220''$	$10'' < r < 100''$	4.17	$6.64 \pm 0.19$	$1.17 \pm 0.06$	235.87/110
26	M/L=const	Schödel+ 2009	stars	$r < 220''$	$10'' < r < 100''$	4.17	$4.87 \pm 0.09$		216.97/111
27	M/L=const	Trippe+ 2008	stars	$r < 220''$	$10'' < r < 100''$	4.17	$7.81 \pm 0.16$		441.13/111
28	M/L=const	Genzel+ 1996	stars	$r < 220''$	$10'' < r < 100''$	4.17	$6.44 \pm 0.13$		241.92/111

Note. — Jeans model fitting of our dynamics and density data, assuming different mass and tracer models, and different selections for the data. The mass model includes in all cases a central point mass.  $M_{100''}$  is the nuclear cluster mass within  $100''$ . If no error is given for a parameter it is fixed. The literature tracer models are from Trippe et al. (2008), Schödel et al. (2009), and Genzel et al. (1996).

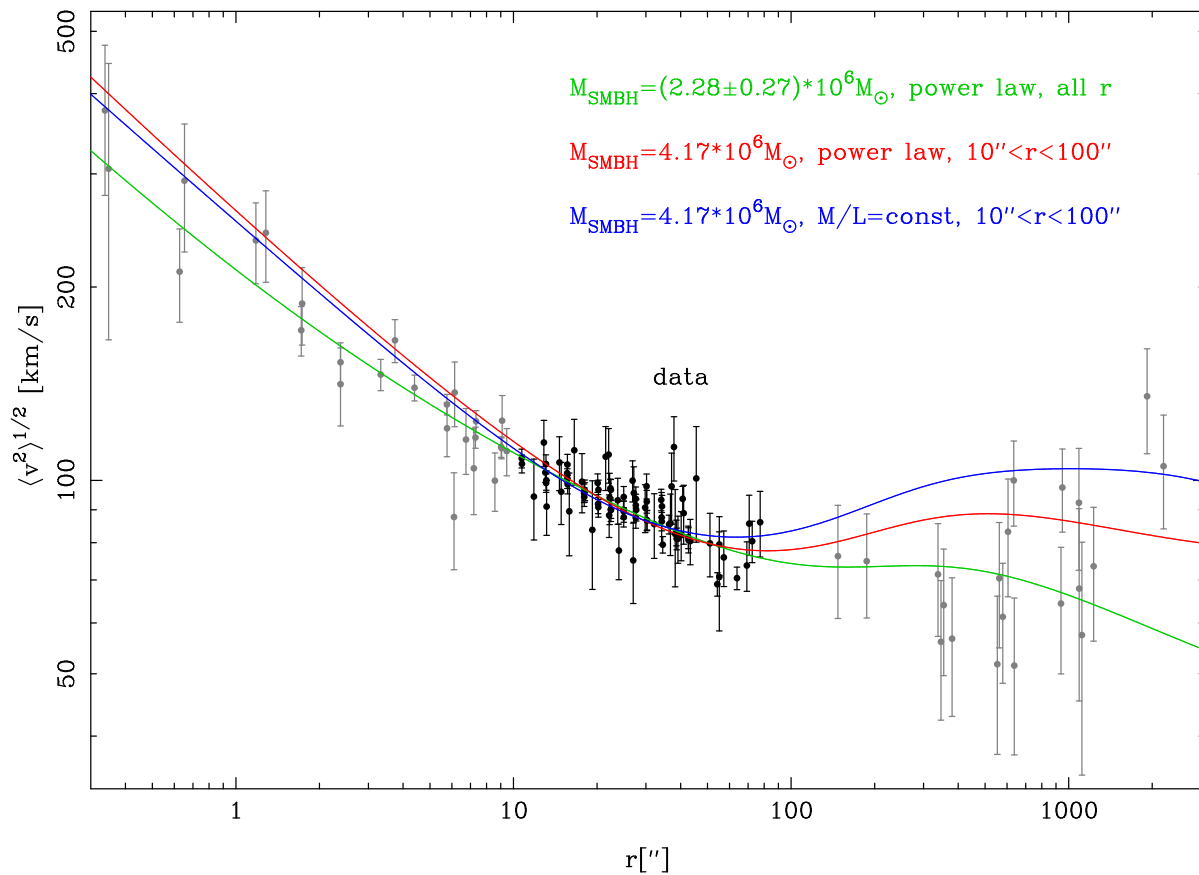


Figure 5.16 Data and fits of the Jeans modeling. The data within  $10''$  and outside  $100''$  (gray dots) are somewhat less consistent with our simple model; the other data is plotted as black dots. The curves show the fits from rows 1 (green), 3 (red), and 5 (blue) of Table 5.3.

the tracer results in a difference of up to 19 % in  $M_{100''}$  (compare rows 5 and 6 in table). The larger value occurs for the flux density profile, since it is steeper (outside the core) and thus places the mass in 3D closer to the center.

Looking at the  $\chi^2$ -values in the table seems to indicate that the fits using the flux density as a tracer profile are worse than the fits using the stellar number counts. However, most of this difference is due to the density data, where because of our error calculation (Appendix 5.8.2) the  $\chi^2$  of the flux density data is worse, see also Section 5.4.3. Hence, we choose to give both density profiles equal weight for the following average.

Overall, we trust the 14 fits in rows 3 - 6 and 9 - 18. The average mass is

$$M_{100''} = (6.02 \pm 0.51) \times 10^6 M_{\odot} . \quad (5.10)$$

The error is dominated by the scatter between the different fit results. Using only rows 3 - 6 yields a very similar result.

The cluster mass slope is between 1.11 and 1.40, where the largest slopes occur in rows 7 and 8, which are affected by the SMBH mass bias. Calculating the mean of the other six values yields  $\delta = 1.19 \pm 0.07$ , where the error again is dominated by the scatter between the different fits. This number is in reasonable agreement with the tracer profile, which has a slope of 1.18 (stellar number count based) or 1.06 (flux based) in the range  $50'' < r < 200''$ .

In order to compare with the models used in the literature, we also fit single Nuker models to our data (Rows 19 - 22). In order to be able to fit a single component model, we in addition restrict the range of the tracer density data inside the break to the nuclear disk, i. e.  $r < 220''$ . With this restriction our mass range is  $5.86 \times 10^6$  to  $7.29 \times 10^6 M_{\odot}$ . Using the literature profiles of Genzel et al. (1996), Trippe et al. (2008), and Schödel et al. (2009) the mass range is larger, from  $4.87 \times 10^6$  to  $7.81 \times 10^6 M_{\odot}$ . Profiles with a steep outer slope (e.g. Trippe et al. 2008) measure the biggest mass, while the mass is smallest when the outer slope is small and the core is large.

Our data set would allow to determine the distance to the GC,  $R_0$ , by means of a statistical parallax (Genzel et al. 2000; Eisenhauer et al. 2003; Trippe et al. 2008). We have more than 2400 radial velocities and even more proper motions. This would yield a statistical precision of  $1.6\% \approx 0.13$  kpc. At that level of precision, however, one needs to take into account the difference in dispersion between  $l^*$  and  $b^*$ . Our spherical model cannot provide that, and we defer this to the follow-up work by Chatzopoulos et al. in preparation, who will present self-consistent flattened models.

We now obtain the mass uncertainty due to the distance uncertainty. We use the latest results for the orbit of the S-stars of  $R_0 = 8.2 \pm 0.34$  kpc (Gillessen et al. 2013). To include this distance error in the error budget we repeat the Jeans modeling for  $R_0$  of 7.86 and 8.54 kpc. We rescale the SMBH mass according to the  $M_{\bullet} - R_0$  relation of Gillessen et al. (2009)  $M_{\bullet} \propto R_0^{2.19}$ . We find following mass distance relation:

$$M_{100''} = (6.02 \pm 0.51) \cdot 10^6 \times \left( \frac{R_0}{8.2 \text{kpc}} \right)^{3.83} \quad (5.11)$$

The distance error of Gillessen et al. (2009) leads to following expression

$$M_{100''} = (6.02 \pm 0.51|_{\text{fix}R_0} \pm 0.96|_{R_0}) \times 10^6 M_{\odot} . \quad (5.12)$$

Thus, the distance-induced error is larger than other errors considered so far.

Finally, we obtain an estimate for the total mass of the nuclear cluster by using our Sersic decomposition. Assuming that the mass scales like the flux, we find a ratio of  $M_{\text{NC}}/M_{100''} = 2.14 \pm 0.41$ . The error is due to the error on the cluster luminosity (Section 5.4.5), excluding however the calibration contributions. This yields a total nuclear cluster mass of

$$M_{\text{NC}} = (12.88 \pm 2.69|_{\text{fix}R_0} \pm 2.05|_{R_0}) \times 10^6 M_{\odot} . \quad (5.13)$$

We expect that this estimate can be further improved by the self-consistent, flattened and rotating model in Chatzopoulos et al in prep.

### 5.5.5 Velocity Distribution and Fast Stars

The Jeans modeling only used the first two moments of the velocity distributions, but they contain information beyond that. In particular, stars with high velocities, in the wings of the distributions, are interesting. The unbiased space velocity for each star is

$$v_{3\text{D}} = \sqrt{v_x^2 + v_y^2 + v_z^2 - \delta v_x^2 - \delta v_y^2 - \delta v_z^2} . \quad (5.14)$$

The errors of  $v_{3\text{D}}$  do not depend on the value, and in particular there is no indication that the higher velocity stars are due to a measurement problem. We divide the sample into radial bins of 32 stars each, and determine in each the maximum and the median 3D-velocity (Figure 5.17). The maximum velocity is not a smooth function of  $r$ , but follows a power law slope of  $-0.47 \pm 0.04$  inside of  $7.5''$ , close to a Keplerian slope of  $-0.5$ . Other high quantiles like the second fastest star follow similar slopes in the center. Outside of  $7.5''$  these slopes appear to be consistent with the slope of the median velocity, of around  $-0.17$ .

### Minimum Binding Mass

We now calculate for all stars the minimum binding mass, i.e. we assume that each star is in the plane of sky and on a parabolic orbit around a point mass. In each radial bin we thus can determine the highest mass (Figure 5.18). Inside of  $8.3''$  the escape mass is close to the SMBH mass. The average escape mass there is  $3.69 \times 10^6 M_{\odot}$ , the most significant mass larger than that of the SMBH occurs for the star S111 with  $4.33 \pm 0.05 \times 10^6 M_{\odot}$ , as was noted already by Trippe et al. (2008) and Gillessen et al. (2009). High escape masses indicate that the stars are not only in projection, but also in 3D close to the SMBH. These fast stars can be used as additional constraints on the late-type density profile close to the SMBH in advanced dynamic modeling.

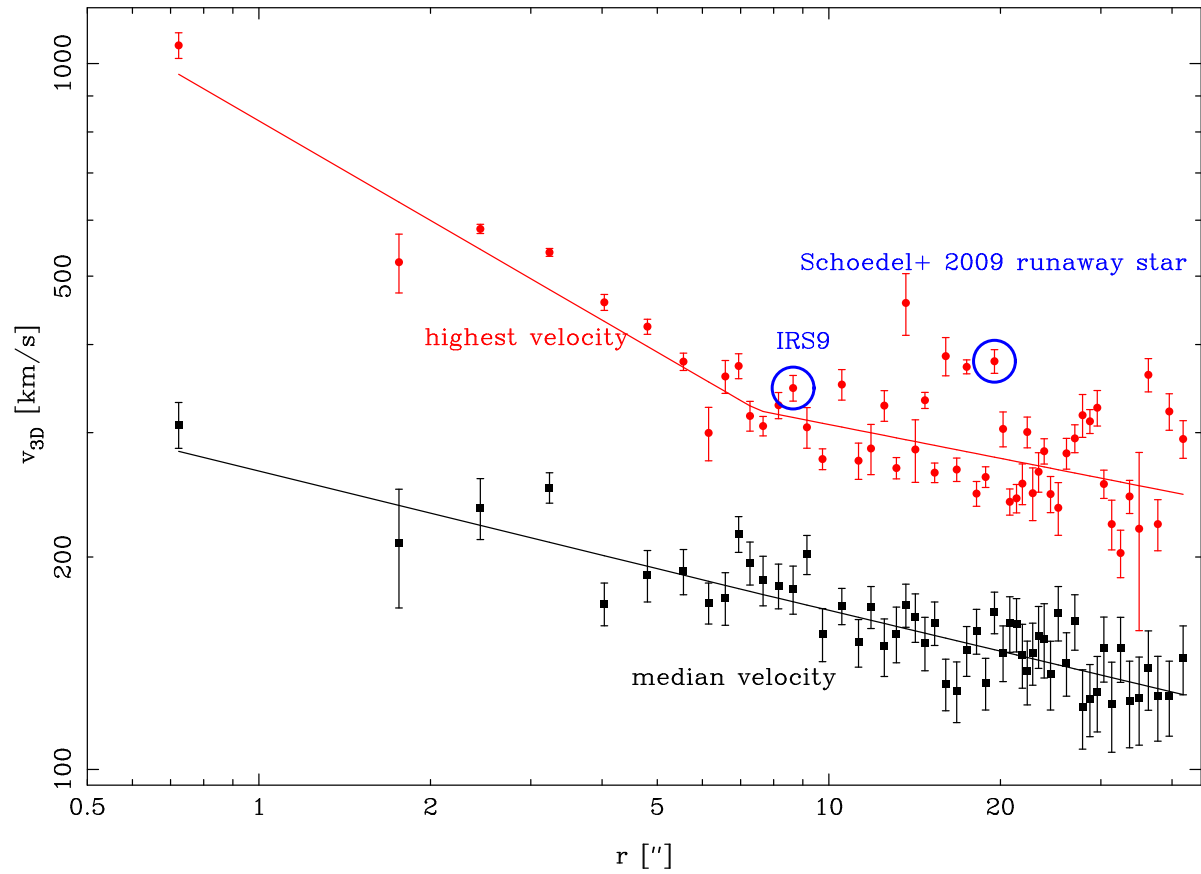


Figure 5.17 Binwise median and maximum three-dimensional velocity. We describe the data with (broken) power laws. The error indicates the velocity error of the median velocity stars and the velocity error of the fastest stars, respectively. Fast stars already discussed by Reid et al. (2007) or Schödel et al. (2009) are marked with open blue circles.

### A Distance Estimate

The number of stars that appear unbound depends on the assumed distance  $R_0$ . Stars whose velocity is dominated by the radial velocity are bound for a large  $R_0$ , while stars with a large proper motion are bound for small  $R_0$ . Our sample contains nine stars, which are unbound for some distances between 7.2 and 9.2 kpc. From these stars we calculate a  $\chi^2$  as a function of  $R_0$  summing up in squares the significances of the differences from the escape mass minus the mass of the SMBH. For the latter we assume  $M_\bullet = (3.95 \pm 0.06) \times 10^6 (R_0/8.0\text{kpc})^{2.19} M_\odot$  (Gillessen et al. 2009). Minimizing this  $\chi^2$  as a function of  $R_0$  yields  $R_0 = 8.51_{-0.14}^{+0.18}$  kpc. The main constraint comes from 2 stars: S111 and a star with high proper motion, id 569 (Figure 5.19).

This estimate relies on some assumptions:

- We assume that all stars are bound. This is justified, since the chance to see an escaping star from a Hills-event (Hills 1988) is very low (Yu & Tremaine 2003; Perets et al. 2007). Also the mechanism, which causes stars faster than the local escape velocity at  $\gtrsim 10''$  is unlikely to play a role, as suggested by the break around  $8''$  visible in Figure 5.17).
- The method relies on the mass-distance scaling of the SMBH mass from stellar orbits. Using the relation from Ghez et al. (2008) we obtain  $R_0 = 8.36_{-0.24}^{+0.20}$  kpc.
- We assume that we have correctly debiased the velocities. Since the total velocity error of the two most important stars is less than 1.5% of their velocity this assumption seems to be uncritical.

Independent of the  $M_\bullet - R_0$  relation fast stars also yield a lower limit on the SMBH mass, which is  $3.6 \times 10^6 M_\odot$  for  $R_0 > 7.2$  kpc, consistent with the orbit-based estimates, and higher than most Jeans-model estimates.

### Fast Stars at $r > 10''$

Outside of  $10''$  most fast stars are unbound to SMBH and nuclear cluster mass (Figure 5.18). Some of these stars were already discussed in Reid et al. (2007) and Genzel et al. (2010). Our improved mass estimate for the nuclear cluster reinforces the statement that these stars are not bound to the GC. Note that placing a star out of the plane of the sky enlarges the discrepancy (Reid et al. 2007), e.g. for a star at  $40''$  the escape velocity decreases out to  $z = 200''$  and then increases only very slowly to about 165 km/s at  $3600''$ , which is still less than in the plane of sky. The fact that maximum velocity decreases for  $r > 8''$  in the same way as the median velocity (Figure 5.17) excludes that the fast stars are foreground objects, for which the velocity would not depend on radius. Furthermore, the extinction appears to be normal for the fast stars.

Reid et al. (2007) also discussed binaries as a solution for the high velocities. This is excluded by our data set since for some stars the high velocity is dominated by long-term proper motions measurements, which cover much more time than what one orbital period

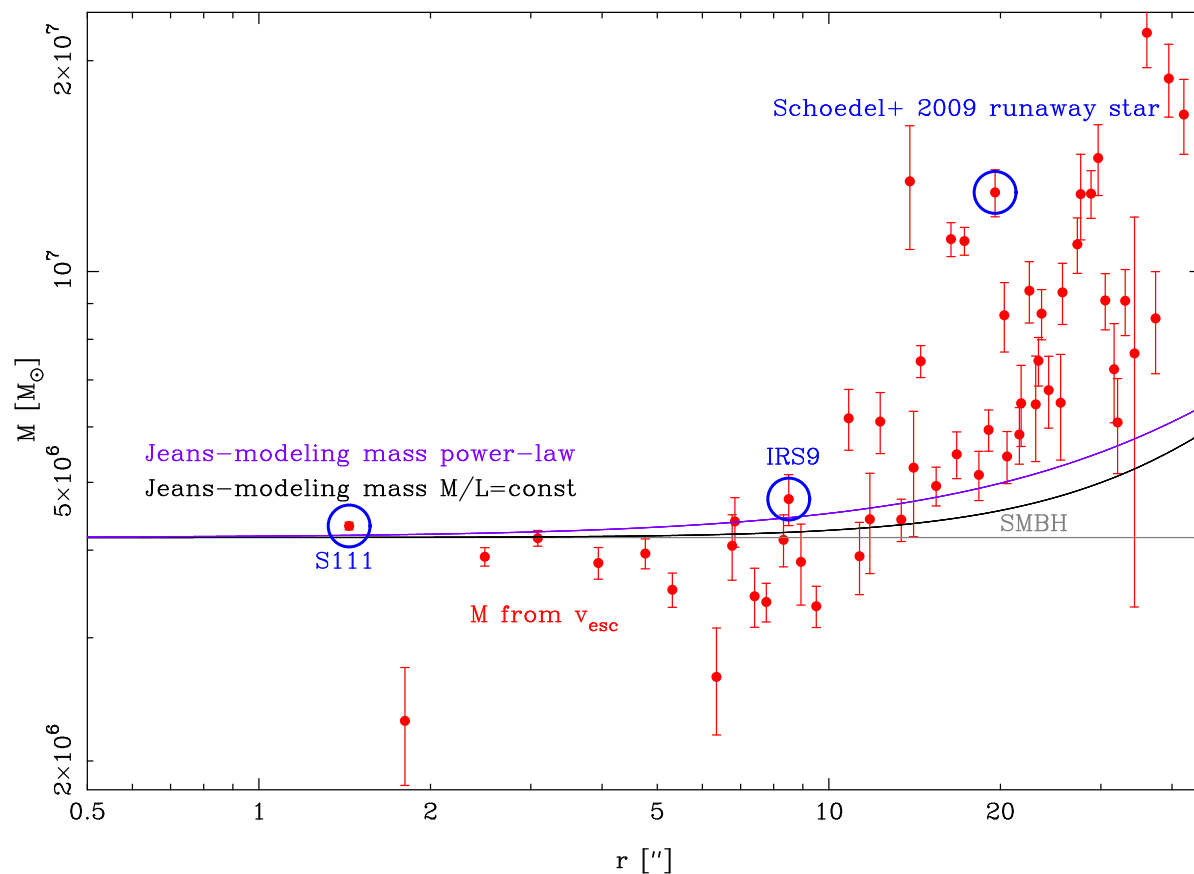


Figure 5.18 Binwise maximum of the minimum binding mass calculated for each star. The mass errors follow from the  $1\sigma$  velocity errors. We compare these masses with the SMBH mass of Gillessen et al. (2009) and two Jeans-models, rows 3 and 5 from Table 5.3. The fast stars from Reid et al. (2007), Trippe et al. (2008) and Schödel et al. (2009) are indicated with open blue circles.

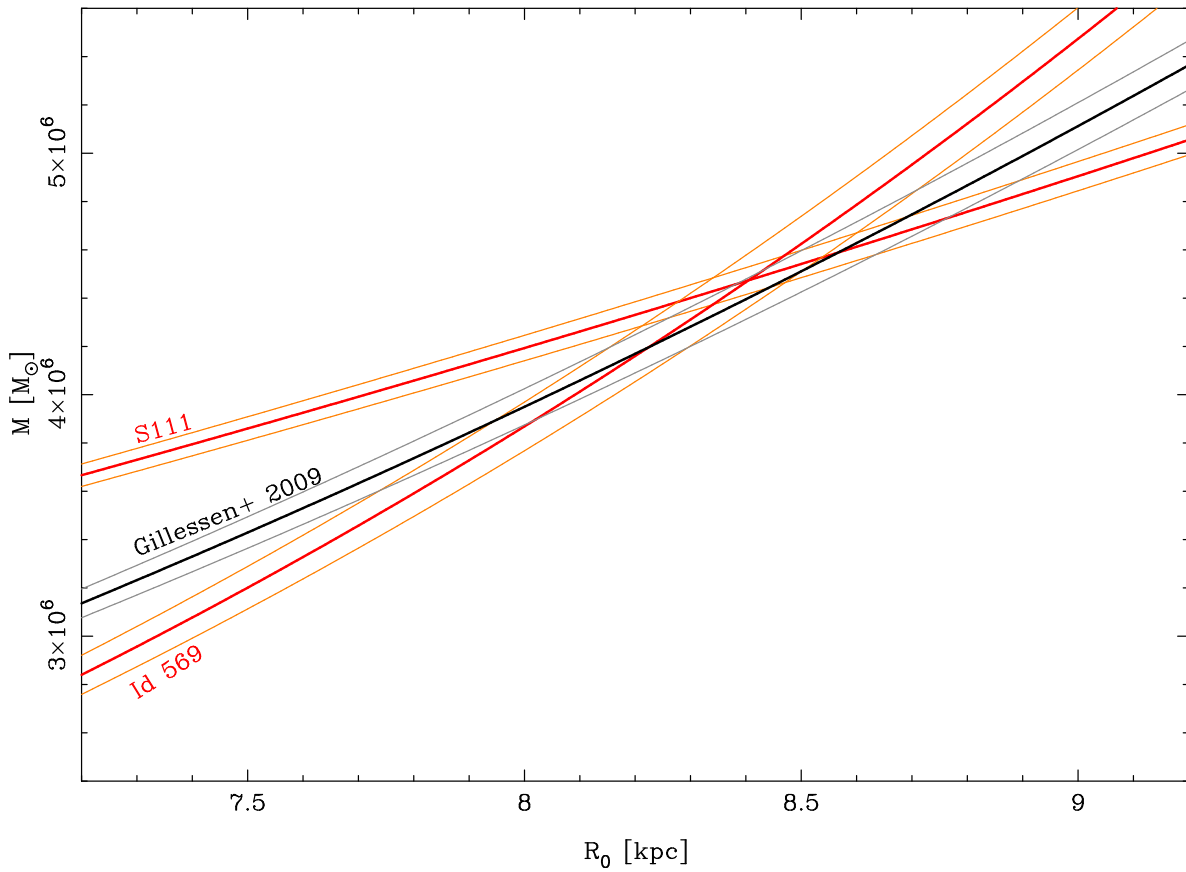


Figure 5.19 Distance constraints from stars that are close to escaping. The figure shows the mass distance relations for the SMBH from Gillessen et al. (2009) and the mass distance relations from the two stars which are closest to escape. Red and black lines mark the value; orange and gray lines the respective  $1\sigma$  error range.

would need to be. Again, the Hills-mechanism origin is unlikely given the comparably large number of fast stars. Probably as already advocated by Reid et al. (2007), the best solution is that these stars are on very eccentric orbits in the large scale potential. Therein they can obtain higher velocities than the local escape velocity.

Since the database Genzel et al. (2010) contained many bright, unbound stars, these authors suggested that preferentially young, unrelaxed, bright TP-AGB stars are on these unbound orbits. This finding might be affected by low number statistics and a bias: Bright stars have smaller velocity errors and are therefore easier to identify as significantly unbound. In our sample and excluding the database of Genzel et al. (2010), we see no evidence that bright stars are dynamically distinct from the other stars. This also holds for the subsample of medium old TP-AGB stars from Blum et al. (2003). Also Pfuhl et al. (2011) found that their two samples of younger and older giants show consistent dynamics.

### Velocity Histograms

In Figure 5.20 we show the velocity histograms of the three dimensions. The proper motion sample is split into two bins,  $r > 7''$  and  $r < 7''$ . For the radial velocities, we use three bins,  $r < 7''$ ,  $7'' < r < 100''$  and  $r > 100''$ . In the latter bin (where the maser stars fall) we have subtracted off the rotation.

We see deviations from Gaussian distributions in many aspects, more than Trippe et al. (2008) did:

- The central part of distributions in  $l^*$  and  $b^*$  are not as peaked as Gaussians. In  $l^*$  the distribution has a flatter peak than a Gaussian (Trippe et al. 2008; Schödel et al. 2009). In  $b^*$  the distribution has a slightly, but significantly ( $> 5\sigma$ ), steeper peak than a Gaussian. This is actually a signature of the flattening of the cluster, as will be discussed in Chatzopoulos et al. in prep.
- The high-velocity wings inside of  $7''$  are not Gaussian. This is due to the fast stars discussed above. Trippe et al. (2008) did not see that because they did not radially subdivide their sample, and furthermore our sample contains twelve more stars in the central  $2''$  with  $v_{3D} > 460$  km/s than the one from Trippe et al. (2008). In that work the only such fast star was S111.
- The varying ratio of maximal and median velocity (Figure 5.17) is also indicative of non-Gaussian wings.
- From the 274 stars in the  $r > 100''$ -bin, roughly 13 are in the high (radial) velocity wings of the distribution. Most of these outliers were already noted by Lindqvist et al. (1992) and Deguchi et al. (2004).

The presence of an SMBH causes non-Gaussian velocity distributions (Gebhardt et al. 2011; van der Marel 1994) close to it. This and the higher number of fast stars make S111 less special than discussed in Trippe et al. (2008).



Table 5.4 gives an overview of the unusually fast stars in our sample. ID 787 is the star Schödel et al. (2009) called a runaway candidate. We find a proper motion that is  $3.8\sigma$  smaller, and derive a rather normal radial velocity from its late-type spectrum, making this star considerably less noteworthy. The difference in proper motion is probably due to our better distortion correction (Section 5.6.1). The star with the highest 3D velocity is the giant ID 4258, but it is (projected) close to another bright late-type star, such that the radial velocity error might well be larger than indicated. Summarizing, about 17 of 5093 stars are somewhat surprisingly fast. But none of these stars is definitely unusually fast. The fraction appears to be smaller than in the maser sample (13/274), but at smaller radii the dispersion is higher and thus the identification of outliers gets more difficult there.

## 5.6 Discussion

We discuss our results in the context of previous results for the nuclear cluster of the Milky Way and of other galaxies.

### 5.6.1 SMBH Mass Bias

Row 1 in Table 5.3 shows that fitting for the SMBH mass with a power law profile yields a mass which is much smaller than the estimates from stellar orbits (Schödel et al. 2002; Gillessen et al. 2009; Ghez et al. 2008). In order to avoid that rotation or flattening influence the results, we use here only the data in the central  $25''$ , where the assumption of spherical symmetry is fulfilled best. The same bias also occurred in earlier works (Genzel et al. 1996; Trippe et al. 2008). However, recently Schödel et al. (2009) and Do et al. (2012) obtained higher masses from Jeans modeling of old stars.

Do et al. (2012) obtained from the three-dimensional motions of 248 late-type stars in the central  $12''$  a mass of  $M_{\bullet} = 4.0 \pm 0.45 \times 10^6 M_{\odot}$ , consistent with the orbit-based estimates. They used anisotropic spherically symmetric Jeans modeling, but their solution is consistent with isotropy. However, they did not include an extended mass. It is not obvious that the late-type star distribution is concentrated enough toward the center that this is allowed. Further, due to the small field of view, Do et al. (2012) cannot constrain the break radius. Also we would obtain the correct SMBH mass when choosing a large break radius, but that is incompatible with the density data. Thus, it is possible that the result of Do et al. (2012) is caused by an implausibly large break radius.

Schödel et al. (2009) obtained from isotropic Jeans modeling  $M_{\bullet} = 3.55 \times 10^6 M_{\odot}$ , larger than our estimate and the earlier works. For their assumed distance of  $R_0 = 8$  kpc the SMBH mass of Gillessen et al. (2009) is within the 90% probability interval, but in their anisotropic modeling it is excluded by 99%. It is interesting to clarify the differences between our analysis and Schödel et al. (2009), using their publicly available data set.

- Using the Schödel et al. (2009) data and our various parametrizations we get results consistent with what these authors found. Hence, the details of the modeling only play a minor role.

- Using our data and the tracer profile of Schödel et al. (2009) we retrieve a smaller SMBH mass. Trials with different tracer profiles show that the differences in the tracer profile are not the main reason for the differences in the mass obtained between our work and Schödel et al. 2009 (Figure 5.21).

Thus, the main reason are the larger dispersion values in the data of Schödel et al. (2009), see Figure 5.21. What is the reason for the different dispersions?

1. The largest differences occur within  $r < 2.5''$ . There, Schödel et al. (2009) still have a few early-type stars polluting their sample, since they used the spectroscopy-based, but slightly outdated star list in Paumard et al. (2006) and the photometric identifications of Buchholz et al. (2009). For example, the well-known early-type star S13 (Eisenhauer et al. 2005), for which an orbit is known, is in their sample. In contrast, we use in the central  $2.5''$  only stars which we positively identify spectroscopically as late-type stars. The issue is critical in the center, since the early-type stars are more concentrated toward the SMBH than the late-type stars and thus show a higher dispersion in the center. Removing the early-type stars from the Schödel et al. (2009) sample yields a dispersion consistent with our value.
2. Within  $2.5$  and  $15''$  the differences are small, and are only caused by the fact that we also use the radial velocity dispersion in this radial range, while Schödel et al. (2009) uses only proper motion data.
3. At  $r > 15''$  differences occur in the proper motion data, which could be caused by differences in the distortion correction. We use the procedure of (Trippe et al. 2008) to correct for distortion. This is particularly important at large radii, in the corners of the NACO field of view. An imperfect distortion correction enlarges dispersions artificially, and thus a smaller measured value is more likely to be correct.

Overall our dispersions are probably more reliable than the of Schödel et al. (2009). This is also supported by the fact that we get a consistent value for the mass parameter  $M_{100''}$ , if we restrict our dynamics data to the range  $r < 25''$ .

We now try to explain why our and other attempts of Jeans-modeling fail to recover the right SMBH mass.

- Neglecting anisotropy cannot cause the bias, since including it yields actually even smaller masses (Schödel et al. 2009).
- The assumed power law tracer profile yields a smaller mass than using a constant M/L:  $M_{\bullet} = (2.47 \pm 0.50) \times 10^6 M_{\odot}$  compared to  $M_{\bullet} = (3.38 \pm 0.16) \times 10^6 M_{\odot}$ , for the restricted range  $r < 25''$  of the dynamics data. Hence, a core in the density may be part of the solution.
- Changing the distance  $R_0$  only can correct to a small part the bias. Even for an unrealistically large value of  $R_0 = 9 \text{ kpc}$  the SMBH mass is not retrieved.

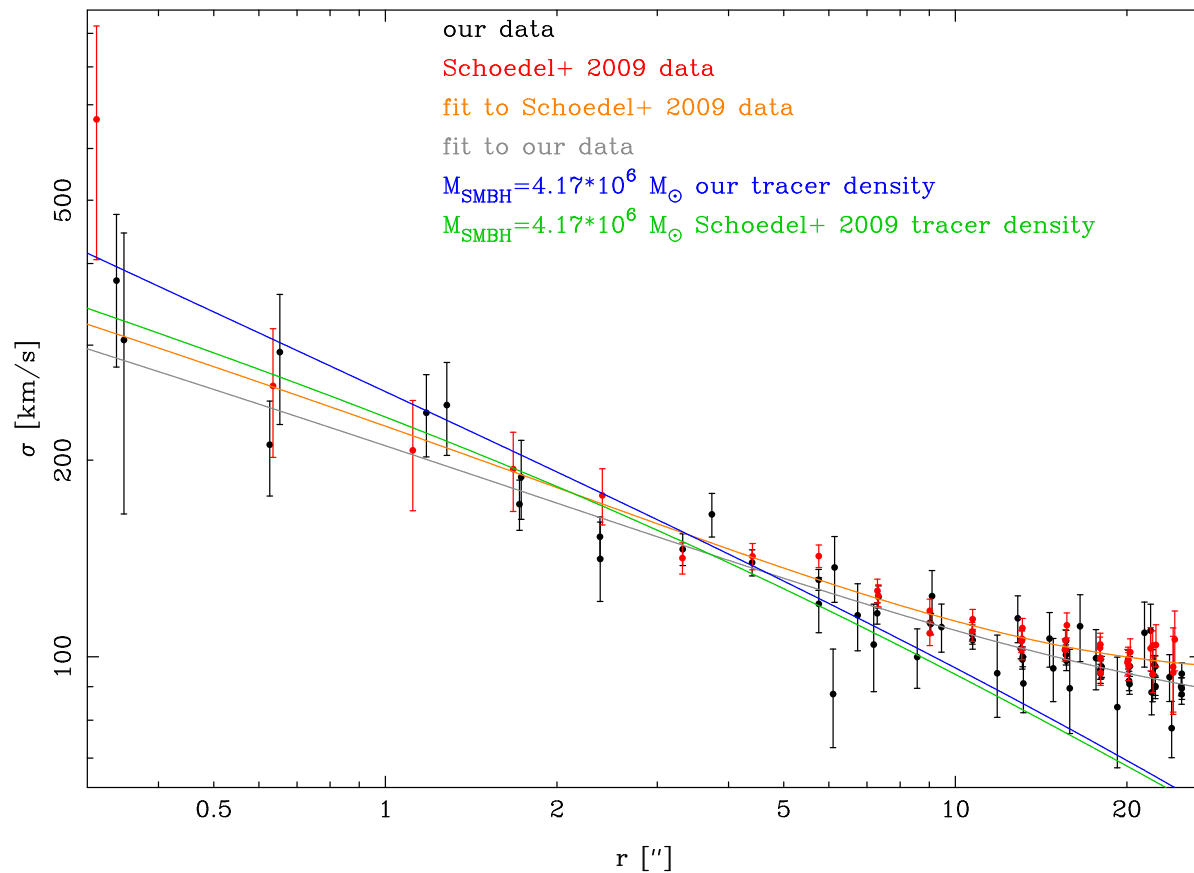


Figure 5.21 Fits of the dispersion in the inner  $25''$  by Jeans models. The black points present our data, red boxes the data from Schödel et al. (2009). Our data include proper motions and radial velocities, the data of Schödel et al. (2009) only proper motions. The blue and green curves show the expected dispersion when only the SMBH is present. We use the tracer profile of Schödel et al. (2009) and the best fit to our tracer density data. In our case we use the fit of the star density data with a double  $\eta$ -model. The orange and gray curves show fits of the different dispersion data using a power law extended mass model. Both use the tracer density of Schödel et al. (2009).

- Inside of  $7''$  the velocity distribution shows non-Gaussian wings (Section 5.5.5). Hence, the error on the dispersion is larger than  $\sigma/\sqrt{2N}$ . However, the dispersions in the different dimensions seem consistent within their errors outside of  $0.5''$ , and hence the effect is probably not large.
- Trippe et al. (2008) and Genzel et al. (2010) argued that a central core-like structure introduces a bias toward low SMBH masses, This, however is only applicable when a tracer profile without core is used for cored data. If the correct profile contains a core and is modeled such, the central core only increases the error on the central mass. In our models such an uncertainty is included via the free density profile, yet the SMBH mass falls outside of the error band. Of course, we cannot exclude, that there is a density profile, different from our model that yields the correct SMBH mass and fits the density data. Perhaps a profile works with a large radial transition region, in which the profile has a constant slope somewhat steeper than in the center.
- Introducing a flat true core is unlikely to solve the issue: It is not only inconsistent with the apparent isotropy, it also underpredicts the number of late-type stars with orbits.
- Also the flattening could influence the SMBH mass via the tracer profile. Using our decomposition (Section 5.4.4) we can artificially increase the contribution of the outer component. Indeed, we find that this reduces the bias significantly, and conclude that modeling including flattening as done in Chatzopoulos et al. in prep. is necessary.

Summarizing, we have tested several potential solutions to the mass bias. For some we have shown quantitatively that they alone cannot correct the bias. Others would requires modeling which goes beyond this work. Flattening and rotation will be investigated in Chatzopoulos et al. in prep. Perhaps maximum likelihood modeling is needed for our discrete data set (D’Souza & Rix 2013), in particular for properly incorporating the information the fast stars carry.

### 5.6.2 Comparison with the Literature

Overall, most values from the literature are similar to our values. The comparison with other works needs some care, since different values for  $R_0$  have been used, and hence we scale to  $R_0 = 8.2$  kpc. We correct the masses in the literature to our distance using a mass scaling with exponent 1 for purely radial velocity based masses, and exponent 3 for purely proper motion based ones. We extrapolate from our best estimate  $M_{100''}$  in two ways: on the one hand we use a broken power law with break radius  $100''$ . The inner slope is  $\delta = 1.242$ , the outer is  $\delta = 1.125$ . (This uses inside of  $100''$  the average  $\delta$  of row 3 and 4 of Table 5.3 and outside the average  $\delta$  of row 11 and 12 there.) On the other hand, we use one of the preferred fit with constant M/L (Row 5 in Table 5.3) Most other mass profiles are similar to one of these cases.

**Schödel et al. (2009)**

The possible mass range of Schödel et al. (2009) within 1 pc is  $(0.5 - 2.2) \times 10^6 M_\odot$ , similar to our result. However, assuming a constant M/L they obtain a mass of  $1.6 \times 10^6 M_\odot$  in the isotropic case, larger than our value of  $0.6 \times 10^6 M_\odot$ . At 4 pc their profile yields a rather large mass of  $16 \times 10^6 M_\odot$ . There are two reasons for the difference:

- The larger core in their profile. It puts the stars after deprojection further out. Consequently, the influence of the SMBH is reduced, and in order to obtain the same observed dispersion, the cluster mass must be higher.
- The larger dispersions at the outer end of their data range.

**Trippe et al. (2008)**

At 100" Trippe et al. (2008) found a mass that is roughly a factor 3 larger than ours. This mass cannot be scaled easily with  $R_0$  since they combined proper motions and radial velocities, but the value used ( $R_0 = 8$  kpc) is close to  $R_0 = 8.2$  kpc. The difference is due to the high rotation at large radii as a result of their selective use of data from McGinn et al. (1989). At 1 pc where rotation is negligible they found a value of  $1.2 \times 10^6 M_\odot$  (their Figure 14, gray dashed curve), similar to our mass in the power law case.

**Inner Circumnuclear Disk**

The gas in the inner circumnuclear disk (CND) can be used to obtain a mass estimate. Serabyn & Lacy (1985) used the emission of [NeII] 12.8  $\mu\text{m}$  from gas streamers at the inner edge (including the Western arc) of the CND to obtain radial velocities. They found  $(3.9 \pm 0.8) \times 10^6 M_\odot$  at 1.4 pc,  $1.7 \sigma$  and  $2.4 \sigma$  smaller than our constant M/L, respectively power law estimate. This value is smaller than the mass of the SMBH. Only an impossibly large core could reconcile the two values. Thus, it seems likely that Serabyn & Lacy (1985) underestimated the mass or at least the error in their measurement. The rotation velocity of the inner CND of 100 km/s is well-determined (Genzel et al. 1985; Serabyn & Lacy 1985; Guesten et al. 1987; Jackson et al. 1993; Christopher et al. 2005), and hence the reason for the discrepancy has to be in the model assumed. Conceptually, the mass derivation of Serabyn & Lacy (1985) was simple: they assumed circular motion of all the gas in one ring with an inclination of  $60 - 70^\circ$ .

In the HCN J-0 data of the inner CND in Guesten et al. (1987) the velocities in the southern and western parts follow the model of Serabyn & Lacy (1985), but not in the northern and eastern parts. The latter can be described by a less inclined ring ( $\approx 45^\circ$ ) with an intrinsic rotation velocity of  $137 \pm 8$  km/s. This velocity results in a total mass  $(6.1 \pm 0.7) \times 10^6 M_\odot$ . This mass is consistent with our power law estimate and  $1.2 \sigma$  larger than our constant M/L estimate. Using an average inclination between Serabyn & Lacy (1985) and Guesten et al. (1987) would hence yield a mass estimate very similar to ours.

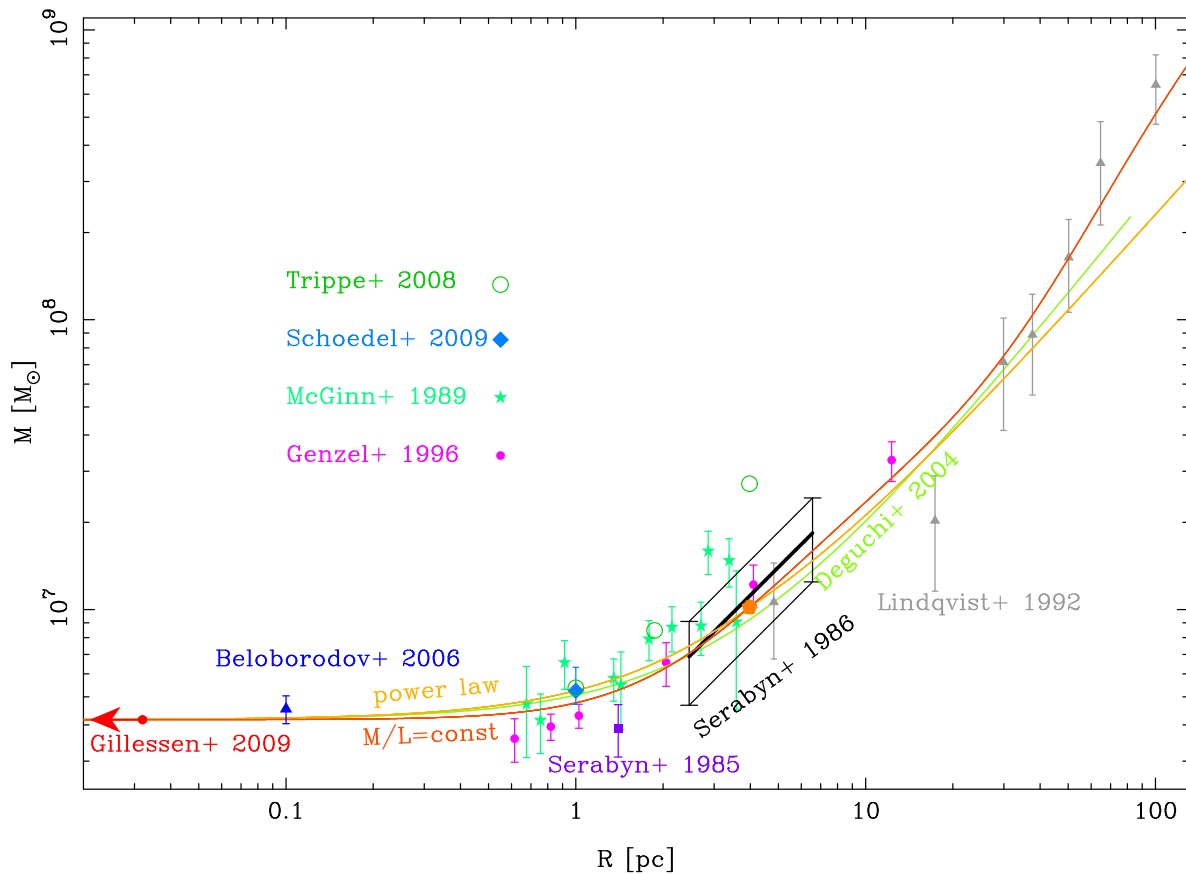


Figure 5.22 Cumulative mass profile of the GC. The main measurement of this work is the orange pentagon at 4 pc, through which the profiles for the power law or constant  $M/L$  case pass. The stellar orbits based value from Gillessen et al. (2009) is at about 0.002 pc. Beloborodov et al. (2006) used an orbit roulette technique to obtain an enclosed mass. In the work of Schödel et al. 2009 (blue diamond) no formal error is given, we show the largest range mentioned. For the masses from Trippe et al. 2008 (green open circles) no errors are given. The value from Serabyn & Lacy (1985) is the violet square. For Serabyn et al. 1986 the thick black line is the value and the thin black lines give the error range. From Lindqvist et al. 1992 (gray triangles) and McGinn et al. 1989 (green stars) we use the Jeans modeling values. In case of Deguchi et al. 2004 (light green line) we show their extended mass model fit using the Boltzmann equation, adapting to our assumed SMBH mass. We plot Jeans-modeling based values from Genzel et al. 1996 (pink dots). We omit the values from Genzel et al. (1996) and McGinn et al. (1989) inside of 0.55 pc, since more accurate values are available there.

Further, the more recent work of Zhao et al. (2009) shows that a single orbit, even a non-circular one, cannot fit all gas streamers in the Western arc, and hence the inner CNB is likely more complicated than assumed by Serabyn & Lacy (1985).

### **Outer Circumnuclear Disk**

Serabyn et al. (1986) used CO 1-0 in the outer parts of the CNB for estimating the mass using the same method as Serabyn & Lacy (1985). This measurement is consistent with our mass. The agreement argues that indeed the gas dynamics is dominated by gravity.

### **Rieke & Rieke (1988)**

At radii larger than 7 pc the gas velocities get unreliable (Serabyn et al. 1986; Guesten et al. 1987), but stellar velocities are available. Rieke & Rieke (1988) used a few bright stars and found a dispersion of 75 km/s between 6'' and 160'', independent of radius. With our data we can reject the hypothesis of McGinn et al. (1989), proposing that a magnitude effect causes the surprisingly flat rotation curve. Possibly, Rieke & Rieke (1988) were limited by the low-number statistics.

### **McGinn et al. (1989)**

These authors covered a similar area in size to ours, using integrated velocities and dispersions in large beams. Broadly their dispersion data is consistent with our data, and they measure a somewhat stronger radial dispersion trend. They obtain masses similar to our estimates and also find a too small SMBH mass, like most works that apply free Jeans modeling. At the outer edge the masses of McGinn et al. (1989) are somewhat larger than ours, due to the high rotation velocity in this work (Section 5.5.3).

### **Lindqvist et al. (1992)**

Using maser velocities and Jeans modeling out to much larger radii Lindqvist et al. (1992) obtained masses consistent with our model. This is not surprising, since we include their velocities in our data set. The main discrepancy occurs around 17 pc, where their estimate is only half of our extrapolation. Possibly, our modeling has not enough flexibility at these large radii. This is obvious for the power law case. In both our and the analysis of Lindqvist et al. (1992) the deviation from spherical symmetry is not considered, which might lead to significant changes at large radii.

### **Deguchi et al. (2004)**

Deguchi et al. (2004) used also maser velocities, but in a somewhat smaller area than Lindqvist et al. (1992). They prefer a result based on a new method developed from the Boltzmann equation. This method includes rotation, but assumes spherical symmetry and a fixed extended mass slope of  $\delta = 1.25$ . To compare their extended mass result with our

work we need to adapt their result to our SMBH mass, which is within their  $1.5\sigma$  range. In the inner parsec their mass of  $(0.90 \pm 0.07) \times 10^6 M_\odot$  is consistent with our range, but at  $100''$  their estimate of  $(5.06 \pm 0.39) \times 10^6 M_\odot$  deviates by  $1.5\sigma$  from our estimate. Due to this fixed slope their mass deviates also at larger radii from the results in Lindqvist et al. (1992). A fixed slope does not describe the stars density in the GC well out to 80 pc.

### Genzel et al. (1996)

This work obtained the mass distribution out to 20 pc from Jeans modeling of radial velocities, using literature radial velocities in combination with own velocities in the center. Also these authors underpredict the SMBH mass. Beyond that, their results are consistent with ours.

### Works Using the Light Distribution

Different works in the past used the light distribution together with a mass to light ratio to estimate the mass of the nuclear cluster (McGinn et al. 1989; Lindqvist et al. 1992; Launhardt et al. 2002). The masses obtained broadly agree with our mass estimate. Mostly, these works used a dynamic mass at a certain radius to obtain M/L there and then extrapolated using the light profile. E. g. Launhardt et al. (2002) used the mass from Genzel et al. (1997) at 1.25 pc to normalize their profile. For best comparison with Launhardt et al. (2002) we extrapolate their mass for the inner parsec to  $100''$  using their radial profile. After distance correction we obtain  $M_{100''} = 6.46 \times 10^6 M_\odot$ , consistent with our value, which however mainly shows the consistency between the stellar mass of Genzel et al. (1997) and our work. Since Genzel et al. (1997) used data from Genzel et al. (1996) outside the very center, this confirms again that Genzel et al. (1996) is consistent with our work.

Using only the light to determine the stellar mass is difficult due to following systematic uncertainties in M/L: the star formation history, the extinction toward the GC and the IMF of the stars. The star formation history and extinction can in principle be derived independent from the mass of the nuclear cluster. The recent establishment of a smaller extinction toward the GC (Nishiyama et al. 2006; Fritz et al. 2011; Schödel et al. 2010) compared to the previously used value from Rieke & Lebofsky (1985) should have decreased the light-derived mass estimates, when only the light was used for mass estimates. The measurement of the star formation history of the GC by Blum et al. (2003) and Pfuhl et al. (2011) can be used to constrain M/L.

In principle it is possible to update the light-derived mass using Fritz et al. (2011) and Pfuhl et al. (2011) together. However, still the mass function is a free parameter. Deriving the mass function of the old stars from their Hertzsprung-Russell diagram is very difficult (Pfuhl et al. 2011). Since the IMF of the GC is an interesting subject, we reverse the argument, and use mass to constrain the IMF (Section 5.6.5).

### 5.6.3 Mass Cusp or Core?

The distribution of old stars does not show the expected cusp (Bahcall & Wolf 1976) with the  $\delta = 1.25$  slope (Buchholz et al. 2009; Do et al. 2009; Bartko et al. 2010). The stars follow a shallower slope, which can either be a true core ( $\delta = 3$ ) or a shallow cusp ( $\delta > 2$ , Do et al. 2009). Also the second case we call core here, since it has much less light in the center than a cusp. Isotropy in the center is preserved for  $\delta < 2.5$  (Schödel et al. 2009). By comparing our power law mass models (with a central cusp) and the constant M/L models (with a core) we can constrain the central mass distribution.

- Given that a core can reduce the SMBH bias, our data favors a core over a cusp. The same is found by Schödel et al. (2009), who used a unrealistically large, fixed break radius. Our results show that the preference of a smaller slope in the center is not only due to the large break radius in Schödel et al. (2009).
- The fact that the binding mass is constant out to  $7''$  (Section 5.5.5) also favors a core.
- The presence of a warped disk of young O-stars (Löckmann & Baumgardt 2009; Bartko et al. 2009) yields an additional constraint. Ulubay-Siddiki et al. (2013) found that with an isothermal cusp of  $M(R < 0.5\text{pc}) = 10^6 M_\odot$  and a flattening of  $q = 0.9$  an initial warped disk is too quickly destroyed and would not be observable today. For of constant M/L we obtain a smaller mass of  $M(R < 0.5\text{pc}) \approx 0.15 \times 10^6 M_\odot$ , which reduces the warping by about a factor five. A core would likewise reduce the destructive forces even more. This conclusion is not firm, since the warping need not be primordial, and a reduced central flattening might also yield less of warping (Kocsis & Tremaine 2011).
- The most reliably mass measurement around 1.4 pc apart from our analysis, that is Serabyn & Lacy (1985), is more consistent with a core than with a cusp.

Overall, it appears likely that the mass profile shows a central core, but better modeling including a solution of the mass bias is necessary. Also better dynamic constraints on the flattening help in the context of Ulubay-Siddiki et al. (2013). Another route for constraining the mass profile worth to follow up is using direct accelerations of stars at radii between  $1''$  and  $7''$  with GRAVITY (Eisenhauer et al. 2008).

Our preference for a core in the mass profile is interesting for theories which aim at explaining the missing light cusp. In some theories the resolvable stars (giants) form a core while dark components (remnants or main sequence stars) form a mass cusp. Thus, our result means that mass segregation is less likely to solve the riddle of missing light cusp. Keshet et al. (2009) derive a similar conclusion from different arguments. Another mechanism that destroys a light cusp, but not a mass cusp, is the destruction of giants by collisions (Dale et al. 2009), and hence our results also disfavor that model. One model that could work is presented in Merritt (2010) who propose that a relatively recent binary black hole (merger) ejected stars. This process would yield a core both in the light and

the mass profile. Still, one would need to fine-tune the timing of such a model, since the early-type stars are concentrated toward the center, but the giants and even the younger red (super-) giants with ages down to 20 Myrs (Blum et al. 2003; Pfuhl et al. 2011) are not.

### 5.6.4 Cumulated Mass Profile

Another way of expressing our results is the cumulative mass profile. In Figure 5.23 we show three cases:

- We use a constant M/L model with the best fitting inner slope of 2.08 (Row 5 in Table 5.3, model A).
- We use a constant M/L model with the shallowest possible inner slope of 2.5 (and otherwise row 5 in Table 5.3, model B).
- We use a power law model with a slope of  $\delta = 1.242$  (model C), the average of row 3 and 4 in Table 5.3<sup>5</sup>.

We normalize these three models to have the overall best-fitting value of  $M_{100''} = 6.02 \times 10^6 M_{\odot}$ . Tabulated values of the profiles can be found in Appendix 5.8.3. The largest mass difference between the M/L=const and the power law model is reached at  $40''$  with  $0.55 \times 10^6 M_{\odot}$ . Since this number exceeds our mass error, it is possible to detect dynamically the cusp, provided the SMBH bias can be solved.

Extrapolating the M/L=const models down to the regime of the S-stars S2 and S55/S0-102 (Meyer et al. 2012) yields a mass there, which is smaller than that of the individual stars. In this regime, the S-stars dominate, and taking into account their Salpeter-like IMF (Bartko et al. 2010) or a potential mass-segregated cusp of stellar remnants (Freitag et al. 2006; Hopman & Alexander 2006) would make the dominance even stronger. (Such a cusp would of course be dynamically interlinked with the old stellar population.) For power law models it is not clear whether the old stars dominate in the central arcsecond the mass, or the other masses.

Outside the central arcsecond the mass of the disks of early-type stars (Bartko et al. 2009; Lu et al. 2009) may be important. The spatial distribution is derived from Figure 2 in Bartko et al. (2010), globally deprojecting to space distances with a factor 1.2 the given projected distances. We estimate the total ZAMS mass of that population to  $1.5 \times 10^4 M_{\odot}$  (Bartko et al. (2010), dominated by the O-stars given the top-heavy shape of the IMF. Across the literature (Paumard et al. 2006; Bartko et al. 2010; Lu et al. 2013) the disk mass is uncertain by a factor 2.5. At  $r = 3''$  the O-stars might be comparable in mass to the old stars, if the constant M/L model is correct.

Further out, the only other component is the circumnuclear disk. Most publications (Genzel et al. 1985; Etxaluze et al. 2011; Mezger et al. 1989; Requena-Torres et al. 2012) agree that its mass is a few  $10^4 M_{\odot}$  and thus irrelevant compared to the old stars. However,

<sup>5</sup>Model C uses outside of  $100''$   $\delta = 1.125$ , the average of row 11 and 12 in Table 5.3.

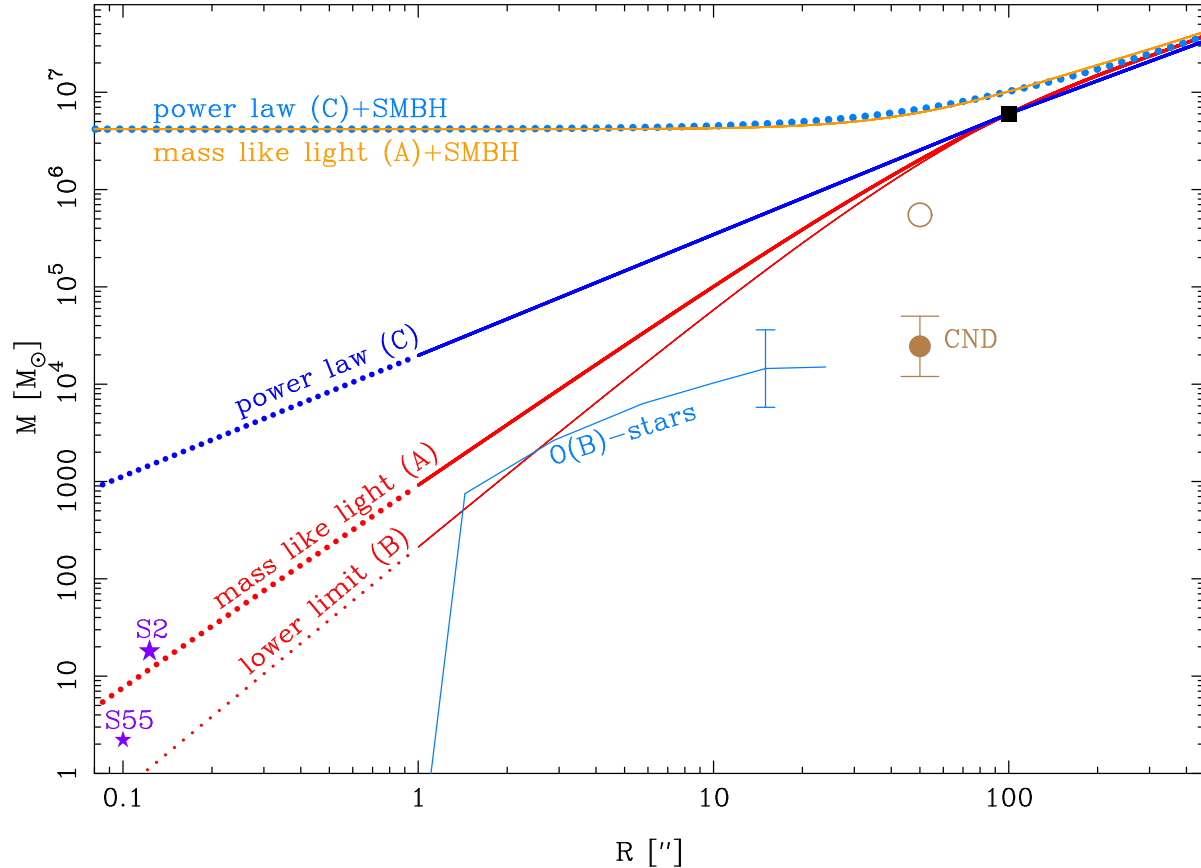


Figure 5.23 Cumulative mass profiles, for a power law model or assuming  $M/L_{K_s} = \text{const.}$  The normalization is done for  $M_{100''} = 6.02 \times 10^6 M_{\odot}$  (black square). Other masses shown are the ZAMS cumulative mass distribution of the O(B)-star population (Bartko et al. 2010) and with a filled disk the CND from Etxaluze et al. (2011), Genzel et al. (1985), Mezger et al. (1989), and Requena-Torres et al. (2012). The open circle is the CND mass estimate from Christopher et al. (2005),

the mass of  $\approx 10^6 M_\odot$  found by Christopher et al. (2005) would be about a third of our mass estimate at that radius.

Our results also yield a new estimate for the sphere of influence of the SMBH (Alexander 2005), which however is completely consistent with previous values (Alexander 2005; Genzel et al. 2010). Using model A and B, we get  $r_{\text{infl}} = 76.9 \pm 5.9'' = 3.06 \pm 0.27 \text{ pc}$ .

### 5.6.5 Mass to Light Ratio

We use our spherically symmetric modeling together with the double  $\eta$ -profile showing the same symmetry to derive a mass to light ratio. Our best mass is  $M_{100''}$ , and hence we use the same radius for the light. From our best fitting double  $\eta$ -profile follows that  $56.1 \pm 5.3 \%$  of the light projected within  $100''$  is also in 3D within  $100''$ . The uncertainty is calculated by comparing the flux respective stellar density profile. We obtain that  $586 \pm 125 \text{ Jy}$  are located within  $R_{3\text{D}} = 100''$ .

This corresponds to  $L_{100''} = (12.12 \pm 2.58) \times 10^6 L_{\odot, \text{Ks}}$  where we used  $M_{\text{Ks}\odot} = 3.28$  (Binney & Merrifield 1998). Hence,  $M/\text{Ks} = 0.50 \pm 0.12 M_\odot / L_{\odot, \text{Ks}}$ . The error consists of the 21.3 % for the light, 8.5 % for the mass, and 7.6 % for the distance uncertainty. The latter number follows from the distance uncertainty of 4.1% (Gillessen et al. 2013) multiplied by the exponent 1.83, which is the scaling M/L with distance given that M scales like 3.83 (Section 5.5.4). Our result is consistent with the values of Pfuhl et al. (2011) and Launhardt et al. (2002). Our error, however, is smaller thanks to the smaller mass error. With the improved mass to light ratio we can constrain the IMF of the old stars further.

To determine the IMF slope  $\alpha$ , we assume the respective star formation histories for the old stars (older than 10 Myrs) from Pfuhl et al. (2011). Their results appear to hold also at the larger radii of interest here (Blum et al. 2003). As in Pfuhl et al. (2011) we use the number of stars with  $m_K < 17.75$  within  $r_{2\text{D}} < 30''$ , plus the conversion from numbers to mass. To convert to  $R_{3\text{D}} < 100''$  we use our density profile, and account for the additional uncertainty of this extrapolation with an additional error of 15 %. Figure 5.24 shows the resulting masses as a function of assumed IMF slope.

A somewhat more top-heavy mass function than the one from Kroupa (2001) is preferred, see also Figure 5.25. This could be obtained by variation of the low mass star fraction. The IMFs from Chabrier (2003) contain less low mass stars (Bastian et al. 2010) and have thus a  $\approx 13\%$  smaller mass to light ratio (Cappellari et al. 2012). This is probably not sufficient to explain our value of M/L, see Figure 5.25.

Formally,  $\alpha = -1.5$  is the best-fitting value with a lower mass limit of  $0.5 M_\odot$ . The even more top-heavy IMFs of the young stars (Paumard et al. 2006; Bartko et al. 2010) are excluded, since then stellar remnants contribute to the total mass. This result was already visible in Pfuhl et al. (2011). Also an IMF with a slope of -0.85 is now excluded by more than  $10\sigma$ . At the other end of the IMF spectrum the IMF from Scalo (1986) results in a significantly too big mass and is thus excluded.

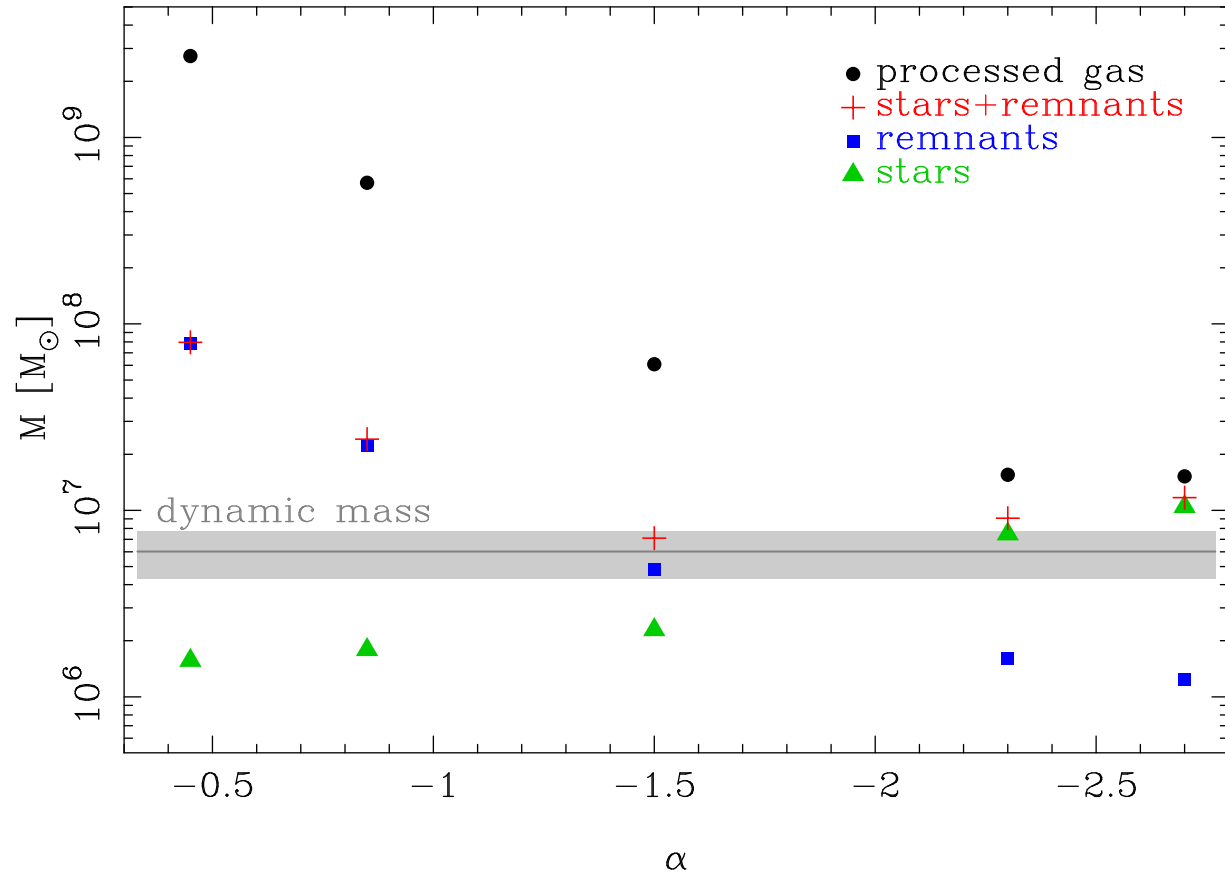


Figure 5.24 Dependence of the mass within  $100''$  on the assumed IMF slope, adapted from Pfuhl et al. (2011). The gray line represents the stellar dynamical mass within  $100''$  and the gray area represents its  $1\sigma$  uncertainty. This error includes also the light uncertainty. Since gas can fall into the SMBH, or be expelled from the central  $100''$ , or be recycled in star formation, the star+remnants points are to be compared with the dynamical mass.

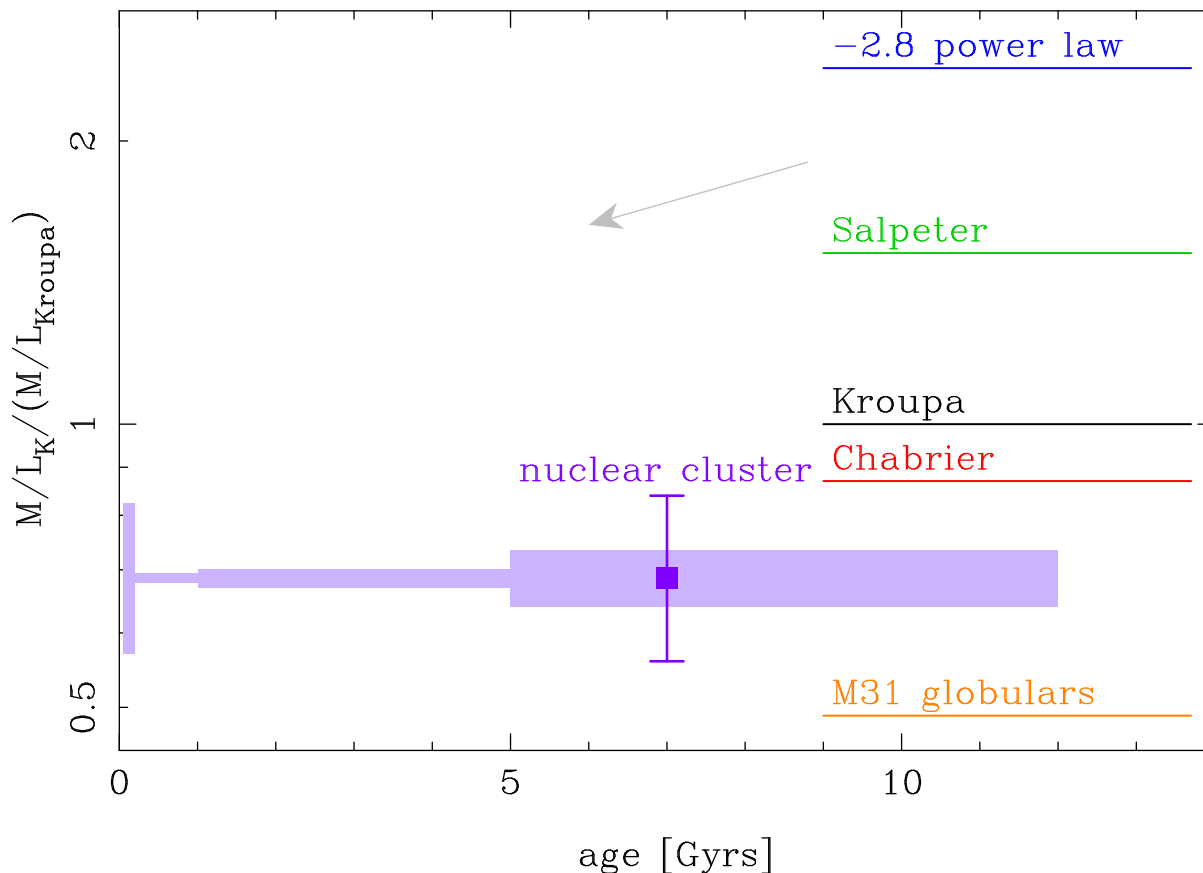


Figure 5.25 Comparison of  $M/L$  within  $R < 100''$  of the nuclear cluster with the literature. The lines indicate  $M/L$  for different mass functions in old star systems (Longhetti & Saracco 2009; Cappellari et al. 2012; Conroy & van Dokkum 2012). The star formation history of the somewhat younger nuclear cluster is indicated by the light violet area. The presence of medium old stars in the GC reduces  $M/L$ . The direction of this effect is indicated by the gray arrow.

We can compare our  $M/L$  with the ones of other old stellar systems<sup>6</sup>, see Figure 5.25. Recent works using population modeling of integrated spectra (van Dokkum & Conroy 2010; Conroy & van Dokkum 2012) and mass to light ratios from advanced dynamic modeling (Cappellari et al. 2006, 2012) indicate that elliptical galaxies, especially massive ones, have a Salpeter IMF (Salpeter 1955) and partly even more bottom heavy IMFs. We can exclude a Salpeter IMF by more than  $3\sigma$ . The Galactic Center shows probably the usual Milky Way IMF, as measured in the Galactic disk and in the bulge (Zoccali et al. 2000; Bastian et al. 2010).

<sup>6</sup> For absolute values of  $M/L$  from the literature we use the old population ratios from Longhetti & Saracco (2009)  $M/L_{\text{Kroupa}} = 0.73 M_{\odot}/L_{\odot, \text{Ks}}$  and  $M/L_{\text{Chabrier}} = 0.64 M_{\odot}/L_{\odot, \text{Ks}}$ , which we scale with the relative  $M/L$  given in the other works to other IMFs.

The IMF of globular clusters appears to contain fewer low mass stars than the Galaxy (Bastian et al. 2010; Sollima et al. 2012). According to Conroy & van Dokkum (2012) and Strader et al. (2011) the mass to light ratios of metal rich ( $[Fe/H] > -1$ ) globular clusters in M31 points to a lack of stars below  $1 M_{\odot}$ . This lack of low mass stars in globular clusters needs not to be primordial, it can also be explained by dynamic effects (Bastian et al. 2010; Marks et al. 2012). These clusters contain about 50% less mass than expected from a Kroupa IMF (Strader et al. 2011; Conroy & van Dokkum 2012). Their M/L is about  $1.4 \sigma$  lower than our result for the nuclear cluster. The comparison is complicated, however, by the fact that M/L does not depend monotonically on  $\alpha$  (Figure 5.24). If the nuclear cluster is fed by globular clusters, one needs to worry about the loss of stars before the cluster reaches the central parsec, and hence M/L might be affected by that, such that the comparison might be wrong also for that reason.

The GC shows an normal ratio of diffuse light to the total light (Pfuhl et al. 2011). This ratio measures the ratio of main sequence stars to giants and decreases monotonically from a bottom-heavy to a top-heavy IMF. Thus it excludes best a cluster dominated by remnants and giants - a possible state of globular clusters inspiraling to the GC. The observed diffuse to total light ratio thus favors an 'in-situ' formation mechanism for the nuclear cluster in a distance of few pc from the SMBH.

### 5.6.6 The Nuclear Cluster of the Milky Way in Comparison

We now compare the nuclear cluster of the Milky Way with nuclear clusters in other galaxies. The literature about the mass of other nuclear clusters (Walcher et al. 2005; Barth et al. 2009) is sparse and biased toward brighter nuclear clusters. We therefore use mainly the light for comparison, for which ample data from HST imaging are available (Carollo et al. 2002; Böker et al. 2004). Böker et al. (2004) studied late-type spiral (Scd to Sm) while Carollo et al. (2002) concentrated on early-type spirals (Sa to Sbc). We color-correct the magnitudes and compare with our GALFIT decomposition for the nuclear cluster (Section 5.4.4) and as a simple measure, not affected by decomposition uncertainties, the cumulative flux as function of radius (Figure 5.26).

The size of the nuclear cluster of the Milky Way is typical. It is smaller than most clusters in Carollo et al. (2002) and larger than most clusters in Böker et al. (2004). This simply might be a consequence from the fact that the galaxy type of the Milky Way is broadly between the two samples.

It is visible in Figure 5.26 that the nuclear cluster of the Milky Way has an unusually high surface brightness. Not only its characteristic brightness is high, but also the cumulative brightness profile lies above nearly all other cluster. What is the reason for that?

- The young ( $\approx 6$  Myrs) and medium old ( $\approx 200$  Myrs) stars in GC are probably not the reason for this offset. They are subdominant compared to the old stars in the Ks-band (Blum et al. 2003; Pfuhl et al. 2011) and Section 5.4.5. Further many nuclear clusters (Rossa et al. 2006; Walcher et al. 2006) contain significant fractions

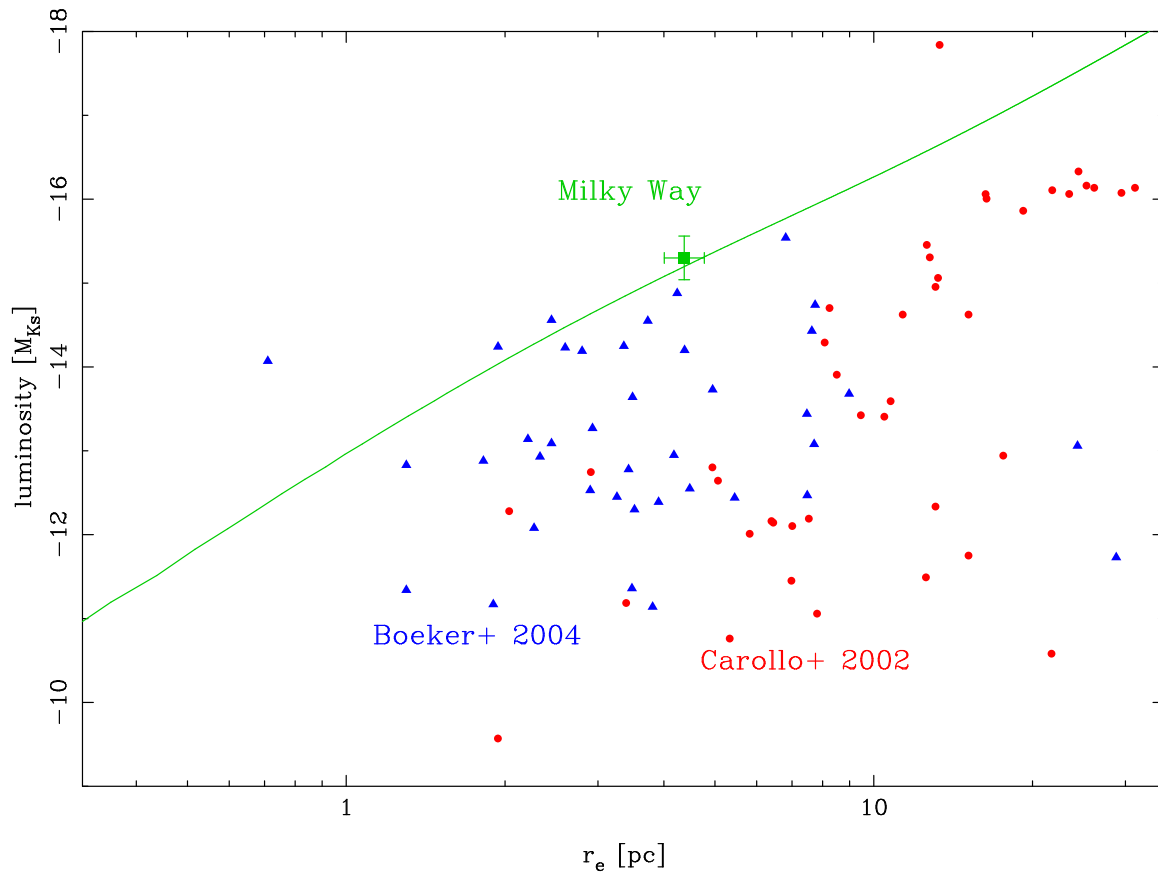


Figure 5.26 Sizes and luminosities of nuclear clusters. We show the half light radii for late-type (Böker et al. 2004) and early-type spiral galaxies (Carollo et al. 2002). For the Milky Way we present the inner component of our GALFIT decomposition (green box) and the cumulative flux as function of the radius.

young or medium old stars. Thus, the M/L of the GC is probably typical.

- Extinction is probably not an issue. We correct for it in the case of the nuclear cluster, and the spirals in the sample of Carollo et al. (2002) and Böker et al. (2004) are seen more or less face-on. Further, the mean IR color in Carollo et al. (2002) yields a small extinction of  $A_{160W} \approx 0.2$ . Also the spectroscopic study of Rossa et al. (2006) obtained small extinctions for the same samples.
- The higher resolution of our data is also not the reason, since we compare the characteristic brightness within 4 pc, a size which can be resolved in most of the galaxies of Carollo et al. (2002) and Böker et al. (2004).
- The nuclear cluster of the Milky Way has a projected mass density of  $\log \Sigma_e = 5.37 \pm 0.17$ . This is larger than for all 11 nuclear clusters in the sample of Walcher et al. (2005).

We conclude that the main reason for high surface density is the high stellar density in the nuclear cluster, compared to other galaxies.

For some near-by galaxies a more detailed comparison is possible. M32 and M33 show central star densities which possibly are larger than in nuclear cluster of the Milky Way (Lauer et al. 1998). M33 does not contain a SMBH (Merritt et al. 2001; Gebhardt et al. 2001), and the old stars - if present at all - are overshadowed by young stars. M32 has a SMBH like the Milky Way, however its core is featureless, consistent with an old population, and it is not a distinct component (Lauer et al. 1992). Thus Kormendy & Kennicutt (2004) did not classify it as a nuclear cluster.

Some nuclear clusters show flattening and rotation, in case of M33 the flattening is 16% (Lauer et al. 1998) combined with some rotation (Kormendy & McClure 1993). The large nuclear cluster in NGC4244 ( $r_e \approx 10$  pc) is visually flattened and has  $v_{\text{rot}}/\sigma \approx 1$  (Seth et al. 2008). NGC404 is a similar case (Seth et al. 2010). Also the nucleus of M31 is not spherical (Lauer et al. 1998). The deviation from spherical is that large that it is uncertain whether it still can be considered as a nuclear cluster. The flattening of the Milky Way nuclear cluster is in the large range of possible shapes.

Carollo (1999) find in their sample that nuclear cluster with  $M_V \lesssim -12$  are typically associated with signs of circumnuclear star formation, like dust lanes and an HII spectrum. In this respect the cluster of the Milky Way with  $M_V \approx -13$  seems typical for its nuclear disk. Preferentially, bright nuclear clusters are observed together with nuclear disks, which might be explained by a physical coupling of the two systems. Since the GC is dominated by old stars this connection is likely not only valid for the recent star formation event but also for the older population.

## 5.7 Conclusions and Summary

The nuclear cluster in the Milky Way is by far the closest and thus can be studied in more detail than other nuclear clusters. In this paper we look not only on its center, but on its

full size to compare it with such clusters in other galaxies. To that aim, we obtain its light profile out to  $1000''$  and measure motions in all three dimensions out to  $100''$ , expanding on the works of Trippe et al. (2008) and Schödel et al. (2009).

- We construct a stellar density map with sufficient resolution for two dimensional structural analysis from the SMBH in the center out to  $r = 1000''$ . This map shows in the central  $70''$  a flattening of about 1.2, while further out the ellipticity increases. We find that this map can be fit by two Sersic functions of different ellipticity. The two components we identify with two different physical entities, the nuclear cluster being the more concentrated and spherical one, and the nuclear disk. The latter can be considered as the stellar analog of the central molecular zone. The nuclear cluster has a half light radius of  $110'' \approx 4.4$  pc, a flattening of 1.1, a Sersic index of  $n = 1.42$ , and a total luminosity of  $M_{Ks} = -15.3 \pm 0.3$ . The outer component has a flattening of 3.85, and contributes 20% of the projected central flux.
- Our dynamical analysis shows that the proper motions are isotropic out to at least  $40''$ . In the center the velocity distribution shows strong wings as expected due to the presence of the SMBH. Assuming that the fastest stars in the center are bound, we set a lower bound to the SMBH mass of  $3.6 \times 10^6 M_{\odot}$ . Assuming in addition that the black hole mass is known to 1.5% (Gillessen et al. 2009) for a given distance, we can estimate  $R_0 = 8.51^{+0.18}_{-0.14}$  kpc. Our new radial velocities show that the projected rotation velocity increases only weakly outside of  $30''$ , and thus the nuclear cluster rotates less than assumed in Trippe et al. (2008).
- We use the motions of 10000 stars for isotropic, spherically symmetric Jeans-modeling. As a tracer profile we use either stellar number counts or the light profile, and the mass model is either a power law model or assumes  $M/L = \text{const}$ . Forcing the mass of the SMBH to its known value we measure for the extended mass a power law slope of  $\delta = 1.19 \pm 0.07$ , consistent with the light profile. Our best mass estimate is obtained at  $R_{3D} = 100''$  as an average over the two mass models. We find  $M_{100''} = (6.02 \pm 0.51|_{\text{fix}R_0} \pm 0.96|_{R_0}) \times 10^6 M_{\odot}$ . The error contains contributions from the uncertain surface density data, from the uncertainty in  $R_0$ . Deviations from isotropy and spherical symmetry are not considered. The modeling yields a total cluster mass of  $M_{NC} = (12.88 \pm 2.69|_{\text{fix}R_0} \pm 2.05|_{R_0}) \times 10^6 M_{\odot}$ .
- The preference for a too small SMBH mass in the Jeans modeling can be interpreted as an argument for a central, core-like structure, opposite to the expected cusp (Bahcall & Wolf 1976). Hence, the deficit in the center would be present not only in the light, but also in the mass profile. That conclusion is also supported by other arguments like the mass measurement of Serabyn & Lacy (1985) at 1.4 pc. The missing mass cusp makes explanations for the missing light cusp, which produce a dark mass cusp, like mass segregation and giants destruction (Dale et al. 2009) less likely. However, we think that it is premature to draw this conclusion firmly. One

would need to develop a model that fits the surface density data and achieves the right SMBH mass. That needs probably at least one of the following elements: (i) a relatively large core in the tracer distribution, which possibly can be found by non-parametric fitting of the density profile, or (ii) the inclusion of an outer background which contributes a significant number of stars also in the center.

- We obtain a mass to light ratio of  $M/Ks = 0.50 \pm 0.12 M_{\odot}/L_{\odot,Ks}$ . This value is slightly lower than expected, even for the usual IMF with the lowest ratio (Chabrier 2003).
- The obtained half light radius of the nuclear cluster of 4.4 pc is typical compared to extragalactic nuclear clusters. However, it is brighter and has a higher light density than nearly all other nuclear clusters. This is also true in the Ks-band, in which recent star formation does not contribute significantly. Possibly, this large luminosity is connected to the nuclear disk further out, for which the brightness also seems high.
- The abundance of young stars and molecular clouds in the nuclear disk and the nuclear cluster supports the idea that at least the young stars in the GC formed in-situ. It is, however, difficult to constrain the origin of the majority of the stars with  $t > 5$  Gyrs. The morphological difference between almost spherical nuclear cluster and the flattened nuclear disk, seems to support that the nuclear cluster built up over time from infalling globular clusters. However, the ratio of diffuse light to total light appears to be normal, which contradicts a globular cluster origin, since they are likely dominated by stellar remnants when they arrive in the GC. Further, the close association of the bright nuclear cluster with the bright nuclear disk is suggestive for a common origin. In conclusion, the formation mechanism of the nuclear cluster is still open.

To improve further the constraints on mass, shape and origin of the nuclear cluster we will first use the data presented here for two-integral modeling (Chatzopoulos et al. in preparation). This will lift the assumptions of spherical symmetry and isotropy.

To improve further the constraints on the origin of the nuclear cluster more data in the transition region to the nuclear region will be useful. By using KMOS it is possible to obtain there at the same time dynamics and star formation history. This information will be useful to decide if nuclear disk and nuclear cluster are distinct in dynamics and star formation history or not.

## 5.8 Appendix

### 5.8.1 Derivation of Proper Motions

In this section we explain how we derive the proper motions. We progress from the center outwards.

Table 5.5. Images used for the extended field

time [mjd]	time	Band	stars on image	fraction of good stars	median position error [mas]
52397.5	2002.334	Ks	4151	0.932	0.98
52769.5	2003.352	Ks	4914	0.974	0.65
53168.5	2004.445	IB2.06	5265	0.981	0.47
53168.5	2004.445	IB2.24	5125	0.961	0.66
53169.5	2004.448	IB2.33	5194	0.961	0.51
53169.5	2004.448	NB2.17	5246	0.905	1.86
53191.5	2004.508	Ks	5271	0.948	1.10
53502.5	2005.359	Ks	6033	0.984	0.71
53540.5	2005.463	Ks	5991	0.807	3.09
53854.5	2006.323	H	5338	0.935	1.16
53854.5	2006.323	Ks	5340	0.964	1.00
53975.5	2006.654	H	5673	0.522	3.28
53975.5	2006.654	Ks	5687	0.698	2.70
54175.5	2007.202	Ks	5768	0.985	0.41
54190.5	2007.243	Ks	5995	0.949	0.73
54561.5	2008.259	Ks	5921	0.974	0.44
54561.5	2008.259	Ks	5746	0.987	0.75
54683.5	2008.593	Ks	5742	0.986	0.36
54725.5	2008.708	Ks	5958	0.977	0.5
54919.5	2009.239	Ks	5982	0.984	0.73
55094.5	2009.718	Ks	5979	0.980	0.45
55325.5	2010.350	H	5971	0.843	1.78
55325.5	2010.350	Ks	5978	0.967	0.99
55467.5	2010.739	Ks	5981	0.948	0.97
55652.5	2011.246	Ks	5975	0.867	1.45
55697.5	2011.369	Ks	6037	0.966	0.61

Note. — All images are obtained with the 27 mas scale with NACO/VLT. A maximum of 6037 stars can be detected on an image. The calculation of the fraction of good stars excludes the stars not on the image.

Table 5.6. Images used for the large and outer field

Telescope/Instrument	epoch	R.A. [']	Dec. [']
Gemini/Hokupa'a	2000-07-02	-13 to 31	-6 to 75
VLT/NACO	2004-05-06	-37 to 36	-38 to 35
VLT/NACO	2006-04-29	-20 to 22	-16 to 25
VLT/MAD	2008-08-21	-37 to 35	-48 to 27
VLT/NACO	2011-05-16	-44 to 44	-44 to 44
VLT/NACO	2011-05-29	0 to 28	45 to 73

Note. — The field of view of the first two datasets is not approximately rectangular.

### The Central Field

In the center ( $r \leq 2''$ ) the crowding is strong. Thus it is difficult to fit the stars on the images with simple Gaussians. Instead, we extract the point spread function (PSF) from the images and deconvolve the image with the Lucy-Richardson algorithm, as in Gillessen et al. (2009). Compared to that work we expand the time baseline and enlarge the field of view from about  $1''$  to  $2''$ .

We fit the data point and their errors for all stars by linear fits. We rescale the  $\chi^2/d.o.f.$  to 1 as in Gillessen et al. (2009). Some of the stars have significant accelerations (Gillessen et al. 2009). However, to avoid complicating our analysis by including acceleration for a very small fraction of the stars, we calculate for all stars only the linear motion. The velocity errors are small, with an average  $0.038$  mas/yr compared to the velocity dispersion of  $5.23$  mas/yr. Furthermore, due to the many data points (more than 100 for many stars) the errors can be determined well from rescaling. For the stars with significant acceleration the errors are not strictly right, since the error calculation assumes random errors. However, since the cubic deviation from linear motion is nearly never significant (Gillessen et al. 2009) the derived velocity is close to the velocity at the mean time of the observing interval. The derived error is slightly too big for this definition, since the scatter is mainly caused by non random accelerations.

All these errors, even the largest of  $0.71$  mas/yr for the velocity of  $-19.09$  mas/yr for S38, are too small to have any influence compared to the large dispersion of  $5.23$  mas/yr and its associated Poisson error of  $0.29$  mas/yr. Therefore, we neglect the error uncertainties for proper motions in the central two arcsecond in our analysis.

### The Extended Field

This data set is an update of Trippe et al. (2008). The field extends out to  $20''$ . We use the same selection of isolated sources as them. We exclude sources which are within the central field. Compared to Trippe et al. (2008) we add new epochs (see Table 5.5 for a list of all images) and a new conversion to absolute coordinates aligned with Gillessen et al. (2009). The positions of the stars in these images are obtained by fitting Gaussian to distortion corrected images. The distortion correction is applied in the same way as in Trippe et al. (2008). Only sources with no close neighbor on the images are included in the dataset. When a source consists in reality of two very close neighbors it can be included in our data set. In such cases the velocity is a flux weighted average, which reduces the absolute velocities and therefore in average also the dispersion. In the center we have also deconvolved images available over 10 years. Checking them shows that source confusion affects less than  $1/10$  of the sources in the extended field. Further out the source density is smaller and thus source confusion introduces no relevant dispersion bias in the extended field data set.

We change the procedure of the outlier rejection and error calculation compared to Trippe et al. (2008). For the first fit we use for each stars the position uncertainty of the Gaussian on the image and rescale the  $\chi^2/d.o.f.$  of the fit to 1. We then calculate for each

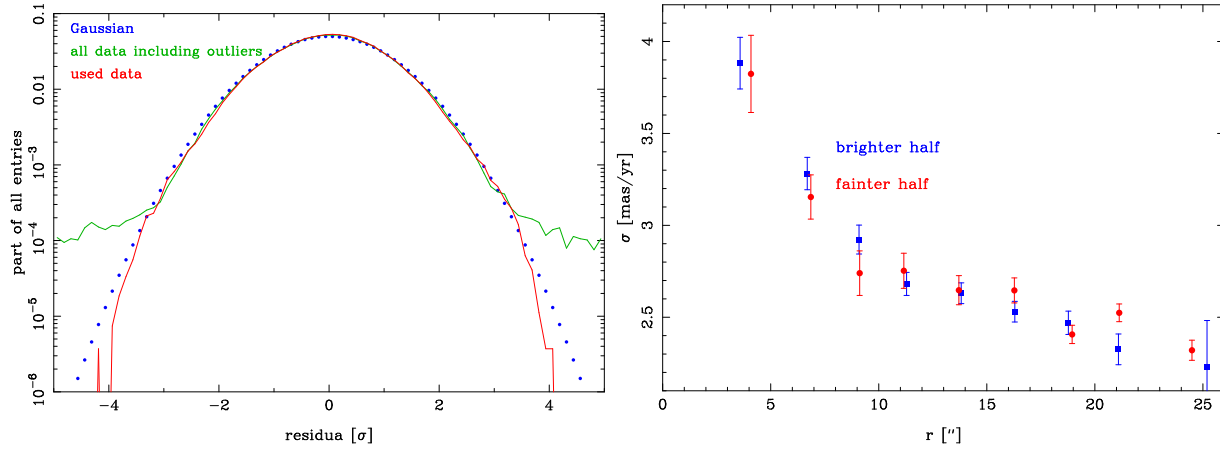


Figure 5.27 Residuals and dispersion in the extended field. Left: Histogram of the position residuals compared to the velocity fits. The red line shows the histogram of the position residuals which we use for our final  $2 \times 6037$  velocity fits. The green line also includes the outliers which are not fit. It can be seen that the residuals to our fit are close to a Gaussian (blue dots). Right: Influence of magnitude on the dispersion. We divide in each bin the stars in two groups by their flux. The same flux threshold is used in all bins.

image the residua distribution of all stars compared to the fit. The width including 68.3 % (W1S) of all entries is often quite different from  $1\sigma$ . To change this we iterate the fitting. In the iteration we rescale the errors on each image by the W1S in  $\sigma$ . We repeat this progress a second time, then the variation of the W1S between different images is less than  $0.1\sigma$ . Other factors are then more important like magnitude with up to  $0.2\sigma$  deviation. However, we ignore these effects because the sign of the deviations is randomly distributed over our 26 images. For the final fit we exclude all  $5\sigma$  outliers and reject outliers between  $2.5$  and  $5\sigma$  by drawing random numbers to approximate a Gaussian distribution. We give in Table 5.5 the median error for all used images. The final residual distribution is approximately Gaussian up to  $|3.7|\sigma$ , see Figure 5.27.

Assuming, only Poisson errors the derived dispersion is  $\sigma_{1D} = 2.671 \pm 0.018$  when using both dimensions together. The error on the dispersion in this field is so small that other error sources could be important. The median and average velocity errors are  $0.150$  and  $0.208$  mas/yr respectively. They are so small, that it does not matter which of them is used. However, this assumes that they are correctly determined. One possible check is to measure the dependence of the dispersion on magnitude (Clarkson et al. 2012). For this test we divide our data in radial bins, to avoid the radial trend diluting a signal, and measure the dispersion in these bins for the brighter and fainter stars, using the same threshold magnitude in all bins, see Figure 5.27. Taking the average of these bins, the difference between fainter and brighter stars is  $\delta\sigma_{1D} = 0.007 \pm 0.041$  mas/yr. The error is the scatter divided by  $\sqrt{N_{\text{bins}}}$  which is consistent with the total number of stars. The consistent dispersions imply that our stars are bright and isolated enough that magnitude

dependent errors like photon and halo noise (Fritz et al. 2010) do not contribute relevantly. Thus, Poisson errors are likely the most important error source for the dispersion and we use only them further on.

### The Large Field

To derive proper motions between 20 and 45'' we use the images listed in Table 5.6. (The last image of this table is used only to derive proper motions between 50 and 70'', the outer field.) We choose as the master image the image from the 16<sup>th</sup> May 2011. This image is the largest in most directions and has, thanks to 0.4'' DIMM seeing, the best resolution. The overlap between its 16 different pointings is too small to obtain a reliable distortion correction in the way of Trippe et al. (2008). The NACO distortion is, however, stable in time within the errors, see Fritz et al. (2010). We therefore use the distortion solution for the distortion correction that is valid during this epoch. Apart from this higher than linear distortion it is also necessary to align the scales and pointings of the images by linear transformations. For this we follow also the procedure of Trippe et al. (2008). Our linear transformation

$$\begin{aligned} x' &= a_0 + a_1 \times x + a_2 \times y \\ y' &= b_0 + b_1 \times x + b_2 \times y \end{aligned} \tag{5.15}$$

contains also crossterms and so automatically corrects for linear effects like differential atmospheric distortion. On this final distortion corrected and aligned image we search for stars and fit them with two-dimensional Gaussians. We thereby exclude stars with close neighbors to reduce the influence of neighboring seeing halos (Fritz et al. 2010) on the position of the target stars. We then translate the pixel positions of the stars to arcseconds by using the known positions and motions of bright stars in the central 20'' using our extended field sample.

For the NACO images in the other epochs we removed the distortion from all single pointing images with the distortion solution valid during this time. For the image from the 6<sup>th</sup> May 2004, the overlap of the different pointings is too small for reliable alignment of the different pointings. In contrast, the pointing of the images from the 29<sup>th</sup> April 2006 overlap enough to apply a reliable alignment. In consequence, we have in most epochs many, mostly single pointing, images of different parts of the GC. The images overlap partly. We identify on all images ten bright stars from the master image for preliminary alignment of the images. We then search on these images around the expected stars positions from 2011 within a radius of 3 pixels for the local maxima. When a maximum is fittable by a Gaussian similar to the PSF core of the image we treat the star as identified on this single pointing image. We then use all stars identified on the single pointing image to obtain the cubic transformation to the master image. This transformation is defined in the following way:

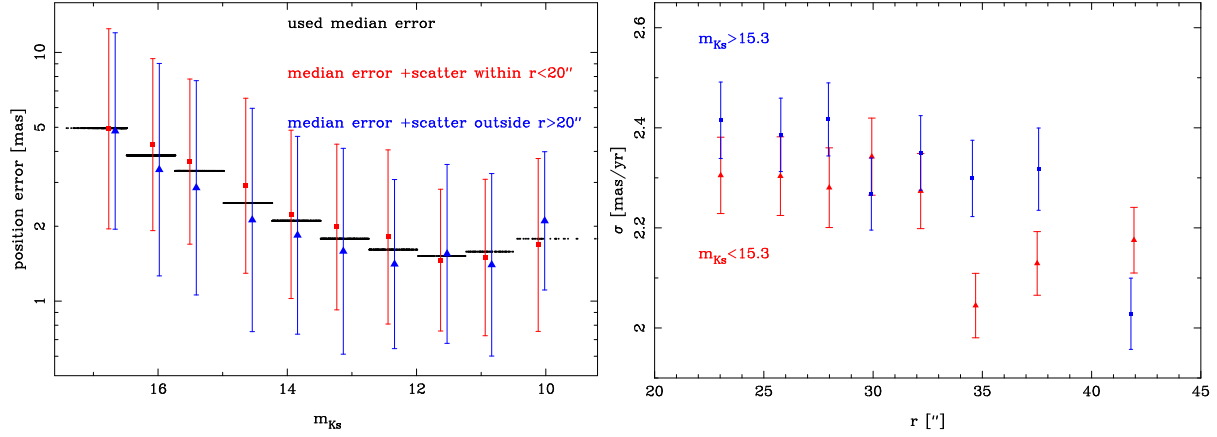


Figure 5.28 Position errors and dispersion in the large field. Left: dependence of the error on magnitude. As the scatter we plot  $1.483 \times$  the median deviation (This measure is identical to  $1 \sigma$  if the distribution is Gaussian.) of the stars in this bin. The errors in magnitude bins for stars within and outside the central  $r = 20''$  box are similar. The black (interrupted) line shows the error as function of magnitude which we use for velocity error calculation. Right: dependence of the dispersion on magnitude. We present in each distance bin the dispersion of brighter and fainter stars.

$$\begin{aligned}
 x' &= a_0 + a_1 \times x + a_2 \times y + a_3 \times x^2 + a_4 \times xy + a_5 \times y^2 \\
 &\quad + a_6 \times x^3 + a_7 \times x^2y + a_8 \times xy^2 + a_9 \times y^3 \\
 y' &= b_0 + b_1 \times x + b_2 \times y + b_3 \times x^2 + b_4 \times xy + b_5 \times y^2 \\
 &\quad + b_6 \times x^3 + b_7 \times x^2y + b_8 \times xy^2 + b_9 \times y^3
 \end{aligned} \tag{5.16}$$

The primary purpose of applying this cubic transformation is to correct unknown distortions together with the other mostly linear effects (Fritz et al. 2010). The number of stars used for the transformation depends on the field of view of the detector and the density of well detected stars. For most epochs we have on average about 4500, and at least 1000 stars. For the single NACO pointings of 6<sup>th</sup> May 2004 there are about 836 stars, and at least 660 stars. Only for the smaller Gemini field of view do we need to use fewer stars. On these image, there are on average 644, and on one only 58. Thus, nearly all images have enough stars to average out the influence of the intrinsic motion of the stars on the cubic transformation. We use the median of all detections in each epoch as the position of the star in this epoch.

To obtain the velocity errors we start with the same position error for all epochs and one that is three times for the master image, because it is the best image and is most free from distortion. We rescale the errors such that the reduced  $\chi^2$  has the expected value. The errors obtained this way vary a lot also at each magnitude: the error of the stars

at the 75 % quantile of the error distribution is 3.4 times bigger than the error at the 25 % quantile of the error distribution. A broad fit error distribution is expected also for perfectly Gaussian distribution of position errors in our case of fitting only three to five data points. Thus, obtaining the errors by rescaling is not so good in our case. Since a clear correlation of the errors with magnitude is visible, see Figure 5.28, we calculate the median error in magnitude bins and use it as the error for most stars. Only if the rescaled error is more than four times larger the median error do we use the rescaled error. We exclude from our sample stars which have in at least one dimension errors larger than 10 mas/yr. When the error is so large, the velocity cannot be determined reliably. For the other stars we use the same error dimensions. The faintest stars have an error three times larger than bright stars (Figure 5.28). This behavior is expected, since many errors are more important for fainter stars, see e.g. Fritz et al. (2010). Due to saturation effects the error increases somewhat again for very bright stars. Another possible error is that the remaining distortion could be larger in the outer parts of the field than in the center. To test this we compare the errors inside and outside the central  $r=20''$  box, see Figure 5.28. We find no major difference between the errors inside and outside this box: the errors inside have a median 23 % bigger than the errors outside, possibly due to the higher source density there.

In principle it is possible to calculate velocities from only two epochs. In this case it is however, not possible to calculate the errors from the fit to the data points. Thus, great care is necessary. To test the reliability of velocity measurement using only two images we compare, in the central part of the field of view, robust dispersion measurements (the median deviation) using all epochs and using only the master epoch (2011) and a single other epoch. We find that the dispersions obtained from two epochs are compatible with the dispersion from most data pairings with the master epoch. The only exception is the 2008 MAD image. The dispersion from this image is about 16 % greater than the dispersion when using all images. The reason for the greater dispersion is probably the small time baseline between 2008 and 2011 together with the fact that two different instruments (with partly unknown distortion) are used for this velocity measurement. By comparison to the dispersion using all data, it follows that the velocity error is 40 % of the dispersion for the 2008-2011 pair. If we could be sure that the error has this value, we could use the dispersion after correcting for the biasing velocity error. However, the errors due to distortion, and maybe others, are probably not constant over the field of view. Even if the errors would increase only to 50 % this would enlarge the values by 8%. This error induced uncertainty is much larger for this data pair than for the other data pairs. We therefore exclude stars only detected in 2011 and 2008 from the analysis. The stars detected only in two other datasets (Due to the covered fields they are mostly in the 2000 and 2004 data sets.) show no higher dispersion. We include them in our analysis.

As in the extended field we further test, if the dispersion depends on the magnitude, see Figure 5.28. For this test we exclude stars with only two measurements. For this comparison, subtracting the errors is more important than further in, since the median error is 0.464 mas/yr. For the subtraction we use  $1.2\times$  the median error, since this is between the median error (which is too low because larger error contribute more to the

overall error) and the average (which is affected by few unrealistic large errors).

The half with  $m_{K_s} > 15.3$  has, after velocity error subtraction by  $0.078 \pm 0.038$  mas/yr, larger errors than the brighter half. Thus, the dispersion possibly increase by  $2\sigma$  with magnitude. This is barely significant. Therefore, we do not include a systematic dispersion error uncertainty for this data set. We then compare this data set with the inner Trippe et al. (2008) data set and exclude all sources within this inner field. In total we add 3831 late-types stars in the large field.

### The Outer Field

Of the two epochs of this field (Gemini in 2000 and NACO in 2011), the NACO data are of the higher quality, so we use it as the master image. We remove distortions with the distortion solution of NACO in this period. We use STARFINDER (Diolaiti et al. 2000) to obtain first estimates for the star positions with a single PSF extracted from the full field. In a second step we fit these stars with two-dimensional Gaussians and keep only the stars which are well fit by a Gaussian. We fit the same stars also on three other NACO images in other filters but with the same pointing. The average for the four filters is the position for 2011 and the scatter is its error. The error in this epoch is negligible compared to the error in the Gemini epoch. The Gemini data of 2000 consists of 12 reduced images, covering 3 pointings. Thereby one pointing creates the overlap between the other two pointings, thus allowing estimates for distortion effects. We use ten stars on each Gemini image to establish a first linear transformation to the NACO data. We search then in a radius of three pixels around the expected star positions for maxima and fit them with two-dimensional Gauss functions. All stars found which are offset by less than 3 pixel from the NACO epoch position are used for a full cubic transformation (equation 5.16) of each Gemini image to the NACO image. These transformations use on average 470 and at least 133 stars.

For the calculation of errors we use stars, which are on more than one pointing. Firstly, we calculate the average position of the different images in one pointing. Secondly, we obtain the final position and its error by using the average and the scatter of the different pointings. Since errors obtained from the scatter of two or three images have a large scatter we construct a magnitude dependent error model. Therefore we bin the stars by magnitude to obtain the median error. We interpolate these data, by a curve which has an error floor for the brightest magnitudes, is then dominated by photon noise and for the faintest level by sky/read-out noise, see Fritz et al. (2010). If a star has an error more than three times the expected error this larger error is used.

We now test if the errors are reliable. Firstly, we test if the distortion is well corrected. For this we compare the dispersion of stars covered by only one pointing, with the stars covered by more than one pointing, see Figure 5.29. We use only relatively bright stars for this comparison. The dispersion of the stars in only one pointing is  $0.33 \pm 0.08$  mas/yr larger than of the stars in more than one pointing. The distortion correction is thus probably not perfect. We exclude the stars which are in only one pointing. The use of more than one pointing likely reduces the effects of distortion by averaging out the residual distortion.

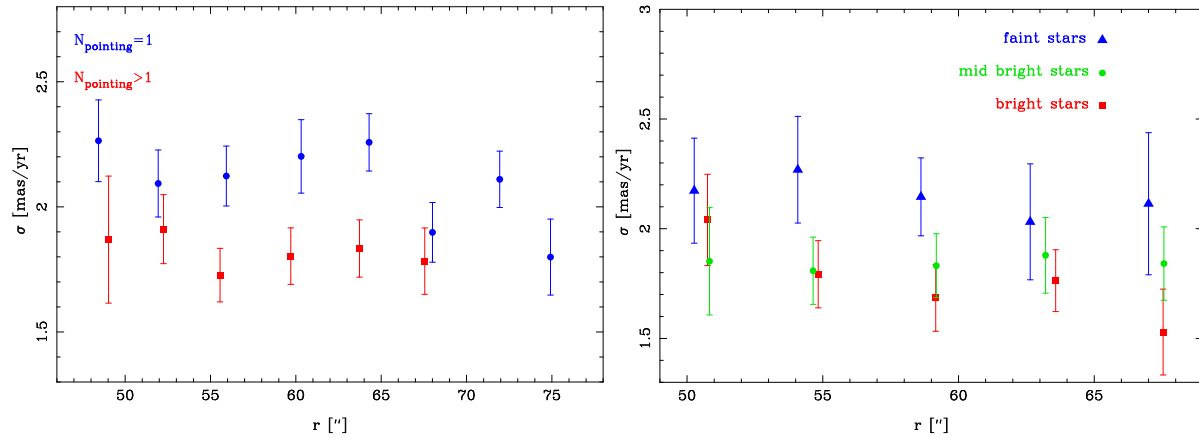


Figure 5.29 Dependence of the dispersion on different parameters in the outer field. Left: dependence of the dispersion on the number of pointings. Only relatively bright stars are used for this comparison. Right: dependence of the dispersion on the magnitude

For a second test we split the stars which are in more than one pointing into three brightness bins, see Figure 5.29. The dispersion in the median brightness bin is only  $0.097 \pm 0.105$  mas/yr larger than in the brightest magnitude bin and thus consistent with it. However, in the faintest magnitude bin, the dispersion is  $0.38 \pm 0.13$  mas/yr higher than in the brightest magnitude bin. We therefore exclude the faintest magnitude bin from the data set. The total dispersion of both dimension together is  $\sigma_{1D} = 1.792 \pm 0.052$  mas/yr. This dispersion is unexpectedly low compared to the proper motion dispersion somewhat further in and the radial velocity dispersion at the same radius. We are therefore not certain if we do not exclude too many stars in the outer field. Nevertheless, we apply the exclusions discussed. Since we do not allow for a radial mass profile break around  $50''$  (between large field and outer field), the dispersion in the outer field being possibly too low balances that further in which is possibly too high. Also, since we have only 297 stars in the outer field the weight of this low dispersion is limited.

### 5.8.2 Obtaining the Luminosity Properties

We describe here in detail how we obtain the luminosity properties. For stars from the VISTA data image we extract point sources from the central  $r = 1000''$  box in H and Ks using STARFINDER (Diolaiti et al. 2000). To progress we divide the field of view into nine subimages, a central image and a ring of 8 images around. We use standard parameters of STARFINDER and a 15 pixel PSF. Since we do not use the faintest stars, the exact parameters do not have a relevant influence on the result. The magnitudes obtained are adjusted to the VISTA catalog by matching bright, but not saturated stars. Essentially all stars outside the central  $20''$  are old stars, see Section 5.3.3. Thus, we do not need to exclude young field stars from the VISTA data. The Arches and Quintuplet clusters are excluded.

For source counts completeness is always a concern. To measure the source confusion we insert in the central Ks-image ( $r_{\text{box}} = 344''$ ) the PSF extracted with STARFINDER. The PSFs are separated by 20 pixels to avoid artificial confusion. In this way we create six images with artificial stars between 11 and 16 magnitude in full magnitude steps, to cover all unsaturated magnitudes for which significant numbers are detected. In all these image we use STARFINDER for detecting the inserted stars in the same way as for the original image. The resulting completeness maps have a resolution of 20 pixels. Locally this may not be sufficient for a good map. However, since we are only interested in the global radial and azimuthal profiles, the number of artificial stars used (10201) is sufficient for our purposes. Outside the central field the confusion is smaller. In the ring fields we measure confusion in the same way for 14 and 16 magnitude and then extrapolate to the other magnitudes using the multi magnitude completeness curve in the center which matches best to the completeness at 14 and 16 magnitude.

We correct for extinction using stellar colors. The H-Ks color is nearly independent of stellar type (Cox 2000): H-K= 0.29 for  $M_K = -6.26$  giants and H-K= 0.15 for  $M_K = -3.46$  giants. We use a color of H-K= 0.2 for all stars. For the extinction correction we use the extinction law toward the GC from Fritz et al. (2011) which implies  $A_{K_s} = (A_H - A_{K_s})/0.753$  for VISTA filters. If possible we use the H - Ks of each star for extinction correction. This way we can better account for extinction dispersion in the line of sight than if we would use a kind of mean extinction. We use this method for Ks-sources with a H counterpart within 2 pixel and no other source within one pixel more distance. The vast majority of all bright Ks-sources has such a H counterpart. For the other sources we use the local extinction distribution of the matched sources in bins  $r_{\text{box}} = 12.7''$ . The primary result of this procedure are star density maps with pixels of size of  $25.5''$ . We made these maps for different extinction corrected magnitudes. The brightest magnitude which is not significantly affected by saturation is, after extinction correction,  $m_{K_s, \text{excor}} = 9$ . For our final density map we use stars fainter than this magnitude and brighter than  $m_{K_s, \text{excor}} = 10.5$  to exclude magnitudes which are severely incomplete in the center. With this faint magnitude cut the completeness is 52 % at  $r \approx 25''$ . The use of stars fainter than  $m_{K_s, \text{excor}} = 9$  also has the advantage that we avoid stars brighter than the tip of the giant branch which are mostly younger than most old stars in the GC. These younger and brighter stars are more concentrated to Sgr A\* (Catchpole et al. 1990).

The result of this procedure is a star density map. Some Ks-dark clouds are still visible on this map. We mask out map pixels which show too low a density compared to their neighbors and others pixels at the same  $|b^*|$  and  $|l^*|$ . This symmetry relative to the Galactic plane and the GC is visible before masking out these areas, see Figure 5.30. A more complicated symmetry is also physically unlikely because the Galactic center is so small compared to its distance that any bar like structure would appear symmetric along its axis, independent of the orientation of the bar to the line of sight. In areas where completeness is no issue at fainter magnitudes we are guided in the masking also by density maps for fainter stars, to reduce the influence of small number statistics. At some radii the masked areas are mostly close to  $l^* = 0$ . At these radii a calculation of the radial profile from the unmasked area would result in a density biased to  $b^* \approx 0$ . To avoid this we replace

in our final map the counts in the masked pixels by the average of the unmasked pixels at the same  $|b^*|$  and  $|l^*|$ , see Figure 5.30. To obtain a radial profile at higher resolution we also binned the stars more finely by a factor 5. Thereby, we use still the larger binning for masking and completeness correction since on smaller areas Poisson noise dominates.

To obtain estimate errors for the general radial profile and the profiles in  $l^*$  and  $b^*$  we first calculate the lowest possible error from Poisson statistics. We obtain a further error estimate by calculating the difference between the upper and lower halves, and the left and right halves of the maps respectively. This second estimate is typically 4.4 % and larger than the first and is used for most radial bins. With this, the reduced  $\chi^2$  of log-polynomials of fourth degree is smaller than 1. To estimate the flattening we measure the density along the major and minor axes using data with less than  $38''$  separation from these axes. (In the center where this method obviously smooths out the flattening we don't use the VISTA data to estimate it.) For these profile we obtain the non-Poisson errors by comparing the two sides and obtain an error of 12.5 % which we scale up by a factor  $\sqrt{2}$  for points which have only data on one side. At large separations polynomial fits yield a  $\chi^2/d.o.f.$  larger than one. We therefore scale up the errors there to obtain  $\chi^2/d.o.f. = 1$ .

For WFC3/IR data we use images in M127 and M153. We use Starfinder (Diolaiti et al. 2000) with standard parameters and a PSF box of  $2''$  diameter. The fluxes obtained with this PSF are converted to magnitudes using the zeropoints for a  $0.4''$  PSF and an infinitely large PSF. We match sources in the two filters and use only sources which are detected in both filters. Precisely, this means that the closest neighbor in M127 is within 1 pixel and second closest is at least 2.3 pixel further away. We use the colors in the following way to apply the extinction correction on a per star basis:  $A_{M153} = 2.12 \cdot (m_{M127} - m_{M153} - 0.374)$ ; The factor is obtained from the -2.11 power law extinction in Fritz et al. (2011). The giant color 0.374 is obtained from observed giant spectra, published in Rayner et al. (2009), approximately K4III.

From these extinction corrected stars we construct stellar density maps in Galactic Coordinates using pixels of  $2''$  size. Primarily we use stars brighter than  $m_{M153\text{excor}} = 12.5$  which in addition have  $m_{M127} - m_{M153} > 2$  in order to exclude foreground stars. With this brightness cut more than 87 % of the unextincted stars, which have typically  $m_{M153\text{excor}} < 12.5$ , have matches in M127. The radial profile is consistent in the center with the higher resolution NACO profile. Thus, we need not to correct for completeness. Saturation is no worry, since only few stars are saturated and many more fainter stars are included in the sample. As in the VISTA data NIR dark clouds can locally block all GC light, see Figure 5.31. We use a density map of all stars with  $m_{M153\text{excor}} < 15$  to identify these clouds and mask them out. This, second density map saturates in the center due to crowding but is superior in areas of low star density, such as these dark clouds.

Early-types are not important in the region of the map we use ( $r > 20''$ ), see Section 5.3.3. For visualization, as in case of the VISTA data, we replace the masked out areas with their symmetry partners, see Figure 5.31. There it can be seen that the cluster is, after extinction correction, much less flattened than at first sight. To quantify the weak flattening we measure the star density separately in  $l^*$  and  $b^*$  using stars in halves which have  $|l^*| > |b^*|$ , and  $|l^*| < |b^*|$  respectively. As the error we use the larger of the following:

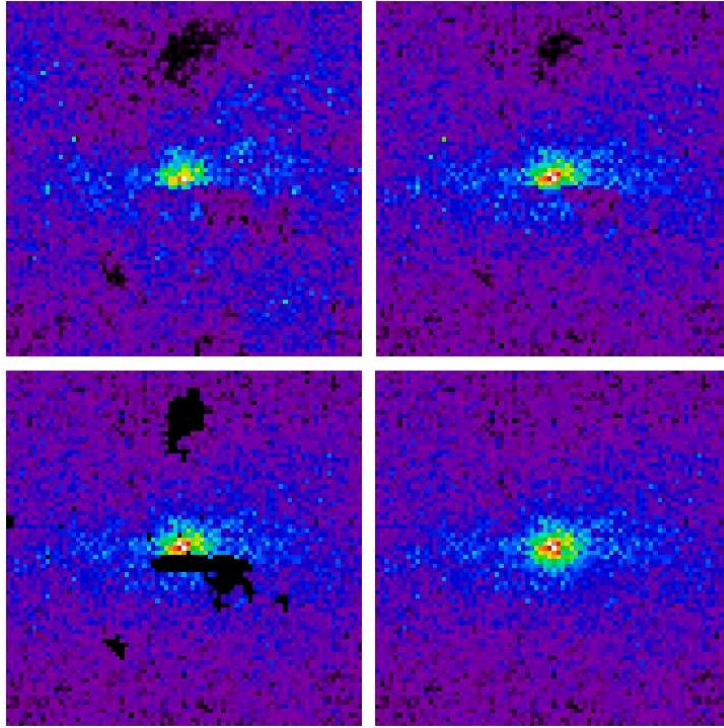


Figure 5.30 Stellar surface density maps in the GC. The number of stars are obtained from VISTA data. The images show  $r = 1000''$  boxes around Sgr A\*. The Galactic plane runs horizontally. The upper left image a shows the completeness corrected star density for stars with  $11.5 < m_{K_s} < 13$ . The upper right image shows the completeness and extinction corrected density of stars with  $9 < m_{K_s, \text{excor}} < 10.5$ . Since each star is corrected for its extinction, the same stars are not necessarily used in the upper left and upper right image. The magnitude range in the raw magnitude map is chosen with the aim to use approximately the same number of stars in both maps. In the lower left image we mask out the pixels in  $b$  with unusually low (high) counts. In the lower right image we replace the masked pixels with the average flux of the pixels at the same  $|l^*|$  and  $|b^*|$  assuming such symmetry with respect to Sgr A\* in these coordinates.

either Poisson statistics or the average difference between the density at  $-l^*$  and  $+l^*$  and  $-b^*$  and  $+b^*$  which is 7.8 %. We obtain the full radial profile from the average of the two profiles in  $l^*$  and  $b^*$ .

In the center we use NACO data. We extract stars from a NACO image with STARFINDER (Diolaiti et al. 2000). We calibrate the magnitudes of these stars locally on the source list of (Schödel et al. 2010). In the center the use of an extinction map is superior to a star by star color since the extinction does not vary much in the light of sight. Thus, a map which uses the local median reduces the noise. We use the extinction map of Schödel et al. (2010) scaled by a factor of 0.976 to align the map with the extinction of Fritz et al. (2011). We select stars with  $m_{\text{Ks,excor}} = 12.65$ . With this magnitude we still have some stars in the central arcsecond, at the same time, are rather complete. In imaging we are essentially complete till this magnitude, we thus do not apply a completeness correction. Dark clouds are no issue in the central  $20''$ , we therefore do not apply masks. In the NACO data the exclusion of early-type stars is important, see Section 5.3.3 for the detailed procedure. For the density profile we use from 0 to  $20''$  the late-type fraction of the spectroscopically typed stars with  $m_{\text{Ks,excor}} = 12.65$  to convert the density profile of all stars to the late-type density profile. To obtain estimates for the flattening in the center we also separately calculate the late-type stellar density in the same two halves of the data as for the WFC3/IR data. The three different profile sources are aligned at their transition radial ranges.

We now describe how we obtain the extinction corrected flux of the GC. For the sky we subtract the median counts toward some dark clouds in the H- and Ks-band. We bin the flux in H and Ks, again in pixels of  $r_{\text{box}} = 12.7''$ . This flux is then used for extinction correction, assuming a somewhat bluer color of  $H - Ks = 0.15$  since bright cool giants are less important in total flux than in source counts of bright stars, especially when as in our case, the brightest stars are saturated. In the extinction corrected flux map the dark clouds are better visibly than in the star density map, since few bright blue foreground stars can bias the extinction estimate toward values that are too low. We therefore construct a new mask for the flux and apply it to the data. To obtain a profile with finer radial sampling we bin the flux finer but still use the same extinction and mask maps.

The final profile is similar but not identical to the star density profile. In the very center of the VISTA image saturation affects many sources. We use there a flux calibrated NACO image and the extinction map discussed above to obtain the light profile there. In the center, a few bright young stars dominated the total flux. From the source list of Schödel et al. (2010) we find the spectroscopic young stars (early-type stars and the young (Pfuhl et al. 2011) red-supergiant IRS7) and subtract their total flux, adapted to our zeropoint. Their flux is only relevant in the inner  $10''$ . Due to their top-heavy IMF (Bartko et al. 2010; Lu et al. 2013), the fact that we do not have spectra for all stars has negligible influence on the total flux. This inner NACO profile is less affected by saturation than the VISTA profile. We therefore use the transition region around  $20''$  to align the VISTA flux to the NACO flux. We estimate the errors on the resulting profile by fitting step wise low order log-polynomials to the data and setting  $\chi^2/d.o.f. = 1$ . As expected in case of Poisson noise which is caused by few bright stars the error decreases with radius.

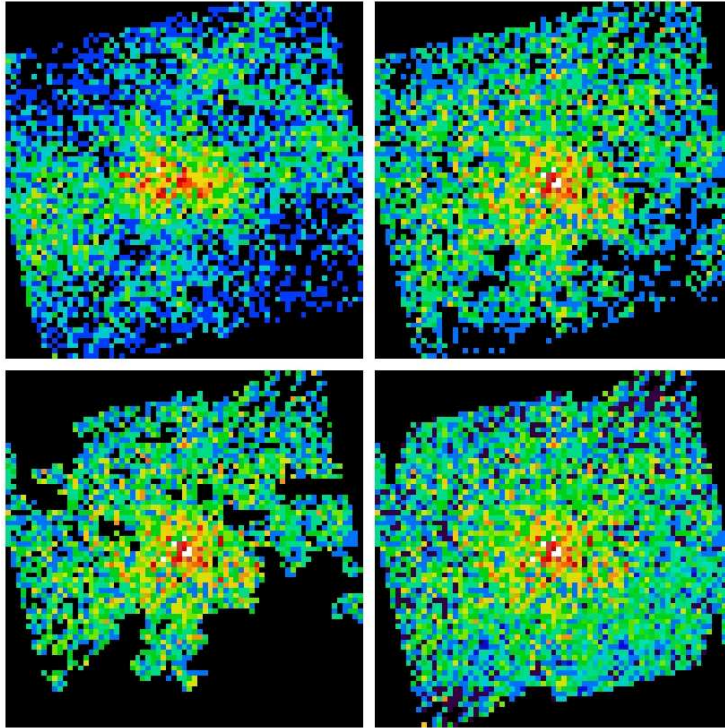


Figure 5.31 Stellar surface density maps in the inner GC. The number of stars is obtained from WFC3/IR data. The images show  $r = 68''$  boxes around Sgr A\*. The Galactic plane runs horizontal. The upper left image shows the star density of stars with  $m_{M153} < 19.0$ . The upper right image shows the extinction corrected density of stars with  $m_{M153,excor} < 12.5$ . Since each star is corrected for its own extinction, not exactly the same stars are used in the upper left and upper right image. The magnitude range in the raw magnitude map is chosen with the aim to use approximately the same number of stars in both maps. In the lower left image we mask out the pixels with unusual low (high) counts. In the lower right image we replace the masked pixels with the average flux of the pixels at the same  $|l^*|$  and  $|b^*|$  assuming such symmetry with respect to Sgr A\* in these coordinates.

Table 5.7. Cumulative mass distribution

R[ $''$ ]	R[pc]	$M_A$ [ $10^6 M_\odot$ ]	$M_B$ [ $10^6 M_\odot$ ]	$M_C$ [ $10^6 M_\odot$ ]
7	0.28	0.049	0.025	0.221
10	0.40	0.101	0.058	0.345
15	0.60	0.223	0.148	0.571
20	0.80	0.388	0.281	0.816
25	0.99	0.590	0.457	1.076
40	1.59	1.381	1.203	1.929
50	1.99	2.030	1.850	2.547
75	2.98	3.914	3.800	4.210

Note. — Cumulative mass of three different extended mass models. All assume  $R_0 = 8.2$  kpc. The model for  $M_A$  uses the preferred constant M/L model, with a inner slope of -0.82 (Row 5 in Table 5.3). The model for  $M_B$  is identical to the previous, however the inner slope is changed to the shallowest possible of -0.5. To obtain  $M_C$  a power law model with  $\delta = 1.242$  is used. All are scaled to  $6.02 \times 10^6 M_\odot$  at  $100''$ . At  $40''$  the mass difference between the power law case and the constant M/L case is maximal.

### 5.8.3 Tabulated Values of Cumulative Mass Profiles

Here, we present our mass models from Figure 5.23 in Table 5.7.

# Conclusions and Outlook

The Galactic Center harbors a variety of interesting phenomena, especially the central supermassive black hole, the nuclear cluster and potentially more unknown phenomena. This study and other recent publications indicate that the Galactic Center is possibly more normal than previously thought:

- It is difficult to find intermediate mass black holes in the GC (Chapter 3).
- The extinction curve toward the Galactic Center is consistent with recent measurements in other lines of sight through the Galaxy (Chapter 4); since the dust that causes the extinction is mostly not in Galactic Center this is not surprising.
- The initial mass function (IMF) of the old stars in Galactic Center is close or identical to the standard IMF found in the Galaxy (Chapter 5 and Pfuhl et al. 2011).

However, some surprises compared to theory persist. The indications that not only the light but also the mass is missing a Bahcall & Wolf (1976) cusp are growing (Chapter 5). Since no other galaxy with a similarly massive nuclear cluster and black hole is close enough to resolve it sufficiently, it is unknown if the missing cusp is a general property of galactic centers or a Milky Way peculiarity.

In Chapter 3, the data were not sufficient to decide whether there is an intermediate mass black hole in IRS13E. Since that paper I have added another five years of images, increasing the precision of accelerations by a factor four. This acceleration accuracy should be enough to determine if the stars in IRS13E orbit around an intermediate mass or around the supermassive black hole. To the near- and mid-infrared extinction curve in Chapter 4 I will soon add the extinction in the far-infrared using the *Herschel Space Observatory* measurements of hydrogen lines. Possibly these measurements will only yield an upper limit on the small extinction there, but still it would be the first measurement of the extinction in the far infrared when using a well understood tracer. To increase the confidence in the missing mass cusp it is necessary to apply a more complex modeling to the nuclear cluster data of Chapter 5. This project has already started. Possibly, the clue to understand why the cusp is missing lies in the fact that the same missing cusp is visible in all stars older than 10 Myrs, see Pfuhl et al. (2011) and Chapter 1. With the spectra and proper motions used in Chapter 5 it is possible to further quantify this similarity and to look for subtle differences in spatial distribution and kinematics. The spatial distribution of stars seems to depend more on their color than on their age, since red supergiants of an age of 20 Myrs

are less concentrated than B-stars which are potentially older. Destruction of supergiant envelopes could be a solution, however the biggest red supergiant IRS7 is rather close to Sgr A\*. Possibly the B-stars are younger than their maximum main sequence lifetime and all belong to a population different from the red stars. Such a young age for the B-stars also fits well to their IMF, which is consistent with a single-age Salpeter IMF.

What is the origin of the red stars which form the nuclear cluster? It needs to be different from the blue stars since they are distributed differently. Thus, local star formation out of gas like in the case of the blue O-stars seems unlikely. However, since the resulting IMF and stellar distribution is a strong function of radius, star formation out of a cloud around one to few parsecs is not impossible. Star clusters that spiral by dynamic friction to the center provide a possible route. In this case the radial distribution would be flatter in the center than further out (Fujii et al. 2009; Antonini et al. 2012). The younger red stars could originate in Arches-like clusters, the older red stars in globular clusters. If the different old clusters arrived at similar times, no population would have had enough time for relaxation to a Bahcall & Wolf (1976) cusp. Since the nuclear disk is much too big to originate from globular clusters, the star formation history and metallicity of these two components would likely be different in this scenario. However, the contemporary arrival of clusters in the GC is artificial, a recent event in the GC acting on all existing stars in the same way is a more natural solution. A merger of galaxies and their black holes (Merritt 2010) is unlikely to have occurred less than 20 Myrs ago. Could it be that the recent formation of the O-stars, which was possibly associated with simultaneous AGN activity, provides an event which could cause the core in light and mass?

For the infrared group the Galactic Center was one main motivation to build instruments like SINFONI and NACO. What follows from this study for planned or possible future VLT instruments and long-term observing strategies? The analysis in Chapter 2 on the astrometry provides direct input for future imaging observations and a future imager. The most important current limitations are distortion and crowding by the high star density. In the case of distortion, it is difficult to improve upon the design of NACO, but still it is important that the new imager ERIS (Amico et al. 2012) has a similarly small distortion. The influence of crowding can be reduced by higher spatial resolution, which is with current telescopes only possible at shorter wavelengths (in the GC the J-band is the shortest possible useful band) or by a higher Strehl ratio. For both, the better AO system of ERIS is a step forward. I prefer an AO system that uses IRS7 as guide star. Although this star is not so close to Sgr A\* that it always outperforms a laser, the GC observations have about once or twice per year such a large coherence angle, that AO on IRS7 is superior to a laser pointed directly on Sgr A\*. Chapter 3 and Chapter 5 show how important it is in astrometry to have a long time base line. While it was possible in Chapter 5 to obtain many motions, more motions would be easily possible, when more images would have been taken some years ago. Thus, in the future it will be important, when the new instrument GRAVITY (Eisenhauer et al. 2008) becomes available, to start astrometric programs on many objects, not just the most interesting ones. A possible aim would be to measure acceleration (limits) of a representative sample of young and old stars. In case of the young stars their origin in two disks and the Hills mechanism can possibly

be proven this way. In case of the old stars the shape of the missing cusp can be probed. Concerning spectroscopy outside the very center, where no AO resolution is necessary, the new K-band multi object spectrograph (KMOS, Sharples et al. 2013) offers an increase in speed of a factor 3 to 24 depending on the source density. This is useful for probing the transition between the nuclear cluster and nuclear disk to decide how related these two components are and to collect more radial velocities to push the precision of the statistical parallax of the GC to the 1% level. Close to the center only AO assisted spectrographs are useful. Possibly, already this year the new laser PARLA provides improvement in the Strehl Ratio and thus reduces the integration time for SINFONI. Certainly, the updated spectrograph SPIFFI in the new environment of ERIS provides much higher Strehl ratios. Progress on top of this level is likely only obtained with a new telescope, the E-ELT (Gilmozzi & Kissler-Patig 2011). Apart from supporting GRAVITY by spectroscopy in the very center, better spectrographs will be useful to obtain more B-stars further out and to be able to dissect them per luminosity.

Of course apart from this planned science, new and old instruments with a field of view sufficient to observe more than one object at once always contain the possibility to detect unexpected objects. Also with the current instruments this is possible even a decade after the instruments come online, as the small gas cloud falling toward Sgr A\* (Gillessen et al. 2012) shows. Thus, I will be surprised if the Galactic Center will not surprise me anymore.



# Bibliography

- Abuter, R., Schreiber, J., Eisenhauer, F., et al. 2006, NAR, 50, 398
- Alard, C. 2001, A&A, 379, L44
- Alexander, T. 2001, ApJL, 553, L149
- Alexander, T. 2005, Phys. Rep., 419, 65
- Alexander, T. 2007, arXiv:0708.0688
- Alexander, D. M., Brandt, W. N., Smail, I., et al. 2008, AJ, 135, 1968
- Alexander, T., & Hopman, C. 2009, ApJ, 697, 1861
- Alig, C., Schartmann, M., Burkert, A., & Dolag, K. 2013, arXiv:1305.2953
- Allen, D. A., Hyland, A. R., & Jones, T. J. 1983, MNRAS, 204, 1145
- Allen, D. A., & Sanders, R. H. 1986, Nature, 319, 191
- Allen, D. A., Hyland, A. R., & Hillier, D. J. 1990, MNRAS, 244, 706
- Alves-Brito, A., Meléndez, J., Asplund, M., Ramírez, I., & Yong, D. 2010, A&A, 513, A35
- Amico, P., Marchetti, E., Pedichini, F., et al. 2012, Proc. SPIE, 8446,
- Amorim, A., Lima, J., Alves, J., et al. 2006, Proc. SPIE, 6269,
- An, D., Ramírez, S. V., Sellgren, K., et al. 2009, ApJL, 702, L128
- An, D., Ramírez, S. V., Sellgren, K., et al. 2011, ApJ, 736, 133
- Andersen, D. R., Walcher, C. J., Böker, T., et al. 2008, ApJ, 688, 990
- Anderson, J., & van der Marel, R. P. 2010, ApJ, 710, 1032
- Angus, G. W., Shan, H. Y., Zhao, H. S., & Famaey, B. 2007, ApJL, 654, L13
- Antonini, F., Lombardi, J. C., Jr., & Merritt, D. 2011, ApJ, 731, 128

- Antonini, F., Capuzzo-Dolcetta, R., Mastrobuono-Battisti, A., & Merritt, D. 2012, *ApJ*, 750, 111
- Arp, H. 1965, *ApJ*, 141, 43
- Asplund, M., Grevesse, N., Sauval, A. J., & Scott, P. 2009, *ARA&A*, 47, 481
- Baade, W. 1944, *ApJ*, 100, 137
- Baade, W. 1946, *PASP*, 58, 249
- Babusiaux, C., Gómez, A., Hill, V., et al. 2010, *A&A*, 519, A77
- Babusiaux, C. 2012, SF2A-2012: Proceedings of the Annual meeting of the French Society of Astronomy and Astrophysics, 77
- Babcock, H. W. 1939, *Lick Observatory Bulletin*, 19, 41
- Backer, D. C. 1996, *Unsolved Problems of the Milky Way*, 169, 193
- Baganoff, F. K., Bautz, M. W., Brandt, W. N., et al. 2001, *Nature*, 413, 45
- Bahcall, J. N., & Wolf, R. A. 1976, *ApJ*, 209, 214
- Baker, J. G., & Menzel, D. H. 1938, *ApJ*, 88, 52
- Balick, B., & Brown, R. L. 1974, *ApJ*, 194, 265
- Bally, J., Stark, A. A., Wilson, R. W., & Henkel, C. 1988, *ApJ*, 324, 223
- Bania, T. M. 1977, *ApJ*, 216, 381
- Banerjee, S., Kroupa, P., & Oh, S. 2012, *MNRAS*, 426, 1416
- Barth, A. J., Strigari, L. E., Bentz, M. C., Greene, J. E., & Ho, L. C. 2009, *ApJ*, 690, 1031
- Bartko, H., Martins, F., Fritz, T. K., et al. 2009, *ApJ*, 697, 1741
- Bartko, H., Martins, F., Trippe, S., et al. 2010, *ApJ*, 708, 834
- Bastian, N., Covey, K. R., & Meyer, M. R. 2010, *ARA&A*, 48, 339
- Becklin, E. E., & Neugebauer, G. 1968, *ApJ*, 151, 145
- Becklin, E. E., & Neugebauer, G. 1975, *ApJL*, 200, L71
- Becklin, E. E., & Neugebauer, G. 1978, *PASP*, 90, 657
- Becklin, E. E., Gatley, I., & Werner, M. W. 1982, *ApJ*, 258, 135
- Bekenstein, J. D. 2004, *Phys. Rev. D*, 70, 083509

- Beloborodov, A. M., Levin, Y., Eisenhauer, F., et al. 2006, *ApJ*, 648, 405
- Beintema, D. A., Salama, A., & Lorente, R. 2003, *The Calibration Legacy of the ISO Mission*, 481, 215
- Bender, R., Kormendy, J., Bower, G., et al. 2005, *ApJ*, 631, 280
- Bensby, T., Adén, D., Meléndez, J., et al. 2011, *A&A*, 533, A134
- Bik, A., Kaper, L., & Waters, L. B. F. M. 2006, *A&A*, 455, 561
- Binney, J., Gerhard, O. E., Stark, A. A., Bally, J., & Uchida, K. I. 1991, *MNRAS*, 252, 210
- Binney, J., Gerhard, O., & Spergel, D. 1997, *MNRAS*, 288, 365
- Binney, J., & Merrifield, M. 1998, *Galactic astronomy / James Binney and Michael Merrifield*. Princeton, NJ : Princeton University Press, 1998. (Princeton series in astrophysics) QB857 .B522 1998 (\$35.00),
- Binney, J., & Tremaine, S. 2008, *Galactic Dynamics: Second Edition*, by James Binney and Scott Tremaine. ISBN 978-0-691-13026-2 (HB). Published by Princeton University Press, Princeton, NJ USA, 2008.,
- Blaauw, A., Gum, C. S., Pawsey, J. L., & Westerhout, G. 1960, *MNRAS*, 121, 123
- Blitz, L., & Spergel, D. N. 1991, *ApJ*, 379, 631
- Blum, R. D., Sellgren, K., & Depoy, D. L. 1996, *ApJ*, 470, 864
- Blum, R. D., Ramírez, S. V., Sellgren, K., & Olsen, K. 2003, *ApJ*, 597, 323
- Böker, T., Sarzi, M., McLaughlin, D. E., et al. 2004, *AJ*, 127, 105
- Böker, T., Laine, S., van der Marel, R. P., et al. 2002, *AJ*, 123, 1389
- Böker, T. 2010, *IAU Symposium*, 266, 58
- Bohlin, R. C., Savage, B. D., & Drake, J. F. 1978, *ApJ*, 224, 132
- Bond, H. E. 1981, *ApJ*, 248, 606
- Bonnell, I. A., & Rice, W. K. M. 2008, *Science*, 321, 1060
- Bonnet, H., Ströbele, S., Biancat-Marchet, F., et al. 2003, *Proc. SPIE*, 4839, 329
- Bovy, J., Rix, H.-W., Liu, C., et al. 2012, *ApJ*, 753, 148
- Bovy, J., Allende Prieto, C., Beers, T. C., et al. 2012, *ApJ*, 759, 131

- Bozza, V., & Mancini, L. 2005, *ApJ*, 627, 790
- Bozza, V., & Mancini, L. 2009, *ApJ*, 696, 701
- Brodie, J. P., & Strader, J. 2006, *ARA&A*, 44, 193
- Bromley, B. C., Kenyon, S. J., Geller, M. J., et al. 2006, *ApJ*, 653, 1194
- Brown, R. L., & Liszt, H. S. 1984, *ARA&A*, 22, 223
- Brown, W. R., Anderson, J., Gnedin, O. Y., et al. 2010, *ApJL*, 719, L23
- Brown, W. R., Geller, M. J., Kenyon, S. J., & Kurtz, M. J. 2005, *ApJL*, 622, L33
- Brown, W. R., Geller, M. J., Kenyon, S. J., & Bromley, B. C. 2009, *ApJL*, 690, L69
- Brown, W. R., Geller, M. J., & Kenyon, S. J. 2012, *ApJ*, 751, 55
- Brunthaler, A., Reid, M. J., Menten, K. M., et al. 2011, *Astronomische Nachrichten*, 332, 461
- Buchholz, R. M., Schödel, R., & Eckart, A. 2009, *A&A*, 499, 483
- Burkert, A., & Tremaine, S. 2010, *ApJ*, 720, 516
- Burkert, A., Schartmann, M., Alig, C., et al. 2012, *ApJ*, 750, 58
- Butchart, I., McFadzean, A. D., Whittet, D. C. B., Geballe, T. R., & Greenberg, J. M. 1986, *A&A*, 154, L5
- Caffau, E., Bonifacio, P., François, P., et al. 2011, *Nature*, 477, 67
- Calzetti, D., Armus, L., Bohlin, R. C., et al. 2000, *ApJ*, 533, 682
- Calzetti, D. 2001, *PASP*, 113, 1449
- Cameron, P. B., Britton, M. C., & Kulkarni, S. R. 2009, *AJ*, 137, 83
- Capelli, R., Warwick, R. S., Porquet, D., Gillessen, S., & Predehl, P. 2012, *A&A*, 545, A35
- Cappellari, M., Bacon, R., Bureau, M., et al. 2006, *MNRAS*, 366, 1126
- Cappellari, M., McDermid, R. M., Alatalo, K., et al. 2012, *Nature*, 484, 485
- Capuzzo-Dolcetta, R., & Miocchi, P. 2008, *ApJ*, 681, 1136
- Cardelli, J. A., Clayton, G. C., & Mathis, J. S. 1989, *ApJ*, 345, 245
- Carignan, C., Chemin, L., Huchtmeier, W. K., & Lockman, F. J. 2006, *ApJL*, 641, L109
- Carollo, C. M., Stiavelli, M., de Zeeuw, P. T., & Mack, J. 1997, *AJ*, 114, 2366

- Carollo, C. M., Stiavelli, M., & Mack, J. 1998, *AJ*, 116, 68
- Carollo, C. M. 1999, *ApJ*, 523, 566
- Carollo, C. M., Stiavelli, M., Seigar, M., de Zeeuw, P. T., & Dejonghe, H. 2002, *AJ*, 123, 159
- Carr, J. S., Sellgren, K., & Balachandran, S. C. 2000, *ApJ*, 530, 307
- Carretti, E., Crocker, R. M., Staveley-Smith, L., et al. 2013, *Nature*, 493, 66
- Catchpole, R. M., Whitelock, P. A., & Glass, I. S. 1990, *MNRAS*, 247, 479
- Chabrier, G. 2003, *PASP*, 115, 763
- Chauvin, G., Lagrange, A.-M., Dumas, C., et al. 2004, *A&A*, 425, L29
- Chiar, J. E., Tielens, A. G. G. M., Whittet, D. C. B., et al. 2000, *ApJ*, 537, 7
- Christlieb, N., Bessell, M. S., Beers, T. C., et al. 2002, *Nature*, 419, 90
- Christopher, M. H., Scoville, N. Z., Stolovy, S. R., & Yun, M. S. 2005, *ApJ*, 622, 346
- Clarkson, W., Sahu, K., Anderson, J., et al. 2008, *ApJ*, 684, 1110
- Clarkson, W. I., Ghez, A. M., Morris, M. R., et al. 2012, *ApJ*, 751, 132
- Clemens, D. P. 1985, *ApJ*, 295, 422
- Cohen, R. S., & Thaddeus, P. 1977, *ApJL*, 217, L155
- Coker, R. F., Pittard, J. M., & Kastner, J. H. 2002, *A&A*, 383, 568
- Compiègne, M., Verstraete, L., Jones, A., et al. 2011, *A&A*, 525, A103
- Conan, R., Fusco, T., Rousset, G., et al. 2004, *Proc. SPIE*, 5490, 602
- Conroy, C., & van Dokkum, P. G. 2012, *ApJ*, 760, 71
- Contopoulos, G., & Mertzaniades, C. 1977, *A&A*, 61, 477
- Contopoulos, G., & Papayannopoulos, T. 1980, *A&A*, 92, 33
- Côté, P., Piatek, S., Ferrarese, L., et al. 2006, *ApJS*, 165, 57
- Cotera, A. S., Erickson, E. F., Colgan, S. W. J., et al. 1996, *ApJ*, 461, 750
- Cox, P., & Mezger, P. G. 1989, *A&A Rev.*, 1, 49
- Cox, A. N. 2000, *Allen's Astrophysical Quantities*,

- Crocker, R. M., Jones, D. I., Aharonian, F., et al. 2011, MNRAS, 413, 763
- Crowther, P. A. 2007, ARA&A, 45, 177
- Crowther, P. A., Schnurr, O., Hirschi, R., et al. 2010, MNRAS, 408, 731
- Cuadra, J., Nayakshin, S., Springel, V., & Di Matteo, T. 2005, MNRAS, 360, L55
- Cunha, K., Sellgren, K., Smith, V. V., et al. 2007, ApJ, 669, 1011
- Dale, J. E., Davies, M. B., Church, R. P., & Freitag, M. 2009, MNRAS, 393, 1016
- Dambis, A. K. 2009, MNRAS, 396, 553
- Dame, T. M., Ungerechts, H., Cohen, R. S., et al. 1987, ApJ, 322, 706
- Dame, T. M., Hartmann, D., & Thaddeus, P. 2001, ApJ, 547, 792
- Das, P., Gerhard, O., Mendez, R. H., Teodorescu, A. M., & de Lorenzi, F. 2011, MNRAS, 415, 1244
- Davies, B., Origlia, L., Kudritzki, R.-P., et al. 2009, ApJ, 694, 46
- Davies, M. B., Church, R. P., Malmberg, D., et al. 2011, The Galactic Center: a Window to the Nuclear Environment of Disk Galaxies, 439, 212
- Deason, A. J., Belokurov, V., & Evans, N. W. 2011, MNRAS, 416, 2903
- de Graauw, T., Haser, L. N., Beintema, D. A., et al. 1996, A&A, 315, L49
- de Graauw, T., Whittet, D. C. B., Gerakines, P. A., et al. 1996, A&A, 315, L345
- Deguchi, S., Imai, H., Fujii, T., et al. 2004, PASJ, 56, 261
- Dehnen, W., & Binney, J. J. 1998, MNRAS, 298, 387
- Diolaiti, E., Bendinelli, O., Bonaccini, D., et al. 2000, Proc. SPIE, 4007, 879
- Dexter, J., Agol, E., Fragile, P. C., & McKinney, J. C. 2010, ApJ, 717, 1092
- Dexter, J., & Fragile, P. C. 2012, arXiv:1204.4454
- Do, T., Ghez, A. M., Morris, M. R., et al. 2009, ApJ, 703, 1323
- Do, T., Ghez, A., Lu, J. R., et al. 2012, Journal of Physics Conference Series, 372, 012016
- Do, T., Lu, J. R., Ghez, A. M., et al. 2013, ApJ, 764, 154
- Dobbs, C. L., & Burkert, A. 2012, MNRAS, 421, 2940
- Dodds-Eden, K., Porquet, D., Trap, G., et al. 2009, ApJ, 698, 676

- Dodds-Eden, K., Sharma, P., Quataert, E., et al. 2010, *ApJ*, 725, 450
- Dodds-Eden, K., Gillessen, S., Fritz, T. K., et al. 2011, *ApJ*, 728, 37
- Doeleman, S. S., Weintraub, J., Rogers, A. E. E., et al. 2008, *Nature*, 455, 78
- Dong, H., Wang, Q. D., Cotera, A., et al. 2011, *MNRAS*, 417, 114
- Dong, H., Wang, Q. D., & Morris, M. R. 2012, *MNRAS*, 425, 884
- Downes, D., & Martin, A. H. M. 1971, *Nature*, 233, 112
- Dotter, A., Sarajedini, A., & Anderson, J. 2011, *ApJ*, 738, 74
- Draine, B. T. 1989, *Infrared Spectroscopy in Astronomy*, 290, 93
- Draine, B. T. 2003, *ARA&A*, 41, 241
- Drimmel, R., & Spergel, D. N. 2001, *ApJ*, 556, 181
- D'Souza, R., & Rix, H.-W. 2013, *MNRAS*, 429, 1887
- Duquennoy, A., & Mayor, M. 1991, *A&A*, 248, 485
- Dwek, E., Arendt, R. G., Hauser, M. G., et al. 1995, *ApJ*, 445, 716
- Dwek, E. 2004, *ApJL*, 611, L10
- Eckart, A., & Genzel, R. 1996, *Nature*, 383, 415
- Eckart, A., & Genzel, R. 1997, *MNRAS*, 284, 576
- Eckart, A., Genzel, R., Ott, T., & Schödel, R. 2002, *MNRAS*, 331, 917
- Eckart, A., Moultaqa, J., Viehmann, T., Straubmeier, C., & Mouawad, N. 2004, *ApJ*, 602, 760
- Eckart, A., Baganoff, F. K., Morris, M., et al. 2004, *A&A*, 427, 1
- Eckart, A., Schödel, R., Meyer, L., et al. 2006, *A&A*, 455, 1
- Eckart, A., Schödel, R., García-Marín, M., et al. 2008, *A&A*, 492, 337
- Edelmann, H., Napiwotzki, R., Heber, U., Christlieb, N., & Reimers, D. 2005, *ApJL*, 634, L181
- Edlen, B. 1953, *Journal of the Optical Society of America (1917-1983)*, 43, 339
- Eddington, A. S. 1926, *The Internal Constitution of the Stars*, Cambridge: Cambridge University Press, 1926. ISBN 9780521337083.,

- Efstathiou, G., Sutherland, W. J., & Maddox, S. J. 1990, *Nature*, 348, 705
- Eggen, O. J., Lynden-Bell, D., & Sandage, A. R. 1962, *ApJ*, 136, 748
- Einasto, J., Saar, E., Kaasik, A., & Chernin, A. D. 1974, *Nature*, 252, 111
- Einstein, A. 1916, *Annalen der Physik*, 354, 76
- Eisenhauer, F., Schödel, R., Genzel, R., et al. 2003, *ApJL*, 597, L121
- Eisenhauer, F., Abuter, R., Bickert, K., et al. 2003, *Proc. SPIE*, 4841, 1548
- Eisenhauer, F., Genzel, R., Alexander, T., et al. 2005, *ApJ*, 628, 246
- Eisenhauer, F., Perrin, G., Brandner, W., et al. 2008, *Proc. SPIE*, 7013
- Emsellem, E., & van de Ven, G. 2008, *ApJ*, 674, 653
- Espinoza, P., Selman, F. J., & Melnick, J. 2009, *A&A*, 501, 563
- Etxaluze, M., Smith, H. A., Tolls, V., Stark, A. A., & González-Alfonso, E. 2011, *AJ*, 142, 134
- Falcke, H., Melia, F., & Agol, E. 2000, *ApJL*, 528, L13
- Farrell, S. A., Webb, N. A., Barret, D., Godet, O., & Rodrigues, J. M. 2009, *Nature*, 460, 73
- Feigelson, E. D., & Jogesh Babu, G. 2012, *Modern Statistical Methods for Astronomy*, by Eric D. Feigelson, G. Jogesh Babu, Cambridge, UK: Cambridge University Press, 2012,
- Felli, M., Testi, L., Schuller, F., & Omont, A. 2002, *A&A*, 392, 971
- Feng, H., & Soria, R. 2011, *NAR*, 55, 166
- Ferrarese, L., & Merritt, D. 2000, *ApJL*, 539, L9
- Ferrarese, L., Côté, P., Dalla Bontà, E., et al. 2006, *ApJL*, 644, L21
- Figer, D. F., McLean, I. S., & Morris, M. 1995, *ApJL*, 447, L29
- Figer, D. F., McLean, I. S., & Morris, M. 1999, *ApJ*, 514, 202
- Figer, D. F., Najarro, F., Gilmore, D., et al. 2002, *ApJ*, 581, 258
- Figer, D. F., Rich, R. M., Kim, S. S., Morris, M., & Serabyn, E. 2004, *ApJ*, 601, 319
- Figer, D. F. 2005, *Nature*, 434, 192

- Figer, D. F. 2009, *Massive Stars: From Pop III and GRBs to the Milky Way*. Space Telescope Science Institute Symposium Series No. 20. Edited by Mario Livio and Eva Villaver. Cambridge University Press, 2009, ISSN 9780521762632, p.40-59, 40
- Fitzpatrick, E. L. 2004, *Astrophysics of Dust*, 309, 33
- Fitzpatrick, E. L., & Massa, D. 2009, *ApJ*, 699, 1209
- Flaherty, K. M., Pipher, J. L., Megeath, S. T., et al. 2007, *ApJ*, 663, 1069
- Forrest, W. J., Shure, M. A., Pipher, J. L., & Woodward, C. E. 1987, *The Galactic Center*, 155, 153
- Förster Schreiber, N. M., Genzel, R., Lutz, D., Kunze, D., & Sternberg, A. 2001, *ApJ*, 552, 544
- Freeman, K. C. 2008, *IAU Symposium*, 245, 3
- Freitag, M., Amaro-Seoane, P., & Kalogera, V. 2006, *ApJ*, 649, 91
- Fritz, T., Gillessen, S., Trippe, S., et al. 2010, *MNRAS*, 401, 1177
- Fritz, T. K., Gillessen, S., Dodds-Eden, K., et al. 2010, *ApJ*, 721, 395
- Fritz, T. K., Gillessen, S., Dodds-Eden, K., et al. 2011, *ApJ*, 737, 73
- Froebrich, D., & del Burgo, C. 2006, *MNRAS*, 369, 1901
- Frogel, J. A. 1988, *ARA&A*, 26, 51
- Fujii, M., Iwasawa, M., Funato, Y., & Makino, J. 2009, *ApJ*, 695, 1421
- Fujii, M., Iwasawa, M., Funato, Y., & Makino, J. 2010, *ApJL*, 716, L80
- Fux, R. 1999, *A&A*, 345, 787
- Gao, Y., & Solomon, P. M. 2004, *ApJ*, 606, 271
- Gao, J., Jiang, B. W., & Li, A. 2009, *ApJ*, 707, 89
- Gao, J., Jiang, B. W., & Li, A. 2010, *Earth, Planets, and Space*, 62, 63
- Galileo, Galilei 1610, *Siderius Nuncius*
- Geballe, T. R., Najarro, F., Rigaut, F., & Roy, J.-R. 2006, *ApJ*, 652, 370
- Gebhardt, K., Bender, R., Bower, G., et al. 2000, *ApJL*, 539, L13
- Gebhardt, K., Lauer, T. R., Kormendy, J., et al. 2001, *AJ*, 122, 2469

- Gebhardt, K., Adams, J., Richstone, D., et al. 2011, *ApJ*, 729, 119
- Gendron, E., Clénet, Y., Fusco, T., & Rousset, G. 2006, *A&A*, 457, 359
- Genzel, R., Crawford, M. K., Townes, C. H., & Watson, D. M. 1985, *ApJ*, 297, 766
- Genzel, R., Hollenbach, D., & Townes, C. H. 1994, *Reports on Progress in Physics*, 57, 417
- Genzel, R., Thatte, N., Krabbe, A., Kroker, H., & Tacconi-Garman, L. E. 1996, *ApJ*, 472, 153
- Genzel, R., Eckart, A., Ott, T., & Eisenhauer, F. 1997, *MNRAS*, 291, 219
- Genzel, R., Pichon, C., Eckart, A., Gerhard, O. E., & Ott, T. 2000, *MNRAS*, 317, 348
- Genzel, R., Schödel, R., Ott, T., et al. 2003, *Nature*, 425, 934
- Genzel, R., Schödel, R., Ott, T., et al. 2003, *ApJ*, 594, 812
- Genzel, R., Burkert, A., Bouché, N., et al. 2008, *ApJ*, 687, 59
- Genzel, R., Eisenhauer, F., & Gillessen, S. 2010, *Reviews of Modern Physics*, 82, 3121
- Gerakines, P. A., Whittet, D. C. B., Ehrenfreund, P., et al. 1999, *ApJ*, 522, 357
- Gerhard, O. 2001, *ApJL*, 546, L39
- Gerhard, O., & Martinez-Valpuesta, I. 2012, *ApJL*, 744, L8
- Ghez, A. M., Klein, B. L., Morris, M., & Becklin, E. E. 1998, *ApJ*, 509, 678
- Ghez, A. M., Morris, M., Becklin, E. E., Tanner, A., & Kremenek, T. 2000, *Nature*, 407, 349
- Ghez, A. M., Duchêne, G., Matthews, K., et al. 2003, *ApJL*, 586, L127
- Ghez, A. M., Becklin, E., Duchjne, G., et al. 2003, *Astronomische Nachrichten Supplement*, 324, 527
- Ghez, A. M., Salim, S., Hornstein, S. D., et al. 2005, *ApJ*, 620, 744
- Ghez, A. M., Salim, S., Weinberg, N. N., et al. 2008, *ApJ*, 689, 1044
- Gillessen, S., Eisenhauer, F., Quataert, E., et al. 2006, *ApJL*, 640, L163
- Gillessen, S., Eisenhauer, F., Trippe, S., et al. 2009, *ApJ*, 692, 1075
- Gillessen, S., Genzel, R., Fritz, T. K., et al. 2012, *Nature*, 481, 51
- Gillessen, S., Eisenhauer, F., Fritz, T. K., et al. 2013, *IAU Symposium*, 289, 29

- Gilmozzi, R., & Kissler-Patig, M. 2011, *The Messenger*, 143, 25
- Gilmore, G., & Reid, N. 1983, *MNRAS*, 202, 1025
- Gilmore, G. 1984, *MNRAS*, 207, 223
- Glass, I. S., Moneti, A., & Moorwood, A. F. M. 1990, *MNRAS*, 242, 55P
- Gonzalez, O. A., Rejkuba, M., Minniti, D., et al. 2011, *A&A*, 534, L1
- Gosling, A. J., Bandyopadhyay, R. M., & Blundell, K. M. 2009, *MNRAS*, 394, 2247
- Goss, W. M., & McGee, R. X. 1996, *The Galactic Center*, 102, 369
- Gould, A., & Quillen, A. C. 2003, *ApJ*, 592, 935
- Graham, A. W., & Spitler, L. R. 2009, *MNRAS*, 397, 2148
- Gratton, R. G., Bragaglia, A., Carretta, E., et al. 2003, *A&A*, 408, 529
- Graves, J. E., Northcott, M. J., Roddier, F. J., Roddier, C. A., & Close, L. M. 1998, *Proc. SPIE*, 3353, 34
- Groenewegen, M. A. T. 2008, *A&A*, 488, 935
- Groenewegen, M. A. T., Udalski, A., & Bono, G. 2008, *A&A*, 481, 441
- Gualandris, A., Portegies Zwart, S., & Sipior, M. S. 2005, *MNRAS*, 363, 223
- Gualandris, A., & Merritt, D. 2009, *ApJ*, 705, 361
- Guesten, R., Walmsley, C. M., & Pauls, T. 1981, *A&A*, 103, 197
- Guesten, R., Genzel, R., Wright, M. C. H., et al. 1987, *ApJ*, 318, 124
- Gültekin, K., Richstone, D. O., Gebhardt, K., et al. 2009, *ApJ*, 698, 198
- Gürkan, M. A., & Rasio, F. A. 2005, *ApJ*, 628, 236
- Guo, F., & Mathews, W. G. 2012, *ApJ*, 756, 181
- Haubois, X., Dodds-Eden, K., Weiss, A., et al. 2012, *A&A*, 540, A41
- Haller, J. W., Rieke, M. J., Rieke, G. H., et al. 1996, *ApJ*, 456, 194
- Hansen, B. M. S., & Milosavljević, M. 2003, *ApJL*, 593, L77
- Harris, W. E. 1976, *AJ*, 81, 1095
- Harris, W. E. 1996, *AJ*, 112, 1487

- Harris, G. L. H., & Harris, W. E. 2011, *MNRAS*, 410, 2347
- Hodapp, K.-W., Hora, J. L., Hall, D. N. B., et al. 1996, *New Astronomy*, 1, 177
- Howard, C. D., Rich, R. M., Clarkson, W., et al. 2009, *ApJL*, 702, L153
- He, L., Whittet, D. C. B., Kilkenny, D., & Spencer Jones, J. H. 1995, *ApJS*, 101, 335
- Heger, A., Fryer, C. L., Woosley, S. E., Langer, N., & Hartmann, D. H. 2003, *ApJ*, 591, 288
- Helmi, A. 2008, *A&A Rev.*, 15, 145
- Hełminiak, K. G. 2009, *New Astronomy*, 14, 521
- Herrnstein, R. M., Zhao, J.-H., Bower, G. C., & Goss, W. M. 2004, *AJ*, 127, 3399
- Herschel, W. 1785, *Royal Society of London Philosophical Transactions Series I*, 75, 213
- Hesser, J. E. 1992, *The Stellar Populations of Galaxies*, 149, 1
- Hill, V., Lecureur, A., Gómez, A., et al. 2011, *A&A*, 534, A80
- Hillier, D. J., & Miller, D. L. 1998, *ApJ*, 496, 407
- Hills, J. G. 1988, *Nature*, 331, 687
- Henry, J. P., Depoy, D. L., & Becklin, E. E. 1984, *ApJL*, 285, L27
- Hobbs, A., & Nayakshin, S. 2009, *MNRAS*, 394, 191
- Hofmann, R., Blietz, M., Duhoux, P., et al. 1992, *European Southern Observatory Conference and Workshop Proceedings*, 42, 617
- Hopman, C., & Alexander, T. 2006, *ApJL*, 645, L133
- Hornstein, S. D., Matthews, K., Ghez, A. M., et al. 2007, *ApJ*, 667, 900
- Hummer, D. G., & Storey, P. J. 1987, *MNRAS*, 224, 801
- Humphreys, R. M., & Larsen, J. A. 1995, *AJ*, 110, 2183
- Hunter, C., & Qian, E. 1993, *MNRAS*, 262, 401
- Hußmann, B., Stolte, A., Brandner, W., Gennaro, M., & Liermann, A. 2012, *A&A*, 540, A57
- Immer, K., Schuller, F., Omont, A., & Menten, K. M. 2012, *A&A*, 537, A121
- Indebetouw, R., Mathis, J. S., Babler, B. L., et al. 2005, *ApJ*, 619, 931

- Inui, T., Koyama, K., Matsumoto, H., & Tsuru, T. G. 2009, PASJ, 61, 241
- Jackson, J. M., Geis, N., Genzel, R., et al. 1993, ApJ, 402, 173
- Jahnke, K., & Macciò, A. V. 2011, ApJ, 734, 92
- Jansky, K. G. 1932, Proceedings of the IRE, 20, 1932
- Jansky, K. G. 1933, Popular Astronomy, 41, 548
- Jiang, B. W., Omont, A., Ganesh, S., Simon, G., & Schuller, F. 2003, A&A, 400, 903
- Jiang, B. W., Gao, J., Omont, A., Schuller, F., & Simon, G. 2006, A&A, 446, 551
- Jofré, P., & Weiss, A. 2011, A&A, 533, A59
- Kahn, F. D., & Woltjer, L. 1959, ApJ, 130, 705
- Kalberla, P. M. W., & Kerp, J. 2009, ARA&A, 47, 27
- Kalirai, J. S. 2012, Nature, 486, 90
- Kauffmann, G., & Haehnelt, M. 2000, MNRAS, 311, 576
- Kemper, F., Vriend, W. J., & Tielens, A. G. G. M. 2004, ApJ, 609, 826
- Kenyon, S. J., Lada, E. A., & Barsony, M. 1998, AJ, 115, 252
- Kervella, P., Mérand, A., Petr-Gotzens, M. G., Pribulla, T., & Thévenin, F. 2013, A&A, 552, A18
- Kerr, R. P. 1963, Physical Review Letters, 11, 237
- Keshet, U., Hopman, C., & Alexander, T. 2009, ApJL, 698, L64
- Kim, S. S., Figer, D. F., Kudritzki, R. P., & Najarro, F. 2006, ApJL, 653, L113
- Knez, C., Boogert, A. C. A., Pontoppidan, K. M., et al. 2005, ApJL, 635, L145
- Kobayashi, S., Hainick, Y., Sari, R., & Rossi, E. M. 2012, ApJ, 748, 105
- Kobulnicky, H. A., & Fryer, C. L. 2007, ApJ, 670, 747
- Kocsis, B., & Tremaine, S. 2011, MNRAS, 412, 187
- Köhler, R., Neuhauser, R., Krämer, S., et al. 2008, A&A, 488, 997
- Kollmeier, J. A., Gould, A., Knapp, G., & Beers, T. C. 2009, ApJ, 697, 1543
- Kolpak, M. A., Jackson, J. M., Bania, T. M., Clemens, D. P., & Dickey, J. M. 2003, ApJ, 582, 75

- Kennicutt, R. C., Jr. 1998, *ApJ*, 498, 541
- Kormendy, J., & McClure, R. D. 1993, *AJ*, 105, 1793
- Kormendy, J., & Richstone, D. 1995, *ARA&A*, 33, 581
- Kormendy, J., Bender, R., Richstone, D., et al. 1996, *ApJL*, 459, L57
- Kormendy, J., & Kennicutt, R. C., Jr. 2004, *ARA&A*, 42, 603
- Kormendy, J. 2004, *Coevolution of Black Holes and Galaxies*, 1
- Kormendy, J., Fisher, D. B., Cornell, M. E., & Bender, R. 2009, *ApJS*, 182, 216
- Kormendy, J., Bender, R., & Cornell, M. E. 2011, *Nature*, 469, 374
- Kormendy, J., & Bender, R. 2011, *Nature*, 469, 377
- Koyama, K., Maeda, Y., Sonobe, T., et al. 1996, *PASJ*, 48, 249
- Krabbe, A., Genzel, R., Drapatz, S., & Rotaciuc, V. 1991, *ApJL*, 382, L19
- Krabbe, A., Genzel, R., Eckart, A., et al. 1995, *ApJL*, 447, L95
- Krabbe, A., Iserlohe, C., Larkin, J. E., et al. 2006, *ApJL*, 642, L145
- Kroupa, P. 2001, *MNRAS*, 322, 231
- Kruijssen, J. M. D., Longmore, S. N., Elmegreen, B. G., et al. 2013, *arXiv:1303.6286*
- Kuijken, K., & Rich, R. M. 2002, *AJ*, 124, 2054
- Lacy, J. H., Baas, F., Townes, C. H., & Geballe, T. R. 1979, *ApJL*, 227, L17
- Lacy, J. H., Townes, C. H., & Hollenbach, D. J. 1982, *ApJ*, 262, 120
- Lagrange, A.-M., Gratadour, D., Chauvin, G., et al. 2009, *A&A*, 493, L21
- Landini, M., Natta, A., Salinari, P., Oliva, E., & Moorwood, A. F. M. 1984, *A&A*, 134, 284
- Larsen, J. A., & Humphreys, R. M. 2003, *AJ*, 125, 1958
- Lauer, T. R., Faber, S. M., Currie, D. G., et al. 1992, *AJ*, 104, 552
- Lauer, T. R., Faber, S. M., Groth, E. J., et al. 1993, *AJ*, 106, 1436
- Lauer, T. R., Ajhar, E. A., Byun, Y.-I., et al. 1995, *AJ*, 110, 2622
- Lauer, T. R., Faber, S. M., Ajhar, E. A., Grillmair, C. J., & Scowen, P. A. 1998, *AJ*, 116, 2263

- Launhardt, R., Zylka, R., & Mezger, P. G. 2002, *A&A*, 384, 112
- Lebofsky, M. J., Rieke, G. H., & Tokunaga, A. T. 1982, *ApJ*, 263, 736
- Lecureur, A., Hill, V., Zoccali, M., et al. 2007, *A&A*, 465, 799
- Lenzen, R., Hartung, M., Brandner, W., et al. 2003, *Proc. SPIE*, 4841, 944
- Leonard, P. J. T., & Merritt, D. 1989, *ApJ*, 339, 195
- Levin, Y., & Beloborodov, A. M. 2003, *ApJL*, 590, L33
- Li, A., & Greenberg, J. M. 1997, *A&A*, 323, 566
- Li, A., & Draine, B. T. 2001, *ApJ*, 554, 778
- Li, A. 2005, *ApJ*, 622, 965
- Li, A. 2007, *The Central Engine of Active Galactic Nuclei*, 373, 561
- Lindqvist, M., Winnberg, A., Habing, H. J., & Matthews, H. E. 1992, *A&AS*, 92, 43
- Lindqvist, M., Habing, H. J., & Winnberg, A. 1992, *A&A*, 259, 118
- Lindgren, L. 1978, *IAU Colloq. 48: Modern Astrometry*, 197
- Lindgren, L., Bastian U., 2006, *GAIA Internal Report*, GAIA-LL-061-2, 1.
- Lis, D. C., & Carlstrom, J. E. 1994, *ApJ*, 424, 18
- Liszt, H. S. 2003, *A&A*, 408, 1009
- Liu, T., Becklin, E. E., Henry, J. P., & Simons, D. 1993, *AJ*, 106, 1484
- Lo, K. Y., & Claussen, M. J. 1983, *Nature*, 306, 647
- Löckmann, U., Baumgardt, H., & Kroupa, P. 2008, *ApJL*, 683, L151
- Löckmann, U., & Baumgardt, H. 2009, *MNRAS*, 394, 1841
- Löckmann, U., Baumgardt, H., & Kroupa, P. 2009, *MNRAS*, 398, 429
- Lombardi, M., Alves, J., & Lada, C. J. 2006, *A&A*, 454, 781
- Longhetti, M., & Saracco, P. 2009, *MNRAS*, 394, 774
- Longmore, S. N., Bally, J., Testi, L., et al. 2013, *MNRAS*, 429, 987
- López-Corredoira, M., Cabrera-Lavers, A., Garzón, F., & Hammersley, P. L. 2002, *A&A*, 394, 883

- Lord, S. D., 1992, NASA Technical Memorandum 103957
- Lu, J. R., Ghez, A. M., Hornstein, S. D., Morris, M., & Becklin, E. E. 2005, *ApJL*, 625, L51
- Lu, J. R., Ghez, A. M., Hornstein, S. D., et al. 2009, *ApJ*, 690, 1463
- Lu, Y., Zhang, F., & Yu, Q. 2010, *ApJ*, 709, 1356
- Lu, J. R., Do, T., Ghez, A. M., et al. 2013, *ApJ*, 764, 155
- Lucas, W. E., Bonnell, I. A., Davies, M. B., & Rice, K. 2013, arXiv:1305.0012
- Lucy, L. B. 1974, *AJ*, 79, 745
- Lützgendorf, N., Kissler-Patig, M., Gebhardt, K., et al. 2012, *A&A*, 542, A129
- Lutz, D., Krabbe, A., & Genzel, R. 1993, *ApJ*, 418, 244
- Lutz, D., Feuchtgruber, H., Genzel, R., et al. 1996, *A&A*, 315, L269
- Lutz, D. 1999, *The Universe as Seen by ISO*, 427, 623
- Lynden-Bell, D. 1969, *Nature*, 223, 690
- Lynden-Bell, D., & Rees, M. J. 1971, *MNRAS*, 152, 461
- Maeda, Y., Baganoff, F. K., Feigelson, E. D., et al. 2002, *ApJ*, 570, 671
- Macintosh, B. A., Graham, J., Poyneer, L., et al. 2003, *Proc. SPIE*, 5170, 272
- Madigan, A.-M., Levin, Y., & Hopman, C. 2009, *ApJL*, 697, L44
- Madigan, A.-M., Hopman, C., & Levin, Y. 2011, *ApJ*, 738, 99
- Madigan, A.-M., Levin, Y., Pfuhl, O., Genzel, R., & Perets, H. B. 2013, arXiv:1305.1625
- Maillard, J. P., Paumard, T., Stolovy, S. R., & Rigaut, F. 2004, *A&A*, 423, 155
- Maiolino, R., Marconi, A., Salvati, M., et al. 2001, *A&A*, 365, 28
- Maness, H., Martins, F., Trippe, S., et al. 2007, *ApJ*, 669, 1024
- Maoz, E. 1995, *ApJL*, 447, L91
- Maraston, C., Greggio, L., Renzini, A., et al. 2003, *A&A*, 400, 823
- Marchetti, E., Brast, R., Delabre, B., et al. 2004, *Proc. SPIE*, 5490, 236
- van der Marel, R. P. 1994, *MNRAS*, 270, 271

- van der Marel, R. P. 2004, *Coevolution of Black Holes and Galaxies*, 37
- van der Marel, R. P., & Anderson, J. 2010, *ApJ*, 710, 1063
- Marks, M., Kroupa, P., Dabringhausen, J., & Pawlowski, M. S. 2012, *MNRAS*, 422, 2246
- Markwardt, C. B. 2009, *Astronomical Data Analysis Software and Systems XVIII*, 411, 251
- Marrone, D. P., Baganoff, F. K., Morris, M. R., et al. 2008, *ApJ*, 682, 373
- Marshall, D. J., Robin, A. C., Reylé, C., Schultheis, M., & Picaud, S. 2006, *A&A*, 453, 635
- Martín-Hernández, N. L., Bik, A., Puga, E., Nürnberger, D. E. A., & Bronfman, L. 2008, *A&A*, 489, 229
- Martins, F., Genzel, R., Hillier, D. J., et al. 2007, *A&A*, 468, 233
- Martins, F., Gillessen, S., Eisenhauer, F., et al. 2008, *ApJL*, 672, L119
- Martins, F., Hillier, D. J., Paumard, T., et al. 2008, *A&A*, 478, 219
- Martins, F., Hillier, D. J., Bouret, J. C., et al. 2009, *A&A*, 495, 257
- Masana, E., Jordi, C., & Ribas, I. 2006, *A&A*, 450, 735
- Mathis, J. S., Rumpl, W., & Nordsieck, K. H. 1977, *ApJ*, 217, 425
- Mathis, J. S. 1990, *ARA&A*, 28, 37
- Mathis, J. S. 1996, *ApJ*, 472, 643
- Matthews, L. D., & Gallagher, J. S., III 1997, *AJ*, 114, 1899
- Matsunaga, N., Kawadu, T., Nishiyama, S., et al. 2009, *MNRAS*, 399, 1709
- Matsunaga, N., Kawadu, T., Nishiyama, S., et al. 2011, *Nature*, 477, 188
- Mauerhan, J. C., Morris, M., Walter, F., & Baganoff, F. K. 2005, *ApJL*, 623, L25
- Mauerhan, J. C., Muno, M. P., Morris, M. R., Stolovy, S. R., & Cotera, A. 2010, *ApJ*, 710, 706
- McConnachie, A. W., Irwin, M. J., Ferguson, A. M. N., et al. 2005, *MNRAS*, 356, 979
- McGee, R. X., & Bolton, J. G. 1954, *Nature*, 173, 985
- McGinn, M. T., Sellgren, K., Becklin, E. E., & Hall, D. N. B. 1989, *ApJ*, 338, 824
- Melia, F., & Falcke, H. 2001, *ARA&A*, 39, 309

- Messineo, M., Habing, H. J., Menten, K. M., et al. 2005, *A&A*, 435, 575
- Merritt, D., & Tremblay, B. 1994, *AJ*, 108, 514
- Merritt, D., Ferrarese, L., & Joseph, C. L. 2001, *Science*, 293, 1116
- Merritt, D., Gualandris, A., & Mikkola, S. 2009, *ApJL*, 693, L35
- Merritt, D. 2010, *ApJ*, 718, 739
- Meyer, L., Eckart, A., Schödel, R., et al. 2006, *A&A*, 460, 15
- Meyer, L., Do, T., Ghez, A., et al. 2009, *ApJL*, 694, L87
- Meyer, L., Ghez, A. M., Schödel, R., et al. 2012, *Science*, 338, 84
- Mezger, P. G., Zylka, R., Salter, C. J., et al. 1989, *A&A*, 209, 337
- Mezger, P. G., Duschl, W. J., & Zylka, R. 1996, *A&A Rev.*, 7, 289
- Milgrom, M. 1983, *ApJ*, 270, 365
- Milosavljević, M. 2004, *ApJL*, 605, L13
- Minniti, D. 1995, *AJ*, 109, 1663
- Minniti, D., & Zoccali, M. 2008, *IAU Symposium*, 245, 323
- Minniti, D., Saito, R. K., Alonso-García, J., Lucas, P. W., & Hempel, M. 2011, *ApJL*, 733, L43
- Mościbrodzka, M., Gammie, C. F., Dolence, J. C., Shiokawa, H., & Leung, P. K. 2009, *ApJ*, 706, 497
- Moneti, A., Cernicharo, J., & Pardo, J. R. 2001, *ApJL*, 549, L203
- Monnier, J. D., Tuthill, P. G., & Danchi, W. C. 2002, *ApJL*, 567, L137
- Moore, T. J. T., Lumsden, S. L., Ridge, N. A., & Puxley, P. J. 2005, *MNRAS*, 359, 589
- Morris, M. 1993, *ApJ*, 408, 496
- Morris, M., & Serabyn, E. 1996, *ARA&A*, 34, 645
- Morris, M. R., Meyer, L., & Ghez, A. M. 2012, *Research in Astronomy and Astrophysics*, 12, 995
- Morrison, R., & McCammon, D. 1983, *ApJ*, 270, 119
- Morrison, H. L. 1993, *AJ*, 106, 578

- Morrison, H. L., Mateo, M., Olszewski, E. W., et al. 2000, *AJ*, 119, 2254
- Moultaka, J., Eckart, A., Schödel, R., Viehmann, T., & Najarro, F. 2005, *A&A*, 443, 163
- Muno, M. P., Pfahl, E., Baganoff, F. K., et al. 2005, *ApJL*, 622, L113
- Muno, M. P., Bower, G. C., Burgasser, A. J., et al. 2006, *ApJ*, 638, 183
- Munyanza, F., & Viollier, R. D. 2002, *ApJ*, 564, 274
- Mužić, K., Eckart, A., Schödel, R., Meyer, L., & Zensus, A. 2007, *A&A*, 469, 993
- Mužić, K., Schödel, R., Eckart, A., Meyer, L., & Zensus, A. 2008, *A&A*, 482, 173
- Naoi, T., Tamura, M., Nakajima, Y., et al. 2006, *ApJ*, 640, 373
- Naoi, T., Tamura, M., Nagata, T., et al. 2007, *ApJ*, 658, 1114
- Narayanan, V. K., Gould, A., & Depoy, D. L. 1996, *ApJ*, 472, 183
- Nataf, D. M., Udalski, A., Gould, A., Fouqué, P., & Stanek, K. Z. 2010, *ApJL*, 721, L28
- Nataf, D. M., & Gould, A. P. 2012, *ApJL*, 751, L39
- Navarro, J. F., Frenk, C. S., & White, S. D. M. 1997, *ApJ*, 490, 493
- Nayakshin, S., & Cuadra, J. 2005, *A&A*, 437, 437
- Ness, M., Freeman, K., Athanassoula, E., et al. 2013, *MNRAS*, 430, 836
- Ness, M., Freeman, K., Athanassoula, E., et al. 2013, *arXiv:1303.6656*
- Neugebauer, G., Becklin, E. E., Beckwith, S., Matthews, K., & Wynn-Williams, C. G. 1976, *ApJL*, 205, L139
- Neuhäuser, R., Seifahrt, A., Röhl, T., Bedalov, A., & Mugrauer, M. 2007, *IAU Symposium*, 240, 261
- Neuhäuser, R., Mugrauer, M., Seifahrt, A., Schmidt, T. O. B., & Vogt, N. 2008, *A&A*, 484, 281
- Nishiyama, S., Nagata, T., Sato, S., et al. 2006, *ApJ*, 647, 1093
- Nishiyama, S., Nagata, T., Kusakabe, N., et al. 2006, *ApJ*, 638, 839
- Nishiyama, S., Nagata, T., Tamura, M., et al. 2008, *ApJ*, 680, 1174
- Nishiyama, S., Tamura, M., Hatano, H., et al. 2009, *ApJ*, 696, 1407
- Nishiyama, S., & Schödel, R. 2013, *A&A*, 549, A57

- Nowak, M. A., Neilsen, J., Markoff, S. B., et al. 2012, arXiv:1209.6354
- Noyola, E., Gebhardt, K., & Bergmann, M. 2008, ApJ, 676, 1008
- Nusser, A., & Broadhurst, T. 2004, MNRAS, 355, L6
- Okuda, H., Shibai, H., Nakagawa, T., et al. 1990, ApJ, 351, 89
- Oort, J. H., Kerr, F. J., & Westerhout, G. 1958, MNRAS, 118, 379
- Oort, J. H. 1977, ARA&A, 15, 295
- Ostriker, J. P., & Peebles, P. J. E. 1973, ApJ, 186, 467
- Ostriker, J. P., Peebles, P. J. E., & Yahil, A. 1974, ApJL, 193, L1
- Ostriker, J. P., & Steinhardt, P. J. 1995, Nature, 377, 600
- Ott, T., Eckart, A., & Genzel, R. 1999, ApJ, 523, 248
- Ott, T., PhD Thesis
- Ozernoy, L. M. 1989, The Center of the Galaxy, 136, 555
- Pasquini, L., Bonifacio, P., Randich, S., et al. 2007, A&A, 464, 601
- Paumard, T., Maillard, J.-P., & Morris, M. 2004, A&A, 426, 81
- Paumard, T., Genzel, R., Martins, F., et al. 2006, ApJ, 643, 1011
- Pendleton, Y. J., & Allamandola, L. J. 2002, ApJS, 138, 75
- Peng, C. Y., Ho, L. C., Impey, C. D., & Rix, H.-W. 2002, AJ, 124, 266
- Peng, C. Y., Impey, C. D., Rix, H.-W., et al. 2006, ApJ, 649, 616
- Peng, C. Y. 2007, ApJ, 671, 1098
- Perets, H. B., Hopman, C., & Alexander, T. 2007, ApJ, 656, 709
- Perets, H. B. 2009, ApJ, 690, 795
- Perets, H. B., & Gualandris, A. 2010, ApJ, 719, 220
- Perlmutter, S., Aldering, G., Goldhaber, G., et al. 1999, ApJ, 517, 565
- Pfuhl, O., Fritz, T. K., Zilka, M., et al. 2011, ApJ, 741, 108
- Phillips, A. C., Illingworth, G. D., MacKenty, J. W., & Franx, M. 1996, AJ, 111, 1566
- Philipp, S., Zylka, R., Mezger, P. G., et al. 1999, A&A, 348, 768

- Piddington, J. H., & Minnett, H. C. 1951, Australian Journal of Scientific Research A Physical Sciences, 4, 459
- Predehl, P., & Schmitt, J. H. M. M. 1995, A&A, 293, 889
- Ponti, G., Terrier, R., Goldwurm, A., Belanger, G., & Trap, G. 2010, ApJ, 714, 732
- Porcel, C., Garzon, F., Jimenez-Vicente, J., & Battaner, E. 1998, A&A, 330, 136
- Porquet, D., Predehl, P., Aschenbach, B., et al. 2003, A&A, 407, L17
- Porquet, D., Grosso, N., Predehl, P., et al. 2008, A&A, 488, 549
- Portegies Zwart, S. F., & McMillan, S. L. W. 2002, ApJ, 576, 899
- Portegies Zwart, S. F., Baumgardt, H., Hut, P., Makino, J., & McMillan, S. L. W. 2004, Nature, 428, 724
- Portegies Zwart, S., Gaburov, E., Chen, H.-C., Guumlrkan, M. A. 2007, MNRAS, 378, L29
- Racca, G., Gómez, M., & Kenyon, S. J. 2002, AJ, 124, 2178
- Ramírez, S. V., Sellgren, K., Carr, J. S., et al. 2000, ApJ, 537, 205
- Ramírez, S. V., Arendt, R. G., Sellgren, K., et al. 2008, ApJS, 175, 147
- Rawlings, M. G., Adamson, A. J., & Whittet, D. C. B. 2003, MNRAS, 341, 1121
- Rayner, J. T., Cushing, M. C., & Vacca, W. D. 2009, ApJS, 185, 289
- Reber, G. 1944, ApJ, 100, 279
- Reid, M. J. 1993, ARA&A, 31, 345
- Reid, M. J., Readhead, A. C. S., Vermeulen, R. C., & Treuhaft, R. N. 1999, ApJ, 524, 816
- Reid, M. J., Menten, K. M., Genzel, R., et al. 2003, ApJ, 587, 208
- Reid, M. J., & Brunthaler, A. 2004, ApJ, 616, 872
- Reid, M. J., Menten, K. M., Trippe, S., Ott, T., & Genzel, R. 2007, ApJ, 659, 378
- Reid, M. J., Menten, K. M., Zheng, X. W., et al. 2009, ApJ, 700, 137
- Reid, M. J., Menten, K. M., Zheng, X. W., Brunthaler, A., & Xu, Y. 2009, ApJ, 705, 1548
- Requena-Torres, M. A., Güsten, R., Weiß, A., et al. 2012, A&A, 542, L21
- Revnivtsev, M., van den Berg, M., Burenin, R., et al. 2010, A&A, 515, A49

- Rhode, K. L. 2012, *AJ*, 144, 154
- Rich, R. M., & Origlia, L. 2005, *ApJ*, 634, 1293
- Rich, R. M., Origlia, L., & Valenti, E. 2012, *ApJ*, 746, 59
- Rieke, G. H., & Lebofsky, M. J. 1985, *ApJ*, 288, 618
- Rieke, G. H., & Rieke, M. J. 1988, *ApJL*, 330, L33
- Rieke, G. H., Rieke, M. J., & Paul, A. E. 1989, *ApJ*, 336, 752
- Rieke, M. J. 1999, *The Central Parsecs of the Galaxy*, 186, 32
- Riess, A. G., Filippenko, A. V., Challis, P., et al. 1998, *AJ*, 116, 1009
- Ritchie, B. W., Clark, J. S., Negueruela, I., & Langer, N. 2010, *A&A*, 520, A48
- Rix, H.-W., & Bovy, J. 2013, arXiv:1301.3168
- Roberts, M. S., & Rots, A. H. 1973, *A&A*, 26, 483
- Roberts, D. A., Goss, W. M., van Gorkom, J. H., & Leahy, J. P. 1991, *ApJL*, 366, L15
- Roberts, D. A., & Goss, W. M. 1993, *ApJS*, 86, 133
- Roberts, D. A., Yusef-Zadeh, F., & Goss, W. M. 1996, *ApJ*, 459, 627
- Robitaille, T. P., & Whitney, B. A. 2010, *ApJL*, 710, L11
- Robin, A. C., Creze, M., & Mohan, V. 1992, *ApJL*, 400, L25
- Rocha-Pinto, H. J., Scalo, J., Maciel, W. J., & Flynn, C. 2000, *ApJL*, 531, L115
- Roche, P. F., & Aitken, D. K. 1984, *MNRAS*, 208, 481
- Roche, P. F., & Aitken, D. K. 1985, *MNRAS*, 215, 425
- Roelfsema, P. R., Goss, W. M., & Mallik, D. C. V. 1992, *ApJ*, 394, 188
- Rogers, A. E. E., Doeleman, S., Wright, M. C. H., et al. 1994, *ApJL*, 434, L59
- Román-Zúñiga, C. G., Lada, C. J., Muench, A., & Alves, J. F. 2007, *ApJ*, 664, 357
- Rosa, M. R., Zinnecker, H., Moneti, A., & Melnick, J. 1992, *A&A*, 257, 515
- Rosenberg, A., Saviane, I., Piotto, G., & Aparicio, A. 1999, *AJ*, 118, 2306
- Rosenthal, D., Bertoldi, F., & Drapatz, S. 2000, *A&A*, 356, 705
- Rossa, J., van der Marel, R. P., Böker, T., et al. 2006, *AJ*, 132, 1074

- Rousset, G., Lacombe, F., Puget, P., et al. 2003, *Proc. SPIE*, 4839, 140
- Rubilar, G. F., & Eckart, A. 2001, *A&A*, 374, 95
- Rubin, V. C., Burstein, D., Ford, W. K., Jr., & Thonnard, N. 1985, *ApJ*, 289, 81
- Russeil, D. 2003, *A&A*, 397, 133
- Saito, R. K., Zoccali, M., McWilliam, A., et al. 2011, *AJ*, 142, 76
- Sakano, M., Warwick, R. S., Decourchelle, A., & Predehl, P. 2004, *MNRAS*, 350, 129
- Salaris, M., & Girardi, L. 2002, *MNRAS*, 337, 332
- Sale, S. E., Drew, J. E., Knigge, C., et al. 2010, *MNRAS*, 402, 713
- Salpeter, E. E. 1955, *ApJ*, 121, 161
- Saha, K., Martinez-Valpuesta, I., & Gerhard, O. 2012, *MNRAS*, 421, 333
- Sana, H., de Mink, S. E., de Koter, A., et al. 2012, *Science*, 337, 444
- Sanders, R. H. 1992, *Nature*, 359, 131
- Sanders, R. H., & McGaugh, S. S. 2002, *ARA&A*, 40, 263
- Savage, B. D., & Mathis, J. S. 1979, *ARA&A*, 17, 73
- Sazonov, S., Sunyaev, R., & Revnivtsev, M. 2012, *MNRAS*, 420, 388
- Scalo, J. M. 1986, *Fund. Cosmic Phys.*, 11, 1
- Schartmann, M., Burkert, A., Alig, C., et al. 2012, *ApJ*, 755, 155
- Schlafly, E. F., Finkbeiner, D. P., Schlegel, D. J., et al. 2010, *ApJ*, 725, 1175
- Schmidt, M. 1963, *Nature*, 197, 1040
- Schödel, R., Ott, T., Genzel, R., et al. 2002, *Nature*, 419, 694
- Schödel, R., Eckart, A., Iserlohe, C., Genzel, R., & Ott, T. 2005, *ApJL*, 625, L111
- Schödel, R., Eckart, A., Alexander, T., et al. 2007, *A&A*, 469, 125
- Schödel, R., Merritt, D., & Eckart, A. 2008, *Journal of Physics Conference Series*, 131, 012044
- Schödel, R., Merritt, D., & Eckart, A. 2009, *A&A*, 502, 91
- Schödel, R., Najarro, F., Muzic, K., & Eckart, A. 2010, *A&A*, 511, A18

- Schödel, R. 2011, *The Galactic Center: a Window to the Nuclear Environment of Disk Galaxies*, 439, 222
- Schönrich, R., & Binney, J. 2009, *MNRAS*, 396, 203
- Schönrich, R., Binney, J., & Dehnen, W. 2010, *MNRAS*, 403, 1829
- Schreiber, J., Thatte, N., Eisenhauer, F., et al. 2004, *Astronomical Data Analysis Software and Systems (ADASS) XIII*, 314, 380
- Schultz, G. V., & Wiemer, W. 1975, *A&A*, 43, 133
- Schultheis, M., Sellgren, K., Ramírez, S., et al. 2009, *A&A*, 495, 157
- Schwarz, U. J., Bregman, J. D., & van Gorkom, J. H. 1989, *A&A*, 215, 33
- Schwarzschild, K. 1916, *Abh. Konigl. Preuss. Akad. Wissenschaften Jahre 1906,92, Berlin,1907*, 189
- Scott, D. W. 1992, *Multivariate Density Estimation*, Wiley, New York, 1992,
- Scoville, N. Z., Stolovy, S. R., Rieke, M., Christopher, M., & Yusef-Zadeh, F. 2003, *ApJ*, 594, 294
- Schuller, F., Omont, A., Glass, I. S., et al. 2006, *A&A*, 453, 535
- Seaton, M. J. 1979, *MNRAS*, 187, 73P
- Sellgren, K., Hall, D. N. B., Kleinmann, S. G., & Scoville, N. Z. 1987, *ApJ*, 317, 881
- Sellgren, K., McGinn, M. T., Becklin, E. E., & Hall, D. N. 1990, *ApJ*, 359, 112
- Serabyn, E., & Lacy, J. H. 1985, *ApJ*, 293, 445
- Serabyn, E., Guesten, R., Walmsley, J. E., Wink, J. E., & Zylka, R. 1986, *A&A*, 169, 85
- Serabyn, E., & Morris, M. 1996, *Nature*, 382, 602
- Serabyn, E., Carlstrom, J., Lay, O., et al. 1997, *ApJL*, 490, L77
- Sersic, J. L. 1968, *Cordoba, Argentina: Observatorio Astronomico*, 1968,
- Seth, A. C., Dalcanton, J. J., Hodge, P. W., & Debattista, V. P. 2006, *AJ*, 132, 2539
- Seth, A. C., Blum, R. D., Bastian, N., Caldwell, N., & Debattista, V. P. 2008, *ApJ*, 687, 997
- Seth, A. C., Cappellari, M., Neumayer, N., et al. 2010, *ApJ*, 714, 713
- Shapley, H. 1918, *PASP*, 30, 42

- Sharples, R., Bender, R., Agudo Berbel, A., et al. 2013, *The Messenger*, 151, 21
- Shcherbakov, R. V., & Baganoff, F. K. 2010, *ApJ*, 716, 504
- Shcherbakov, R. V., Penna, R. F., & McKinney, J. C. 2012, *ApJ*, 755, 133
- Shukla, H., Yun, M. S., & Scoville, N. Z. 2004, *ApJ*, 616, 231
- Silk, J., & Rees, M. J. 1998, *A&A*, 331, L1
- Snedden, C., Gehrz, R. D., Hackwell, J. A., York, D. G., & Snow, T. P. 1978, *ApJ*, 223, 168
- Sollima, A., Bellazzini, M., & Lee, J.-W. 2012, *ApJ*, 755, 156
- Soltan, A. 1982, *MNRAS*, 200, 115
- Springel, V., White, S. D. M., Jenkins, A., et al. 2005, *Nature*, 435, 629
- Stanek, K. Z., Mateo, M., Udalski, A., et al. 1994, *ApJL*, 429, L73
- Stead, J. J., & Hoare, M. G. 2009, *MNRAS*, 400, 731
- Stecker, F. W., Solomon, P. M., Scoville, N. Z., & Ryter, C. E. 1975, *ApJ*, 201, 90
- Strader, J., Caldwell, N., & Seth, A. C. 2011, *AJ*, 142, 8
- Strader, J., Chomiuk, L., Maccarone, T. J., et al. 2012, *ApJL*, 750, L27
- Straižys, V., & Laugalys, V. 2008, *Baltic Astronomy*, 17, 253
- Su, M., Slatyer, T. R., & Finkbeiner, D. P. 2010, *ApJ*, 724, 1044
- Šubr, L., Schovancová, J., & Kroupa, P. 2009, *A&A*, 496, 695
- Sumi, T. 2004, *MNRAS*, 349, 193
- Sunyaev, R. A., Markevitch, M., & Pavlinsky, M. 1993, *ApJ*, 407, 606
- Sutton, E. C., Danchi, W. C., Jaminet, P. A., & Masson, C. R. 1990, *ApJ*, 348, 503
- Tamblyn, P., Rieke, G. H., Hanson, M. M., et al. 1996, *ApJ*, 456, 206
- Terrier, R., Ponti, G., Bélanger, G., et al. 2010, *ApJ*, 719, 143
- Thuan, T. X., Sauvage, M., & Madden, S. 1999, *ApJ*, 516, 783
- Tokunaga, A. T., & Vacca, W. D. 2005, *PASP*, 117, 421
- Torres, D. F., Capozziello, S., & Lambiase, G. 2000, *Phys. Rev. D*, 62, 104012
- Tran, Q. D., Lutz, D., Genzel, R., et al. 2001, *ApJ*, 552, 527

- Trap, G., Goldwurm, A., Dodds-Eden, K., et al. 2011, *A&A*, 528, A140
- Treffers, R. R., Fink, U., Larson, H. P., & Gautier, T. N., III 1976, *ApJL*, 209, L115
- Tremaine, S. D., Ostriker, J. P., & Spitzer, L., Jr. 1975, *ApJ*, 196, 407
- Tremaine, S., Richstone, D. O., Byun, Y.-I., et al. 1994, *AJ*, 107, 634
- Tremaine, S., Gebhardt, K., Bender, R., et al. 2002, *ApJ*, 574, 740
- Trippe, S., Gillessen, S., Gerhard, O. E., et al. 2008, *A&A*, 492, 419
- Trippe, S., Davies, R., Eisenhauer, F., et al. 2010, *MNRAS*, 402, 1126
- Trumpler, R. J. 1930, *Lick Observatory Bulletin*, 14, 154
- Udalski, A. 2003, *ApJ*, 590, 284
- Ulubay-Siddiki, A., Bartko, H., & Gerhard, O. 2013, *MNRAS*, 428, 1986
- van Breemen, J. M., Min, M., Chiar, J. E., et al. 2011, *A&A*, 526, A152
- van Dokkum, P. G., & Conroy, C. 2010, *Nature*, 468, 940
- van Loon, J. T., Gilmore, G. F., Omont, A., et al. 2003, *MNRAS*, 338, 857
- Viehmann, T., Eckart, A., Schödel, R., et al. 2005, *A&A*, 433, 117
- Viollier, R. D., Trautmann, D., & Tupper, G. B. 1993, *Physics Letters B*, 306, 79
- Vollmer, B., Zylka, R., & Duschl, W. J. 2003, *A&A*, 407, 515
- Voshchinnikov, N. V., Il'in, V. B., Henning, T., & Dubkova, D. N. 2006, *A&A*, 445, 167
- Walcher, C. J., van der Marel, R. P., McLaughlin, D., et al. 2005, *ApJ*, 618, 237
- Walcher, C. J., Böker, T., Charlot, S., et al. 2006, *ApJ*, 649, 692
- Wang, Q. D., Lu, F. J., & Gotthelf, E. V. 2006, *MNRAS*, 367, 937
- Wang, Q. D., Dong, H., Cotera, A., et al. 2010, *MNRAS*, 402, 895
- Weinberg, N. N., Milosavljević, M., & Ghez, A. M. 2005, *ApJ*, 622, 878
- Weingartner, J. C., & Draine, B. T. 2001, *ApJ*, 548, 296
- Weintraub, J. 2008, *Journal of Physics Conference Series*, 131, 012047
- Weitzel, L., Krabbe, A., Kroker, H., et al. 1996, *A&AS*, 119, 531
- White, S. D. M., & Rees, M. J. 1978, *MNRAS*, 183, 341

- Whitford, A. E. 1958, *AJ*, 63, 201
- Whitford, A. E. 1978, *ApJ*, 226, 777
- Whittet, D. C. B. 1988, *MNRAS*, 230, 473
- Whittet, D. C. B., Bode, M. F., Longmore, A. J., et al. 1988, *MNRAS*, 233, 321
- Whittet, D. C. B., Boogert, A. C. A., Gerakines, P. A., et al. 1997, *ApJ*, 490, 729
- Wieprecht, E., Lahuis, F., Bauer, O. H., et al. 1998, *Astronomical Data Analysis Software and Systems VII*, 145, 279
- Willner, S. P., Russell, R. W., Puetter, R. C., Soifer, B. T., & Harvey, P. M. 1979, *ApJL*, 229, L65
- Witzel, G., Eckart, A., Bremer, M., et al. 2012, *ApJS*, 203, 18
- Wollman, E. R., Geballe, T. R., Lacy, J. H., Townes, C. H., & Rank, D. M. 1977, *ApJL*, 218, L103
- Wyse, R. F. G., Gilmore, G., & Franx, M. 1997, *ARA&A*, 35, 637
- Yu, Q., & Tremaine, S. 2003, *ApJ*, 599, 1129
- Yuan, F., Quataert, E., & Narayan, R. 2003, *ApJ*, 598, 301
- Yuan, F., Quataert, E., & Narayan, R. 2004, *ApJ*, 606, 894
- Yusef-Zadeh, F., & Wardle, M. 1993, *ApJ*, 405, 584
- Yusef-Zadeh, F., Roberts, D. A., & Biretta, J. 1998, *ApJL*, 499, L159
- Yusef-Zadeh, F., Roberts, D., Wardle, M., Heinke, C. O., & Bower, G. C. 2006, *ApJ*, 650, 189
- Yusef-Zadeh, F., Hewitt, J. W., Arendt, R. G., et al. 2009, *ApJ*, 702, 178
- Yusef-Zadeh, F., Bushouse, H., Wardle, M., et al. 2009, *ApJ*, 706, 348
- Yusef-Zadeh, F., Bushouse, H., & Wardle, M. 2012, *ApJ*, 744, 24
- Zhang, F., Lu, Y., & Yu, Q. 2012, *arXiv:1210.1901*
- Zoccali, M., Cassisi, S., Frogel, J. A., et al. 2000, *ApJ*, 530, 418
- Zoccali, M., Renzini, A., Ortolani, S., et al. 2003, *A&A*, 399, 931
- Zoccali, M., Barbuy, B., Hill, V., et al. 2004, *A&A*, 423, 507

- Zoccali, M., Lecureur, A., Barbuy, B., et al. 2006, *A&A*, 457, L1
- Zoccali, M., Hill, V., Lecureur, A., et al. 2008, *A&A*, 486, 177
- Zoccali, M. 2012, *Chemical Evolution of the Milky Way*,
- Zasowski, G., Majewski, S. R., Indebetouw, R., et al. 2009, *ApJ*, 707, 510
- Zhao, J.-H., & Goss, W. M. 1998, *ApJL*, 499, L163
- Zhao, J.-H., Young, K. H., Herrnstein, R. M., et al. 2003, *ApJL*, 586, L29
- Zhao, J.-H., Morris, M. R., Goss, W. M., & An, T. 2009, *ApJ*, 699, 186
- Zinn, R. 1985, *ApJ*, 293, 424
- Zubko, V., Dwek, E., & Arendt, R. G. 2004, *ApJS*, 152, 211
- Zubovas, K., & Nayakshin, S. 2012, *MNRAS*, 424, 666
- Zucker, S., Alexander, T., Gillessen, S., Eisenhauer, F., & Genzel, R. 2006, *ApJL*, 639, L21

# Acknowledgements

First of all I want to thank all the people, which now are or once were in the IR-group. Many of you helped me in science related to the thesis. Others saved me from being totally immersed totally in the Galactic Center by talking about other science and sometimes even not science related topics. The greatest thanks of all goes to Stefan for all its assistance at MPE since I joined the IR group. In between Katie you replaced him partly in science, but not only there. It was the nicest time in the office when you were there. Thanks also to Peter for a lot of advice in not Galactic Center matters and for the cakes. I still need to demonstrate you, that I can bake too. I thank Thomas for his help in computer related problems and elsewhere. Thanks to the students in the IR-group, especially Oliver, Laura, Sascha and Christina for your company. From the non-GCs I emphasize here by gratitude for company and advice to Emily, Ric, Albrecht and Javier. Thanks to Frank for many things, also the sometimes nasty, but good questions. Thanks to Reinhard to give me so much freedom in choosing the research topics within the GC. I usually pursued the question which I wanted. Thanks also for few but good suggestions for my projects.

Also thanks to the other scientists with who I have learned to collaborate, especially at the end with Sotiris and Ortwin. Thanks to Nitya to give the most convincing reason to finish this summer the PhD. Linda, Reinhard Genzel and Frank you also made sure that I finished finally. Finally, thanks to Reinhard and the MPG who enabled me to graduate in a group for which 4 meter telescopes on the ground and 20 hours VLT projects are small. Of course without ESO and its member states who run this great observatory with such qualified staff that even I can take data there the thesis would also not be possibly. I always enjoy to be on Paranal.

Of course I also want not forget family and friends, especially Leonore, Hendrik, Michael, Gertrud, Elwin, Manuela and Hilli and her family. Thanks for mom and dad to help all the long way to the thesis. Although, my strengths in math and physics are not yours you still supported my way. In the last few years I think you were more worried that I forgot the world immersed in science than that I do not invest enough time in science. At least in Freiburg you and the Breisgau have been usually successful that I neglect science when I am there. Thanks also to my sister and Peter, it was also great to be together with you and having fun and getting sometimes advice. Now, there is again as much fun with you Dorothee as many years ago since Emu is there, too.